

Developing scalable processing techniques for perovskite solar cells using X-ray scattering

Joel A. Smith

Department of Physics & Astronomy

The University of Sheffield



The
University
Of
Sheffield.



EPSRC CENTRE FOR DOCTORAL TRAINING
NEW AND SUSTAINABLE
PHOTOVOLTAICS

March 2021

A thesis submitted in partial fulfilment of the requirements for the degree of

Doctor of Philosophy

“Science is magic that works.”

Kurt Vonnegut, *Cat's Cradle*.

Acknowledgements

Firstly, thank you to my supervisor David Lidzey for taking a chance on a physicist on sabbatical enticed by the shining AM1.5G. In particular, thank you for encouraging me to be creative with the topics I could pursue, for always enjoying a good scientific discussion and for keeping the big picture in mind. I am also grateful to the Centre for Doctoral Training in New and Sustainable Photovoltaics (CDT-PV) for this excellent PhD experience and to EPSRC for funding this. Without this foundation, I wouldn't understand the many intertwining areas of solar energy research in the UK. Thank you also to C3, the best group of nerds to be traipsing around the country with for a year, it was the best of times.

Thank you everyone in the Electronic and Photonic Molecular Materials group at the University of Sheffield. In particular, thank you to Onkar Game for the many hours of discussion and debate on perovskites, and honest advice at every stage of my PhD. Thank you to Michael Wong-Stringer for instilling me with a positive work ethic from the beginning, to James Bishop for your impressive completer-finisher mentality and memes of varying quality and to Tom Routledge for being the voice of reason in the lab. Thank you to Ben Freestone for raising difficult questions and going deep to answer them. Thank you to Claire Greenland for investigating things the right way for too long in dark rooms. More recently, thank you to Rachel Kilbride, Emma Spooner, Tarek Alanazi, Elena Cassella and Mary O'Kane for many excellent discussions, projects and fun, it's been great working with you. Thanks as well to Rahul Jayaprakash, David Coles, Kyriakos Georgiou and Kirsty McGhee for your unique spectroscopic insight. Thank you to Adam Shnier for endless useful structural discussions and to the START collaboration for enabling this friendship. Thank you to Tao Wang and to Jinlong Cai for teaching us so much. Thank you Natalia for giving me a taste of quantum chemistry with your insightful simulations. Thank you to Andy Parnell for hours of assistance in a basement with X-rays and to Andrew Pearson and Alan Dunbar for hours of time in a room with stronger X-rays. Thank you to the beamline scientists at I07, I14, I22, KMC2 and PTB for showing me the ropes.

Furthermore thank you to Antonio Abate for encouraging and enabling my visit to your group at Helmholtz Zentrum Berlin and to Erasmus+ for funding time there. It was an unforgettable experience thanks to Jorge Mielgo, Marion Flatken, Nga Phung, Oleksandra Shargaieva, Qiong Wang, Amran Al-Ashouri, Hans Köbler, Laura Canil, Carolin Rehermann, Silver-Hamill Turren-Cruz, Hampus Näsström and everyone in the HySprint labs. Thank you for being so welcoming and for the varied discussions, food, collaborations, late night science and Späti night kicker.

Thank you dearly to my parents Elspeth and Steve for keeping me asking questions, encouraging my interests and supporting every diversion.

Lastly thank you to Amy, for everything.

Abstract

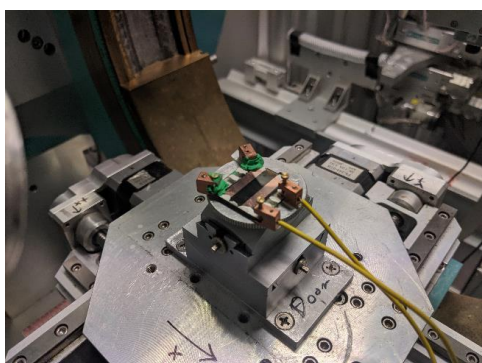
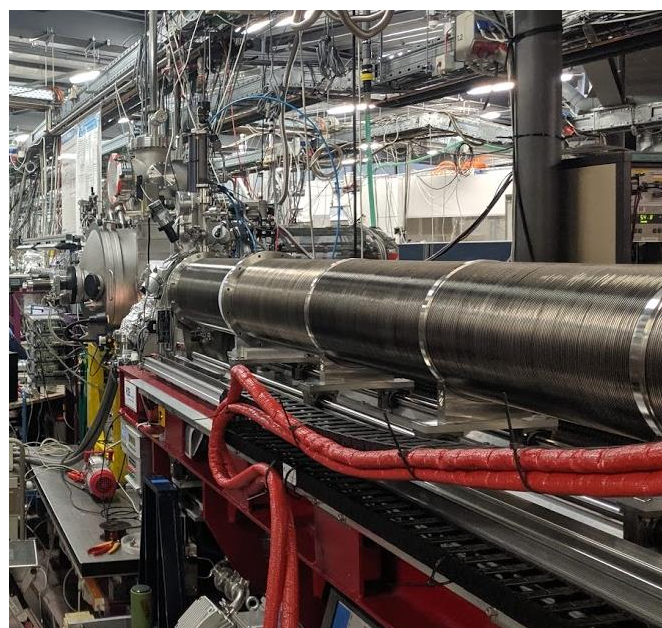
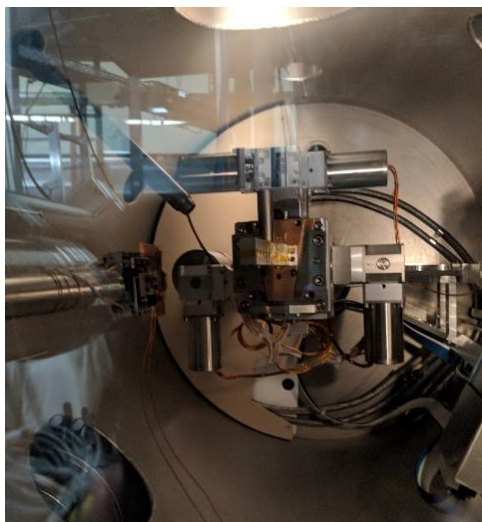
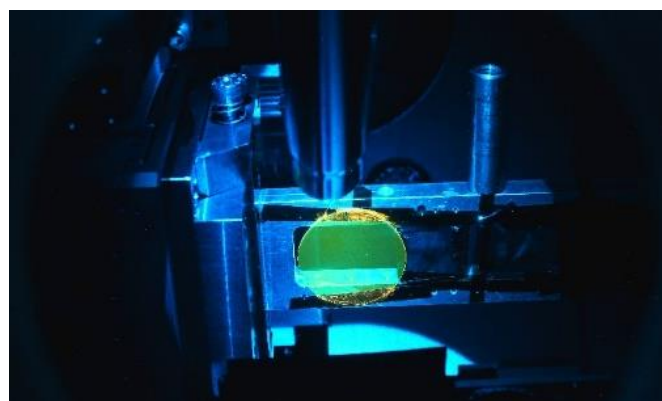
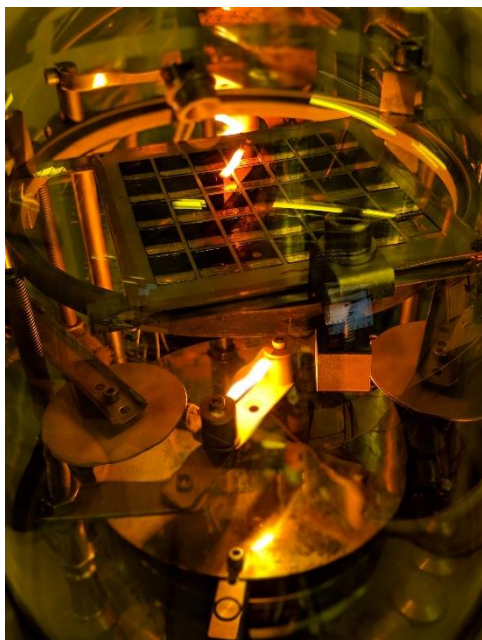
Metal halide perovskites have fascinated physicists, chemists, materials scientists and more since their emergence for optoelectronic applications little over a decade ago. Their use in photovoltaic devices offers the promise of a new era of mass-produced, low-cost, thin-film solar cells made from Earth-abundant materials if the interlinked challenges of photovoltaic efficiency, scalability and stability can be met. This thesis aims to primarily address the issue of scalability by developing processes that are compatible with transfer from small lab-scale devices to photovoltaic module production. In particular, by understanding the formation, crystallisation and recrystallisation of nanoscale layers used in perovskite solar cells (PSCs). Specifically, this research has focused on use cases related to the potential second generation of commercial perovskite solar cells (beyond silicon-perovskite tandems) which could be processed via continuous roll-to-roll production. Here, the economic case is clear: process duration is the critical factor underpinning the potential growth of the technology, with this growth rate ultimately determining the material's utility in comparison to silicon. To achieve rapid processability, significant challenges remain in developing suitably rapid processes, with X-ray diffraction offering an ideal set of methods to structurally characterise them.

In the first chapter, a potentially stable, low-cost metal oxide nanoparticle solution system was investigated for use in perovskite solar cells. Tin oxide was scalably deposited via spray-coating, with high efficiency devices achieved. Using small-angle X-ray diffraction, photoelectron spectroscopy and electrical measurements, the nanoparticle formation process was studied in depth. Through this insight, a rapid thermal treatment was developed with greatly reduced process duration, suitable for high-throughput manufacture.

Considering next the crystallisation of the perovskite, an approach to relax the processing requirements for the deposition of these layers is to post-treat them with a recrystallising solvent-vapour. Here it was found that small changes in solution stoichiometry can dramatically affect the outcome of this solvent vapour annealing process. Specifically, the effects on stability and microstructure were characterised. For inorganic-rich compositions an intermediate solvate phase was formed, observed using X-ray diffraction. The solvent-vapour annealing process was found to induce stoichiometric changes and a mechanism of solvent-organic cation hydrogen bonding is proposed as the cause.

Finally, much interest has surrounded the mechanism by which methylamine gas is able to recrystallise methylammonium lead halide perovskite films, which reforms with beneficial film texture and morphology. The mechanism for this industrially applicable process is not well understood, so this process was monitored using in-situ synchrotron X-ray scattering. It is revealed intermediate crystalline phases are found to govern this process, with the resulting

film exhibiting more complex non-uniaxial grain orientation than presently thought. This behaviour is facilitated by both homo-conjugated acid-base complex formation and then in the fully dissolved state we conclude that methylamine is co-ordinating to lead. These behaviours are compared to those in related rapidly crystallising solution chemistries. The compositional limits for the recrystallisation process are explored, with irreversible cation decomposition found to limit the use of methylamine with formamidinium perovskites.



Front matter

Declaration of originality

This thesis is a summary of work undertaken in the Department of Physics and Astronomy at the University of Sheffield from October 2016 to March 2021 under the supervision of Prof. David Lidzey. I declare that the work contained within is my own except where specific reference is made to the contribution of others.

Joel A. Smith, March 2021

Thesis format

This thesis is in Alternative Format, such that the results chapters are formatted as research papers which have been either published or are intended for submission. Each results chapter is preceded by a Foreword summarising the work, its relation to the thesis and to the wider field. For the published works, the papers have been reformatted from the accepted version into the style of the thesis for continuity (results chapter sections X.2). For ease of readability, numeration of content aside from page numbers is specific to each chapter. Supplementary Figures are numerated as such and presented after each results chapter (sections X.3).

Collaborating authors

For Chapters 4 and 6, the experimental work, data analysis, interpretation and writing was primarily completed by myself. In the case of Chapter 5, the work was prepared in close collaboration with Dr Onkar Game who is the first author on the associated paper, in this case the Chapter Foreword describes my specific contributions for clarity. All the collaborating authors who I have been fortunate enough to work with on publications in this thesis are listed below and I am grateful for their contributions to the works, which are explained in the Author Contributions for each chapter.

Adam Shnier
Alvaro Tejada
Andre Dallman
Andrew J. Parnell
Antonio Abate
Claire Greenland
Cornelia Rodenburg
Daniel Wamwangi
David G. Billing
David G. Lidzey
Deborah B. Hammond

Elena J. Cassella
Emma L.K. Spooner
Eva Unger
Ganna Chistiakova
Hampus Näsström
James E. Bishop
Jonathan Rawle
Jorge Mielgo
Marion Flatken
Mary O’Kane
Michael Wong-Stringer

Natalia Martsinovich
Nick J. Terrill
Nik Reeves-Mclaren
Oleksandra Shargaieva
Onkar S. Game
Rachel C. Kilbride
Rachel Kilbride
Rahul Jayaprakash
Tarek I. Alanazi
Thomas J. Routledge
Vikas Kumar

Publications

Chapter 4: "Rapid Scalable Processing of Tin Oxide Transport Layers for Perovskite Solar Cells". ACS Appl. Energy Mater. **2020**, 3 (6), 5552–5562. **Smith, J. A.**; Game, O. S.; Bishop, J. E.; Spooner, E. L. K.; Kilbride, R. C.; Greenland, C.; Jayaprakash, R.; Alanazi, T. I.; Cassella, E. J.; Tejada, A.; Chistiakova, G.; Wong-Stringer, M.; Routledge, T. J.; Parnell, A. J.; Hammond, D. B.; Lidzey, D. G. DOI: 10.1021/acsaem.0c00525.

Chapter 5: "Solvent Vapour Annealing of Methylammonium Lead Halide Perovskite: What's the Catch?". J. Mater. Chem. A **2020**, 8 (21), 10943–10956. Game, O. S.; **Smith, J. A.**; Alanazi, T. I.; Wong-Stringer, M.; Kumar, V.; Rodenburg, C.; Terrill, N. J.; Lidzey, D. G. DOI: 10.1039/d0ta03023f.

Chapter 6: "Understanding the role of methylamine in the crystallisation of halide perovskites using *in-situ* X-ray scattering". **Smith, J. A.**; Shnier, A.; Shargaieva, O. S.; Martsinovich, N.; Kilbride, R. C.; O'Kane, M. E.; Pascual, J.; Flatken, M.; Näsström, H.; Rawle, J. S.; Dallman, A.; Wamwangi, D.; Billing, D. G.; Reeves-Mclaren, N.; Game, O. S.; Unger, E. S.; Abate, A.; Lidzey, D. G. *In preparation.*

"Efficient Perovskite Photovoltaic Devices Using Chemically Doped PCDTBT as a Hole-Transport Material". J. Mater. Chem. A **2017**, 5 (30), 15714–15723. Wong-Stringer, M.; Bishop, J. E.; **Smith, J. A.**; Mohamad, D. K.; Parnell, A. J.; Kumar, V.; Rodenburg, C.; Lidzey, D. G. DOI: 10.1039/c7ta03103c.

"Degradation of Inverted Architecture $\text{CH}_3\text{NH}_3\text{PbI}_{3-x}\text{Cl}_x$ Perovskite Solar Cells Due to Trapped Moisture". Energy Sci. Eng. **2018**, 6 (1), 35–46. Bracher, C.; Freestone, B. G.; Mohamad, D. K.; **Smith, J. A.**; Lidzey, D. G. DOI: 10.1002/ese3.180.

"High-Performance Multilayer Encapsulation for Perovskite Photovoltaics". Adv. Energy Mater. **2018**, 1801234, 1801234. Wong-Stringer, M.; Game, O. S.; **Smith, J. A.**; Routledge, T. J.; Alqurashy, B. A.; Freestone, B. G.; Parnell, A. J.; Vaenas, N.; Kumar, V.; Alawad, M. O. A.; Iraqi, A.; Rodenburg, C.; Lidzey, D. G. DOI: 10.1002/aenm.201801234.

"High-Efficiency Spray-Coated Perovskite Solar Cells Utilizing Vacuum-Assisted Solution Processing". ACS Appl. Mater. Interfaces **2018**, 10 (46), 39428–39434. Bishop, J. E.; **Smith, J. A.**; Greenland, C.; Kumar, V.; Vaenas, N.; Game, O. S.; Routledge, T. J.; Wong-Stringer, M.; Rodenburg, C.; Lidzey, D. G. DOI: 10.1021/acsaami.8b14859.

"Low-Temperature, High-Speed Reactive Deposition of Metal Oxides for Perovskite Solar Cells". J. Mater. Chem. A **2019**, 7 (5), 2283–2290. Routledge, T. J.; Wong-Stringer, M.; Game, O.

S.; **Smith, J. A.**; Bishop, J. E.; Vaenas, N.; Freestone, B. G.; Coles, D. M.; McArdle, T.; Buckley, A. R.; Lidzey, D. G. DOI: 10.1039/c8ta10827g.

"Low-Dimensional Emissive States in Non-Stoichiometric Methylammonium Lead Halide Perovskites". *J. Mater. Chem. A* **2019**, Freestone, B. G.;* **Smith, J. A.**;* Piana, G.; Kilbride, R.; Parnell, A.; Sortino, L.; Coles, D. M.; Ball, O. B.; Martsinovich, N.; Thompson, C.; Alanazi, T. I.; Game, O. S.; Tartakovskii, A.; Lagoudakis, P. G.; Lidzey, D. G. DOI: 10.1039/C8TA12184B.

*Authors contributed equally.

"A Flexible Back-Contact Perovskite Solar Micro-Module". *Energy Environ. Sci.* **2019**, 12 (6), 1928–1937. Wong-Stringer, M.; Routledge, T. J.; McArdle, T.; Wood, C. J.; Game, O. S.; **Smith, J. A.**; Bishop, J. E.; Vaenas, N.; Coles, D. M.; Buckley, A. R.; Lidzey, D. G. DOI: 10.1039/c8ee03517b.

"Correlating the Electron-Donating Core Structure with Morphology and Performance of Carbon–Oxygen-Bridged Ladder-Type Non-Fullerene Acceptor Based Organic Solar Cells". *Nano Energy* **2019**, 61 (April), 318–326. Li, W.; Xiao, Z.; Cai, J.; **Smith, J. A.**; Spooner, E. L. K.; Kilbride, R. C.; Game, O. S.; Meng, X.; Li, D.; Zhang, H.; Chen, M.; Gurney, R. S.; Liu, D.; Jones, R. A. L.; Lidzey, D. G.; Ding, L.; Wang, T. DOI: 10.1016/j.nanoen.2019.04.053.

"13.9% Efficiency Ternary Nonfullerene Organic Solar Cells Featuring Low-Structural Order". *ACS Energy Lett.* **2019**, 4 (10), 2378–2385. Du, B.; Geng, R.; Li, W.; Li, D.; Mao, Y.; Chen, M.; Zhang, X.; **Smith, J. A.**; Kilbride, R. C.; O’Kane, M. E.; Liu, D.; Lidzey, D. G.; Tang, W.; Wang, T. DOI: 10.1021/acsenerylett.9b01630.

"Tin(IV) Dopant Removal through Anti-Solvent Engineering Enabling Tin Based Perovskite Solar Cells with High Charge Carrier Mobilities". *J. Mater. Chem. C* **2019**, 7 (27), 8389–8397. Bandara, R. M. I.; Jayawardena, K. D. G. I.; Adeyemo, S. O.; Hinder, S. J.; **Smith, J. A.**; Thirimanne, H. M.; Wong, N. C.; Amin, F. M.; Freestone, B. G.; Parnell, A. J.; Lidzey, D. G.; Joyce, H. J.; Sporea, R. A.; Silva, S. R. P. DOI: 10.1039/c9tc02003a.

"Enhancing the Efficiency of PTB7-Th:COi8DFIC-Based Ternary Solar Cells with Versatile Third Components". *Appl. Phys. Rev.* **2019**, 6 (4), 041405. Li, W.; Xiao, Z.; **Smith, J. A.**; Cai, J.; Li, D.; Kilbride, R. C.; Spooner, E. L. K.; Game, O. S.; Meng, X.; Liu, D.; Jones, R. A. L.; Lidzey, D. G.; Ding, L.; Wang, T. DOI: 10.1063/1.5125438.

"Correlating Phase Behavior with Photophysical Properties in Mixed-Cation Mixed-Halide Perovskite Thin Films". *Adv. Energy Mater.* **2020**, 10 (4), 1901350. Greenland, C.; Shnier, A.; Rajendran, S. K.; **Smith, J. A.**; Game, O. S.; Wamwangi, D.; Turnbull, G. A.; Samuel, I. D. W.; Billing, D. G.; Lidzey, D. G. DOI: 10.1002/aenm.201901350.

"Fluorinated Solid Additives Enable High Efficiency Non-Fullerene Organic Solar Cells". *J. Mater. Chem. A* **2020**, 8 (8), 4230–4238. Cai, J.; Wang, H.; Zhang, X.; Li, W.; Li, D.; Mao, Y.; Du, B.; Chen, M.; Zhuang, Y.; Liu, D.; Qin, H. L.; Zhao, Y.; **Smith, J. A.**; Kilbride, R. C.; Parnell, A. J.; Jones, R. A. L.; Lidzey, D. G.; Wang, T. DOI: 10.1039/c9ta13974e.

"Non-Fullerene Acceptor Fibrils Enable Efficient Ternary Organic Solar Cells with 16.6% Efficiency". *Sci. China Chem.* **2020**. Li, D.; Chen, X.; Cai, J.; Li, W.; Chen, M.; Mao, Y.; Du, B.; **Smith, J. A.**; Kilbride, R. C.; O’Kane, M. E.; Zhang, X.; Zhuang, Y.; Wang, P.; Wang, H.; Liu, D.; Jones, R. A. L.; Lidzey, D. G.; Wang, T. DOI: 10.1007/s11426-019-9681-8.

"Managing Phase Purities and Crystal Orientation for High-Performance and Photostable Cesium Lead Halide Perovskite Solar Cells". *Sol. RRL* **2020**, 2000213. Wang, Q.; **Smith, J. A.**; Skroblin, D.; Steele, J. A.; Wolff, C. M.; Caprioglio, P.; Stolterfoht, M.; Köbler, H.; Li, M.; Turren-Cruz, S. H.; Gollwitzer, C.; Neher, D.; Abate, A. DOI: 10.1002/solr.202000213.

"Fully Spray-Coated Triple-Cation Perovskite Solar Cells". *Sci. Rep.* **2020**, 10 (1), 1–8. Bishop, J. E.; Read, C. D.; **Smith, J. A.**; Routledge, T. J.; Lidzey, D. G. DOI: 10.1038/s41598-020-63674-5.

"Ion Migration-Induced Amorphization and Phase Segregation as a Degradation Mechanism in Planar Perovskite Solar Cells". *Adv. Energy Mater.* **2020**, 2000310. Di Girolamo, D.; Phung, N.; Kosasih, F. U.; Di Giacomo, F.; Matteocci, F.; **Smith, J. A.**; Flatken, M. A.; Köbler, H.; Turren Cruz, S. H.; Mattoni, A.; Cinà, L.; Rech, B.; Latini, A.; Divitini, G.; Ducati, C.; Di Carlo, A.; Dini, D.; Abate, A. DOI: 10.1002/aenm.202000310.

"Origin of Sn(ii) Oxidation in Tin Halide Perovskites". *Mater. Adv.* **2020**. Pascual, J.; Nasti, G.; Aldamasy, M. H.; **Smith, J. A.**; Flatken, M.; Phung, N.; Di Girolamo, D.; Turren-Cruz, S.-H.; Li, M.; Dallmann, A.; Avolio, R.; Abate, A. DOI: 10.1039/D0MA00245C.

"Potassium Iodide Reduces the Stability of Triple-Cation Perovskite Solar Cells". *RSC Adv.* **2020**, 10 (66), 40341–40350. Alanazi, T. I.; Game, O. S.; **Smith, J. A.**; Kilbride, R. C.; Greenland, C.; Jayaprakash, R.; Georgiou, K.; Terrill, N. J.; Lidzey, D. G. DOI: 10.1039/d0ra07107b.

"Development of Spray-Coated Perovskite Solar Cells". *ACS Appl. Mater. Interfaces* **2020**. Bishop, J. E.; **Smith, J. A.**; Lidzey, D. G. DOI: 10.1021/acsami.0c14540.

"Hybrid Perovskite Crystallization from Binary Solvent Mixtures: Interplay of Evaporation Rate and Binding Strength of Solvents". *Mater. Adv.* **2020**. Shargaieva, O.; Näsström, H.; **Smith, J. A.**; Többens, D.; Munir, R.; Unger, E. L. DOI: 10.1039/D0MA00815J.

"Emissive Spin-0 Triplet-Pairs Are a Direct Product of Triplet–Triplet Annihilation in Pentacene Single Crystals and Anthradithiophene Films". *Nat. Chem.* **2020**. Bossanyi, D. G.; Matthiesen, M.;

Wang, S.; **Smith, J. A.**; Kilbride, R. C.; Shipp, J. D.; Chekulaev, D.; Holland, E.; Anthony, J. E.; Zaumseil, J.; Musser, A. J.; Clark, J. DOI: 10.1038/s41557-020-00593-y.

"Monolithic Perovskite/Silicon Tandem Solar Cell with >29% Efficiency by Enhanced Hole Extraction". *Science*. **2020**, 370 (6522), 1300–1309. Al-Ashouri, A.; Köhnen, E.; Li, B.; Magomedov, A.; Hempel, H.; Caprioglio, P.; Márquez, J. A.; Vilches, A. B. M.; Kasparavicius, E.; **Smith, J. A.**; Phung, N.; Menzel, D.; Grischek, M.; Kegelmann, L.; Skroblin, D.; Gollwitzer, C.; Malinauskas, T.; Jošt, M.; Matič, G.; Rech, B.; Schlatmann, R.; Topič, M.; Korte, L.; Abate, A.; Stannowski, B.; Neher, D.; Stolterfoht, M.; Unold, T.; Getautis, V.; Albrecht, S. DOI: 10.1126/science.abd4016.

"Controlling PbI_2 Stoichiometry during Synthesis to Improve the Performance of Perovskite Photovoltaics". *Chem. Mater.* **2021**, 33 (2), 554–566. Tsevas, K.; **Smith, J. A.**; Kumar, V.; Rodenburg, C.; Fakis, M.; Mohd Yusoff, A. R. bin; Vasilopoulou, M.; Lidzey, D. G.; Nazeeruddin, M. K.; Dunbar, A. D. F. DOI: 10.1021/acs.chemmater.0c03517.

"Perovskites on ice: An Additive-Free Approach to Increase the Stability of Triple-Cation Perovskite Precursor Solutions". *ChemSusChem*. **2021**, 14(12), 2537. O'Kane M. E.; **Smith, J. A.**; Alanazi, T. I.; Cassella, E. J.; Game, O. S.; Van Meurs, S.; Lidzey, D. G. DOI: 10.1002/cssc.202100332

Presentations

Conference talks

- “Understanding fast recrystallisation processes in hybrid perovskite materials using in situ synchrotron scattering.” CDT-PV Showcase, Bath, 2019. *Awarded prize for best presentation.*
- “Scalable deposition of SnO₂ transport layers for perovskite solar cells.” 7th EuCheMS Chemistry Congress, Liverpool, 2018.
- “Perovskite solar cell research at the University of Sheffield.” Synchrotron Techniques for African Research and Technology (START) meeting, Johannesburg, 2018.
- “Scalable deposition of SnO₂ transport layers for perovskite solar cells.” UK Semiconductors, Sheffield, 2018.
- “Scalable deposition of SnO₂ transport layers for perovskite solar cells.” E-MRS Spring, Strasbourg, 2018.

Poster presentations

- “Solvent Vapour Annealing of Methylammonium Lead Halide Perovskite: What’s the Catch?”, HOPV20 online, 2020.*
- “Understanding texture formation in methylamine-recrystallised MAPbI₃” NanoGE Fall Meeting, Berlin, 2019 (*awarded poster prize*) and BESSY II User Meeting, Berlin, 2019.*
- “Electron beam evaporation of tin oxide transport layers for perovskite solar cells.” HOPV18, Benidorm, 2018. *and* CDT PV showcase, Liverpool, 2018.*
- “Performance and stability of planar perovskite solar cells using SnO₂ electron transport layers.” University of Sheffield Faculty of Science Graduate School Showcase, Sheffield, 2018.
- “Solution and vacuum processing of SnO₂ electron transport layers for perovskite solar cells.” Next Generation Materials for Solar Photovoltaics, Royal Society of Chemistry, London, 2018 *and* Energy CDTs Summer Masterclass 2018, Sheffield, 2018.
- “Performance and stability of planar perovskite solar cells using SnO₂ electron transport layers.” CDT PV showcase, Liverpool, 2017.
- “Performance and stability of planar perovskite solar cells using SnO₂ electron transport layers.” PSCO 2017, Oxford, 2017.*

* Examples of these presented posters are given in the Appendices.

Table of contents

Chapter 1: Introduction	1
1.1: The climate is changing	1
1.2: The economics of solar energy.....	2
1.3: The case for halide perovskites.....	3
1.4: Thesis motivation.....	4
1.5: Thesis overview	5Joel
1.6: References.....	7
Chapter 2: Background theory	9
2.0: Introduction.....	9
2.1: Solids	9
2.1.1: Atoms	9
2.1.2: Bonding.....	11
2.1.3: Solid crystals	13
2.1.4: Diffraction.....	16
2.1.5: Reciprocal lattice	17
2.1.6: Miller indices	19
2.1.7: Observed reflections	20
2.1.8: Band formation.....	24
2.1.9: Semiconductors.....	26
2.2: Solar cells.....	28
2.2.1: The photovoltaic effect.....	28
2.2.2: Quantum efficiency	30
2.2.3: Recombination and carrier extraction	32
2.2.4: Solar cell operation.....	33
2.2.5: Efficiency limits.....	35
2.2.6: Performance metrics	35
2.3: Perovskites	36
2.3.1: Structures	36
2.3.2: Metal halide perovskites	37
2.3.3: Related materials	40
2.3.4: Perovskite solar cells.....	42
2.3.5: Potential for solution processing.....	43
2.3.6: The early years.....	43
2.3.7: Novel crystallisation approaches	44

2.3.8: Diversifying compositions for high efficiency.....	45
2.3.9: Device architectures.....	47
2.4: References.....	49
Chapter 3: Methods	55
3.0: Introduction.....	55
3.1: Materials.....	55
3.2: Fabrication techniques.....	56
3.2.1: Chemical etching.....	56
3.2.2: Substrate cleaning.....	57
3.2.3: Spin coating.....	57
3.2.4: Slot-die coating.....	57
3.2.5: Spray coating.....	58
3.2.6: Device fabrication.....	59
3.3: Characterisation techniques.....	61
3.3.1: Device characterisation.....	61
3.3.2: X-ray diffraction.....	62
3.3.3: 2D X-ray scattering.....	65
3.3.4: X-ray sources.....	68
3.3.5: Data processing.....	68
3.3.6: Nuclear magnetic resonance (NMR) spectroscopy.....	73
3.3.7: Optical spectroscopies.....	74
3.3.8: Surface characterisation.....	74
3.3.9: Photoelectron spectroscopy.....	75
3.4: References.....	76
Chapter 4: Rapid Scalable Processing of Tin Oxide Transport Layers for Perovskite Solar Cells.....	79
4.0: Publication Foreword.....	80
4.1: Author contributions.....	80
4.2: Publication - Rapid Scalable Processing of Tin Oxide Transport Layers for Perovskite Solar Cells.....	81
4.2.1: Abstract.....	81
4.2.2: Introduction.....	82
4.2.3: Results and discussion.....	83
4.2.3.1: Electron transport layer deposition.....	83
4.2.3.2: Slot-die coating.....	84
4.2.3.3: Spray-coating.....	85
4.2.3.4: Topography and device performance.....	86

4.2.3.5: Scalable processing.....	88
4.2.3.6: The Effect of Thermal Annealing.....	89
4.2.3.7: Post deposition treatments.....	91
4.2.3.8: Photoelectron Spectroscopy.....	93
4.2.3.9: Device physics	95
4.2.3.10: Rapid processing	96
4.2.4: Conclusions	97
4.2.5: Acknowledgements.....	98
4.3: Supporting Information	98
4.3.1: Methods	98
4.3.1.1: Device fabrication	98
4.3.1.2: Characterisation.....	100
4.3.2: SI Note 1 – Solvent mixtures	103
4.3.3: SI Note 2 – Optical E_{gap} determination.....	104
4.3.4: Note 3 – GISAXS modelling.....	105
4.3.5: Supplementary Figures & Tables.....	106
4.4: References	124

Chapter 5: Solvent Vapour Annealing of Methylammonium Lead Halide Perovskite:	
What's the catch?	128
5.0: Publication Foreword	129
5.1: Author contributions.....	129
5.2: Publication - Solvent Vapour Annealing of Methylammonium Lead Halide Perovskite: What's the catch?	130
5.2.1: Abstract.....	130
5.2.2: Introduction.....	131
5.2.3: Results and discussion.....	133
5.2.3.1: Influence of SVA on PbI_2 -excess MAPbI_3 - insights from pc-AFM.....	133
5.2.3.2: Mitigating loss of organic halides during SVA	136
5.2.3.3: Influence of stoichiometry and SVA on device performance	140
5.2.3.4: Influence of SVA on material stability - in-situ GIWAXS study	142
5.2.3.5: Influence of SVA on device stability	143
5.2.3.6: Proposed mechanism of observed stoichiometric changes following SVA	147
5.2.4: Conclusions.....	150
5.2.5: Experimental section.....	150
5.2.5.1: Materials and methods	150
5.2.5.2: Characterization	151
5.2.6: Acknowledgements.....	153
5.3: Supporting Information.....	154

5.4: Additional data.....	167
5.5: References.....	170
Chapter 6: Understanding the role of methylamine in the crystallisation of halide perovskites using <i>in-situ</i> X-ray scattering.....	172
6.0: Publication Foreword.....	172
6.1: Author contributions.....	173
6.2 Publication: Understanding the role of methylamine in the crystallisation of halide perovskites using <i>in-situ</i> X-ray scattering.....	173
6.2.1: Abstract	174
6.2.2: Introduction	174
6.2.3: Results.....	177
6.2.3.1: In-situ recrystallisation.....	177
6.2.3.2: Phase identification.....	179
6.2.3.3: Temperature and orientation	182
6.2.3.4: Relating to solution chemistry	186
6.2.3.5: Compositions beyond MAPbI ₃	192
6.2.4: Conclusions.....	196
6.2.5: Methods.....	196
6.2.6: Acknowledgements.....	202
6.3: Supporting Information.....	203
6.4: References.....	222
Chapter 7: Conclusions.....	226
Appendix A: Key poster presentations.....	233
Appendix B: Available solar energy.....	239

Chapter 1

Introduction

1.1: The climate is changing

Anthropogenic global warming is the greatest challenge ever faced by human society, and has driven the most dramatic changes in the Earth's temperature for at least 10,000 years.¹ Our consumption of energy, primarily through burning of fossil fuels, has caused ever increasing CO₂ emissions into the atmosphere, destabilising the natural environment in myriad ways.² With mounting international pressure to strategically combat global warming, and with global power consumption projected to increase by 60% by 2050,³ there is increasing pressure on scientists and engineers to develop new and sustainable energy technology to meet this demand. Undoubtedly, this century will be defined by the growth and mass adoption of low-carbon energy systems. Solar energy offers an abundant supply of renewable energy that if exploited could vastly exceed global energy usage (Figure 1). As a technology, it is uniquely capable of supplying power at various levels throughout the grid; low-cost utility-scale installations, rooftop generation at the point of use, 'internet of things' low-power distributed devices, or in off-grid and micro-grid applications.

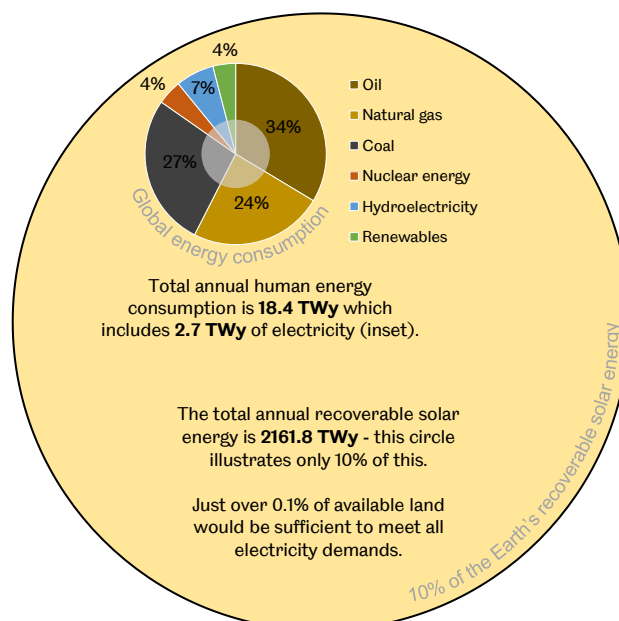


Figure 1: Estimated total photovoltaic energy availability globally, calculated for each country's suitable area for solar PV (52% of all land) and the local annual specific yield for that area (with a mean of 1529.8 kWh/kWp/yr),⁴ full methodology is given in Appendix B. Inset (to scale) is a comparison of annual energy consumption by fuel type in 2018, illustrating <1% of land would be sufficient to meet all human energy consumption.⁵

1.2: The economics of solar energy

Since their initial commercialisation in the 1960s, solar photovoltaics (PV) have plummeted in price and market forces continue to underpin their growth. As solar PV becomes more widely adopted, costs decrease; an approximate 20% reduction in cost per doubling of module shipments (the learning rate) was predicted in 2006 and has largely held true, recently estimated as 23.5%.^{6,7} Between 2010 and 2019, the levelised cost of electricity (LCOE) for utility-scale PV fell by 82%, and for newly commissioned PV installations, 40% were cheaper than any fossil fuel alternative.⁸

Crystalline silicon dominates the PV market, despite there being significant disadvantages to using silicon as a photovoltaic material. Silicon has relatively low light absorption, partly because of its indirect bandgap, so requires a relatively thick absorbing layer to generate sufficient photocurrent (~180 μm).⁷ With a narrow bandgap (~1.1 eV), below the detailed-balance limit, significant voltage losses are incurred due to carrier thermalisation by above-bandgap photons (described in the following chapter). Perhaps most importantly, silicon PV production requires multiple high temperature processes. Notably, the Czochralski process, used for the formation of single ingot silicon before slicing into wafers, must take place above the melting point of silicon at 1,414 °C.⁹ In addition, multiple factories with associated energy and transport costs operate in the supply chain for each stage of production - from polysilicon to wafers to cells and finally modules.⁷ There has been a significant reduction in the energy payback time (EPBT) - the time for a PV module to recover the input energy used in its production - down to as little as 0.4-1.5 years,¹⁰ but the required processing conditions set a lower bound to the required energy input.^{11,12} This energy budget for solar panel fabrication sets a physical limit on production capacity growth, with the required capital expenditure (CapEx) ultimately determining the possible growth rate of any PV technology.¹³

Regarding the economics of solar installations, the overall system cost must include the balance of systems (BoS); the additional material costs related to a solar installation, in addition to installation costs, shipping and other expenses. Currently, module costs are only a small percentage of the system installation cost. Whilst efficiency is important, it is uneconomical to install the most efficient 47.1% concentrating multi-junction (MJ) III-V solar cells on rooftops,¹⁴ as the intrinsic production cost is so large that they would dominate the system cost. These MJ modules are typically employed for space applications where the specific power (power per weight) is the most critical determining factor. As such, with photovoltaics there is a constant trade-off between efficiency and economic considerations, with factors such as weight, flexibility, durability and processability dictating the requirements for specific applications.

Thin film photovoltaics emerged with the potential for improving on several of these fronts, predominantly processability and EPBT, meaning lower material and infrastructure costs. Prominent mature thin film technologies such as cadmium telluride (CdTe), copper indium gallium diselenide (CIGS) and amorphous silicon (a-Si) each have their own benefits, and despite silicon currently dominating the global PV market, each has had some success. Many “third-generation” thin film technologies are now the subject of research interest, such as organic/polymer solar cells (OSCs), dye-sensitized solar cells (DSSCs), quantum dot solar cells (QDs) and as well as other more exotic materials and phenomena to surpass the single-junction efficiency limit.

1.3: The case for halide perovskites

Perovskite solar cells (PSCs) have become the subject of frenzied research in the photovoltaic community since their usage in 2006 by Miyasaka and co-workers for DSSC applications.^{15,16} Since then, record power conversion efficiencies (PCEs) of 25.5% have been achieved in single-junction architectures.¹⁷ Their unique material properties – low intra-band trap density (relatively benign defect population, particularly in the bulk), a large dielectric constant (generation of free, mobile charge-carriers), long charge-carrier lifetimes, direct bandgap (leading to strong light absorption with typically ~500 nm absorber layer) and compositionally tuneable bandgaps - make them highly suitable candidates for photovoltaics.^{18–21} Building upon the DSSC and OSC fields, numerous device architectures, deposition techniques and processes have been proposed with a variety of suitable options for commercialisation. Nevertheless, there remain significant challenges to be addressed before PSCs can reach the market, most critically the issues of stability (comparable to that of silicon modules) and scalability (transitioning lab processes to low-cost manufacture²²). Specifically, perovskites must achieve a lower LCOE, EPBT or otherwise demonstrate a clear economic benefit over established PV technologies if they are to avoid being consigned to history as fascinating but ultimately useless.

The closest-to-market approach aims to achieve a lower LCOE by fabricating silicon/perovskite tandem PV modules with higher efficiency than silicon at a marginally increased cost.²³ In situations where the BoS costs dominates (where the module cost is a small fraction of the cost of installation), then marginal improvements in efficiency significantly increase the economic value of PV. In the highly competitive silicon industry this has driven the adoption of more complex, higher efficiency architectures. Notably, Passivated Emitter and Rear Cell (PERC²⁴) and related architectures have grown their market share over the course of this PhD (2016 to 2020) from 14% to over 70%,⁷ illustrating the capability of the industry to adopt novel

architectures. Against this backdrop, with the world record silicon single-junction PCE remaining static at 26.7%, monolithic silicon-perovskite tandems have emerged with the capability to surpass this limit. This architecture overcomes the sub-optimal silicon bandgap with a wider-bandgap perovskite top cell to more efficiently recover the photon energy available in the solar spectrum, as will be discussed in the following chapter. The current world record silicon-perovskite tandem is over 29.5% PCE after rapid advancements over the last few years.^{17,25} By building on the existing silicon infrastructure it is hoped that perovskite materials can prove their capability, and achieve LCOEs 15-20% lower than single-junction silicon cells.²⁶

Beyond silicon/perovskite tandems in the short term, ultimately the lowest cost approach for PSCs is high-throughput roll-to-roll (R2R) manufacturing, either of single-junction or all-perovskite tandem and multi-junction modules.²⁷⁻²⁹ Replacing the ecosystem of factories required for silicon modules with a single material-to-product factory, with high-throughput processing, could dramatically increase solar cell adoption by accelerating growth. Cost models by Bruening *et al.* and Matthews *et al.* highlight this potential for PSCs.^{30,31} Here, their models consider perovskite modules fabricated on a continuous production line, with the largest CapEx costs being the factory and associated production equipment (fixed assets), in addition to ongoing operational costs (equipment maintenance, staffing). As the throughput speed of such a factory is increased, only the materials costs (raw perovskite precursors, substrates, encapsulation) are scaled, and the cost per module decreases.^{30,32} In turn the operating profit margin increases, enabling larger investment for growth of production capacity, with the possible growth rate estimated to be between 15-30% per annum, compared with only ~8% for silicon in their model.³⁰ Underpinning this most enticing economic prospect is the necessity for researchers to prove that this fast fabrication of PSCs is technologically possible.

1.4: Thesis motivation

If they are to aid humanity in preventing runaway climate change, PSCs must become a commercially viable technology capable of faster deployment than silicon, or provide competitive impetus for the silicon industry to greatly improve efficiencies. To meet this requirement, researchers must develop low-cost processes to enable the rapid crystallisation of stable perovskite materials and formation of device layers. This thesis aims to develop and understand these scalable crystallisation processes, to enable the future - and parallel - transfer of these processes to scalable manufacture. Specifically, the objectives of the research will be to:

- Develop new lab-scale methods for processing functional optoelectronic layers for perovskite solar cells which are suitable with the requirements for scalable manufacture and rapid processing.
- Understand the fundamental crystallisation processes occurring during these deposition processes to gain new insight and enable the rational design of future novel processing routes.
- Elucidate the relationship between solution chemistry and early-stages crystallisation to bridge between a chemical and materials understanding of halide perovskites.
- At all stages, consider the efficiency/stability/cost triangle for economically viable PSC manufacture.

Three key investigations will be undertaken related to this. Firstly, the development of a low-cost, spray-coating process for an electron transport material which could enable rapid module fabrication. Secondly, a potential route to relax the perovskite layer deposition constraints to increase the initial processing speed through a solvent vapour post-treatment. Finally, a fundamental study into the rapid crystallisation of perovskite materials enabled by methylamine gas, directly as a vapour treatment and in rapidly-crystallising solvent systems.

1.5: Thesis overview

Chapter 2 details background theory relating to materials in the solid state, periodic crystals and diffraction, semiconductor principles and their use in photovoltaics. An overview of photovoltaics, perovskite materials and a brief history of perovskite solar cells is provided to contextualise the thesis in this relatively new field. In addition, a summary of scalable processing techniques is discussed, including high speed R2R fabrication techniques and perovskite device architectures.

Chapter 3 is an overview of the fabrication and characterisation techniques used in the thesis. This covers the materials and device preparation methods used in the research, including scalable deposition by spray-coating. Here, explanations are given for the various optoelectronic approaches to understand the physics of halide perovskites and to determine the performance of photovoltaic cells, with specific methods given in each chapter. A particular focus is on the use of lab- and synchrotron-based diffraction techniques which are of specific importance to the studies in later chapters.

Chapter 4 is an investigation into the use of SnO₂ as an electron transport layer (ETL) for scalably-processed perovskite solar cells. Specifically, the research addressed the possibility of using spray-coated nanoparticle SnO₂ layers combined with rapid post-processing to

achieve layers that would be suitable for use in a high-throughput manufacturing environment. Typical post-processing treatments, such as thermal annealing, are unsuitable for R2R manufacture, where each process duration dictates the maximum throughput speed, which in turn dictates the economic viability of module production.

Chapter 5 looks into understanding the effects of solvent-vapour annealing, a common post-processing technique used to recrystallise halide perovskite materials for enhanced grain growth. Processes like this could be used to simplify the initial perovskite deposition allowing for faster processing. In literature, this process is reported to be purely beneficial, however the more subtle effects of this process on material composition and device stability are explored. Specifically, we identify using X-ray diffraction that for certain solution stoichiometries, the vapour treatment leads to a stable intermediate phase. This, as well as strong solvent-cation interactions, significantly impact the perovskite film microstructure and device stability.

Chapter 6 probes the mechanisms underlying the use of methylamine gas in perovskite crystallisation and unconventional solvents. Specifically, methylamine has been shown to rapidly liquify solid films, inducing a transparent phase. When the vapour is removed, the film recrystallises with strong texturing and extended crystalline domains throughout the film thickness. This is ideal for charge transport in the light-absorbing layer, minimising defects which could parasitically affect the solar cell efficiency. More generally, methylamine has been used to form and maintain this liquid state inside other solvents which would otherwise be unsuitable for the dissolution of the perovskite precursor materials. In this work, the fundamental bonding mechanisms and structural interactions underpinning both the texturing during recrystallisation and the related solution chemistry are explored.

Chapter 7 concludes the thesis with a discussion of each results chapter, contextualised within the wider field. Future research directions related to the key investigations are outlined with an outlook for the different approaches, as well as some perspective on the remaining challenges for halide perovskites to transition into commercial usage.

Appendix A provides four examples of posters presenting various aspects of this and other research at international conferences.

Appendix B discusses and shows the calculation of the total recoverable photovoltaic energy available on Earth.

1.6: References

- (1) Kaufman, D.; McKay, N.; Routson, C.; Erb, M.; Dätwyler, C.; Sommer, P. S.; Heiri, O.; Davis, B. Holocene Global Mean Surface Temperature, a Multi-Method Reconstruction Approach. *Sci. Data* **2020**, *7* (1), 201. <https://doi.org/10.1038/s41597-020-0530-7>.
- (2) IPCC. *Climate Change 2014: Synthesis Report*; Pachauri, R. K., Meyer, L. A., Eds.; Cambridge University Press: Geneva, Switzerland, 2014; Vol. 9781107025. <https://doi.org/10.1017/CBO9781139177245.003>.
- (3) BloombergNEF. Bloomberg New Energy Outlook 2020; 2020.
- (4) *ESMAP Global Solar Atlas*; World Bank, Washington, DC: Washinton DC, 2020. <https://doi.org/10.1596/34102>.
- (5) Ameri, T.; Li, N.; Brabec, C. J. Highly Efficient Organic Tandem Solar Cells: A Follow up Review. *Energy Environ. Sci.* **2013**, *6* (8), 2390. <https://doi.org/10.1039/c3ee40388b>.
- (6) Swanson, R. M. A Vision for Crystalline Silicon Photovoltaics. *Prog. Photovolt Res. Appl.* **2006**, *14*, 443–453. <https://doi.org/10.1002/pip.709>.
- (7) VDMA. International Technology Roadmap for Photovoltaic (ITRPV) 11th Edition. **2020**, No. April.
- (8) Taylor, M.; Ralon, P.; Anuta, H.; Al-Zoghoul, S. *Renewable Power Generation Costs in 2019*; 2020.
- (9) Czochralski, J. Ein Neues Verfahren Zur Messung Der Kristallisationsgeschwindigkeit Der Metalle. *Zeitschrift für Phys. Chemie* **1918**, *92U* (1), 219–221. <https://doi.org/10.1515/zpch-1918-9212>.
- (10) Fraunhofer ISE: Photovoltaics Report; 2020.
- (11) Koppelaar, R. H. E. M. Solar-PV Energy Payback and Net Energy: Meta-Assessment of Study Quality, Reproducibility, and Results Harmonization. *Renew. Sustain. Energy Rev.* **2017**, *72* (August 2016), 1241–1255. <https://doi.org/10.1016/j.rser.2016.10.077>.
- (12) Pickard, W. F. A Simple Lower Bound on the EROI of Photovoltaic Electricity Generation. *Energy Policy* **2017**, *107* (May), 488–490. <https://doi.org/10.1016/j.enpol.2017.05.022>.
- (13) Powell, D. M.; Fu, R.; Horowitz, K.; Basore, P. A.; Woodhouse, M.; Buonassisi, T. The Capital Intensity of Photovoltaics Manufacturing: Barrier to Scale and Opportunity for Innovation. *Energy Environ. Sci.* **2015**, *8* (12), 3395–3408. <https://doi.org/10.1039/c5ee01509j>.
- (14) Geisz, J. F.; France, R. M.; Schulte, K. L.; Steiner, M. A.; Norman, A. G.; Guthrey, H. L.; Young, M. R.; Song, T.; Moriarty, T. Six-Junction III–V Solar Cells with 47.1% Conversion Efficiency under 143 Suns Concentration. *Nat. Energy* **2020**, *5* (4), 326–335. <https://doi.org/10.1038/s41560-020-0598-5>.
- (15) Kojima, A.; Teshima, K.; Shirai, Y.; Miyasaka, T. Novel Photoelectrochemical Cell with Mesoscopic Electrodes Sensitized by Lead-Halide Compounds. *Meet. Abstr.* **2006**, *MA2008-02* (1), 27.
- (16) Kojima, A.; Teshima, K.; Shirai, Y.; Miyasaka, T. Organometal Halide Perovskites as Visible-Light Sensitizers for Photovoltaic Cells. *J. Am. Chem. Soc.* **2009**, *131* (17), 6050–6051. <https://doi.org/10.1021/ja809598r>.
- (17) National Renewable Energy Laboratory. Best Research-Cell Efficiencies <https://www.nrel.gov/pv/cell-efficiency.html> (accessed Jan 1, 2021).
- (18) Egger, D. A.; Bera, A.; Cahen, D.; Hodes, G.; Kirchartz, T.; Kronik, L.; Lovrincic, R.; Rappe, A. M.; Reichman, D. R.; Yaffe, O. What Remains Unexplained about the Properties of Halide Perovskites? *Adv. Mater.* **2018**, *30* (20), 1–11. <https://doi.org/10.1002/adma.201800691>.
- (19) Stranks, S. D. Nonradiative Losses in Metal Halide Perovskites. *ACS Energy Lett.* **2017**, 1515–1525. <https://doi.org/10.1021/acsenenergylett.7b00239>.
- (20) Jacobsson, J. T.; Correa Baena, J. P.; Pazoki, M.; Saliba, M.; Schenk, K.; Grätzel, M.; Hagfeldt, A. An Exploration of the Compositional Space for Mixed Lead Halogen Perovskites for High Efficiency Devices - *Sl. Energy Environ. Sci.* **2016**, *41* (0), 1–35. <https://doi.org/10.1039/C6EE00030D>.

- (21) Tress, W. Perovskite Solar Cells on the Way to Their Radiative Efficiency Limit – Insights Into a Success Story of High Open-Circuit Voltage and Low Recombination. *Adv. Energy Mater.* **2017**, *7* (14). <https://doi.org/10.1002/aenm.201602358>.
- (22) Song, Z.; McElvany, C. L.; Phillips, A. B.; Celik, I.; Krantz, P. W.; Wathage, S. C.; Liyanage, G. K.; Apul, D.; Heben, M. J. A Technoeconomic Analysis of Perovskite Solar Module Manufacturing with Low-Cost Materials and Techniques. *Energy Environ. Sci.* **2017**, *10* (6), 1297–1305. <https://doi.org/10.1039/c7ee00757d>.
- (23) Case, C.; Beaumont, N.; Kirk, D. Industrial Insights into Perovskite Photovoltaics. *ACS Energy Lett.* **2019**, *4* (11), 2760–2762. <https://doi.org/10.1021/acsenergylett.9b02105>.
- (24) Green, M. A. The Passivated Emitter and Rear Cell (PERC): From Conception to Mass Production. *Sol. Energy Mater. Sol. Cells* **2015**, *143*, 190–197. <https://doi.org/10.1016/j.solmat.2015.06.055>.
- (25) Al-Ashouri, A.; Köhnen, E.; Li, B.; Magomedov, A.; Hempel, H.; Caprioglio, P.; Márquez, J. A.; Vilches, A. B. M.; Kasparavicius, E.; Smith, J. A.; Phung, N.; Menzel, D.; Grischek, M.; Kegelmann, L.; Skroblin, D.; Gollwitzer, C.; Malinauskas, T.; Jošt, M.; Matič, G.; Rech, B.; Schlatmann, R.; Topič, M.; Korte, L.; Abate, A.; Stannowski, B.; Neher, D.; Stolterfoht, M.; Unold, T.; Getautis, V.; Albrecht, S. Monolithic Perovskite/Silicon Tandem Solar Cell with >29% Efficiency by Enhanced Hole Extraction. *Science* (80-.). **2020**, *370* (6522), 1300–1309. <https://doi.org/10.1126/science.abd4016>.
- (26) Sofia, S. E.; Wang, H.; Bruno, A.; Cruz-Campa, J. L.; Buonassisi, T.; Peters, I. M. Roadmap for Cost-Effective, Commercially-Viable Perovskite Silicon Tandems for the Current and Future PV Market. *Sustain. Energy Fuels* **2020**, *4* (2), 852–862. <https://doi.org/10.1039/c9se00948e>.
- (27) Jean, J.; Woodhouse, M.; Bulović, V. Accelerating Photovoltaic Market Entry with Module Replacement. *Joule* **2019**, *3* (11), 2824–2841. <https://doi.org/10.1016/j.joule.2019.08.012>.
- (28) Li, Z.; Zhao, Y.; Wang, X.; Sun, Y.; Zhao, Z.; Li, Y.; Zhou, H.; Chen, Q. Cost Analysis of Perovskite Tandem Photovoltaics. *Joule* **2018**, *2* (8), 1559–1572. <https://doi.org/10.1016/j.joule.2018.05.001>.
- (29) Dou, B.; Whitaker, J. B.; Bruening, K.; Moore, D. T.; Wheeler, L. M.; Ryter, J.; Breslin, N. J.; Berry, J. J.; Garner, S. M.; Barnes, F. S.; Shaheen, S. E.; Tassone, C. J.; Zhu, K.; van Hest, M. F. A. M. Roll-to-Roll Printing of Perovskite Solar Cells. *ACS Energy Lett.* **2018**, *3* (10), 2558–2565. <https://doi.org/10.1021/acsenergylett.8b01556>.
- (30) Bruening, K.; Dou, B.; Simonaitis, J.; Lin, Y.; van Hest, M. F. A. M.; Tassone, C. J. Scalable Fabrication of Perovskite Solar Cells to Meet Climate Targets. *Joule* **2018**, *2* (11), 2464–2476. <https://doi.org/10.1016/j.joule.2018.09.014>.
- (31) Mathews, I.; Sofia, S.; Ma, E.; Jean, J.; Laine, H. S.; Siah, S. C.; Buonassisi, T.; Peters, I. M. Economically Sustainable Growth of Perovskite Photovoltaics Manufacturing. *Joule* **2020**, 1–18. <https://doi.org/10.1016/j.joule.2020.01.006>.
- (32) Bishop, J. E.; Smith, J. A.; Lidzey, D. G. Development of Spray-Coated Perovskite Solar Cells. *ACS Appl. Mater. Interfaces* **2020**. <https://doi.org/10.1021/acsami.0c14540>.

Chapter 2

Background theory

2.0: Introduction

In this chapter, the physical and materials chemistry basis for the investigations is presented. The theory discussed here is an overview of the more comprehensive treatments on some of these topics by Kittel,¹ Hook and Hall,² Nelson³ and Mullin.⁴ This covers a broad overview of the properties of solids from both a structural and electronic standpoint. A particular focus is placed on crystalline photovoltaic materials, and the related semiconductor physics are discussed, as well as the principles for the incorporation of these materials into devices. These understandings are then related to perovskite structures, which are explained from their early discovery through to the unique properties of the metal-halide family. Here, an overview of metal-halide perovskites (and related materials) covers their structural properties, a brief history of the field, crystallisation for solution-processing techniques and photovoltaic device incorporation.

2.1: Solids

2.1.1: Atoms

Each atom is comprised of a positively charged nucleus and a surrounding distribution of electrons in a configuration governed by quantum mechanical principles. In the simple atomic orbital model, electrons occupy discretized energy levels, or orbitals, surrounding the nucleus. The occupancy of these orbitals is in accordance with the Pauli exclusion principle, such that no two or more electrons can reside in the same quantum state, as described by the four quantum numbers shown in Table 1. These numbers dictate the available states, or energy levels, for electrons to occupy. Electronic transitions to, from or between certain levels is facilitated by excitation by other particles, in this field typically photons, resulting in an excited state with higher energy than the ground state. By the Aufbau principle, for atoms or ions in the ground state, electrons will always occupy the lowest energy state available. Together these orbitals form the shells and subshells which underpin the chemistry of each element.

Table 1: The four quantum numbers which define the quantum mechanical behaviour of an atomic electron.

Symbol	Name	Values
n	principal quantum number	$n = 1, 2, 3 \dots$
l	azimuthal quantum number	$0 \leq l \leq n - 1$
m_l	magnetic quantum number	$-l \leq m_l \leq +l$
m_s	spin quantum number	$1/2$ or $-1/2$

Within these orbitals, the position of an electron is wave-like, where the electron distribution is probabilistic. In many cases, the configuration or shape of these orbital nodes can be calculated as solutions to the nonrelativistic time-independent Schrödinger equation,

$$\left[\frac{-\hbar^2}{2m} \nabla^2 + V(\mathbf{r}) \right] \psi(\mathbf{r}) = E\psi(\mathbf{r}) \quad (2.1)$$

with the distribution of electron density described by a wavefunction ψ at a position in 3D space denoted by a vector \mathbf{r} . Here, \hbar is the reduced Planck constant ($h/2\pi$), ∇ is the gradient operator, $V(\mathbf{r})$ is the potential energy as a function of position and E is the energy of the system. Typical examples of the resulting s , p and d orbitals surrounding a hydrogenic nucleus and their relation to the quantum numbers are shown in Figure 1. It should be noted that, in reality, these orbitals are not isolated quantum states but are instead a mixture of states due to wavefunction interactions (hybridisation).

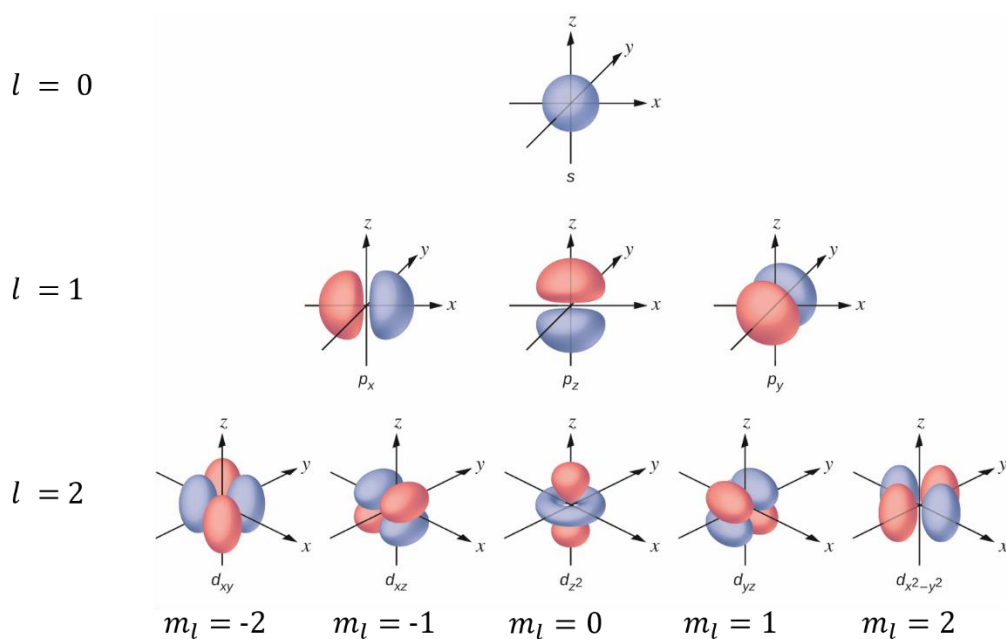


Figure 1: Illustration of the shapes of s , p and d orbital nodes, showing the distribution of single-electron density in these quantum states. Modified under Creative Commons licence from ref [5].

As Pb is a heavy element, the nonrelativistic treatment is insufficient to describe its orbital arrangement, instead the Dirac relativistic formalism is required.^{6,7} Relativistic spin-orbit coupling effects are caused by the heavy Pb nucleus attracting inner *s* orbitals towards it, increasing the electron velocities close enough to the speed of light that their mass becomes non-negligible.⁸ This additional mass attracts *s* and *p* orbitals to the nucleus (reducing the Bohr radius – the most probable nucleus to electron distance).⁹ Indirectly, this slightly shields *d* and *f* orbitals, repelling them from the nucleus. Coupling between the electron's spin and orbital motion affects the shape of the *p*, *d*, and *f* orbitals. Considering the relativistic effects, the p_x , p_y and p_z orbitals (Figure 1) no longer have the same symmetry, and therefore have different energies. The new relativistic $p_{1/2}$ orbital has spherical symmetry, which promotes mixing with *s* orbitals.⁸ Taken together, this leads to remarkable effects on the chemical and material properties. Most notably, it results in atoms having a smaller than expected atomic radius, causing metallic Pb to be dense and with high electron density. This causes strong X-ray absorption and scattering, meriting the common use of Pb for X-ray shielding as well as facilitating many of the experimental techniques used in this research.

2.1.2: Bonding

As matter is assembled, the interatomic forces between atoms are similarly driven by atomic electrons minimising their energy through interaction with surrounding atoms or molecules. It is therefore useful to divide the electrons into the core electrons, which occupy inner orbitals and are tightly bound to the nucleus, and valence electrons, in the outermost shell. These higher energy, valence electrons are most critical in determining the chemical bonding of an element. Where the valence electrons occupy a filled - or “closed” – shell, the already stable electronic configuration prevents chemical interactions. With partially filled shells, bonding can occur between atoms by the sharing or donation of electrons. This can take many forms with varying degrees of electron donation or withdrawal from the atomic form. The most important types here are: i) purely ionic bonding character, where the cation has fully donated electrons to the anion; and ii) covalent, where the electron density is fully shared (with a spectrum existing between these extremes). The possible forms of an element are the allowed “oxidation states” – an integer approximation of the stable (pseudo-ionic) forms in which an atom has donated electrons. Through these chemical bonds, atoms are combined, resulting in larger structures.

For Pb, the aforementioned relativistic effects modify the most stable oxidation state compared to the other group 14 elements (C, Si, Ge, Sn). These elements all have electronic structures with four valence electrons split between *s* and *p* orbitals ($6s^2 6p^2$ in the case of

Pb). Moving down the group, relativistic effects play a greater role, as the electrons in the outermost *s* orbital are pulled towards the nucleus. For Pb, this actually results in the 6*s* electrons being more tightly bound than the 5*s* and so are less available for bonding (the so-called 'inert pair').⁸ As such, where the majority of the group prefers to exist in the +4 oxidation state, Pb is more stable as +2 - or "Pb(II)". This stable Pb(II) oxidation state is critical to the stoichiometry required for metal halide perovskites, and in turn hinders the development of Sn-based perovskites, as Sn(II) is far more readily oxidised through loss of its 5*s* valence electrons.

The electronic interaction between elements is described well by molecular orbital (MO) theory. The research in this thesis has focused primarily on lattices with free charge carriers, hence a detailed description of molecular excitons and covalent bonding is beyond its scope. However, MO theory is important with respect to ligand field theory for Pb compounds in solution and for the mechanism of band formation in metal halide perovskites, which gives rise to many of their unique characteristics. In brief, the available electronic states in a molecular system of atoms approximates to be a linear combination of their atomic orbitals – a superposition of the wavefunctions associated with the constituent atoms, as shown in Figure 2. As two atoms are moved into proximity, their associated orbitals can be spatially co-located resulting in orbital overlap, defined by the overlap integral of their wavefunctions. Where these orbitals lie between the two atoms, with energies below the otherwise filled atomic orbitals, electrons will prefer to occupy these states. This strengthens the chemical bond, and so the resulting molecular orbitals which form are known as bonding orbitals. In contrast, for antibonding orbitals, electron density is concentrated behind one atom, away from the bonding axis. This has a withdrawing effect, pulling the atoms apart and weakening their bond. Non-bonding orbitals are molecular orbitals which do not affect the bond strength because the orbitals have comparable energies to the atomic energy levels, which may be due to their orthogonality with respect to the bonding axis.

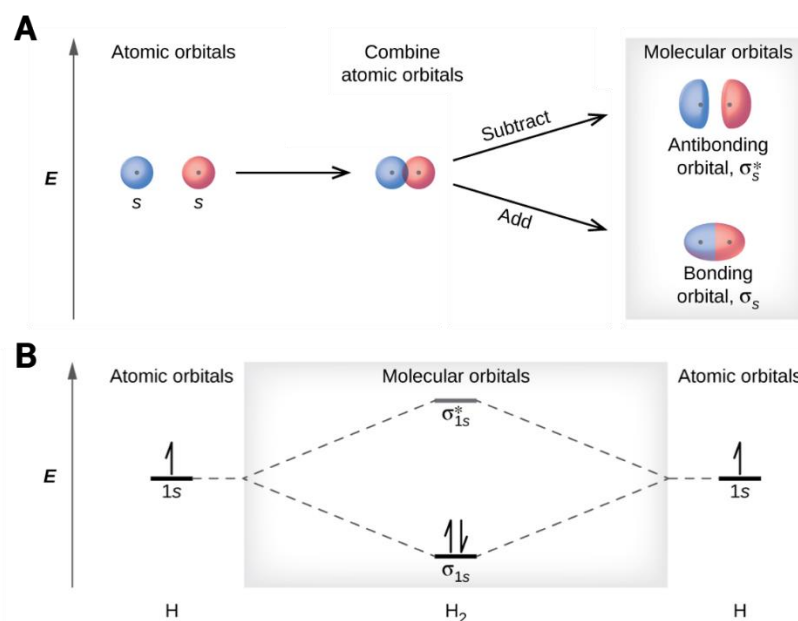


Figure 2: Molecular orbital theory. A) Depiction of the wavefunctions of two atomic s orbitals which are combined, resulting in bonding (σ_s) and antibonding (σ_s^*) orbitals. B) Energy level diagram showing hydrogen (H) $1s$ spin up ($m_s = 1/2$) electrons combining as molecular hydrogen (H_2), with electrons filling the σ_{1s} orbital.

Adapted from ¹⁰ under Creative Commons licence.

2.1.3: Solid crystals

The shape and symmetry of the electron densities surrounding atoms and molecules determines their possible arrangements in solid form. Solids can be broadly divided into amorphous and crystalline materials. In simple terms, amorphous solids exhibit minimal regular ordering, whereas crystalline materials exhibit periodicity in space, forming ordered arrays of material known as lattices. During crystallisation, atoms or molecules will occupy equilibrium positions with respect to each other, which will vary with direction, forming different ordering along different axes.¹¹ This long-range structural ordering of the positions in a crystal lattice results in various possible symmetries which are used to classify them. These can be symmetries about a point (a centre), about a line (an axis) or about a plane.

This is best visualised by first considering a lattice in two dimensions. For example, the graphene lattice is a periodic arrangement of carbon atoms situated at each corner of a flat grid of hexagons (Figure 3). We can consider this as a boundless 2D repeating pattern and analyse it by first denoting an origin at one of the carbon sites. It quickly becomes apparent that while several nearby carbon sites are completely equivalent to this origin, others are not. Those that are equivalent are termed lattice points. We can define two possible vector translations **a** and **b** which would take us between two lattice points. The set of possible vector translations between identical lattice points is therefore:

$$\mathbf{r} = u\mathbf{a} + v\mathbf{b} \quad (2.2)$$

where u and v are integers. As this lattice is hexagonal, the angle α between these two vectors is 120° . With this angle and the magnitudes of each lattice vector (the lattice parameters, here $|\mathbf{a}| = |\mathbf{b}| = 2.46 \text{ \AA}$), we have described the geometry of the 2D unit cell: the repeating, tessellating polygon which makes up this lattice.

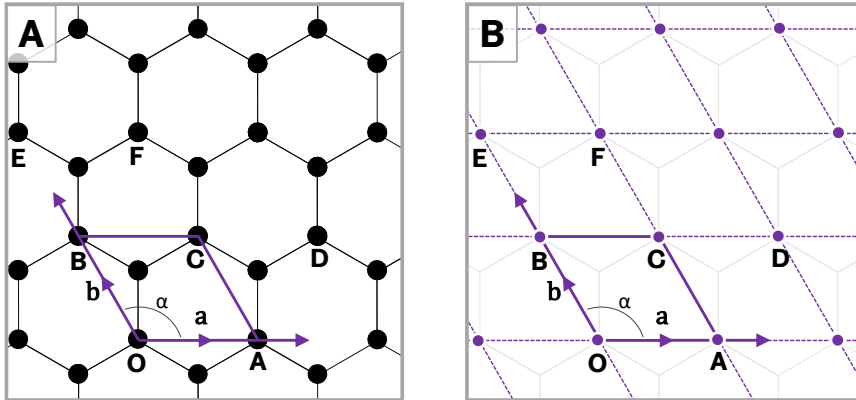


Figure 3: Representations of a 2D graphene lattice with carbon atoms positioned at the corners of a grid of regular hexagons. A) All carbon atoms in the layer are shown, with the origin marked O . However only those marked with A, B, \dots are equivalent to O . B) The same lattice but now with only the equivalent lattice points marked. Translations between these points are described by integer multiples of the lattice vectors \mathbf{a} and \mathbf{b} as in equation (2.2). The angle between \mathbf{a} and \mathbf{b} ($\alpha = 120^\circ$) defines this unit cell (purple) as being a hexagonal system.

By the same principle of identical points within a repeating periodic arrangement, we can describe any three-dimensional crystal lattice. Here the set of lattice translation vectors are extended to:

$$\mathbf{T} = u\mathbf{a} + v\mathbf{b} + w\mathbf{c} \quad (2.3)$$

with the \mathbf{c} vector describing an additional possible translation along the third crystallographic axis. A translation - or direction - through a crystal can be denoted with square brackets, in the form $[u \ v \ w]$. A set of symmetrically equivalent directions are given in angle brackets, $\langle u \ v \ w \rangle$ – as in the case of a simple cubic structure where $[100] = [010] = [001]$. Describing the unit cell in three dimensions therefore requires three lattice parameters, a, b , and c , and three angles, α, β , and γ , forming a parallelepiped as shown in Figure 4.

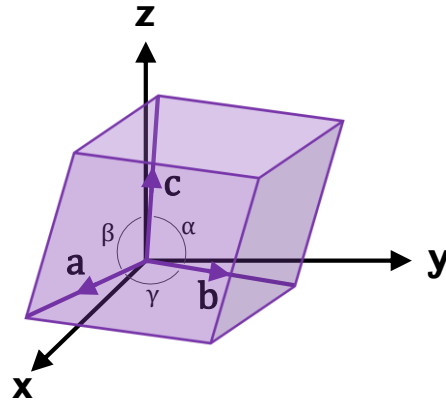


Figure 4: Representation of the unit cell of a three-dimensional crystal lattice. The shape of this unit cell is defined by the lattice parameters a , b , and c , as well as the angles between them, α , β , and γ .

All possible unit cell geometries in three dimensions fall into one of 7 broad crystal systems, based on their rotational symmetry (Table 2). Within these geometries are 4 possible atomic centre positions, showing the occupied lattice points in the unit cell which describe the translational symmetry (P, C, I and F, as shown in Figure 5).

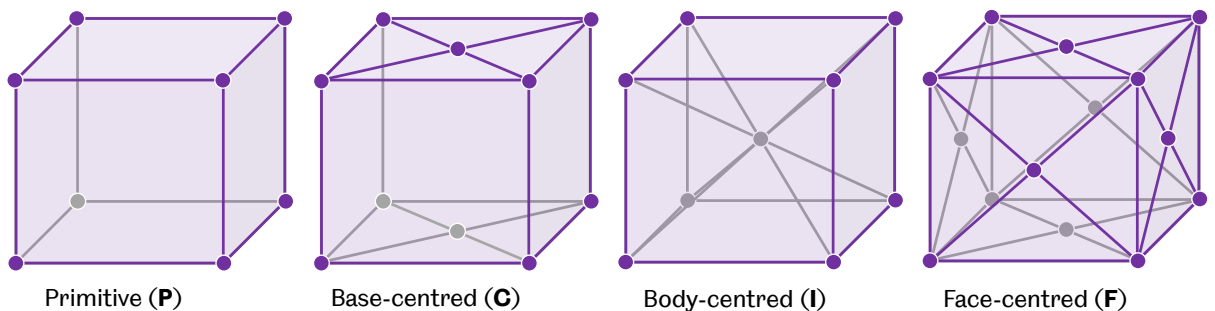


Figure 5: The four possible centering types for an orthorhombic unit cell, with lattice points as indicated.

This would give $7 \times 4 = 28$ possible combinations, however due to the equivalency of some of these configurations through judicious choice of crystal axes, this number is reduced. A total of 15 space lattices was first suggested by M.L. Frankenheim in 1842,¹² before being reduced to 14 by Auguste Bravais in 1848.¹³ These conventional “Bravais lattices” are all of the possible configurations of 3D repeating units (atoms or otherwise) within a crystal, and will tessellate, without any overlap or unfilled space between the units. The possible configurations are further extended by considering additional atomic sites in relation to the lattice points (such as the additional carbon atoms not on the unit cell boundary in Figure 3b). These sites are described by a generalised position vector, the fractional coordinates of a site within the unit cell of a similar form as (2.3):

$$\mathbf{r} = a\mathbf{x} + b\mathbf{y} + c\mathbf{z} \quad (2.4)$$

where $0 \leq x \leq 1$, $0 \leq y \leq 1$ and $0 \leq z \leq 1$. The possible rotational, translational, mirror and inversion symmetries of a crystal unit cell results in 32 possible “point” symmetry groups in 3D space. With the possible combinations of Bravais lattices and point groups, this gives a total of 230 possible crystallographic “space groups”, when also accounting for chiral symmetry (summarised in Table 2).

Table 2: Summary of the seven crystal systems, their unit cell geometries and crystallographic arrangements.

Crystal systems	Axis lengths	Axial angles	Centerings				Bravais lattices	Point groups	Space groups
			P	C	I	F			
Triclinic	$a \neq b \neq c$	$\alpha \neq \beta \neq \gamma \neq 90^\circ$	X				1	2	2
Monoclinic	$a \neq b \neq c$	$\alpha = \beta = 90^\circ \neq \gamma$	X	X			2	3	13
Orthorhombic	$a \neq b \neq c$	$\alpha = \beta = \gamma = 90^\circ$	X	X	X	X	4	3	59
Tetragonal	$a = b \neq c$	$\alpha = \beta = \gamma = 90^\circ$	X		X		2	7	68
Trigonal	$a = b = c$	$\alpha = \beta = \gamma \neq 90^\circ, < 120^\circ$	X				1	5	25
Hexagonal	$a = b \neq c$	$\alpha = \beta = 120^\circ, \gamma = 90^\circ$	X				1	7	27
Cubic	$a = b = c$	$\alpha = \beta = \gamma = 90^\circ$	X		X	X	3	5	36
Total:							14	32	230

2.1.4: Diffraction

The periodicity of the 230 space groups with their various symmetries gives each material a structural fingerprint which can be probed through diffraction methods. Using X-ray photons, electrons or neutrons of comparable wavelengths to the interatomic distances in a crystal, periodic crystal structures will behave like a 3D diffraction grating to the incoming particle waves, resulting in interference. Max von Laue and co-workers first investigated this diffraction with X-ray beams in 1911, and observed that where the distances in a crystal are known, the wavelength of the radiation can be calculated from the diffraction pattern. More importantly, if the wavelength is known, the interatomic distances within crystals could now be measured.

Consider a coherent beam incident at an angle θ on a set of parallel planes evenly spaced by a distance d , where scattering from the planes is elastic (the kinetic energy of the beam is conserved). We can show geometrically (Figure 6) that the difference in path length for the reflected beam from successive planes is $2d \sin \theta$. For an incident wavelength λ , where the difference in path length is an integer multiple (n) of the wavelength, the wave will be in phase and result in constructive interference:

$$2d \sin \theta = n\lambda \quad (2.5)$$

which is satisfied for wavelengths where $\lambda \leq 2d$. This is the Bragg condition, named after W. H. and W. L. Bragg who first demonstrated the angular dependence of X-ray scattering intensity from a variety of crystal structures in 1913.¹⁴

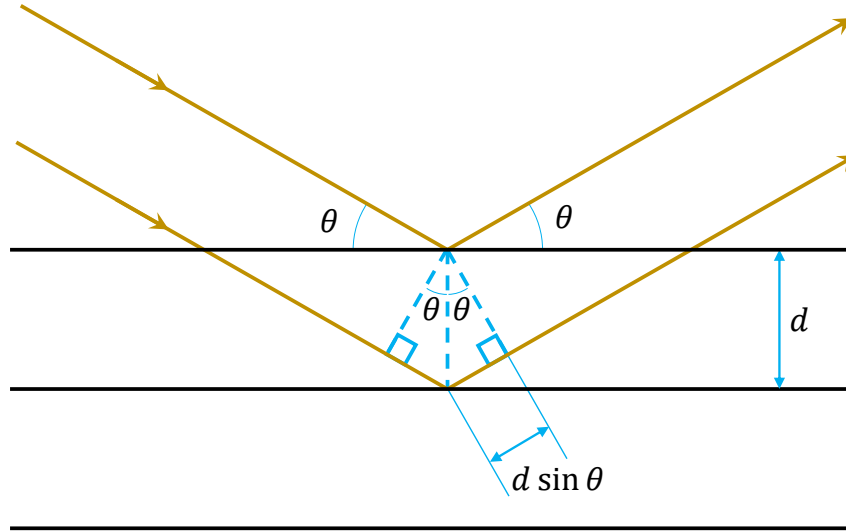


Figure 6: Understanding the path length difference for an elastically scattered wave from parallel crystal planes.

2.1.5: Reciprocal lattice

It is important to introduce the concept of the reciprocal lattice – the Fourier transform of the real space crystal lattice. The reciprocal lattice can be a convenient representation of a crystal (in length units) in reciprocal space (with units of inverse length), also referred to as k -space or momentum space. For a distance d in real space, there is an equivalent Q and vice-versa,

$$Q = \frac{2\pi}{d} \quad d = \frac{2\pi}{Q}, \quad (2.6)$$

such that Bragg's law (2.5) becomes:

$$Q = \frac{4\pi \sin \theta}{n\lambda} \quad (2.7)$$

as will be demonstrated. For scattered X-rays, the diffraction intensity (amplitude) is related to the distribution of electron density in the crystal, with some atomic scattering sites having significantly higher electron density (eg Pb). As this distribution is periodic, the electron number density $n(\mathbf{r})$ is also a periodic function of \mathbf{r} , the position vector, with the periods \mathbf{a} , \mathbf{b} and \mathbf{c} being the periodicity along each crystal axis. From the translational invariance, with \mathbf{r} being a possible position vector (2.4) and with \mathbf{T} a translation (2.3):

$$n(\mathbf{r} + \mathbf{T}) = n(\mathbf{r}). \quad (2.8)$$

This periodicity might also be relevant to the reciprocal lattice, and clearly lends itself well to Fourier analysis.¹ For the one-dimensional case, with an electron density function $n(x)$ in the x direction and with period a we can express this as the Fourier series:

$$n(x) = n_0 + \sum_{p>0} \left[C_p \cos\left(\frac{2\pi p x}{a}\right) + S_p \sin\left(\frac{2\pi p x}{a}\right) \right] \quad (2.9)$$

with p being a positive integer and C_p and S_p being real constants. Testing the translational invariance in (2.8) in 1D (with period a), we find:

$$n(x+a) = n_0 + \sum_{p>0} \left[C_p \cos\left(\frac{2\pi p x}{a} + 2\pi p\right) + S_p \sin\left(\frac{2\pi p x}{a} + 2\pi p\right) \right] \quad (2.10)$$

which is equal to (2.9) because of the $2\pi/a$ term and the periodicity of both functions. The points given by $2\pi p/a$ are the points on the reciprocal lattice of the crystal. Using Euler's identity, (2.9) is more completely represented over all integers by the complex function:

$$n(x) = \sum_p n_p e^{i2\pi p x/a} . \quad (2.11)$$

This can be extended to the 3D case with spatially varying electron density by now considering vectors \mathbf{G} which will satisfy the requirement for translational invariance with the Fourier sum:

$$n(\mathbf{r}) = \sum_{\mathbf{G}} n_{\mathbf{G}} e^{i\mathbf{G}\cdot\mathbf{r}} . \quad (2.12)$$

To do this, we can define the primitive reciprocal lattice vectors \mathbf{a}^* , \mathbf{b}^* , and \mathbf{c}^* from their real space analogues:

$$\mathbf{a}^* = 2\pi \frac{\mathbf{b} \times \mathbf{c}}{\mathbf{a} \cdot (\mathbf{b} \times \mathbf{c})} \quad \mathbf{b}^* = 2\pi \frac{\mathbf{c} \times \mathbf{a}}{\mathbf{a} \cdot (\mathbf{b} \times \mathbf{c})} \quad \mathbf{c}^* = 2\pi \frac{\mathbf{a} \times \mathbf{b}}{\mathbf{a} \cdot (\mathbf{b} \times \mathbf{c})} . \quad (2.13)$$

where the common denominator is the unit cell volume. These are defined in such a way that each is orthogonal to two of the lattice vectors, resulting in the relations,

$$\mathbf{a}^* \cdot \mathbf{a} = \mathbf{b}^* \cdot \mathbf{b} = \mathbf{c}^* \cdot \mathbf{c} = 2\pi \quad (2.14)$$

but with all other possible vector dot products returning 0. The points on the reciprocal lattice are therefore vectors of the form:

$$\mathbf{G} = h\mathbf{a}^* + k\mathbf{b}^* + l\mathbf{c}^* \quad (2.15)$$

where h , k , and l are integers. For a translation \mathbf{T} (2.3) in the Fourier form (2.12):

$$n(\mathbf{r} + \mathbf{T}) = \sum_{\mathbf{G}} n_{\mathbf{G}} e^{i\mathbf{G}\cdot\mathbf{r}} e^{i\mathbf{G}\cdot\mathbf{T}} . \quad (2.16)$$

The $e^{i\mathbf{G}\cdot\mathbf{T}}$ term can be expanded with the real and reciprocal vectors, given (2.14):

$$e^{i\mathbf{G}\cdot\mathbf{T}} = \exp[i(h\mathbf{a}^* + k\mathbf{b}^* + l\mathbf{c}^*) \cdot (u\mathbf{a} + v\mathbf{b} + w\mathbf{c})] = \exp[i2\pi(hu + kv + lw)] . \quad (2.17)$$

Because the terms in brackets in the argument of the exponential are all integers, they sum to another integer n , and again using Euler's identity:

$$\exp[i2\pi(hu + kv + lw)] = \exp[i2\pi n] = \cos(2\pi n) + i\sin(2\pi n) = 1 . \quad (2.18)$$

Thus (2.16) and (2.12) are identical and therefore the reciprocal lattice is also translationally invariant.

2.1.6: Miller indices

It is useful at this point to introduce the concept of Miller indices, which are used to describe sets of parallel planes in the real space lattice (Figure 7). Because of the orthogonality between a reciprocal lattice vector and two other (real-space) lattice vectors, the hkl integer values describing the vectors \mathbf{G} in (2.15) can also denote planes passing through the unit cell at the points:

$$x = \frac{a}{h} \quad y = \frac{b}{k} \quad z = \frac{c}{l}. \quad (2.19)$$

Some examples of these planes through a unit cell are shown in Figure 7. The shortest distance between adjacent planes is the d spacing. This is clearly a normal vector from the plane, and is thus conveniently defined by the magnitude of the reciprocal lattice vector:

$$d_{hkl} = \frac{2\pi}{|\mathbf{G}_{hkl}|}. \quad (2.20)$$

This general form can be expanded by taking the square and substituting for the unit cell parameters, which is non-trivial for lower symmetry unit cells with complex geometry. For brevity, as an example the orthorhombic case is given by:

$$\frac{1}{d_{hkl}^2} = \frac{h^2}{a^2} + \frac{k^2}{b^2} + \frac{l^2}{c^2} \quad (2.21)$$

which clearly simplifies for the tetragonal (cubic) cases where $a = b (= c)$ to

$$\frac{1}{d_{hkl}^2} = \frac{h^2 + k^2}{a^2} + \frac{l^2}{c^2}, \quad \frac{1}{d_{hkl}^2} = \frac{h^2 + k^2 + l^2}{a^2} \quad (2.22)$$

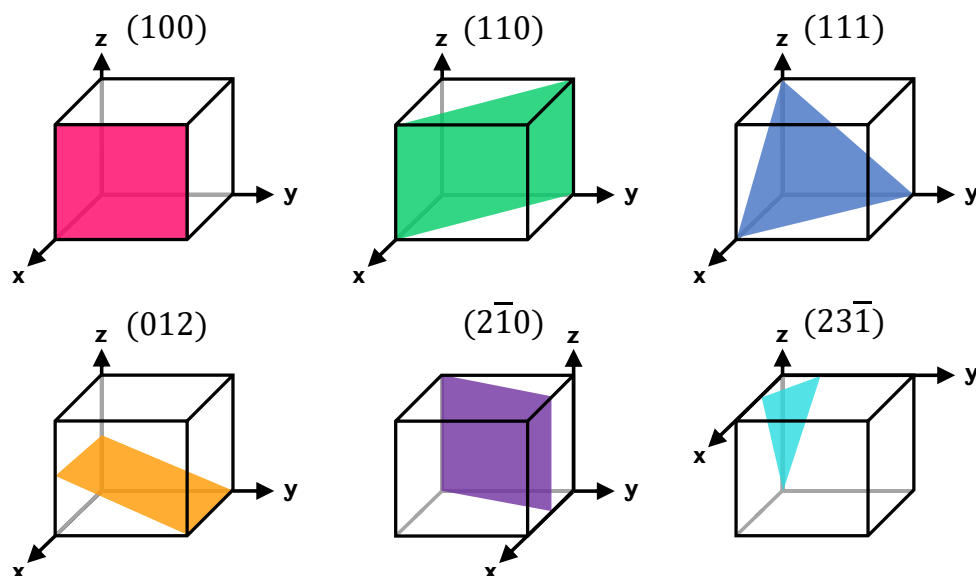


Figure 7: Example crystal planes described by Miller indices of the form (hkl) . Here, negative numbers are represented with a superscript bar.

2.1.7: Observed reflections

We can understand how the varying electron density within a material can result in constructive interference by considering a probing electromagnetic wave in a sample. The electromagnetic radiation (X-ray beam) is described by a plane wave $e^{i\mathbf{k}\cdot\mathbf{r}}$, with an incident wavevector \mathbf{k} in reciprocal space, and the elastically scattered exit beam by \mathbf{k}' . We can define the momentum transfer between the two waves as a third vector between their endpoints in reciprocal space, $\mathbf{Q} = \mathbf{k} - \mathbf{k}'$. For two scattering volumes dV in the sample, at an origin \mathbf{O} and at a position \mathbf{r} , we find there is a phase factor of $\exp[i(\mathbf{k} - \mathbf{k}') \cdot \mathbf{r}]$ between the incoming and outgoing beams, as shown in Figure 8.

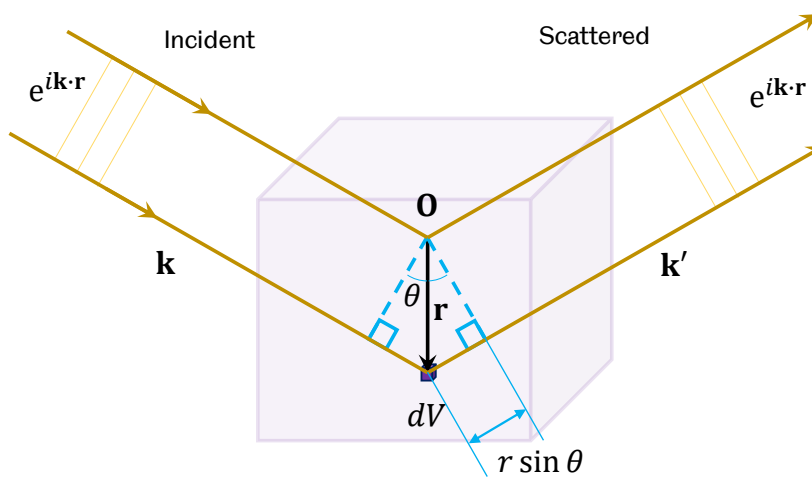


Figure 8: The phase difference between incident and scattered waves from a sample. The path length difference for the incident beam between the origin and a point \mathbf{r} is $r \sin \theta$, analogous to the path length difference in Bragg scattering. This changes the phase angle by $(2\pi r \sin \theta)/\lambda$, which is $\mathbf{k} \cdot \mathbf{r}$. For the scattered wave this is $-\mathbf{k}' \cdot \mathbf{r}$ to give $(\mathbf{k} - \mathbf{k}') \cdot \mathbf{r}$ in total. The phase factor between two volume elements at the origin and \mathbf{r} is therefore $\exp[i(\mathbf{k} - \mathbf{k}') \cdot \mathbf{r}]$.

The intensity of the diffracted wave from a volume dV with an electron density distribution $n(\mathbf{r})$ in the direction \mathbf{k}' thus has this phase factor $\exp(i\mathbf{Q} \cdot \mathbf{r})$ applied. The discrete scattering volumes therefore contribute to a total intensity over the whole sample:

$$F = \int dV n(\mathbf{r}) \exp(i\mathbf{Q} \cdot \mathbf{r}) \quad (2.23)$$

where F is the total scattering amplitude. Substituting $n(\mathbf{r})$ for the Fourier form in (2.12):

$$F = \sum_{\mathbf{G}} \int dV n_{\mathbf{G}} \exp[i(\mathbf{G} - \mathbf{Q}) \cdot \mathbf{r}]. \quad (2.24)$$

Why does this matter? Because for any momentum transfer where

$$\mathbf{Q} = \mathbf{G} \quad (2.25)$$

i.e. where the scattering vector is equal to a reciprocal lattice vector, the exponential term in (2.24) tends to 1 and the integral becomes $F = Vn_G$. This is constructive interference. For any scattering vectors away from this (where $\mathbf{Q} \neq \mathbf{G}$) the interference is quickly destructive, and so diffraction is only observed close to the reciprocal lattice vectors \mathbf{G} .

For elastic scattering, $|\mathbf{k}| = |\mathbf{k}'|$ (i.e. the magnitudes of the incident and scattered waves are equal), as all momentum is transferred. This is neatly depicted in the Ewald sphere construction in Figure 9. A sphere is defined in reciprocal space with radius $2\pi/\lambda$ about the scattering centre, and the reciprocal lattice is drawn such that the incident vector \mathbf{k} touches a reciprocal lattice point. Now wherever the surface of this sphere intersects the reciprocal lattice, we will observe diffraction. Geometrically in Figure 9, from the isosceles triangle centred at the origin, we can see that

$$Q = 2 \sin \theta * \frac{2\pi}{\lambda} = \frac{4\pi \sin \theta}{\lambda} \quad (2.26)$$

which proves Bragg's law in Q-space (2.7). This visualisation is also useful in understanding the practical aspects of a variety of X-ray detector geometries, which will be discussed further in Chapter 3.

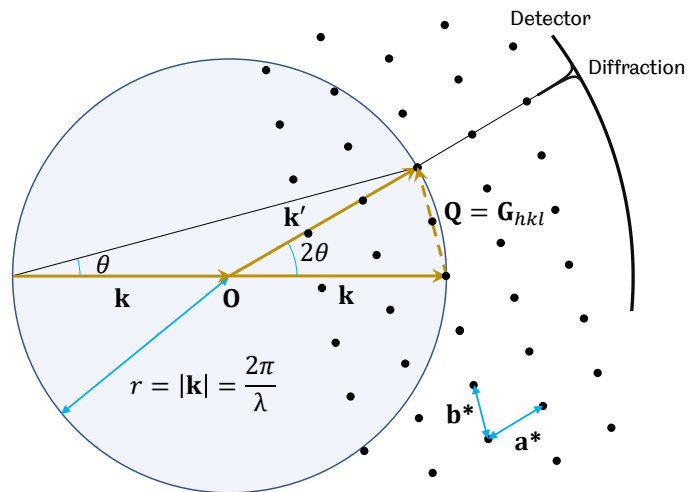


Figure 9: Ewald's sphere for elastic scattering from a crystal. By appropriately setting the radius and position of the sphere in real space, nodes of the reciprocal lattice intersect its surface and diffraction would be observed on the detector. This occurs only when $\mathbf{Q} = \mathbf{G}$ - the momentum transfer is equal to a reciprocal lattice vector with miller indices hkl .

The possible observed reflections from a particular crystal are also contingent on the integer values for the reciprocal lattice vectors. In the case of a primitive cubic lattice with side

length a , combining the possible interplanar distances (2.22) into Bragg's law (2.26) and rearranging*,

$$Q^2 = \frac{4\pi^2}{a^2} (h^2 + k^2 + l^2). \quad (2.27)$$

As the sum of the squares of the integers $h^2 + k^2 + l^2$ must also be an integer, we will therefore observe reflections equally spaced in Q^2 by a factor $4\pi^2/a^2$. However, as certain sums of three integer squares are impossible, these will be absent in the diffraction pattern. As illustrated in Table 3, the 7th reflection will be absent.

Table 3: Allowed reflections for a primitive cubic lattice.

hkl	$h^2 + k^2 + l^2$
100	1
110	2
111	3
200	4
210	5
211	6
220	8

Along certain directions through a crystal, due to the centerings as shown in Figure 5, specific reflections will also be absent. In simple terms, this occurs due to perfectly destructive interference where an atom is positioned at a location corresponding to the second order of a diffracting plane. This is shown in Figure 10 for the case of a face-centred (F) structure, where the scattering from the face-centred sites is perfectly out-of-phase with the scattering from the corner sites. This causes the (100) reflection in the scattering pattern to disappear.

* Equation (2.27) also neatly shows the benefit of scattering data presented in Q , with inverse length units - the reflection positions are wavelength independent. Given the simplicity of conversion by simple re-arrangement of (2.7) and the obvious benefit for data "Interoperability",¹⁵⁷ reporting diffraction data in 2θ for non-standard wavelengths (e.g. Cu K α emission with $\lambda = 1.5406 \text{ \AA}$) remains frustratingly commonplace.

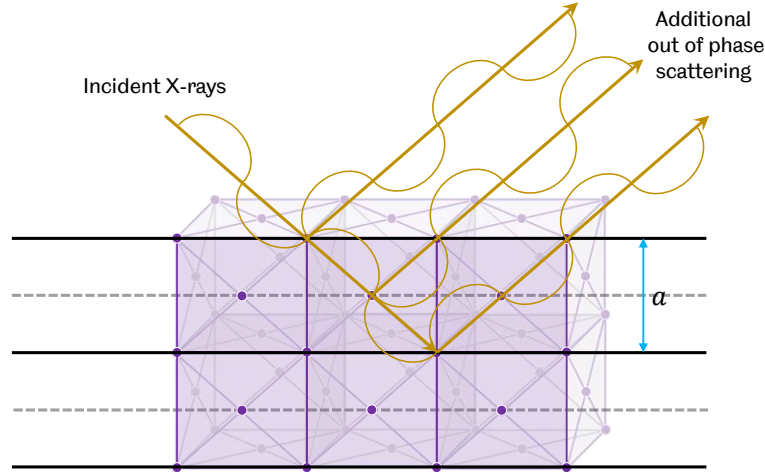


Figure 10: Illustration of the effect of the face-centred atoms on the scattering pattern from this F-centred crystal. The additional atoms (with the same electron density/atomic form factor) are offset by half the unit cell parameter a , and so are perfectly out of phase with (100) reflections causing destructive interference.

More rigorously, the total diffraction (constructive or destructive) is caused by the structure factor of the crystal, which is the sum of the individual atomic scattering contributions in the basis to the diffraction. For a crystal with atoms j , the structure factor F can be derived from (2.24) where $\mathbf{Q} = \mathbf{G}$:

$$F(hkl) = \sum_j f_j \exp(-i\mathbf{G} \cdot \mathbf{r}_j) \quad (2.28)$$

where \mathbf{r}_j is the position vector to an atomic centre, as in (2.4),

$$\mathbf{r}_j = a\mathbf{x}_j + b\mathbf{y}_j + c\mathbf{z}_j \quad (2.29)$$

and f_j is the atomic form factor for that atom. The atomic form factor describes the scattering at any position with respect to the atomic centre. By the same expansion as given in (2.17), the structure factor in (2.28) becomes:

$$F(hkl) = \sum_j f_j \exp[-2\pi i(hx_j + ky_j + lz_j)]. \quad (2.30)$$

In the case of the face-centred structure shown in Figure 10, the unit cell has atoms at the sites (\mathbf{r}_j): 000 , $0\frac{1}{2}\frac{1}{2}$, $\frac{1}{2}0\frac{1}{2}$ and $\frac{1}{2}\frac{1}{2}0$. The structure factor summed over these positions then becomes:

$$F(hkl) = f\{1 + \exp[-i\pi(k+l)] + \exp[-i\pi(h+l)] + \exp[-i\pi(h+k)]\}. \quad (2.31)$$

Now for any values where hkl are all even or all odd, the exponential terms go to 1 and $F = 4f$. For any other combination of even or odd values, two of the arguments in the exponents are odd multiples of $-i\pi$ and $F = 0$. This leads to the so-called selection rules for the common lattice centerings which determine whether a reflection will be observed or is systematically

absent (Table 4). Various other glide and screw translations will also cause systematic absences. By extension, variations in atomic form factors for any unit cell will cause different crystal reflections to have greater or lower scattering intensity according to its structure factor. A scattering pattern therefore contains a huge wealth of information about a crystal structure, from the intensity of reflections to the broadening of peaks providing insight on the atomic structure.

Table 4: Diffraction selection rules for common lattice centerings.

Centering	Reflection condition
P	None
C	$h + k = 2n$
I	$h + k + l = 2n$
F	h, k, l all even or odd

2.1.8: Band formation

Each of these possible spatial configurations of electron density has implications for the possible electronic states in a material, which in turn affect its bulk electrical properties. For a completely unbounded, free electron in a solid, the electron dispersion relation dictates how the energy E of the electron wave varies as a function of its wavevector \mathbf{k} :

$$E(\mathbf{k}) = \frac{\hbar^2 k^2}{2m} \tag{2.32}$$

where \hbar is the reduced Planck constant and m is the mass of the electron. This is a parabolic relationship as shown in Figure 11.

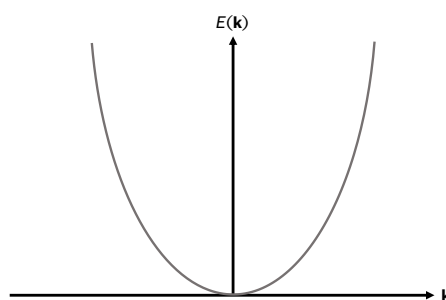


Figure 11: Energy of a free electron as a function of its momentum wavevector.

However, the periodicity in electron density of a crystal affects the propagation of electron waves through it, in the same way that photons are Bragg reflected. The periodic potential of the crystal $U(\mathbf{r})$ modulates the electron plane wave $e^{i\mathbf{k}\cdot\mathbf{r}}$, such that solutions to the Schrödinger equation (2.1) become:

$$\psi_{\mathbf{k}}(\mathbf{r}) = U_{\mathbf{k}}(\mathbf{r})e^{i\mathbf{k}\cdot\mathbf{r}}. \quad (2.33)$$

known as Bloch's theorem. While solutions are dependent on the wavevector \mathbf{k} , the periodicity occurs along the directions of the reciprocal lattice vectors \mathbf{G} . It is therefore useful to consider the unit cell in a related form. In the same way that planes with indices hkl in the real space unit cell can be defined by reciprocal lattice vectors orthogonal to them, we can define a similar set of planes which bisect the same vectors in reciprocal space. If we construct these planes from the origin at half the length of the vector and join them as a surface, over the whole set \mathbf{G} these represent periodic boundaries which can perturb an otherwise free electron, enclosing volumes known as Brillouin zones.

Considering the translational invariance of the lattice, the potential of the lattice is invariant:

$$U_{\mathbf{k}}(\mathbf{r}) = U_{\mathbf{k}}(\mathbf{r} + \mathbf{T}) \quad (2.34)$$

where \mathbf{T} is a translation vector between lattice points as defined in (2.3). It follows that solutions to Bloch's theorem (2.33) along a wavevector are periodic in $2\pi/a$, as demonstrated earlier for the reciprocal lattice in (2.8)-(2.10). This is also apparent given the symmetry of (2.32) that $E(\mathbf{k}) = E(-\mathbf{k})$ and $E(\mathbf{k}) = E(\mathbf{k} + 2\pi/a)$. The consequence is that unique solutions to the Bloch equation only exist for:

$$-\frac{\pi}{a} < k < \frac{\pi}{a} \quad (2.35)$$

which is the first Brillouin zone, or the smallest zone which can be enclosed by the perpendicular bisectors of the reciprocal lattice vectors drawn from the origin as described above. In this nearly-free electron model, the boundaries diffract the electron wave and by equation (2.35), there exist discontinuities in the possible electron energy states at the zone boundaries, as depicted in Figure 12.

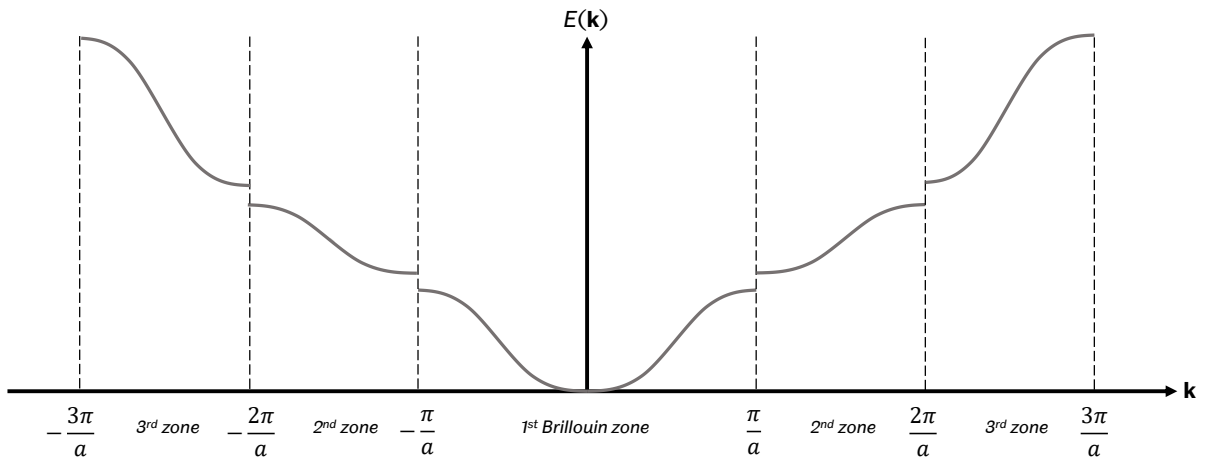


Figure 12: Extended Brillouin zone scheme in 1D.

2.1.9: Semiconductors

Because of the periodic nature of the lattice and $E(\mathbf{k})$, the extended Brillouin zone scheme can be reduced onto a smaller momentum space. In the simple 1D case presented in Figure 12, we map the energy eigenstates onto the first Brillouin zone here by the $2\pi/a$ periodicity. This results in the reduced scheme shown in Figure 13, with all eigenstates shown in the first Brillouin zone. In reality beyond 1D, the point group symmetry leads to critical points for each Brillouin zone along unique \mathbf{k} directions, which then completely describe the energy eigenstates within a crystal. As we can see, the consequence of the discontinuity at the Brillouin zone boundary introduces forbidden bands between the allowed energy states.

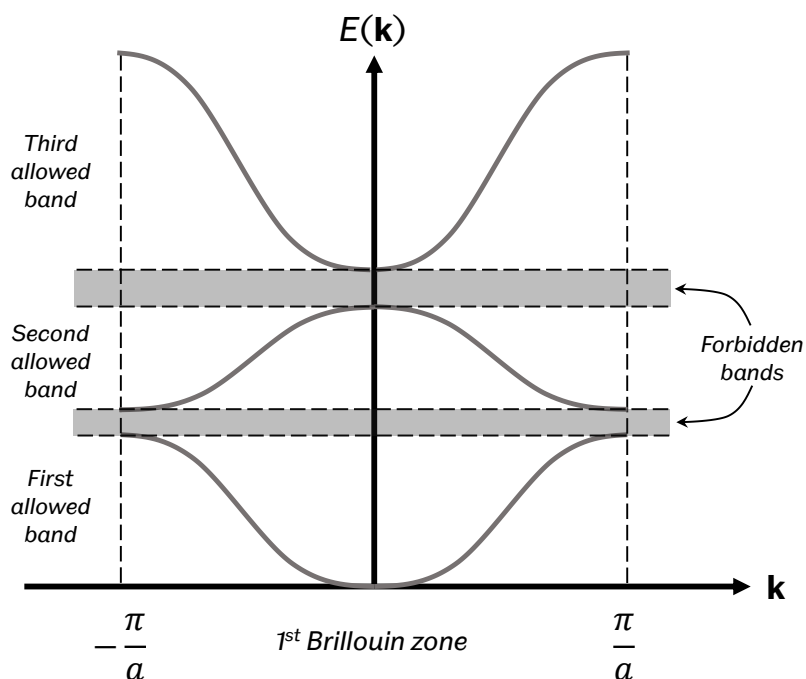


Figure 13: The reduced Brillouin zone in 1D illustrating the available and forbidden energy bands for electrons.

The forbidden energy bands are known as bandgaps, and these are critical to the electrical conductivity of a material. These can be divided into three major types of materials, illustrated in Figure 14:

- Insulators: all of the energy bands are either completely filled or empty. The forbidden band is wide enough that electrons cannot be promoted across it – the magnitude of the bandgap is too large. This means that electrons are immobilised in the crystal.
- Metals: at least one energy band is partially filled, or several bands overlap such that electrons effectively see no energy gap. In this way, electrons are free to move with any applied electromotive force.

- Semiconductors: a combination of partially filled bands, one mostly empty and one mostly full. The gap between the two bands is sufficiently narrow that electrons can be promoted from the lower band to the higher band. In a pure semiconductor, at absolute zero (0 K), there is no excitation energy, which immobilises electrons in the lower band, and the semiconductor behaves as an insulator.

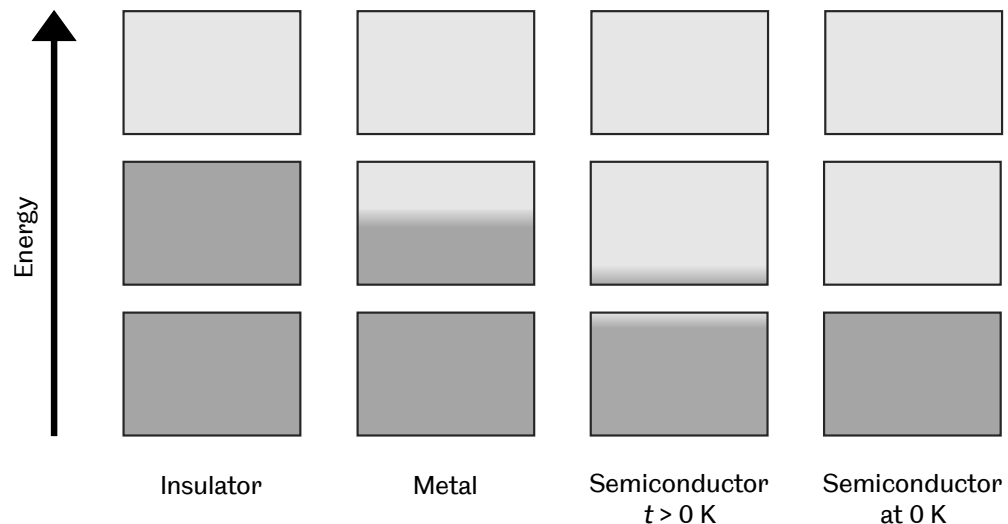


Figure 14: Illustration of the band filling for different solids categorised by electrical conductivity, where the darker colour indicates filling by a population of electrons.

An alternative model for the construction of band structures in solids is the tight-binding model, which is highly appropriate for covalently bonded solids. Here, as with the concept of orbital hybridisation discussed in section 2.1.2, we can think of the individual wavefunctions of atoms being brought together and hybridising to form bulk wavefunctions in the material. In the case of diamond, carbon atoms arrange in such a way that they are perfectly packed with no space, and so the distance between atomic centres is defined by the lattice. The available energy states are hybridised 2s and 2p orbitals as a function of the distance between the nuclei, and therefore the available energy states are uniquely dependent on the possible packing distance. The lattice parameter associated with this is indicated as a_0 in Figure 15, demonstrating the continuum of states available as a function of the interatomic distance.

In this picture, it becomes clearer that the highest energy electrons in the resting state are the atomic valence electrons, and so the lower (filled) band is known as the valence band. The upper band is the conduction band, into which electrons can be excited. The filling of the energy states in these bands is governed by Fermi-Dirac statistics, with a distribution:

$$f(E) = \frac{1}{\exp\left(\frac{E - E_F}{k_B T}\right) + 1} \quad (2.36)$$

where k_B is the Boltzmann constant, T is the temperature and E is the energy of a given state. Here, E_F is the Fermi level, the 'midpoint' of the distribution of energies. Where $E = E_F$, the exponential term in (2.36) goes to 1, such that $f(E) = 0.5$. This is also the work required to add an additional electron to the system, and in a semiconductor, this point lies within the bandgap. As might be expected for a thermodynamic distribution, and from (2.36), at temperatures $T > 0$ K for a semiconductor this results in the slight filling of the conduction band shown in Figure 14. Because of the statistical nature of the distribution of states in both bands, it is useful to define the valence band maximum (VBM) - or highest occupied molecular orbital (HOMO) in the picture of hybridised orbitals – as the uppermost point of the lower band which has an energy E_V . Conversely, the lowest point of the conduction band is known as the conduction band minimum (CBM) or lowest unoccupied molecular orbital (LUMO), with energy E_C . These energies are marked in Figure 15, with the difference between them being the band gap energy E_g .

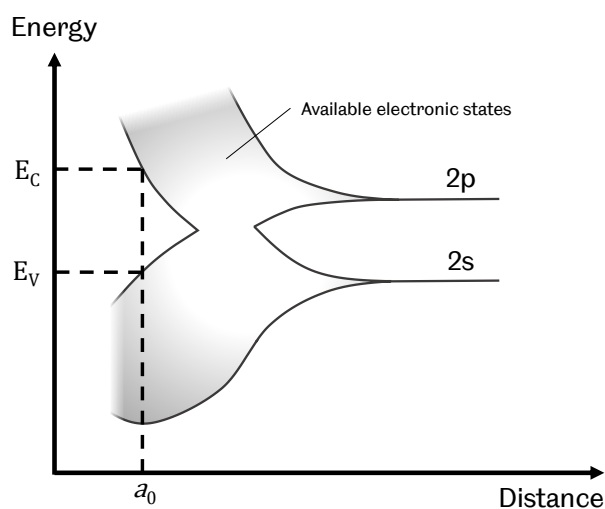


Figure 15: The available electronic states in a bulk solid formed of carbon atoms (diamond). Here the atomic orbitals are hybridised, with the lattice parameter a_0 of the structure dictating the possible electronic states.

2.2: Solar cells

2.2.1: The photovoltaic effect

Central to this research are light-absorbing semiconducting materials. In the simplest terms, photovoltaic (PV) materials are designed to absorb sunlight and convert it to electricity, allowing the transfer of energy from photons to electrons, an effect first observed by Edmond

Becquerel in 1839.¹⁵ This requires the efficient absorption of photons, generating excitons or immediately dissociated electron-hole pairs and extracting these charge carriers to their respective selective contacts, retaining as much of the input energy as possible. Each massless photon carries an energy E inversely proportional to its wavelength λ ,

$$E = \frac{hc}{\lambda} = h\nu = pc \quad (2.37)$$

where h is Planck's constant, c is the speed of light, the frequency ν is equivalent c/λ , and p is the photon's momentum. PV materials are semiconductors, with electrons predominantly occupying the valence band. When an electron in the valence band absorbs a photon of sufficient energy $h\nu$ greater than the bandgap E_g , it can be excited into the conduction band, leaving a hole in the valence band.³ Any excess kinetic energy that the photon has imparted into the electron greater than E_g is lost through thermalisation as both the hot electrons and holes rapidly (femtoseconds) decay back to the typical energies within their band, as shown in Figure 16.

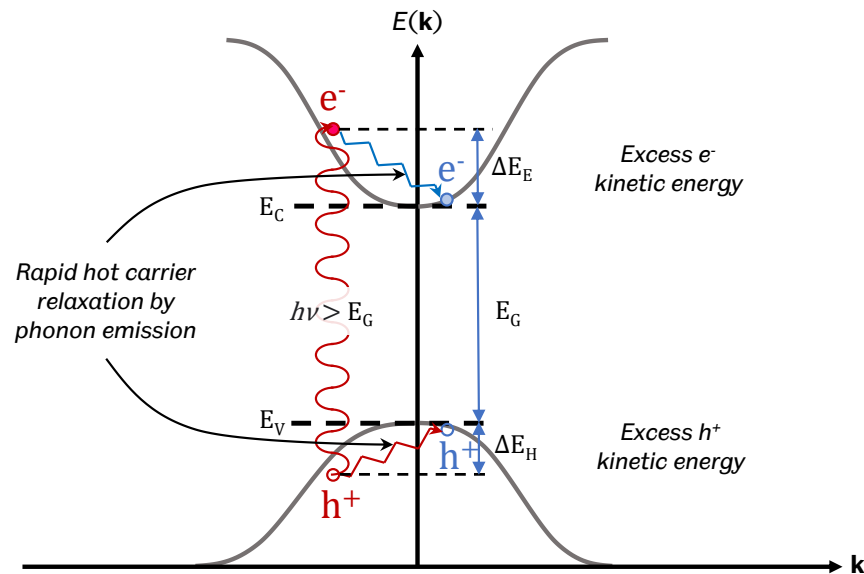


Figure 16: Energy level diagram illustrating the absorption of a photon with energy greater than the material bandgap ($h\nu > E_g$). An electron is promoted to the conduction band leaving a hole in the valence band. Carriers relax to the band edges (E_c and E_v) releasing the excess energy ($E_g - h\nu$).

For the case shown in Figure 16, the band structure of the material is such that the valence and conduction bands are aligned in momentum space. This means that all photons above the bandgap can be absorbed by electrons, such that optical absorption is continuous above E_g – giving a sharp absorption onset. This is known as a direct bandgap, as shown in Figure 17. However, it is also possible for the CBM to be offset from the VBM by a wavevector \mathbf{k} ; an

“indirect bandgap”. Photons have very little momentum (rearranging (2.37) $p = h/\lambda$, which is close to negligible), so for an electron-hole pair to be created, an additional lattice phonon with appropriate momentum is required to bridge the gap in momentum space. This reduces the probability of a photon absorption event for $h\nu > E_g$, giving a shallower absorption onset rather than the typically sharp onset above E_g for direct bandgap materials. Indirect bandgap PV materials therefore require much thicker layers to absorb the same photon energy (around 200 μm in the case of silicon, compared to only 500 nm for a halide perovskite). This does however also mean that radiative recombination – the reverse process where a conduction band electron recombines with a valence band hole – is suppressed by the requirement for this transition to also be phonon-assisted.

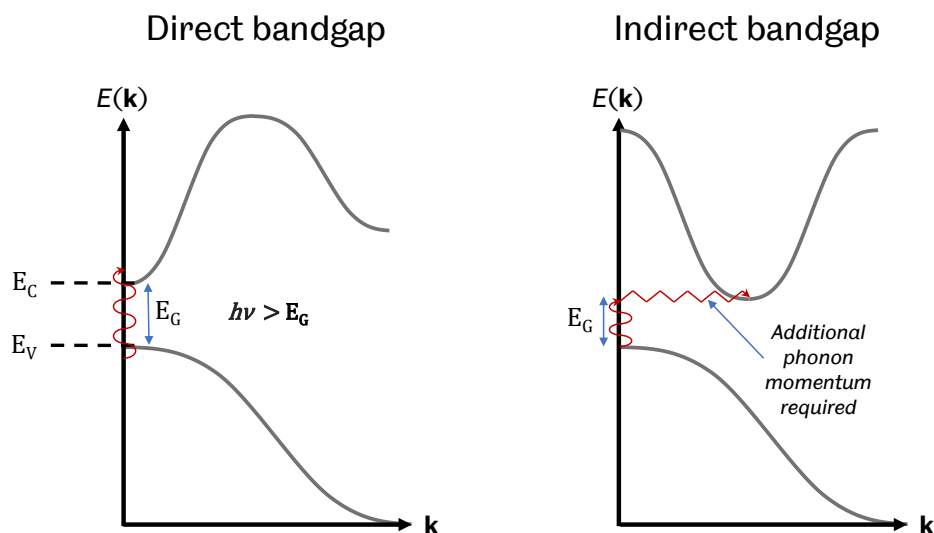


Figure 17: Direct and indirect bandgap semiconductor excitation processes.

2.2.2: Quantum efficiency

The quantum efficiency of a material can be defined as the ratio of the photons incident on a solar absorber to the number of carriers collected by the PV cell.³ For low E_g materials there is a proportionally greater number of photons above the band gap which can be absorbed, however the extracted potential energy per carrier is reduced through the thermalisation process described above. Considering the Sun’s spectrum (shown in Figure 18), which closely resembles that of a black body at 5778 K, we see that most of the available energy is close to the visible spectrum. For a given material, with an E_g energy which also corresponds to a wavelength, any photons with shorter wavelengths (higher energies) can be absorbed. Therefore, the maximum available energy yield is the area under the spectrum to the left of (above) the bandgap energy. For example, a 2500 nm wavelength corresponds to $E_g \approx 0.5$ eV.

and so almost all photons could be absorbed by a material with this bandgap under ideal conditions. Unfortunately, the energy recovered per photon would be <0.5 eV after carrier thermalisation to the bandgap (as shown in Figure 16): a large proportion of the incident photon energy is lost for most photons in the spectrum.

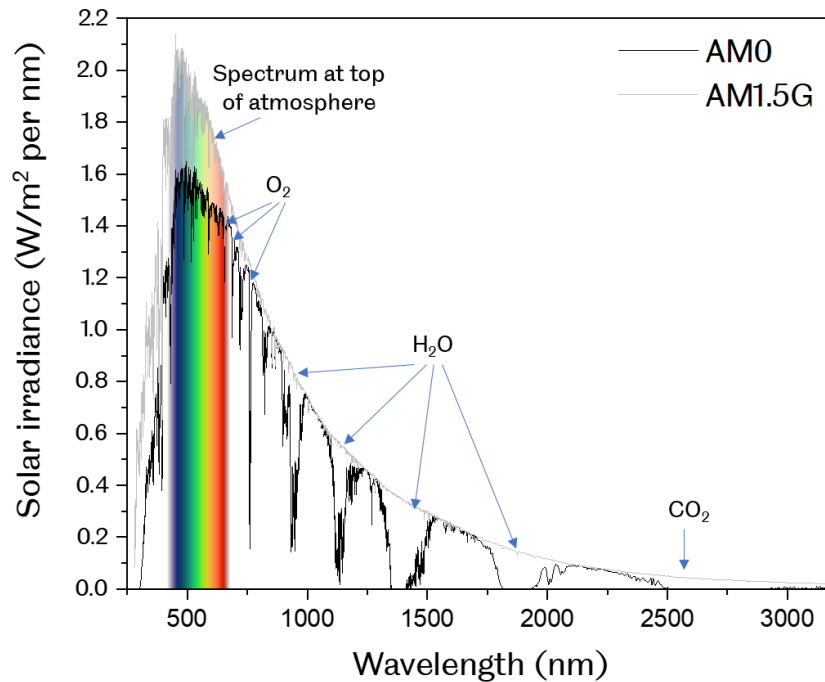


Figure 18: Wavelength dependent solar irradiance at the Earth's surface and atmosphere. The spectrum at the top of the atmosphere closely matches that of theoretical black body radiation, with the highest irradiance at shorter wavelengths. Parts of the spectrum are absorbed by greenhouse gases such as H_2O and CO_2 . The standard spectrum at the top of the atmosphere is known as air mass 0 (AM0) and at the ground is AM1.5G.¹⁶

Clearly, whilst it is important to have a high quantum efficiency – absorbing as many photons as possible and converting them to electrons – it is also important to extract charge carriers from the valence band with as much energy as possible. For higher E_G materials there are fewer photons of sufficient energy to promote electrons to the valence band, but for each photon which is absorbed the energy per photon is greater – the energy lost through carrier thermalisation is reduced.

This trade-off between having higher energy carriers (wider bandgap) and extracting as many carriers as possible (lower bandgap), as well as other intrinsic losses even in the idealised case, gives rise to the “detailed balance limit” (Figure 19).¹⁷ This limit defines the theoretical maximum power conversion efficiency of a single-junction solar cell for a given bandgap under AM1.5G illumination (the standardised solar spectrum at the Earth's surface considering atmospheric losses). The detailed balance limit considers the spectral losses (below bandgap,

thermalisation) and intrinsic radiative losses. The practical efficiency limit is significantly reduced by other loss mechanisms in the absorber and at/in the selective contacts – the adjacent layers which extract the generated charges.¹⁸

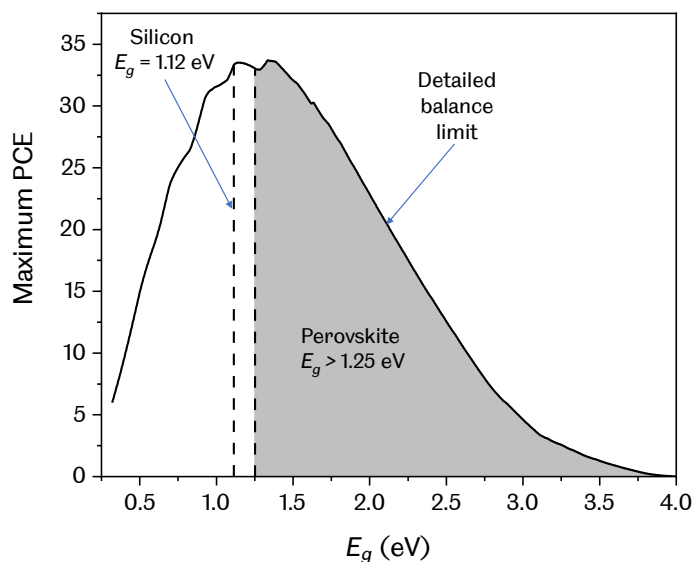


Figure 19: The radiative efficiency limit for an ideal solar cell at different E_G . The available photon energy is reduced by carrier relaxation to band edges (thermalisation), unabsorbed photons below the bandgap and other intrinsic radiative losses. The maximum theoretical efficiency attainable for an ideal single junction has a power conversion efficiency (PCE) of 33.7% at $E_G = 1.34$ eV, however the optimum bandgap shifts with more detailed consideration.

2.2.3: Recombination and carrier extraction

Following an absorption event, a coupled electron-hole pair will form – an “exciton”. In materials with efficient charge screening (as in perovskites – see section 2.3.4), the exciton quickly becomes a dissociated electron-hole pair. After this excitation, a number of processes can happen to the electron, which are highly dependent on the carrier density in the material.¹⁹ The carrier may radiatively recombine with a hole, which will in turn re-emit a photon with a probability of being absorbed.²⁰ The electron may however recombine *non-radiatively* via a trap state in the bandgap, or at an interface, at which point the re-emitted photon is below the bandgap and cannot be absorbed by the material, and so the energy is lost.

Various solar cell architectures exist designed to efficiently separate the electron-hole pairs, the most common being the p-n junction. In this architecture, two semiconducting materials are grown adjacent to each other with significantly different “doping”; doping can be used in crystalline semiconductors to modify the majority and minority carrier types to be either electrons (n-type) or holes (p-type). With these two materials electrically contacted to each

other, a dipole is therefore introduced as the Fermi levels in the two materials align, resulting in a “built-in field” which drives charge separation.

Perovskites behave differently to this in that the photon absorber layer is an intrinsic (“i”) semiconductor, i.e. the Fermi level is close to the middle of the bandgap. The electrons and holes within the layer experience their own “quasi-Fermi levels”, and the splitting (QFLS) between these levels gives the maximum possible voltage (V_{OC}) which can be extracted from a cell.²² At the two interfaces with this are placed an n-type electron extraction and a p-type hole extraction layer. These layers are designed to be highly selective to the correct carrier, have good band alignment to minimise energy losses and to prevent parasitic currents (reverse currents back into the cell or interfacial traps, non-radiative recombination channels²³). In ideal materials, all recombination is radiative and therefore excellent absorber materials are in turn highly luminescent. Any reduction in luminescence efficiency indicates a reduction in the QFLS and thus the available voltage from a cell.²¹

Figure 20 illustrates the configuration of layers for a perovskite device with an intrinsic active layer. If the cathode depicted here was at the substrate, then the n-type layer is deposited prior to the active layer and the p-type after (*n-i-p* if illuminated from the substrate side). When this configuration is connected in a circuit and illuminated, we have an operational solar cell.

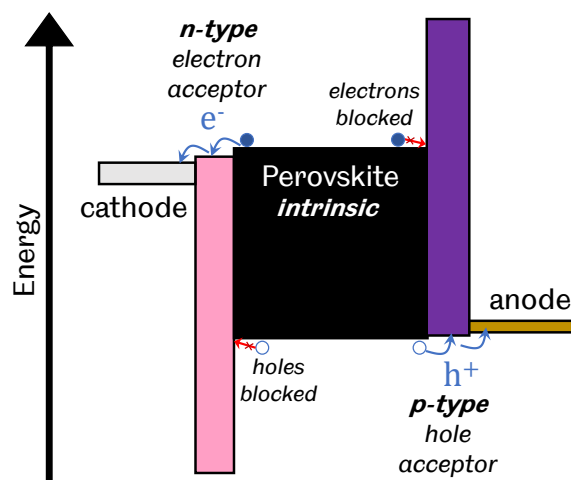


Figure 20: A perovskite solar cell device configuration illustrating the role of the electron- and hole- accepting materials in generating current under illumination.

2.2.4: Solar cell operation

Clearly the electrical nature of the cell under operation (at equilibrium) must be considered for a complete picture of photovoltaic behaviour. For a given E_G , the total available current for a cell (the short circuit current density or J_{sc}) can be described as the integral of the photon

fluxes at each wavelength multiplied by the cell's external quantum efficiency (EQE) at that wavelength (λ).²⁴ In short,

$$J_{sc} = -q \int_{\lambda_1}^{\lambda_2} EQE(\lambda) \Phi_{ph,\lambda}^{AM1.5G} d\lambda \quad (2.38)$$

where q is the fundamental charge, and $\Phi_{ph,\lambda}^{AM1.5G}$ is the spectral photon flux at AM1.5G (Figure 18).²⁴ Note, it is typical for the photocurrent to be represented as positive in solar cell physics. Without illumination and under an applied bias voltage, solar cells behave like a diode, such that a larger current is observed for positive bias voltages. This dark current behaviour can be described using the ideal diode equation,

$$J_{dark}(V) = J_0 \left(e^{\frac{qV}{kT}} - 1 \right) \quad (2.39)$$

with J_0 being the dark saturation current (the current leakage of the diode without illumination), V is the applied voltage, k is Boltzmann's constant and T is the operating temperature.^{3,24} This is modified by an "ideality factor" $n = 1 - 2$,

$$J_{dark}(V) = J_0 \left(e^{\frac{qV}{nkT}} - 1 \right) \quad (2.40)$$

where n is related to the dominant carrier recombination channels within a cell (traps at interfaces, in the bulk).²⁵ This is highly characteristic to a technology and cell architecture, and can evolve under operation.²⁶ Under illumination, the net current density is therefore given by:

$$J(V) = J_{sc} - J_{dark}(V) = J_{sc} - J_0 \left(e^{\frac{qV}{nkT}} - 1 \right) \quad (2.41)$$

The measured currents in the dark and under illumination for a range of positive bias voltages are shown in Figure 21, and the equivalent circuit is shown in Figure 22a.

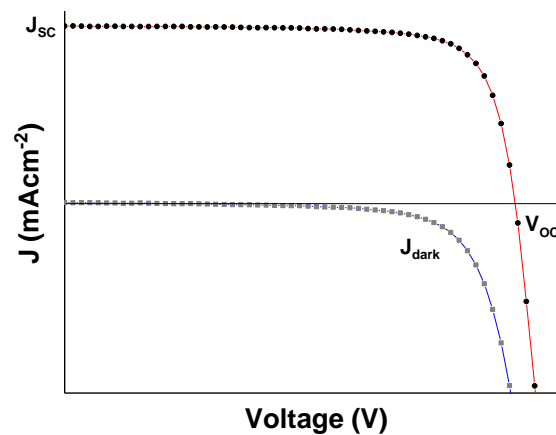


Figure 21: Current-voltage (J - V) measurements for an ideal solar cell in the dark (blue) and under illumination (red). J_{sc} is the short-circuit current, and V_{oc} is the open-circuit voltage – the maximum voltage with no current flowing.

2.2.5: Efficiency limits

Parasitic losses also contribute to the overall efficiency of the system. Series resistance (R_S) must be kept as low as possible to allow carriers to move freely in the cell. R_S could be caused by an overly thick transport layer - thus resulting in undesirable carrier recombination - or the effect of poor charge transport at an interface. The ideal cell model considers only directional charge transport with no reverse saturation current, such that an infinite resistance is in parallel to the diode. In reality, shunting pathways - due to pinholes in a layer or other leakage current effects - in poorly rectifying cells lead to a reduction in “shunt resistance” (R_{sh}).³ This can be represented by a modification to the diode equation,

$$J(V) = J_{sc} - J_0 \left(e^{\frac{q(V+JAR_S)}{nkT}} - 1 \right) - \frac{V + JAR_S}{R_{sh}} \quad (2.42)$$

The equivalent circuit representing the diode equation with series and shunt resistances is shown in Figure 22b.

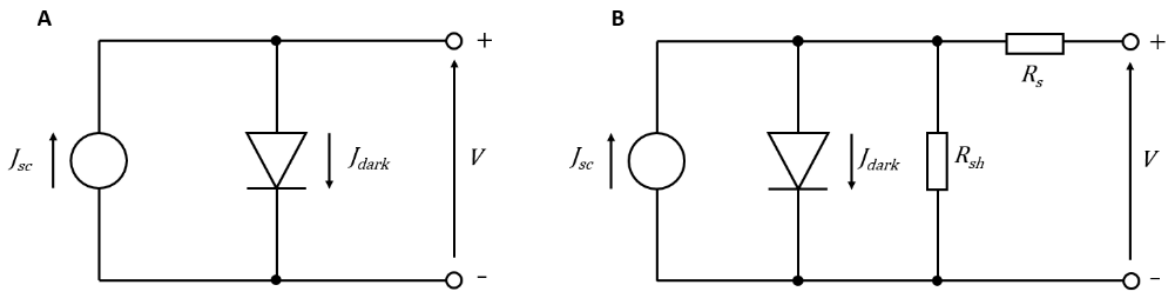


Figure 22: Equivalent circuits for a) an ideal solar cell and b) ideal solar cell with parasitic losses.

2.2.6: Performance metrics

The impact of parasitic losses must be effectively managed to ensure high performance solar cells. Both voltage and current must be maximised to deliver the highest power density,

$$P = JV \quad (2.43)$$

The maximum power point (MPP) of a solar cell is defined by the optimum applied voltage to achieve the highest power output (Figure 23). The ratio of the maximum power area to the total area of $J_{sc} * V_{oc}$ is referred to as the fill factor (FF),

$$FF = \frac{P_{max}}{J_{sc}V_{oc}} = \frac{J_{mpp}V_{mpp}}{J_{sc}V_{oc}} \quad (2.44)$$

which can be thought of geometrically as the ‘squareness’ of the current-voltage sweep.³ Parasitic resistances affect this, such that the gradient of the curve at J_{sc} is roughly

proportional to $1/R_{sh}$ and at V_{oc} is approximately $1/R_s$. Consequently, with the effect of these resistances, the fill factor is reduced.

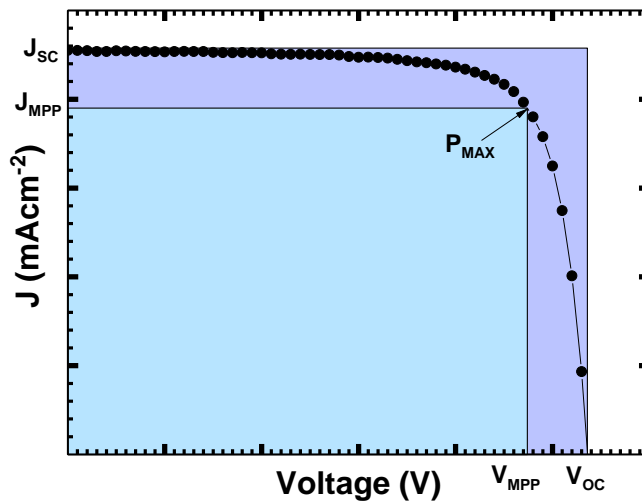


Figure 23: Typical current-voltage sweep for a solar cell where J is the current density. The fill factor is defined as the area of maximum power over the area of the external points V_{oc} and J_{sc} .

Finally, we come to the golden metric of solar cell performance, the power conversion efficiency (η or PCE). This is the ratio of the power generated by the solar cell to the power of the light incident upon it from the sun (P_s),

$$\eta = \frac{J_{mpp}V_{mpp}}{P_s} = \frac{J_{sc}V_{oc}FF}{P_s} \quad (2.45)$$

so J_{sc} , V_{oc} and the fill factor must all be maximised to make higher efficiency cells.

2.3: Perovskites

2.3.1: Structures

Perovskites are ionic crystals with the general chemical formula ABX_3 , where A and B are cations and X is an anion. The first perovskite crystal structure was discovered by Gustav Rose in the Ural mountains in 1839 and was named in honour of his friend, the Russian mineralogist Lev Aleksevich von Perovski.²⁷ This material was the naturally occurring mineral calcium titanate, $CaTiO_3$, with titanium and oxygen forming BX_6 octahedral units, with 12 oxygen atoms then caging in the calcium cation (Figure 24). Since then, thousands of naturally occurring and synthesised perovskite and related compounds have been identified, and it is Earth's most abundant crystal structure in the form of bridgmanite and related silicate perovskites in the mantle.²⁸

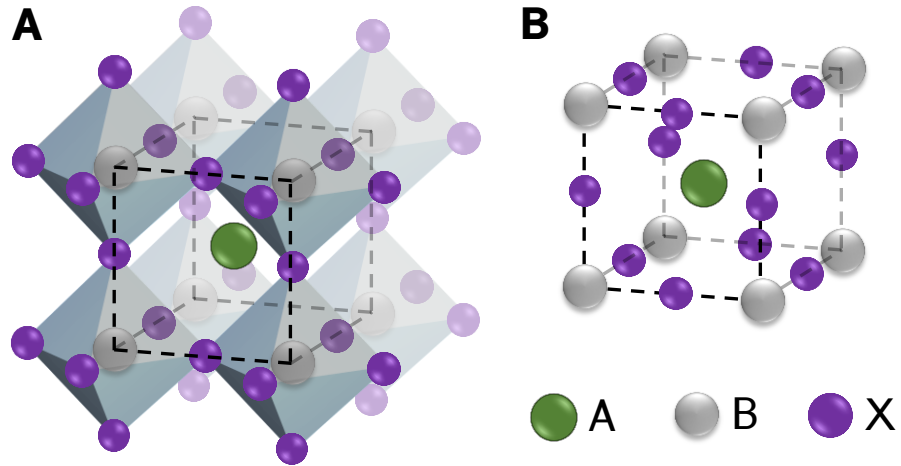


Figure 24: Crystal structure of ABX_3 perovskite, (a) Corner sharing BX_6 octahedra stabilised by the central A-site cation, (b) Unit cell for a cubic perovskite crystal centred on the A-site cation.

The formation of perovskite crystal structures was extensively considered in 1926 by V. M. Goldschmidt, who defined the principles of cubic perovskite tolerances based on the ionic radii of the constituent elements.²⁹ In this work, the tolerance factor t was defined as:

$$t = \frac{r_A + r_X}{\sqrt{2}(r_B + r_X)} \quad (2.46)$$

where r_A , r_B and r_X are the ionic radii of the A, B and X-site ions. It was proposed that where $0.8 < t < 1.0$, a perovskite structure can form, with $t = 1.0$ being the geometric 'ideal'. Unfortunately, t is a rather imperfect measure and inaccurately predicts structure formation with many compositions (in particular with halide anions).³⁰ For these perovskite phases to form, the B-site must be large enough to separate the X-site anions. From geometrical considerations this gives the octahedral factor,

$$\mu = \frac{r_B}{r_X} \quad (2.47)$$

which must have $\mu \geq 0.41$ for octahedra to form. Beyond this, the relative ionic sizes and competing A-X and B-X bonding interactions result in many possible stable octahedral distortions – patterns along a crystal direction or between planes such that the B-X-B bond angle $\neq 180^\circ$. These distortions were classified by A. M. Glazer in 1972, who categorised the possible tilting effects in perovskite crystals.³¹

2.3.2: Metal halide perovskites

For metal-halide perovskite structures with ABX_3 composition, A is a monovalent cation, B is a divalent (doubly charged) cation and X is an anion (as opposed to the oxide perovskites where the X-site is divalent). For photoactive hybrid organic-inorganic halide PSCs, the A-site cation

is typically all or partly organic, such as methylammonium (CH_3NH_3^+ , or MA), formamidinium ($\text{HC}(\text{NH}_2)_2^+$, or FA) or Cs^+ , the B-site is a metal, commonly Pb^{2+} or Sn^{2+} , and the anion is a halide (I^- , Br^- , Cl^-) or combination of halides. Alkali lead halides of this form were first synthesized in 1893 by H. L. Wells, who reported cesium- and potassium-based structures, including CsPbI_3 , CsPbBr_3 and CsPbCl_3 .³² The first detailed crystallographic study on these inorganic cesium-based perovskites was conducted in 1966 by Christiaan Møller who identified photoconductivity, indicative of semiconductor-like behaviour, a hint of the exciting future for this material.³³

Hybrid organic-inorganic methylammonium lead and tin perovskites were first reported by Dieter Weber in 1978, where it was also noted there was colour variation due to the composition.^{34,35} Perovskites of this '3D' form and other variants were extensively researched for their optoelectronic properties by David Mitzi and co-workers at IBM in the 1990s-2000s, during which many of the synthesis approaches used today were developed.³⁶⁻⁴¹

The term 3D here refers to a continuous network of corner-sharing octahedra. Within this, because of the aforementioned variety of ionic size and octahedral tilting effects, a number of phases can form, with some typical examples shown in Figure 25. The simplest case is the idealised primitive cubic ($Pm\bar{3}m$ space group) perovskite in Figure 25A, with no octahedral tilting ($a^0a^0a^0$ in Glazer notation), for example room-temperature methylammonium lead bromide (MAPbBr_3) with a tolerance factor $t = 0.927$ from (2.46). Two common tilts where the octahedra are tilted in a single plane result in the phases shown in Figure 25B and C. Here the difference between them is whether the tilts alternate ($a^0a^0c^-$) or are the same ($a^0a^0c^+$) between planes in the c -axis, which is shown in Figure 25 going into the page.

The tilting means that a cubic space group is insufficiently descriptive and tetragonal space groups are required, such that the diagonal (110) plane of the cubic phase becomes the (100) of a larger tetragonal cell. For instance, at room temperature the archetypal perovskite MAPbI_3 , with a slightly less ideal $t = 0.912$, adopts an $I4/mcm$ (or similar⁴²) symmetry shown in Figure 25C. The subtle balance between the two bonding interactions with the halide seem to underpin the stable tetragonal-type distortions for a given composition.⁴³ It is also possible for the octahedral tilting to vary in another axis (such that the B- and X-site are no longer colinear into the page in Figure 25D), as in the case of the photo-active CsPbI_3 phase, which has a tolerance factor of $t = 0.807$ and crystallises only at high temperature (>550 K). This is commensurate with a mismatch between the a and b lattice parameters (as were equivalent

for the tetragonal cells) and by the atomic sites is described by the orthorhombic $Pnma$ space group.

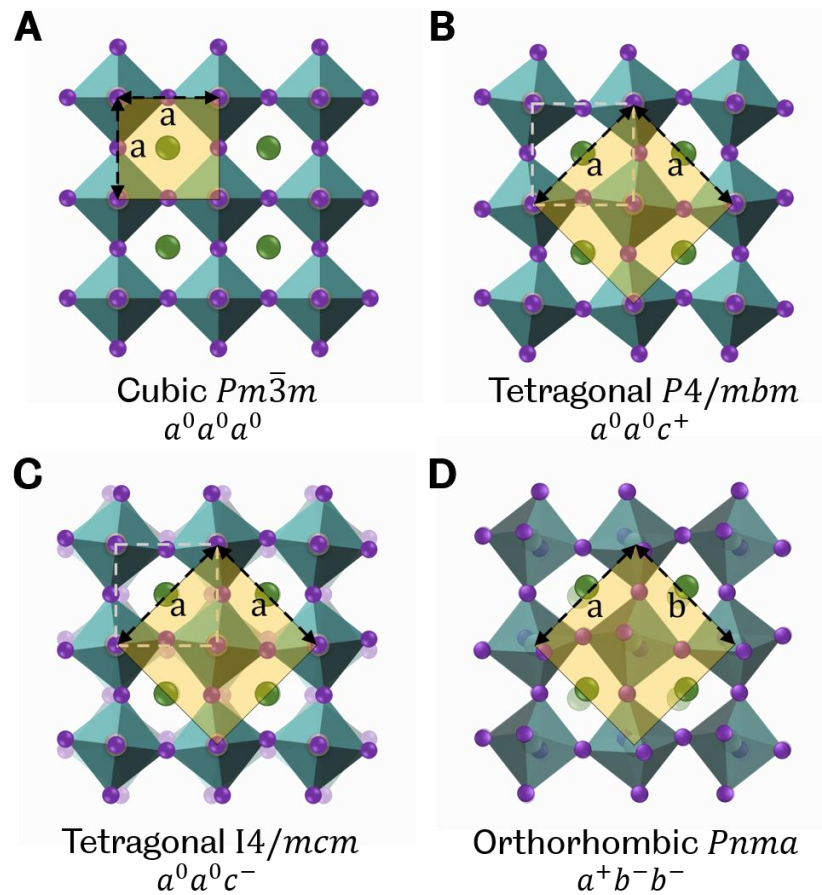


Figure 25: Four typical perovskite structures as described in the main text.

Recent attempts have been made to improve upon the Goldschmidt approach, for example through modification of the typically used Shannon ionic radii⁴⁴ for suitability with halide perovskites.⁴⁵ Computational approaches have also been used across large datasets, proposing a more limited region of perovskite formation considering both the octahedral and Goldschmidt factors.⁴⁶ Perhaps most interesting is the so-called Bartel tolerance factor, τ , developed through the screening of many possible factors that could determine the phase stability.³⁰ Encompassed in this factor is the oxidation state of the A-site, n_A , as well as the octahedral factor:

$$\tau = \frac{1}{\mu} - n_A \left(n_A - \frac{r_A/r_B}{\ln(r_A/r_B)} \right) \quad (2.48)$$

where $\tau < 4.18$ predicts perovskite formation across a wide range of compounds with 91% accuracy.³⁰

2.3.3: Related materials

The huge compositional space in the 3D variants gives rise to facile tunability of parameters, as is discussed in the following section and is expanded further by an extensive variety of other perovskite-related materials. These include perovskite-like quasi-2D layered structures (Ruddlesden-Popper, Aurivilius, Dion-Jacobson and more⁴⁷) with many having interesting optoelectronic properties.⁴⁸ In these compounds, sheets of metal halide octahedra (continuous in two dimensions) are spaced apart by larger cations, creating multiple quantum well structures.⁴⁹ These structures can be classified in simple terms by the ‘*n*-dimensionality’ ($n = 1, 2, \dots$) of the quasi-2D structure, meaning the number of metal halide octahedral layers between organic spacer layers, as shown in Figure 26. Consequently, these quantum wells have related excitonic effects contingent upon the organic layer spacing (which can also be functionalised) and configuration, as well as the rigidity of the organic molecules in these structures.^{50,51} Mixed-phase 2D-3D compositions have also attracted significant research for both novel optoelectronic devices, and as a highly effective strategy for grain boundary and interface passivation.^{52,53} That such mixed-phase films can be fabricated with relative ease is a unique benefit of hybrid perovskite materials, although the long-term phase stability of these mixtures remains unclear.

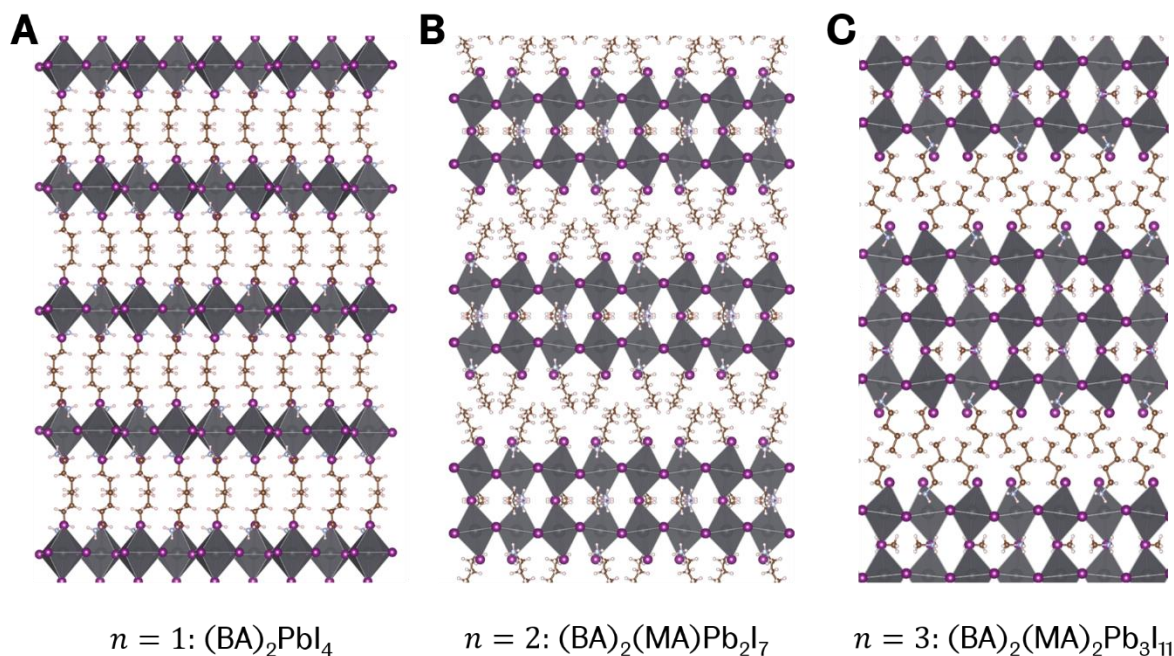


Figure 26: Illustration of the A) $n = 1$ B) $n = 2$ and C) $n = 3$ layered quasi-2D butylammonium(BA) methylammonium lead iodide Ruddlesden-Popper phases. Renders produced using Crystallographic Information Files in refs. ^{50,54,55}.

A wide range of so-called low-dimensional “0D” and “1D” compounds are also reported. These are of importance to this work primarily as either undesirable secondary phases during film formation or degradation,^{56–59} or as intermediate phases during crystallisation with intercalated solvent molecules.^{60,61} Some examples of these 1D phases are shown in Figure 27.

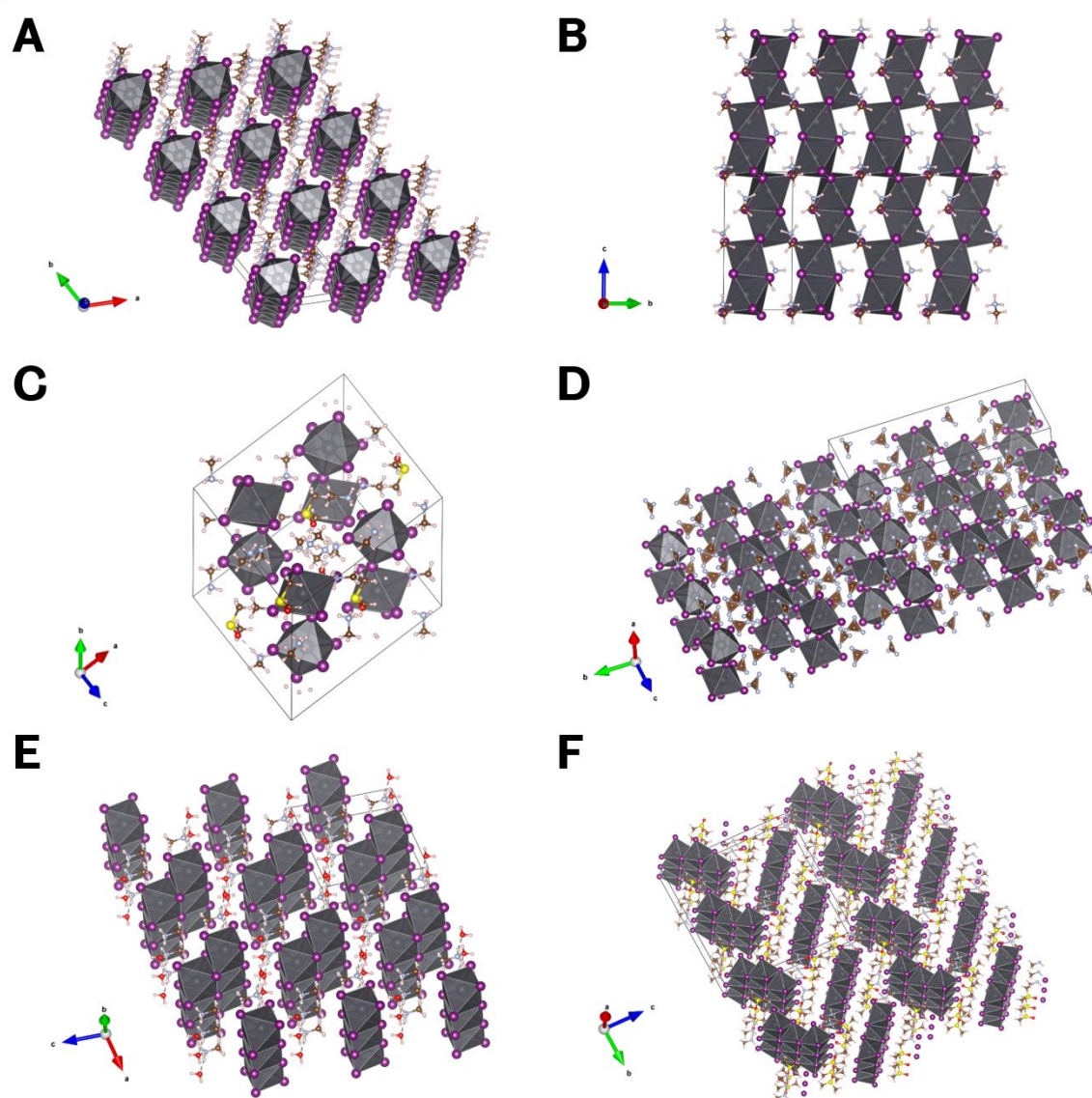


Figure 27: Structural diversity of 1D and quasi-2D perovskite-related materials, rendered from CIFs in the cited references. A) MAPbI_3 delta phase, or 2H polytype, a 1D compound with face-sharing PbI_3^- iodoplumbate chains charge neutralised by intercalated organic cations.⁶² B) 4H polytype, a similar compound with an alternating arrangement of face- (as with 2H) and then corner-sharing octahedra.⁶² C) $(\text{MA})_3\text{PbI}_5 \cdot \text{DMF}$, a fully corner-sharing 1D intermediate structure with Pb-deficient stoichiometry compared to a 3D structure, and intercalated DMF solvent molecules.⁶³ D) $(\text{Gua})_2\text{PbI}_4$, a quasi-2D corner-sharing phase forming corrugated sheets spaced by guanidinium cations.⁶⁴ E) $\text{MAPbI}_3 \cdot \text{H}_2\text{O}$, the reversibly formed 1D ‘monohydrate’ degradation phase, comprised of a mixture of face- and edge- sharing octahedra.⁶⁵ F) $(\text{MA})_2\text{Pb}_3\text{I}_8 \cdot 2\text{DMSO}$, a commonly formed 1D intermediate phase with strongly-coordinating DMSO intercalated between 3-wide octahedral ribbons with an alternating motif, in contrast to the co-aligned monohydrate.⁶³

2.3.4: Perovskite solar cells

Certain underlying material properties make metal-halide PSCs very good materials for solar applications. The valence bands in these materials are formed of hybridised metal-halide orbitals (coupling between Pb 6s and I 5p antibonding orbitals in the case of lead iodide perovskites, with a low density of states at the VBM), with the conduction band forming from empty Pb 6p orbitals (with the A-site cation only indirectly contributing to the band edges through stabilising the metal halide lattice).^{66–68} This leads to a direct bandgap, giving ideal optical absorption properties – a sharp and steep absorption onset, and good luminescence properties. In addition, the antibonding character of the valence band means that, while the formation energy of some vacancy or interstitial defects is low, the defects are formed close to the band edges - the density of intra-band or deep trap states is very low in the perovskite bulk.^{69–71} In other words, in many typical compositions, the defects are relatively electronically benign and so have little impact on performance (high “defect tolerance”). As a result, perovskites also exhibit long carrier diffusion lengths and carrier lifetimes.⁷² Halide perovskite materials generally have a high dielectric constant.^{73,74} This results in rapid exciton dissociation (electron-hole pairs formed directly) and charge screening, which contributes to a low capture cross-section by electronically active recombination centres, leading to low trap assisted recombination.⁴⁸

The huge range of possible bandgaps (highlighted in Figure 28) also introduces the potential for multi-junction architectures which can overcome the detailed balance limit.⁷⁵ By combining a wider bandgap perovskite top cell (capturing the high energy portion of the solar spectrum) with a lower bandgap bottom cell (eg silicon, 1.12 eV), the large carrier thermalisation losses can be reduced. This has been demonstrated with high efficiency perovskite-perovskite,^{76,77} perovskite-silicon,^{78–80} perovskite-CIGS,^{81–83} and perovskite-organic^{84,85} cells.

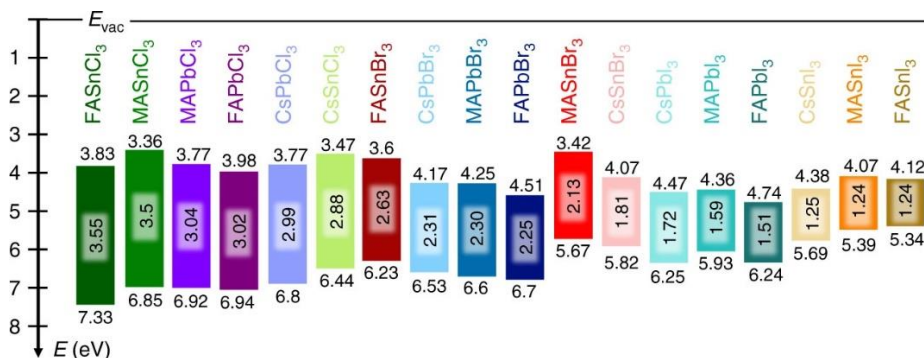


Figure 28: Energy level diagrams for unalloyed metal halide perovskites using FA, MA and Cs cations, reproduced from ref. ⁶⁷ under Creative Commons licence. The energies E_v (top) and E_c (bottom) are marked with respect to the vacuum energy and the optical E_g bandgaps (middle) are also shown in eV units.

2.3.5: Potential for solution processing

Beyond the unique physics, the study of perovskites is further motivated because the materials can be produced from a variety of scalable methods, including solution processing methods which can allow for R2R coating (Figure 29). These methods are possible due to the ionicity of the crystal,⁸⁶ allowing for crystallisation at room temperature in some cases. The solubility of the inorganic lead halide species is enhanced by the addition of the organo-halide, which makes additional halide species available for the formation of metal-halide complexes in solution.^{87,88} Perovskite research has benefitted greatly from experience in related established fields such as DSSCs, OPVs and printed electronics in the huge range of successfully employed deposition techniques. Particular success has been with contact coating methods such as slot-die^{89,90} and blade coating,⁹¹ as well as non-contact methods like spray-coating and inkjet printing,^{92,93} with spray-coating being a particular speciality in our labs since the first reported spray-coated perovskite in 2014.⁹⁴

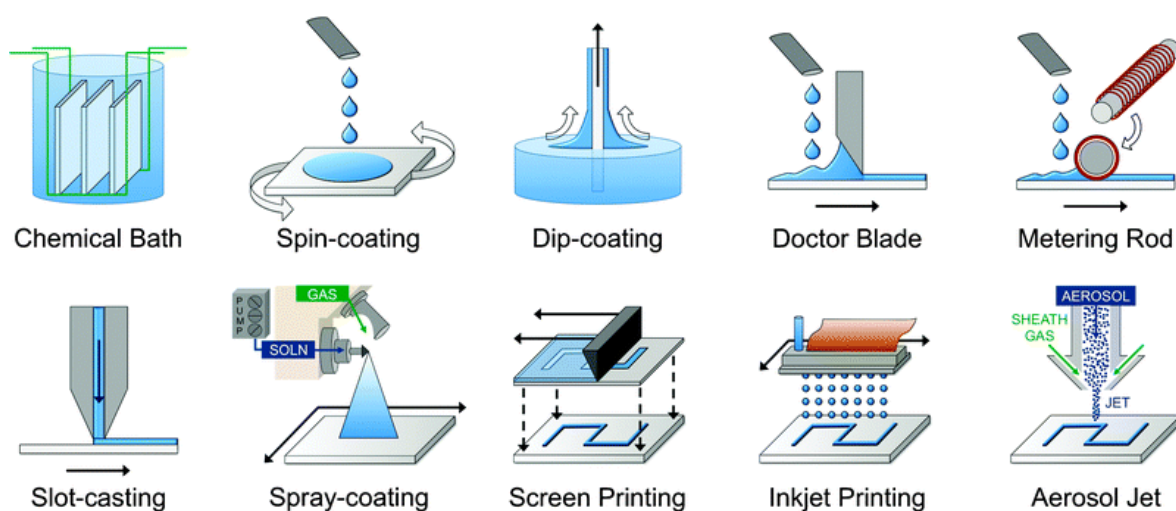


Figure 29: Various scalable solution processing deposition methods which can be used for layer manufacture in PSCs. Reprinted with permission from ref. 95.

2.3.6: The early years

The potential for perovskites in photovoltaic applications was recognised by Miyasaka and colleagues from 2006 onwards, where MAPbBr_3 was used in a novel photoelectrochemical cell. Here the perovskite was used as an equivalent to a sensitizer on electron-accepting mesoporous titanium dioxide (TiO_2) in a dye-sensitizing architecture, achieving an efficiency of 2.2%.⁹⁶ Upon publication in 2009, the scope of their work had extended to MAPbI_3 and an efficiency of 3.8% has been reached.⁹⁷ Nevertheless, these early cells showed poor stability, with the perovskite quickly degrading in the liquid electrolyte.⁹⁸ Progress in efficiency and

stability was made in 2011 by Park and co-workers by changing the electrolyte formulation, surface treating the TiO_2 and by using perovskite nanoparticles, which led to 6.5% efficiency.⁹⁹ The continued issue of degradation motivated the inclusion of a solid-state hole transport material (HTM), spiro-OMeTAD, which was developed for organic LEDs and later transferred for use in solid state DSSCs. In 2012 Grätzel and colleagues reached 9.7% efficiency using an architecture in which perovskite covers a mesoporous scaffold of TiO_2 , residing on the surface, followed by infiltration of the HTM throughout; as expected there was enhanced stability.¹⁰⁰

Several simultaneous breakthroughs occurred with the work of Snaith and co-workers soon after in mid-2012.¹⁰¹ By swapping TiO_2 to an electrically-insulating Al_2O_3 scaffold, they surprisingly reached higher device efficiencies peaking at 9.7%, which demonstrated that the scaffold was not critical for electron extraction, challenging the prevailing wisdom of the necessity for mesoporous layers in perovskite solar cells. This demonstrated the perovskite was able to act beyond the role of a sensitizer and could itself transport charge carriers to the cell terminals.¹⁰² This seminal work also presented planar configuration (scaffold-free) PSCs for the first time, as well as compositional variation with a mixed-halide perovskite $\text{CH}_3\text{NH}_3\text{PbI}_{3-x}\text{Cl}_x$ with improved carrier mobility and stability. A further improvement to 12.0% PCE was realised by the combined efforts of the groups of Seok and Grätzel, with a mesoporous layer combined with perovskite capping layer and a selection of HTMs including spiro-OMeTAD, but with the best performance instead using poly-triarylamine (PTAA).¹⁰³ Seok's group at KRICT pushed this further using a mixed halide composition $\text{MAPbI}_{3-x}\text{Br}_x$.¹⁰⁴ Almost simultaneously, Snaith's group at Oxford University achieved 12.3% efficiency using an optimised low temperature planar architecture with a similar perovskite to their earlier paper.¹⁰⁵

2.3.7: Novel crystallisation approaches

Soon after this, Burschka *et al.* based at EPFL achieved a certified 14.1% efficient device using a sequential, or *two-step*, deposition protocol.¹⁰⁶ For MAPbI_3 , this method involves the initial formation of a PbI_2 layer which then has MAI deposited on it, in this case through dipping. Following dipping, the MAI infiltrates the PbI_2 lattice forming a high-quality perovskite layer. Since then, this process has been repeated through various combinations of deposition protocols for the lead halide first step and organo-halide second step.

The group of Seok at KRICT next took the certified record efficiency with a 16.2% bilayer architecture, utilising PTAA as a hole transporter, and utilising the structure of the intermediate adduct MAI- PbI_2 -DMSO.^{107,108} These intermediate adduct structures (as illustrated in Figure 27) have proved a common feature in high efficiency solar cells, where the

adduct formation is dependent on the physical and chemical properties of the solvents and their mixtures.^{109,110} In general, the adduct phase is achieved through the use of an “antisolvent quench” in the one-step deposition protocol. This quenching rapidly removes some of the volatile solvent to induce supersaturation of the solution and initiate crystallisation.¹¹¹ Solvent removal can also be achieved using air flows, either by vacuum or gas quenching, which are more suitable for scalable processing.

Taking a different approach that avoids the use of solvents entirely, towards the end of 2013 Liu *et al.* from Oxford University used a dual source vapour-deposition (thermal evaporation) system to develop a highly uniform perovskite active layer with 15.4% efficiency.¹¹² This novel processing route demonstrated scalability using a mature technology with widespread industrial usage, if losing some of the benefit of solution processing (additives and solution engineering, rapid processing). Several recent works have shown PCEs over 20%, albeit with slow film growth rates that are most likely impractical at scale (process durations of 100-120 minutes).^{113,114} Interestingly, these devices exhibit apparently enhanced stability over comparable solution-processed devices, which may be related to the avoidance of trapped solvent, cation degradation, stoichiometric changes (explored in Chapter 5) or other contamination introduced during solution processing.^{115–118}

2.3.8: Diversifying compositions for high efficiency

Early work by Eperon *et al.* had recognised the potential for usage of formamidinium (FA) as an alternative cation to MA; this narrowly increased the record solution-processed planar architecture efficiency at the time to 14.2%.¹¹⁹ Their work identified that using a mixed iodide-bromide system allowed for a broad range of mid-to-high bandgap perovskites. In early 2015, building on the use of alternative cations to methylammonium (which by this point had been identified as temperature unstable above 85 °C¹²⁰) KRICT developed a mixed-cation, mixed-halide perovskite of the form $(\text{FAPbI}_3)_{0.83}(\text{MAPbBr}_3)_{0.17}$. With this they achieved over 18% efficiency, combining the temperature stability of the FA perovskites and the perovskite structural stability of the MA perovskites. In 2016, advancement came from partial inclusion of Cs in mixed cation recipes to stabilise the structure and achieve 21.1% efficiency by Saliba, Matsui and co-workers at EPFL, resulting in a *triple-cation* composition which became the cornerstone for the most commonly used formulations today.¹²¹ An overview of these various common alloyed compositions is shown in Figure 30.

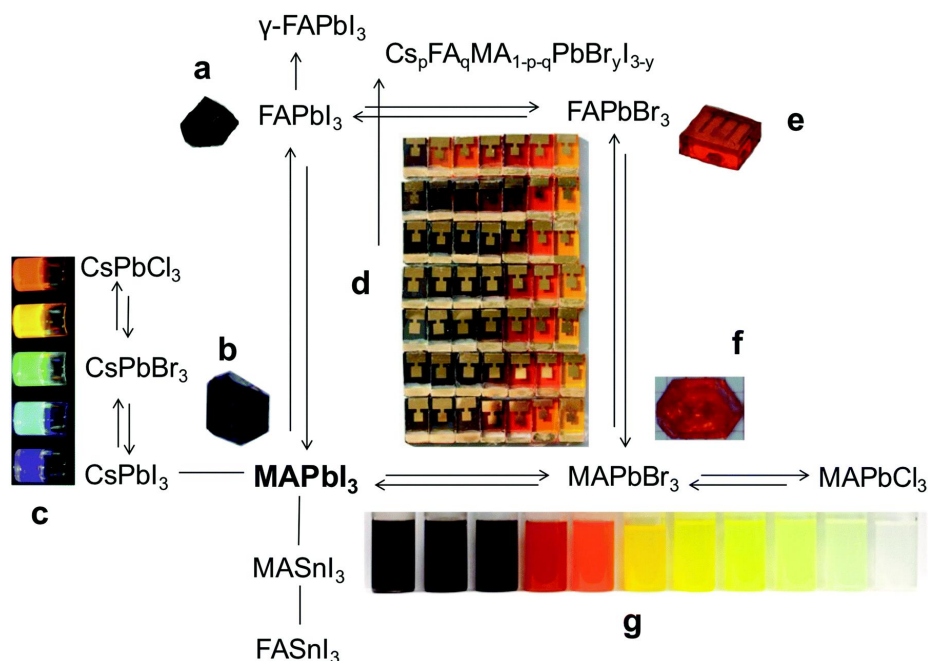


Figure 30: Some of the many photoactive halide perovskite materials and their bandgap tunability, composite image reproduced from ref. 122 with permission. Insets show (a) single crystal of FAPbI₃,¹²³ (b) single crystal of MAPbI₃,¹²⁴ (c) colloidal solutions of CsPbX₃ (X = Cl, Br, I) perovskites,¹²⁵ (d) solar cells of 49 different compositions in the MA_xFA_{1-x}Pb(I_yBr_{1-y})₃ compositional space,¹²⁶ (e) single crystal of FAPbBr₃,¹²³ (f) single crystal of MAPbBr₃,¹²⁴ and (g) colloidal nanocrystals of MAPbX₃ (X = Cl, Br, I) perovskites.¹²⁷

The seminal work using Cs was later extended to a *quadruple cation* absorber with the small addition of rubidium (Rb), and a stabilised 21.6% PCE was reached.¹²⁸ This is perhaps surprising as Rb is too small to form a phase pure iodide composition (Bartel $\tau = 6.07$, well over the required $\tau = 4.18$). The even smaller potassium (K) ion has also been shown to have benefit in passivating the perovskite, suggesting these alkali metal species may be playing a more significant role as additives rather than structural cations.¹²⁹ The role of the Cs and Rb salts has since been identified to be related to the crystallisation of the film more than the formed composition.^{130,131} This seems to result in both the direct crystallisation of the 3D perovskite phase rather than any polytypic phases, and gives films with more uniform distribution of halide species (better alloying) where the concentration of salts is well optimised.¹³² The case of K inclusion is less clear, however there is evidence that this forms a surface passivation layer which inhibits the formation of surface traps,^{18,133} but may also be a cause of film and device-level instability.¹³⁴

More recently, for single-junction devices the field has returned to FA- and I-rich compositions which have a lower E_g of ~1.4 eV that is closer to the detailed balance limit (discussed in Figure 19) than more Br- and MA-rich compositions such as the popular triple-cation approach (E_g ~1.55-1.7 eV). This shift arguably began when researchers at KRICT developed the DMSO adduct

technique from their previous work, to form pure FAPbI₃ perovskites via intramolecular exchange and achieved over 20% efficiency.¹³⁵ Previously, FAPbI₃ had been thought to be overly phase-unstable to a 2H polytype phase (δ -FAPbI₃),¹¹⁹ where the instability is explained by the large size of the FA cation, resulting in a less-than-ideal Goldschmidt tolerance factor $t = 0.987$. More recently, several innovations by KRICT, MIT and UNIST have resulted in the world record single-junction perovskite cell hitting 25.5% PCE.¹⁰⁸ Of the available reports at the time of writing, all devices over 24% have relied on well-engineered FAPbI₃ derived materials with small amounts of additives to influence the crystallization and passivate the perovskite.^{53,136–138}

2.3.9: Device architectures

Taking stock of the field, Figure 31 shows the four most prevalent single-junction device architectures. These configurations are defined based on the doping character of the charge extraction layers and their arrangement with respect to the absorber with the n-type/p-type layer above or below the intrinsic perovskite (see section 2.2.3). Each architecture has advantages and shortcomings. *Standard architecture*, *n-i-p* mesoporous devices typically use an inorganic electron-transporting layer (ETL) such as TiO₂ with an additional mesoporous layer in which the perovskite is infiltrated. This may minimise the required electron diffusion length, or have some stability benefit in distributing the n-i junction.^{139–141} These devices have achieved the highest efficiencies so far, however, using metal oxides for the compact and mesoporous ETLs generally requires high temperature processing. This is problematic for scalability, despite some progress in this area.^{142–144} Planar *n-i-p* perovskite devices remove the mesoporous layer but use otherwise similar materials, typically topped with spiro-OMeTAD hole-transporting later (HTL) and an Au or Ag anode. So-called *inverted architecture* (*p-i-n*) planar devices generally use organic transport layers with experience drawn from OPVs such as PTAA or poly-TPD, or a hole-transporting metal oxide (NiO) as the base layer onto which the perovskite is deposited.^{145–147} Whilst historically lower efficiencies have been achieved with this architecture, recent progress with self-assembled monolayer materials (SAMs) as HTLs has shown huge potential, with these ultrathin transport layers exhibiting incredible charge-extraction characteristics.^{80,148,149} The possible layers in inverted and standard architectures are largely driven by optical management and processing, with light transparency and insolubility in any of the perovskite layer solvents being required for the substrate transport layer.

The HTM-free n-i-p mesoscopic design is an alternative, scalable, stable perovskite design used in modules.¹⁵⁰ Here, TiO₂/SnO₂ and ZrO₂ layers are typically deposited from slurries by screenprinting, where a thick carbon electrode capping layer mitigates extrinsic stability issues

(such as moisture ingress).^{151,152} The perovskite is then drop cast to infiltrate the whole stack, resulting in a much thicker active layer than is typical in perovskite solar cells. Here, the metal oxide layers are still annealed at high temperature for 2 hours, although recently there has been progress in using a near-infrared fast heating procedure to reduce this,¹⁵³ as has been a research focus in this thesis in Chapter 4. The precise mechanism of operation in these cells is unclear, however it has been suggested that the front of the cell has a high electron density and holes are more uniformly distributed throughout the active layer, gradually diffusing to the back electrode of the device.¹⁵⁴

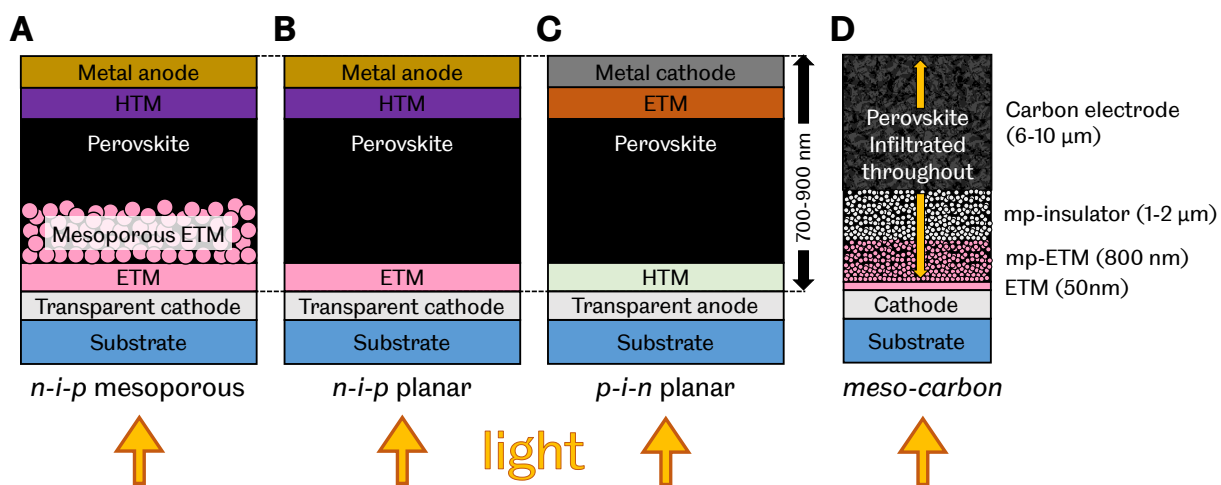


Figure 31: Common PSC device architectures. A) *n-i-p* mesoporous architecture, with typically $\text{TiO}_2/\text{mp-TiO}_2$ ETM, spiro-OMeTAD HTM and Au/Ag anode. B) *n-i-p* planar architecture usually with SnO_2 ETM and ITO transparent cathode. C) *p-i-n* ("inverted") planar architecture with PTAA or SAM HTM, fullerene ETM Al/Ag cathode. D) HTM-free *n-i* mesoscopic architecture. Inspired by refs 155 and 156.

2.4: References

- (1) Charles Kittel. *Introduction to Solid State Physics, 8th Edition*; 2004.
- (2) Hook, J. R.; Hall, H. E. *Solid State Physics, 2nd Edition*; Wiley, 1991.
- (3) Nelson, J. *The Physics of Solar Cells*; Imperial College Press: London, 2003.
- (4) Mullin, J. W. *Crystallization, 4th Edition*; Butterworth-Heinemann, 2001.
- (5) Flowers, P.; Theopold, K.; Langley, R.; Robinson, W. R. Chapter 6.3 Development of Atomic Theory. In *Chemistry 2e*; OpenStax: Houston, Texas, 2019.
- (6) Dirac, P. The Quantum Theory of the Electron. *Proc. R. Soc. London. Ser. A. Contain. Pap. a Math. Phys. Character Contain. Pap. a Math. Phys. Character* **1928**, *117* (778), 610–624. <https://doi.org/10.1098/rspa.1928.0023>.
- (7) Dirac, P. Quantum Mechanics of Many-Electron Systems. *Proc. R. Soc. London. Ser. A. Contain. Pap. a Math. Phys. Character* **1929**, *123* (792), 714–733. <https://doi.org/10.1098/rspa.1929.0094>.
- (8) Claudio, E. S.; Godwin, H. A.; Magyar, J. S. Fundamental Coordination Chemistry, Environmental Chemistry, and Biochemistry of Lead(II). In *Progress in Inorganic Chemistry, Volume 51*; John Wiley & Sons, Inc.: New York, USA, 2002; Vol. 51, pp 1–144. <https://doi.org/10.1002/0471267287.ch1>.
- (9) Pyykkö, P. Relativistic Effects in Chemistry: More Common than You Thought. *Annu. Rev. Phys. Chem.* **2012**, *63*, 45–64. <https://doi.org/10.1146/annurev-physchem-032511-143755>.
- (10) Flowers, P.; Theopold, K.; Langley, R.; Robinson, W. R. Chapter 8.4: Molecular Orbital Theory. In *Chemistry*; OpenStax: Houston, Texas, 2015.
- (11) Klug, H. P.; Alexander, L. E. *X-Ray Diffraction Procedures: For Polycrystalline and Amorphous Materials, 2nd Edition*; Wiley, 1974.
- (12) Frankenheim, M. L. Die Gesetze Der Hemiedrie. *Ann. der Phys. und Chemie* **1842**, *132* (6), 275–294. <https://doi.org/10.1002/andp.18421320608>.
- (13) Bravais, A. Sur Les Propriétés Géométriques Des Assemblages de Points Régulièrement Distribués Dans l'espace. *Comptes Rendus des Séances de l'Académie des Sciences*. Gauthier-Villars: Paris 1848, pp 601–604.
- (14) Bragg, P. W. H.; Bragg, W. L. The Reflection of X-Rays by Crystals. *Proc. R. Soc. London. Ser. A. Contain. Pap. a Math. Phys. Character* **1913**, *88* (605), 428–438. <https://doi.org/10.1098/rspa.1913.0040>.
- (15) Becquerel, E. Mémoire Sur Les Effets Électriques Produits Sous l'influence Des Rayons Solaires. *Comptes rendus l'académie des Sci.* **1839**, *9*, 561–567.
- (16) ASTM G173-03(2020) Standard Tables for Reference Solar Spectral Irradiances: Direct Normal and Hemispherical on 37° Tilted Surface. West Conshohocken, Philadelphia 2020. <https://doi.org/10.1520/G0173-03R20>.
- (17) Shockley, W.; Queisser, H. J. Detailed Balance Limit of Efficiency of P-n Junction Solar Cells. *J. Appl. Phys.* **1961**, *32* (3), 510–519. <https://doi.org/10.1063/1.1736034>.
- (18) Stolterfoht, M.; Grischek, M.; Caprioglio, P.; Wolff, C. M.; Gutierrez-Partida, E.; Peña-Camargo, F.; Rothhardt, D.; Zhang, S.; Raoufi, M.; Wolansky, J.; Abdi-Jalebi, M.; Stranks, S. D.; Albrecht, S.; Kirchartz, T.; Neher, D. How To Quantify the Efficiency Potential of Neat Perovskite Films: Perovskite Semiconductors with an Implied Efficiency Exceeding 28%. *Adv. Mater.* **2020**, 2000080. <https://doi.org/10.1002/adma.202000080>.
- (19) Kirchartz, T.; Márquez, J. A.; Stolterfoht, M.; Unold, T. Photoluminescence-Based Characterization of Halide Perovskites for Photovoltaics. *Adv. Energy Mater.* **2020**, *1904134*, 1904134. <https://doi.org/10.1002/aenm.201904134>.
- (20) Bowman, A. R.; Anaya, M.; Greenham, N. C.; Stranks, S. D. Quantifying Photon Recycling in Solar Cells and Light-Emitting Diodes: Absorption and Emission Are Always Key. *Phys. Rev. Lett.* **2020**, *125* (6), 67401. <https://doi.org/10.1103/PhysRevLett.125.067401>.
- (21) Miller, O. D.; Yablonovitch, E.; Kurtz, S. R. Strong Internal and External Luminescence as Solar Cells Approach the Shockley-Queisser Limit. *IEEE J. Photovoltaics* **2012**, *2* (3), 303–311. <https://doi.org/10.1109/JPHOTOV.2012.2198434>.
- (22) Stolterfoht, M.; Caprioglio, P.; Wolff, C. M.; Márquez, J. A.; Nordmann, J.; Zhang, S.; Rothhardt, D.; Hörmann, U.; Amir, Y.; Redinger, A.; Kegelmann, L.; Zu, F.; Albrecht, S.; Koch, N.; Kirchartz, T.; Saliba, M.; Unold, T.; Neher, D. The Impact of Energy Alignment and Interfacial Recombination on the Internal and External Open-Circuit Voltage of Perovskite Solar Cells. *Energy Environ. Sci.* **2019**, 1–27. <https://doi.org/10.1039/C9EE02020A>.
- (23) Wolff, C. M.; Caprioglio, P.; Stolterfoht, M.; Neher, D. Nonradiative Recombination in Perovskite Solar Cells: The Role of Interfaces. *Adv. Mater.* **2019**, *1902762*, 1902762. <https://doi.org/10.1002/adma.201902762>.
- (24) Smets, A.; Jäger, K.; Isabella, O.; Swaaij, R. van; Zeman, M. *Solar Energy: The Physics and Engineering of Photovoltaic Conversion, Technologies and Systems*; UIT Cambridge, 2016.
- (25) Caprioglio, P.; Wolff, C. M.; Sandberg, O. J.; Armin, A.; Rech, B.; Albrecht, S.; Neher, D.; Stolterfoht, M. On the Origin of the Ideality Factor in Perovskite Solar Cells. *Adv. Energy Mater.* **2020**, *10* (27), 1–9. <https://doi.org/10.1002/aenm.202000502>.
- (26) Calado, P.; Burkitt, D.; Yao, J.; Troughton, J.; Watson, T. M.; Carnie, M. J.; Telford, A. M.; Regan, B. C. O.; Nelson, J.; Barnes, P. R. F. Identifying Dominant Recombination Mechanisms in Perovskite Solar Cells by Measuring the Transient Ideality Factor. *Phys. Rev. Appl.* **2019**, *10* (1), 1. <https://doi.org/10.1103/PhysRevApplied.11.044005>.
- (27) Rose, G. Beschreibung Einiger Neuen Mineralien Des Urals. *Ann. Phys.* **1840**, *126* (8), 652–656. <https://doi.org/10.1002/andp.18401260807>.
- (28) Tschauer, O.; Chi, M.; Beckett, J. R.; Prescher, C.; Prakapenka, V. B.; Rossman, G. R. Discovery of Bridgmanite, the Most Abundant Mineral in Earth, in a Shocked Meteorite. *Science* (80-.). **2014**, *346* (6213), 1100–1102. <https://doi.org/10.1126/science.1259369>.
- (29) Goldschmidt, V. M. Die Gesetze Der Krystallochemie. *Naturwissenschaften* **1926**, *14* (21), 477–485. <https://doi.org/10.1007/BF01507527>.
- (30) Bartel, C. J.; Sutton, C.; Goldsmith, B. R.; Ouyang, R.; Musgrave, C. B.; Ghiringhelli, L. M.; Scheffler, M. New Tolerance Factor to Predict the Stability of Perovskite Oxides and Halides. *Sci. Adv.* **2019**, *5* (2), 1–10. <https://doi.org/10.1126/sciadv.aav0693>.
- (31) Glazer, A. M. The Classification of Tilted Octahedra in Perovskites. *Acta Crystallogr. Sect. B Struct. Crystallogr. Cryst. Chem.* **1972**, *28* (11), 3384–3392. <https://doi.org/10.1107/S0567740872007976>.

- (32) Wells, H. L. Über Die Cäsium- Und Kalium- Bleihalogenide. *Zeitschrift für Anorg. und Allg. Chemie* **1893**, *3* (1), 195–210. <https://doi.org/10.1002/zaac.18930030124>.
- (33) Møller, C. K.; Marstrander, A. The Structure of White Cesium Lead (II) Bromide, CsPbBr₃. **1966**, *5* (5).
- (34) Weber, D. CH₃NH₃PbX₃, a Pb(II)-System with Cubic Perovskite Structure. *Z. Naturforsch* **1978**, *1445* (August 1978), 1443–1445.
- (35) Weber, D. CH₃NH₃SnBr_{3-x} (x = 0–3), a Sn(II)-System with Cubic Perovskite Structure. *Z. Naturforsch* **1978**, *33b*, 862–865.
- (36) Mitzi, D. B.; Feild, C. A.; Harrison, W. T. A.; Guloy, A. M. Conducting Tin Halides with a Layered Organic-Based Perovskite Structure. *Nature* **1994**, *369* (6480), 467–469. <https://doi.org/10.1038/369467a0>.
- (37) Mitzi, D. B.; Feild, C. a.; Schlesinger, Z.; Laibowitz, R. B. Transport, Optical, and Magnetic Properties of the Conducting Halide Perovskite CH₃NH₃SnI₃. *J. Solid State Chem.* **1995**, *114* (1), 159–163. <https://doi.org/10.1006/jssc.1995.1023>.
- (38) Liang, K.; Mitzi, D. B.; Prikas, M. T. Synthesis and Characterization of Organic–Inorganic Perovskite Thin Films Prepared Using a Versatile Two-Step Dipping Technique. *Chem. Mater.* **1998**, *10* (1), 403–411. <https://doi.org/10.1021/cm970568f>.
- (39) Mitzi, D. B. Templating and Structural Engineering in Organic–Inorganic Perovskites. *J. Chem. Soc. Dalton Trans.* **2001**, No. 1, 1–12. <https://doi.org/10.1039/b007070j>.
- (40) Chondroudis, K.; Kagan, C. R.; Mitzi, D. B. Organic – Inorganic Electronics. **2001**, *45* (1), 29–45.
- (41) Mitzi, D. B. Synthesis, Structure, and Properties of Organic-Inorganic Perovskites and Related Materials. In *Progress in Inorganic Chemistry*; 1999; Vol. 48, pp 1–122. <https://doi.org/10.1002/9781118148235>.
- (42) Breternitz, J.; Lehmann, F.; Barnett, S. A.; Nowell, H.; Schorr, S. Role of the Iodide–Methylammonium Interaction in the Ferroelectricity of CH₃NH₃PbI₃. *Angew. Chemie - Int. Ed.* **2020**, *59* (1), 424–428. <https://doi.org/10.1002/anie.201910599>.
- (43) Butler, K. T. The Chemical Forces Underlying Octahedral Tilting in Halide Perovskites. *J. Mater. Chem. C* **2018**, *6* (44), 12045–12051. <https://doi.org/10.1039/c8tc02976h>.
- (44) Shannon, R. D. Revised Effective Ionic Radii and Systematic Studies of Interatomic Distances in Halides and Chalcogenides. *Acta Crystallogr. Sect. A* **1976**, *32* (5), 751–767. <https://doi.org/10.1107/S0567739476001551>.
- (45) Travis, W.; Glover, E. N. K.; Bronstein, H.; Scanlon, D. O.; Palgrave, R. G. On the Application of the Tolerance Factor to Inorganic and Hybrid Halide Perovskites: A Revised System. *Chem. Sci.* **2016**, *7* (7), 4548–4556. <https://doi.org/10.1039/c5sc04845a>.
- (46) Filip, M. R.; Giustino, F. The Geometric Blueprint of Perovskites. *Proc. Natl. Acad. Sci. U. S. A.* **2018**, *115* (21), 5397–5402. <https://doi.org/10.1073/pnas.1719179115>.
- (47) Marchenko, E. I.; Fateev, S. A.; Petrov, A. A.; Korolev, V. V.; Mitrofanov, A.; Petrov, A. V.; Goodilin, E. A.; Tarasov, A. B. Database of Two-Dimensional Hybrid Perovskite Materials: Open-Access Collection of Crystal Structures, Band Gaps, and Atomic Partial Charges Predicted by Machine Learning. *Chem. Mater.* **2020**, *32* (17), 7383–7388. <https://doi.org/10.1021/acs.chemmater.0c02290>.
- (48) Park, N.-G.; Grätzel, M.; Miyasaka, T. *Organic-Inorganic Halide Perovskite Photovoltaics*; 2016. https://doi.org/10.1007/978-3-319-35114-8_4.
- (49) Stoumpos, C. C.; Cao, D. H.; Clark, D. J.; Young, J.; Rondinelli, J. M.; Jang, J. I.; Hupp, J. T.; Kanatzidis, M. G. Ruddlesden-Popper Hybrid Lead Iodide Perovskite 2D Homologous Semiconductors. *Chem. Mater.* **2016**, *28* (8), 2852–2867. <https://doi.org/10.1021/acs.chemmater.6b00847>.
- (50) Stoumpos, C. C.; Malliakas, C. D.; Kanatzidis, M. G. Semiconducting Tin and Lead Iodide Perovskites with Organic Cations: Phase Transitions, High Mobilities, and Near-Infrared Photoluminescent Properties. *Inorg. Chem.* **2013**, *52* (15), 9019–9038. <https://doi.org/10.1021/ic401215x>.
- (51) Seitz, M.; Magdaleno, A. J.; Alcázar-Cano, N.; Meléndez, M.; Lubbers, T. J.; Walraven, S. W.; Pakdel, S.; Prada, E.; Delgado-Buscalioni, R.; Prins, F. Exciton Diffusion in Two-Dimensional Metal-Halide Perovskites. *Nat. Commun.* **2020**, *11* (1), 1–8. <https://doi.org/10.1038/s41467-020-15882-w>.
- (52) Tong, J.; Song, Z.; Kim, D. H.; Chen, X.; Chen, C.; Palmstrom, A. F.; Ndione, P. F.; Reese, M. O.; Dunfield, S. P.; Reid, O. G.; Liu, J.; Zhang, F.; Harvey, S. P.; Li, Z.; Christensen, S. T.; Teeter, G.; Zhao, D.; Al-Jassim, M. M.; van Hest, M. F. A. M.; Beard, M. C.; Shaheen, S. E.; Berry, J. J.; Yan, Y.; Zhu, K. Carrier Lifetimes of >1 Ms in Sn-Pb Perovskites Enable Efficient All-Perovskite Tandem Solar Cells. *Science (80-.)*, **2019**, *7911* (April), eaav7911. <https://doi.org/10.1126/science.aav7911>.
- (53) Kim, G.; Min, H.; Lee, K. S.; Lee, D. Y.; Yoon, S. M.; Seok, S. I. Impact of Strain Relaxation on Performance of A-Formamidinium Lead Iodide Perovskite Solar Cells. *Science (80-.)*, **2020**, *370* (6512), 108–112. <https://doi.org/10.1126/science.abc4417>.
- (54) Billing, D. G.; Lemmerer, A. Synthesis, Characterization and Phase Transitions in the Inorganic–Organic Layered Perovskite-Type Hybrids [(C_nH_{2n} + 1NH₃)₂PbI₄], n = 4, 5 and 6. *Acta Crystallogr. Sect. B Struct. Sci.* **2007**, *63* (5), 735–747. <https://doi.org/10.1107/S0108768107031758>.
- (55) Paritmongkol, W.; Dahod, N. S.; Stollmann, A.; Mao, N.; Settens, C.; Zheng, S.; Tisdale, W. A. Synthetic Variation and Structural Trends in Layered Two-Dimensional Alkylammonium Lead Halide Perovskites. *Chem. Mater.* **2019**, *31* (15), 5592–5607. <https://doi.org/10.1021/acs.chemmater.9b01318>.
- (56) Gratia, P.; Zimmermann, I.; Schouwink, P.; Yum, J.-H.; Audinot, J.-N.; Sivula, K.; Wirtz, T.; Nazeeruddin, M. K. The Many Faces of Mixed Ion Perovskites: Unraveling and Understanding the Crystallization Process. *ACS Energy Lett.* **2017**, 2686–2693. <https://doi.org/10.1021/acsenenergylett.7b00981>.
- (57) Jong, U.-G.; Yu, C.-J.; Ri, G.-C.; Walsh, A.; Barnes, P. R. F. Influence of Water Intercalation and Hydration on Chemical Decomposition and Ion Transport in Methylammonium Lead Halide Perovskites. *J. Mater. Chem. A Mater. energy Sustain.* **2017**, *00*, 1–8. <https://doi.org/10.1039/C7TA09112E>.
- (58) Marchezi, P. E.; Therézio, E. M.; Szostak, R.; Loureiro, H. C.; Bruening, K.; Gold-Parker, A.; Melo, M. A.; Tassone, C. J.; Tolentino, H. C. N.; Toney, M. F.; Nogueira, A. F. Degradation Mechanisms in Mixed-Cation and Mixed-Halide Cs: XFA1-XPb(BryI- y)₃ Perovskite Films under Ambient Conditions. *J. Mater. Chem. A* **2020**, *8* (18), 9302–9312. <https://doi.org/10.1039/d0ta01201g>.
- (59) Mundt, L. E.; Schelhas, L. T. Structural Evolution During Perovskite Crystal Formation and Degradation: In Situ and Operando X-Ray Diffraction Studies. *Adv. Energy Mater.* **2019**, *1903074*, 1903074. <https://doi.org/10.1002/aenm.201903074>.
- (60) Cao, J.; Jing, X.; Yan, J.; Hu, C.; Chen, R.; Yin, J.; Li, J.; Zheng, N. Identifying the Molecular Structures of Intermediates for Optimizing the Fabrication of High-Quality Perovskite Films. *J. Am. Chem. Soc.* **2016**, *138* (31), 9919–9926. <https://doi.org/10.1021/jacs.6b04924>.

- (61) Petrov, A. V. A. V. A. V. A.; Structure, C.; Phases, D.; Zubavichus, Y. V. V.; Khrustalev, V. N. N.; Petrov, A. V. A. V. A. V. A.; Grätzel, M.; Sokolova, I. P. P.; Belich, N. A. A.; Peters, G. S. S.; Dorovatovskii, P. V. V.; Zubavichus, Y. V. V.; Khrustalev, V. N. N.; Petrov, A. V. A. V. A. V. A.; Grätzel, M.; Goodilin, E. A. A.; Tarasov, A. B. B. Crystal Structure of DMF-Intermediate Phases Uncovers the Link Between $\text{CH}_3\text{NH}_3\text{PbI}_3$ Morphology and Precursor Stoichiometry. *J. Phys. Chem. C* **2017**, *121* (38), acs.jpcc.7b08468. <https://doi.org/10.1021/acs.jpcc.7b08468>.
- (62) Thind, A. S.; Huang, X.; Sun, J.; Mishra, R. First-Principles Prediction of a Stable Hexagonal Phase of $\text{CH}_3\text{NH}_3\text{PbI}_3$. *Chem. Mater.* **2017**, *29* (14), 6003–6011. <https://doi.org/10.1021/acs.chemmater.7b01781>.
- (63) Cao, J.; Jing, X.; Yan, J.; Hu, C.; Chen, R.; Yin, J.; Li, J.; Zheng, N. Identifying the Molecular Structures of Intermediates for Optimizing the Fabrication of High-Quality Perovskite Films. *J. Am. Chem. Soc.* **2016**, *138* (31), 9919–9926. <https://doi.org/10.1021/jacs.6b04924>.
- (64) Szafranski, M.; Katrusiak, A. Phase Transitions in the Layered Structure of Diguandinium Tetraiodoplumbate. *Phys. Rev. B* **2000**, *61* (2), 1026–1035. <https://doi.org/10.1103/PhysRevB.61.1026>.
- (65) Imler, G. H.; Li, X.; Xu, B.; Dobreiner, G. E.; Dai, H.-L.; Rao, Y.; Wayland, B. B. Solid State Transformation of the Crystalline Monohydrate (CH_3NH_3) $_2\text{PbI}_4$ to the (CH_3NH_3) $_2\text{PbI}_4$ Perovskite. *Chem. Commun.* **2015**, *51* (56), 11290–11292. <https://doi.org/10.1039/C5CC03741G>.
- (66) Egger, D. A.; Bera, A.; Cahen, D.; Hodes, G.; Kirchartz, T.; Kronik, L.; Lovrincic, R.; Rappe, A. M.; Reichman, D. R.; Yaffe, O. What Remains Unexplained about the Properties of Halide Perovskites? *Adv. Mater.* **2018**, *30* (20), 1–11. <https://doi.org/10.1002/adma.201800691>.
- (67) Tao, S.; Schmidt, I.; Brocks, G.; Jiang, J.; Tranca, I.; Meerholz, K.; Olthof, S. Absolute Energy Level Positions in Tin- and Lead-Based Halide Perovskites. *Nat. Commun.* **2019**, *10* (1), 1–10. <https://doi.org/10.1038/s41467-019-10468-7>.
- (68) Frost, J. M.; Butler, K. T.; Brivio, F.; Hendon, C. H.; Van Schilfgaarde, M.; Walsh, A. Atomistic Origins of High-Performance in Hybrid Halide Perovskite Solar Cells. *Nano Lett.* **2014**, *14* (5), 2584–2590. <https://doi.org/10.1021/nl500390f>.
- (69) Berry, J.; Buonassisi, T.; Egger, D. A.; Hodes, G.; Kronik, L.; Loo, Y.-L.; Lubomirsky, I.; Marder, S. R.; Mastai, Y.; Miller, J. S.; Mitzi, D. B.; Paz, Y.; Rappe, A. M.; Riess, I.; Rybtchinski, B.; Stafsudd, O.; Stevanovic, V.; Toney, M. F.; Zitoun, D.; Kahn, A.; Ginley, D.; Cahen, D. Hybrid Organic-Inorganic Perovskites (HOIPs): Opportunities and Challenges. *Adv. Mater.* **2015**, n/a-n/a.
- (70) Brandt, R. E.; Stevanovic, V.; Ginley, D. S.; Buonassisi, T. Identifying Defect-Tolerant Semiconductors with High Minority-Carrier Lifetimes: Beyond Hybrid Lead Halide Perovskites. *MRS Commun.* **2015**, *5* (2), 1–11. <https://doi.org/10.1557/mrc.2015.26>.
- (71) Ball, J. M.; Petrozza, A. Defects in Perovskite-Halides and Their Effects in Solar Cells. *Nat. Energy* **2016**, *1* (11), 16149. <https://doi.org/10.1038/nenergy.2016.149>.
- (72) Shi, D.; Adinolfi, V.; Comin, R.; Yuan, M.; Alarousu, E.; Buin, A.; Chen, Y.; Hoogland, S.; Rothenberger, A.; Katsiev, K.; Losovyj, Y.; Zhang, X.; Dowben, P. A.; Mohammed, O. F.; Sargent, E. H.; Bakr, O. M. Low Trap-State Density and Long Carrier Diffusion in Organolead Trihalide Perovskite Single Crystals. *Science* (80-.). **2015**, *347* (6221), 519–522. <https://doi.org/10.1126/science.aaa2725>.
- (73) Onoda-Yamamuro, N.; Matsuo, T.; Suga, H. Dielectric Study of $\text{CH}_3\text{NH}_3\text{PbX}_3$ (X = Cl, Br, I). *J. Phys. Chem. Solids* **1992**, *53* (7), 935–939.
- (74) Poglitsch, A.; Weber, D. Dynamic Disorder in Methylammoniumtrihalogenoplumbates (II) Observed by Millimeter-Wave Spectroscopy. *J. Chem. Phys.* **1987**, *87* (11), 6373. <https://doi.org/10.1063/1.453467>.
- (75) Vos, A. De. Detailed Balance Limit of the Efficiency of Tandem Solar Cells. *J. Phys. D: Appl. Phys.* **1980**, *13* (5), 839–846. <https://doi.org/10.1088/0022-3727/13/5/018>.
- (76) Xiao, K.; Lin, R.; Han, Q.; Hou, Y.; Qin, Z.; Nguyen, H. T.; Wen, J.; Wei, M.; Yeddu, V.; Saidaminov, M. I.; Gao, Y.; Luo, X.; Wang, Y.; Gao, H.; Zhang, C.; Xu, J.; Zhu, J.; Sargent, E. H.; Tan, H. All-Perovskite Tandem Solar Cells with 24.2% Certified Efficiency and Area over 1 cm^2 Using Surface-Anchoring Zwitterionic Antioxidant. *Nat. Energy* **2020**, *5* (11), 870–880. <https://doi.org/10.1038/s41560-020-00705-5>.
- (77) Eperon, G. E.; Leijtens, T.; Bush, K. A.; Prasanna, R.; Green, T.; Wang, J. T.-W.; McMeekin, D. P.; Volonakis, G.; Milot, R. L.; May, R.; Palmstrom, A.; Slotcavage, D. J.; Belisle, R. A.; Patel, J. B.; Parrott, E. S.; Sutton, R. J.; Ma, W.; Moghadam, F.; Conings, B.; Babayigit, A.; Boyen, H.-G.; Bent, S.; Giustino, F.; Herz, L. M.; Johnston, M. B.; McGehee, M. D.; Snaith, H. J. Perovskite-Perovskite Tandem Photovoltaics with Optimized Band Gaps. *Science* (80-.). **2016**, *354* (6314), 861–865. <https://doi.org/10.1126/science.aaf9717>.
- (78) Bush, K. A.; Palmstrom, A. F.; Yu, Z. (Jason); Boccard, M.; Cheacharoen, R.; Mailoa, J. P.; McMeekin, D. P.; Hoyer, R. L. Z.; Bailie, C. D.; Leijtens, T.; Peters, I. M.; Minichetti, M. C.; Rolston, N.; Prasanna, R.; Sofia, S. E.; Harwood, D.; Ma, W.; Moghadam, F.; Snaith, H. J.; Buonassisi, T.; Holman, Z. C.; Bent, S. F.; McGehee, M. D. 23.6%-Efficient Monolithic Perovskite/Silicon Tandem Solar Cells with Improved Stability. *Nat. Energy* **2017**, No. February, 1–7. <https://doi.org/10.1038/nenergy.2017.9>.
- (79) Xu, J.; Boyd, C. C.; Yu, Z. J.; Palmstrom, A. F.; Witter, D. J.; Larson, S. W.; France, R. M.; Werner, J.; Harvey, S. P.; Wolf, E. J.; Weigand, W.; Manzoor, S.; van Hest, M. F. A. M.; Berry, J. J.; Luther, J. M.; Holman, Z. C.; McGehee, M. D. Triple-Halide Wide-Band Gap Perovskites with Suppressed Phase Segregation for Efficient Tandems. *Science* (80-.). **2020**, *367* (6482), 1097–1104. <https://doi.org/10.1126/science.aaz5074>.
- (80) Al-Ashouri, A.; Köhnen, E.; Li, B.; Magomedov, A.; Hempel, H.; Caprioglio, P.; Márquez, J. A.; Vilches, A. B. M.; Kasparavicius, E.; Smith, J. A.; Phung, N.; Menzel, D.; Grischek, M.; Kegelmann, L.; Skroblin, D.; Gollwitzer, C.; Malinauskas, T.; Jošt, M.; Matič, G.; Rech, B.; Schlatmann, R.; Topič, M.; Korte, L.; Abate, A.; Stannowski, B.; Neher, D.; Stolterfoht, M.; Unold, T.; Getautis, V.; Albrecht, S. Monolithic Perovskite/Silicon Tandem Solar Cell with >29% Efficiency by Enhanced Hole Extraction. *Science* (80-.). **2020**, *370* (6522), 1300–1309. <https://doi.org/10.1126/science.abd4016>.
- (81) Todorov, T.; Gershon, T.; Gunawan, O.; Lee, Y. S.; Sturdevant, C.; Chang, L. Y.; Guha, S. Monolithic Perovskite-CIGS Tandem Solar Cells via in Situ Band Gap Engineering. *Adv. Energy Mater.* **2015**, *5* (23), 1–6. <https://doi.org/10.1002/aenm.201500799>.
- (82) Jošt, M.; Bertram, T.; Koushik, D.; Marquez, J. A.; Verheijen, M. A.; Heinemann, M. D.; Köhnen, E.; Al-Ashouri, A.; Braunger, S.; Lang, F.; Rech, B.; Unold, T.; Creatore, M.; Lauermaun, I.; Kaufmann, C. A.; Schlatmann, R.; Albrecht, S. 21.6%-Efficient Monolithic Perovskite/Cu(In,Ga)Se₂ Tandem Solar Cells with Thin Conformal Hole Transport Layers for Integration on Rough Bottom Cell Surfaces. *ACS Energy Lett.* **2019**, *4* (2), 583–590. <https://doi.org/10.1021/acsenergylett.9b00135>.
- (83) Jošt, M.; Kegelmann, L.; Korte, L.; Albrecht, S. Monolithic Perovskite Tandem Solar Cells: A Review of the Present Status and Advanced Characterization Methods Toward 30% Efficiency. *Adv. Energy Mater.* **2020**, *10* (26), 1904102. <https://doi.org/10.1002/aenm.201904102>.
- (84) Chen, X.; Jia, Z.; Chen, Z.; Jiang, T.; Bai, L.; Tao, F.; Chen, J.; Chen, X.; Liu, T.; Xu, X.; Yang, C.; Shen, W.; Sha, W. E. I.; Zhu, H.; Yang, Y. (Michael). Efficient and Reproducible Monolithic Perovskite/Organic Tandem Solar Cells with Low-Loss Interconnecting Layers. *Joule* **2020**, *4* (7), 1594–1606. <https://doi.org/10.1016/j.joule.2020.06.006>.

- (85) Brinkmann, K. O.; Becker, T.; Florian Zimmermann; Gahlmann, T.; Theisen, M.; Haeger, T.; Olthof, S.; Kreusel, C.; Gunster, M.; Maschwitz, T.; F. Gobelsmann; Koch, C.; Hertel, D.; Caprioglio, P.; Perdigon, L.; Al-Ashouri, A.; Merten, L.; Hinderhofer, A.; Schreiber, F.; Albrecht, S.; Meerholz, K.; Neher, D.; Stolterfoht, M.; Riedl, T. 23.5% Efficient Monolithic Perovskite/Organic Tandem Solar Cells Based on an Ultra-Thin Metal-like Metal-Oxide Interconnect. *ResearchSquare*. <https://doi.org/10.21203/rs.3.rs-125381/v1>.
- (86) Kelley, S. P.; Narita, A.; Holbrey, J. D.; Green, K. D.; Reichert, W. M.; Rogers, R. D. Understanding the Effects of Ionicity in Salts, Solvates, Co-Crystals, Ionic Co-Crystals, and Ionic Liquids, Rather than Nomenclature, Is Critical to Understanding Their Behavior. *Cryst. Growth Des.* **2013**, *13* (3), 965–975. <https://doi.org/10.1021/cg4000439>.
- (87) Radicchi, E.; Mosconi, E.; Elisei, F.; Nunzi, F.; De Angelis, F.; Angelis, F. De; De Angelis, F. Understanding the Solution Chemistry of Lead Halide Perovskites Precursors. *ACS Appl. Energy Mater.* **2019**, *2* (5), 3400–3409. <https://doi.org/10.1021/acsam.9b00206>.
- (88) Shargaieva, O.; Kuske, L.; Rappich, J.; Unger, E.; Nickel, N. H. Building Blocks of Hybrid Perovskites: A Photoluminescence Study of Lead-Iodide Solution Species. *ChemPhysChem* **2020**, *21* (20), 2327–2333. <https://doi.org/10.1002/cphc.202000479>.
- (89) Patidar, R.; Burkitt, D.; Hooper, K.; Richards, D.; Watson, T. Slot-Die Coating of Perovskite Solar Cells: An Overview. *Mater. Today Commun.* **2020**, *22* (December 2019), 100808. <https://doi.org/10.1016/j.mtcomm.2019.100808>.
- (90) Dou, B.; Whitaker, J. B.; Bruening, K.; Moore, D. T.; Wheeler, L. M.; Ryter, J.; Breslin, N. J.; Berry, J. J.; Garner, S. M.; Barnes, F. S.; Shaheen, S. E.; Tassone, C. J.; Zhu, K.; van Hest, M. F. A. M. Roll-to-Roll Printing of Perovskite Solar Cells. *ACS Energy Lett.* **2018**, *3* (10), 2558–2565. <https://doi.org/10.1021/acsenerylett.8b01556>.
- (91) Wu, W. Q.; Rudd, P. N.; Wang, Q.; Yang, Z.; Huang, J. Blading Phase-Pure Formamidinium-Alloyed Perovskites for High-Efficiency Solar Cells with Low Photovoltage Deficit and Improved Stability. *Adv. Mater.* **2020**, *32* (28), 1–8. <https://doi.org/10.1002/adma.202000995>.
- (92) Mathies, F.; List-Kratochvil, E. J. W.; Unger, E. L. Advances in Inkjet-Printed Metal-Halide Perovskite Photovoltaic and Optoelectronic Devices. *Energy Technol.* **2019**, *81* (11), ente.201900991. <https://doi.org/10.1002/ente.201900991>.
- (93) Bishop, J. E.; Smith, J. A.; Lidzey, D. G. Development of Spray-Coated Perovskite Solar Cells. *ACS Appl. Mater. Interfaces* **2020**. <https://doi.org/10.1021/acsami.0c14540>.
- (94) Barrows, A.; Pearson, A.; Kwak, C.; Dunbar, A.; Buckley, A.; Lidzey, D. Efficient Planar Heterojunction Mixed-Halide Perovskite Solar Cells Deposited via Spray-Deposition. *Energy Environ. Sci.* **2014**, *7*, 2945. <https://doi.org/10.1039/C4EE01546K>.
- (95) Pasquarelli, R. M.; Ginley, D. S.; O'Hayre, R. Solution Processing of Transparent Conductors: From Flask to Film. *Chem. Soc. Rev.* **2011**, *40* (11), 5406–5441. <https://doi.org/10.1039/c1cs15065k>.
- (96) Kojima, A.; Teshima, K.; Shirai, Y.; Miyasaka, T. Novel Photoelectrochemical Cell with Mesoscopic Electrodes Sensitized by Lead-Halide Compounds. *Meet. Abstr.* **2006**, *MA2008-02* (1), 27.
- (97) Kojima, A.; Teshima, K.; Shirai, Y.; Miyasaka, T. Organometal Halide Perovskites as Visible-Light Sensitizers for Photovoltaic Cells. *J. Am. Chem. Soc.* **2009**, *131* (17), 6050–6051. <https://doi.org/10.1021/ja809598r>.
- (98) Grätzel, M. The Light and Shade of Perovskite Solar Cells. *Nat. Mater.* **2014**, *13* (9), 838–842. <https://doi.org/10.1038/nmat4065>.
- (99) Im, J.-H.; Lee, C.-R.; Lee, J.-W.; Park, S.-W.; Park, N.-G. 6.5% Efficient Perovskite Quantum-Dot-Sensitized Solar Cell. *Nanoscale* **2011**, *3* (10), 4088. <https://doi.org/10.1039/c1nr10867k>.
- (100) Kim, H.-S.; Lee, C.-R.; Im, J.-H.; Lee, K.-B.; Moehl, T.; Marchioro, A.; Moon, S.-J.; Humphry-Baker, R.; Yum, J.-H.; Moser, J. E.; Grätzel, M.; Park, N.-G. Lead Iodide Perovskite Sensitized All-Solid-State Submicron Thin Film Mesoscopic Solar Cell with Efficiency Exceeding 9%. *Sci. Rep.* **2012**, *2*, 591. <https://doi.org/10.1038/srep00591>.
- (101) Lee, M. M.; Teuscher, J.; Miyasaka, T.; Murakami, T. N.; Snaith, H. J. Efficient Hybrid Solar Cells Based on Meso-Superstructured Organometal Halide Perovskites. *Science (80-.)*. **2012**, *338* (6107), 643–647. <https://doi.org/10.1126/science.1228604>.
- (102) Green, M. A.; Ho-Baillie, A.; Snaith, H. J. The Emergence of Perovskite Solar Cells. *Nat. Photonics* **2014**, *8* (7), 506–514. <https://doi.org/10.1038/nphoton.2014.134>.
- (103) Noh, J. H.; Jeon, N. J.; Choi, Y. C.; Nazeeruddin, M. K.; Grätzel, M.; Seok, S. II. Nanostructured TiO₂/CH₃NH₃PbI₃ Heterojunction Solar Cells Employing Spiro-OMeTAD/Co-Complex as Hole-Transporting Material. *J. Mater. Chem. A* **2013**, *1* (38), 11842–11847. <https://doi.org/10.1039/C3TA12681A>.
- (104) Noh, J. H.; Im, S. H.; Heo, J. H.; Mandal, T. N.; Seok, S. II. Chemical Management for Colorful, Efficient, and Stable Inorganic-Organic Hybrid Nanostructured Solar Cells. *Nano Lett.* **2013**, *13* (4), 1764–1769. <https://doi.org/10.1021/nl400349b>.
- (105) Ball, J. M.; Lee, M. M.; Hey, A.; Snaith, H. J. Low-Temperature Processed Meso-Superstructured to Thin-Film Perovskite Solar Cells. *Energy Environ. Sci.* **2013**, *6* (6), 1739. <https://doi.org/10.1039/c3ee40810h>.
- (106) Burschka, J.; Pellet, N.; Moon, S.-J.; Humphry-Baker, R.; Gao, P.; Nazeeruddin, M. K.; Grätzel, M. Sequential Deposition as a Route to High-Performance Perovskite-Sensitized Solar Cells. *Nature* **2013**, *499* (7458), 316–319. <https://doi.org/10.1038/nature12340>.
- (107) Jeon, N. J.; Noh, J. H.; Kim, Y. C.; Yang, W. S.; Ryu, S.; Seok, S. II. Solvent Engineering for High-Performance Inorganic-Organic Hybrid Perovskite Solar Cells. *Nat. Mater.* **2014**, *13* (9), 1–7. <https://doi.org/10.1038/nmat4014>.
- (108) National Renewable Energy Laboratory. Best Research-Cell Efficiencies <https://www.nrel.gov/pv/cell-efficiency.html> (accessed Jan 1, 2021).
- (109) Shargaieva, O.; Näsström, H.; Smith, J. A.; Töbrens, D.; Munir, R.; Unger, E. L. Hybrid Perovskite Crystallization from Binary Solvent Mixtures: Interplay of Evaporation Rate and Binding Strength of Solvents. *Mater. Adv.* **2020**. <https://doi.org/10.1039/D0MA00815J>.
- (110) Munir, R.; Sheikh, A. D.; Abdelsamie, M.; Hu, H.; Yu, L.; Zhao, K.; Kim, T.; Tall, O. El; Li, R.; Smilgies, D.; Amassian, A. Hybrid Perovskite Thin-Film Photovoltaics: In Situ Diagnostics and Importance of the Precursor Solvate Phases. **2017**. <https://doi.org/10.1002/adma.201604113>.
- (111) Lou, L.; Liu, T.; Xiao, J.; Xiao, S.; Long, X.; Zheng, S.; Yang, S. Controlling Apparent Coordinated Solvent Number in the Perovskite Intermediate Phase Film for Developing Large-Area Perovskite Solar Modules. **2019**, *1900972*, 1–8. <https://doi.org/10.1002/ente.201900972>.
- (112) Liu, M.; Johnston, M. B.; Snaith, H. J. Efficient Planar Heterojunction Perovskite Solar Cells by Vapour Deposition. *Nature* **2013**, *501* (7467), 395–398. <https://doi.org/10.1038/nature12509>.
- (113) Roß, M.; Gil-Escrig, L.; Al-Ashouri, A.; Tockhorn, P.; Jošt, M.; Rech, B.; Albrecht, S. Co-Evaporated p-i-n Perovskite Solar Cells beyond 20% Efficiency: Impact of Substrate Temperature and Hole-Transport Layer. *ACS Appl. Mater. Interfaces* **2020**, *12* (35), 39261–39272. <https://doi.org/10.1021/acsami.0c10898>.

- (114) Li, J.; Wang, H.; Chin, X. Y.; Dewi, H. A.; Vergeer, K.; Goh, T. W.; Lim, J. W. M.; Lew, J. H.; Loh, K. P.; Soci, C.; Sum, T. C.; Bolink, H. J.; Mathews, N.; Mhaisalkar, S.; Bruno, A. Highly Efficient Thermally Co-Evaporated Perovskite Solar Cells and Mini-Modules. *Joule* **2020**, *4* (5), 1035–1053. <https://doi.org/10.1016/j.joule.2020.03.005>.
- (115) Dou, B.; Wheeler, L. M.; Christians, J. A.; Moore, D. T.; Harvey, S. P.; Berry, J. J.; Barnes, F. S.; Shaheen, S. E.; Van Hest, M. F. A. M. Degradation of Highly Alloyed Metal Halide Perovskite Precursor Inks: Mechanism and Storage Solutions. *ACS Energy Lett.* **2018**, *3* (4), 979–985. <https://doi.org/10.1021/acscenergylett.8b00305>.
- (116) Hamill, J. C.; Sorli, J. C.; Pelczar, I.; Schwartz, J.; Loo, Y. L. Acid-Catalyzed Reactions Activate DMSO as a Reagent in Perovskite Precursor Inks. *Chem. Mater.* **2019**, *31* (6), 2114–2120. <https://doi.org/10.1021/acs.chemmater.9b00019>.
- (117) Wang, X.; Fan, Y.; Wang, L.; Chen, C.; Li, Z.; Liu, R.; Meng, H.; Shao, Z.; Du, X.; Zhang, H.; Cui, G.; Pang, S. Perovskite Solution Aging: What Happened and How to Inhibit? *Chem* **2020**, 1–10. <https://doi.org/10.1016/j.chempr.2020.02.016>.
- (118) Game, O. S.; Smith, J. A.; Alanazi, T. I.; Wong-Stringer, M.; Kumar, V.; Rodenburg, C.; Terrill, N. J.; Lidzey, D. G. Solvent Vapour Annealing of Methylammonium Lead Halide Perovskite: What's the Catch? *J. Mater. Chem. A* **2020**, *8* (21), 10943–10956. <https://doi.org/10.1039/D0TA03023F>.
- (119) Eperon, G. E.; Stranks, S. D.; Menelaou, C.; Johnston, M. B.; Herz, L. M.; Snaith, H. J. Formamidinium Lead Trihalide: A Broadly Tunable Perovskite for Efficient Planar Heterojunction Solar Cells. *Energy Environ. Sci.* **2014**, *7* (3), 982. <https://doi.org/10.1039/c3ee43822h>.
- (120) Conings, B.; Drijkoningen, J.; Gauquelin, N.; Babayigit, A.; D'Haen, J.; D'Olieslaeger, L.; Ethirajan, A.; Verbeeck, J.; Manca, J.; Mosconi, E.; Angelis, F. De; Boyen, H. Intrinsic Thermal Instability of Methylammonium Lead Trihalide Perovskite. *Adv. Energy Mater.* **2015**.
- (121) Saliba, M.; Matsui, T.; Seo, J.-Y.; Domanski, K.; Correa-Baena, J.-P.; Mohammad K., N.; Zakeeruddin, S. M.; Tress, W.; Abate, A.; Hagfeldt, A.; Grätzel, M.; Nazeeruddin, M. K.; Zakeeruddin, S. M.; Tress, W.; Abate, A.; Hagfeldt, A.; Grätzel, M. Cesium-Containing Triple Cation Perovskite Solar Cells: Improved Stability, Reproducibility and High Efficiency. *Energy Environ. Sci.* **2016**, *9* (6). <https://doi.org/10.1039/C5EE03874J>.
- (122) Correa-Baena, J.-P.; Abate, A.; Saliba, M.; Tress, W.; Jesper Jacobsson, T.; Grätzel, M.; Hagfeldt, A. The Rapid Evolution of Highly Efficient Perovskite Solar Cells. *Energy Environ. Sci.* **2017**, *10* (3), 710–727. <https://doi.org/10.1039/C6EE03397K>.
- (123) Saidaminov, M. I.; Abdelhady, A. L.; Maculan, G.; Bakr, O. M. Retrograde Solubility of Formamidinium and Methylammonium Lead Halide Perovskites Enabling Rapid Single Crystal Growth. *Chem. Commun.* **2015**, *51* (100), 17658–17661. <https://doi.org/10.1039/C5CC06916E>.
- (124) Su, J.; Chen, D. P.; Lin, C. T. Growth of Large CH₃NH₃PbX₃ (X=I, Br) Single Crystals in Solution. *J. Cryst. Growth* **2015**.
- (125) Yakunin, S.; Protesescu, L.; Krieg, F.; Bodnarchuk, M. I.; Nedelcu, G.; Humer, M.; De Luca, G.; Fiebig, M.; Heiss, W.; Kovalenko, M. V. Low-Threshold Amplified Spontaneous Emission and Lasing from Colloidal Nanocrystals of Caesium Lead Halide Perovskites. *Nat. Commun.* **2015**, *6*, 8056. <https://doi.org/10.1038/ncomms9056>.
- (126) Jacobsson, J. T.; Correa Baena, J. P.; Pazoki, M.; Saliba, M.; Schenk, K.; Grätzel, M.; Hagfeldt, A. An Exploration of the Compositional Space for Mixed Lead Halogen Perovskites for High Efficiency Devices - SI. *Energy Environ. Sci.* **2016**, *41* (0), 1–35. <https://doi.org/10.1039/C6EE00030D>.
- (127) Jang, D. M.; Park, K.; Kim, D. H.; Park, J.; Shojaei, F.; Kang, H. S.; Ahn, J.-P. P.; Lee, J. W.; Song, J. K. Reversible Halide Exchange Reaction of Organometal Trihalide Perovskite Colloidal Nanocrystals for Full-Range Band Gap Tuning. *Nano Lett.* **2015**, *15* (8), 5191–5199. <https://doi.org/10.1021/acs.nanolett.5b01430>.
- (128) Saliba, M.; Matsui, T.; Domanski, K.; Seo, J.-Y.; Ummadisingu, A.; Zakeeruddin, S. M.; Correa-Baena, J.-P.; Tress, W. R.; Abate, A.; Hagfeldt, A.; Grätzel, M. Incorporation of Rubidium Cations into Perovskite Solar Cells Improves Photovoltaic Performance. *Science (80-.)*. **2016**, *5557* (September). <https://doi.org/10.1126/science.aah5557>.
- (129) Abdi-Jalebi, M.; Andaji-Garmaroudi, Z.; Cacovich, S.; Stavarakas, C.; Philippe, B.; Richter, J. M.; Alsari, M.; Booker, E. P.; Hutter, E. M.; Pearson, A. J.; Lilliu, S.; Savenije, T. J.; Rensmo, H.; Divitini, G.; Ducati, C.; Friend, R. H.; Stranks, S. D. Maximizing and Stabilizing Luminescence from Halide Perovskites with Potassium Passivation. *Nature* **2018**, *555* (7697), 497–501. <https://doi.org/10.1038/nature25989>.
- (130) Qin, M.; Tse, K.; Lau, T. K.; Li, Y.; Su, C. J.; Yang, G.; Chen, J.; Zhu, J.; Jeng, U. S.; Li, G.; Chen, H.; Lu, X. Manipulating the Mixed-Perovskite Crystallization Pathway Unveiled by In Situ GIWAXS. *Adv. Mater.* **2019**, *31* (25), 1–10. <https://doi.org/10.1002/adma.201901284>.
- (131) Dang, H. X.; Wang, K.; Ghasemi, M.; Tang, M.-C.; De Bastiani, M.; Aydin, E.; Dauzon, E.; Barrit, D.; Peng, J.; Smilgies, D.-M.; De Wolf, S.; Amassian, A. Multi-Cation Synergy Suppresses Phase Segregation in Mixed-Halide Perovskites. *Joule* **2019**, *3*, 1–19. <https://doi.org/10.1016/j.joule.2019.05.016>.
- (132) Correa-Baena, J. P.; Luo, Y.; Brenner, T. M.; Snaider, J.; Sun, S.; Li, X.; Jensen, M. A.; Hartono, N. T. P.; Nienhaus, L.; Wiegold, S.; Poindexter, J. R.; Wang, S.; Meng, Y. S.; Wang, T.; Lai, B.; Holt, M. V.; Cai, Z.; Bawendi, M. G.; Huang, L.; Buonassisi, T.; Fenning, D. P. Homogenized Halides and Alkali Cation Segregation in Alloyed Organic-Inorganic Perovskites. *Science (80-.)*. **2019**, *363* (6427), 627–631. <https://doi.org/10.1126/science.aah5065>.
- (133) Zheng, F.; Chen, W.; Bu, T.; Ghiggino, K. P.; Huang, F.; Cheng, Y.; Tapping, P.; Kee, T. W.; Jia, B.; Wen, X. Triggering the Passivation Effect of Potassium Doping in Mixed-Cation Mixed-Halide Perovskite by Light Illumination. *Adv. Energy Mater.* **2019**, *1901016*, 1–11. <https://doi.org/10.1002/aenm.201901016>.
- (134) Alanazi, T. I.; Game, O. S.; Smith, J. A.; Kilbride, R. C.; Greenland, C.; Jayaprakash, R.; Georgiou, K.; Terrill, N. J.; Lidzey, D. G. Potassium Iodide Reduces the Stability of Triple-Cation Perovskite Solar Cells. *RSC Adv.* **2020**, *10* (66), 40341–40350. <https://doi.org/10.1039/d0ra07107b>.
- (135) Yang, W. S.; Noh, J. H.; Jeon, N. J.; Kim, Y. C.; Ryu, S.; Seo, J.; Seok, S. I. High-Performance Photovoltaic Perovskite Layers Fabricated through Intramolecular Exchange. *Science (80-.)*. **2015**, *348* (May), science.aaa9272-. <https://doi.org/10.1126/science.aaa9272>.
- (136) Min, H.; Kim, M.; Lee, S. U.; Kim, H.; Kim, G.; Choi, K.; Lee, J. H.; Seok, S. I. Efficient, Stable Solar Cells by Using Inherent Bandgap of a-Phase Formamidinium Lead Iodide. *Science (80-.)*. **2019**, *366* (6466), 749–753. <https://doi.org/10.1126/science.aay7044>.
- (137) Jeong, M.; Choi, I. W.; Go, E. M.; Cho, Y.; Kim, M.; Lee, B.; Jeong, S.; Jo, Y.; Choi, H. W.; Lee, J.; Bae, J. H.; Kwak, S. K.; Kim, D. S.; Yang, C. Stable Perovskite Solar Cells with Efficiency Exceeding 24.8% and 0.3-V Voltage Loss. *Science (80-.)*. **2020**, *369* (6511), 1615–1620. <https://doi.org/10.1126/science.abb7167>.
- (138) Yoo, J. J.; Seo, G.; Chua, M. R.; Park, T. G.; Lu, Y.; Rotermund, F.; Kim, Y.; Moon, C. S.; Jeon, N. J.; Bulović, V.; Shin, S. S.; Bawendi, M. G. Efficient Perovskite Solar Cells via Improved Carrier Management. *Nature* **2021**, *590* (June 2020). <https://doi.org/10.1038/s41586-021-03285-w>.
- (139) Gagliardi, A.; Abate, A. Mesoporous Electron Selective Contacts Enhance the Tolerance to Interfacial Ions Accumulation in Perovskite Solar Cells. *ACS Energy Lett.* **2017**, acscenergylett.7b01101. <https://doi.org/10.1021/acscenergylett.7b01101>.

- (140) Roose, B.; Wang, Q.; Abate, A. The Role of Charge Selective Contacts in Perovskite Solar Cell Stability. *Adv. Energy Mater.* **2018**, *1803140*, 1803140. <https://doi.org/10.1002/aenm.201803140>.
- (141) Yang, J.; Fransishyn, K. M.; Kelly, T. L. Comparing the Effect of Mesoporous and Planar Metal Oxides on the Stability of Methylammonium Lead Iodide Thin Films. *Chem. Mater.* **2016**, *28* (20), 7344–7352. <https://doi.org/10.1021/acs.chemmater.6b02744>.
- (142) Fakhruddin, A.; Di Giacomo, F.; Palma, A. L.; Matteocci, F.; Ahmed, I.; Razza, S.; D'Epifanio, A.; Licoccia, S.; Ismail, J.; Di Carlo, A.; Brown, T. M.; Jose, R. Vertical TiO₂ Nanorods as a Medium for Stable and High-Efficiency Perovskite Solar Modules. *ACS Nano* **2015**, *9* (8), 8420–8429. <https://doi.org/10.1021/acs.nano.5b03265>.
- (143) Hooper, K.; Carnie, M.; Charbonneau, C.; Watson, T. Near Infrared Radiation as a Rapid Heating Technique for TiO₂ Films on Glass Mounted Dye-Sensitized Solar Cells. *Int. J. Photoenergy* **2014**, *2014* (1). <https://doi.org/10.1155/2014/953623>.
- (144) Das, S.; Gu, G.; Joshi, P. C.; Yang, B.; Aytug, T.; Rouleau, C. M.; Gehegan, D. B.; Xiao, K. Low Thermal Budget, Photonic-Cured Compact TiO₂ Layers for High-Efficiency Perovskite Solar Cells. *J. Mater. Chem. A* **2016**, *4* (24), 9685–9690. <https://doi.org/10.1039/c6ta02105k>.
- (145) Stolterfoht, M.; Caprioglio, P.; Wolff, C. M.; Márquez Prieto, J. A.; Nordmann, J.; Zhang, S.; Rothhardt, D.; Hörmann, U.; Amir, Y.; Redinger, A.; Kegelmann, L.; Zu, F.; Albrecht, S.; Koch, N.; Kirchartz, T.; Saliba, M.; Unold, T.; Neher, D. The Impact of Energy Alignment and Interfacial Recombination on the Open-Circuit Voltage of Perovskite Solar Cells. *Energy Environ. Sci.* **2019**. <https://doi.org/10.1039/C9EE02020A>.
- (146) Wang, J. T. W.; Wang, Z.; Pathak, S.; Zhang, W.; Dequillettes, D. W.; Wisnivesky-Rocca-Rivarola, F.; Huang, J.; Nayak, P. K.; Patel, J. B.; Mohd Yusof, H. A.; Vaynzof, Y.; Zhu, R.; Ramirez, I.; Zhang, J.; Ducati, C.; Grovenor, C.; Johnston, M. B.; Ginger, D. S.; Nicholas, R. J.; Snaith, H. J. Efficient Perovskite Solar Cells by Metal Ion Doping. *Energy Environ. Sci.* **2016**, *9* (9), 2892–2901. <https://doi.org/10.1039/c6ee01969b>.
- (147) Di Girolamo, D.; Di Giacomo, F.; Matteocci, F.; Marrani, A. G.; Dini, D.; Abate, A.; Di Girolamo, D. Progress, Highlights and Perspectives on NiO in Perovskite Photovoltaics. *Chem. Sci.* **2020**, *11* (30), 7746–7759. <https://doi.org/10.1039/d0sc02859b>.
- (148) Magomedov, A.; Al-Ashouri, A.; Kasparavičius, E.; Strazdaite, S.; Niaura, G.; Jošt, M.; Malinauskas, T.; Albrecht, S.; Getautis, V. Self-Assembled Hole Transporting Monolayer for Highly Efficient Perovskite Solar Cells. *Adv. Energy Mater.* **2018**, *8* (32). <https://doi.org/10.1002/aenm.201801892>.
- (149) Al-Ashouri, A.; Magomedov, A.; Roß, M.; Jošt, M.; Talaikis, M.; Chistiakova, G.; Bertram, T.; Márquez, J. A.; Köhnen, E.; Kasparavičius, E.; Levenco, S.; Gil-Escrig, L.; Hages, C. J.; Schlattmann, R.; Rech, B.; Malinauskas, T.; Unold, T.; Kaufmann, C. A.; Korte, L.; Niaura, G.; Getautis, V.; Albrecht, S. Conformal Monolayer Contacts with Lossless Interfaces for Perovskite Single Junction and Monolithic Tandem Solar Cells. *Energy Environ. Sci.* **2019**, *12* (11), 3356–3369. <https://doi.org/10.1039/C9EE02268F>.
- (150) Mei, A.; Li, X.; Liu, L.; Ku, Z.; Liu, T.; Rong, Y.; Xu, M. M.; Hu, M.; Chen, J.; Yang, Y.; Grätzel, M.; Han, H.; Grätzel, M.; Han, H. A Hole-Conductor-Free, Fully Printable Mesoscopic Perovskite Solar Cell with High Stability. *Science* (80-.). **2014**, *345* (6194), 295–298. <https://doi.org/10.1126/science.1254763>.
- (151) Wang, Q.; Liu, S.; Ming, Y.; Guan, Y.; Li, D.; Zhang, C.; Wang, Z.; Rong, Y.; Hu, Y.; Han, H. Improvements in Printable Mesoscopic Perovskite Solar Cells: Via Thinner Spacer Layers. *Sustain. Energy Fuels* **2018**, *2* (11), 2412–2418. <https://doi.org/10.1039/c8se00332g>.
- (152) Guan, Y.; Xu, M.; Zhang, W.; Li, D.; Hou, X.; Hong, L.; Wang, Q.; Zhang, Z.; Mei, A.; Chen, M.; Zhou, Y.; Padture, N. P.; Hu, Y.; Rong, Y.; Han, H. In Situ Transfer of CH₃NH₃PbI₃ Single Crystals in Mesoporous Scaffolds for Efficient Perovskite Solar Cells. *Chem. Sci.* **2019**, *68* (20), 42–61. <https://doi.org/10.1039/C9SC04900B>.
- (153) Baker, J.; Hooper, K.; Meroni, S.; Pockett, A.; McGettrick, J.; Wei, Z.; Escalante, R.; Oskam, G.; Carnie, M. J.; Watson, T. M. High Throughput Fabrication of Mesoporous Carbon Perovskite Solar Cells. *J. Mater. Chem. A* **2017**. <https://doi.org/10.1039/C7TA05674E>.
- (154) Kerremans, R.; Sandberg, O. J.; Meroni, S.; Watson, T.; Armin, A.; Meredith, P. On the Electro-Optics of Carbon Stack Perovskite Solar Cells. *Sol. RRL* **2019**, *1900221*, 1900221. <https://doi.org/10.1002/solr.201900221>.
- (155) Song, Z.; Waththage, S. C.; Phillips, A. B.; Heben, M. J. Pathways toward High-Performance Perovskite Solar Cells: Review of Recent Advances in Organo-Metal Halide Perovskites for Photovoltaic Applications. *J. Photonics Energy* **2016**, *6* (2), 22001. <https://doi.org/10.1117/1.JPE.6.022001>.
- (156) Grancini, G.; Roldán-Carmona, C.; Zimmermann, I.; Mosconi, E.; Lee, X.; Martineau, D.; Narbey, S.; Oswald, F.; De Angelis, F.; Graetzel, M.; Nazeeruddin, M. K. One-Year Stable Perovskite Solar Cells by 2D/3D Interface Engineering. *Nat. Commun.* **2017**, *8* (14), 1–8. <https://doi.org/10.1038/ncomms15684>.
- (157) Wilkinson, M. D.; Dumontier, M.; Aalbersberg, I. J.; Appleton, G.; Axton, M.; Baak, A.; Blomberg, N.; Boiten, J. W.; da Silva Santos, L. B.; Bourne, P. E.; Bouwman, J.; Brookes, A. J.; Clark, T.; Crosas, M.; Dillo, I.; Dumon, O.; Edmunds, S.; Evelo, C. T.; Finkers, R.; Gonzalez-Beltran, A.; Gray, A. J. G.; Groth, P.; Goble, C.; Grethe, J. S.; Heringa, J.; t Hoen, P. A. C.; Hooft, R.; Kuhn, T.; Kok, R.; Kok, J.; Lusher, S. J.; Martone, M. E.; Mons, A.; Packer, A. L.; Persson, B.; Rocca-Serra, P.; Roos, M.; van Schaik, R.; Sansone, S. A.; Schultes, E.; Sengstag, T.; Slater, T.; Strawn, G.; Swertz, M. A.; Thompson, M.; Van Der Lei, J.; Van Mulligen, E.; Velterop, J.; Waagmeester, A.; Wittenburg, P.; Wolstencroft, K.; Zhao, J.; Mons, B. Comment: The FAIR Guiding Principles for Scientific Data Management and Stewardship. *Sci. Data* **2016**, *3*, 1–9. <https://doi.org/10.1038/sdata.2016.18>.

Chapter 3

Methods

3.0: Introduction

In this chapter, an overview of the fabrication protocols and characterization techniques used in this thesis are given. The specific methods and materials employed in the research are comprehensively explained within each results chapter, detailing the exact process parameters or other particulars. Here, the basic principles of the most important methods are outlined, including how they relate to the theory in Chapter 2. An overview of the additional techniques is given but the reader is referred to the results chapters for further details.

3.1: Materials

All solar cells have been fabricated using glass/TCO substrates, where the transparent conducting oxide (TCO) is either fluorine-doped tin oxide (FTO) or indium tin oxide (ITO). The former benefits from lower usage of rare-earth metals, with In being of particular concern for future resource scarcity. ITO substrates generally offer the benefit of higher transmission, higher conductivity and lower roughness. Hence, for many of the devices using thin transport layers, this is the ideal material.

In all cases, devices were fabricated in a planar *n-i-p* architecture, with an SnO₂ electron-transporting layer (ETL) and spiro-OMeTAD hole-transporting layer (HTL).

The SnO₂ was typically a nanoparticle solution first introduced by Jiang et al.¹ which has become a staple for high-efficiency planar devices with several reports achieving over 23% PCE.^{2,3} The nanoparticle-SnO₂ (np-SnO₂) benefits from relatively low-temperature and short-duration processing (150 °C for 30 min), with attempts made in Chapter 4 to reduce this. This is deposited from a colloidal solution, an aqueous (non-toxic) suspension, although the potassium hydroxide (KOH) stabilising agent may cause corrosion of some deposition equipment (we did not observe this).⁴

The perovskite layer employed was generally either a triple-cation perovskite with PbI₂ excess (Chapter 4) or MAPbI₃. The triple-cation perovskite had a nominal stoichiometry (in solution) of Cs_{0.05}FA_{0.79}MA_{0.16}PbI_{2.5}Br_{0.5}.⁵ This is deposited from a mixture of two solvents, the non-toxic

dimethyl sulfoxide (DMSO) and highly toxic dimethyl formamide (DMF). MAPbI₃ solution was prepared according to the method introduced by Noel *et al.* by which MAI and PbI₂ precursor powders are added to acetonitrile (ACN) with methylamine (MA⁰) gas flowed through to dissolve the material. The exact setup used for the preparation of this solution (referred to as ACN MA⁰·MAPbI₃) as well as the underlying mechanism for this process are elicited in Chapter 6.

The HTL is comprised of the small organic molecule spiro-OMeTAD, first engineered for use in DSSCs. This is doped with two bis(trifluoromethane)sulfonimide (TFSI⁻) compounds - a lithium salt to increase conductivity (Li-TFSI), and FK209, a cobalt co-ordination compound. Additionally *tert*-butyl pyridine is included as an additive, which may play a role in solubilising the perovskite top-surface, enhancing hole-selectivity at this interface, and even introducing localised doping to the perovskite top surface.⁶ Spiro-OMeTAD benefits from a deep LUMO, ideal for hole extraction from the perovskite. Unfortunately, this requires rather precise multi-component solution preparation (aging and mixing), as well as transient charge transport characteristics in air, which can lead to large variation and evolution of photovoltaic device performances (the author notes that 1-2 days of aging in air leads to maximum PV performance at the solution composition used). Spiro-OMeTAD is also intrinsically expensive to synthesize and parasitically absorbs light, making use in tandem configurations difficult.

The back contact material (anode) used throughout is gold (Au), another expensive material which is essentially irrecoverable from the completed devices and evaporation chambers in which it is used. This can be deposited by thermal or electron-beam evaporation.

3.2: Fabrication techniques

3.2.1: Chemical etching

The TCO layers used were either *pre-patterned* to define the layout of the cell areas on a substrate, or were *etched* to define the regions without a TCO. This is done to minimise the potential for undesired recombination channels (e.g. pinholes) between the top layers and TCO, which would reduce the R_{SH} (which would ideally be infinite). Etching is achieved using dilute hydrochloric acid (HCl) together with zinc powder, which react to form zinc chloride and active hydrogen. The hydrogen then reacts to reduce the metal oxide layer to the metal (Sn or In) which is then etched by further HCl. This allows facile removal of portions of the substrate to define the layout of a device.

3.2.2: Substrate cleaning

An often-overlooked aspect for those seeking high-performance devices is the removal of surface contaminants and particulates before any layers are deposited. This is completed in several stages using a range of solvents.⁷ Firstly (before etching) any large particulates are removed by N₂ blowing. After etching, the substrates are scrubbed with a soap solution (Hellmanex) diluted with deionised (DI) water. Then the substrates are placed in a rack and cleaned by ultrasonication at an elevated temperature in boiling soap solution. These are then rinsed extensively and sonicated in boiling de-ionised water to remove any remaining soap solution. They are then rinsed with acetone and isopropyl alcohol (IPA), and then immersed in IPA for a final period of ultrasonication. Finally, the substrates are placed in a UV-ozone cleaning system which creates free radical species to remove further carbon contaminants. This UVO process is also applied after annealing of the np-SnO₂ layer and its effect is discussed in Chapter 4.

3.2.3: Spin coating

Spin coating has been used widely throughout this research and thin-film fabrication generally. This works by spreading a solution over the substrate surface by the centrifugal force forming a uniform *wet film*. The spinning continues to drive volatile solvent evaporation, thinning the wet film and then finally inducing crystallisation (or drying) of a layer.⁸ The resultant film thickness t depends on the concentration of the solution, the wetting of the solution to the substrate and by the rotation speed ω . Thus for a given solution the thickness is proportional with the relation - $t \approx k/\omega^2$ where k is a constant. In this way from a known ω and t , the required speed to achieve a desired thickness can be estimated.

In this work, spin coating was used to deposit the ETL, perovskite and HTL. A program is defined for the rotations-per-minute (RPM) of the chuck, with a series of ramping speeds (acceleration) to control the film formation. A substrate is then mounted at the centre of a spinning “chuck”, held in place either by vacuum or a physical recess. A volume (10-100 μ l) of the layer solution is then deposited on the film surface either *statically* (substrate not rotating) or *dynamically*, where the substrate is already rotating; the latter can be beneficial for enhancing wetting or in initiating crystallisation in some circumstances.

3.2.4: Slot-die coating

Slot-die coating is a contact coating method used in Chapter 4, whereby the wet film thickness (here a meniscus) is defined by a coating head passing over a substrate surface (Figure 1). This is comparable in terms of drying and crystallization to doctor-blading or bar coating, where

the solution reservoir is behind the coating head on the substrate surface, but in contrast here the solution is fed directly into the coating head. This is arguably a more suitable approach for high-throughput PSC coating than the other two methods, where prolonged interaction between the active layer solvent and the substrate may be undesirable. Problems can arise with improper solution rheology, discontinuities in the meniscus formation from uneven solution flow,⁹ or improper process design (the coating speed and solution flow must be well-matched¹⁰).

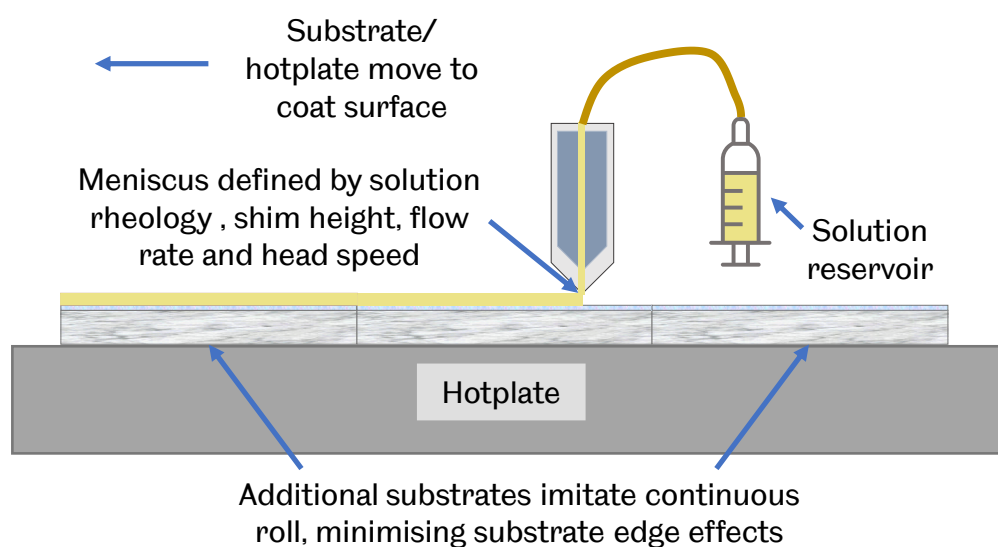


Figure 1: Illustration of the slot-die coating system used in this work.

3.2.5: Spray coating

Spray coating has been used extensively in Chapter 4, in addition to various other published work during this PhD. Ultrasonic spray-coating has been used throughout, in which a solution is fed to a spray-head comprised of a piezoelectric transducer and a shaping gas flow. The transducer breaks up the flowing solution into small droplets, which are then directed onto a substrate by a shaping gas. This forms a wet film, a process critically reliant on the physics of droplet formation and impact, in addition to the chemistry of surface wetting through appropriate surface preparation and solution composition.¹¹ A uniform coating is further dependent on the solvent volatility, and the mutual droplet interactions on the film surface, with various morphological instabilities possible.^{12,13}

In contrast to contact coating methods, the wet film thickness and uniformity is defined by the solution, which presents an additional solvent engineering challenge. This does however mean that non-uniform surfaces can be coated, and that – at least in present literature – much faster speeds are achievable for metal halide perovskite deposition, as explored in our recent

overview on this topic.¹⁴ The practical operation of a spray coater hence relies on control of many parameters:

- Solvent surface tension.
- Solution concentration.
- Atmospheric composition, pressure and air flow.
- Hotplate temperature.
- Surface energy of the coating surface.
- Spray head speed and height.
- Flow rate/solution reservoir pressure.

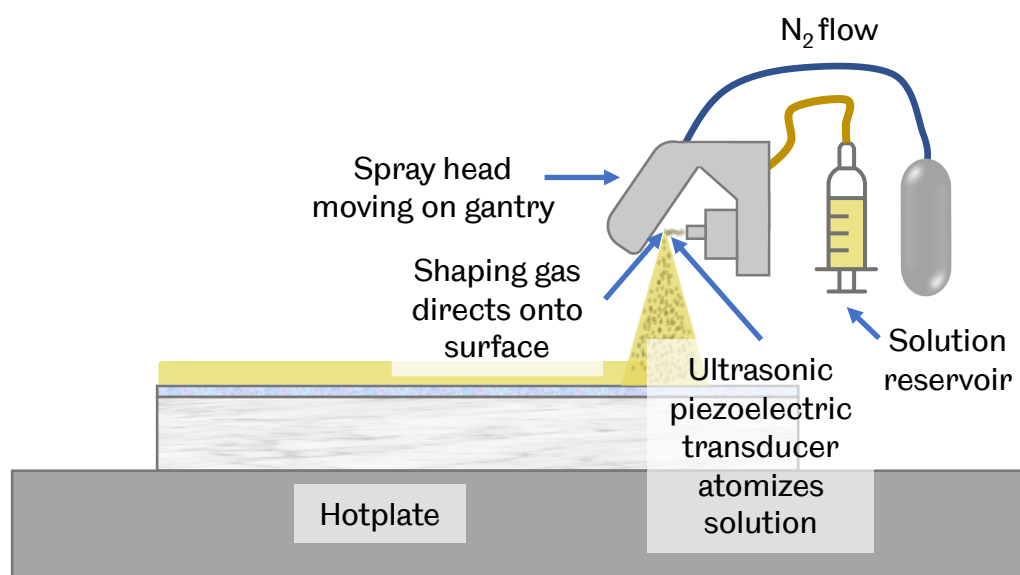


Figure 2: Illustration of the spray coating system used herein.

3.2.6: Device fabrication

The above processes can be succinctly summarised in the process diagram shown in Figure 3A. These are initial substrate cleaning, followed by chemical etching, thorough cleaning and UVO treatment. Immediately following this (to avoid atmospheric contamination and changes to the surface energy of the substrate), the np-SnO₂ is deposited by static spin, spray or slot-die coating. A cotton bud with DI water is then used to remove the np-SnO₂ in the area where the TCO will be contacted. The films are then annealed on a hotplate or with a hot air gun (Chapter 4), before again being UVO treated (both UVO and O₂ plasma treatments are also investigated in Chapter 4) and then transferred into a glovebox.

After cleaning with an N₂ gun to remove any particulates, the yellow triple cation perovskite solution is spin-coated, forming a thin wet film (translucent yellow). Prior to the end of the

deposition, an *antisolvent quench* of chlorobenzene is applied by pipetting onto the film surface which removes excess solvent and crystallises an intermediate solvate phase, with black spots also visible in the film. This is then transferred to a hotplate for annealing, and rapidly forms a black film with a specular (mirror-like) surface as the intermediate phase converts to the perovskite. In Chapters 5 and 6, ACN MA⁰·MAPbI₃ is used as the perovskite. This bypasses the previous steps (antisolvent is not required), directly forming a specular black film after ~1-2 s of spinning (dynamic or static coating) due to the higher volatility of the two components in this mixture.

After perovskite annealing and further N₂ cleaning, the spiro-OMeTAD is spin-coated dynamically, forming a colourful interference pattern during spinning with yellow/green/purple colour depending on the film thickness (which is greater at the substrate edge due to meniscus effects). The films are then transferred to a dark drybox to oxidise, enhancing the spiro-OMeTAD conductivity, a particularly important step without the FK209 additive. The perovskite and spiro-OMeTAD layers are then partially removed using a razor blade and sometimes acetonitrile/chlorobenzene (particularly beneficial on the rougher FTO).

Finally, the samples are N₂ cleaned and transferred into recesses in a patterned evaporation mask. This defines the Au electrode area(s) which are either a single *pixel* per device or 6 small pixels. The Au is then thermally evaporated in an Edwards 306 bell jar evaporator, initially slowly (0.1 Ås⁻¹) to form a good contact with the spiro-OMeTAD,⁷ before evaporating at a higher speed; the trade-off here being time under vacuum vs. substrate temperature, which can be mitigated through larger throw distances or substrate cooling during evaporation. The film thicknesses are calibrated using a quartz crystal monitor during evaporation, and a tooling factor corrects for the evaporation geometry (this is added based on ellipsometry measurements of measured vs. target film thicknesses).

Each process is designed to minimise possible shunt pathways through the device, most critical being small particulates which can interpenetrate between layers, pinholes in a layer due to poor film formation, and direct contact pathways. The latter here are *shorting devices*, where undesired current paths reduce the R_{SH} to effectively zero. The layout on the substrate is shown in Figure 3B, with the cell active area marked in green, indicating the region exposed to illumination for performance testing.

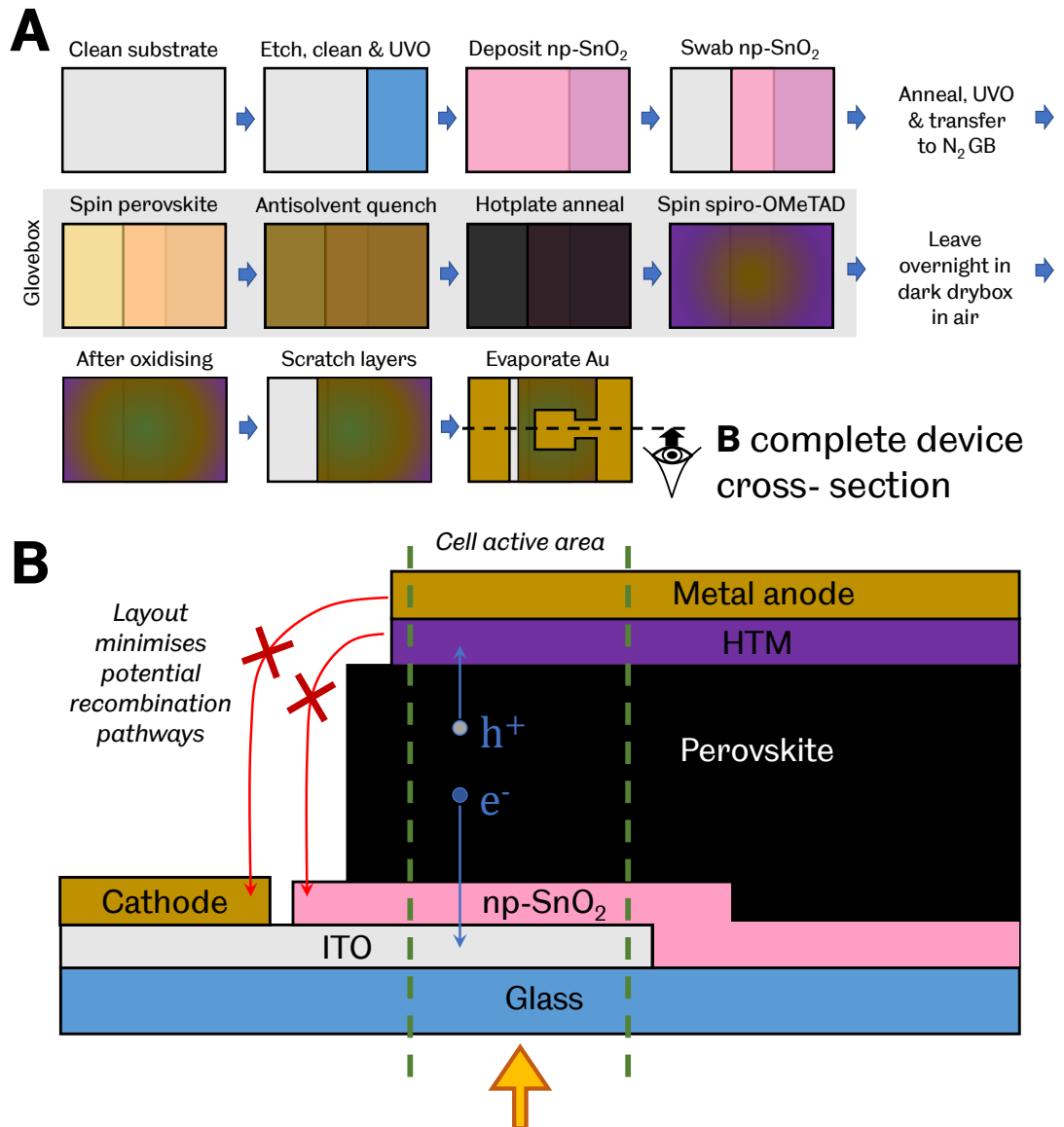


Figure 3: A) Overview of device fabrication processes for an n-i-p configuration solar cell. B) Cross-section through a completed device illustrating the role of etching, swabbing & scratching in mitigating potential recombination channels. Illumination through the glass side allows for photovoltaic performance assessment.

3.3: Characterisation techniques

3.3.1: Device characterisation

Completed devices are placed upside down into a recessed holder with spring-loaded pins pushing up to contact the anode and the cathode. An illumination mask is placed on top, with a well-defined area (just smaller than the cell active area) measured precisely using an optical microscope. The cell is then illuminated by a *solar simulator*, a device generating a temporally and spatially uniform spectrum of light. In our system (Newport 92251A-1000) this is produced by a Xenon arc lamp, which passes through optical filters, to give a spectral output closely

matching the AM1.5G spectrum. Prior to testing, an NREL-certified Si reference cell (including a Schott KG5 filter to remove the infra-red) is used to tune the exact output power of the solar simulator to $1000.0 \pm 0.5 \text{ W/m}^2$.

Next, a bias voltage is applied from a source measure unit to the cell to measure the current as a function of applied bias. Current-voltage (J - V) curves for all pixels are acquired by electrically connecting to each in turn by mechanically switching between them, from which the performance metrics described in the previous chapter are extracted: J_{SC} , V_{OC} , FF and PCE. Devices are tested in both the forward (J_{SC} to V_{OC}) and reverse (V_{OC} to J_{SC}) sweep directions to account for any hysteresis behaviour in the cell,¹⁵ which is fortunately reasonably low with the transport layers employed here.

The hysteresis effect is better accounted for in perovskites by measuring the stabilised power output (SPO) of a cell. Here, the bias voltage is not varied and instead is set to the J - V determined V_{mpp} and the current output is measured. This is equivalent to using the solar cell under real-world conditions but without use of an MPP tracking algorithm to optimise the cell output. Generally, after tens of seconds the cell achieves a stable power output and the J and PCE at this point are reported.

Additional insight can be gained by varying the illumination intensity from the typical 1000 W/m^2 (1 sun) and acquiring electrical measurements. In Chapter 4, light-intensity dependent V_{OC} measurements were acquired using an LED solar simulator (Oriel LSH-7320 ABA LED) which can be varied from 0.1 to 1.1 suns intensity. Here the deviation of the V_{OC} from a theoretical ideal can indicate certain recombination mechanisms at play in the solar cell.^{16,17}

Device stability measurements were also acquired in Chapter 5 using a *lifetime testing* solar simulator (Atlas Suntest CPS+). This system also uses a 1500 W Xenon bulb, but has a far greater spectral mismatch to AM1.5G, including a significant infra-red component, as shown in Bovill *et al.*¹⁸ Here, pixels are sequentially measured (reverse sweep direction) in turn with automatic switching between, and held at open-circuit in between measurements. The system also does not allow for an illumination mask and irradiation is from all directions, so the data are normalised with respect to calibrated intensity measurements using the solar simulator.

3.3.2: X-ray diffraction

The main principles underlying diffraction measurements on crystalline materials are explained in the previous chapter, here we focus on the experimental geometries and

equipment used to investigate perovskite thin films. The explanations here are largely based on works by Klug & Alexander, and Als-Nielsen & McMorrow.^{19,20}

In conventional lab-based 1D XRD, a heated cathode filament is used to generate thermionic electrons which are directed onto a copper (Cu) target anode. This results in the emission of electromagnetic radiation (X-rays) with a continuous distribution of wavelengths. For a Cu target with electronic structure, the incident electrons can also remove core shell electrons, leaving vacant inner orbitals. Outer electrons quickly drop to fill the vacant core shell, emitting a photon with a quantised transition energy, resulting in characteristic emission lines in the radiation. The most important lines for Cu (electronic structure $1s^2 2s^2 2p^6 3s^2 3p^6 3d^{10} 4s^1$) in XRD are the $K_{\alpha 1}$ and $K_{\alpha 2}$ emission lines corresponding to transitions from the $2p_{3/2}$ and $2p_{1/2}$ orbitals to the $1s$ orbital. These generate X-rays with a wavelength of 1.541 and 1.544 Å, smaller than typical interatomic lattice distances and thus ideal for diffraction.

The generated X-rays pass through various optics to limit the beam divergence, parallelise the beam (Soller slits) and monochromate the beam - unwanted transitions such as K_{β} will cause additional scattering. A final slit is changed by the user to optimise the source beam for minimising beam divergence (narrow slit) or maximising scattering intensity (wider slit). A second slit is used on the X-ray detector, with the same trade-off. To acquire a diffraction pattern, the source and the detector are mounted on a goniometer, which is rotated in one axis about the sample centre. A *beam knife* is optionally employed, sitting above the sample surface to restrict scattering away from the sample centre by both blocking the scattering from the left of the sample and blocking the beam from hitting right-of-centre. This is particularly beneficial at low incidence angles where the source would otherwise be almost incident on the detector. During measurement, the sample is usually rotated in the plane orthogonal to the measurement axis to account for any sample non-uniformity such as preferential orientation in the plane of the sample. One of the diffractometers used in this research (Bruker D8 Advance) is shown in Figure 4 with these features marked.

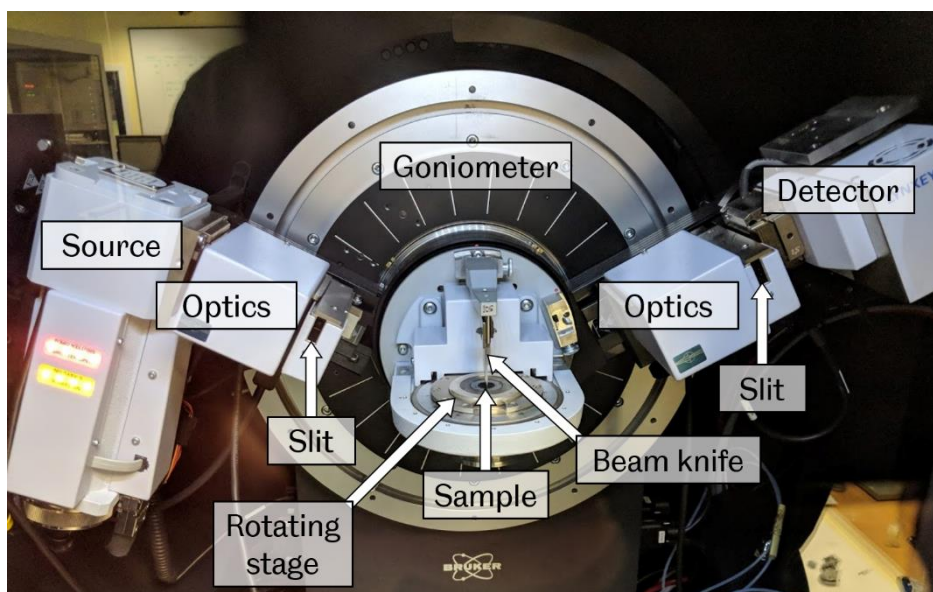


Figure 4: Bruker D8 Advance diffractometer with key components indicated.

Perhaps the most widely used method for the acquisition of XRD patterns uses the Bragg-Brentano, or *reflection*, geometry (Figure 5A). Here the X-ray source and detector arms are both symmetrically rotated on the goniometer by an angle θ above the horizontal sample plane, in this way the range of 2θ Bragg angles are probed. This is ideal for thick samples, however at higher angles with thin films the X-ray beam will pass through a reduced scattering volume, altering the peak intensity. This can also cause intense reflections from the substrate in the case of weakly scattering thin films.

An alternative geometry is *grazing-incidence* (Figure 5B), in which the beam is at a constant incidence angle α_i with respect to the sample surface, and only the detector arm is rotated through 2θ . This has the benefit of always maintaining the same beam attenuation through the sample (minimal substrate contribution), but does however mean that the *sample footprint* over which scattering occurs is longer. The effect is a larger instrumental contribution to peak broadening (particularly at larger 2θ angles), whereas at most angles in Bragg-Brentano the scattering is effectively from a point.

These 1D-XRD methods are unfortunately of lower utility for highly oriented or textured thin film samples, in which scattering can occur away from the measurement plane in either of these geometries, necessitating the use of 2D X-ray scattering methods.

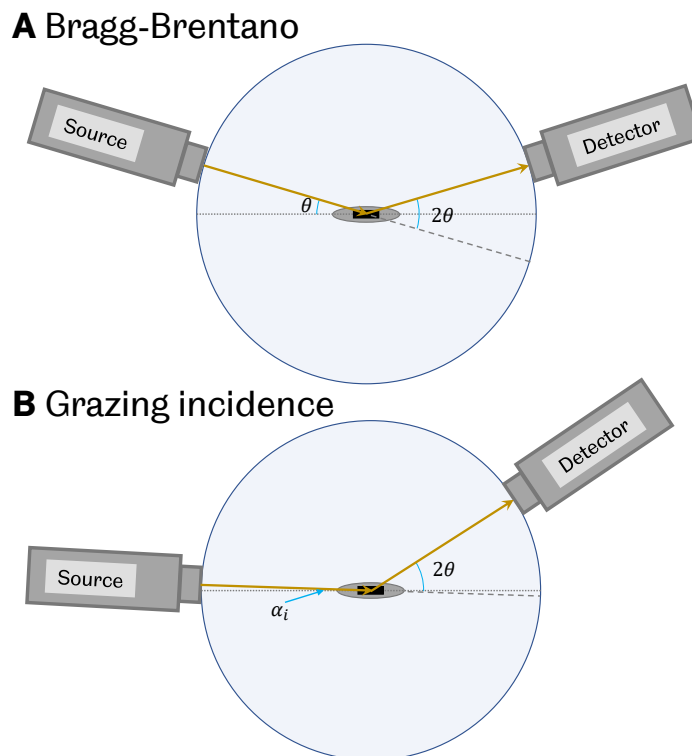


Figure 5: Two common 1D-XRD geometries. A) Bragg-Brentano geometry, in which the source and detector are rotated through an angle θ to satisfy the Bragg condition. B) Grazing-incidence, where the X-ray source is held at a constant incidence angle α_i greater than the critical angle of the material (typically 0.5-3°).

3.3.3: 2D X-ray scattering

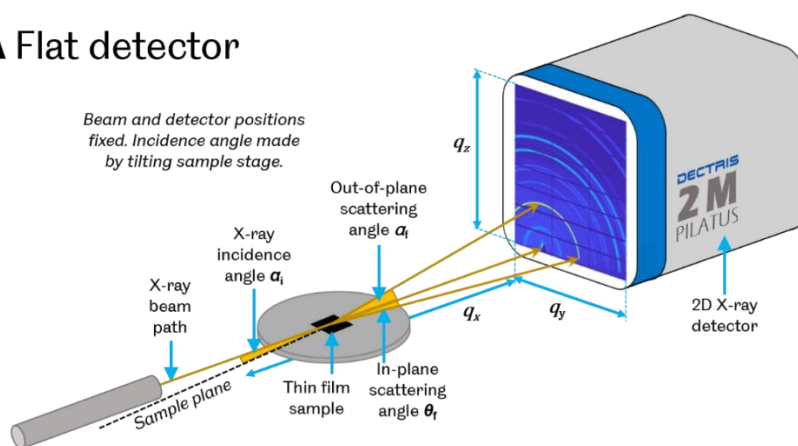
Wide-angle X-ray scattering (WAXS), in particular in grazing-incidence geometry (GIWAXS), overcomes these shortcomings of 1D X-ray scattering methods for thin films. This technique emerged from an offshoot of the small-angle X-ray scattering (SAXS) community, working on grazing-incidence SAXS, which was introduced in 1989.²¹ Initial reports focused on film formation, nanoparticle assembly, and GISAXS became widely used in response to the difficulties in measuring weakly scattering organic thin films.²² This progressed into extensive possibilities for characterisation of thin film morphologies, buried interfaces, and most importantly, by acquiring a large region of reciprocal space simultaneously, *in-situ* process monitoring.^{23,24}

In a GISAXS measurement, a flat X-ray detector is positioned at a large distance from the scattering centre to monitor very low Q reciprocal space, corresponding to large distances in real space. In contrast, GIWAXS (and related/analogous techniques such as 2D GI-XRD, GIXS etc) monitors the much smaller scattering features, typically $q = 0.1\text{-}3 \text{ \AA}^{-1}$, or real space distances $d \sim 2\text{-}60 \text{ \AA}$ – covering a range of interatomic distances. Depending on the X-ray source, scattering intensity and 2D detector, impressive time resolutions can be achieved - in

Chapter 6 as high as 10 frames per second - but with much faster acquisition possible with the latest generation detector materials.²⁵

A standard GIWAXS experimental configuration using a flat 2D detector at a static position is shown in Figure 6A, with the required incidence angle α_i implemented by tilting the sample stage. Alternatively, a smaller 2D detector on a goniometer can be used which more closely samples the surface of the Ewald sphere (Figure 6B).²⁶ This is at the expense of temporal resolution as data for a complete scattering pattern must be acquired at multiple detector positions,²⁷ and so is unsuitable for monitoring fast processes. This setup is analogous to 1D GI-XRD but without slits at the detector to minimise the scattering background, so high brilliance X-ray sources are required. A range of sample environments can be used surrounding the sample, including *in-situ* coating apparatus,^{28,29} environmental chambers,³⁰⁻³² or vacuum environments to remove background air scatter or perform vapour depositions.^{26,33}

A Flat detector



B Rotating detector

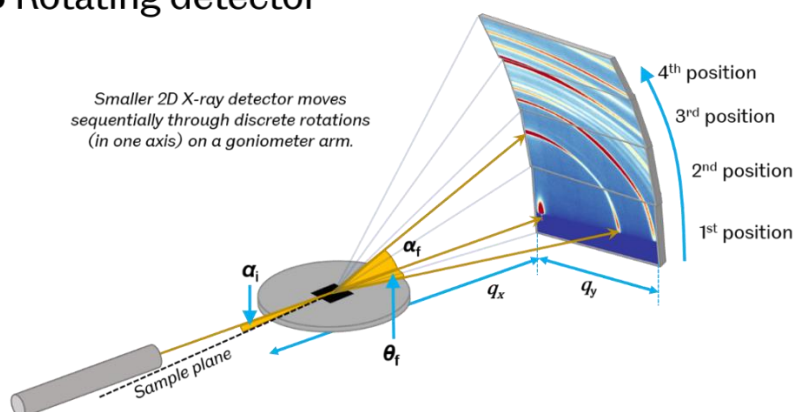


Figure 6: A) Typical GIWAXS experimental setup. If sufficiently scattering and transmissive, the sample can also be mounted in a transmission configuration, normal to the beam path. This has the benefit of reducing sample footprint broadening, but prevents analysis of film texture. B) Alternatively, a smaller 2D detector rotated about the sample centre can be used.

For many materials, crystal formation in thin films is not isotropic; the equilibrium point for crystal nucleation is not uniform throughout a wet film.³⁴ Instead, the air/liquid or liquid/solid interfaces may be sites which seed crystal growth, and could then proceed in a specific orientation direction through a film. This results in crystal structure which has preferentially grown along some axes, exhibiting strong orientation or “texturing”. In these highly oriented materials, GIWAXS is particularly invaluable, as they will exhibit scattering features but not along the q_z axis which is probed by 1D-XRD methods (Figure 7). Peaks outside of this region will not be observed in traditional XRD, and for phases with out-of-plane texture, the peak intensity will be greatly exaggerated. This is frequently the case in the halide perovskite field with PbI_2 commonly forming with strong out-of-plane texture and often scattering more strongly than the perovskite phase.³⁵ This could be easily misinterpreted as being the dominant phase in a film, when in fact it is merely the phase with the largest “coherent scattering domain” in the plane of the measurement, but may be a much smaller phase fraction of the overall film. In the case of randomly oriented (“isotropic”) samples (such as uniform powder samples), the scattering peaks observed in a 1D XRD pattern will appear as complete Debye-Scherrer rings on the 2D detector surface.

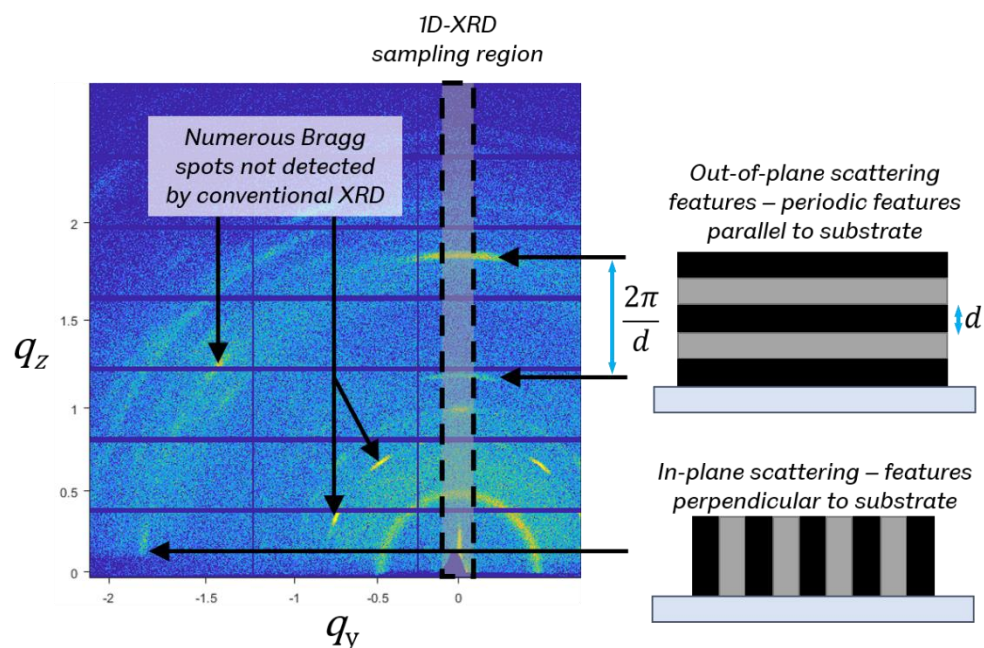
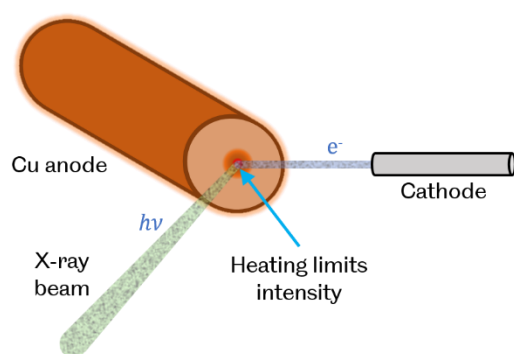


Figure 7: A GIWAXS detector image acquired from a highly oriented sample. The marked region indicates the region observed in a 1D-XRD measurement. The illustrations to the right show periodic structure either parallel or perpendicular to the sample substrate, resulting in reciprocal space scattering in the marked directions (regular orders of the same plane are spaced by $Q = 2\pi/d$). It should be noted that aside from epitaxial samples, polycrystalline film orientation is generally isotropic in the q_{xy} plane, so while the detector image samples reciprocal space orthogonal to the q_x direction (Figure 6), the full in-plane scattering is still acquired.

3.3.4: X-ray sources

To acquire 2D X-ray scattering data, high intensity, collimated beams are required. With a solid-state Cu anode, the X-ray flux is proportional to the electron flux, and reaches a maximum when the anode begins to melt (Figure 8A). This limits the practical electron beam intensity to typically ~ 2-3 kW with some cooling of the anode, with tens of kW achievable with a rotating anode or other innovative cooling.^{36,37} The most exciting development for lab-based measurements has been the advent of liquid-metal jet X-ray sources.³⁸ In these systems, the solid-state anode is replaced by a rapidly flowing jet of a liquid metal, typically indium-gallium alloys. In this way, the anode is continuously replenished, avoiding the melting that would occur for a solid-state source, and allowing for much higher power electron beams (up to 250 kW).³⁹ An Excillum MetalJet source as part of a Xenocs Xeuss 2.0 system based in the Department of Chemistry at the University of Sheffield was used extensively throughout all aspects of the research undertaken, enabling acquisition of GIWAXS patterns from perovskite films in as little as 60 seconds. For fast in situ processes or rapid data acquisition, synchrotron radiation sources are required. Here the X-ray photon intensity is several orders of magnitude higher (10^{14} photons/second), concentrated in a small area, low divergence beam with advanced X-ray optics to enhance the monochromaticity.

A Solid state



B Liquid-metal jet

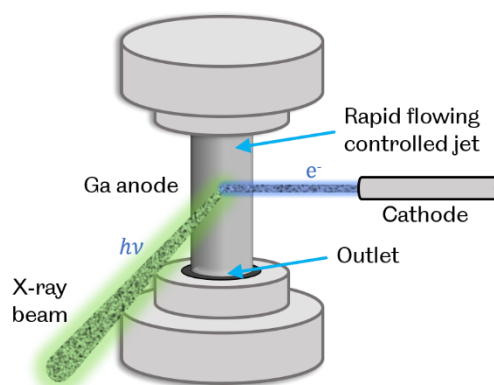


Figure 8: Comparison of solid-state and liquid anodes for X-ray generation. A) A solid Cu anode is limited by the melting of the material, which can be partially overcome by rotating or actively cooling it. B) With a constantly flowing Ga anode, the cathode beam intensity can be an order of magnitude higher intensity.

3.3.5: Data processing

X-ray data acquired as GIWAXS must be corrected, masked and processed (data reduction) before being analysed. The raw 2D detector images are acquired at a sample-to-detector distance (SDD) and the correct reciprocal space mapping for this position is calibrated using

a measurement from a strongly scattering standard material with well-defined lattice parameters, such as silver behenate or ideally lanthanum hexaboride (LaB₆, specifically NIST standard SRM660c). The data is masked to remove faulty pixels on the detector, and to remove known background scattering features such as the direct beam, or scattering below the sample horizon. Data must also be corrected for other factors such as the polarisation of the X-ray beam, for instance in the case of horizontally polarised synchrotron light, or the detector solid angle, a correction accounting for the angle-dependent path-length of a diffracted photon through a finite thickness detector.⁴⁰ In the case of shallow α_i , refraction can cause not insignificant shifts of peak positions in q_z which must be considered for certain samples.⁴¹

From this, because incidence and scattering angles are not equal, the outgoing momentum transfer vector has an in-plane scattering component, therefore some data from the otherwise spherical Ewald surface are not captured.⁴² This results in a “missing wedge” of data which is dependent on the scattering and incidence angles, as well as the detector angle.^{40,43} The raw 2D detector image must therefore be “reshaped”, and from this we can take linecuts through the data, with an “azimuthal linecut” (confusingly also variously termed a “radial linecut”) integrating over a range of χ angles, producing a 1D plot of q vs. intensity, which is interpretable in the same way as XRD, but with total scattering including the contribution from off-axis scattering vectors (Figure 9A,C). For *in-situ* process monitoring, by azimuthally integrating a series of 2D images we can produce “waterfall” (or “contour”) plots of diffraction over time, acquired simultaneously at a range of length scales (Figure 9D). To better understand orientation of a specific lattice plane, one can also take a “azimuthal profile” (or sector profile) around, or along, a specific Debye-Scherrer ring, returning a plot of χ vs. intensity (Figure 9B). Short of a more rigorous texture analysis, this orientation distribution can be analysed by a number of parameters such as Hermans’s orientation function, Maier-Saupe orientation parameter,⁴⁴ a mosaicity factor,⁴⁵ or a Lotgering factor.^{46,47}

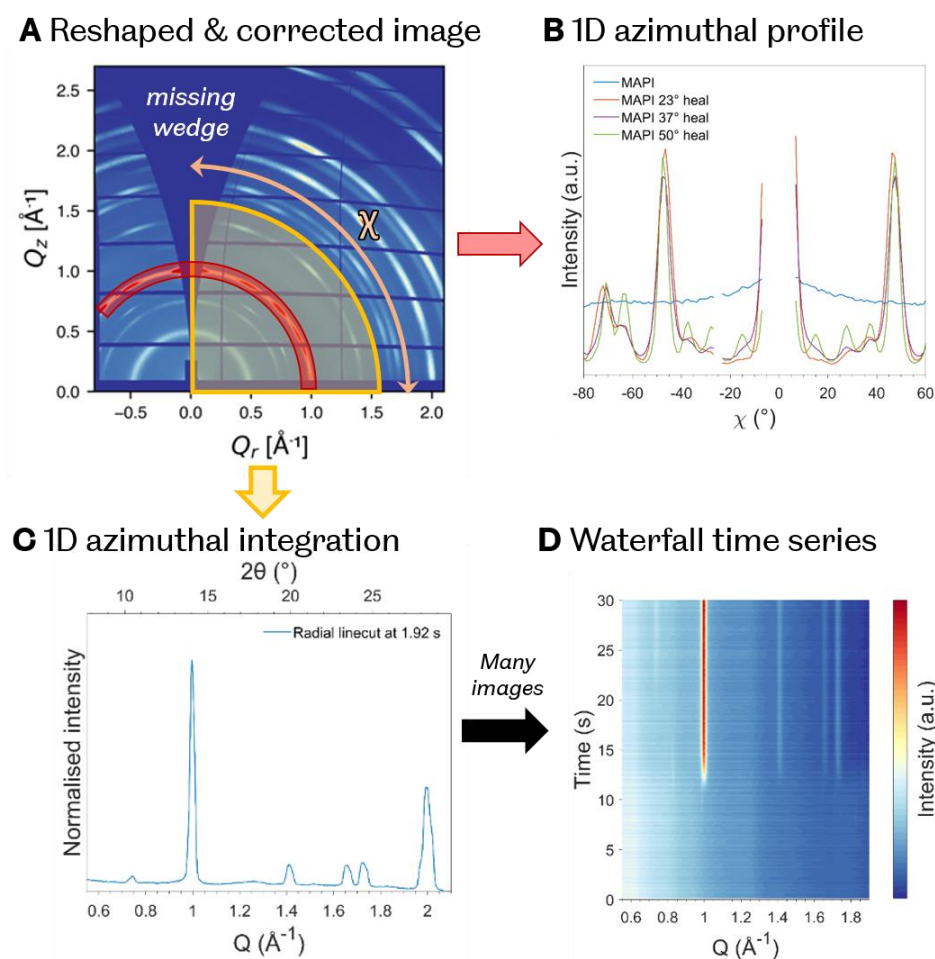


Figure 9: GIWAXS data reduction. A) A raw 2D detector image has been corrected and reshaped, introducing the missing wedge of data, the portion of the Ewald sphere not sampled by the flat detector. The angle χ on the 2D image is marked, indicating the axis along all Debye-Scherrer scattering rings. B) Radially integrating along a single scattering ring gives the orientation distribution for a specific reflection. C) An azimuthal integration over all χ angles gives the equivalent to a powder-XRD pattern – an orientation independent q vs. intensity plot. D) Taking a series of azimuthal integrations we can monitor multiple reflections simultaneously for *in-situ* measurements.

Whilst the GIWAXS community is obviously not as large as the wider field of crystallography, there is a growing ecosystem of software packages for data reduction and analysis. Most useful to this thesis has been GIXSGUI, developed by Zhang Jiang at the Advanced Photon Source.⁴⁰ This is a MATLAB toolbox with wide-ranging functionality from data processing, applying corrections, 1D linecut processing and 2D image reshaping to account for the missing wedge.⁴⁸ This software has only limited capability for batch-processing, so additionally a GUI was developed for this purpose to handle large datasets. This was designed to simplify data processing and has been invaluable, particularly for *in-situ* experiments with large kinetic datasets.

More recently, Python Fast Azimuthal Integrator (PyFAI), has been employed with great success.⁴⁹ This program has been designed by researchers at the European Synchrotron Radiation Facility for the computationally efficient reduction of large 2D datasets in transmission geometry. This has the benefit of being open-source code, well supported, and has a range of tools, such as for implementing sample alignment and reciprocal space mapping. Developing work by Dane *et al.*⁵⁰ to modify the PyFAI library for use with grazing incidence geometry, numerous codes were written to automatically process 1D azimuthal integrations, reshape 2D data and waterfall plots, benefitting from the more extensive set of Python libraries than are available within Matlab.

In addition, both SimDiffraction and GIXSGUI have been useful to analyse and simulate 2D diffraction patterns. GIXSGUI allows for the calculation of expected scattering positions for a generic unit cell for any of the 230 space groups when given the unit cell parameters a, b, c, α, β and γ . With an orientation vector $[uvw]$ of the unit cell, the expected positions in q_{xy} and q_z are calculated and can be directly overlaid onto the measured diffraction data (Figure 10). This has been useful for quickly identifying dominant orientations for known crystal structures in a material. SimDiffraction, a Matlab package developed and maintained by Dag Breiby *et al.*,⁵¹ offers an even more powerful tool which was particularly useful in Chapter 6. Here, it is possible to directly simulate 2D diffraction data by defining an extensive range of parameters relating to the beam (shape, polarization), sample (correlation length, X-ray absorption properties), crystal structure (crystallographic information file [CIF] import, structure factor, atomic positions) and preferred orientation (uniaxial/biaxial models, sample tilts, peak broadening). The interface, processing and example data output are shown in Figure 11.

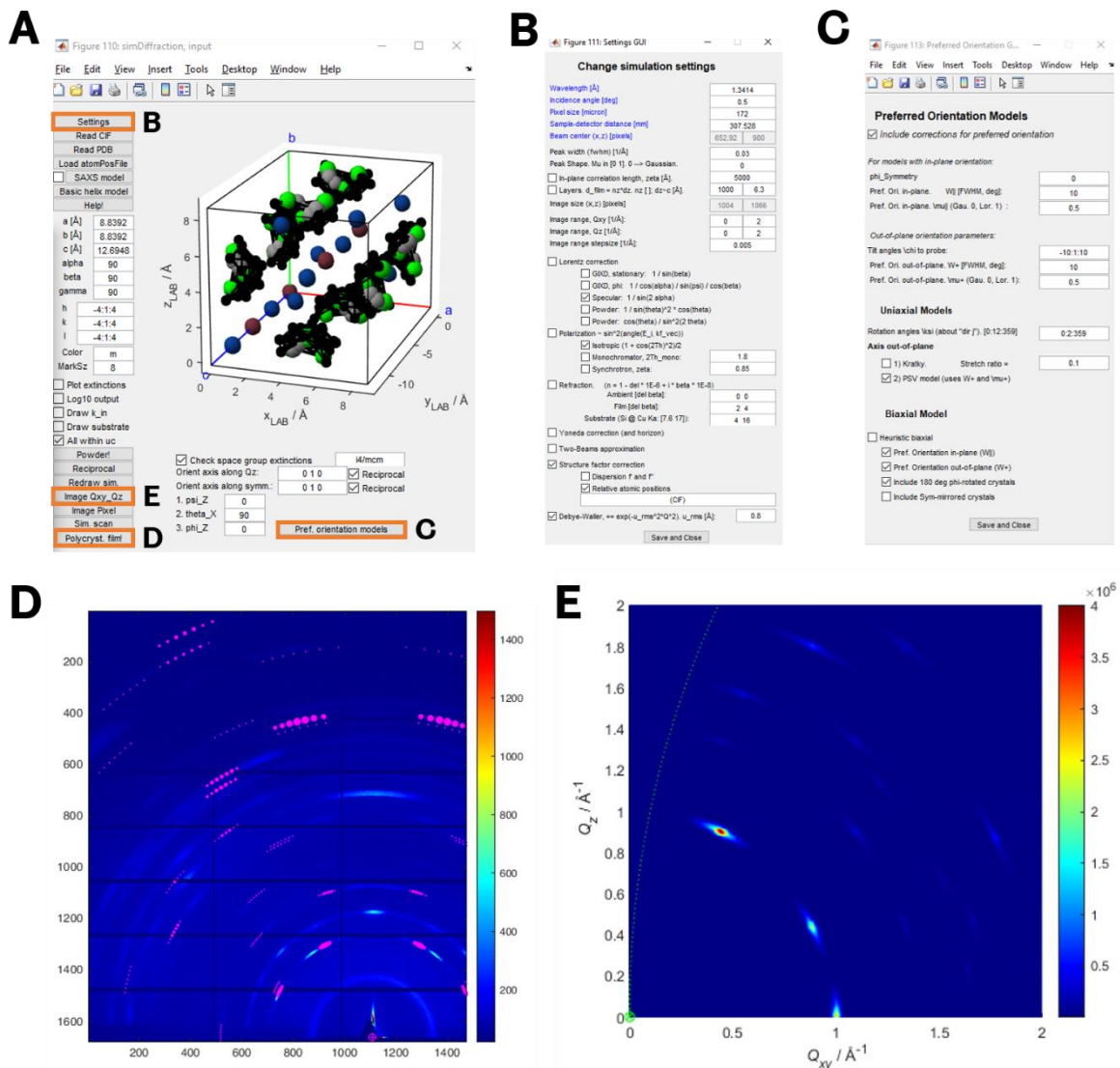


Figure 11: SimDiffraction tool for simulating 2D diffraction data. A) The core input window, illustrating an imported CIF structure, unit cell parameters, orientation vector and other options. From here, the settings B) define the experimental parameters for the imported data and various corrections which can be applied. C) The preferred orientation model parameters for a simulation, accounting for sample tilting, rotation in the xy plane, chirality and other possible sources of scattering intensity. D) A simple overlay of expected scattering positions on the acquired data (analogous to Figure 10B in GIXSGUI, with peak broadening, but unfortunately without Miller indices). E) Example of a fully-simulated 2D diffraction pattern using the applied corrections and orientation model output as in part D.

3.3.6: Nuclear magnetic resonance (NMR) spectroscopy

NMR has been used, particularly in the later stages of the research, to identify chemical environments in solution. This relies on isotopes of certain elements which have an intrinsic magnetic moment, which can be perturbed by applying magnetic fields and observing the spin relaxation, with various types of pulse sequence providing detailed information on the surroundings of an element in a sample.^{52,53} To do this, samples (~600 μ l) are prepared inside

standard NMR tubes unless otherwise mentioned, in an N₂ glovebox to minimise contamination, free from particulates and usually in deuterated solvents as stated for each sample.⁵⁴ Several types of spectra were acquired in 1D (¹H, ¹³C, ²⁰⁷Pb) and 2D (1H-1H COrelated Spectroscopy [COSY] and 1H-13C Heteronuclear Single Quantum Coherence [HSQC]), generally using standardised parameters. Data was acquired on a Bruker Avance II 400MHz or Bruker Avance III 400MHz and all data were analysed using TopSpin (Bruker).

3.3.7: Optical spectroscopies

White-light absorption, photoluminescence (PL) and spectroscopic ellipsometry (SE) were used to characterise np-SnO₂ and perovskite films in Chapter 4.

Absorption allowed for the estimation of the optical E_g of these layers by comparing a white light spectrum with and without an absorbing sample. Absorption measurements were also used for solutions in a cuvette, with absorption bands corresponding to different iodoplumbate species in solution.

Bandgap measurements on films were complemented by PL which provides a fast method to look at the emission spectrum of photons after excitation by above bandgap photons (typically 532 nm). We note there are some subtleties in measuring PL on perovskite films due to optical effects,⁵⁵ the presence of mixtures of phases,⁵⁶ and evolution of these multiple phases (such as by light-induced halide segregation),⁵⁷ and light-intensity dependence.

SE was used to analyse the thicknesses of np-SnO₂ thin films, making use of the change of polarisation between a transmitted and a reflected beam of light. This is done by fitting a model to the phase difference of the incident and reflected light. This was further developed by combining ellipsometry and transmission data to obtain the complex refractive index self-consistently for individual wavelengths via a global error minimization.⁵⁸ Some of this data was fitted with a band fluctuations model with an equation describing the direct absorption edge and Urbach tail.^{58,59}

3.3.8: Surface characterisation

Surface profilometry, atomic force microscopy (AFM), photo-conducting AFM (pc-AFM) and scanning electron microscopy (SEM) were all used to characterise film thicknesses, microstructure, roughness and electronic properties. All samples were prepared according to the procedures for device fabrication.

Profilometry was used on individual layers and completed devices both in line-scan mode (to check layer thicknesses) and with 2D map profiles to look at morphology over large areas. Data was processed in Gwyddion to remove sample tilting, and correct for other distortions over large areas.

AFM measurements were acquired over small areas to look at film topography. A scanning force microscope was used in tapping mode and again Gwyddion was used to process images and determine localised film roughnesses.

A scanning probe microscope was used to acquire pc-AFM on half-stack devices (ITO/SnO₂/perovskite). These were illuminated through the substrate by a blue LED with no applied bias to generate free charges, and the AFM tip connected to a ground to acquire the photocurrent at short-circuit conditions. Additionally the surface topology is measured, as with standard AFM.

SEM images of both film surfaces and device cross-sections were measured using various SEM systems, with success using a Carl Zeiss modified Raith Nanofabrication SEM. This was operated at low voltage (1-1.5 kV) to prevent excess charging which both damages samples and distorts images.⁶⁰ This was also mitigated by forming a good electrical contact between the perovskite and the sample holder using silver conductive paint, which was particularly important for cross-section sample preparation. Here, films were fractured using a diamond scribe applied to the back side of the sample, before snapping from the film side, and then mounted in a holder and coated with silver paint close to the measurement area. Backscattered secondary electrons were captured using a detector inside the beam column to allow for short working distances of 1-3 mm. Grain size analysis from these images utilised ImageJ, through carefully controlling the contrast of grain boundaries.

3.3.9: Photoelectron spectroscopy

Ultraviolet photoelectron spectroscopy (UPS) and X-ray photoelectron spectroscopy (XPS) measurements were acquired for thin films in ultra-high vacuum. These consist of photons being incident on a sample, which can remove electrons from the core levels of the elements present. Because the photoelectrons must be able to escape the film, these are highly surface-sensitive techniques. XPS can give extensive information about the chemical state of the elements present in a sample. UPS uses lower energy photons to probe orbital energies, giving information about the energy levels present in a sample, so it is ideal for analysing band alignment effects, assuming sample degradation can be avoided. XPS and UPS was collected using a Kratos AXIS Supra with either monochromatic aluminium radiation (1486.6 eV) for XPS

or helium (21.22 eV). Samples were electrically contacted to the sample holder to provide a conductive path from the top surface to the sample holder and prevent charging. The data was primarily analysed using CasaXPS and OriginPro, with further fitting of the XPS core level spectra in Fityk.⁶¹ A plasma cleaned Au foil was used as a reference film for UPS measurements (to confirm the Fermi energy for a metal sample of 0 eV).

3.4: References

- (1) Jiang, Q.; Zhang, L.; Wang, H.; Yang, X.; Meng, J.; Liu, H.; Yin, Z.; Wu, J.; Zhang, X.; You, J. Enhanced Electron Extraction Using SnO₂ for High-Efficiency Planar-Structure HC(NH₂)₂PbI₃-Based Perovskite Solar Cells. *Nat. Energy* **2017**, *2* (1), 16177. <https://doi.org/10.1038/nenergy.2016.177>.
- (2) Jiang, Q.; Zhao, Y.; Zhang, X.; Yang, X.; Chen, Y.; Chu, Z.; Ye, Q.; Li, X.; Yin, Z.; You, J. Surface Passivation of Perovskite Film for Efficient Solar Cells. *Nat. Photonics* **2019**. <https://doi.org/10.1038/s41566-019-0398-2>.
- (3) Lu, H.; Liu, Y.; Ahlawat, P.; Mishra, A.; Tress, W. R.; Eickemeyer, F. T.; Yang, Y.; Fu, F.; Wang, Z.; Avalos, C. E.; Carlsen, B. I.; Agarwalla, A.; Zhang, X.; Li, X.; Zhan, Y.; Zakeeruddin, S. M.; Emsley, L.; Rothlisberger, U.; Zheng, L.; Hagfeldt, A.; Grätzel, M. Vapor-Assisted Deposition of Highly Efficient, Stable Black-Phase FAPbI₃ Perovskite Solar Cells. *Science* (80-.). **2020**, *370* (6512). <https://doi.org/10.1126/science.abb8985>.
- (4) Bu, T.; Li, J.; Zheng, F.; Chen, W.; Wen, X.; Ku, Z.; Peng, Y.; Zhong, J.; Cheng, Y.-B.; Huang, F. Universal Passivation Strategy to Slot-Die Printed SnO₂ for Hysteresis-Free Efficient Flexible Perovskite Solar Module. *Nat. Commun.* **2018**, *9* (1), 4609. <https://doi.org/10.1038/s41467-018-07099-9>.
- (5) Saliba, M.; Matsui, T.; Seo, J.-Y.; Domanski, K.; Correa-Baena, J.-P.; Nazeeruddin, M. K.; Zakeeruddin, S. M.; Tress, W.; Abate, A.; Hagfeldt, A.; Grätzel, M. Cesium-Containing Triple Cation Perovskite Solar Cells: Improved Stability, Reproducibility and High Efficiency. *Energy Environ. Sci.* **2016**, *9* (6), 1989–1997. <https://doi.org/10.1039/C5EE03874J>.
- (6) Habisreutinger, S. N.; Noel, N. K.; Snaith, H. J.; Nicholas, R. J. Investigating the Role of 4-Tert Butylpyridine in Perovskite Solar Cells. *Adv. Energy Mater.* **2016**, 1601079. <https://doi.org/10.1002/aenm.201601079>.
- (7) Saliba, M.; Correa-Baena, J. P.; Wolff, C. M.; Stolterfoht, M.; Phung, N.; Albrecht, S.; Neher, D.; Abate, A. How to Make over 20% Efficient Perovskite Solar Cells in Regular (n-i-p) and Inverted (p-i-n) Architectures. *Chem. Mater.* **2018**, *30* (13), 4193–4201. <https://doi.org/10.1021/acs.chemmater.8b00136>.
- (8) Danglad-Flores, J.; Eickelmann, S.; Riegler, H. Deposition of Polymer Films by Spin Casting: A Quantitative Analysis. *Chem. Eng. Sci.* **2018**, *179*, 257–264. <https://doi.org/10.1016/j.ces.2018.01.012>.
- (9) Patidar, R.; Burkitt, D.; Hooper, K.; Richards, D.; Watson, T. Slot-Die Coating of Perovskite Solar Cells: An Overview. *Mater. Today Commun.* **2020**, *22* (December 2019), 100808. <https://doi.org/10.1016/j.mtcomm.2019.100808>.
- (10) Ding, X.; Liu, J.; Harris, T. A. L. A Review of the Operating Limits in Slot Die Coating Processes. *AIChE J.* **2016**, *62* (7), 2508–2524. <https://doi.org/10.1002/aic.15268>.
- (11) Eslamian, M. Spray-on Thin Film PV Solar Cells: Advances, Potentials and Challenges. *Coatings* **2014**, *4* (1), 60–84. <https://doi.org/10.3390/coatings4010060>.
- (12) Bishop, J. E.; Routledge, T. J.; Lidzey, D. G. Advances in Spray-Cast Perovskite Solar Cells. *J. Phys. Chem. Lett.* **2018**, 1977–1984. <https://doi.org/10.1021/acs.jpcllett.8b00311>.
- (13) Majumder, M.; Rendall, C.; Li, M.; Behabtu, N.; Eukel, J. A.; Hauge, R. H.; Schmidt, H. K.; Pasquali, M. Insights into the Physics of Spray Coating of SWNT Films. *Chem. Eng. Sci.* **2010**, *65* (6), 2000–2008. <https://doi.org/10.1016/j.ces.2009.11.042>.
- (14) Bishop, J. E.; Smith, J. A.; Lidzey, D. G. Development of Spray-Coated Perovskite Solar Cells. *ACS Appl. Mater. Interfaces* **2020**. <https://doi.org/10.1021/acsami.0c14540>.
- (15) Snaith, H. J.; Abate, A.; Ball, J. M.; Eperon, G. E.; Leijtens, T.; Noel, N. K.; Stranks, S. D.; Wang, J. T. W.; Wojciechowski, K.; Zhang, W. Anomalous Hysteresis in Perovskite Solar Cells. *J. Phys. Chem. Lett.* **2014**, *5* (9), 1511–1515. <https://doi.org/10.1021/jz500113x>.
- (16) Tress, W.; Yavari, M.; Domanski, K.; Yadav, P. K.; Niesen, B.; Correa-Baena, J.-P.; Hagfeldt, A.; Grätzel, M. Interpretation and Evolution of Open-Circuit Voltage, Recombination, Ideality Factor and Subgap Defect States during Reversible Light-Soaking and Irreversible Degradation of Perovskite Solar Cells. *Energy Environ. Sci.* **2017**. <https://doi.org/10.1039/C7EE02415K>.
- (17) Calado, P.; Burkitt, D.; Yao, J.; Troughton, J.; Watson, T. M.; Carnie, M. J.; Telford, A. M.; Regan, B. C. O.; Nelson, J.; Barnes, P. R. F. Identifying Dominant Recombination Mechanisms in Perovskite Solar Cells by Measuring the Transient Ideality Factor. *Phys. Rev. Appl.* **2019**, *10* (1), 1. <https://doi.org/10.1103/PhysRevApplied.11.044005>.
- (18) Bovill, E.; Scarratt, N.; Griffin, J.; Yi, H.; Iraqi, A.; Buckley, A. R.; Kingsley, J. W.; Lidzey, D. G. The Role of the Hole-Extraction Layer in Determining the Operational Stability of a Polycarbazole:Fullerene Bulk-Heterojunction Photovoltaic Device. *Appl. Phys. Lett.* **2015**, *106* (7). <https://doi.org/10.1063/1.4909530>.
- (19) Klug, H. P.; Alexander, L. E. *X-Ray Diffraction Procedures: For Polycrystalline and Amorphous Materials, 2nd Edition*; Wiley, 1974.
- (20) Als-Nielsen, J.; McMorrow, D. *Elements of Modern X-Ray Physics: Second Edition*; 2011. <https://doi.org/10.1002/9781119998365>.
- (21) Levine, J. R.; Cohen, J. B.; Chung, Y. W.; Georgopoulos, P. Grazing-Incidence Small-Angle X-Ray Scattering: New Tool for Studying Thin Film Growth. *J. Appl. Crystallogr.* **1989**, *22* (6), 528–532. <https://doi.org/10.1107/s002188988900717x>.
- (22) Renaud, G.; Lazzari, R.; Leroy, F. Probing Surface and Interface Morphology with Grazing Incidence Small Angle X-Ray Scattering. *Surf. Sci. Rep.* **2009**, *64* (8), 255–380. <https://doi.org/10.1016/j.surfrep.2009.07.002>.

- (23) Renaud, G.; Lazzari, R.; Revenant, C.; Barbier, A.; Noblet, M.; Ulrich, O.; Leroy, F.; Jupille, J.; Borensztein, Y.; Henry, C. R.; Deville, J. P.; Scheurer, F.; Mane-Mane, J.; Fruchart, O. Real-Time Monitoring of Growing Nanoparticles. *Science* (80-.). **2003**, *300* (5624), 1416–1419. <https://doi.org/10.1126/science.1082146>.
- (24) Smilgies, D.; Busch, P.; Papadakis, C. M.; Posselt, D. Characterization of Polymer Thin Films with Small-angle X-ray Scattering under Grazing Incidence (GISAXS). *Synchrotron Radiation News*. 2002, pp 35–42. <https://doi.org/10.1080/08940880208602975>.
- (25) Müller, M.; Donath, T.; Rissi, M.; Ott, H.; Graf, J.; Stuerzer, T.; Ruf, M. PILATUS3 R CdTe Large-Area Detectors for Laboratory Applications. *Acta Crystallogr. Sect. A* **2016**, *A72* (September), 2016.
- (26) Skroblin, D.; Schavkan, A.; Pflüger, M.; Pilet, N.; Lüthi, B.; Krumrey, M. Vacuum-Compatible Photon-Counting Hybrid Pixel Detector for Wide-Angle x-Ray Scattering, x-Ray Diffraction, and x-Ray Reflectometry in the Tender x-Ray Range. *Rev. Sci. Instrum.* **2020**, *91* (2). <https://doi.org/10.1063/1.5128487>.
- (27) Rosales, B. A.; Mundt, L. E.; Allen, T. G.; Moore, D. T.; Prince, K. J.; Wolden, C. A.; Rumbles, G.; Schelhas, L. T.; Wheeler, L. M. Reversible Multicolor Chromism in Layered Formamidinium Metal Halide Perovskites. *Nat. Commun.* **2020**, *11* (1), 1–12. <https://doi.org/10.1038/s41467-020-19009-z>.
- (28) Munir, R.; Sheikh, A. D.; Abdelsamie, M.; Hu, H.; Yu, L.; Zhao, K.; Kim, T.; Tall, O. E.; Li, R.; Smilgies, D.; Amassian, A. Hybrid Perovskite Thin-Film Photovoltaics : In Situ Diagnostics and Importance of the Precursor Solvate Phases. **2017**. <https://doi.org/10.1002/adma.201604113>.
- (29) Szostak, R.; Marchezi, P. E.; Marques, A. D. S.; Da Silva, J. C.; De Holanda, M. S.; Soares, M. M.; Tolentino, H. C. N.; Nogueira, A. F. Exploring the Formation of Formamidinium-Based Hybrid Perovskites by Antisolvent Methods: In Situ GIWAXS Measurements during Spin Coating. *Sustain. Energy Fuels* **2019**, *3* (9), 2287–2297. <https://doi.org/10.1039/c9se00306a>.
- (30) Schelhas, L. T.; Li, Z.; Christians, J. A.; Goyal, A.; Kairys, P.; Harvey, S. P.; Kim, D. H.; Stone, K. H.; Luther, J. M.; Zhu, K.; Stevanovic, V.; Berry, J. J. Insights into Operational Stability and Processing of Halide Perovskite Active Layers. *Energy Environ. Sci.* **2019**, 1341–1348. <https://doi.org/10.1039/c8ee03051k>.
- (31) Fransishyn, K. M.; Kundu, S.; Kelly, T. L. Elucidating the Failure Mechanisms of Perovskite Solar Cells in Humid Environments Using in Situ Grazing-Incidence Wide-Angle X-Ray Scattering. *ACS Energy Lett.* **2018**, *3* (9), 2127–2133. <https://doi.org/10.1021/acsenerylett.8b01300>.
- (32) Nicklin, C.; Arnold, T.; Rawle, J.; Warne, A. Diamond Beamline I07: A Beamline for Surface and Interface Diffraction. *J. Synchrotron Radiat.* **2016**, *23*, 1245–1253. <https://doi.org/10.1107/S1600577516009875>.
- (33) Nicklin, C.; Martinez-Hardigree, J.; Warne, A.; Green, S.; Burt, M.; Naylor, J.; Dorman, A.; Wicks, D.; Din, S.; Riede, M. MINERVA: A Facility to Study Microstructure and Interface Evolution in Realtime under Vacuum. *Rev. Sci. Instrum.* **2017**, *88* (10). <https://doi.org/10.1063/1.4989761>.
- (34) Mullin, J. W. *Crystallization, 4th Edition*; Butterworth-Heinemann, 2001.
- (35) Jiang, Q.; Zhao, Y.; Zhang, X.; Yang, X.; Chen, Y.; Chu, Z.; Ye, Q.; Li, X.; Yin, Z.; You, J. Surface Passivation of Perovskite Film for Efficient Solar Cells. *Nat. Photonics* **2019**, *13* (7), 460–466. <https://doi.org/10.1038/s41566-019-0398-2>.
- (36) Rigaku SmartLab product information <https://www.rigaku.com/products/xrd/smartlab> (accessed Sep 20, 2020).
- (37) I μ S – Incoatec Microfocus Source <https://www.incoatec.de/files/downloads/flyer/IDO-F20-005B-IMS-8seiter-A4einzeln-xs.pdf> (accessed Sep 20, 2020).
- (38) Espes, E.; Andersson, T.; Björnsson, F.; Gratorp, C.; Hansson, B. A. M.; Hemberg, O.; Johansson, G.; Kronstedt, J.; Otendal, M.; Tuohimaa, T.; Takman, P. Liquid-Metal-Jet x-Ray Tube Technology and Tomography Applications. *Dev. X-Ray Tomogr. IX* **2014**, *9212* (September 2014), 92120J. <https://doi.org/10.1117/12.2061612>.
- (39) Excillum. *MetalJet D2+ 160 KV - The World's Brightest Microfocus X-Ray Source*; Kista, 2019.
- (40) Jiang, Z. GIXSGUI: A MATLAB Toolbox for Grazing-Incidence X-Ray Scattering Data Visualization and Reduction, and Indexing of Buried Three-Dimensional Periodic Nanostructured Films. *J. Appl. Crystallogr.* **2015**, *48* (3), 917–926. <https://doi.org/10.1107/S1600576715004434>.
- (41) Savikhin, V.; Steinrück, H.-G.; Liang, R.-Z.; Collins, B. A.; Oosterhout, S. D.; Beaujuge, P. M.; Toney, M. F. GIWAXS-SIRKit : Scattering Intensity, Indexing and Refraction Calculation Toolkit for Grazing-Incidence Wide-Angle X-Ray Scattering of Organic Materials. *J. Appl. Crystallogr.* **2020**, *53* (4), 1108–1129. <https://doi.org/10.1107/S1600576720005476>.
- (42) Baker, J. L.; Jimison, L. H.; Mannsfeld, S.; Volkman, S.; Yin, S.; Subramanian, V.; Salleo, A.; Alivisatos, A. P.; Toney, M. F.; Science, M.; Synchrotron, S.; Lightsource, R.; Park, M. Quantification of Thin Film Crystallographic Orientation Using X-Ray Diffraction with an Area Detector. *Langmuir* **2010**, *26* (11), 9146–9151. <https://doi.org/10.1021/la904840q>.
- (43) Dane, T. G.; Cresswell, P. T.; Pilkington, G. A.; Lilliu, S.; Macdonald, J. E.; Prescott, S. W.; Bikondoa, O.; Faul, C. F. J.; Briscoe, W. H. Oligo(Aniline) Nanofilms: From Molecular Architecture to Microstructure. *Soft Matter* **2013**, *9* (44), 10501. <https://doi.org/10.1039/c3sm51407b>.
- (44) Dou, B.; Whitaker, J. B.; Bruening, K.; Moore, D. T.; Wheeler, L. M.; Ryter, J.; Breslin, N. J.; Berry, J. J.; Garner, S. M.; Barnes, F. S.; Shaheen, S. E.; Tassone, C. J.; Zhu, K.; van Hest, M. F. A. M. Roll-to-Roll Printing of Perovskite Solar Cells. *ACS Energy Lett.* **2018**, *3* (10), 2558–2565. <https://doi.org/10.1021/acsenerylett.8b01556>.
- (45) Ogle, J.; Powell, D.; Amerling, E.; Smilgies, D. M.; Whittaker-Brooks, L. Quantifying Multiple Crystallite Orientations and Crystal Heterogeneities in Complex Thin Film Materials. *CrystEngComm* **2019**, *21* (38), 5707–5720. <https://doi.org/10.1039/c9ce01010f>.
- (46) Lotgering, F. K. Topotactical Reactions with Ferrimagnetic Oxides Having Hexagonal Crystal Structures-I. *J. Inorg. Nucl. Chem.* **1959**, *9* (2), 113–123. [https://doi.org/10.1016/0022-1902\(59\)80070-1](https://doi.org/10.1016/0022-1902(59)80070-1).
- (47) Furushima, R.; Tanaka, S.; Kato, Z.; Uematsu, K. Orientation Distribution-Lotgering Factor Relationship in a Polycrystalline Material - As an Example of Bismuth Titanate Prepared by a Magnetic Field. *J. Ceram. Soc. Japan* **2010**, *118* (1382), 921–926. <https://doi.org/10.2109/jcersj2.118.921>.
- (48) Zhang Jiang. Documentation for GIXSGUI - 1.6.2 <https://www.aps.anl.gov/Sector-8/8-ID/Operations-and-Schedules/Useful-Links/Sector-8-GIXSGUI> (accessed Aug 20, 2020).
- (49) Ashiotis, G.; Deschildre, A.; Nawaz, Z.; Wright, J. P.; Karkoulis, D.; Picca, F. E.; Kieffer, J. The Fast Azimuthal Integration Python Library: PyFAI. *J. Appl. Crystallogr.* **2015**, *48*, 510–519. <https://doi.org/10.1107/S1600576715004306>.
- (50) Dane, T. G. The pygix library <https://github.com/tgdane/pygix>.

- (51) Breiby, D. W.; Bunk, O.; Andreasen, J. W.; Lemke, H. T.; Nielsen, M. M. Simulating X-Ray Diffraction of Textured Films. *J. Appl. Crystallogr.* **2008**, *41* (2), 262–271. <https://doi.org/10.1107/S0021889808001064>.
- (52) Claudio, E. S.; Godwin, H. A.; Magyar, J. S. Fundamental Coordination Chemistry, Environmental Chemistry, and Biochemistry of Lead(II). In *Progress in Inorganic Chemistry, Volume 51*; John Wiley & Sons, Inc.: New York, USA, 2002; Vol. 51, pp 1–144. <https://doi.org/10.1002/0471267287.ch1>.
- (53) Claridge, T. D. W. *High-Resolution NMR Techniques in Organic Chemistry, 3rd Edition*; Elsevier Science, 2016.
- (54) Torres, A. M.; Price, W. S. Common Problems and Artifacts Encountered in Solution-State NMR Experiments. *Concepts Magn. Reson. Part A* **2016**, *45A* (2), e21387. <https://doi.org/10.1002/cmr.a.21387>.
- (55) Fassl, P.; Lami, V.; Berger, F. J.; Falk, L. M.; Zaumseil, J.; Richards, B. S.; Howard, I. A.; Vaynzof, Y.; Paetzold, U. W. Revealing the Internal Luminescence Quantum Efficiency of Perovskite Films via Accurate Quantification of Photon Recycling. *Matter* **2021**, 1–83. <https://doi.org/10.1016/j.matt.2021.01.019>.
- (56) Andaji-Garmaroudi, Z.; Abdi-Jalebi, M.; Guo, D.; Macpherson, S.; Sadhanala, A.; Tennyson, E. M.; Ruggeri, E.; Anaya, M.; Galkowski, K.; Shivanna, R.; Lohmann, K.; Frohna, K.; Mackowski, S.; Savenije, T. J.; Friend, R. H.; Stranks, S. D. A Highly Emissive Surface Layer in Mixed-Halide Multication Perovskites. *Adv. Mater.* **2019**, *31* (42). <https://doi.org/10.1002/adma.201902374>.
- (57) Knight, A. J.; Herz, L. M. Preventing Phase Segregation in Mixed-Halide Perovskites: A Perspective. *Energy Environ. Sci.* **2020**, *13* (7), 2024–2046. <https://doi.org/10.1039/d0ee00788a>.
- (58) Guerra, J. A.; Tejada, A.; Korte, L.; Kegelmann, L.; Töfflinger, J. A.; Albrecht, S.; Rech, B.; Weingärtner, R. Determination of the Complex Refractive Index and Optical Bandgap of CH₃NH₃PbI₃ Thin Films. *J. Appl. Phys.* **2017**, *121* (17), 173104. <https://doi.org/10.1063/1.4982894>.
- (59) Guerra, J. A.; Tejada, A.; Töfflinger, J. A.; Grieseler, R.; Korte, L. Band-Fluctuations Model for the Fundamental Absorption of Crystalline and Amorphous Semiconductors: A Dimensionless Joint Density of States Analysis. *J. Phys. D: Appl. Phys.* **2019**, *52* (10), 105303. <https://doi.org/10.1088/1361-6463/aaf963>.
- (60) Rothmann, M. U.; Li, W.; Zhu, Y.; Liu, A.; Ku, Z.; Bach, U.; Etheridge, J.; Cheng, Y. Structural and Chemical Changes to CH₃NH₃PbI₃ Induced by Electron and Gallium Ion Beams. *Adv. Mater.* **2018**, *30* (25), 1800629. <https://doi.org/10.1002/adma.201800629>.
- (61) Wojdyr, M. Fityk: A General-Purpose Peak Fitting Program. *J. Appl. Crystallogr.* **2010**, *43* (5 PART 1), 1126–1128. <https://doi.org/10.1107/S0021889810030499>.

Chapter 4

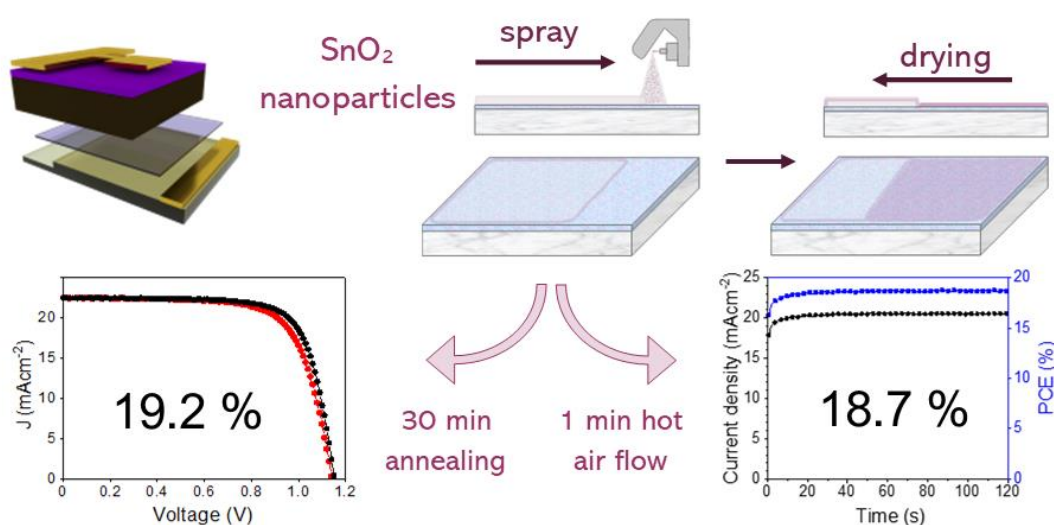
Rapid Scalable Processing of Tin Oxide Transport Layers for Perovskite Solar Cells

ACS **APPLIED**
ENERGY MATERIALS

Volume 3, Issue 6, Pages 5552-5562

May 8, 2020

DOI: 10.1021/acsaem.0c00525



4.0: Publication Foreword

The perovskite field has naturally diversified to investigate the complex electronic and ionic behaviour in the light-absorbing perovskite layer, the numerous transient instabilities in devices and the thousands of potential interface materials, each with their own chemical interactions. In this project, the goal was to develop a stable electron transport layer which could be scalably deposited and post-processed in timescales feasible for industrial fabrication. SnO₂ was chosen as a potentially more UV-stable metal oxide than TiO₂, which had by this point been identified as photocatalytic with UV light, which would seriously limit its potential use in PV modules. After extensive investigations with electron-beam deposited materials, spin-coated *pre-crystallised* nanoparticles (using non-toxic solvent) were found to be an attractive route to reproducibly high efficiency devices. New processes were developed to transfer this spin-coating protocol to scalable deposition procedures and understand the effects of post-processing procedures. The economic need for rapid processing of PSCs has been outlined in the introduction, and so a fast annealing step was developed enabling good efficiency devices. Despite the importance of processing at speed, this area is still relatively unexplored in perovskite literature and it is hoped that this paper will encourage further research in this area.

4.1: Author contributions

J.A.S. conceived the experiments, prepared the devices, performed or assisted with all measurements/analysis and wrote the manuscript. O.G. assisted with device fabrication, manuscript preparation and light V_{OC} measurements. J.E.B. assisted with the spray-coating layer design and fabrication. E.L.K.S. optimised the slot-die coating layers. R.C.K. took the AFM, ellipsometry and assisted with GIWAXS and analysis. C.G. acquired the TRPL data. R.J. took the PL and absorption measurements. T.I.A., M.W-S and T.J.R. assisted with sample fabrication. E.C. took profilometry measurements and assisted with XPS/UPS analysis. A.J.P. assisted with GIWAXS measurements. D.H. took UPS/XPS and supervised this data analysis. D.G.L. supervised the project.

4.2: Publication - Rapid Scalable Processing of Tin Oxide Transport Layers for Perovskite Solar Cells

Joel A. Smith,¹ Onkar S. Game,¹ James E. Bishop,¹ Emma L.K. Spooner,¹ Rachel C. Kilbride,¹ Claire Greenland,¹ Rahul Jayaprakash,¹ Tarek I. Alanazi,^{1,2} Elena J. Cassella,¹ Alvaro Tejada,^{3,4} Ganna Chistiakova,³ Michael Wong-Stringer,¹ Thomas J. Routledge,¹ Andrew J. Parnell,¹ Deborah B. Hammond⁵ and David G. Lidzey.^{1*}

- 1) Department of Physics & Astronomy, University of Sheffield, Sheffield, S3 7RH, UK
- 2) Department of Physics, College of Science, Northern Border University, Arar 73222, Kingdom of Saudi Arabia.
- 3) Helmholtz-Zentrum Berlin für Materialien und Energie GmbH, Institut für Silizium-Photovoltaik, Kekuléstraße 5, 12489 Berlin, Germany.
- 4) Departamento de Ciencias, Sección Física, Pontificia Universidad Católica del Perú, Av. Universitaria 1801, Lima 32, Peru.
- 5) Department of Chemistry, University of Sheffield, S3 7HF, UK.

*Corresponding Author - e-mail: d.g.lidzey@sheffield.ac.uk

4.2.1: Abstract

The development of scalable deposition methods for perovskite solar cell materials is critical to enable the commercialisation of this nascent technology. Herein, we investigate the use and processing of nanoparticle SnO₂ films as electron transport layers in perovskite solar cells, and develop deposition methods for ultrasonic spray-coating and slot-die coating, leading to photovoltaic device efficiencies over 19%. The effects of post-processing treatments (thermal annealing, UV ozone and O₂ plasma) are then probed using structural and spectroscopic techniques to characterise the nature of the np-SnO₂/perovskite interface. We show that a brief 'hot air flow' method can be used to replace an extended thermal anneal, confirming that this approach is compatible with high-throughput processing. Our results highlight the importance of interface management to minimise nonradiative losses, as well as providing a deeper understanding of the processing requirements for large area deposition of nanoparticle metal oxides.

4.2.2: Introduction

Organic-inorganic hybrid perovskite materials have generated excitement and extensive research interest in the photovoltaic community since their demonstration in 2009, with the record single-junction power conversion efficiency (PCE) now reaching above 25%.^{1,2} This has been made possible by a distinctive set of characteristics in this family of materials, including high optical absorption, long charge-carrier lifetimes enabled by low non-radiative recombination rates, and extensive possibilities for compositional tuning.^{3,4} Typically, high efficiency n-i-p cell architectures have relied on a compact and mesoporous TiO₂ electron transport layer (ETL) architecture.⁵ However, a primary concern with TiO₂ is the inherent instability caused by UV light interacting with molecular O₂ adsorbed at surface defect sites. This process may then lead to decomposition of the organic component of the active layer, with many stability studies on devices utilising TiO₂ typically making use of UV filters to negate such effects.^{6,7} TiO₂ based systems also commonly require processing steps at temperatures above 450°C.⁵ This temperature is, however, incompatible with many roll to roll (R2R) or sheet-to-sheet substrates such as polyethylene terephthalate (PET), and will also limit their use in tandem devices that may have other temperature-sensitive layers.

One approach to mitigate ETL UV instability and reduce the processing temperature is to replace TiO₂ (bandgap ~3.3 eV) with a wider bandgap metal oxide such as SnO₂ (3.6 – 4.2 eV), with the wider bandgap also reducing parasitic absorption.^{8,9} Compared to TiO₂, crystalline SnO₂ exhibits nearly two orders of magnitude higher electron mobility;¹⁰ a property that suggests it should act as a highly effective ETL. Atomic layer deposition (ALD) has been used to deposit amorphous SnO₂ and it is thought that its conduction band is well aligned for barrier-free electron transfer from various perovskites.¹¹ Various routes have been used to deposit planar SnO₂ including chemical bath deposition (CBD), sol-gel conversion,¹² chemical vapour deposition (CVD),¹³ plasma-enhanced ALD,¹⁴ electron-beam evaporation,¹⁵ thermal evaporation,¹⁶ sputtering,¹⁷ spin-coated sol-gel precursor in combination with CBD,¹⁸ nanoparticle routes,^{19,20} and mesoporous SnO₂.^{21,22} Importantly, mesoporous SnO₂ has also been demonstrated to have improved UV stability relative to mesoporous TiO₂, although has so far been processed at high temperature, preventing the use of fluorine-SnO₂ (FTO) layers due to fluorine migration.^{21,22} Two key papers on planar SnO₂-only ETL deposition routes have reported efficiencies of over 20%,^{18,19} with work by Jiang *et al.* using an off-the-shelf nanoparticle SnO₂ (np-SnO₂) product leading to a record-breaking planar n-i-p device PCE of 23.3%.²³ This np-SnO₂ system has the advantage of not undergoing temperature-sensitive

phase formation during annealing, which can impact the reproducibility of other SnO₂ ETL deposition processes.

In this paper, we utilise a np-SnO₂ system with a triple cation, mixed-halide perovskite⁵ with solution composition Cs_{0.05}FA_{0.79}MA_{0.16}PbI_{2.45}Br_{0.55} and demonstrate highly reproducible stabilised power output (SPO) efficiencies of up to 19.7% and good batch-to-batch reproducibility. We explore two scalable np-SnO₂ coating methods (spray-coating and slot-die coating) and achieve peak PCEs of over 18% SPO. To demonstrate a rapid process compatible with roll-to-roll (R2R) manufacture, we investigate both annealing-free and hot air flow (HAF) flash drying processes (120°C for 1 minute) combined with other low-temperature post-treatments (ultraviolet-ozone (UVO) and O₂ plasma) to replace or reduce the commonly used annealing step (10-30 minutes at 150°C).^{19,24} Using such techniques, we develop a rapid process that combines spray-coating, HAF at 120°C, and UVO treatment to achieve 18.7% SPO using a fully scalable ETL deposition process. These results demonstrate the benefit of *ex-situ* crystallised nanoparticle metal oxides for achieving efficient, rapidly processed photovoltaic devices.

4.2.3: Results and discussion

4.2.3.1: Electron transport layer deposition

To establish a stable baseline for experiments using more scalable techniques, we explored the fabrication of perovskite solar cell (PSC) devices in which the ETL was deposited by spin-coating np-SnO₂ from a diluted commercially available dispersion. Full details of the techniques used are given in Experimental Methods. Figure 1 shows the *n-i-p* configuration of the device, together with a scanning electron micrograph (SEM) cross-section of a completed device. Here, the full device structure is as follows: indium tin oxide (ITO), np-SnO₂ ETL, triple cation perovskite Cs_{0.05}FA_{0.79}MA_{0.16}PbI_{2.45}Br_{0.55} absorbing layer, doped spiro-OMeTAD hole transport layer (HTL) and Au top contact.

We achieved a narrow distribution of device efficiencies on ITO for large 0.16 cm² cells (see Figure 1c), with a champion device PCE of 19.8% reverse sweep (V_{OC} to J_{SC}) efficiency (Figure 1d) with the stabilised power output (SPO) closely matching the reverse sweep PCE at 19.7% (see Figure 1e). The batch-to-batch reproducibility and device metrics are promising; multiple devices were realised with a V_{OC} of 1.17 V, corresponding to a loss-in-voltage (V_{loss}) from the 1.62 eV bandgap of 0.45 eV in the best cells (Figure S1). Comparable efficiencies of up to 18.8% were demonstrated for smaller devices fabricated on fluorine-doped tin oxide (FTO)

substrates (see Figure S2). For comparison, we also show data in Figure S3 for small cells fabricated using the $\text{SnCl}_4 \cdot 5\text{H}_2\text{O}$ spin-coating method proposed by Ke *et al.* and developed by Anaraki *et al.*^{8,18} Here we found similar performance in some devices, however, we find the process to have low reproducibility (a broader distribution compared to np-SnO₂ devices in Figure S2), with full cell performance parameters given in Table S1. The process also requires a drying step at 100°C followed by a longer annealing time at higher temperature (180°C for 60 minutes).¹⁸ Taken together, we believe that the low reproducibility, and temperature requirements to convert to SnO₂, makes the $\text{SnCl}_4 \cdot 5\text{H}_2\text{O}$ conversion process unsuitable for use in scalable device architectures, with nanoparticle metal oxides being an attractive solution for rapid processing.

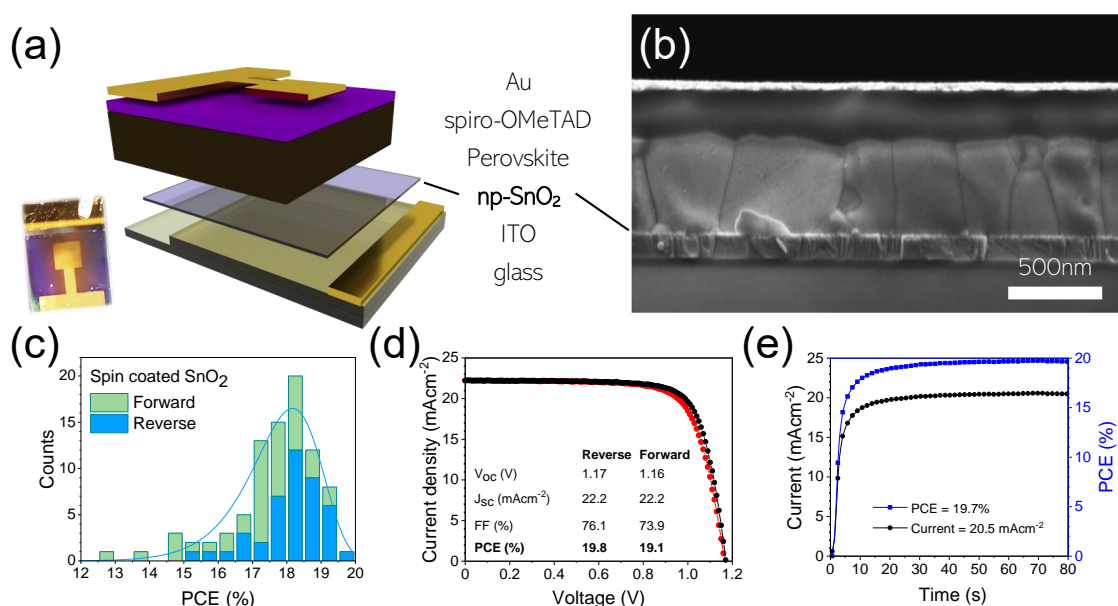


Figure 1: np-SnO₂ device structure and performance. a) Illustration of n-i-p layer architecture with a photo of a completed device in the inset. b) Cross-sectional SEM image of a completed device showing densely packed perovskite grains and ultrathin np-SnO₂ layer. c) Histogram of all spin-coated device efficiencies (forward and reverse sweep), showing excellent reproducibility. Champion cell performance is illustrated by d) a current-voltage sweep and e) stabilised device performance at the J-V determined MPP.

4.2.3.2: Slot-die coating

Two scalable deposition methods were investigated to deposit the ETL layer. Slot-die coating is widely used in industry in R2R processes and has the key benefit of minimal wasted material during coating.^{25,26} To deposit a range of thicknesses, we used a set solution concentration and flow speed and then explored a range of head speeds. Surface wetting was enhanced by UVO treatment of the ITO prior to deposition, with a 3 wt% np-SnO₂ solution prepared by diluting with H₂O. Improved wetting for contact coating methods can also be promoted by mixing the

primary solvent with ethanol by dropwise addition.²⁶ We note that when diluting using only H₂O (which has a high surface tension of >70 mN m⁻¹ at RT) a meniscus forms around the slot die head and at the substrate edges. Here, we mitigated this effect by placing the target substrate between two other substrates to ensure a uniform flow across the intended device area (see Figure S4), with the meniscus defining the thickness of the deposited layer (found to be ~38 nm see Figure S5). This is confirmed by process optimisation results, showing device efficiencies that are comparable across a range of head speeds from 3 to 15 mm s⁻¹ (see Figure S6a). Champion and average device performance metrics are shown in Table S1 for all devices in both sweep directions, with a maximum PCE of 18.5% and only mild hysteresis for the reverse sweep direction (Figure S6b).

4.2.3.3: Spray-coating

As a non-contact scalable deposition technique, spray-coating offers the benefit of higher throughput than is achievable using slot-die or other contact coating methods.²⁷ However, care must be taken to ensure good wetting of the substrate, the formation of a uniform, levelled wet film and homogenous drying. In the case of perovskite films, the solvent optimisation is particularly critical as it is also necessary to control nucleation and crystallisation behaviour. This can be achieved through careful post-deposition treatments such as vacuum exposure;²⁸ a technique that has also been used in inkjet printing.²⁹ For the methods outlined here, we are using an ultrasonic spray coater, which atomises the coating solution using a piezoelectric transducer into droplets from a moving head, which are directed with gas flow onto a static coating surface.²⁷ Here we have adopted a single-pass coating approach, operating in ambient conditions and using non-toxic solvents.

Typically, low surface tension and low boiling point solvents are used for spray-coating. When using H₂O as a solvent to spray-coat SnO₂, its high surface tension can lead to the formation of thick wet films despite its good wetting properties (indeed 30 seconds of UVO exposure is sufficient to encourage complete wetting, see Figure S7). The thickness of the wet film is also dictated by the volume of solution that lands on the substrate, the surface energy of the substrate and meniscus effects at the edge of the substrate. We have optimised the spray-deposition process to deposit SnO₂ films on ITO glass and find that the use of a low concentration solution (1:70 np-SnO₂:H₂O), together with a UVO treatment leads to the formation of a homogeneous wet film. From this wet film, drying proceeds over the substrate surface in around 60 seconds. We show this process schematically in Figure 2, with images of this process and uniform conformal coatings shown in Figure S8. We note that in an industrial

process, drying could be further controlled by use of an air-blade²⁴ or hot air flow (HAF) across the surface, a process that we describe later.

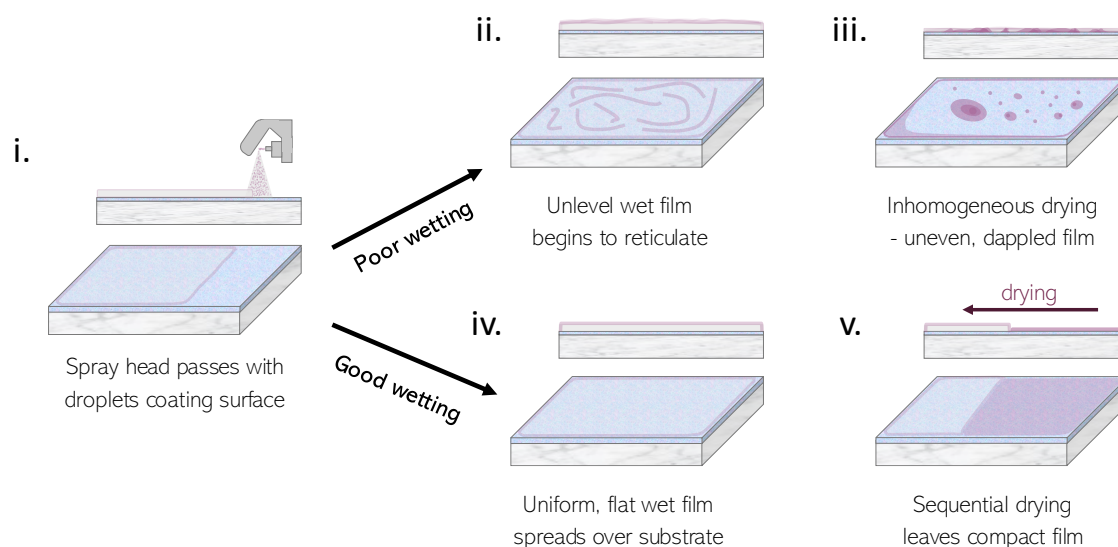


Figure 2: Scheme illustrating the optimised $np\text{-SnO}_2$ drying process across the UVO-treated ITO surface: i) spray-coating, ii) fast reticulation, iii) dry film with poor uniformity, iv) ideal wet film and v) drying proceeds across the substrate.

4.2.3.4: Topography and device performance

To investigate the uniformity and roughness of the deposited films, we performed atomic force microscopy (AFM) on spin- and spray-coated $np\text{-SnO}_2$ (see Figure 3a-c). We found spin-coating significantly reduced the film root mean square surface roughness (R_{RMS}) from 2.46 nm for the uncoated ITO to 1.37 nm, with the spray-coated film being slightly rougher ($R_{\text{RMS}} = 2.20$ nm). Examining the topography of the coated surfaces, we find that the $np\text{-SnO}_2$ film (prepared by both deposition techniques) significantly reduces the surface density of voids in the ITO. We have compared spin- and slot-die coated surfaces and find that slot-die coated $np\text{-SnO}_2$ films exhibit comparable roughness to spin-coated films (1.37 nm) with annealing having little effect on film morphology (see Figure S9). We find that the spray-coated films have a reduced layer thicknesses, which is ~ 17 nm (measured by spectroscopic ellipsometry), with this thickness being apparently insensitive to spray-coater head speed (see Figure S5). We speculate that this thin sprayed $np\text{-SnO}_2$ film dries conformally over the surface, with its greater roughness possibly reflecting the roughness of the underlying ITO (see Figure 2).

We have also performed surface profilometry mapping on completed devices (glass/ITO/ $np\text{-SnO}_2$ /perovskite/spiro-OMeTAD/Au) to explore film morphology over larger length-scales (2 mm x 2 mm). A surface map is shown in Figure 3d that was recorded from the surface of a

device incorporating a spray-coated np-SnO₂ layer deposited from an IPA/H₂O/np-SnO₂ solvent mixture, with similar mixtures having been used with slot-die coating to improve wetting.²⁶ However, we found that de-mixing of this two-solvent system occurs during the atomisation process in the ultrasonic spray head, as illustrated in Figure S10. Consequently, this poor uniformity bottom layer leads to a significant number of pinholes, with ring-like morphological defects resulting from undulations in the np-SnO₂ layer apparently propagating through subsequent layers in the completed device. However, this behaviour can be largely suppressed by judicious choice of spray-solvent. Here, Figure 3e shows a topographic image of a device surface in which H₂O solvent was used to spray-coat the np-SnO₂, leading to greatly reduced density of pinholes and no ring-like features evident. This result highlights the different challenges with solvent engineering for spray-coating as compared to contact methods; further details on creating stable solvent mixtures for spray-coating are given in SI Note 1.

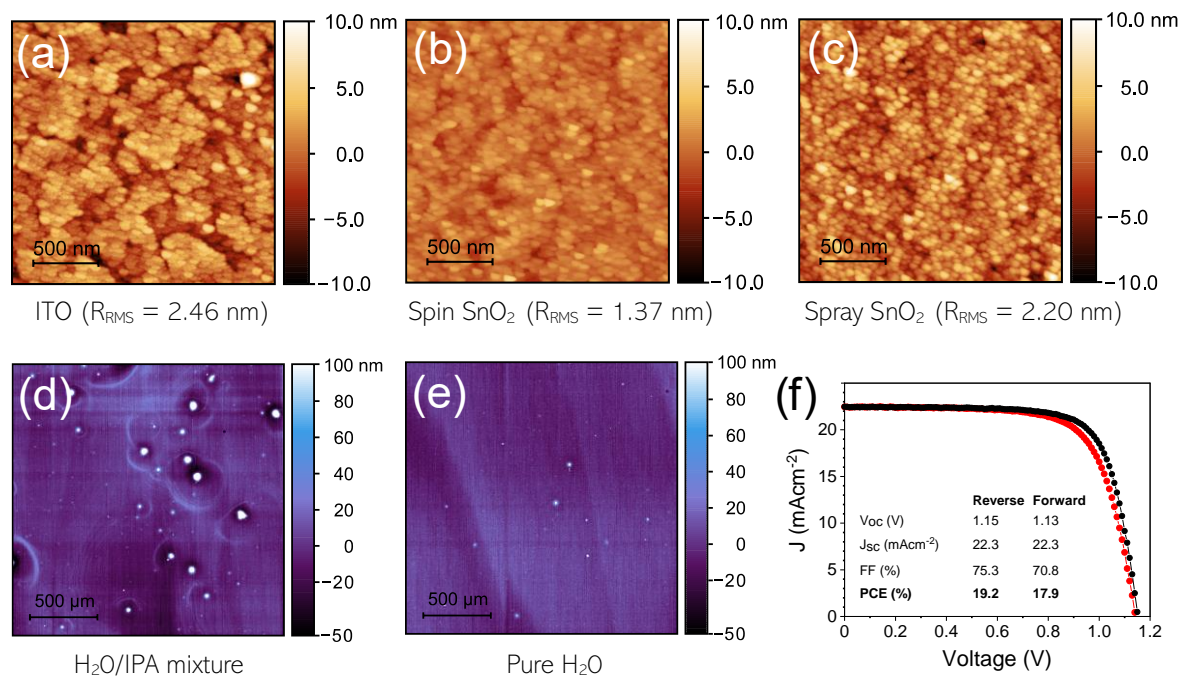


Figure 3: AFM height maps for uniformity and roughness of a) ITO, b) spin-coated and c) spray-coated np-SnO₂ layers. Profilometric mapping of completed devices using spray-deposited np-SnO₂ with d) IPA/H₂O mixed solvent and e) H₂O-only solution; here np-SnO₂ layer inhomogeneity in the IPA/H₂O cast film leads to pinholes in subsequent layers. f) J-V curve for the best performing spray np-SnO₂ device.

Device performance metrics for all devices are shown in Table 1. For optimised spray-coated np-SnO₂ devices, we achieved a champion PCE of 19.2% with a SPO for the best performing cell of 18.6% (see Figure S11). We find that devices fabricated using a spray-coated np-SnO₂ layer exhibit increased J-V hysteresis; a result consistent with a reduced uniformity in layer

thickness. Despite this, we find that other performance metrics for spray-coated and slot-die fabricated devices closely match those of average spin-coated cells.

Note that we have found it is imperative to use the np-SnO₂ films directly after the application of annealing and UV ozone treatments. We observed that leaving annealed np-SnO₂ films in ambient conditions, even if subject to a UVO treatment directly before coating with perovskite, leads to a substantial loss in V_{oc} (see Table 1). This effect most likely results from the adsorption of organic species at the surface that cannot be effectively removed through UVO treatment alone.

Table 5: Champion device performance metrics for spin- and spray-coated np-SnO₂ devices, with average & standard deviation in parenthesis. All devices are thermally annealed (150°C for 30 min) and post-treated with UVO. Performance for spray-coated cells with np-SnO₂ layers left in air for 2 days following annealing is also shown, highlighting the issue of loss of performance resulting from surface contamination.

Coating	Treatment	Sweep	PCE (%)	J _{sc} (mAcm ⁻²)	V _{oc} (V)	FF (%)	No. of cells
Spin	Annealed + 15 mins UVO	Forward	19.29 (17.21±1.40)	22.93 (22.13±0.43)	1.16 (1.12±0.03)	75.30 (69.23±4.80)	43
		Reverse	19.82 (18.17±0.97)	22.94 (22.15±0.46)	1.17 (1.13±0.03)	76.14 (72.58±2.38)	
Spray	Annealed + 15 mins UVO	Forward	17.86 (16.62±1.75)	22.26 (22.13±0.26)	1.13 (1.13±0.01)	70.76 (66.24±6.13)	13
		Reverse	19.22 (18.45±1.18)	22.29 (22.19±0.20)	1.15 (1.14±0.01)	75.27 (72.76±3.75)	
Spray	Annealed + delayed 15 mins UVO	Forward	14.92 (11.32±2.68)	22.21 (22.01±0.20)	1.01 (0.94±0.09)	66.28 (53.76±8.73)	13
		Reverse	17.01 (15.08±3.18)	22.39 (22.11±0.23)	1.06 (1.00±0.11)	72.38 (67.09±10.07)	

4.2.3.5: Scalable processing

The methods outlined so far have utilised an annealing step of 150°C for 30 minutes to dry, crystallise and remove solvent from the np-SnO₂ layer. However, such an extended thermal treatment is incompatible with rapid R2R or continuous processing, where the duration of the longest process dictates the maximum web speed. Furthermore, our standard process also involves a UVO surface preparation treatment for 15 minutes to increase the surface energy for perovskite wetting and remove surface contaminants. In the following sections, we describe techniques that we have developed to reduce process time and temperature, whilst maintaining good device performance.

4.2.3.6: The Effect of Thermal Annealing

To minimise the cost and duration of film processing, it is desirable to remove the transport layer thermal annealing step. Fortunately, as the SnO₂ nanoparticle system is already composed of pre-crystallised nanoparticle domains, there is no phase change or oxidation process required to form the SnO₂ phase. However, it is necessary to understand the effects played by any thermal treatments and UVO exposure on the transport layer and the SnO₂/perovskite interface. Previous reports on the optical absorption of np-SnO₂ suggest a bandgap of 3.79 eV – 3.94 eV for annealed np-SnO₂ films, but with only limited wavelength range below the bandgap, required for accurate fitting.^{19,30} Tauc-like plots from our transmission measurements indicate optical bandgap values of 4.43 eV for non-annealed and 4.39 eV for annealed np-SnO₂ films (Figure S12). These values are significantly higher than those typically expected for phase-pure SnO₂, so we applied a band fluctuations fitting model to spectroscopic ellipsometry data.³¹ This confirmed the wide bandgap of 4.48 eV and 4.45 eV for as-deposited and thermally-annealed at 150°C respectively (see Table S2); this model discussed in SI Note 2.

Grazing incidence small-angle X-ray scattering (GISAXS) techniques can provide a wealth of information about thin-film material structure, and has been used extensively for characterisation of photovoltaic materials. Here, we collected 2D X-ray scattering patterns of np-SnO₂ films (see Figure S13), and fitted an empirical Guinier-Porod model³² to in-plane cuts through this data (see Figure 4) to investigate changes that occur in the lateral structure during annealing. Using this approach, we determine typical correlation lengths for crystalline domains within our films of between 1.1 and 1.2 nm (see Table 2), with such values agreeing with the manufacturer's data. Here, GISAXS measurements were designed to preferentially probe the np-SnO₂ layer averaging over the irradiated sample surface, where changes induced by annealing are most likely to be evident (our complete methodology is explained in SI Note 3). From the fitted values shown in Table 2 (with further parameters presented in Table S3), thermal annealing increases the typical domain size for grains in the film from ~1.17 nm to ~1.22 nm;* a result that confirms that thermal annealing increases the average size of the crystalline domains. We also determine a reduction in the Porod exponent d from ~4 (corresponding to an ideal, smooth surface) to ~3.6; a result that indicates the presence of less well-defined spherical boundaries between SnO₂ domains following annealing. We therefore conclude that

* It is noted that this range is in accordance with the manufacturer's data indicating 1-2 nm particles, as described in the Supporting Information Methods. We also note that the original work by Jiang et al. (ref. 23) observed some slightly larger crystalline domains using transmission electron microscopy, suggesting a potentially broader size distribution than from our calculation or the manufacturer's data.

the annealed film can be considered as a densely-packed layer of fused spheres that become joined and then continue their growth during thermal annealing.

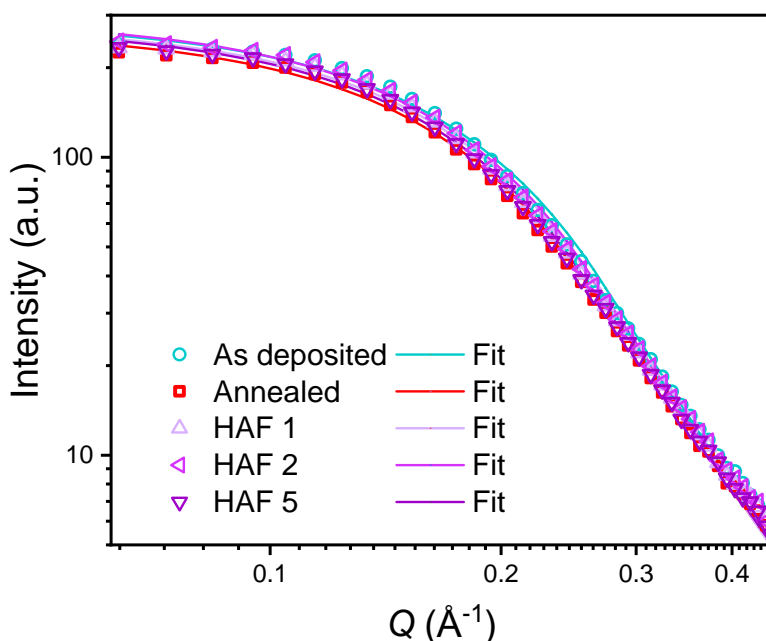


Figure 4: In-plane linecuts and Guinier-Porod fitting of GISAXS from $np\text{-SnO}_2$ layers with different annealing conditions; as deposited, 30 mins 150°C annealed and hot air flow (HAF) for 1, 2 and 5 mins. 2D GISAXS patterns for all samples are shown in Figure S13.

Various rapid thermal processing techniques have been used to process perovskite layers, notably photonic curing, flash infra-red annealing, intense pulsed light (IPL) and rapid thermal processing.^{33–36} Such techniques have also been used to replace TiO_2 sintering,^{37–39} however the high transmissivity of thin $np\text{-SnO}_2$ complicates their use for this material; for example, photonic curing or extended thermal annealing will instead cause damage to flexible plastic substrates like PET or PEN. To replace thermal annealing, we have explored the use of a rapid thermal hot-air flow (HAF) process at a temperature of $(120 \pm 10)^\circ\text{C}$ for between 1 and 5 minutes, as has been used to process perovskite films.⁴⁰ Here, a temperature-controlled heat gun was used to replicate the typical hot-plate thermal annealing process and represents a technique consistent with R2R processing in air. Our experimental setup is shown in Figure S14. Guinier-Porod fit parameters extracted from in-plane scatter measurements (Figure 4) from films processed using HAF show similar trends to those extracted following extended thermal annealing, with an increase in grain radius and reduction of smoothness determined for increasing HAF process times (see Table 2). Indeed, both the Porod exponent and grain radius are found to closely match the extended anneal after only 5 minutes of HAF.

Table 6: Guinier-Porod fitting parameters for GISAXS profiles of np-SnO₂ films. Typical grain size is determined assuming spherical domains, with full details given in SI Note 3.

Sample	R_g (Å ⁻¹)	d (Porod exponent)	Fitted domain size (nm)
As deposited	9.09 ± 0.05	3.984 ± 0.31	1.173 ± 0.006
Annealed	9.43 ± 0.05	3.612 ± 0.24	1.218 ± 0.006
HAF 1 min	9.27 ± 0.05	3.829 ± 0.28	1.197 ± 0.006
HAF 2 min	9.31 ± 0.05	3.831 ± 0.27	1.202 ± 0.006
HAF 5 min	9.42 ± 0.05	3.661 ± 0.24	1.216 ± 0.006

4.2.3.7: Post deposition treatments

Various options exist to clean/process layers for R2R fabrication, including exposure to a plasma. We note that the UVO system used here did not include an O₂ gas feed, so we expect that process times could be significantly reduced by including an oxygen feed or by using more intense UV light sources. UVO has been widely used as a surface treatment for SnO₂ and has been reported to enhance carrier extraction.⁴¹ The UVO process is believed to enhance surface hydroxylation⁴² (increasing the surface energy) and to reduce the surface-density of oxygen vacancies. Again, our objective is to explore an industrially applicable process, so we have also investigated a 5-minute O₂ plasma treatment, which is extensively used in industry and explore its impact on the np-SnO₂ surface and the SnO₂/perovskite interface. O₂ plasma treatment combines UV cleaning under vacuum with cleaning by various ionised oxygen species. In optoelectronic devices this has been used to modify surface electronic properties for enhanced carrier injection or extraction.^{43,44}

We first investigated the effect of removing the thermal annealing process on device performance. Here PV devices were prepared by either drying np-SnO₂ in air, or by using a one-minute annealing step at 120°C to match the fastest HAF process that would be compatible with processing on a flexible substrate. In each case, a further 15-minute UVO (here termed '120 + UVO') or O₂ plasma (termed '120 + O₂') post-treatment was applied to the np-SnO₂ ETL to understand its effect on cell performance. Table S4 shows device efficiencies following each treatment, with optimum device performance achieved using the 120 + UVO process, where a maximum reverse sweep PCE of 18.9% was recorded (champion device shown in Figure 5). This encouraging result suggests that high performance can be achieved using both reduced processing time and relatively low annealing temperatures, with even brief annealing having performance benefit. Table S4 also indicates a reduction in V_{oc} by around 80 mV for devices treated using an O₂ plasma compared with those treated using UVO (average ~1.05 V compared with ~1.13 V respectively). This reduction is accompanied by an increase in hysteresis during

scanning, where the J - V sweep for the best performing 120 + O₂ device (see Figure 5) shows a significant difference in the forward and reverse sweep PCE, V_{OC} and FF compared with that processed using the 120 + UVO np-SnO₂.

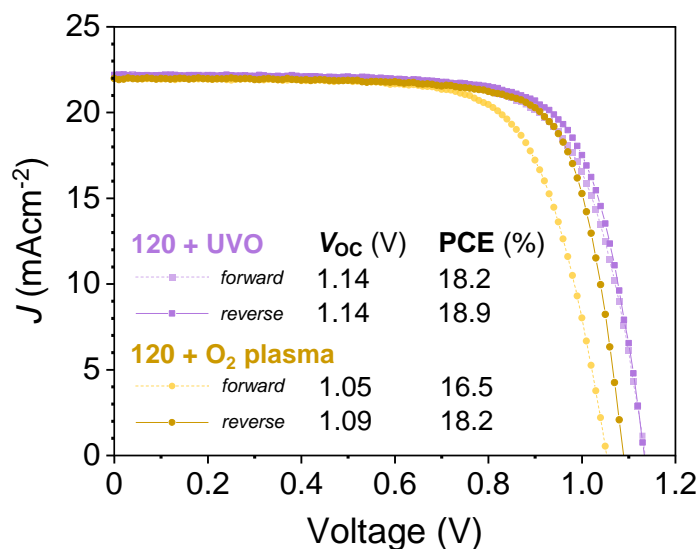


Figure 5: J - V curves for the best performing cells using np-SnO₂ treated with 1 minute 120°C drying and either 15 minutes UVO or 5 minutes O₂ plasma prior to perovskite deposition. Key sweep parameters are inset (full parameters in Table S4), with the O₂ plasma-treated np-SnO₂ device exhibiting lower V_{OC} and increased hysteresis.

To first confirm whether these changes in device performance result from changes in the perovskite deposited on the treated surfaces, we performed white light absorption and steady-state photoluminescence (SSPL) measurements on bilayer np-SnO₂/perovskite samples, with the np-SnO₂ exposed to various processing conditions. Figure S15 shows the optical density for np-SnO₂/perovskite samples and corresponding Tauc-like plots where we assume a direct bandgap. In all cases, films were found to have a similar optical bandgap of ~1.62 eV, corresponding well with PL emission (see Figure S16) at ~1.63 eV in all samples (Table S5). To further confirm whether changes observed in device performance are due to changes in the perovskite layer, we recorded grazing-incidence wide-angle X-ray scattering (GIWAXS) patterns for samples using np-SnO₂ substrates with either 120 + UVO or 120 + O₂ plasma treatment (Figure S17). Here, we found no substrate-dependent effects on the perovskite crystallinity or orientation. From these observations we conclude the perovskite bulk composition and structure is comparable in both cases, irrespective of the np-SnO₂ layer treatment; a result that suggests that the observed changes in device performance result from modification at the SnO₂/perovskite interface.

4.2.3.8: Photoelectron Spectroscopy

To investigate the effect of UVO and O₂ plasma treatments on the band structure and composition of the np-SnO₂, we performed ultraviolet (UPS) and X-ray (XPS) photoelectron spectroscopy (PES) measurements. These highly surface sensitive techniques give a wealth of information on the electronic nature of surfaces and interfaces, with many reports investigating doped and undoped SnO_x for many applications, from TCOs to gas sensing.^{45–48} Here we prepared np-SnO₂ films on ITO at the same thickness as used in completed devices. PES measurements will also include the effect of surface contaminants and adsorbates, which will be heavily dependent on the SnO₂ surface.⁴⁹ Samples might typically be prepared by thorough cleaning, followed by Ar⁺ sputtering to remove adventitious carbon or other detectable species, and remain under high vacuum after preparation.⁵⁰ Here, however, cleaning/sputtering of the SnO₂ will affect its surface composition,⁵¹ so following UVO or O₂ treatments in air, samples were sealed under vacuum and then rapidly transferred to high vacuum for PES measurements.

By measuring XPS spectra across an extended binding energy range we investigate the surface elemental composition of the np-SnO₂ layers. We note that the np-SnO₂ suspension used here is stabilised using KOH (with a solution pH of ~11.5, see Figure S18). From survey (wide) scan spectra shown in Figure S19, we find that the O₂ plasma-treated samples are characterised by reduced emission from K 2p core levels and weakly detectable emission from In 3d levels. This indicates that the O₂ plasma partially removes KOH from the np-SnO₂ surface, and also etches the np-SnO₂ layer, allowing indium in the ITO substrate to be detected. We also find significantly increased F 1s intensity which we attribute to fluorine contamination arising from degraded PTFE coatings within the plasma reactor.⁵² Indeed, if fluorine is incorporated into the SnO₂ surface, it may increase the optical bandgap.⁵³ We also compared the effect of each processing step on the adventitious carbon with C 1s core-level spectra (see Figure S20). As expected, we found that annealing does not remove carbon contaminants, whereas UVO and O₂ plasma both significantly reduce carbon species present at the surface.

Various other stable adsorbates are expected to be present at SnO₂ surfaces, notably O₂, H₂O and hydroxide species, with their concentration heavily dependent on the SnO₂ surface and stoichiometry.^{49,54,55} We probed the O 1s core-level XPS emission to understand changes in surface oxygen species, with spectra and fits for 120 + UVO and 120 + O₂ plasma shown in Figure S21. Two components were fitted (in most cases) using a lower energy feature having a binding energy of 531.1-531.3 eV together with a higher energy shoulder at 532.4-532.6 eV (fitting methodology is described in the experimental methods). The peak at 531.2 eV is ascribed to

lattice oxygen (O-Sn bonds) with the second broader feature originating from adsorbed species such as -OH groups and carboxides.^{55,56} In the O₂ plasma-treated samples, a distinct third peak was detected at 533.3 eV which we suspect is related to an additional adsorbate species induced by fluorine modifying the surface.⁵⁷ In Table S6 we compare the relative areas of O 1s and Sn 3d, and find that Annealed and 120 + UVO samples have the highest area ratio for both [O 1s]/[Sn 3d] and Sn-O/[Sn 3d], which is reduced following an O₂ plasma treatment. Whilst these values should be treated with caution because of the effect of adsorbates, our results suggest that 5 minutes of O₂ plasma treatment can significantly modify the surface species, apparently leading to an Sn-rich, O-poor surface.⁵⁸ A reduced O/Sn ratio has previously been observed following an O₂ plasma treatment,⁵⁹ but the reverse has also been reported for reduced SnO₂ surfaces.⁶⁰ In summary, the SnO₂ surface following treatment will be impacted by the initial stoichiometry and crystallinity of the surface, the proportion of different ionised oxygen species in the plasma, the nature of fluorine contamination and the process duration.^{49,53}

To analyse the electronic structure from UPS spectra, the secondary electron edge (or E_{cutoff}) was used to determine the work-function (WF) for each layer, with the onset energy (E_{onset}) used to find the valence band maximum (VBM) with respect to the Fermi level (E_F) (see Figure S22). To confirm the VBM positions (ionisation energy, I_E) for all samples, we also extracted E_{onset} values from XPS valence spectra (see Figure S23). These values agreed with those determined from UPS measurements (see Tables S5 and S6). As noted above, the energy level determination will be affected by extrinsic band bending due to adsorbates, with adsorbed moisture expected to lead to the formation of an accumulation layer at the SnO₂/perovskite interface.⁵⁴ Noting this, we show an apparent energy level diagram for ITO and key np-SnO₂ samples in Figure 6a, illustrating the position of Fermi level, the VBM and estimated conduction band minimum (CBM) using our previously determined optical bandgap values for np-SnO₂ (Figure S24 illustrates the energy level determination). Here, it is immediately apparent that the O₂ plasma treatment has caused a significant shift of the Fermi level and ionisation energy. Changes to the chemical species present, together with reduced layer thickness and modified oxidation state have significantly altered the surface of the 120 + O₂ sample surface; a conclusion confirmed by the 'As deposited + O₂' sample exhibiting similar shifted energy levels (see Table S7). We note that this is consistent with literature reports on TCOs treated with O₂ plasma; a process that has been shown to down-shift the Fermi level in FTO and ITO surfaces by 0.5-0.6 eV.^{43,49} We also note that the energy levels determined for the annealed sample are significantly modified following UVO treatment, an observation that may partly result from

removal of carbon species, as identified in Figure S20. For completeness, we give typical triple cation perovskite and spiro-OMeTAD energy levels (predominantly measured by UPS at the top surface combined with optical bandgap) in Table S9, with the triple-cation perovskite CBM typically in the range -3.79 to -4.46 eV.

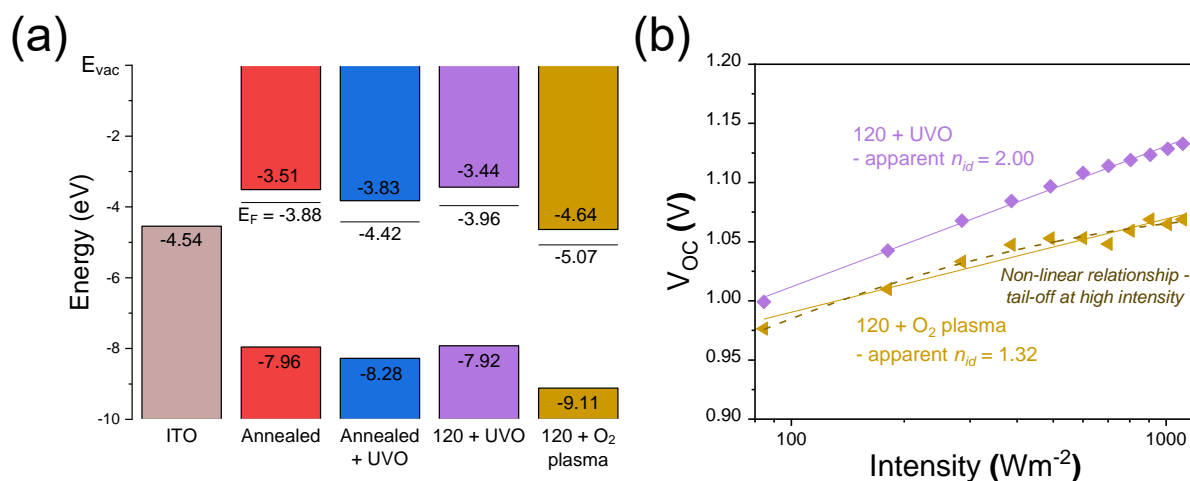


Figure 6: Understanding the effect of UVO and O₂ plasma treatments. a) Electronic structure at the np-SnO₂ surface with Fermi level (E_F) from UPS measurements, valence band from UPS and XPS and estimated conduction band from optical bandgap. b) Stabilised light- V_{OC} measurements for 120 + UVO and 120 + O₂ devices, showing reduced V_{OC} for plasma treatment. Apparent n_{id} from linear fits are shown, and in the O₂ plasma case behaviour indicates increased non-radiative recombination at the ETL interface.^{64,67}

4.2.3.9: Device physics

Previous work has shown that the illumination intensity-dependent variation of V_{OC} can provide information about the dominant recombination mechanisms in photovoltaic devices. Classically, the light ideality factor (n_{id}) extracted using this approach determines whether recombination is primarily bimolecular (band-to-band) or monomolecular (trap-assisted), in cases with comparable electron and hole densities.^{61,62} With varied carrier densities, trap energies and trap locations (bulk or interface), n_{id} can take a range of values ($n_{id} \sim 1-2$); analysis is complicated in hybrid perovskite devices by the influence of mobile ions, which lead to transient modification of interfaces, and therefore carrier extraction behaviour.^{62,63} Adopting the approach modelled by Tress *et al.*, we recorded stabilised V_{OC} measurements after a set illumination period, and find the 120 + O₂ sample exhibits behaviour consistent with poor charge selectivity (see Figure 6b).⁶⁴ This result suggests increased interface recombination in this case, despite a lower apparent n_{id} extracted from a linear fit (1.32 compared to 2.00 in the 120 + UVO sample). Transient photovoltage measurements recorded at 1 sun are shown in Figure S25 and show slower voltage stabilisation for O₂ plasma-treated devices. Over tens of seconds, these changes in V_{OC} are likely to result from dynamic processes at the ETL interface

caused by the interaction of both mobile ions and charge carriers, modifying carrier extraction behaviour.^{63,65}

We conclude therefore that the observed V_{OC} loss shown in Figure 5 and Table S4 for devices utilising the 120 + O₂ ETL results from a significant modification of the surface chemistry. This leads to an apparent downshift of the VBM, Fermi level and CBM of the SnO₂, resulting in a loss of electron selectivity, with reduced quasi-Fermi level splitting in the device. While the observed energy-shifts are significant, they are affected by adsorbates which also affect the extrinsic electron density at the interface, and may even evolve dynamically under operation.^{54,55} However, it is clear that both misalignment and modified doping density will change the charge and ionic screening behaviour of the interface; a process that most likely causes the increased hysteresis observed in O₂ plasma-treated samples.⁶⁶ It is unclear however whether band alignment and doping effects can be independently modified with O₂ plasma.^{30,67} It has also been reported that ALD SnO₂ with different oxidants (such as O₂ plasma or ozone) can lead to changes in the electronic properties of the ETL layer, as well as modifying the subsequent perovskite growth;⁶⁸ a process that may also be influenced by the observed reduction in KOH.²⁶ It is clear that further research is needed to characterise chemical reactivity between different substrate transport materials and the perovskite layer during film formation.^{9,68}

Overall, it is evident that O₂ plasma can have a detrimental impact on the SnO₂/perovskite interface if not properly controlled, however promising results using shorter treatment times have been achieved.⁶⁹ Surface preparation equipment (both UVO and O₂ plasma) used in research laboratories varies greatly in device performance, power and process control, making exact methods difficult to reproduce between research labs. As such further efforts must be made to replicate industrially relevant plasma cleaning approaches used in interface preparation.

4.2.3.10: Rapid processing

Combining the optimised spray-coating, 1-minute HAF and UVO treatment, PV devices were prepared using this series of processes that has the potential to be fully transferrable to R2R or other low-cost processing. In Figure 7 we show a histogram of all device efficiencies, as well as the current-voltage performance and SPO for the champion device with a stabilised PCE of 18.7%. To accompany this, average and champion performance parameters are shown in Table 3, showing comparable metrics to annealed spin- and spray-coated devices presented earlier, albeit with increased hysteresis and slightly reduced average V_{OC} and FF. The total processing

time here is around 1 minute (mainly determined by the annealing step), with spatial atomic layer deposition (SALD) being the only comparably rapid, low-temperature deposition technique that operates in ambient atmosphere able to create functional SnO_x layers for application in perovskite solar cells. We note that Hoffmann *et al.* fabricated p-i-n devices incorporating a SnO_x ETL (that also acted as an impermeable barrier layer), with devices with over 12% PCE. Here devices were fabricated using a substrate processing speed and temperature of 20-80 mm s⁻¹ and 80°C respectively (compared with 25°C and up to 180 mm s⁻¹ achieved in our process), but with no further annealing required.⁷⁰

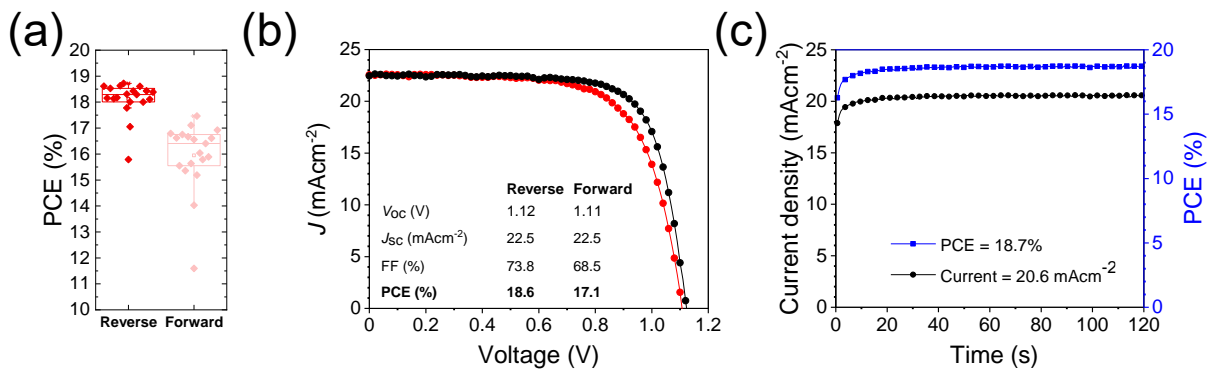


Figure 7: Photovoltaic performance for devices prepared using fast processing: spray-coating, 1-minute HAF and UVO treatment. a) Reverse and forward sweep efficiencies for 19 operational cells, b) J-V sweep and c) SPO of the best performing cell.

Table 7: Fast-processed device performance using sprayed np-SnO₂, 1-minute HAF and UVO treatment.

Coating	Treatment	Sweep	PCE (%)	J _{sc} (mAcm ⁻²)	V _{oc}	FF	No. of cells
Spray	HAF 1 minute + UVO	Forward	17.11 (15.95±1.29)	22.55 (22.54±0.18)	1.11 (1.09±0.03)	68.52 (65.08±3.62)	19
		Reverse	18.62 (18.11±0.66)	22.45 (22.55±0.17)	1.12 (1.11±0.01)	73.81 (72.32±1.93)	

4.2.4: Conclusions

We have explored the deposition of SnO₂ nanoparticle layers using two scalable deposition processes (spray-coating and slot-die coating) and fabricated perovskite devices with performance and morphology comparable to spin-coating. The effect of annealing is investigated using GISAXS, where we quantify the fusing of nanoparticles into a densely packed ETL. The effect of annealing, UV ozone and O₂ plasma post-treatments were also investigated using UPS, XPS, optical and electrical measurements. We observed significant modification to adsorbed species, concomitant with shifts of apparent np-SnO₂ energy levels. Using an O₂

plasma treatment, a significant reduction in the Fermi level led to a loss of V_{oc} and increased current-voltage hysteresis. Finally, we demonstrated an optimised fast deposition technique involving annealing the SnO_2 layer in hot air to create photovoltaic devices yielding stabilised power conversion efficiencies close to 19%. This work outlines the future design requirements for rapid processing of functional metal oxide nanoparticle layers, deposited at high speed and under ambient conditions - conditions compatible with R2R processing.

4.2.5: Acknowledgements

We thank the EPSRC for PhD studentships through the Centre for Doctoral Training in New and Sustainable PV, EP/L01551X/1 (J.A.S., E.L.K.S, C.G.) and via the University of Sheffield DTG account (J.E.B., R.C.K.). T.I.A. thanks the Saudi Government for funding via a PhD studentship. We also acknowledge funding from EPSRC to support this work via grants 'Hybrid Polaritonics' (EP/M025330/1), 'High resolution mapping of performance and degradation mechanisms in printable photovoltaic devices' (EP/M025020/1), 'The integration of photovoltaic devices with carbon-fibre composites' (EP/S009213/1) and from the Global Challenges Research Fund (GCRF) through Science & Technology Facilities Council (STFC), grant number ST/R002754/1 'Synchrotron Techniques for African Research and Technology (START)'. J.A.S. also thanks the Erasmus+ exchange program for support. We also thank Thomas Featherstone for assistance with XPS data analysis, Carolin Rehermann for helping with UV-Vis measurements as well as Selina Olthof and Aboma Merdasa for useful discussions. The XPS instrument belongs to the Sheffield Surface Analysis Centre, a facility run from the Department of Chemistry, University of Sheffield, and is led by Professor Graham Leggett. We thank the company Xenocs for their help and ongoing support in the X-ray scattering user program at Sheffield, and we thank the EPSRC for funding the purchase of this instrument.

4.3: Supporting Information

4.3.1: Methods

4.3.1.1: Device fabrication

Materials: All materials were purchased from Sigma Aldrich unless otherwise specified. ITO coated glass substrates (Ossila, $20\Omega/\text{sq}$) were patterned using powdered Zn and 4 M diluted HCl. Substrates were cleaned by ultrasonication for at least 15 minutes in a 2% aqueous

Hellmanex solution before rinsing extensively with DI water then acetone, sonicated for a further 15 minutes in IPA, dried with N₂ and UV ozone treated for 15 minutes.

Electron transport layer: Tin oxide nanoparticle (np-SnO₂) electron transport layers were deposited from a colloidal solution (15 wt% in H₂O, Alfa Aesar) containing 1-2 nm particles in H₂O, stabilised by KOH (with a solution pH of ~11.5, Figure S18). We confirmed this solution to contain 20 wt% by evaporating the H₂O and calculating the mass loss. For spin coated SnO₂, this was diluted with DI water to 2.67% (6.5:1). This solution was statically spin coated at 3000 rpm for 30 s followed by annealing at 150 °C for 30 min.

Slot-die coated layers were deposited using an Ossila Slot Die Coater with a solution concentration of 6.5:1 H₂O:np-SnO₂. To ensure uniform coating two similar substrates were placed before and after the substrate to be coated (see Figure S4). A two-step flow process was programmed, with the first step controlled to dispense a uniform meniscus, at a coating speed of 0.5 mm s⁻¹ and a flow rate of 30 μl s⁻¹. The second step then dispensed this over the substrate area, with a coating speed of 3-15 mm s⁻¹ and a flow rate of 2 μl s⁻¹. The substrate temperature was held at 80 °C throughout with a gap height of 150 μm.

Spray-coated SnO₂ layers were deposited using a Prism Ultra-coat 300 system (Ultrasonic Systems Inc.) which is operated in low humidity conditions. Head speeds between 120-180 mm s⁻¹ (Figure S5) were used at a head height of 30 mm, with pressure ~10 mbar, on a hot plate at 20 °C. Solution concentration was optimised to a volume ratio of 1:70 SnO₂ NPs:H₂O (17.5 ml H₂O + 250 μl NPs), corresponding to a solution concentration of 0.29 wt% (using 20 wt% calculated above). For the mixed IPA:H₂O np-SnO₂ system used in devices, 5 ml of IPA was added by dropwise addition to a solution containing 12.5 ml H₂O and 250 μl np-SnO₂ solution. In all cases, np-SnO₂ was removed from the ITO in the metal contact evaporation area by fine swabbing with H₂O. Where used, the Hot Air Flow (HAF) heating was performed used a 2000 W Heat Gun (Tacklife HGP73AC) operating at ~120 ± 10 °C determined using a thermocouple attached to a test substrate.

Where used, the sol-gel SnO₂ spin-coating process was completed exactly following the method outlined by Ke *et al.* and Anaraki *et al.*^{8,18} Briefly, SnCl₄.5H₂O in IPA is spin coated at 3000 rpm, followed by drying at 100°C and annealing at 180°C.

Prior to perovskite deposition, SnO₂ layers were UV ozone cleaned (Ossila UV ozone cleaner with no O₂ flow) for 15 minutes before transferring to a nitrogen glovebox. Where used, O₂ plasma treatment was performed for 5 minutes in a custom-built chamber with pressure 2

mbar that was flushed with O₂ three times before treating for 5 minutes at approximately 400 W.

Perovskite: Triple-cation perovskites were deposited via the one-step deposition method from a precursor ink containing (per ml of solvent, not accounting for volume change) FAI (1M, Ossila), MABr (0.2M, Ossila), PbI₂ (1.1M, TCI) and PbBr₂ (0.2M, TCI) in fresh anhydrous DMF/DMSO (4:1 volume ratio) with 50 µl of a 1.5M CsI solution in DMSO added per ml to give the desired solution composition Cs_{0.05}FA_{0.79}MA_{0.16}PbI_{2.45}Br_{0.55}. The solution was heated to 65 °C for 15 minutes to aid dissolution if required. Films were spin coated statically in a two-step program: 1000 rpm for 10 s then 6000 rpm for 20 s with 100 µl of chlorobenzene antisolvent dripped on the film around 5 s before the end, with the film immediately turning translucent brown when using Cs. Films were then transferred to a hotplate for annealing at 100 °C for 60 min. In measurements where perovskite layers were prepared for optical characterisation, films were simply deposited using the above protocol on cleaned, UV-ozone treated quartz-coated glass substrates.

Hole transport layer/contact: Spiro-OMeTAD hole transport layer was deposited from a solution containing 86 mg ml⁻¹ spiro-OMeTAD (sublimed 99.5%, Ossila) in chlorobenzene. To each 1 ml was added 34 µl of 4-tert-butyl-pyridine (tBP, 96.6%), 20 µl of lithium bis(trifluoromethanesulfonyl)imide solution (LiTFSI, 500 mgml⁻¹ in acetonitrile) and 11 µl of FK209 solution (FK209 Co(II) PF₆, Dyesol, 300 mg ml⁻¹ in acetonitrile). This solution was vortex mixed and filtered before spin-coating dynamically at 4000 rpm for 20 s. Layers were partially removed using a razor blade to pattern devices before 80 nm of Au (Cooksongold) was thermally evaporated under high vacuum as the electrode (area 0.25 cm²) with one cell created per substrate unless otherwise stated.

4.3.1.2: Characterisation

Current-voltage measurements: J-V curves were used to determine device performance under ambient conditions using a Newport 92251A-1000 solar simulator. Prior to testing, an NREL certified KG5 filtered silicon reference cell was used to calibrate the simulated AM1.5G light to 100 mWcm⁻² at the sample location. A sample holder was used to ensure consistent positioning and illumination. A metal illumination aperture mask defined a cell area of 0.155 cm² (accurately determined using optical microscope and ImageJ area analysis) to compensate for any geometric distortion in the electrode evaporation. J-V measurements were recorded using a Keithley 237 source measure unit sweeping between -0.1 and 1.2 V at 100 mVs⁻¹ with all performance metrics extracted from the curve. Stabilised power output measurements were

taken by holding the devices for several minutes at a bias voltage defined by the reverse sweep V_{mpp} . J-V scans were typically recorded on the second or third day after device fabrication and no light-soaking or voltage pre-biasing was used.

X-ray scattering: Grazing incidence X-ray scattering was performed using a Xeuss 2.0 (Xenocs) system with 9.243 keV X-rays from a liquid Ga MetalJet source (Excillum). X-rays were incident on the sample surface, which were 100 nm thick np-SnO₂ with various heat treatments, at an angle of 0.32°. The sample and flight tube were held under vacuum during operation to remove background scatter. Scattered X-rays were then detected with a PILATUS3R 1M (DECTRIS), with a sample to detector distance of ~300 mm. This data was corrected, reduced and reshaped using the GIXSGUI MATLAB toolbox.⁷¹ For GISAXS profile fitting, a shape independent Guinier-Porod fitting model was applied using SasView,⁷² with further details given in SI Note 3.

Scanning electron microscopy: Device cross-section images were recorded from films using a Carl Zeiss-modified Raith Nanofabrication SEM operating at a beam energy of 1.5 kV at a working distance of 2-3 mm with backscattered electrons collected with an in-lens detector.

Light V_{oc} : Oriel LSH-7320 ABA LED solar simulator with ability to control illumination intensity between 0.1 Sun to 1.1 Sun was used to perform intensity depended V_{oc} and transient photovoltage measurements. V_{oc} was measured as a function of time using Keithley 2420 meter controlled through LabTracer 2.9. In our analysis, we use a fitting relation from a modified ideal diode equation for an illuminated cell operating at V_{oc} ⁶⁴; $eV_{oc} = E_{gap} - n_{ID}k_B T \ln\left(\frac{I_0}{I}\right)$.

Atomic force microscopy: AFM measurements were performed in tapping mode using a scanning force microscope (Veeco Dimension 3100) with a nanoscope 3A feedback controller. The AFM tips were TESPA-V2 probes (Bruker) with a resonance of around 320 kHz and spring constant of 42 N/m. Gwyddion 2.54 software was used to process the AFM images and roughness values were calculated using the Gwyddion statistical quantities tool.

Profilometry: A Bruker DektakXT profilometer was used to investigate the morphology of completed devices. Here, 2 x 2 mm map profiles were collected at a 1 μ m line resolution. Data was processed by cropping for touchdown error, plane levelling to remove tilt from stage, base flattening and step line correcting in both x and y.

Spectroscopic ellipsometry: A M2000v ellipsometer (J.A. Woolam Co.) was used to determine the thickness of np-SnO₂ thin films deposited on silicon substrates (Ossila Ltd). Using CompleteEASE software, a Cauchy model was fitted to Ψ (the ratio of the incident and reflected amplitudes) and Δ (the ratio of the phase difference of the incident and reflected light) over the wavelength range where the films are optically transparent (500-1000 nm).

SnO₂ E_{gap} determination (ellipsometry and transmission): Optical measurements were performed with a Sentech SE850 ellipsometer (210-850 nm) and a Perkin Elmer Lambda 1050 spectrophotometer (transmission, 250-700 nm). The complex refractive index was obtained self-consistently for each individual wavelength using the combined ellipsometry and transmission data via a global error minimization.⁷³ The resulting absorption coefficient was fitted with a band fluctuations model which describes the direct absorption edge and Urbach tail in a single equation.^{31,73}

Transmission measurements: Measurements were performed using an Andor Shamrock SR-193i-A double-grating imaging spectrograph, with a focal length of 0.193 m. The spectra were recorded using a 150 grooves/mm grating blazed at 500 nm. The collimated white light from a custom-built tungsten lamp source was focused on to a vertically mounted sample at normal incidence. The transmitted light was then collimated using a 50X Mitutoyo Plan Apo SL infinity corrected objective and focussed into the spectrometer using a final collection lens. These were converted to absorbance units using the relation $A = 2 - \log(T)$. Perovskite layer thickness was determined to be approximately 500 nm using profilometry and confirmed using SEM cross-section, from this absorption coefficients were calculated using $\alpha = 2.303(A/t)$ for Tauc plots used for E_{gap} determination.

Photoluminescence: Measurements were performed using an Andor Shamrock SR-303i-A triple-grating imaging spectrograph, with a focal length of 0.303 m. The spectra were recorded using a 150 grooves/mm grating blazed at 500 nm. The horizontally mounted collection arm of a goniometer was employed to measure the emission at around normal incidence following excitation from a 400 nm diode laser, which was directed to the sample using a vertically displaced arm such that the angle of incidence was ~ 15°. The PL was collected using a pair of lenses on the collection arm which was then fibre coupled into the spectrometer. All samples were collected at five locations with data presented averaged across all locations. To determine optical E_{gap}, an exponentially modified Gaussian (EMG) function was fitted to the data, with peak values given in Table S5.

X-ray photoelectron spectroscopy: XPS data was collected using a Kratos AXIS Supra under UHV conditions ($\sim 10^{-9}$ mbar). Monochromated aluminium radiation (1486.6 eV) of power 225 Watts was used to collect XPS survey scans (wide scans) with a pass energy of 160 eV, between 1200 to 0 eV at 1 eV intervals and 300 seconds sweep time. High-resolution XPS spectra were collected over the C 1s, O 1s, Sn 3d, In 3d and Sn valence band regions at 20 eV pass energy, 0.1 eV intervals and one sweep of 300 seconds over an appropriate energy range. Samples were clamped to the sample bar using a contact to provide a conductive path from the top surface to the sample holder. Charge neutralisation was not used. The area analysed was 700 μm by 300 μm , and two areas per sample were collected. The data was primarily analysed using CasaXPS and OriginPro software. A transmission function characteristic of our Supra instrument is attached to the data by the Kratos software and subsequently used by the Casa software. The sensitivity factors used are the theoretical Scofield factors adjusted for the variation in mean free path with kinetic energy. No correction for angular distribution was made as the angle between the sample and the X-ray source on the Supra is 54° (the magic angle). Analysis and fitting of the XPS elemental core level spectra was conducted using Fityk.⁷⁴ The spectra for the same core levels with different post-treatments were fitted simultaneously using Voigt profiles with coupled Gaussian and Lorentzian line widths with linear background subtraction. For the O 1s peaks, the FWHM was locked relative to the first region for all bonds, and the distance between peaks was fixed.

Ultraviolet photoelectron spectroscopy: UPS was carried out using the Kratos AXIS Supra with the HeI (21.22 eV) emission line employed for excitation. The samples were mounted as described above. The data were acquired at a bias of -9V , from an area that was 110 μm in diameter, at 10 eV pass energy, 0.025 eV energy resolution over an appropriate energy range for one 300 second sweep. UPS data was also collected from an Au foil control sample mounted with the samples to confirm the measured Fermi energy level for a metal sample was 0 eV.

4.3.2: SI Note 1 – Solvent mixtures

Improved wetting of the np-SnO₂ system for slot-die coating has been achieved by diluting with ethanol by dropwise addition.²⁶ Without dropwise addition, the colloidal suspension is unstable and aggregates form when mixing with isopropanol or ethanol and demixing occurs during the spray process as discussed in the main text (Figure S10).

We conducted initial investigations to improve wettability using a range of other low surface tension polar solvents, as well as with additional KOH to modify the np-SnO₂ stabilisation.

Whilst improved wetting and a metastable solvent:H₂O ratio was achieved with acetonitrile (ACN), the system reacted with KOH over 24 hours causing aggregates to form. It is likely that the low concentration KOH base is catalysing hydrolysis of the ACN to various degradation products - likely ammonia, then acetamide and acetic acid.⁷⁵ Having a mixed solvent system also leads to two phase drying, which can lead to further layer inhomogeneity, causing thicker regions of material to form.²⁷ Consequently, the requirements for an ideal second solvent here are:

- 1) Low surface tension for enhanced wetting.
- 2) Low boiling point for more rapid drying.
- 3) Miscibility with water.
- 4) Chemical stability in the presence of KOH.
- 5) Reduced basicity than KOH to ensure no competition for np-SnO₂ suspension.
- 6) In an ideal case, a continuous azeotrope with H₂O to lower the boiling point.

4.3.3: SI Note 2 – Optical E_{gap} determination

Bandgap values are commonly determined from the absorption coefficient by extrapolating from the region of the absorption edge where the parabolic band approximation is valid. For direct semiconductors, this region behaves linearly in a $(\alpha E)^2$ vs. E plot, and so the intercept of a linear fit with the horizontal axis yields the optical E_{gap}. This type of procedure was originally developed for amorphous materials, for which it is commonly known as a Tauc plot.²⁶

This approach has two limitations. Firstly, the selection of the appropriate data points for the fit is somewhat arbitrary and it can be challenging to differentiate the parabolic band edge from the Urbach tail and higher order absorption regions. Secondly, if the Urbach tail is large, there may only be few or no suitable data points available for the linear fit. In these cases, calculated E_{gap} values can be strongly affected by which points are used. Consequently, it is advantageous to use a procedure that considers both the Urbach tail and parabolic band edge regions, which significantly increases the number of available points and reduces the human error involved in their selection. For this reason, bandgap values are extracted by fitting the absorption coefficient with a band fluctuations model that considers both the Urbach tail and parabolic band edge in a single equation,³¹ and has the following form:

$$\alpha(E) = -\frac{\alpha_0}{E} \sqrt{E_u} \text{Li}_{1/2} \left(e^{\frac{E-E_{\text{gap}}}{E_u}} \right)$$

where α_0 is a constant, $\text{Li}_{1/2}(x)$ is the 1/2-order polylogarithm function of x , E_{gap} is the optical bandgap and E_u is the Urbach energy. Our measurements of absorption (assuming direct E_{gap}

behaviour) and spectroscopic ellipsometry indicate values of 4.43-4.48 and 4.39-4.44 eV for non-annealed and annealed np-SnO₂ films respectively (see Figure S12). The unexpectedly high values of E_{gap} for np-SnO₂ could be explained by partial incorporation of organic contaminants into the film. Alternatively, film porosity through voids between joined nanoparticles could lead to a lower effective absorption coefficient, which might then modify the apparent optical E_{gap} values. As such, the E_{gap} values reported are considered an approximation.

4.3.4: Note 3 – GISAXS modelling

We prepared 100 nm thick films (confirmed by ellipsometry on SiO₂), and calculated the approximate critical angle (θ_c) for SnO₂ at a photon energy of 9.243 keV to be 0.32°.⁷⁶ By working close to the critical angle for SnO₂ and taking in-plane line-cuts (integrating $0 \leq Q_z \leq 0.2 \text{ \AA}^{-1}$) through the data, we are able to probe the lateral structure of the film surface, as an aggregate measurement of the whole film. With no well-defined length scales apparent in the small-angle data (as would be indicated by defined scattering features, or peaks), an approach using a shape-independent fitting model was required. Here, the so-called radius of gyration (R_G) is a measure of the characteristic length scale within the film.

Considering the nanoparticles as spheres, and noting the clear Guinier and Porod regions of the scattering curve, we fitted an empirical Guinier-Porod model³² to our data. This allows us to confirm the expected particle shape and smoothness based on the model fit. This model takes the form:

$$I(Q) = \begin{cases} G/Q^s \exp\left(\frac{-Q^2 R_G^2}{3-s}\right) & \text{for } Q \leq Q_1 \\ D/Q^d & \text{for } Q \geq Q_1 \end{cases}$$

where G and D are the Guinier and Porod scale factors, d is the Porod exponent (which describes the smoothness of particle surfaces), s is a dimensionality parameter to describe the particle shape and Q_1 is the continuity region between the Guinier and Porod regimes:

$$Q_1 = \frac{1}{R_G} \left[\frac{(d-s)(3-s)}{2} \right]^{1/2}$$

The dimensionality parameter s here adds the shape dependent factor to the Guinier model by fitting the Porod region $Q \geq Q_1$. Specifically, $s = 0$ indicates spherical objects, $s = 1$ indicates objects such as rods and $s = 2$ indicates plates. This model can therefore be used to probe the shape of, and interfaces between, domains within the film. From the data presented

in the main text and in Table S3, it can be seen that R_G increases during annealing and from this we can use the relation for spherical bodies with radius R , $R_G^2 = \frac{3}{5}R^2$, to calculate sizes of the spherical film domains. In all cases, this is valid as fitting for s in the above model tended to 0, so any deviation from spherical particle shape is within the margin of error.

4.3.5: Supplementary Figures & Tables

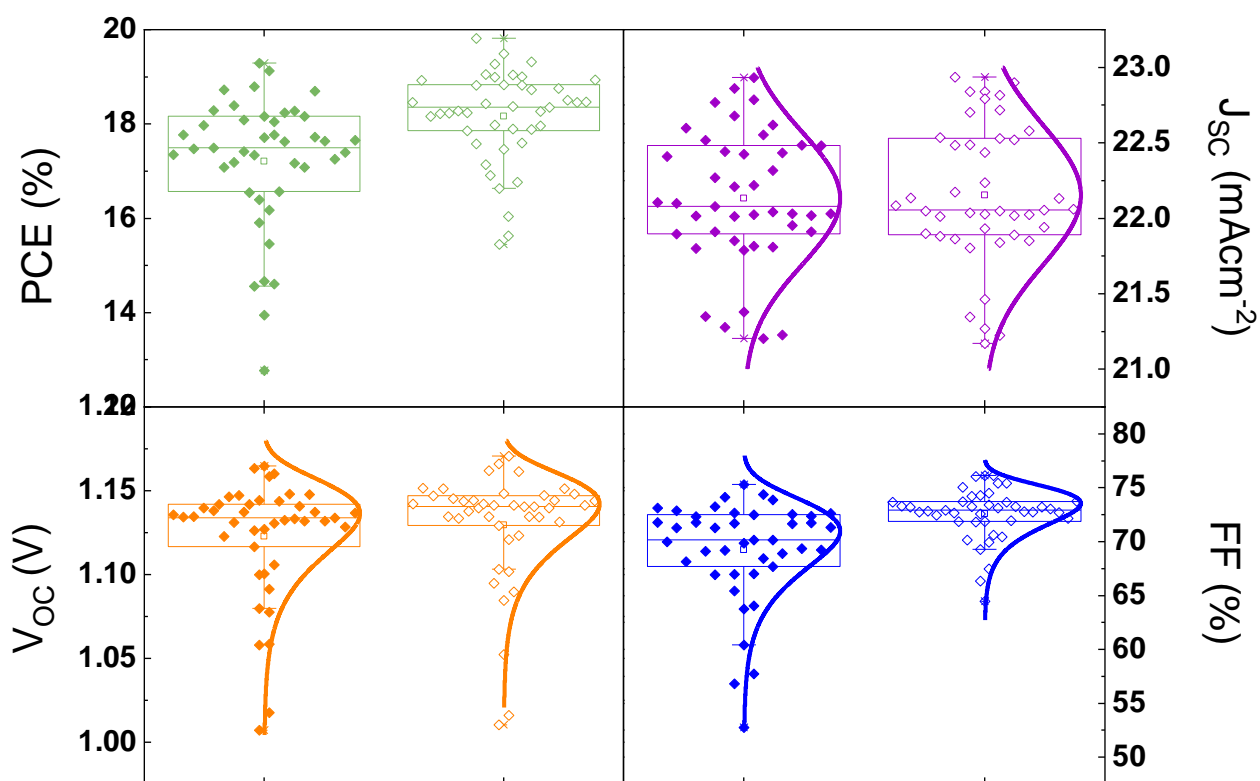


Figure S1: All reverse (hollow, right) and forward (filled, left) sweep device metrics for spin coated np-SnO₂ devices, showing excellent reproducibility between batches of devices.

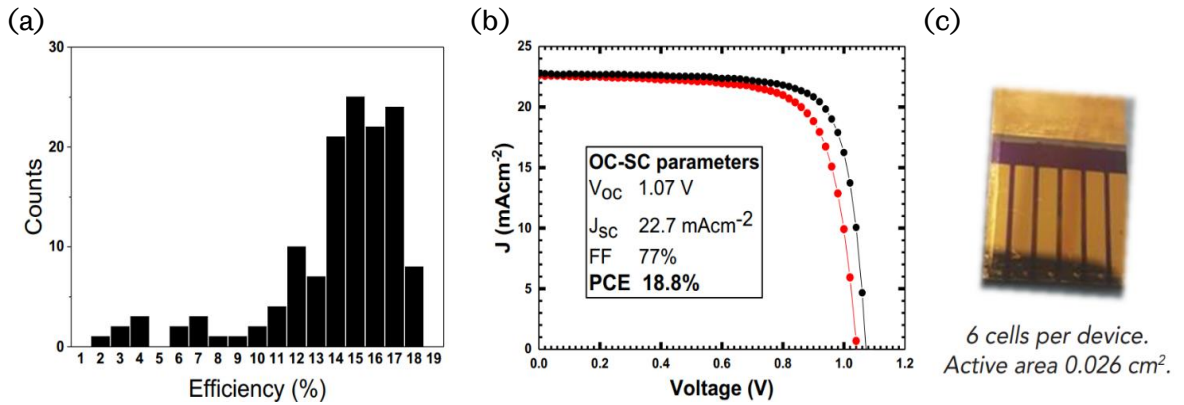


Figure S2: Performance of all functioning small area np-SnO₂ perovskite devices on FTO substrates with architecture FTO/np-SnO₂/perovskite/spiro-OMeTAD/Au. a) Histogram of device efficiencies (reverse sweep), b) J-V curve for champion cell, c) image of complete device with 6 small cells per substrate. The greater performance variation compared to ITO cells (Figure 1c) could be due to the higher roughness of FTO, which may lead to pinholes through the ETL layer. Alternatively, with the smaller cell layout used here, fabricated cells may have a broader PCE distribution due to np-SnO₂ thickness variation over the substrate surface. We note that recent work has confirmed that np-SnO₂ is highly thickness tolerant, with thicker layers on FTO substrates still resulting in highly efficiency devices.²⁶

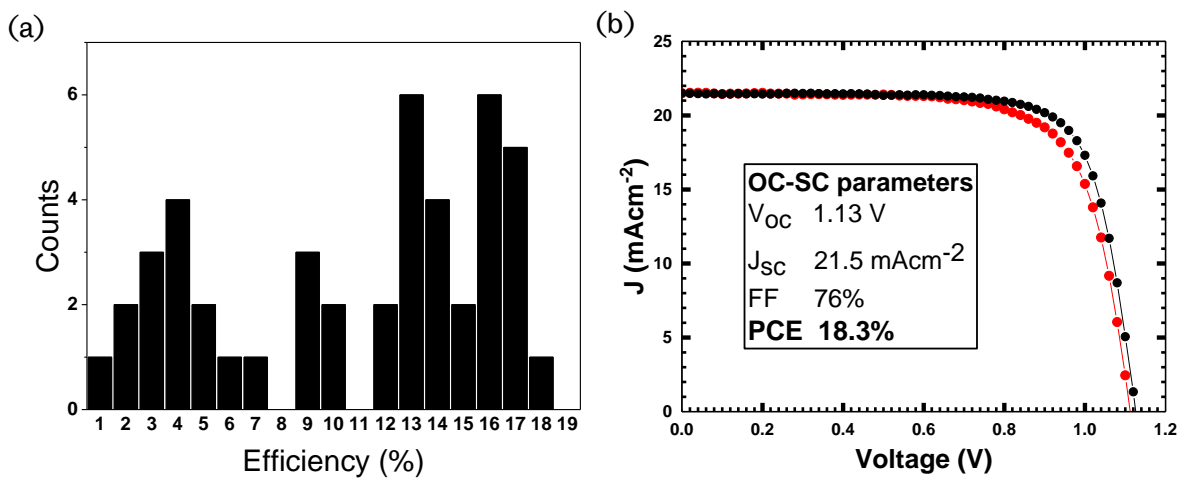


Figure S3: Device performances for small area devices using spin-coated SnCl₄.5H₂O method based on the architecture FTO/np-SnO₂/perovskite/spiro-OMeTAD/Au. a) Histogram of reverse sweep efficiencies and b) J-V curve of the champion device. Significant performance variation is observed compared to FTO/np-SnO₂, as well as requiring a longer and higher temperature deposition protocol.

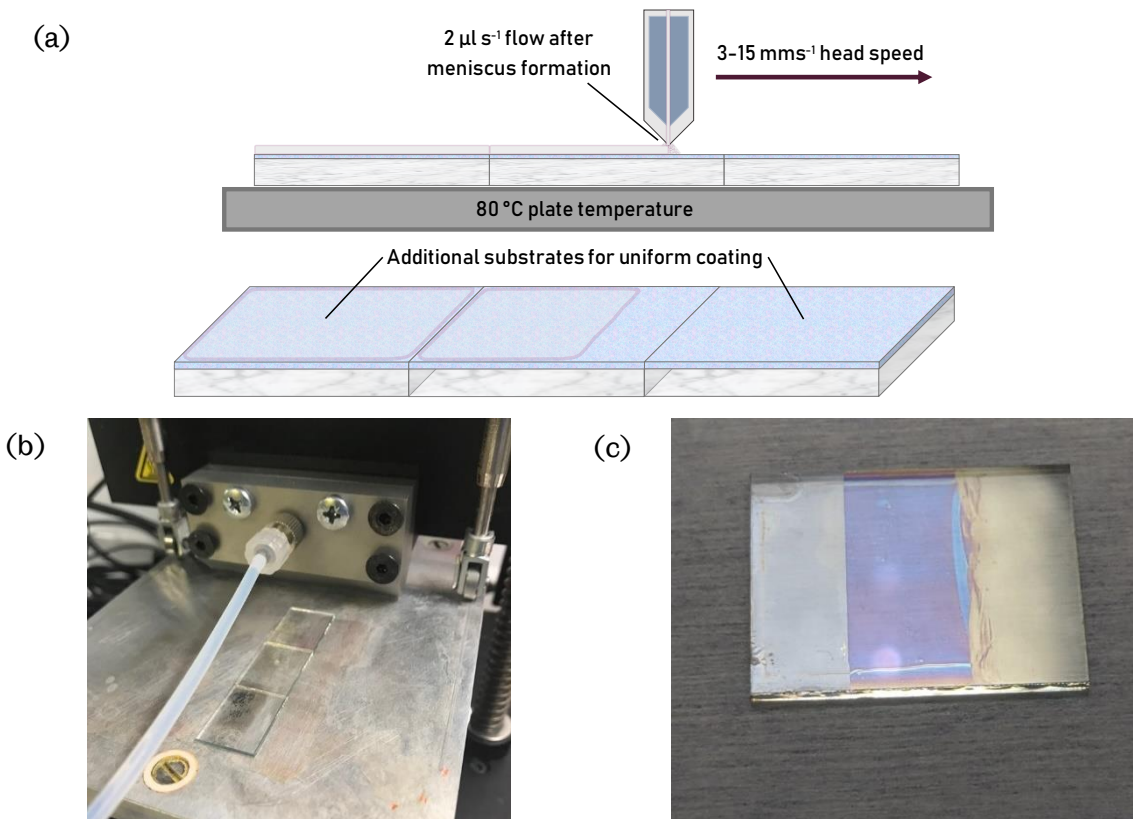


Figure S4: a) Scheme illustrating slot-die coating process. b) Layout during slot-die coating with additional substrates to ensure uniform coating of the central substrate. c) Typical slot-die coated film with $np\text{-SnO}_2$ layer removed at one side for top contact evaporation.

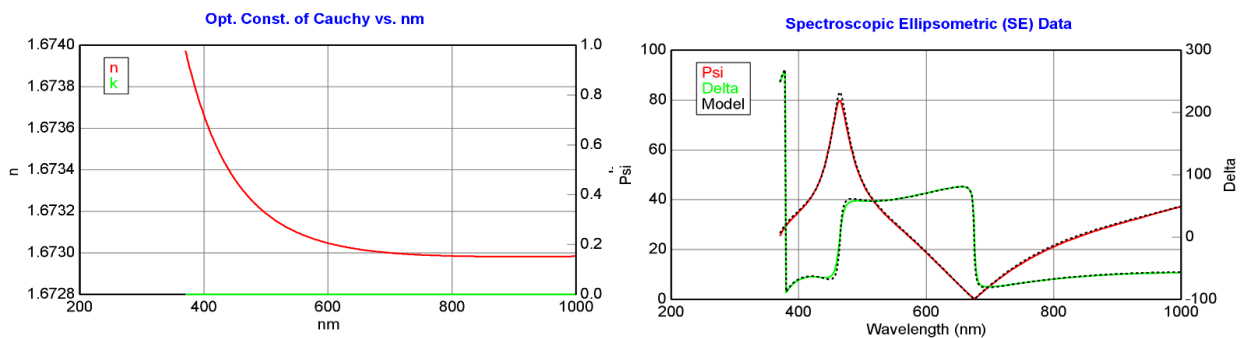


Figure S5: Typical spectroscopic ellipsometry data and Cauchy model fitting for spray-coated $np\text{-SnO}_2$ layers (here 19.01 nm). Approximate layer thicknesses on SiO_2 substrates were found to be 17.67 ± 3.41 for spray-coated cells ($N = 5$) and 38.21 ± 8.44 for slot-die coated ($N = 2$). The values given here are considered estimates, as the wetting behaviour of $np\text{-SnO}_2$ on SiO_2 will differ from that on ITO (see also note in Table S1).

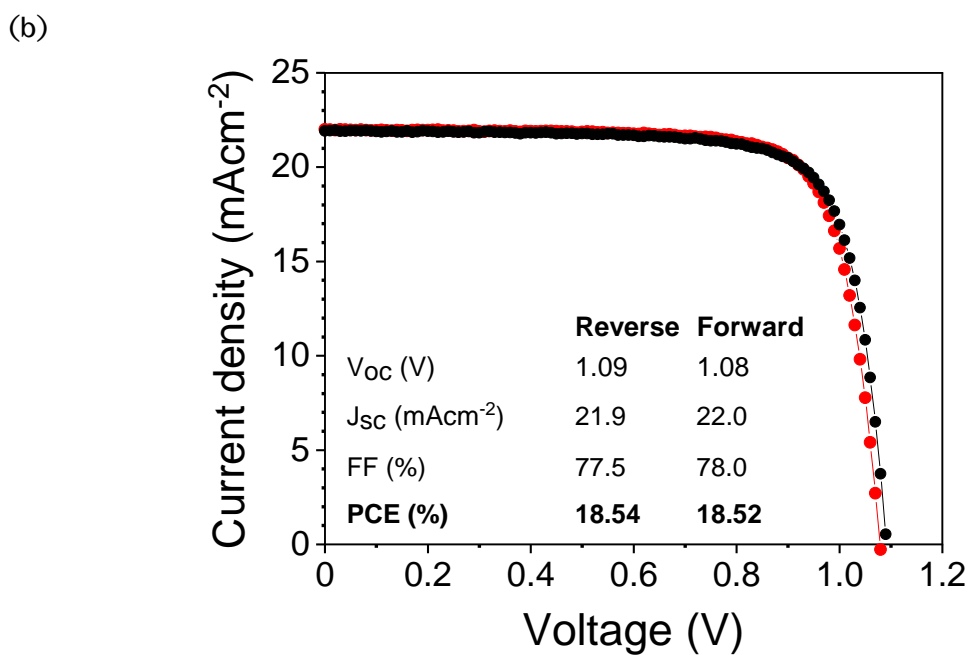
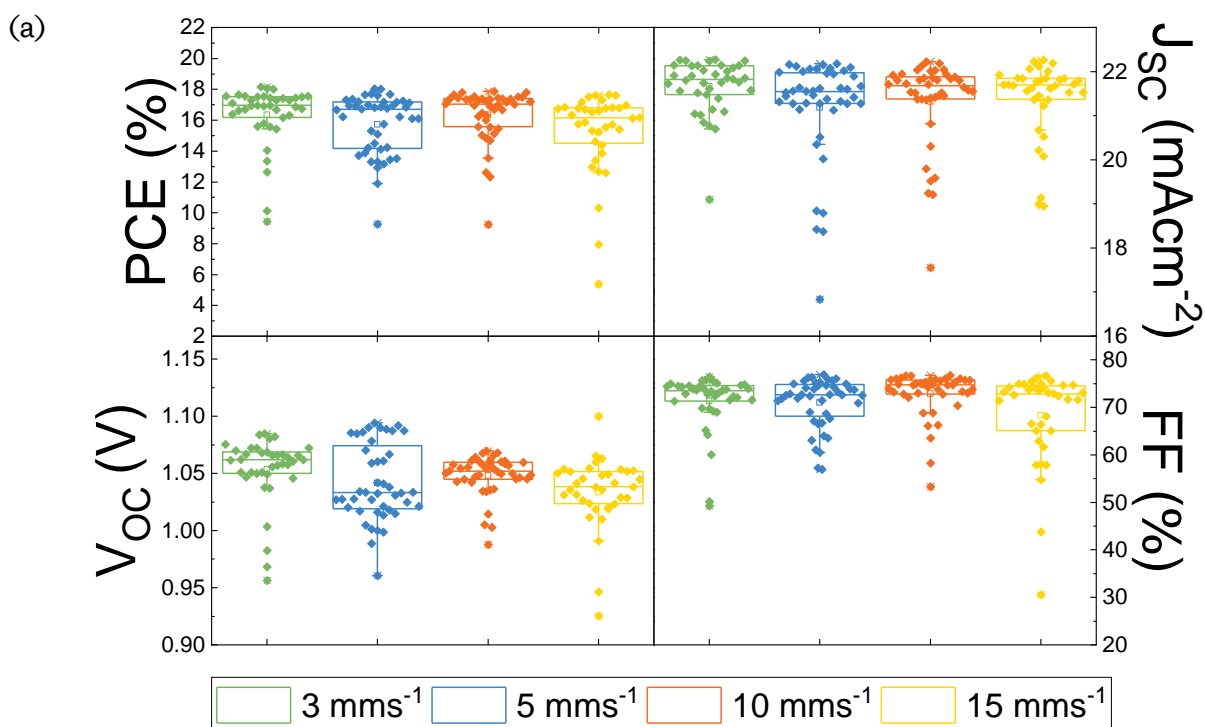


Figure S6: a) Device performance metrics for all slot-die coated np-SnO₂ layers showing comparable efficiencies and parameters across a range of coating speeds. b) J-V curve of the champion slot-die coated cell.

Electron transport layer	Treatment	Sweep	PCE (%)	J_{sc} (mAcm^{-2})	V_{oc} (V)	FF (%)	No. of cells
FTO/np-SnO ₂ (Spin-coat)	Annealed + 15 mins UVO	Forward	17.19 (13.65±2.73)	22.62 (21.56±1.36)	1.04 (1.02±0.05)	72.94 (61.80±9.02)	78
		Reverse	18.80 (14.07±3.96)	22.75 (21.77±1.31)	1.07 (1.02±0.13)	77.05 (61.76±13.11)	
FTO/SnO ₂ (SnCl ₄ .5H ₂ O)	As per methods	Forward	17.27 (11.07±3.94)	21.50 (20.82±1.13)	1.11 (0.88±0.19)	72.23 (57.79±12.02)	56
		Reverse	18.33 (10.38±6.10)	21.50 (20.77±1.19)	1.13 (0.82±0.33)	75.73 (53.85±19.54)	
ITO/np-SnO ₂ (Slot-die)	Annealed + 15 mins UVO	Forward	18.52 (16.47±1.66)	22.00 (21.51±0.79)	1.08 (1.05±0.03)	78.04 (73.08±4.91)	79
		Reverse	18.54 (15.55±2.54)	21.92 (21.31±1.07)	1.09 (1.05±0.03)	77.48 (69.26±8.07)	

Table S1: Cell performance for all operational small area cells shown in Figures S2, S3 and S6, with FTO/np-SnO₂, FTO/SnO₂ (tin chloride pentahydrate conversion route) and slot-die coated ITO/np-SnO₂ cells. Slot-die cells are found to exhibit reduced VOC compared to spin-coated devices, however the different cell architectures may lead to such variations. Variations in performance may also be result from non-uniformity in the SnO₂ layer thickness across the substrate area.

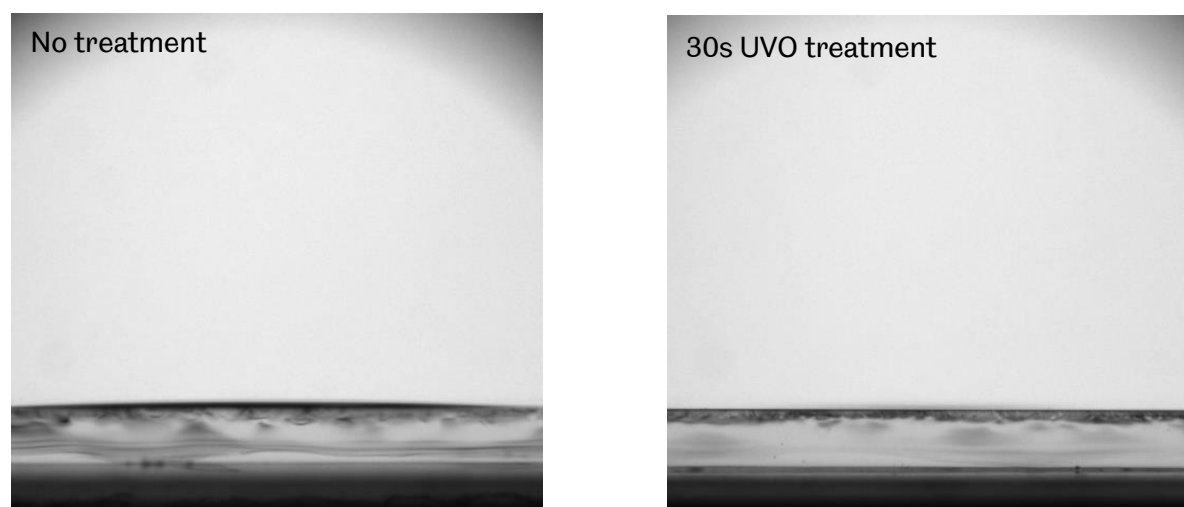


Figure S7: Contact angle measurement showing good wetting of an H₂O droplet on ITO after cleaning procedure (finishing with IPA sonication and N₂ drying) and perfect wetting after a further 30s UVO treatment.

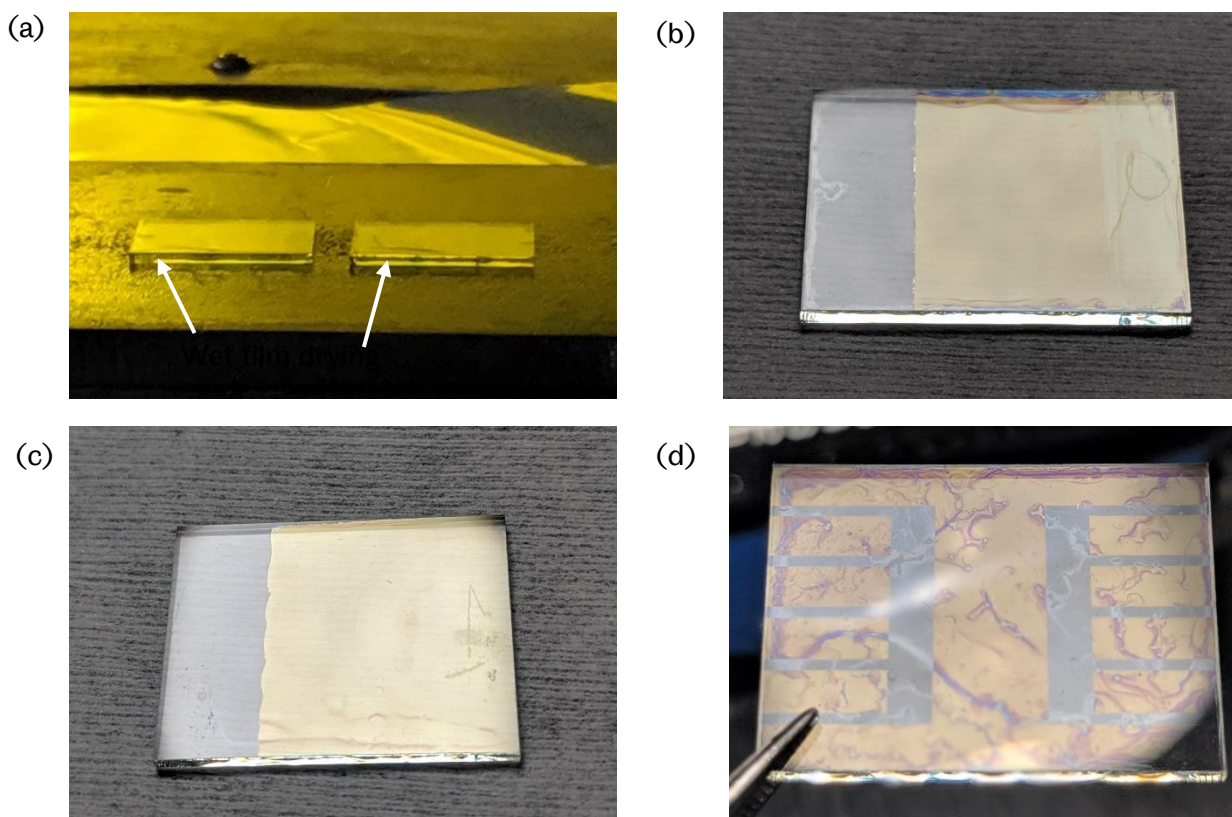


Figure S8: Photographs of spray-coated np-SnO₂. a) Photograph during sequential drying, with wet film receding to one corner. b) Typical np-SnO₂ film with uniform layer formation. Here np-SnO₂ is removed on the right for Au to contact to ITO, with perovskite/spiro-OMeTAD subsequently removed by razor blade. c) np-SnO₂ layer with insufficient UV ozone treatment prior to deposition and d) with higher solution concentration than the optimised 1:70 dilution, both leading to inhomogeneous mottled films.

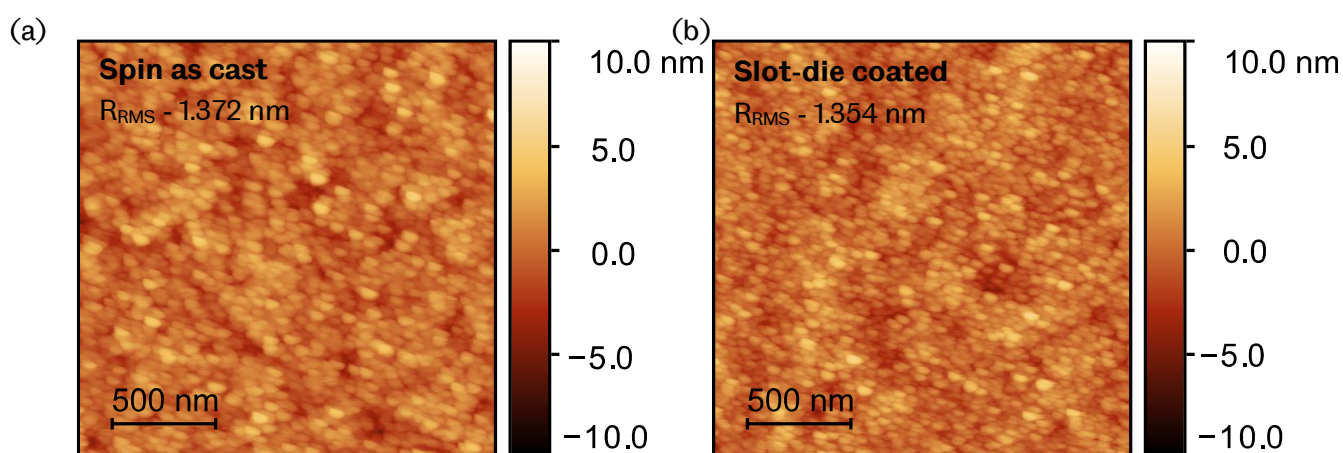


Figure S9: AFM height topography of a) spin-coated np-SnO₂ before annealing and b) slot-die coated np-SnO₂. The SnO₂ film exhibits slightly decreased roughness following annealing.

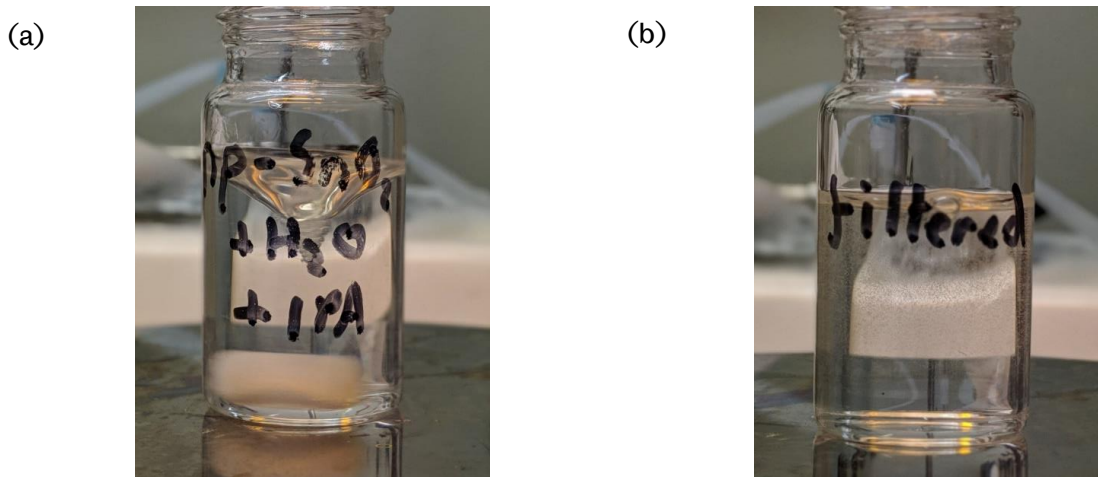


Figure S10: $np\text{-SnO}_2$ solution containing 1 ml of 20 wt% $np\text{-SnO}_2$, 5 ml H_2O and 5 ml IPA (added dropwise) a) before and b) after filtering through a PVDF filter, mimicking the atomisation in the ultrasonic spray coater. Here the IPA/ H_2O solvent de-mixes, leading to regions of aggregation in the as-sprayed $np\text{-SnO}_2$ film.

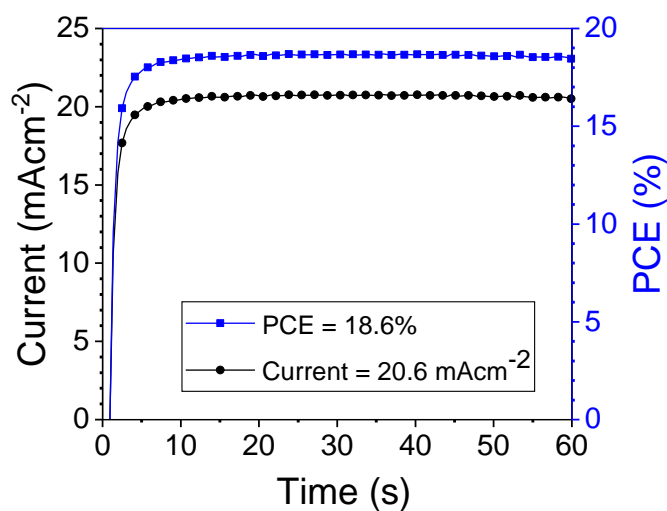


Figure S11: Stabilised power output for the champion spray-coated $np\text{-SnO}_2$ device.

Sample	Thickness (nm)	E_{gap} (SE, eV)	E_{gap} (Tauc, eV)	E_U (meV)
As deposited	94.69	4.476	4.433	159
Annealed	101.42	4.446	4.391	144

Table S2: Optical E_{gap} determination from Tauc plots (shown in Figure S12) and fitting to combined spectroscopic ellipsometry (SE) and transmission data. From the modelling to the SE data described in SI Note 2, the Urbach energy (E_U) is also determined. The thickness value here for the annealed films (on quartz) is in good agreement with that determined for films on SiO_2 in the process design of 100 nm layers for GISAXS measurements (SI Note 3).

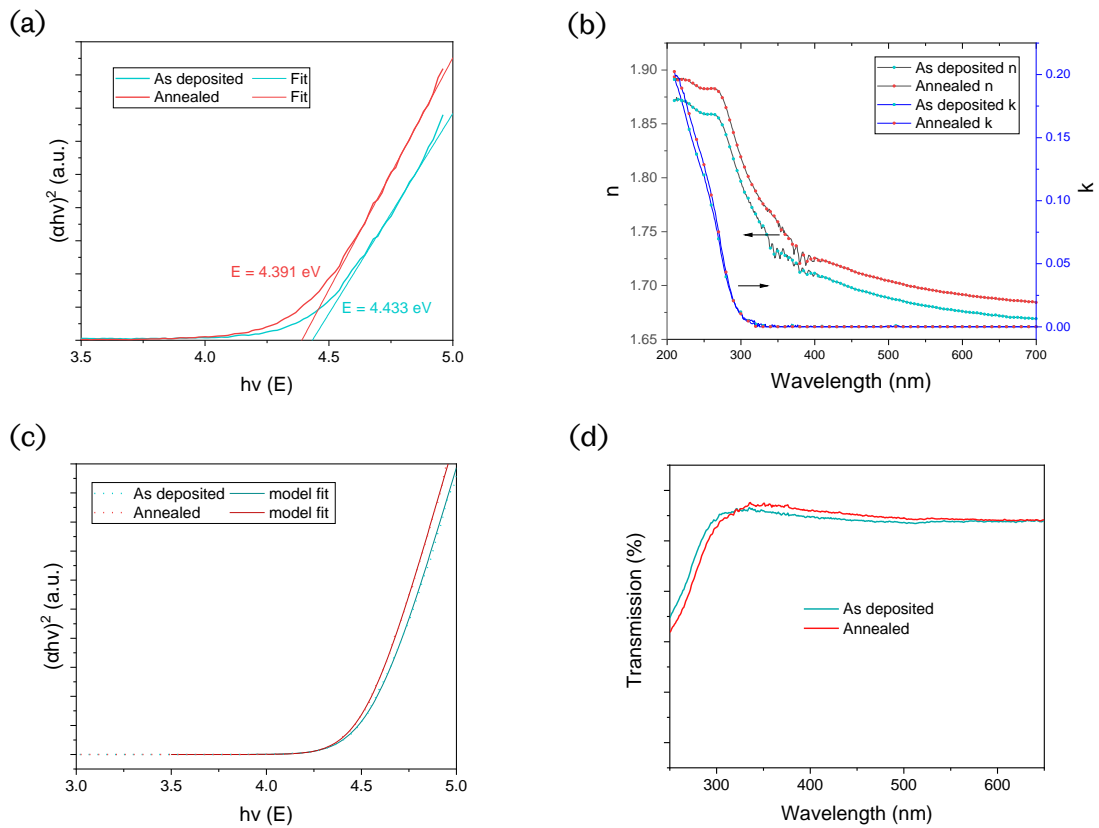


Figure S12: Optical E_{gap} determination for np-SnO₂. a) Tauc plots for as deposited and annealed np-SnO₂ from transmission measurements. b) Corresponding real (n) and imaginary (k) complex refractive index components from fitting to spectroscopic ellipsometry (SE) and transmission (T) data. c) Tauc plot using $\alpha = 2\pi k/\lambda$ for combined SE and T data, with the band fluctuation model fit overlaid. d) Transmission data used for the Tauc plots in part a).

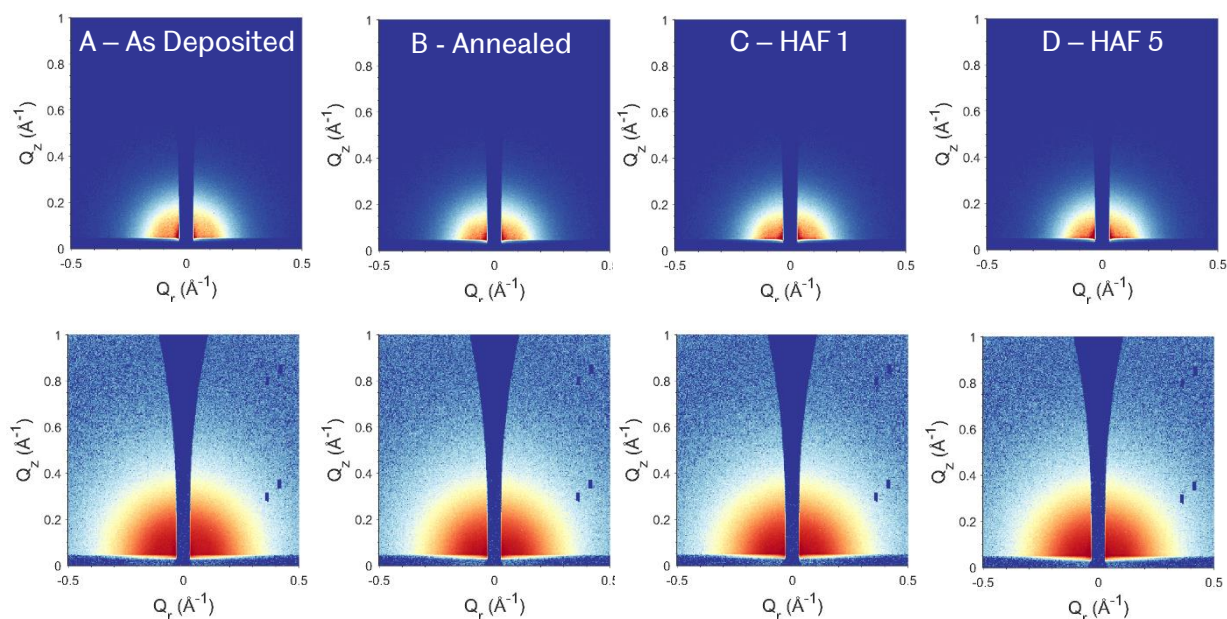


Figure S13: 2D GISAXS scattering patterns with linear (top) and log (bottom) intensity plot scales for four np-SnO₂ annealing conditions. In-plane cuts through this data are shown in Figure 4.

Sample	Fit parameters			Repeated from Table 2		
	Scale	Background	Q ₁	R _g (Å ⁻¹)	d (Porod exponent)	Grain radius
As deposited	286.49 ± 1.08	0.00 ± 1.25	0.2468	9.09 ± 0.05	3.984 ± 0.31	1.173 ± 0.006
Annealed	267.44 ± 1.12	0.00 ± 1.20	0.269	9.43 ± 0.05	3.612 ± 0.24	1.218 ± 0.006
HAF 1	279.60 ± 1.10	0.00 ± 1.22	0.2586	9.27 ± 0.05	3.829 ± 0.28	1.197 ± 0.006
HAF 2	290.96 ± 1.09	0.00 ± 1.21	0.2575	9.31 ± 0.05	3.831 ± 0.27	1.202 ± 0.006
HAF 5	276.95 ± 1.11	0.00 ± 1.20	0.2487	9.42 ± 0.05	3.661 ± 0.24	1.216 ± 0.006

Table S3: Extended fit parameters and Q₁ for Guinier-Porod fitting model applied to GISAXS linecuts. Full details are given in SI Note 3.



Figure S14: Photo of heat gun setup used for HAF annealing. Temperature was stabilised to 120 ± 10 °C, confirmed with a thermocouple connected to a suspended substrate, matching the conditions during HAF annealing.

Annealing	Treatment	Sweep direction	PCE (%)	J_{sc} (mAcm ⁻²)	V_{oc} (V)	FF	No. of cells
Air dried	None	Forward	17.59 (16.70 ±0.74)	22.69 (22.39 ±0.16)	1.11 (1.11 ±0.01)	70.09 (67.30 ±2.30)	9
		Reverse	18.56 (17.30 ±0.78)	22.79 (22.36 ±0.20)	1.12 (1.12 ±0.01)	72.63 (69.31 ±2.21)	
Air dried	15 mins UVO	Forward	17.73 (17.23 ±0.92)	22.79 (22.40 ±0.17)	1.12 (1.12 ±0.01)	69.25 (68.73 ±3.34)	10
		Reverse	18.62 (17.79 ±0.60)	22.81 (22.36 ±0.18)	1.13 (1.13 ±0.01)	72.17 (70.69 ±1.94)	
Air dried	5 mins O ₂ plasma	Forward	16.91 (15.21 ±0.94)	22.17 (22.22 ±0.18)	1.09 (1.02 ±0.04)	70.02 (66.88 ±1.90)	9
		Reverse	18.21 (17.26 ±0.53)	22.20 (22.22 ±0.20)	1.11 (1.07 ±0.03)	73.97 (72.81 ±1.05)	
120 °C 1 min	15 mins UVO	Forward	18.19 (16.86 ±1.29)	22.18 (22.30 ±0.31)	1.14 (1.12 ±0.04)	72.19 (67.70 ±3.93)	8
		Reverse	18.93 (17.98 ±0.86)	22.16 (22.31 ±0.29)	1.14 (1.13 ±0.03)	74.69 (71.50 ±2.28)	
120 °C 1 min	5 mins O ₂ plasma	Forward	16.49 (14.47 ±1.72)	21.99 (22.19 ±0.25)	1.05 (1.00 ±0.05)	71.21 (65.01 ±5.38)	9
		Reverse	18.26 (17.15 ±0.82)	21.98 (22.27 ±0.24)	1.09 (1.05 ±0.03)	76.28 (73.21 ±2.34)	

Table S4: Device performances for devices using annealing-free and flash-dried spin-coated np-SnO₂ layers. Best cells in both sweep directions are given as well as average and standard deviation.

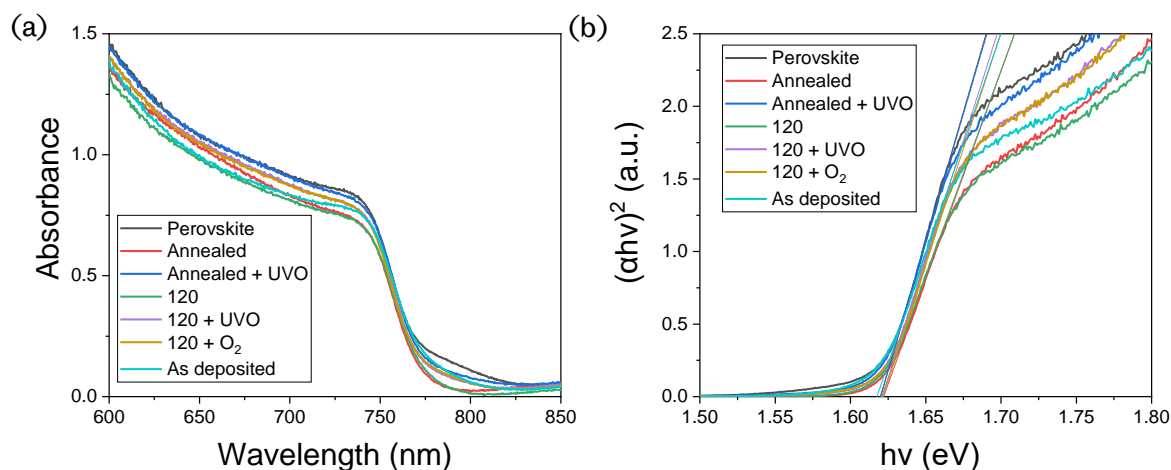


Figure S15: a) Absorbance and b) Tauc plots for $np\text{-SnO}_2/\text{perovskite}$ interface samples with various $np\text{-SnO}_2$ processing conditions, and comparable optical E_{gap} in all cases (Table S5). A quartz-coated glass/perovskite sample is also shown for reference, with apparent sub-bandgap absorption being a measurement artefact that is likely to lead to a small error in the optical E_{gap} as derived from the Tauc plot.

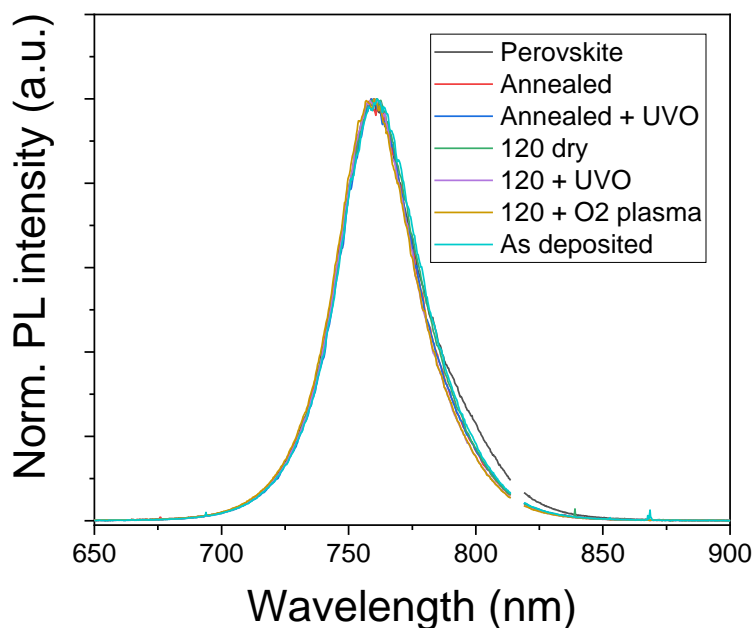


Figure S16: Normalised PL for $np\text{-SnO}_2/\text{perovskite}$ interface samples showing no significant changes to the perovskite layer with different interface treatments. Excitation and collection were from the glass side. An extended tail is observed for the quartz-coated glass/perovskite sample, due to improved perovskite film formation on the $np\text{-SnO}_2$ layer.

Sample	PL (nm)	PL (eV)	Tauc E_{gap} (nm)	Tauc E_{gap} (eV)
Perovskite	759.9	1.63	765.1	1.62
Annealed	759.9	1.63	764.2	1.62
Annealed + UVO	760.3	1.63	765.3	1.62
As deposited	761.2	1.63	766.3	1.62
As dep + UVO	761.0	1.63	765.2	1.62
As dep + O ₂	759.3	1.63	764.4	1.62
120 dry	760.7	1.63	764.9	1.62
120 + UVO	759.6	1.63	764.6	1.62
120 + O ₂	759.3	1.63	764.2	1.62

Table S5: Optical E_{gap} determination for perovskite on np-SnO₂ substrates from extrapolation of linear region of Tauc plots (Figure S15) and SSPL measurements (Figure S16) fitted with an exponentially-modified Gaussian.

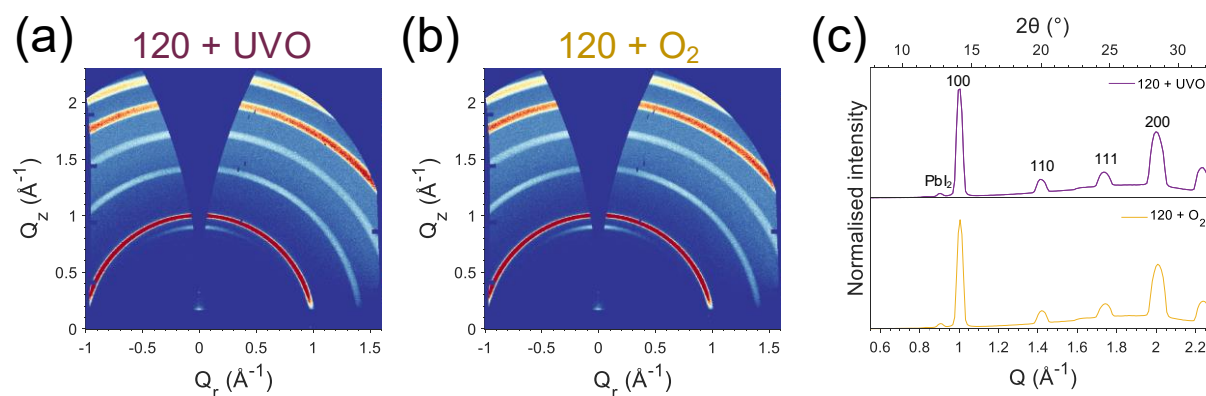


Figure S17: GIWAXS patterns for perovskite layer grown on a) 120 + UVO and b) 120 + O₂ plasma np-SnO₂ layers. c) Azimuthal integrations through the 2D patterns, confirming the presence of some out-of-plane oriented PbI₂ and pseudo-cubic perovskite in both samples, with no observable differences between samples.



Figure S18: pH strip confirming pH of the undiluted np-SnO₂ to be ~11.5, with strong basicity due to the KOH stabiliser.

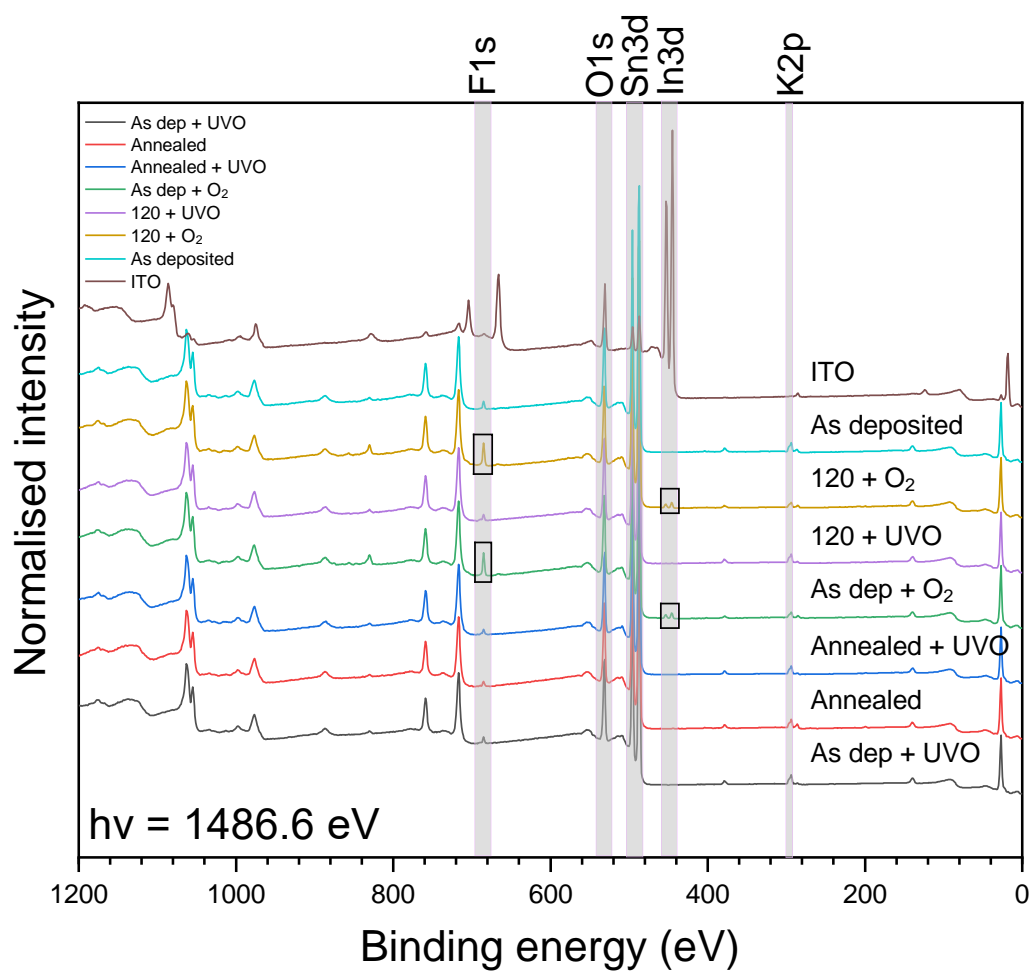


Figure S19: XPS wide scan spectra for all samples. Both 120 + O₂ plasma and 'As deposited + O₂' plasma samples show comparatively increased F 1s and In 3d intensity, with reduced K 2p.

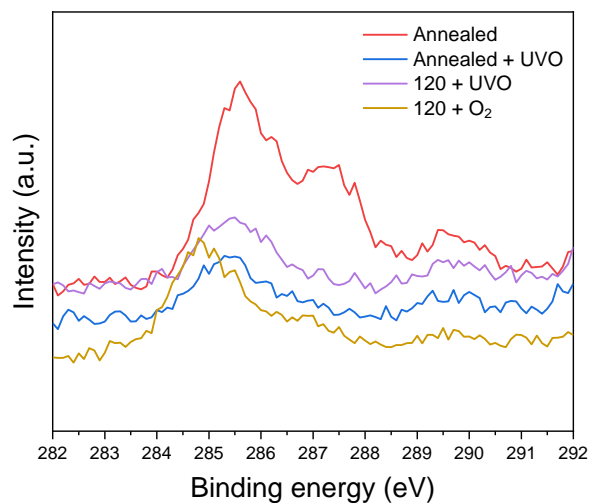


Figure S20: XPS spectra of C 1s core level emission for each process step. We find that UVO and O₂ plasma reduce adventitious carbon at the sample surface.

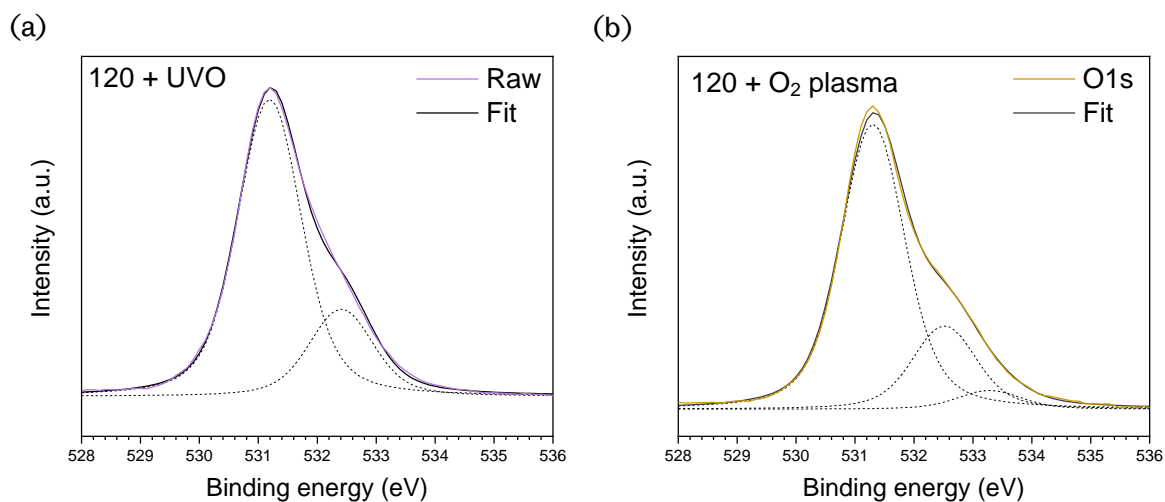


Figure S21: XPS spectra for O 1s core levels for a) 120 + UVO and b) 120 + O₂ plasma samples. Three peaks are required to fit O₂ plasma treated samples, with this third environment ascribed to a contaminant species most likely related to fluorine. The fitting methodology is described in the Experimental Methods section above.

Sample	O 1s peak areas			Area ratios	
	O-Sn	-OH/O _{ads}	HES	O-Sn/[Sn 3d]	[O 1s]/[Sn 3d]
Annealed	0.78	0.22		0.45	0.57
Annealed + UVO	0.77	0.23		0.43	0.56
As deposited	0.77	0.23		0.42	0.55
As dep + UVO	0.78	0.22		0.43	0.55
As dep + O ₂	0.72	0.21	0.07	0.38	0.53
120 + UVO	0.79	0.21		0.44	0.56
120 + O ₂	0.73	0.22	0.05	0.40	0.54

Table S6: Fitted peak areas from XPS O 1s core level spectra for all samples. Two species, ascribed to Sn-O (or lattice oxygen) and -OH/O_{ads} (hydroxides and other adsorbed species) are fitted for all samples. Both O₂ plasma treated samples show a third peak (denoted here as high energy shoulder, HES) ascribed to a contaminant species or defect introduced with the fluorine contamination. Both O₂ plasma species show a reduction in peak area ratios; O-Sn/[Sn 3d] (comparing Sn 3d area with only the lattice oxygen peak) and [O 1s]/[Sn 3d] (comparing with all O 1s peak areas), which may indicate a more oxygen-deficient surface.

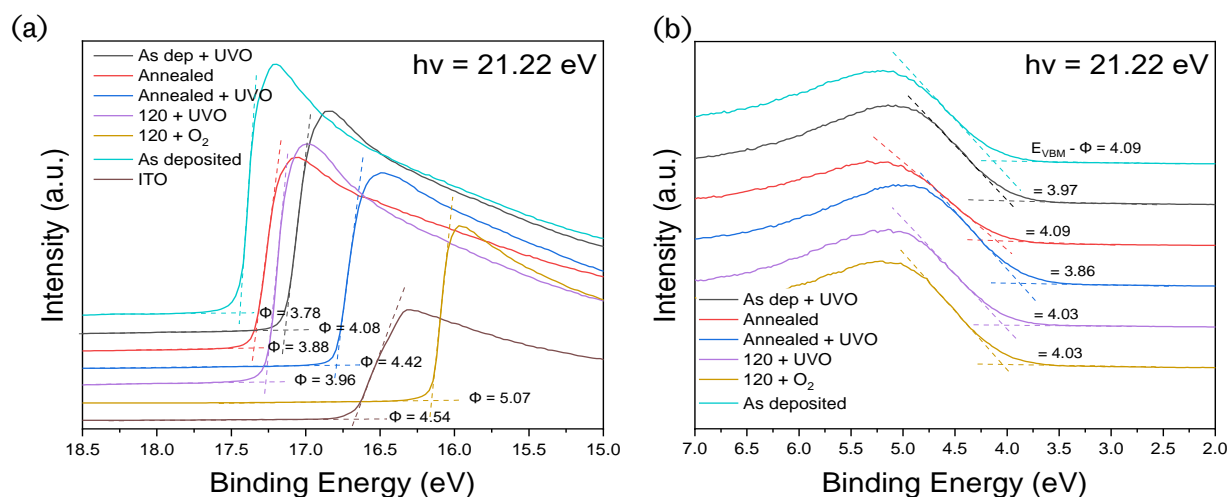


Figure S22: UPS spectra showing a) secondary electron edge with E_{cutoff} measured to determine work function (Φ) and b) E_{onset}/E_B to find the valence band maximum.

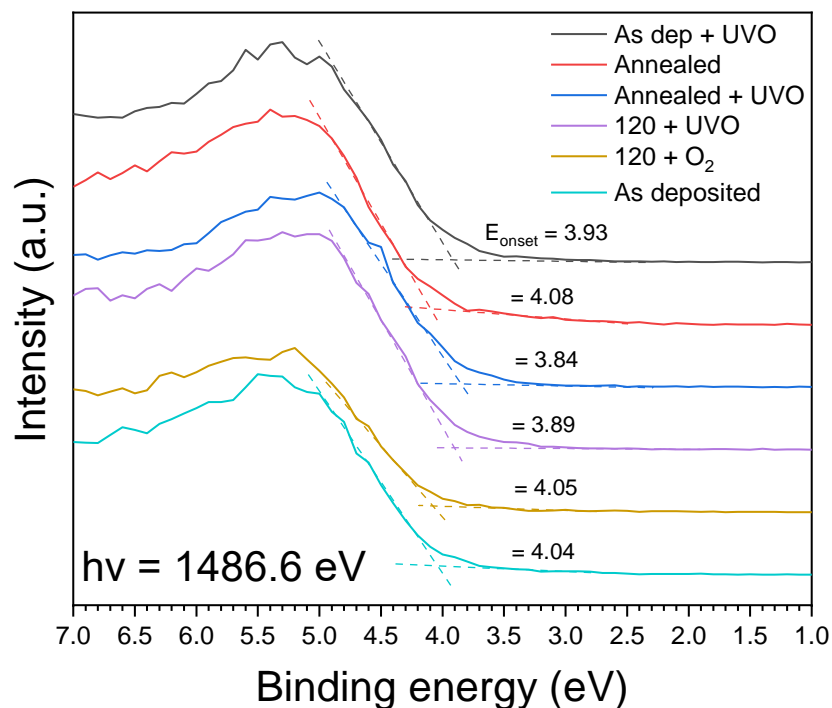


Figure S23: XPS valence spectra used to confirm E_{onset} for IE/valence band determination.

Sample	E_{cutoff} Secondary electron edge	WF Φ	$E_{\text{onset}} (E_{\text{B}})$		Ionisation energy (IE)		Optical E_{gap}	Estimated electron affinity (EA)	
			UPS	XPS	UPS	XPS		UPS	XPS
SnO ₂ NPs (literature) ¹⁹		4.36	3.74		8.10		3.79	4.31	
ITO + UVO	16.68	4.54	3.09	3.15	7.64	7.69			
Annealed	17.34	3.88	4.09	4.08	7.96	7.95	4.45	3.51	3.50
Annealed + UVO	16.80	4.42	3.86	3.84	8.29	8.26	4.45	3.84	3.81
As deposited	17.44	3.78	4.09	4.04	7.86	7.82	4.48	3.38	3.34
As dep + UVO	17.14	4.08	3.97	3.93	8.05	8.01	4.48	3.57	3.53
As dep + O ₂	16.22	5.00	4.04	4.10	9.03	9.10	4.48	4.55	4.62
120 + UVO	17.26	3.96	4.03	3.89	7.99	7.85	4.48	3.51	3.37
120 + O ₂ plasma	16.15	5.07	4.03	4.05	9.11	9.13	4.48	4.63	4.65

Table S7: Electronic structure of np-SnO₂ determined from UPS and XPS measurements, with all energies in eV. EA is estimated using optical E_{gap} (Figure S12). All UPS and XPS values are shown without error due to fitting.

	W.r.t. E_{vac}			W.r.t. E_f		
	VBM ($-E_i$)	WF (Φ)	CBM ($-EA$)	VBM	WF	CBM
ITO + UVO		-4.54				
Annealed	-7.96	-3.88	-3.51	-4.08	0	0.37
Annealed + UVO	-8.28	-4.42	-3.83	-3.85	0	0.60
As deposited	-7.84	-3.78	-3.36	-4.06	0	0.42
As dep + UVO	-8.03	-4.08	-3.55	-3.95	0	0.53
As dep + O ₂	-9.07	-5.00	-4.59	-4.07	0	0.41
120 + UVO	-7.92	-3.96	-3.44	-3.96	0	0.52
120 + O ₂ plasma	-9.12	-5.07	-4.64	-4.04	0	0.44

Table S8: Energy levels used, averaging UPS and XPS, as shown in Figure 6a (with respect to vacuum) and w.r.t. the Fermi level. Values are given without errors related to the fitting.

Stated composition (reference)	Substrate	Methods	Perovskite		spiro-OMeTAD	
			IE (eV)	EA (eV)	IE (eV)	EA (eV)
Cs ₆ (MA _{0.17} FA _{0.83}) ₉₄ Pb(I _{0.83} Br _{0.17}) ₃ (77)	ZnO	UPS/Tauc	6.08	4.46	5.7	2.2
CsI _{0.05} ((FAPbI ₃) _{0.87} (MAPbBr ₃) _{0.13}) _{0.95} (78)	Unknown	UPS	5.7	est. 4.1	5.4	
Cs _{0.05} ((FAPbI ₃) _{0.85} (MAPbBr ₃) _{0.15}) _{0.95} (79)	TiO ₂	UPS/Tauc	5.4	3.79	5.22	
Cs _{0.05} FA _{0.79} MA _{0.16} Pb(I _{0.83} Br _{0.17}) ₃ (80)	PEDOT:PSS	UPS	5.87	4.26		

Table S9: Typical energy level literature values for various triple-cation perovskite compositions and spiro-OMeTAD layers deposited on different transport layers.

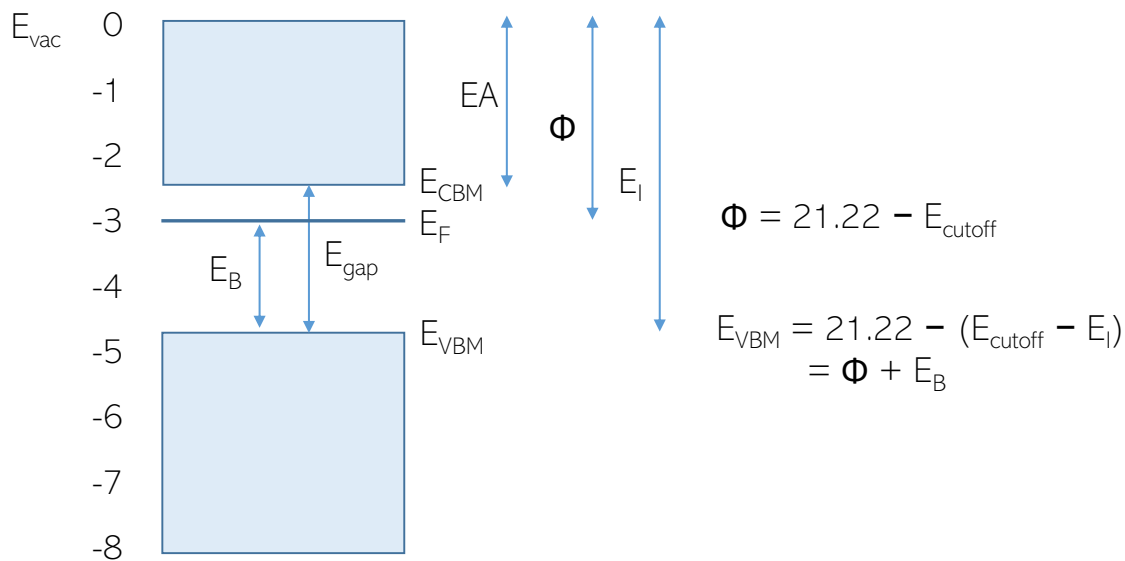


Figure S24: Illustration of energy level determination from UPS measurements.

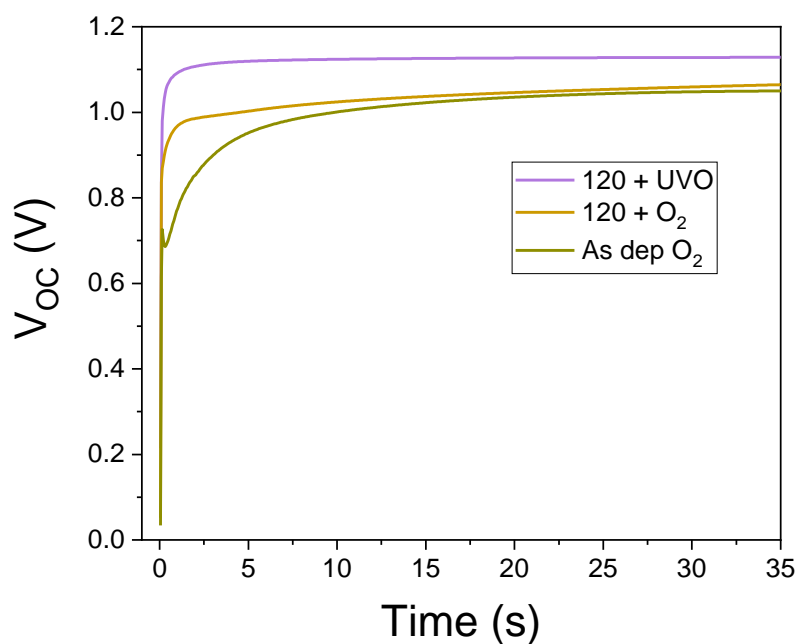


Figure S25: Transient photovoltage measurements showing the evolution of V_{OC} for completed devices with different np-SnO₂ interface treatments, with both O₂ plasma treated samples stabilising more gradually.

4.4: References

- (1) Kojima, A.; Teshima, K.; Shirai, Y.; Miyasaka, T. Organometal Halide Perovskites as Visible-Light Sensitizers for Photovoltaic Cells. *J. Am. Chem. Soc.* **2009**, *131* (17), 6050–6051. <https://doi.org/10.1021/ja809598r>.
- (2) National Renewable Energy Laboratory. Best Research-Cell Efficiencies <https://www.nrel.gov/pv/cell-efficiency.html> (accessed Jan 1, 2021).
- (3) Stranks, S. D. Nonradiative Losses in Metal Halide Perovskites. *ACS Energy Lett.* **2017**, 1515–1525. <https://doi.org/10.1021/acsenenergylett.7b00239>.
- (4) Egger, D. A.; Bera, A.; Cahen, D.; Hodes, G.; Kirchartz, T.; Kronik, L.; Lovrincic, R.; Rappe, A. M.; Reichman, D. R.; Yaffe, O. What Remains Unexplained about the Properties of Halide Perovskites? *Adv. Mater.* **2018**, *30* (20), 1–11. <https://doi.org/10.1002/adma.201800691>.
- (5) Saliba, M.; Matsui, T.; Seo, J.-Y.; Domanski, K.; Correa-Baena, J.-P.; Nazeeruddin, M. K.; Zakeeruddin, S. M.; Tress, W.; Abate, A.; Hagfeldt, A.; Grätzel, M. Cesium-Containing Triple Cation Perovskite Solar Cells: Improved Stability, Reproducibility and High Efficiency. *Energy Environ. Sci.* **2016**, *9* (6), 1989–1997. <https://doi.org/10.1039/C5EE03874J>.
- (6) Berhe, T. A.; Su, W.-N.; Chen, C.-H.; Pan, C.-J.; Cheng, J.-H.; Chen, H.-M.; Tsai, M.-C.; Chen, L.-Y.; Dubale, A. A.; Hwang, B.-J. Organometal Halide Perovskite Solar Cells: Degradation and Stability. *Energy Environ. Sci.* **2016**, *9* (2), 323–356. <https://doi.org/10.1039/C5EE02733K>.
- (7) Leijtens, T.; Eperon, G. E.; Pathak, S.; Abate, A.; Lee, M. M.; Snaith, H. J. Overcoming Ultraviolet Light Instability of Sensitized TiO₂ with Meso-Superstructured Organometal Tri-Halide Perovskite Solar Cells. *Nat. Commun.* **2013**, *4*, 2885. <https://doi.org/10.1038/ncomms3885>.
- (8) Ke, W.; Fang, G.; Liu, Q.; Xiong, L.; Qin, P.; Tao, H.; Wang, J.; Lei, H.; Li, B.; Wan, J.; Yang, G.; Yan, Y. Low-Temperature Solution-Processed Tin Oxide as an Alternative Electron Transporting Layer for Efficient Perovskite Solar Cells. *J. Am. Chem. Soc.* **2015**, *137* (21), 6730–6733. <https://doi.org/10.1021/jacs.5b01994>.
- (9) Christians, J. A.; Schulz, P.; Tinkham, J. S.; Schloemer, T. H.; Harvey, S. P.; Tremolet de Villers, B. J.; Sellinger, A.; Berry, J. J.; Luther, J. M. Tailored Interfaces of Unencapsulated Perovskite Solar Cells for >1,000 Hour Operational Stability. *Nat. Energy* **2018**, *3* (1), 68–74. <https://doi.org/10.1038/s41560-017-0067-y>.
- (10) Tiwana, P.; Docampo, P.; Johnston, M. B.; Snaith, H. J.; Herz, L. M. Electron Mobility and Injection Dynamics in Mesoporous ZnO, SnO₂, and TiO₂ Films Used in Dye-Sensitized Solar Cells. *ACS Nano* **2011**, *5* (6), 5158–5166. <https://doi.org/10.1021/nn201243y>.
- (11) Baena, J. P. C.; Steier, L.; Tress, W.; Saliba, M.; Neutzner, S.; Matsui, T.; Giordano, F.; Jacobsson, T. J.; Kandada, A. R. S.; Zakeeruddin, S. M.; Petrozza, A.; Abate, A.; Nazeeruddin, M. K.; Grätzel, M.; Hagfeldt, A. Highly Efficient Planar Perovskite Solar Cells through Band Alignment Engineering. *Energy Environ. Sci.* **2015**, *8* (10), 2928–2934. <https://doi.org/10.1039/C5EE02608C>.
- (12) Dong, Q.; Shi, Y.; Wang, K.; Li, Y.; Wang, S.; Zhang, H.; Xing, Y.; Du, Y.; Bai, X.; Ma, T. Insight into Perovskite Solar Cells Based on SnO₂ Compact Electron-Selective Layer. *J. Phys. Chem. C* **2015**, *119* (19), 10212–10217. <https://doi.org/10.1021/acs.jpcc.5b00541>.
- (13) Bush, K. A.; Palmstrom, A. F.; Yu, Z. (Jason); Boccard, M.; Cheacharoen, R.; Mailoa, J. P.; McMeekin, D. P.; Hoyer, R. L. Z.; Bailie, C. D.; Leijtens, T.; Peters, I. M.; Minichetti, M. C.; Rolston, N.; Prasanna, R.; Sofia, S. E.; Harwood, D.; Ma, W.; Moghadam, F.; Snaith, H. J.; Buonassisi, T.; Holman, Z. C.; Bent, S. F.; McGehee, M. D. 23.6%-Efficient Monolithic Perovskite/Silicon Tandem Solar Cells with Improved Stability. *Nat. Energy* **2017**, No. February, 1–7. <https://doi.org/10.1038/nenergy.2017.9>.
- (14) Wang, C.; Zhao, D.; Grice, C. R.; Liao, W.; Yu, Y.; Cimaroli, A.; Shrestha, N.; Roland, P. J.; Chen, J.; Yu, Z.; Liu, P.; Cheng, N.; Ellingson, R. J.; Zhao, X.; Yan, Y. Low-Temperature Plasma-Enhanced Atomic Layer Deposition of Tin Oxide Electron Selective Layers for Highly Efficient Planar Perovskite Solar Cells. *J. Mater. Chem. A* **2016**, *4* (31), 12080–12087. <https://doi.org/10.1039/C6TA04503K>.
- (15) Ma, J.; Zheng, X.; Lei, H.; Ke, W.; Chen, C.; Chen, Z.; Yang, G.; Fang, G. Highly Efficient and Stable Planar Perovskite Solar Cells With Large-Scale Manufacture of E-Beam Evaporated SnO₂ Toward Commercialization. *Sol. RRL* **2017**, *1* (10), 1700118. <https://doi.org/10.1002/solr.201700118>.
- (16) Guo, Y.; Yin, X.; Liu, J.; Chen, W.; Wen, S.; Que, M.; Xie, H.; Yang, Y.; Que, W.; Gao, B. Vacuum Thermal-Evaporated SnO₂ as Uniform Electron Transport Layer and Novel Management of Perovskite Intermediates for Efficient and Stable Planar Perovskite Solar Cells. *Org. Electron.* **2019**, *65* (September 2018), 207–214. <https://doi.org/10.1016/j.orgel.2018.11.021>.
- (17) Qiu, L.; Liu, Z.; Ono, L. K.; Jiang, Y.; Son, D.; Hawash, Z.; He, S.; Qi, Y. Scalable Fabrication of Stable High Efficiency Perovskite Solar Cells and Modules Utilizing Room Temperature Sputtered SnO₂ Electron Transport Layer. *Adv. Funct. Mater.* **2019**, *29* (47), 1806779. <https://doi.org/10.1002/adfm.201806779>.
- (18) Anaraki, E. H.; Kermanpur, A.; Steier, L.; Domanski, K.; Matsui, T.; Tress, W.; Saliba, M.; Abate, A.; Grätzel, M.; Hagfeldt, A.; Correa-Baena, J.-P. Highly Efficient and Stable Planar Perovskite Solar Cells by Solution-Processed Tin Oxide. *Energy Environ. Sci.* **2016**, *9* (September), 3128–3134. <https://doi.org/10.1039/C6EE02390H>.

- (19) Jiang, Q.; Zhang, L.; Wang, H.; Yang, X.; Meng, J.; Liu, H.; Yin, Z.; Wu, J.; Zhang, X.; You, J. Enhanced Electron Extraction Using SnO₂ for High-Efficiency Planar-Structure HC(NH₂)₂PbI₃-Based Perovskite Solar Cells. *Nat. Energy* **2017**, *2* (1), 16177. <https://doi.org/10.1038/nenergy.2016.177>.
- (20) Duan, J.; Xiong, Q.; Feng, B.; Xu, Y.; Zhang, J.; Wang, H. Low-Temperature Processed SnO₂ Compact Layer for Efficient Mesoporous Perovskite Solar Cells. *Appl. Surf. Sci.* **2017**, *391*, 677–683. <https://doi.org/10.1016/j.apsusc.2016.06.187>.
- (21) Roose, B.; Baena, J.-P. C.; Gödel, K. C.; Graetzel, M.; Hagfeldt, A.; Steiner, U.; Abate, A. Mesoporous SnO₂ Electron Selective Contact Enables UV-Stable Perovskite Solar Cells. *Nano Energy* **2016**, *30* (August), 517–522. <https://doi.org/10.1016/j.nanoen.2016.10.055>.
- (22) Li, Y.; Zhu, J.; Huang, Y.; Liu, F.; Lv, M.; Chen, S. H.; Hu, L. H.; Tang, J. W.; Yao, J. X.; Dai, S. Y. Mesoporous SnO₂ Nanoparticle Films as Electron-Transporting Material in Perovskite Solar Cells. *Rsc Adv.* **2015**, *5* (36), 28424–28429. <https://doi.org/10.1039/c5ra01540e>.
- (23) Jiang, Q.; Zhao, Y.; Zhang, X.; Yang, X.; Chen, Y.; Chu, Z.; Ye, Q.; Li, X.; Yin, Z.; You, J. Surface Passivation of Perovskite Film for Efficient Solar Cells. *Nat. Photonics* **2019**. <https://doi.org/10.1038/s41566-019-0398-2>.
- (24) Liu, J.; Ge, Q.-Q.; Chen, Y.-X.; Han, Q.; Ma, J.-Y.; Hu, J.-S.; Xue, D.; Mitzi, D. B.; Zhao, B.; Ding, J.; Han, Q.; Ge, Q.-Q.; Xue, D.; Ma, J.-Y.; Zhao, B.; Chen, Y.-X.; Liu, J.; Mitzi, D. B.; Hu, J.-S. Fully Air-Bladed High-Efficiency Perovskite Photovoltaics. *Joule* **2018**, 1–15. <https://doi.org/10.1016/j.joule.2018.10.025>.
- (25) Dou, B.; Whitaker, J. B.; Bruening, K.; Moore, D. T.; Wheeler, L. M.; Ryter, J.; Breslin, N. J.; Berry, J. J.; Garner, S. M.; Barnes, F. S.; Shaheen, S. E.; Tassone, C. J.; Zhu, K.; van Hest, M. F. A. M.; Sean, E.; Tassone, C. J.; Zhu, K.; Hest, M. F. A. M. Van. Roll-to-Roll Printing of Perovskite Solar Cells. *ACS Energy Lett.* **2018**, *3* (10), 2558–2565. <https://doi.org/10.1021/acsenergylett.8b01556>.
- (26) Bu, T.; Li, J.; Zheng, F.; Chen, W.; Wen, X.; Ku, Z.; Peng, Y.; Zhong, J.; Cheng, Y.-B.; Huang, F. Universal Passivation Strategy to Slot-Die Printed SnO₂ for Hysteresis-Free Efficient Flexible Perovskite Solar Module. *Nat. Commun.* **2018**, *9* (1), 4609. <https://doi.org/10.1038/s41467-018-07099-9>.
- (27) Bishop, J. E.; Routledge, T. J.; Lidzey, D. G. Advances in Spray-Cast Perovskite Solar Cells. *J. Phys. Chem. Lett.* **2018**, 1977–1984. <https://doi.org/10.1021/acs.jpcclett.8b00311>.
- (28) Bishop, J. E.; Smith, J. A.; Greenland, C.; Kumar, V.; Vaenas, N.; Game, O. S.; Routledge, T. J.; Wong-Stringer, M.; Rodenburg, C.; Lidzey, D. G. High-Efficiency Spray-Coated Perovskite Solar Cells Utilizing Vacuum-Assisted Solution Processing. *ACS Appl. Mater. Interfaces* **2018**, *10* (46), 39428–39434. <https://doi.org/10.1021/acsami.8b14859>.
- (29) Mathies, F.; Eggers, H.; Richards, B. S.; Hernandez-Sosa, G.; Lemmer, U.; Paetzold, U. W. Inkjet-Printed Triple Cation Perovskite Solar Cells. *ACS Appl. Energy Mater.* **2018**, *1* (5), 1834–1839. <https://doi.org/10.1021/acsaem.8b00222>.
- (30) Yun, A. J.; Kim, J.; Hwang, T.; Park, B. Origins of Efficient Perovskite Solar Cells with Low-Temperature Processed SnO₂ Electron Transport Layer. *ACS Appl. Energy Mater.* **2019**, *2* (5), 3554–3560. <https://doi.org/10.1021/acsaem.9b00293>.
- (31) Guerra, J. A.; Tejada, A.; Töfflinger, J. A.; Grieseler, R.; Korte, L. Band-Fluctuations Model for the Fundamental Absorption of Crystalline and Amorphous Semiconductors: A Dimensionless Joint Density of States Analysis. *J. Phys. D: Appl. Phys.* **2019**, *52* (10), 105303. <https://doi.org/10.1088/1361-6463/aaf963>.
- (32) Hammouda, B. A New Guinier-Porod Model. *J. Appl. Crystallogr.* **2010**, *43* (4), 716–719. <https://doi.org/10.1107/S0021889810015773>.
- (33) Troughton, J.; Carnie, M. J.; Davies, M. L.; Charbonneau, C.; Jewell, E. H.; Worsley, D. A.; Watson, T. M. Photonic Flash-Annealing of Lead Halide Perovskite Solar Cells in 1 Ms. *J. Mater. Chem. A* **2016**, *4* (9), 3471–3476. <https://doi.org/10.1039/c5ta09431c>.
- (34) Sanchez, S.; Hua, X.; Phung, N.; Steiner, U.; Abate, A. Flash Infrared Annealing for Antisolvent-Free Highly Efficient Perovskite Solar Cells. *Adv. Energy Mater.* **2018**, *1702915*, 1702915. <https://doi.org/10.1002/aenm.201702915>.
- (35) Ghahremani, A. H.; Martin, B.; Gupta, A.; Bahadur, J.; Ankireddy, K.; Druffel, T. Rapid Fabrication of Perovskite Solar Cells through Intense Pulse Light Annealing of SnO₂ and Triple Cation Perovskite Thin Films. *Mater. Des.* **2020**, *185*, 108237. <https://doi.org/10.1016/j.matdes.2019.108237>.
- (36) Ouyang, Z.; Yang, M.; Whitaker, J.; Li, D.; van Hest, M. F. A. M. Towards Scalable Perovskite Solar Modules Using Blade-Coating and Rapid Thermal Processing. *ACS Appl. Energy Mater.* **2020**. <https://doi.org/10.1021/acsaem.0c00180>.
- (37) Charbonneau, C.; Holliman, P. J.; Davies, M. L.; Watson, T. M.; Worsley, D. A. Facile Self-Assembly and Stabilization of Metal Oxide Nanoparticles. *J. Colloid Interface Sci.* **2015**, *442*, 110–119. <https://doi.org/10.1016/j.jcis.2014.11.042>.
- (38) Das, S.; Gu, G.; Joshi, P. C.; Yang, B.; Aytug, T.; Rouleau, C. M.; Geohegan, D. B.; Xiao, K. Low Thermal Budget, Photonic-Cured Compact TiO₂ Layers for High-Efficiency Perovskite Solar Cells. *J. Mater. Chem. A* **2016**, *4* (24), 9685–9690. <https://doi.org/10.1039/c6ta02105k>.
- (39) Feleki, B.; Bex, G.; Andriessen, R.; Galagan, Y.; Di Giacomo, F. Rapid and Low Temperature Processing of Mesoporous TiO₂ for Perovskite Solar Cells on Flexible and Rigid Substrates. *Mater. Today Commun.* **2017**, *13* (June), 232–240. <https://doi.org/10.1016/j.mtcomm.2017.09.007>.
- (40) Liu, Y.; Shin, I.; Hwang, I. W.; Lee, J.; Kim, S.; Lee, D. Y.; Lee, S. H.; Jang, J. W.; Jung, Y. K.; Jeong, J. H.; Park, S. H.; Kim, K. H. Effective Hot-Air Annealing for Improving the Performance of Perovskite Solar Cells. *Sol. Energy* **2017**, *146*, 359–367. <https://doi.org/10.1016/j.solener.2017.03.005>.

- (41) Dong, Q.; Shi, Y.; Zhang, C.; Wu, Y.; Wang, L. Energetically Favored Formation of SnO₂ Nanocrystals as Electron Transfer Layer in Perovskite Solar Cells with High Efficiency Exceeding 19%. *Nano Energy* **2017**, *40*, 336–344. <https://doi.org/10.1016/j.nanoen.2017.08.041>.
- (42) Méndez, P. F.; Muhammed, S. K. M.; Barea, E. M.; Masi, S.; Mora-Seró, I. Analysis of the UV–Ozone-Treated SnO₂ Electron Transporting Layer in Planar Perovskite Solar Cells for High Performance and Reduced Hysteresis. *Sol. RRL* **2019**, *3* (9), 1900191. <https://doi.org/10.1002/solr.201900191>.
- (43) Milliron, D. J.; Hill, I. G.; Shen, C.; Kahn, A.; Schwartz, J. Surface Oxidation Activates Indium Tin Oxide for Hole Injection. *J. Appl. Phys.* **2000**, *87* (1), 572–576. <https://doi.org/10.1063/1.371901>.
- (44) Lee, K. H. Mechanism for the Increase of Indium-Tin-Oxide Work Function by O₂ Inductively Coupled Plasma Treatment. *J. Appl. Phys.* **2004**, *95* (2), 586. <https://doi.org/10.1063/1.1633351>.
- (45) Themlin, J. M.; Sporken, R.; Darville, J.; Caudano, R.; Gilles, J. M.; Johnson, R. L. Resonant-Photoemission Study of SnO₂: Cationic Origin of the Defect Band-Gap States. *Phys. Rev. B* **1990**, *42* (18), 11914–11925. <https://doi.org/10.1103/PhysRevB.42.11914>.
- (46) McGuinness, C.; Stagarescu, C. B.; Ryan, P. J.; Downes, J. E.; Fu, D.; Smith, K. E.; Egdell, G. Influence of Shallow Core-Level Hybridization on the Electronic Structure of Post-Transition-Metal Oxides Studied Using Soft X-Ray Emission and Absorption. *Phys. Rev. B - Condens. Matter Mater. Phys.* **2003**, *68* (16), 1–10. <https://doi.org/10.1103/PhysRevB.68.165104>.
- (47) Batzill, M. Surface Science Studies of Gas Sensing Materials: SnO₂. *Sensors* **2006**, *6* (10), 1345–1366. <https://doi.org/10.3390/s6101345>.
- (48) Das, S.; Jayaraman, V. SnO₂: A Comprehensive Review on Structures and Gas Sensors. *Prog. Mater. Sci.* **2014**, *66*, 112–255. <https://doi.org/10.1016/j.pmatsci.2014.06.003>.
- (49) Weidner, M. Fermi Level Determination in Tin Oxide by Photoelectron Spectroscopy. *Ph.D. Thesis* **2015**, TU Darmstadt. <https://doi.org/10.13140/RG.2.1.3999.0809>.
- (50) Helander, M. G.; Greiner, M. T.; Wang, Z. B.; Lu, Z. H. Pitfalls in Measuring Work Function Using Photoelectron Spectroscopy. *Appl. Surf. Sci.* **2010**, *256* (8), 2602–2605. <https://doi.org/10.1016/j.apsusc.2009.11.002>.
- (51) Egdell, R. G.; Eriksen, S.; Flavell, W. R. A Spectroscopic Study of Electron and Ion Beam Reduction of SnO₂(110). *Surf. Sci.* **1987**, *192* (1), 265–274. [https://doi.org/10.1016/S0039-6028\(87\)81175-5](https://doi.org/10.1016/S0039-6028(87)81175-5).
- (52) Karulkar, P. C. XPS/AES Investigation of Cross Contamination in a Plasma Etcher. *J. Vac. Sci. Technol. B Microelectron. Nanom. Struct.* **1985**, *3* (3), 889. <https://doi.org/10.1116/1.583077>.
- (53) Swallow, J. E. N.; Williamson, B. A. D.; Whittles, T. J.; Birkett, M.; Featherstone, T. J.; Peng, N.; Abbott, A.; Farnworth, M.; Cheetham, K. J.; Warren, P.; Scanlon, D. O.; Dhanak, V. R.; Veal, T. D. Self-Compensation in Transparent Conducting F-Doped SnO₂. *Adv. Funct. Mater.* **2018**, *28* (4), 1–10. <https://doi.org/10.1002/adfm.201701900>.
- (54) Trost, S.; Becker, T.; Polywka, A.; Görrn, P.; Oszejca, M. F.; Luechinger, N. A.; Rogalla, D.; Weidner, M.; Reckers, P.; Mayer, T.; Riedl, T. Avoiding Photoinduced Shunts in Organic Solar Cells by the Use of Tin Oxide (SnO_x) as Electron Extraction Material Instead of ZnO. *Adv. Energy Mater.* **2016**, *6* (15). <https://doi.org/10.1002/aenm.201600347>.
- (55) Roose, B.; Friend, R. H. Extrinsic Electron Concentration in SnO₂ Electron Extracting Contact in Lead Halide Perovskite Solar Cells. *Adv. Mater. Interfaces* **2019**, *1801788* (5), 1801788. <https://doi.org/10.1002/admi.201801788>.
- (56) Chistiakova, G.; Mews, M.; Wilks, R. G.; Bär, M.; Korte, L. In-System Photoelectron Spectroscopy Study of Tin Oxide Layers Produced from Tetrakis(Dimethylamino)Tin by Plasma Enhanced Atomic Layer Deposition. *J. Vac. Sci. Technol. A Vacuum, Surfaces, Film.* **2018**, *36* (2), 02D401. <https://doi.org/10.1116/1.5015967>.
- (57) Noonuruk, R.; Mekprasart, W.; Vittayakorn, N.; Sritharathikhun, J. Physical, Electrical and Optical Properties of F / Sb Codoped SnO₂ Synthesized Via Sonochemical Process Physical, Electrical and Optical Properties of F / Sb Codoped SnO₂ Synthesized Via Sonochemical. **2016**, *0193*. <https://doi.org/10.1080/00150193.2015.1072694>.
- (58) Jiang, J. C.; Lian, K.; Meletis, E. I. Influence of Oxygen Plasma Treatment on the Microstructure of SnO_x Thin Films. *Thin Solid Films* **2002**, *411* (2), 203–210.
- (59) Mathur, S.; Ganesan, R.; Grobelsek, I.; Shen, H.; Ruegamer, T.; Barth, S. Plasma-Assisted Modulation of Morphology and Composition in Tin Oxide Nanostructures for Sensing Applications. *Adv. Eng. Mater.* **2007**, *9* (8), 658–663. <https://doi.org/10.1002/adem.200700086>.
- (60) Cavicchi, R.; Tarlov, M.; Semancik, S. Preparation of Well-ordered, Oxygen-rich SnO₂ (110) Surfaces via Oxygen Plasma Treatment. *J. Vac. Sci. Technol. A Vacuum, Surfaces, Film.* **1990**, *8* (3), 2347–2352. <https://doi.org/10.1116/1.576696>.
- (61) Wolff, C. M.; Caprioglio, P.; Stolterfoht, M.; Neher, D. Nonradiative Recombination in Perovskite Solar Cells: The Role of Interfaces. *Adv. Mater.* **2019**, *1902762*, 1902762. <https://doi.org/10.1002/adma.201902762>.
- (62) Calado, P.; Burkitt, D.; Yao, J.; Troughton, J.; Watson, T. M.; Carnie, M. J.; Telford, A. M.; Regan, B. C. O.; Nelson, J.; Barnes, P. R. F. Identifying Dominant Recombination Mechanisms in Perovskite Solar Cells by Measuring the Transient Ideality Factor. *Phys. Rev. Appl.* **2019**, *10* (1), 1. <https://doi.org/10.1103/PhysRevApplied.11.044005>.
- (63) Moia, D.; Gelmetti, I.; Calado, P.; Fisher, W.; Stringer, M.; Game, O.; Hu, Y.; Docampo, P.; Lidzey, D.; Palomares, E.; Nelson, J.; Barnes, P. R. F. Ionic-to-Electronic Current Amplification in Hybrid Perovskite Solar Cells: Ionically Gated Transistor-Interface Circuit Model Explains Hysteresis and Impedance of Mixed Conducting Devices. *Energy Environ. Sci.* **2019**, *12* (4), 1296–1308. <https://doi.org/10.1039/C8EE02362J>.

- (64) Tress, W.; Yavari, M.; Domanski, K.; Yadav, P.; Niesen, B.; Correa Baena, J. P.; Hagfeldt, A.; Graetzel, M. Interpretation and Evolution of Open-Circuit Voltage, Recombination, Ideality Factor and Subgap Defect States during Reversible Light-Soaking and Irreversible Degradation of Perovskite Solar Cells. *Energy Environ. Sci.* **2018**, *11* (1), 151–165. <https://doi.org/10.1039/c7ee02415k>.
- (65) Walter, D.; Fell, A.; Wu, Y.; Duong, T.; Barugkin, C.; Wu, N.; White, T.; Weber, K. Transient Photovoltage in Perovskite Solar Cells: Interaction of Trap-Mediated Recombination and Migration of Multiple Ionic Species. *J. Phys. Chem. C* **2018**, *122* (21), 11270–11281. <https://doi.org/10.1021/acs.jpcc.8b02529>.
- (66) Courtier, N. E.; Cave, J. M.; Foster, J. M.; Walker, A. B.; Richardson, G. How Transport Layer Properties Affect Perovskite Solar Cell Performance: Insights from a Coupled Charge Transport/Ion Migration Model. *Energy Environ. Sci.* **2019**, *12* (1), 396–409. <https://doi.org/10.1039/C8EE01576G>.
- (67) Aygüler, M. F.; Hufnagel, A. G.; Rieder, P.; Wussler, M.; Jaegermann, W.; Bein, T.; Dyakonov, V.; Petrus, M. L.; Baumann, A.; Docampo, P. Influence of Fermi Level Alignment with Tin Oxide on the Hysteresis of Perovskite Solar Cells. *ACS Appl. Mater. Interfaces* **2018**, *10* (14), 11414–11419. <https://doi.org/10.1021/acsami.8b00990>.
- (68) Hu, T.; Becker, T.; Pourdavoud, N.; Zhao, J.; Oliver, K.; Heiderhoff, R.; Gahlmann, T.; Olthof, S.; Meerholz, K.; Többs, D.; Cheng, B.; Chen, Y.; Riedl, T.; Brinkmann, K. O.; Heiderhoff, R.; Gahlmann, T.; Huang, Z.; Olthof, S.; Meerholz, K.; Többs, D.; Cheng, B.; Chen, Y.; Riedl, T. Indium-Free Perovskite Solar Cells Enabled by Impermeable Tin-Oxide Electron Extraction Layers. *Adv. Mater.* **2017**, *29* (27), 1–9. <https://doi.org/10.1002/adma.201606656>.
- (69) Luan, Y.; Yi, X.; Mao, P.; Wei, Y.; Zhuang, J.; Chen, N.; Lin, T.; Li, C.; Wang, J. High-Performance Planar Perovskite Solar Cells with Negligible Hysteresis Using 2,2,2-Trifluoroethanol-Incorporated SnO₂. *iScience* **2019**, *16*, 433–441. <https://doi.org/10.1016/j.isci.2019.06.004>.
- (70) Hoffmann, L.; Brinkmann, K. O.; Malerczyk, J.; Rogalla, D.; Becker, T.; Theirich, D.; Shutsko, I.; Görrn, P.; Riedl, T. Spatial Atmospheric Pressure Atomic Layer Deposition of Tin Oxide as an Impermeable Electron Extraction Layer for Perovskite Solar Cells with Enhanced Thermal Stability. *ACS Appl. Mater. Interfaces* **2018**, *10* (6), 6006–6013. <https://doi.org/10.1021/acsami.7b17701>.
- (71) Jiang, Z. GIXSGUI: A MATLAB Toolbox for Grazing-Incidence X-Ray Scattering Data Visualization and Reduction, and Indexing of Buried Three-Dimensional Periodic Nanostructured Films. *J. Appl. Crystallogr.* **2015**, *48* (3), 917–926. <https://doi.org/10.1107/S1600576715004434>.
- (72) SasView software package www.sasview.org.
- (73) Guerra, J. A.; Tejada, A.; Korte, L.; Kegelmann, L.; Töfflinger, J. A.; Albrecht, S.; Rech, B.; Weingärtner, R. Determination of the Complex Refractive Index and Optical Bandgap of CH₃NH₃PbI₃ Thin Films. *J. Appl. Phys.* **2017**, *121* (17), 173104. <https://doi.org/10.1063/1.4982894>.
- (74) Wojdyr, M. Fityk: A General-Purpose Peak Fitting Program. *J. Appl. Crystallogr.* **2010**, *43* (5 PART 1), 1126–1128. <https://doi.org/10.1107/S0021889810030499>.
- (75) Wang, Z.; Richter, S. M.; Rozema, M. J.; Schellinger, A.; Smith, K.; Napolitano, J. G. Potential Safety Hazards Associated with Using Acetonitrile and a Strong Aqueous Base. *Org. Process Res. Dev.* **2017**, *21* (10), 1501–1508. <https://doi.org/10.1021/acs.oprd.7b00158>.
- (76) Henke, B. L.; Gullikson, E. M.; Davis, J. C. X-Ray Interactions: Photoabsorption, Scattering, Transmission, and Reflection at E = 50–30,000 EV, Z = 1–92. *At. Data Nucl. Data Tables* **1993**, *54* (2), 181–342. <https://doi.org/10.1006/adnd.1993.1013>.
- (77) Song, J.; Liu, L.; Wang, X. F.; Chen, G.; Tian, W.; Miyasaka, T. Highly Efficient and Stable Low-Temperature Processed ZnO Solar Cells with Triple Cation Perovskite Absorber. *J. Mater. Chem. A* **2017**, *5* (26), 13439–13447. <https://doi.org/10.1039/c7ta03331a>.
- (78) Prochowicz, D.; Tavakoli, M. M.; Kalam, A.; Chavan, R. D.; Trivedi, S.; Kumar, M.; Yadav, P. Influence of A-Site Cations on the Open-Circuit Voltage of Efficient Perovskite Solar Cells: A Case of Rubidium and Guanidinium Additives. *J. Mater. Chem. A* **2019**, *7* (14), 8218–8225. <https://doi.org/10.1039/c9ta00272c>.
- (79) Deepa, M.; Salado, M.; Calio, L.; Kazim, S.; Shivaprasad, S. M.; Ahmad, S. Cesium Power: Low Cs⁺ Levels Impart Stability to Perovskite Solar Cells. *Phys. Chem. Chem. Phys.* **2017**, *19* (5), 4069–4077. <https://doi.org/10.1039/c6cp08022g>.
- (80) Ji, L.; Zhang, X.; Zhang, T.; Wang, Y.; Wang, F.; Zhong, Z.; Chen, Z. D.; Xiao, Z.; Chen, L.; Li, S. Band Alignment of Pb–Sn Mixed Triple Cation Perovskites for Inverted Solar Cells with Negligible Hysteresis. *J. Mater. Chem. A* **2019**, *7* (15), 9154–9162. <https://doi.org/10.1039/c8ta11891d>.

Chapter 5

Solvent Vapour Annealing of Methylammonium Lead Halide Perovskite: What's the catch?

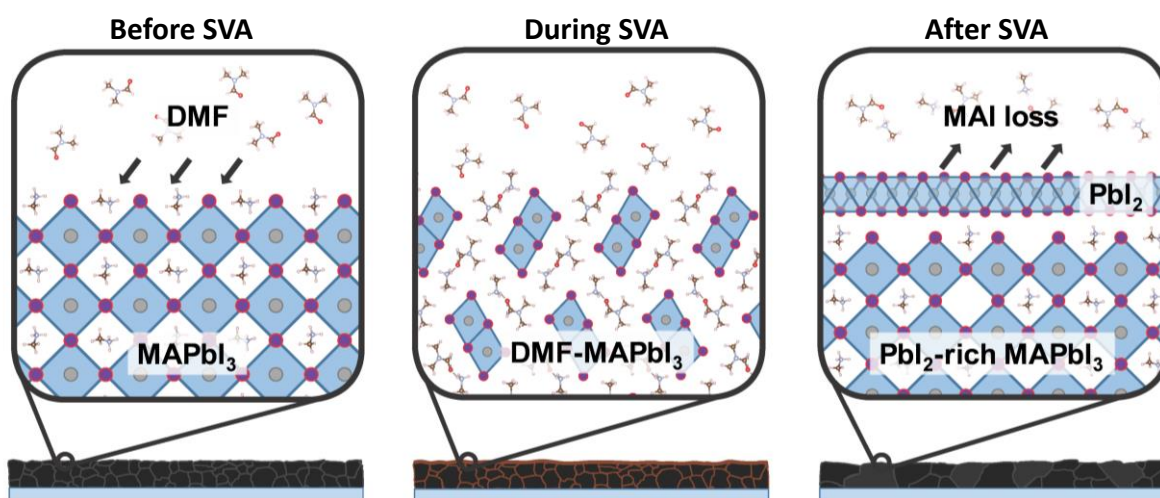
Journal of
Materials Chemistry A



Volume 8, Issue 21, Pages 10943-10956

May 13, 2020

DOI: 10.1039/D0TA03023F



5.0: Publication Foreword

With the case for rapid processing made clear, one approach to achieve this with the perovskite layer is through recrystallisation of the film. Recrystallisation has gained significant interest as it would allow for less stringent controls on the perovskite deposition and could result in better microstructural engineering for performance and stability. In this project, we investigated the effect of DMF vapour recrystallisation of MAPbI₃ on film structure and device stability. We had noted in earlier work that the solvent vapour annealing process led to device instability despite some initial performance benefit.²⁷ At that time, we used vibrational spectroscopy methods on powdered films to determine if there was any remnant DMF which could be destabilising films, but did not observe any. In this work, by investigating with a more extensive approach across a range of MAI:PbI₂ stoichiometries and by minimising ambient air contact, we were able to observe a weakly scattering intermediate phase containing DMF, indicating a potential source of ongoing instability. The issue of prolonged solvent coordination and possible hydrogen-bonding interactions leading to loss of organic material most likely renders this process unsuitable in its current form for commercialisation. It also points to the issue of trapped solvent being a more widespread issue in perovskite materials than is currently assumed.

This project was led by my colleague Dr Onkar Game, who I am grateful to have had the chance to work with on it and many other projects during the PhD. My contributions to the work included acquisition and analysis of *in-situ* and *ex-situ* GIWAXS data and related analysis, some of the SEM and XRD data and analysis, as well as extensive input into the interpretation and writing of the manuscript, including design of the scheme once we had refined our understanding of the mechanism. Some further data which could not be included in the manuscript due to the length has also been provided after the supporting information.

5.1: Author contributions

OG conceived the project, fabricated and tested the devices and their stability, performed pc-AFM measurements, and wrote the first version of the manuscript. JAS assisted with sample fabrication, acquired and analysed the GIWAXS data, edited the manuscript and produced additional figures. JAS & VK acquired SEM images, TA & JAS acquired XRD data; both were analysed by OG and JAS. MW-S assisted with device fabrication and conceptualisation of the project. NJT assisted during the synchrotron-based measurements. CR and DGL supervised the project. All authors gave input into the final manuscript.

5.2: Publication - Solvent Vapour Annealing of Methylammonium Lead Halide Perovskite: What's the catch?

Onkar S. Game,^{1*} Joel A. Smith,¹ Tarek I. Alanazi,¹ Michael Wong-Stringer,¹ Vikas Kumar,² Cornelia Rodenburg,² Nick J. Terrill,³ and David G. Lidzey.^{1*}

6) Department of Physics & Astronomy, University of Sheffield, Sheffield, S3 7RH, UK.

7) Department of Material Science and Engineering, University of Sheffield, Sheffield, S1 3JD, UK.

8) Diamond Light Source Ltd, Diamond House, Harwell Science & Innovation Campus, Didcot, Oxfordshire, OX11 0DE, UK.

*Corresponding Authors - e-mail: o.game@sheffield.ac.uk, d.g.lidzey@sheffield.ac.uk

5.2.1: Abstract

Solvent vapour annealing (SVA) is a common post-processing technique used to increase the average grain size of lead halide perovskite films and thus enhance device performance. The prevailing wisdom is that large grained perovskite films lead to enhanced stability, however, we observed the reverse in $\text{CH}_3\text{NH}_3\text{PbI}_3$ (MAPbI_3) with dimethylformamide vapour treatment compared to non-SVA controls. Using a range of microstructural characterisation techniques, we reveal that SVA is not a chemically benign grain-growth process, but leads to substantial stoichiometric changes in the perovskite films. Intrinsic material degradation is investigated under external loading with in-situ X-ray scattering, and combined with lifetime testing on full devices. We show that the operational stability of SVA devices greatly depends on the initial stoichiometry of the MAPbI_3 with PbI_2 -excess compositions being least stable. However, the incorporation of excess organic-halides in the precursor solution helps to mitigate the deleterious effects of SVA on device stability. This work critically re-evaluates current thinking around grain structure and stoichiometry in achieving long-term stability for perovskite solar cells.

5.2.2: Introduction

The remarkable optoelectronic properties of hybrid lead halide perovskites (LHP), combined with their ease of processing via low-temperature solution routes have made LHPs one of the most promising new-generation photovoltaic materials.²⁻⁵ Recent progress in the development of deposition techniques, compositional engineering and passivation strategies have led to outstanding improvement in device power conversion efficiency (PCE), with perovskite single-junction devices reaching 25.2% and Si-perovskite monolithic tandem solar cells now at 28%.⁶ Although LHP solar cells have reached such efficiencies in a short period (~7 years of focused research activity), their transition from lab to industrial scale still faces challenges such as developing appropriate device manufacture routes and enhancing operational stability to the level of established inorganic photovoltaic technologies.⁷

One of the most significant properties of LHP materials is their ability to be fabricated into thin films having a high degree of crystallinity, despite being processed from solution at low temperature (80 – 180 °C).⁸ Most processing routes used to create LHPs result in the formation of polycrystalline films having an average grain size that is smaller than the film thickness required to maximize light harvesting. Unfortunately, films composed of small crystalline grains contain a high density of grain-boundaries that can adversely affect the photovoltaic performance of the resultant device. This results from grain boundaries distributed along carrier transport pathways which cause resistive and recombination losses.⁹ Grain-boundaries within LHP films have also been shown to facilitate potentially undesirable effects such as ion migration^{10, 11} that result in hysteretic effects in the current-voltage (*J-V*) characteristics of photovoltaic (PV) devices. Interestingly, the extrinsic stability of LHPs may also depend on grain size, with grain-boundaries acting as diffusion pathways for the ingress of moisture and oxygen.¹²⁻¹⁴ Therefore, PV devices based on LHP thin films containing a low density of grain-boundaries are expected to have improved optoelectronic performance and enhanced extrinsic stability. It has been found that grain growth in LHP films following extended thermal annealing often occurs at the expense of compositional degradation.¹⁵ Furthermore, the use of process additives and compositional engineering strategies to enhance grain size can also result in the formation of secondary phases that may have detrimental effects on overall device performance.^{16, 17}

Researchers interested in controlling grain-size in LHPs have turned to the use of solvent vapour annealing (SVA).¹⁸⁻²⁰ This commonly used post-processing technique has been shown to reduce grain-boundary density and form grains that extend continuously between the anode

and cathode contacts in operational PV devices. The SVA process involves annealing LHP films in the presence of a polar-aprotic solvent vapour (e.g. dimethylformamide, DMF), resulting in a level of grain growth that is usually significantly greater than that can be achieved using thermal annealing or additive engineering methods.²¹ Due to the simplicity of the method and the presumption that material composition is unaffected, SVA has been used in fundamental studies that investigate the influence of grain size on stability²² and the optoelectronic properties of LHPs.²³⁻²⁶ There have been several literature reports describing the SVA mechanism, which usually report its beneficial effects on PV device efficiency.^{1, 18-20} Indeed, in our recent study on multilayer encapsulation of $\text{CH}_3\text{NH}_3\text{PbI}_3$ (MAPbI₃) based perovskite solar cells, we observed an improvement in photovoltaic parameters with SVA.²⁷ However, despite effective device encapsulation, we found that SVA processed devices had a significantly lower intrinsic operational stability than comparable “small-grain” thermally annealed devices. This surprising finding stands in contrast to the general wisdom that suggests films having larger grains should be more robust towards extrinsic degradation processes.¹²

In this paper, we investigate the effect of the SVA process on the operational stability of LHP solar cells, and use photoconductive atomic force microscopy (pc-AFM), X-ray diffraction (XRD), scanning electron microscopy (SEM) and energy-dispersive X-ray spectroscopy (EDS) to understand the effects of SVA on phase and optoelectronic properties of MAPbI₃ films. We show that annealing MAPbI₃ films in the presence of DMF vapour results in compositional changes in the film, with the initial stoichiometry of the MAPbI₃ precursor solution playing an important role in determining the relative rate of film and device degradation. Using *in situ* grazing incidence wide-angle X-ray scattering (GIWAXS) to monitor the degradation of thin-films subjected to stress (elevated temperature, humidity, illumination) together with continuous illumination lifetime testing on full devices, we demonstrate the deleterious effect of SVA. We ascribe the rapid loss in performance of SVA-treated perovskite solar cells to a loss of volatile organic halide species (MAI in the case of MAPbI₃) caused by the acid-base interaction of (polar) DMF with the ammonium moiety of MA⁺. It is then shown that the incorporation of excess cationic species in the precursor solution helps to mitigate the detrimental effects of SVA on the operational stability of devices.

Although the primary focus of this study is an investigation into the effects of SVA, we can draw more general conclusions and insights into the effect of material stoichiometry on the long-term stability of MAPbI₃-based solar cells. We expect our results can be generalised to other mixed-cation perovskite compositions that contain methylammonium cations or possibly

formamidinium ($\text{HC}(\text{NH}_2)_2$), or to other SVA processes that involve the use of polar aprotic solvents that generate strong hydrogen bonding interactions.

5.2.3: Results and discussion

5.2.3.1: Influence of SVA on PbI_2 -excess MAPbI_3 - insights from pc-AFM

We have studied SVA on MAPbI_3 thin films deposited from methylamine-bubbled acetonitrile (ACN/MA) solutions.²⁷⁻²⁹ This solvent system was chosen to avoid repeated exposure of the films to common solvents used in the SVA process and therefore allowed us to study the influence of DMF exclusively during the vapour annealing stage. Details of film and device fabrication can be found in the Experimental Methods section of the Supporting Information (SI). Briefly, precursor solutions containing a mixture of MAI: PbI_2 were bubbled with methylamine gas to ensure the complete dissolution of MAI and PbI_2 . Several reports on MAPbI_3 and multi-cation perovskite films have shown that the excess lead iodide (PbI_2) in precursor solutions and films results in passivation of grain-boundaries, leading to enhanced photovoltaic performance.³⁰⁻³³ However, in our earlier study, we observed accelerated degradation in devices with SVA-treated PbI_2 -excess stoichiometry.²⁷ Therefore, to understand our previous results, we initially used ACN/MA ink having a PbI_2 -excess composition (PbI_2 :MAI = 1.06:1). Thin films were cast from the precursor solutions by spin coating. Following this, films were thermally annealed at 100°C for 3 minutes after which they were SVA treated by exposure to a DMF vapour (also at 100°C) for 7 minutes. Films were then thermally annealed for a further 5 minutes to remove any residual DMF. In all cases, non-SVA controls were also prepared.

To understand how SVA affects the physical morphology of perovskite films, we have imaged SVA films and their relevant controls using photoconductive AFM (pc-AFM). This technique creates simultaneous images of topography and photocurrent at nanoscale resolution, allowing morphological features (e.g. grain size/grain boundaries) to be correlated with the photo-response of the active layer.^{34,35} To record pc-AFM measurements, a series of perovskite films were prepared on ITO/ SnO_2 hole-blocking layers³⁴ and imaged using a Pt-Ir coated AFM probe. This structure effectively acts as a PV device (albeit without a hole-transport layer), with the AFM probe acting as the device top contact. Such 'devices' were then illuminated through the ITO/ SnO_2 using a blue (448 nm) LED, with the photocurrent generated measured at zero applied bias to obtain a short-circuit current density map.

Figure 1(a) shows the measured topography of 6% PbI_2 molar excess MAPbI_3 film that was not subjected to vapour annealing (henceforth referred to as Pb-NVA). We find that typical

perovskite grains have a lateral size between 100 and 300 nm; a value typical for MAPbI₃ made by the acetonitrile solvent route.²⁸ Interestingly, we find that such films are characterised by a population of much larger crystallites (200 nm – 1 μm) that protrude from the film surface. We believe that such structures result from phase separation of the excess PbI₂ from the MAPbI₃ matrix. This finding is in contrast to several previous reports^{31, 33} in which it was claimed that excess PbI₂ crystalized uniformly along grain boundaries in MAPbI₃, thereby resulting in a trap-passivation effect (See ESI Note 1). Figure 1(a) shows the corresponding photocurrent maps recorded from a Pb-NVA film in Figure 1(b). Here, dark patches can be seen mostly at positions corresponding to the presumed PbI₂ crystallites, suggesting that such PbI₂ domains do not allow the extraction of photo-carriers. We have performed an analysis of the photocurrent recorded across a typical 3 × 3 μm photocurrent scan, and find the average photocurrent to be 350 pA.

In Figure 1(c) we plot an AFM topograph of a PbI₂-excess film that had undergone solvent vapour annealing (henceforth denoted as Pb-VA). Here, we observe that the SVA process results in grain growth with the average grain size now being between 300 and 700 nm. Significantly, most of the grains in the Pb-VA film generate a higher photocurrent in the corresponding photocurrent map (see Figure 1(d)) than was observed in the Pb-NVA film (Figure 1(b)), with the average photocurrent being 670 pA.

Comparing Figure 1(b) and (d), we find that the area of dark-patches appears to have substantially increased in the Pb-VA film compared to Pb-NVA, with several large crystallites being almost completely dark (*vide infra*) in the photocurrent map in Figure 1(d). For completeness, we plot a pixel frequency vs current histogram for Pb-NVA and Pb-VA films in Figure S1 (a) and (b). Here, we find a substantial increase in the number of pixels producing a photocurrent greater than 1 nA in the Pb-VA film, although there is still a significant fraction of pixels in the Pb-VA film that produce a near-zero photocurrent. We ascribe this apparent higher photocurrent in SVA films to a reduction in recombination losses at lateral grain boundaries (parallel to the plane of the substrate). In small grain Pb-NVA perovskite films, high recombination rates at lateral grain-boundaries are one of the major factors that limit out-of-plane charge transport and photocurrent generation in a PV device.^{36, 37} In contrast, SVA-induced grain growth often creates grains that span the entire active layer thickness in a PV device; a process that reduces carrier recombination at the grain boundaries.

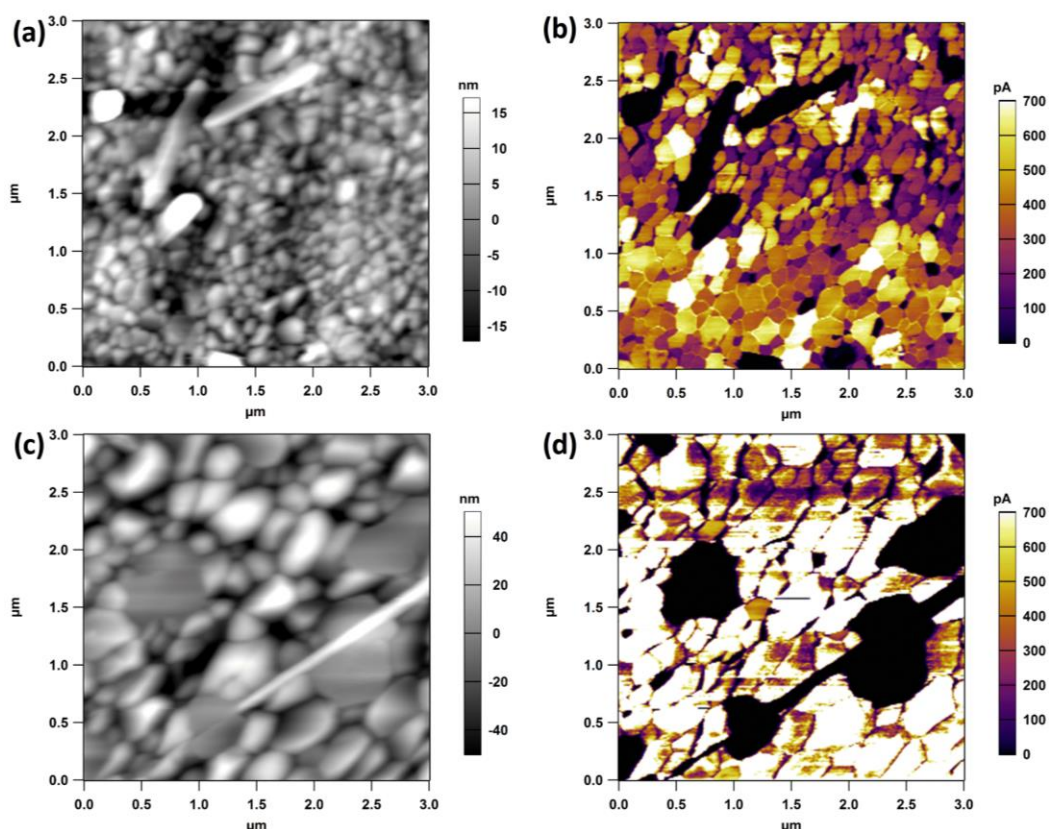


Figure 1: Contact mode AFM (height profile) for (a) Pb-NVA and (c) Pb-VA films. Photocurrent maps for (b) Pb-NVA and (d) Pb-VA simultaneously acquired with topography using pc-AFM under blue (448 nm) LED illumination and short-circuit conditions.

To investigate the nature of the photo-inactive phases in Pb-VA films, we have performed XRD and SEM-EDS measurements on SVA and non-treated films. This is shown in Figure 2(a) where we plot XRD patterns of Pb-NVA and Pb-VA films. Here we find a small increase in the intensity of the PbI_2 (001) peak ($2\theta = 12.6^\circ$) after solvent vapour annealing. This change in film composition suggests a change in the stoichiometry of the Pb-NVA film via loss of methylammonium iodide, which presumably occurs during and after the DMF solvent vapour annealing process. This conclusion is strengthened by SEM-EDS measurements performed on the same films as shown in Figure 2(b) and (c). Here, PbI_2 rich (or MAI deficient) crystallites in the Pb-NVA film can be evidenced from the distinct contrast between stoichiometric MAPbI_3 grains (which appear darker) and PbI_2 -rich grains (which appear brighter) due to their different electron densities.

Similar well-defined bright features have been identified as being PbI_2 using secondary electron hyperspectral imaging of MAPbI_3 pellets prepared with a 5% molar excess of PbI_2 ³⁸. We have measured the proportion of the film area occupied by these PbI_2 -rich grains in the SEM images (total area $\sim 8.0 \mu\text{m}^2$) as shown in Figure S2. These occupy approximately 3% of the total area

of the Pb-NVA SEM image in Figure 2 (b), a value that increases five-fold to 13% for the Pb-VA film in Figure 2 (c). Figure S3 (b) shows an EDS spectrum recorded from one of the representative brighter grains (circled yellow) together with that from a darker grain (circled red) in a Pb-VA film. This measurement indicates that the brighter grains contain a greater fraction of Pb and I, and a relatively lower fraction of C and N than is observed in the darker grains (noting that some EDS signal collection will come from outside the grain area). We conclude that the low MAI content in 'bright' grains results from a loss of MAI during the DMF vapour annealing; a result in accord with our XRD measurements recorded on bulk films (see Figure 2(a)). Clearly, the SVA process results in a change in film stoichiometry, with such changes occurring predominantly at the top surface.

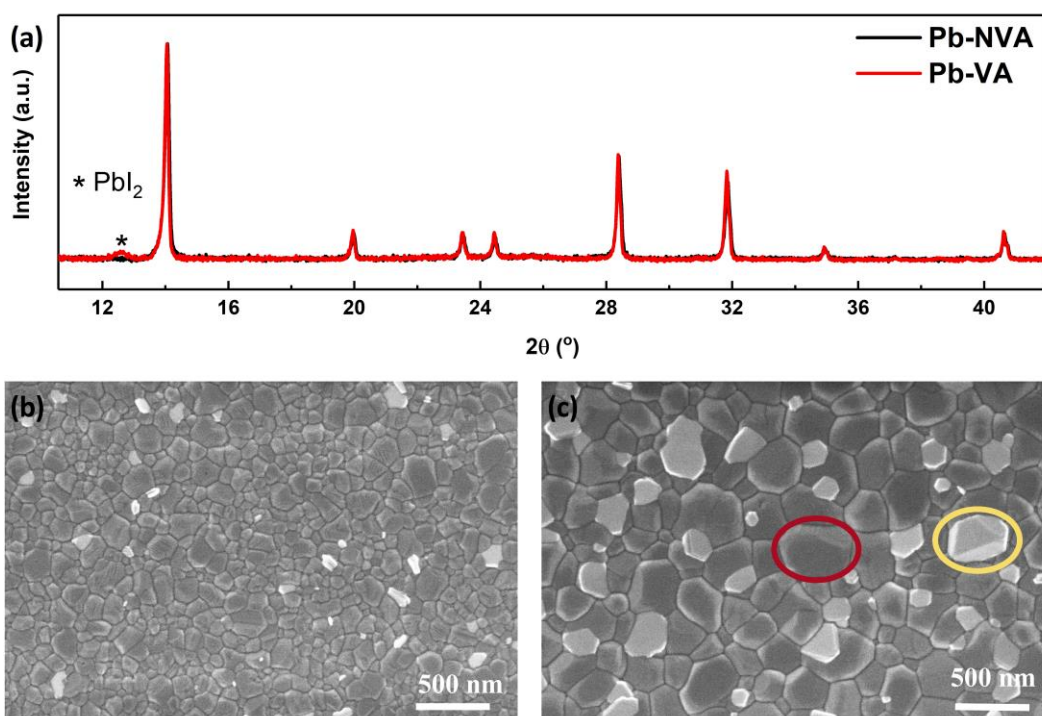


Figure 2: a) XRD of PbI_2 -excess $MAPbI_3$ before (Pb-NVA) and after (Pb-VA) solvent vapour annealing; (b) and (c) show SEM images of Pb-NVA and Pb-VA respectively.

5.2.3.2: Mitigating loss of organic halides during SVA

To mitigate the loss of MAI during SVA, we have prepared films using solutions that contain an initial 3% stoichiometric excess of MAI (henceforth denoted as MA-NVA) and have explored their response to the SVA process. A typical AFM scan of an MA-NVA film is shown in Figure 3(a), with the film having a uniform morphology and grains with an average size of 100 to 300 nm. Significantly, there is no evidence for the platelet/rod-shaped structures that were observed in PbI_2 -rich films (see Figure 1). This suggests that the 3% MAI excess in solution

prevents the formation of phase-separated PbI_2 or PbI_2 -rich grains during film formation. Although there is again contrast between the photocurrent brightness of individual grains, there are no large grains that appear dark in photocurrent maps. This observation has been made over both large areas ($10\ \mu\text{m} \times 10\ \mu\text{m}$) as shown in Figure S4 (b) and over small areas ($5\ \mu\text{m} \times 5\ \mu\text{m}$) as shown in Figure 3 (b).

When such MAI excess films were solvent vapour annealed (here termed as MA-VA) we observe an increase in average grain sizes to between 300 and 700 nm as observed in Figure 3(c). Again, there is an absence of completely dark grains in the accompanying photocurrent map as shown in Figure 3(d). This indicates that the excess-MAI stoichiometry prevents the formation of PbI_2 rich grains even when the films are solvent vapour treated.

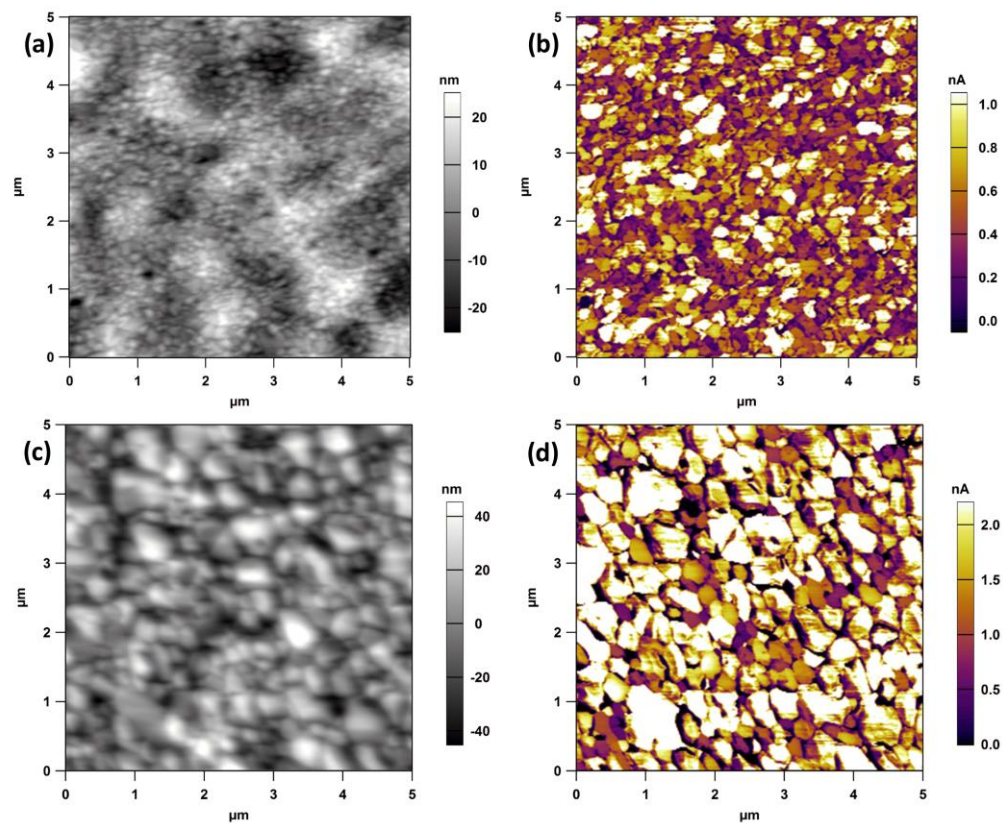


Figure 3: Contact mode AFM (height profile) for (a) MA-NVA and (c) MA-VA films. Photocurrent maps (simultaneously acquired with topography) of (b) MA-NVA and (d) MA-VA using pc-AFM under 1-sun equivalent LED illumination and short circuit conditions.

To further understand the observed photocurrent behaviour, we have performed a statistical analysis of the pc-AFM data for both compositions from their photocurrent histograms. Comparing Figure S1 (a) and S5 (a) we find that the photocurrent distribution in MA-NVA and Pb-NVA films is similar (except there is a higher fraction of zero photocurrent pixels in Pb-

NVA). Interestingly, we find that the peak of the photocurrent histogram in the MA-VA film is shifted to a higher value (1.2 nA) than in MA-NVA (0.5 nA) (see Figure S5 (b)) with a higher mean photocurrent also observed in MA-VA compared to MA-NVA (880 pA and 360 pA respectively). The number of pixels that produce a near-zero photocurrent was higher in MA-VA than MA-NVA; an effect that results from the grain boundary regions of MA-VA which appear photo-inactive (which is evident from the darker grain boundaries in the pc-AFM map of MA-VA compared with MA-NVA in Figure 3). This indicates that the loss of MAI during solvent vapour annealing can at least be partially compensated for by the addition of excess MAI into the MAPbI₃ precursor, although not eliminated.

To gain further insight into the effect of the solvent anneal process, we have used XRD to characterise the material phases present in the different stoichiometric samples. This is shown in Figure 4(a) where we observe a two-fold increase in scattering intensity from the (110) plane for MA-NVA compared to Pb-VA films. However, we find that the scattering intensity from (310) planes at $2\theta \sim 31.9^\circ$ in MA-NVA is similar to that from Pb-VA. As the average size of crystalline grains in MA-NVA and Pb-NVA films are very similar, this suggests that the two-fold increase in X-ray diffraction intensity of the (110)/(220) peaks observed in the MA-NVA films may result from an increased density of coherent scattering from domains oriented in the [110] direction. As shown in Figure 4(a), the diffraction intensity of (110)/(220) peaks in the MA-VA film also increases by ~ 2.5 times in comparison to the MA-NVA film. Note that we did not observe such coherent scattering along [110] in the XRD for non-annealed freshly spin-cast films (see Figure S6) and thus we conclude that temperature, material composition and casting-environment may each play a role. Figure S6 (b) also demonstrates that the FWHM of the (110) diffraction peak in the MA-VA film is narrower than its equivalent peak in MA-NVA (0.100 and 0.115° respectively). This finding is consistent with the larger apparent grain size of MA-VA films shown in the SEM image presented in Figure 4(c) (MA-VA and MA-NVA films have an average grain size of 300 – 700 nm and 100 – 300 nm respectively). Importantly, no PbI₂ diffraction peak is observed from MA-NVA or MA-VA films around $2\theta \sim 12.6^\circ$ (see the inset of Figure 4 (a)). This finding is confirmed by the fairly uniform SEM image contrast observed in the MA-NVA and MA-VA films as shown in Figure 4(b) and (d); a result implying a high degree of compositional homogeneity between the grains.³⁸ This result is in accord with the pc-AFM maps of MA-NVA and MA-VA (see Figure 3(b) and (d)) in which an absence of photo-inactive grains (dark regions) was observed. For the sake of comparison, Figure S7 (a) and (b) shows the XRD and SEM of PbI₂-excess and MAI-excess compositions both with and without solvent vapour annealing. Taken together, our results indicate that an excess MAI in the precursor solution has

both suppressed the formation of phase-separated PbI_2 crystallites (both with and without SVA) and has resulted in the formation of films in which crystalline grains form domains that scatter more efficiently in the [110] direction. Note however that enhanced scattering along [110] in MA-NVA or MA-VA is not on its own sufficient to indicate that perovskite grains undergo preferential orientation.

To gain further insight into structural changes caused as a result of varying the solution stoichiometry or the SVA process, we have used lab-based *ex situ* grazing incidence wide-angle X-ray scattering (GIWAXS) to characterise representative thin films. The 2D scattering patterns for all four samples are similar (see Figure S8), with the primary MAPbI_3 (110)/(002) reflection at $Q \approx 1.01 \text{ \AA}^{-1}$ (equivalent to $2\theta \approx 14.2^\circ$) present in all films. We observed characteristic scattering from PbI_2 at $Q \approx 0.9 \text{ \AA}^{-1}$ in both Pb-NVA and Pb-VA samples, which was not present in MAI excess samples (MA-NVA and MA-VA). Figure S9 (b) plots 1D radial profiles after azimuthal integration of 2D patterns for all samples. We find that Pb-VA sample is characterised by enhanced scatter from PbI_2 ($Q \approx 0.9 \text{ \AA}^{-1}$) compared to that from the Pb-NVA film, indicating the loss of organic species due to SVA. In contrast, radial line profiles from the MAI-excess samples show a complete absence of crystalline PbI_2 and an increase in (110) scattering intensity; a trend that is also observed in the XRD patterns shown in Figure 4 (a). Significantly, we find that freshly prepared Pb-VA samples exhibited scattering from a set of low-intensity peaks at $Q = 0.26, 0.44, 0.53$ and 0.63 \AA^{-1} (equivalent to $2\theta = 3.7^\circ, 6.2^\circ, 7.5^\circ$ and 8.9°), with scattering plots shown in Figs S8 and S10. We note that such features are comparable to the previously reported phase $(\text{MA})_2(\text{DMF})_2\text{Pb}_3\text{I}_8$ that contains $(\text{Pb}_3\text{I}_8)^{2-}$ octahedral chains that are intercalated with MA and DMF³⁹. This phase is formed as an intermediate when MAPbI_3 is processed under PbI_2 -rich conditions (using DMF as the solvent) and has an orthorhombic structure (space group *Pnmm*) with expected reflections at 6.5° (110), 8.0° (020) and 9.5° (120). We have found that this phase is metastable and can be removed from the film upon prolonged exposure to ambient air/moisture or extended heat treatment (see Figure S10 (b)). The significance of such intermediate DMF complexes is discussed later in the manuscript.

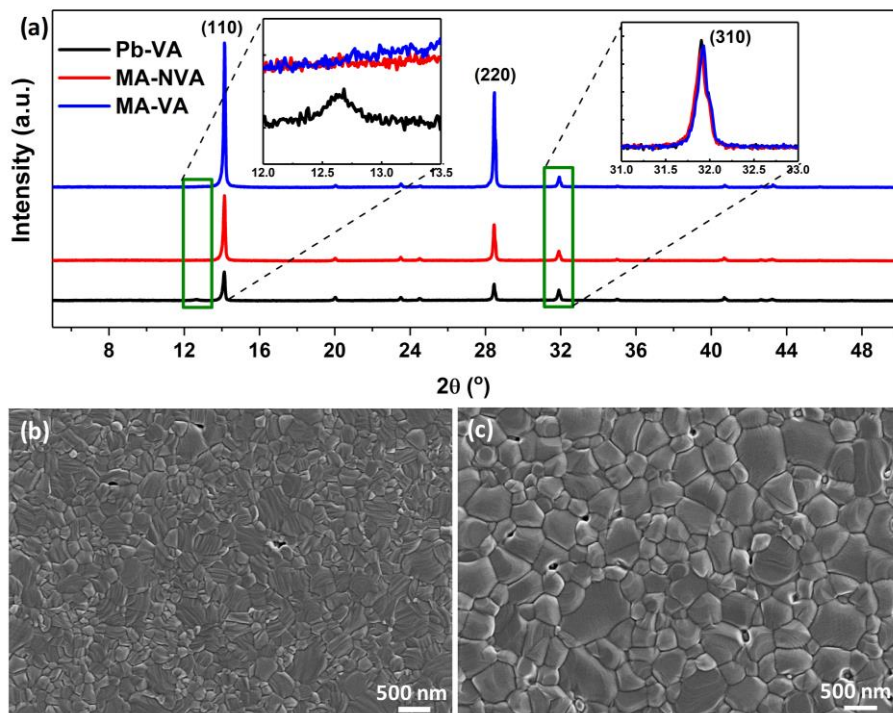


Figure 4: XRD patterns of Pb-NVA, Pb-VA, MA-NVA and MA-VA (vertically offset for comparison and clarity), inset shows a magnified view of XRD patterns, showing no PbI_2 scattering at 12.6° . Parts (b) and (c) show SEM images of MA-NVA and MA-VA respectively.

5.2.3.3: Influence of stoichiometry and SVA on device performance

To understand the effect of the initial stoichiometry of MAPbI_3 films and SVA on photovoltaic performance a series of photovoltaic devices were fabricated having the general structure ITO/np- SnO_2 / MAPbI_3 /spiro-MeOTAD/Au. Figure 5 plots J - V curves of the best devices fabricated using Pb-NVA, Pb-VA, MA-NVA and MA-VA films (corresponding device metrics listed in Table S1). We find that in PbI_2 -rich films that have not undergone SVA (Pb-NVA), the peak PCE determined using a reverse-scan ($V_{oc} \rightarrow J_{sc}$) and a forward-scan ($J_{sc} \rightarrow V_{oc}$) were $\sim 16\%$ and $\sim 12.3\%$ respectively (a moderate degree of J - V hysteresis). On SVA, the reverse-scan PCE of the best performing Pb-VA device was found to be similar ($\sim 15.8\%$) but the forward-scan efficiency was significantly reduced to 6.9% ; a substantial increase in J - V hysteresis. We note that the reduction in fill factor (FF) in Pb-VA containing devices when measured using a forward-scan indicates shunt losses at one of the charge-extracting interfaces. We speculate that this results from a depletion of MAI at the perovskite top surface following solvent vapour annealing, thus adversely affecting carrier recombination at the MAPbI_3 /spiro-MeOTAD interface.*

* The dramatic increase in hysteresis for Pb-NVA and (to a greater extent) Pb-VA could have other explanations, such as the reduction of the MAPbI_3 /HTL interface area with large PbI_2 grains formed, a substantial increase in bulk defects (most likely iodide or MA^+ vacancies) altering the ion mobility or greatly increased interfacial charge-trapping defects (interstitial iodide defects).

On addition of excess MAI, we observe an improvement in all photovoltaic parameters in non-SVA films (see Table S1), leading to higher reverse and forward-scan efficiencies of 17.8% and 16.2% respectively. On SVA, we find that devices based on MAI-excess films retain a high forward-scan efficiency of 15.9%. An improvement in interface quality in MAI-excess compositions is also evident from the low J - V hysteresis observed in MA-NVA and MA-VA based devices. For completeness, we have also explored perovskite films having a stoichiometric composition in PV devices, in which the MAI:PbI₂ molar ratio was 1:1. Figure S11 and Table S1 plot J - V curves and photovoltaic parameters of stoichiometric MAPbI₃ devices with and without solvent vapour annealing, termed MAPI-VA and MAPI-NVA respectively. We find that both MAPI-NVA/VA films performed better in PV devices than corresponding PbI₂-excess compositions but were lower performing than MAI-excess devices.

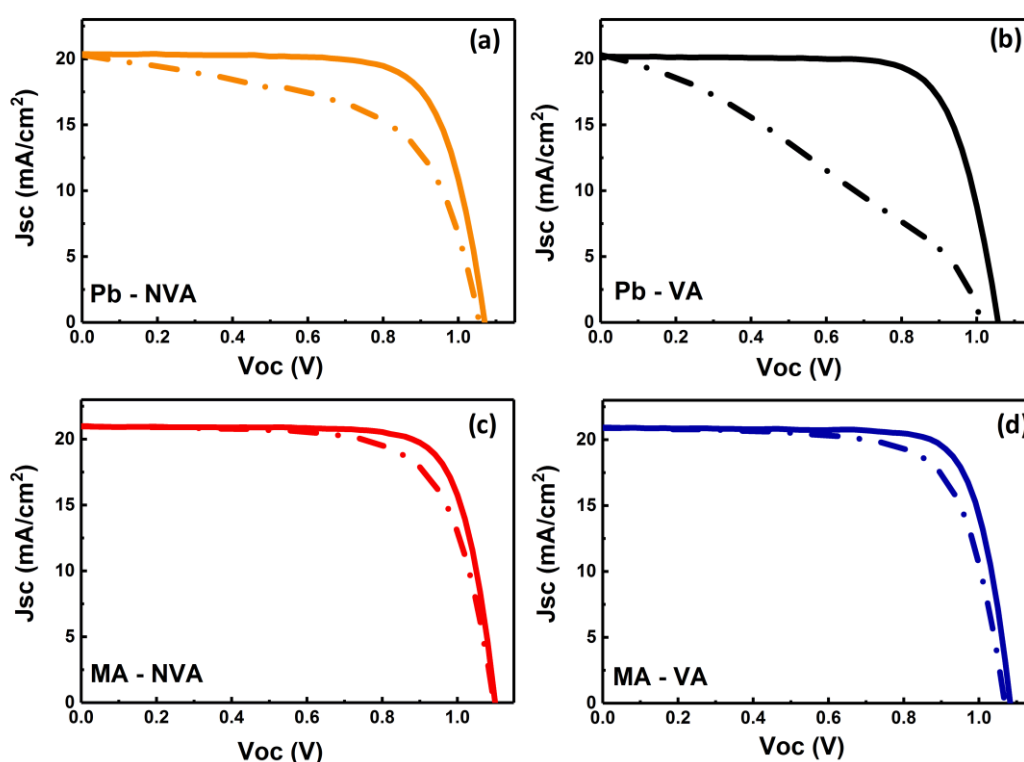


Figure 5: J - V curves of (a) Pb-NVA, (b) Pb-VA, (c) MA-NVA and (d) MA-VA fabricated in planar n - i - p architecture (Glass/FTO/SnO₂/MAPbI₃/spiro-MeOTAD/Au).

We summarise full device statistics obtained from 32 pixels per film preparation condition in Figure S12. We find that without solvent vapour-annealing, all photovoltaic parameters increase monotonically as film composition is tuned from being deficient in MAI to having an MAI excess. This trend of increased device metrics as MAI concentration is increased is also observed following solvent vapour annealing, albeit with lower statistical significance. Importantly, the negative effects of vapour-annealing on forward-scan metrics were found to reduce with the

addition of MAI, with MAI-excess compositions being the least affected by this process. We conclude that MAI-excess compositions lead to both better device performance without SVA perovskite treatment, and appear to be least susceptible to the detrimental effects of SVA. Interestingly, we did not observe improvements in the device performance parameters after SVA in both PbI_2 -excess and MAI-excess compositions; a finding that is in contrast to previous reports^{18,19}. One of the main reasons for enhancements in photovoltaic efficiency following SVA includes healing of voids present at the substrate-perovskite interface in apparent smooth and compact perovskite films^{19,40,41}. Here, the ACN/MA process used in this paper resulted in films that were free of voids around the SnO_2 -perovskite interface (see the cross-sectional SEM image shown in Figure S17 (a) and (b)). Therefore, in the devices reported here, we suspect that changes in stoichiometry following SVA likely play a dominant role in reducing the observed device performance.

5.2.3.4: Influence of SVA on material stability - in-situ GIWAXS study

Although it is useful to determine the effect of material composition on initial device performance, the long-term operational stability of devices is equally as important when considering the practical deployment of any photovoltaic technology. We have previously demonstrated that certain film-treatments and perovskite-compositions that seemingly improve initial device performance can result in reduced operational stability when devices are measured over extended timescales.²⁷ We have found degradation to be stoichiometry-dependent and can result in different degradation pathways specific to local composition.^{22,38} We therefore studied the intrinsic material stability of the various perovskite compositions under accelerated stress factors (high-humidity, enhanced-temperature and intense optical illumination) using synchrotron radiation at Diamond Light Source I22 beamline. Here, GIWAXS scattering measurements were made on films placed in a humidity-controlled chamber incorporating a hotplate, while illuminated with a white light LED. Humidity was maintained by mixing moist air and dry-nitrogen using two mass flow controllers with an in-line feedback sensor at the point of mixing. Figure S13 shows a photograph of the humidity-controlled chamber, with GIWAXS measurements typically at $\sim 40 \pm 5\%$ relative humidity, 50°C hotplate temperature and $200 \pm 10 \text{ mW/cm}^2$ irradiation.

In these measurements, we have monitored time-dependent changes in the MAPbI_3 (110) peak intensity to determine relative degradation rates under high stress (accelerated degradation) conditions. Our experiments confirm that perovskite composition strongly influences the rate at which MAPbI_3 films undergo degradation. This is shown in Figure 6(a), where we show NVA films containing an MAI-excess undergo degradation at a slightly slower rate than PbI_2 -excess

when tested under identical conditions, with degradation being complete in both types of films after ~1 hour. However, more significant differences in film stability were observed following SVA as shown in Figure 6(b). Here, the perovskite phase in films containing a PbI_2 -excess (Pb-VA) were almost completely degraded after 35 - 40 minutes. Our results indicate that films containing an MAI-excess are more stable both with and without SVA; suggesting that PV devices based on this material composition should have enhanced operational lifetime.

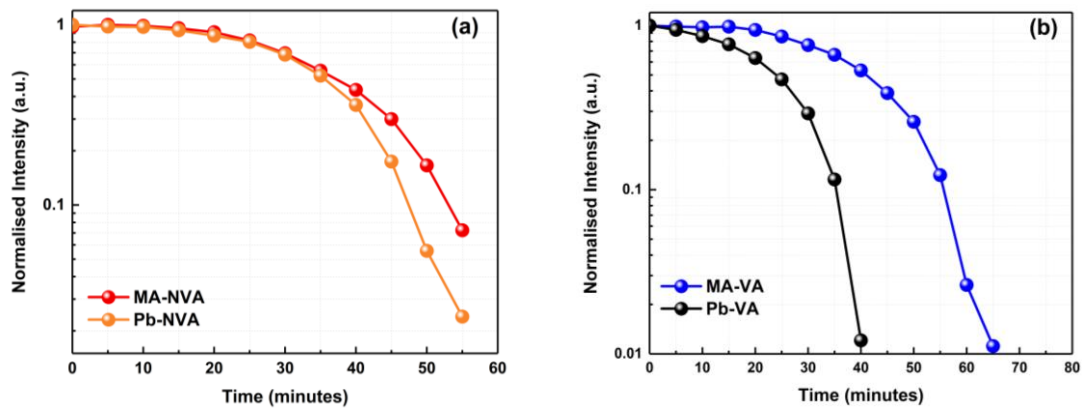


Figure 6: Semi-log plots of normalised intensity from the MAPbI_3 (110) peak over time for (a) non-solvent vapour annealed and (b) solvent annealed MAI-excess and PbI_2 -excess composition, acquired in a GIWAXS geometry. Panel (a) shows the influence of stoichiometry on accelerated degradation while panel (b) shows the degradation of solvent vapour annealed perovskite films with different stoichiometry (MAI-excess and PbI_2 -excess)

5.2.3.5: Influence of SVA on device stability

To determine whether such findings can be translated to device lifetime, we have followed the operational performance of un-encapsulated PV devices under continuous 1-sun equivalent illumination for ~120 hours, with J - V sweeps recorded every 20 min, and devices held at open-circuit between measurements. Specific details about the methodology used for device lifetime testing can be found in the experimental section. We note that the presence of an internal electric field and the flow of current (i.e. under short-circuit condition) or the accumulation of charged species (i.e. under open-circuit conditions) or both (under maximum power point conditions) has been shown to significantly affect the stability of photovoltaic devices.⁴²

In Figure 7, we plot the metrics of PV devices based on the four different perovskite conditions (Pb-NVA, Pb-VA, MA-NVA, MA-VA) over 120 hours. We find that device stability is strongly dependent on the composition of the active layer and the application (or not) of the SVA treatment. The most dramatic reduction in device efficiency during aging is seen in solvent vapour annealed PbI_2 -excess composition (Pb-VA). Here, a near exponential decrease in J_{SC} is

observed over time (see Figure 7(c)) that results in a significant loss in PCE (see Figure 7(d)). Interestingly, PbI_2 -excess films that were not subjected to SVA (Pb-NVA) underwent a slower (linear) reduction in J_{SC} ; a result that suggests that different degradation pathways may exist in such films. To determine whether such losses in J_{SC} of Pb-VA devices result from an increased vulnerability of the perovskite layer to moisture/oxygen, we performed similar lifetime measurements on Pb-VA cells that had been encapsulated with 150 nm of SiO_2 . Significantly, we observed similar degradation rates in Pb-VA devices with SiO_2 encapsulation (see Figure S14). This indicates that the degradation process is intrinsic to the perovskite material, with the effects of illumination and J - V cycling being the primary mechanisms that cause such a loss in performance in encapsulated PV devices. The near-complete loss in performance of Pb-VA based devices at the end of lifetime testing is evident from the photograph of the aged device shown in Figure 7. Here, the Pb-VA film has turned yellowish, rather than the strongly absorbing dark film expected for MAPbI_3 . The Pb-NVA devices appeared to have retained some of their optical density at the end of the testing period – consistent with their higher performance and operational stability. In all cases, the degradation of MAPbI_3 will limit the ability of the device to absorb light, and will also alter the charge carrier extraction rate, recombination dynamics and hence shunt resistance.

Significantly, devices based on an MAI-excess composition without solvent vapour annealing (MA-NVA) had the highest stability (see Figure 7(d)). Here, the V_{OC} of MA-NVA devices maintained 97% of its initial value over 120 hrs, although the fill factor decreased by ~10% over this period. Notably, device J_{SC} underwent a positive burn-in, increasing by 5-10% over the first 20 hrs and then maintaining this value over the rest of the testing period. We note that we have previously observed similar improvements in J_{SC} (and decrease in FF) in fully-encapsulated inverted architecture (p - i - n) devices²⁷ based on a PbI_2 -excess composition, indicating that material stoichiometry may not be the sole reason for these changes. We suspect that improvements in J_{SC} over short periods (~20 hrs) most likely result from favourable changes in interface structure caused by ion migration processes during testing. The beneficial effect of excess-MAI on the stability of unencapsulated MA-NVA devices can be seen in Figure 7(d), with such devices retaining ~90% of their original efficiency after 120 hrs of continuous illumination. Devices using MAI-excess films that had been SVA (MA-VA) also largely retained their initial V_{OC} , demonstrated a short-time increase in J_{SC} and underwent a decrease in FF. However, a reduction in V_{OC} (~95%), J_{SC} (~83%) and FF (~77%) resulted in a final PCE of around 63% of its original level after 120 hrs testing. This loss in PCE under continuous illumination

testing in MA-VA as compared to MA-NVA indicates that the loss of cationic species during solvent vapour annealing may not be completely mitigated by the excess MAI.

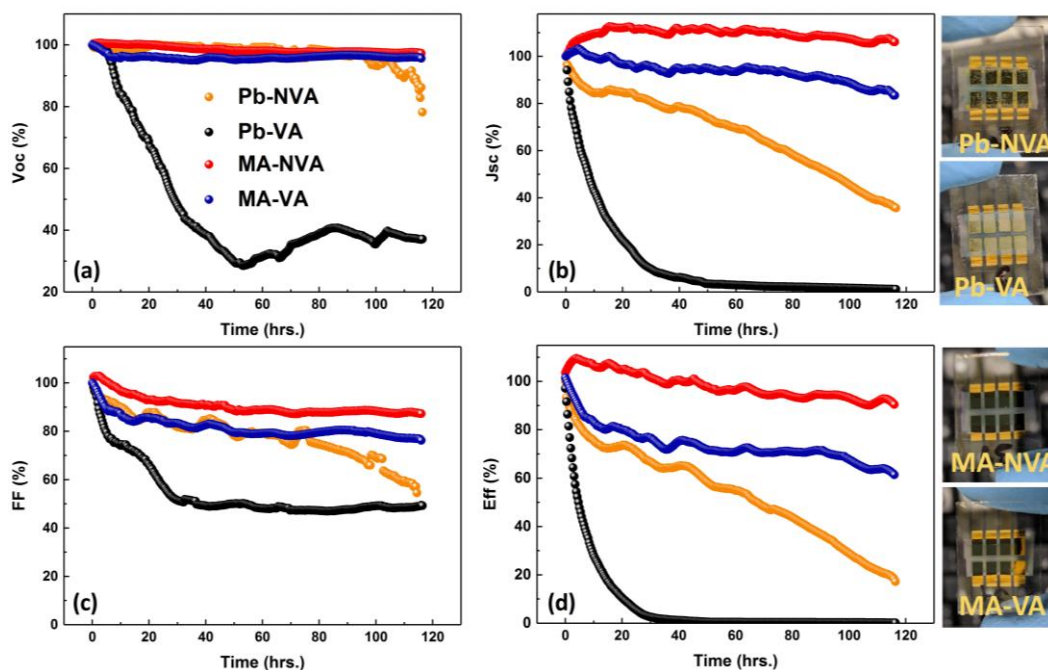


Figure 7: Evolution of unencapsulated device (a) V_{OC} , (b) J_{SC} , (c) fill factor and (d) PCE (all normalized to initial values) under continuous illumination (~120 hrs). Right side column shows photographs of rear side of devices after 120 hr continuous illumination J-V testing.

For completeness, we also compared the lifetimes of films made with stoichiometric solutions (MAI:PbI₂ 1:1) without (MAPI-NVA) and with (MAPI-VA) solvent vapour annealing. Figure S15 shows that devices using MAI-excess (with or without SVA) had better stability than either PbI₂-excess or stoichiometric perovskites. We conclude that the incorporation of excess cation (here MAI) in precursor solution can be used to both improve device performance metrics, device stability as well as to mitigate the loss of cationic species during solvent vapour annealing.

To further understand the dependence of material composition and solvent vapour annealing on device degradation, we recorded cross-sectional SEM images of selected PV devices after lifetime testing, with representative images shown in Figure 8. Here, all devices were encapsulated with a 150 nm thick SiO₂ encapsulation layer. We first compare device cross-sections containing Pb-NVA and MA-NVA perovskites (see Figure 8 (a) and (c) respectively). Here, the effect of excess MAI content is striking; after 120 hours of continuous illumination, the cross-section of the MA-NVA based device shown in Figure 8(c) is characterised by a well-defined grain structure, indicating negligible changes in the microstructure of the perovskite

phase despite J - V cycling and being held at open-circuit conditions. The initial device cross-section of Pb-NVA sample before subjecting to lifetime testing (Figure S16) had a similar appearance to the MAI-excess sample without SVA treatment in Figure 8 (c), with the grain boundary structure within the perovskite film being initially well-defined with grain size ranging from 100 – 300 nm. However, after the continuous illumination lifetime testing, the Pb-NVA device cross-section (see Figure 8 (a)) was characterised by a series of voids (marked with yellow circles in the Figure 8) along with a less-distinct grain boundary structure. This evolution in grain-structure suggests both the degradation and dynamic reconstruction of the perovskite during device operation. It has been previously shown that PbI_2 can undergo photodecomposition to metallic Pb and molecular iodine (I_2) at temperatures relevant to solar cell operation (40 – 80 °C)⁴³. Wang *et al.*⁴⁴ have also demonstrated that the evolution of gaseous I_2 from a perovskite film, combined with migration and accumulation of I^- ions under illumination and open-circuit conditions, sets up a chain reaction that results in further perovskite phase degradation to gaseous methylamine (CH_3NH_2), I_2 and H_2 . We illustrate this process using the reaction scheme shown in the supplementary information (Scheme S18). Such a chain reaction would require vacancy-mediated migration of I^- ions.⁴⁵ As PbI_2 -excess films (Pb-NVA or Pb-VA) are deficient in MAI, they are expected to be more susceptible to the formation of vacancy defects (V_{I} and V_{MA}), with the density of such defects likely to increase during SVA for the PbI_2 -excess composition.

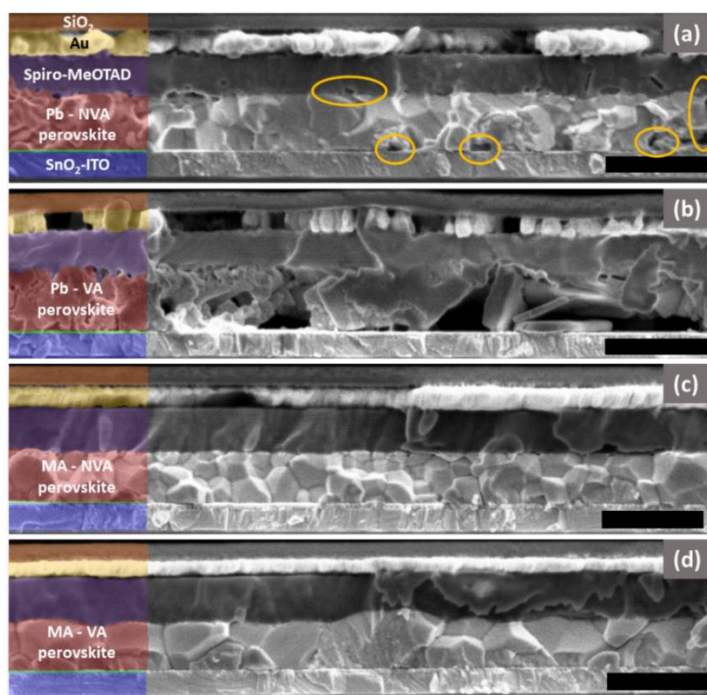


Figure 8: SEM cross-sections of encapsulated (150 nm SiO_2) (a) Pb-NVA, (b) Pb-VA, (c) MA-NVA and (d) MA-VA device after ~300 hrs of continuous illumination lifetime testing. Yellow circles in (a) denote the voids induced by degradation in the Pb-NVA sample. All the scale bars are 500 nm.

We expect that the density of MA⁺ and I⁻ related vacancy/interstitial defects in MAI-excess films to be lower than in Pbl₂-excess films⁴⁶. We suggest that this is likely to lead to a more stable perovskite phase under operational conditions. Excess-MAI will likely act as a “reservoir” that replenishes the loss of methylammonium and iodide, thereby limiting the formation of interface defects or degradation products during device operation. This conclusion is consistent with the observation of increased hysteresis in the *J-V* sweeps of Pbl₂-excess devices compared to those made with an excess of MAI in the precursor solution.*

We now compare device cross-sections in which the perovskite was subjected to SVA treatment. Here, cross-section images of SVA treated Pbl₂-excess and MAI-excess films after lifetime testing are shown in Figure 8(b) and (d) respectively. The catastrophic failure of the Pb-VA device compared to the MA-VA device is evident as a decomposed active layer. The aged Pb-VA device (Figure 8(b)) is characterised by large voids and platelet-like structures that are likely Pbl₂ crystallites along with other hydrate phases⁴⁷; a conclusion that is consistent with the bleached appearance of Pb-VA devices after lifetime testing (see Figure 7 Pb-VA). We also note that the SiO₂ encapsulation layer has undergone a degree of deformation - a process likely driven by strain within the device resulting from the conversion from MAPbl₃ to Pbl₂ (or other degradation products^{47, 48}). In contrast, the MA-VA device (Figure 8(d)) is characterised by a continuous grain structure, with such grains being relatively large as a result of the SVA process. Here, the SiO₂ encapsulation layer appears flat, indicating an absence of strain within the device caused by degradation induced phase transitions.

5.2.3.6: Proposed mechanism of observed stoichiometric changes following SVA

We now propose a general mechanism to explain our results. Our mechanism is based on work by Guo *et al.*⁴⁹ who suggested that when processing MAPbl₃ using DMF/DMSO solvents, nucleation and growth of crystal grains takes place via the formation of intermediate polymeric plumbates. On heating, such intermediate phases lose solvent molecules and then crystallise into a perovskite phase. Petrov *et al.*³⁹ then showed that the nature of such intermediate plumbates in DMF strongly depends on precursor stoichiometry. Specifically, it was proposed that (MA)₂(DMF)₂Pb₃I₈, (MA)₂(DMF)₂Pb₂I₆ and (MA)₃(DMF)PbI₅ would form under Pbl₂-rich, stoichiometric and MAI-rich conditions respectively. It is important to note that such

* It is also possible that the additional I⁻ compensates for an initial I⁻ deficiency in the Pbl₂, and that during SVA this inhibits undercoordinated Pb before the SVA process.

intermediate phases act as dominant pathways that drive nucleation and growth when DMF (or DMSO) is used as the primary processing solvent.

We illustrate the SVA process in Figure 9(a). Here, polar aprotic solvents (such as DMF or DMSO) are good solvents for PbI_2 and organic-halide compounds such as $\text{CH}_3\text{NH}_3\text{I}$. As the amount of solvent used in SVA is usually low ($\sim 10 \mu\text{L}$), a complete dissolution of the film is unlikely to occur. Instead, the solvent vapours are likely to form a thin layer of the intermediate plumbate complexes at regions having a high interfacial energy (such as the film surface and grain boundaries) as shown in previous studies^{1,19} and illustrated in Figure 9(b). The formation of such intermediate complexes involves structural transitions from a 3D MAPbI_3 perovskite to the quasi-1D fibrous plumbate phases (e.g. $(\text{MA})_2(\text{DMF})_2\text{Pb}_3\text{I}_8$) in which MA^+ molecules are extracted from between the PbI_6 octahedral cages. The polar aprotic nature of DMF/DMSO plays an important role in this process, as they act as a hydrogen-bond acceptor and remove the relatively acidic MA^+ ions. Structurally, the incorporation of DMF in MAPbI_3 involves hydrogen bonding⁵⁰ between $-\text{C}=\text{O}^{\delta-}$ of DMF and $-\text{H}_3\text{N}^{\delta+}$ of MA^+ , with this bond being stronger than the hydrogen bond of $-\text{H}_3\text{N}^{\delta+}$ with the $\text{I}^{\delta-}$ of the Pb-I octahedra. This allows an extraction of MA^+ ions from between the PbI_6 octahedral cages and helps the temporary formation of plumbate structures. We speculate that three factors are important in the removal of weakly bound MA^+ ions; (1) the removal of MA^+ from the PbI_6^- perovskite cage by DMF, (2) the strong hydrogen bonding between the $-\text{C}=\text{O}^{\delta-}$ (in DMF) and $-\text{H}_3\text{N}^{\delta+}$ (in MA^+), and (3) the use of annealing temperatures of $100 \text{ }^\circ\text{C}$. This process leads to the formation of MAI-deficient perovskite grains, possibly with PbI_2 present on the surface of these grains as illustrated in Figure 9 (c).

Our experiments further suggest that the presence of excess unbound MAI at grain boundary regions helps to replenish the SVA-induced loss of MA^+ and I^- from MAPbI_3 that results from SVA. Note that excess-MAI in the form of a salt during SVA is unlikely to be strongly affected by this process due to the strong ionic-bond between MA^+ and I^- .

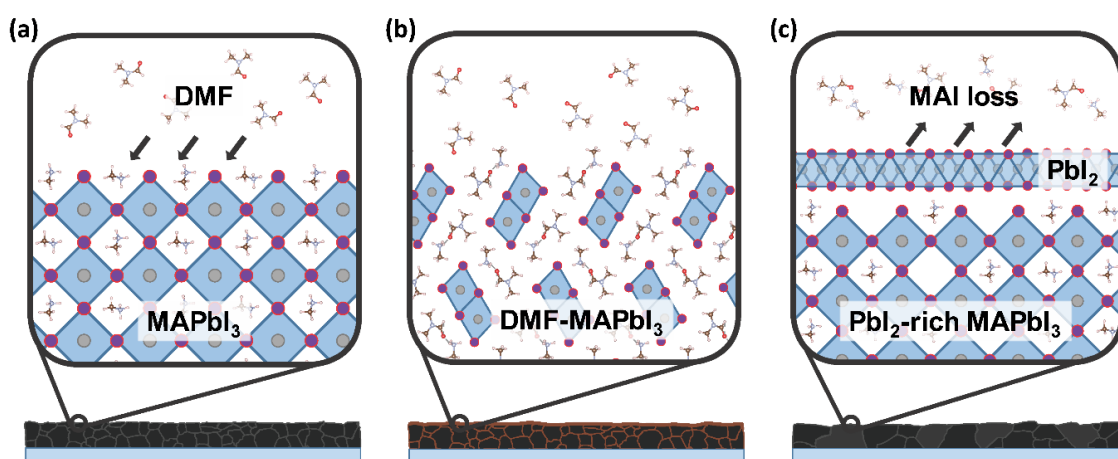


Figure 9: Proposed schematic illustrating the effect of DMF-SVA on the stoichiometry of MAPbI₃ films. In part (a), DMF molecules interact at high surface energy interfaces at the top-surface and grain boundaries. In part (b), SVA at 100 °C results in a temporary structural transition from 3D MAPbI₃ to a plumbate complex (e.g. (MA)₂(DMF)₂Pb₃I₉) in a thin layer near the grain surfaces and boundaries. Part (c) illustrates the interaction between DMF and MA⁺, which when combined with an annealing temperature of 100 °C leads to loss of MAI. This results in the formation of a MAI-deficient MAPbI₃ perovskite, with PbI₂ located at the grain surface.

We speculate that this mechanism is likely to occur during SVA using other polar solvents such as dimethyl sulfoxide (DMSO), *N*-methyl-2-pyrrolidone (NMP) and gamma-butyrolactone (GBL) which also have an electronegative $\text{-C=O}^{\delta-}$ group. The conclusions drawn in this manuscript are also likely to apply when SVA is applied to mixed-cation perovskite compositions that contain MA cations, and may also apply to FA compositions. We note that a recent *in situ* synchrotron study on triple cation (FAMACs) perovskite devices concluded that the presence of MA⁺ leads to more thermodynamically stable structures than occur in double-cation FACs lead halide perovskites.⁵¹ The extent of loss of cationic species will thus depend on bonding strength between the cation and solvent, the nature of the SVA process solvent⁵⁰ and the thermodynamic stability of the perovskite composition.^{52, 53} MA⁺ loss during SVA is likely to be enhanced compared to FA⁺ as the cation is more polar and acidic. Indeed, the negative impact of the SVA process is expected to be more significant for MAPbI₃ and mixed cation perovskites with MA⁺ cations due to the volatility of methylammonium.⁵⁴⁻⁵⁶

Finally, we expect the loss of cationic species due to solvent-solute interaction may well happen in cases where DMF/DMSO are used simply as process solvents, with films being fabricated by a standard thermal annealing route. However, the extent of this loss is far more severe during the SVA process than thermal annealing due to the large excess of solvent vapours. We note that recent quantitative nuclear magnetic resonance (NMR) measurements on perovskite precursor solutions and spin-cast films (without SVA) showed that the stoichiometry of

thermally-annealed films is different to that of the precursor solution⁵⁷ with a loss of cationic species observed during fabrication. We suggest that the influence of SVA on perovskite stoichiometry should be considered when exploring the effect of grain size effect on optoelectronic properties of hybrid perovskites, and this process cannot be considered as benign.^{23, 25}

5.2.4: Conclusions

In summary, we have studied the effect of annealing hybrid perovskite (MAPbI₃) films in the presence of polar solvent vapours in a process known as solvent vapour annealing (SVA). We use a range of different characterisation techniques (pc-AFM, XRD, SEM-EDS) to show that films subjected to SVA are characterised by increased grain size that occurs at the expense of altered stoichiometry compared to the initial film. We show that SVA leads to a loss of organic halide species (MAI in case of MAPbI₃) due to interactions between the MA⁺ cation and polar solvent such as DMF. Device lifetime measurements and accelerated degradation studies show that the loss of operational stability with SVA depends on the initial stoichiometry of the MAPbI₃ film, with PbI₂-excess compositions being the least stable. The results presented here agree with previous reports on the poor stability of PbI₂-excess MAPbI₃ compositions, despite short-term improvements in the device performance parameters^{58, 59}. We then demonstrate that the incorporation of excess organic halides into the precursor solution partially mitigates the deleterious effects of SVA. Our work highlights the importance of considering material stoichiometry, particularly when highly polar aprotic solvents are used to process perovskite solar cells. We emphasize that the conclusions drawn here are also likely to be relevant in other mixed cation perovskite compositions containing methylammonium cations and we speculate that similar effects may occur with formamidinium.

5.2.5: Experimental section

5.2.5.1: Materials and methods

MAPbI₃ films for microstructure characterisation and devices were prepared using a protocol similar to Noel *et al.*²⁸ All the chemicals were bought from commercial sources and used without purification. Specifically, lead iodide (PbI₂, TCI 99.99% Product No. L0279) and methylammonium iodide (MAI 99.9%, Ossila UK) were mixed in acetonitrile (ACN, Sigma Aldrich, 99.8% anhydrous) with different PbI₂/MAI molar ratios to get the solute weight percentage of 29% in ACN. Complete dissolution of MAI and PbI₂ occurred after bubbling the methylamine gas generated from a methylamine solution using a setup as described in ref. 28.

Three ACN/MA inks with different composition viz. PbI_2 -excess ($\text{PbI}_2 : \text{MAI} = 1.06 : 1$), stoichiometric ($\text{PbI}_2 : \text{MAI} = 1 : 1$) and MAI excess ($\text{PbI}_2 : \text{MAI} = 1 : 1.03$) were prepared. All the films were made by static spin coating at 3000 rpm for 30 seconds. Control samples with only thermal treatment were annealed at 100 °C for 15 min. For solvent vapour annealing, eight as-spun-coated films were placed equidistant (~4 cm) from the centre of the hotplate and were first thermally annealed for 3 min at 100 °C. 15 μL DMF was then dropped at the centre of the hotplate and the substrates were immediately covered with a shallow petri-dish to trap solvent vapours. The petri-dish was removed after 7 minutes (after all the DMF was converted to vapour form and utilised in the SVA process). Thermal annealing at 100 °C was continued for five more minutes. The total time for which the substrates are heated at 100 °C in no vapour annealed (NVA) or solvent vapour annealed (SVA) cases was kept the same (15 min).

For perovskite solar cell fabrication, cleaned ITO (Ossila, 20 ohm/sq, 8 pixel) substrates were spin-coated at 3000 rpm with SnO_2 nanoparticle solution (Alfa Aesar, 15 wt% nanoparticle dispersion) diluted to 1:4 (volume) in de-ionised water. SnO_2 coated ITO substrates were heated at 150°C for 30 min followed by UV-Ozone treatment for 10 min. MAPbI_3 films were spin-coated and subjected to thermal or solvent vapour annealing using the protocol outlined above. Spiro-MeOTAD (Ossila, 99.5% sublimed) hole-transport layer was spin-coated dynamically at 4000 rpm. The composition of the hole-transport layer solution included 86 mg spiro-MeOTAD in 1 mL Chlorobenzene (Sigma-Aldrich) doped with LiTFSI (Sigma Aldrich, 20 μL from 500 mg/mL stock in ACN), FK (II) 209 PF6 (GreatCell Solar, 11 μL from 300 mg/mL stock in ACN) and 4-*tert*-butylpyridine (34 μL). The cells were left overnight in dry air for oxidation of the spiro-MeOTAD and then an 80 nm gold layer was deposited using thermal evaporation at up to 1 \AA s^{-1} . For encapsulation (where used), the devices were coated with 150 nm of SiO_2 using e-beam evaporation at a rate of 1 \AA s^{-1} grown in two steps to minimise sample heating.

5.2.5.2: Characterization

Microstructural characterization: X-ray diffraction patterns were collected on perovskite films using a PANalytical X'Pert Pro diffractometer with Cu $\text{K}\alpha$ source. SEM images of films and device cross-sections were acquired using an FEI Helios NanoLab G3 UC and Carl Zeiss modified Raith Nanofabrication SEM at 1 - 1.5 kV accelerating voltage and an InLens detector at ~2.5 mm working distance. Grain size analysis was performed using ImageJ through control of grain boundary contrast. EDS spectra were collected using an Oxford Instruments EDS spectrometer and AZtecEnergy spectral analysis software with the Helios NanoLab SEM.

Photoconductive AFM (pc-AFM): pc-AFM maps were acquired using an Asylum Research MFP-3D scanning probe microscope. Samples for pc-AFM were prepared in a similar way as for full devices but without spiro-OMeTAD and gold top electrodes. The HTL-free devices were illuminated from the ITO side using a blue LED (448 nm, LXML-PR02-A900) biased in constant current mode with 700 mA. Platinum-Iridium coated conductive-AFM tips (Asylum Research Econo-SCM-PIC) with low spring constant (0.2 N/m) were used in contact mode to probe topography and photocurrent maps simultaneously. The pc-AFM tip was connected to the virtual ground. Photocurrent maps were acquired at zero applied bias to get short-circuit current maps under 448 nm illumination.

Device Testing: Devices were tested for their photovoltaic performance under a Newport 92251A-1000 solar simulator calibrated to 100 mW/cm² using a KG5 calibrated NREL silicon reference cell. JV curves were captured at a 400 mV/s scan rate using a Keithley 237 source measure unit. The active area (0.0256 cm²) of devices was defined using a metal aperture mask.

Device Lifetime-Testing: Encapsulated/non-encapsulated devices were tested for their lifetime under continuous illumination using Atlas Suntest CPS+ (1500 W xenon source with quartz IR reducing filters and internal reflectors). The lamp spectrum and irradiance approximately matches the AM 1.5G. The performance parameters were determined using reverse sweep (1.2 V to 0 V at 0.5 V/s) *J-V* curves after every 22 min. Devices were held at open circuit in between the consecutive JV measurements. During operation, the temperature and relative humidity reached 42 ± 3 °C and 38 ± 6% respectively. Since devices were not masked with a metal aperture mask, the performance parameters were normalised to their initial value.

Grazing incidence wide-angle X-ray scattering (GIWAXS): *In situ* GIWAXS was performed at the I22 beamline at Diamond Light Source with 14 keV X-rays incident on a controlled sample environment with a hotplate set at 50°C, LED illumination (200 ± 10 mW/cm² irradiation) and moisture control (-40 ± 5% relative humidity). The X-ray beam (size: 80×300 μm, flux: ~ 6 × 10¹² photons/sec) was attenuated through 0.2 mm Mo and incident at 0.3° on to the samples. Ambient moisture was controlled by passing N₂ through two mass-flow controllers, with one output passing through a moisture bubbler and the second passing directly into a mixing valve before entering the sample chamber, as shown in Figure S13. Data reduction, analysis and perovskite peak integration for intensity monitoring was done using the DAWN software package⁶⁰. *Ex situ* GIWAXS was performed using a Xeuss 2.0 (XENOCs) system with 9.243 keV X-rays produced using a Ga liquid MetalJet source (Excillum). Here, X-rays were directed onto

the sample surface at 0.3-1.5°, under vacuum to reduce background scatter. Scattered X-rays were then incident on a PILATUS3R 1M 2D detector (DECTRIS), with a sample to detector distance of ~330 mm. *Ex situ* GIWAXS data was corrected, reduced and reshaped using the GIXSGUI MATLAB toolbox⁶¹.

5.2.6: Acknowledgements

This work was supported through the Global Challenges Research Fund (GCRF) through Science & Technology Facilities Council (STFC), grant number ST/R002754/1: Synchrotron Techniques for African Research and Technology (START) and by the Engineering and Physical Sciences Research Council (EPSRC) via grant EP/M025020/1 'High-resolution mapping of performance and degradation mechanisms in printable photovoltaic devices' and via 'Secondary electron emission microscopy for organics with reliable engineering-properties' (EP/N008065/1). J.A.S. and M.S. thank the EPSRC for PhD studentships from the Centre for Doctoral Training in New and Sustainable PV, EP/L01551X/1 and T.A. thanks the Saudi Government for funding via a PhD studentship. GIWAXS studies at the Diamond Light Source were performed on I22 using beam-time allocation SM18563-1. We thank Dr. Andrew J. Parnell for his help with Xeuss 2.0 instrumentation setup, and we are indebted to Xenocs for their ongoing help and support in the user program at The University of Sheffield.

5.3: Supporting Information

5.3.1: SI Note 1: PbI_2 crystallization

The crystallization behaviour of PbI_2 and its location in mixed-phase perovskite films is a matter of ongoing research within the field. Most of the reports using ACN/MA solvent system for PbI_2 -excess compositions demonstrate the crystallization of PbI_2 as phase-separated grains or segregated regions in the films.^{29,62} However, we believe that this behaviour is not unique to the ACN/MA solvent system. Some of the early reports on PbI_2 excess in MAPbI_3 claimed a uniform distribution of PbI_2 around grain boundaries.³¹ However, recent reports on excess- PbI_2 in precursor solutions made with DMF/DMSO⁶³⁻⁶⁵ or GBL/DMSO⁶⁶ solvents also showed crystallization of PbI_2 grains, distributed throughout the film. We believe that such differences could have their origin in different annealing temperatures and durations, solvent ratios, fabrication environment (air vs nitrogen) and occasionally in batch-to-batch variation.

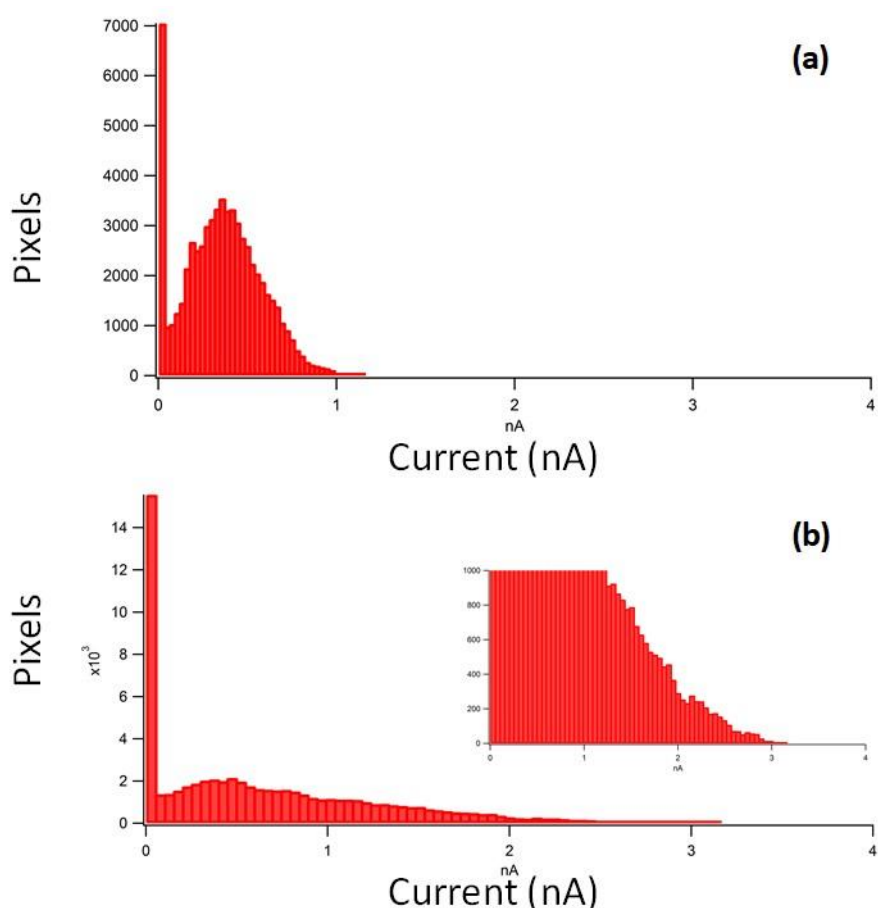


Figure S1 (a) and (b) show histogram of pixel frequency vs photocurrent for Pb-NVA and Pb-VA pc-AFM map in Figure 1(b) and (d) respectively. Inset of Figure S1 (b) shows the magnified view of Pb-VA histogram indicating the presence of pixels (regions/grains) with photocurrent magnitude higher than 1 nA.

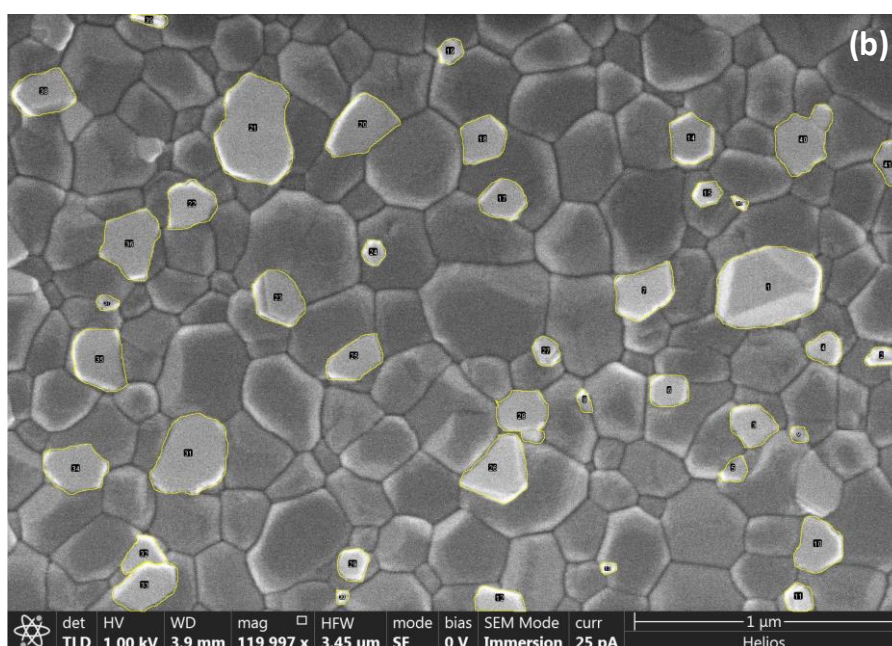
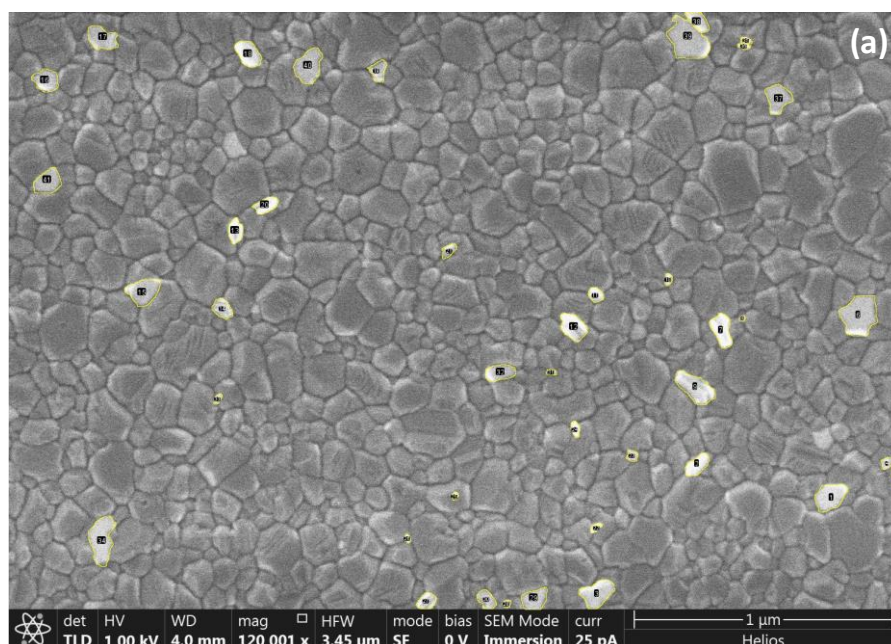


Figure S2: The total areas occupied by grains showing brighter contrast (highlighted in yellow) than surrounding grains in SEM images (with a total area of $8.02 \mu\text{m}^2$) were calculated using ImageJ software. These bright contrast PbI_2 -rich grains occupied $\sim 0.22 \mu\text{m}^2$ area in the SEM image of (a) Pb-NVA (3% of the surface) which on solvent vapour annealing increased to $\sim 1.04 \mu\text{m}^2$ for (b) Pb-VA (13% of the surface).

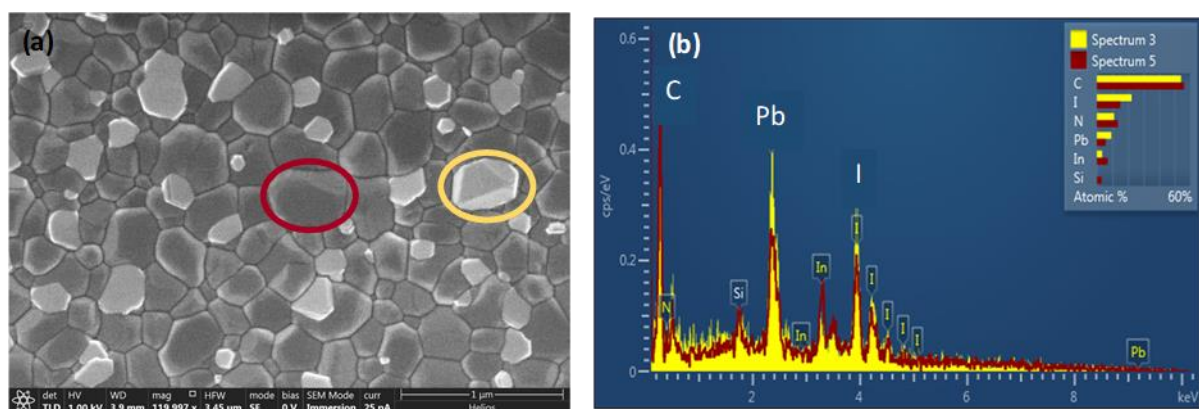


Figure S3 (a) shows the SEM of PbI_2 excess solvent vapour annealed (Pb-VA) film. Representative grains with dark and bright contrast are marked in red and yellow circles respectively. (b) shows the point EDS spectra of Pb-VA film at two locations marked red and yellow in (a).

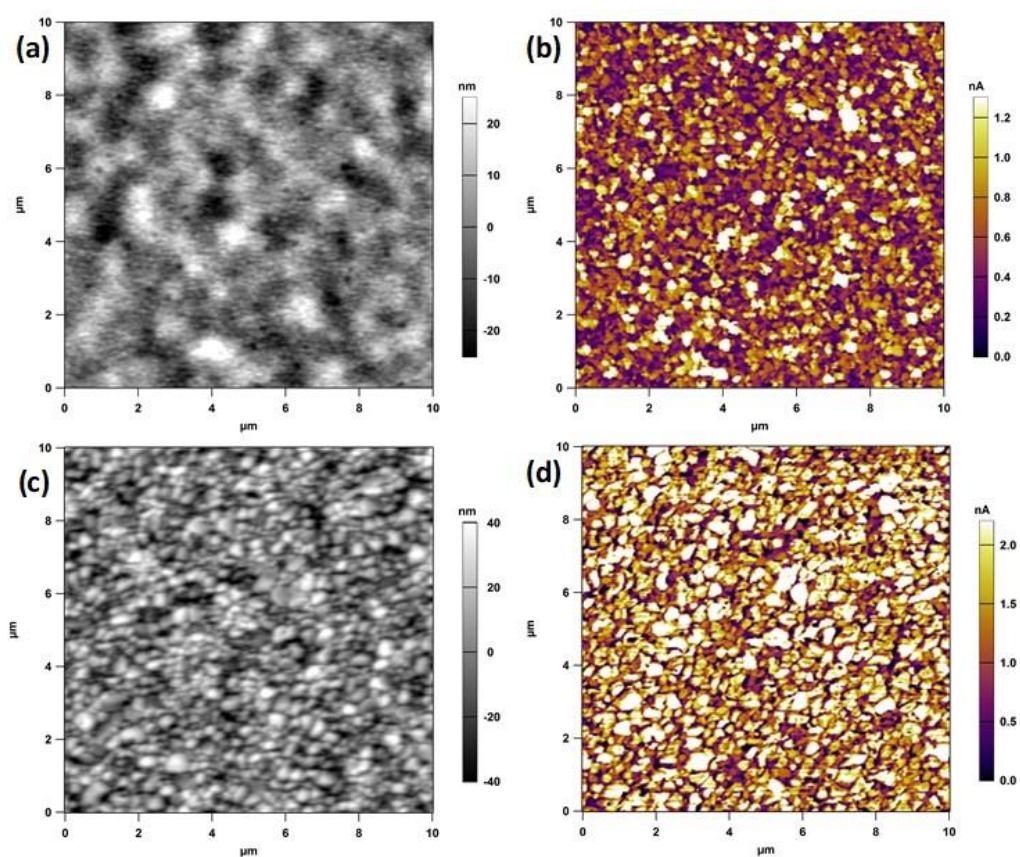


Figure S4: (a) and (c) shows the contact mode AFM (height profile) for MA-NVA and MA-VA films $10 \mu\text{m} \times 10 \mu\text{m}$ scan; (b) and (d) show photocurrent maps ($10 \mu\text{m} \times 10 \mu\text{m}$) simultaneously acquired with topography using pc-AFM under illumination for MA-NVA and MA-VA respectively.

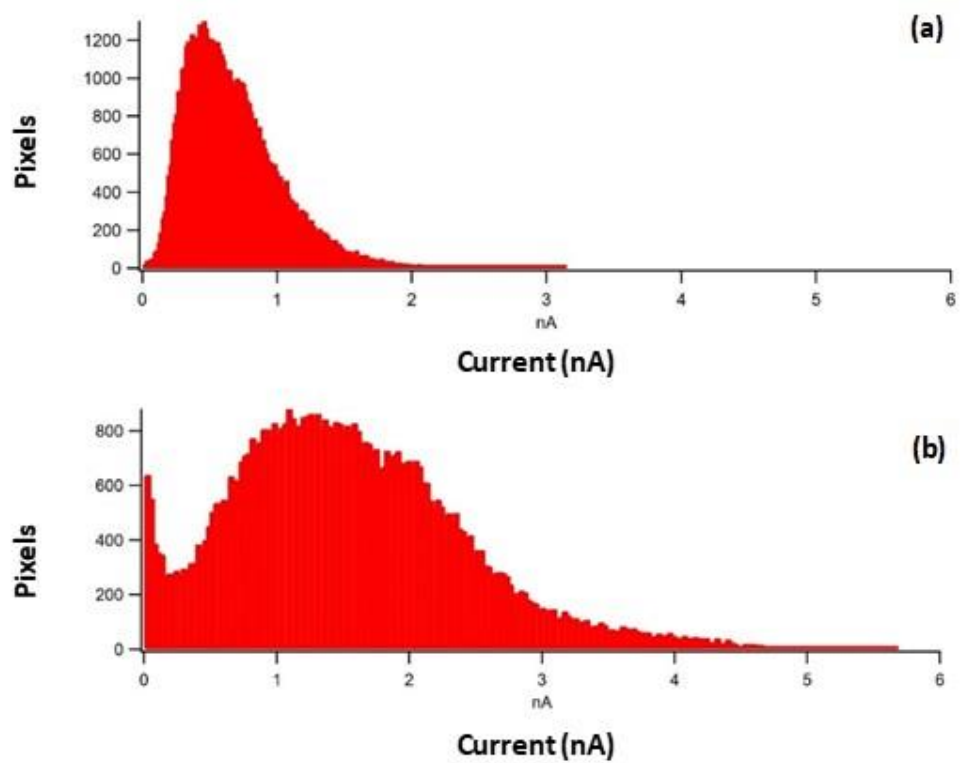


Figure S5: (a) and (b) show histogram of pixels vs photocurrent in *pc*-AFM map (from Figure 3 (b), (d)) for MA-NVA and MA-VA films respectively.

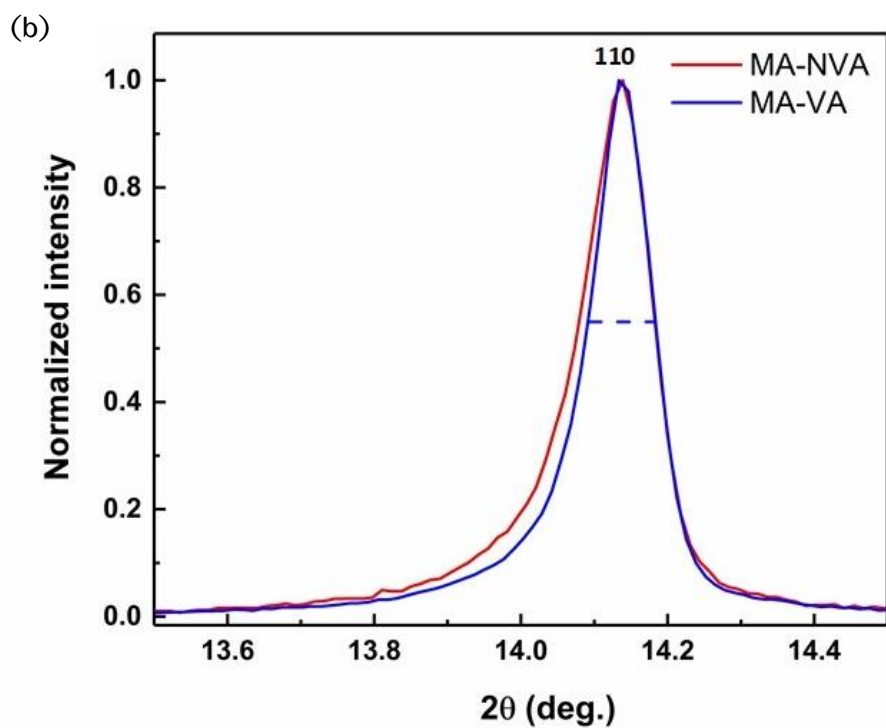
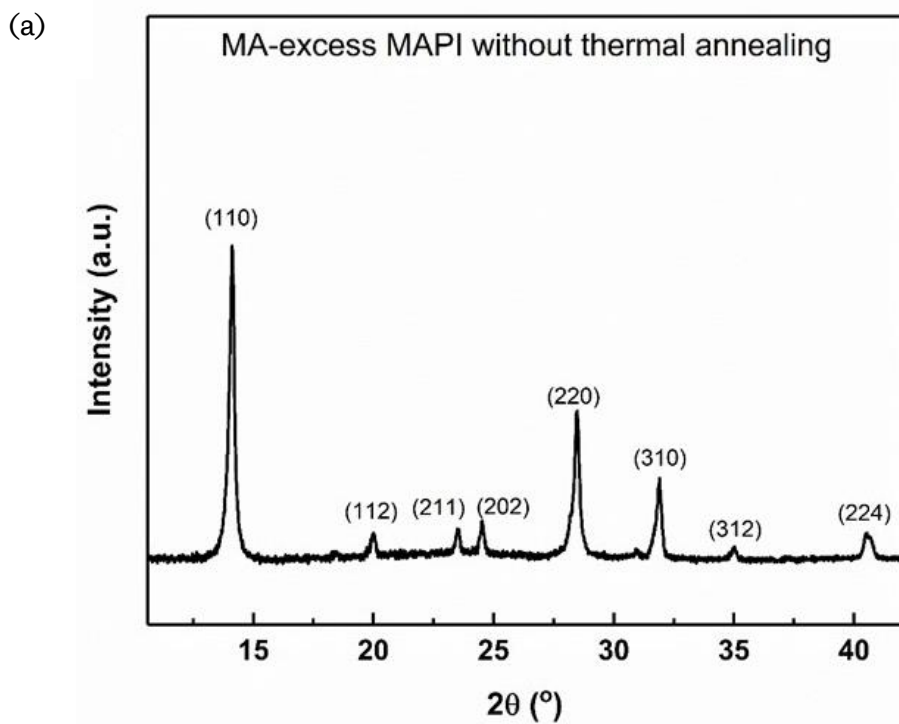
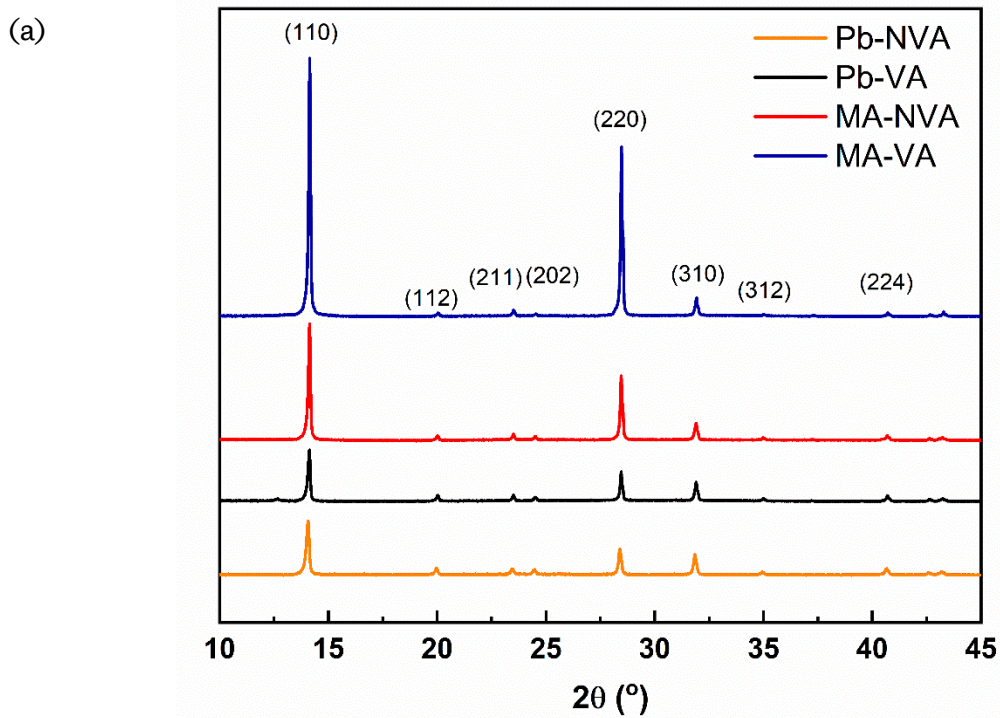


Figure S6: (a) XRD of as spin cast MAI excess MAPbI_3 without any thermal or solvent treatment. (b) Normalized (110) XRD peak of MA-NVA and MA-VA showing reduced FWHM in MA-VA implying grain growth post solvent vapour annealing.



(b)

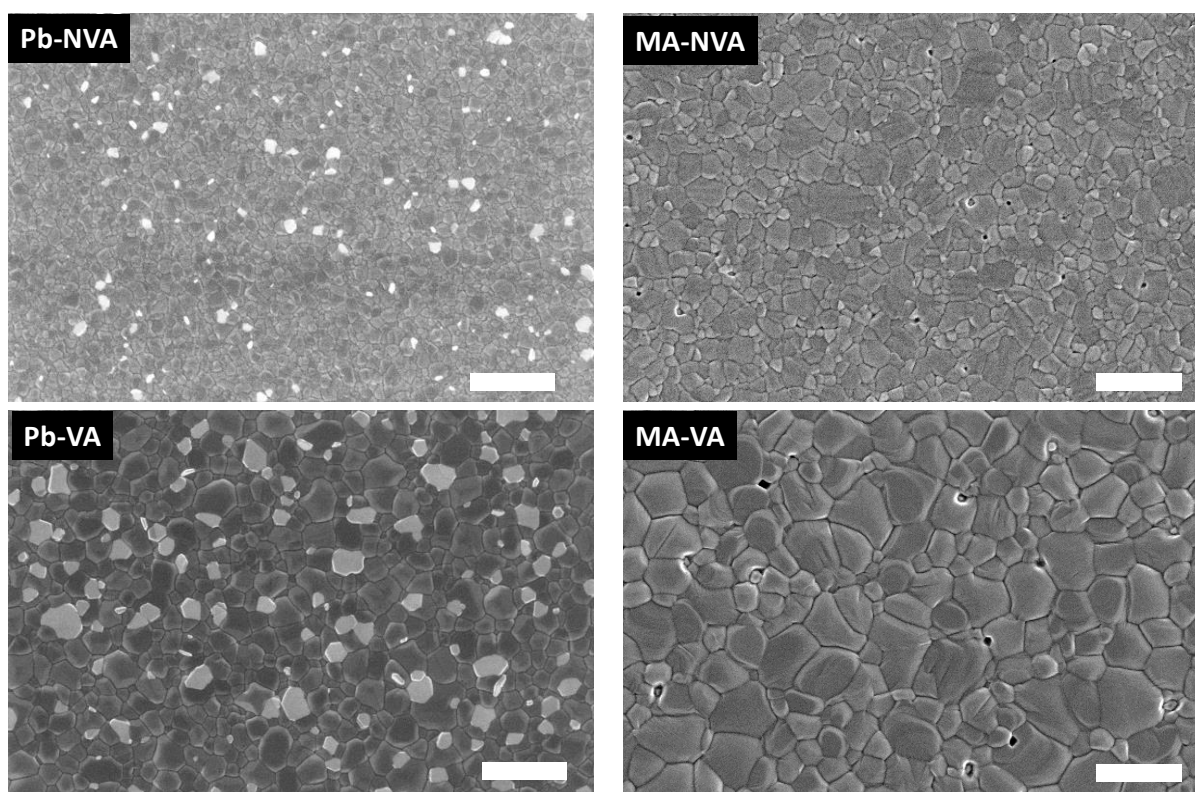


Figure S7: (a) XRD of PbI_2 -excess and MAI-excess compositions with and without solvent vapour annealing. (b) SEM of PbI_2 -excess and MAI-excess compositions with and without solvent vapour annealing. In all cases, the scale bar represents $1\ \mu\text{m}$.

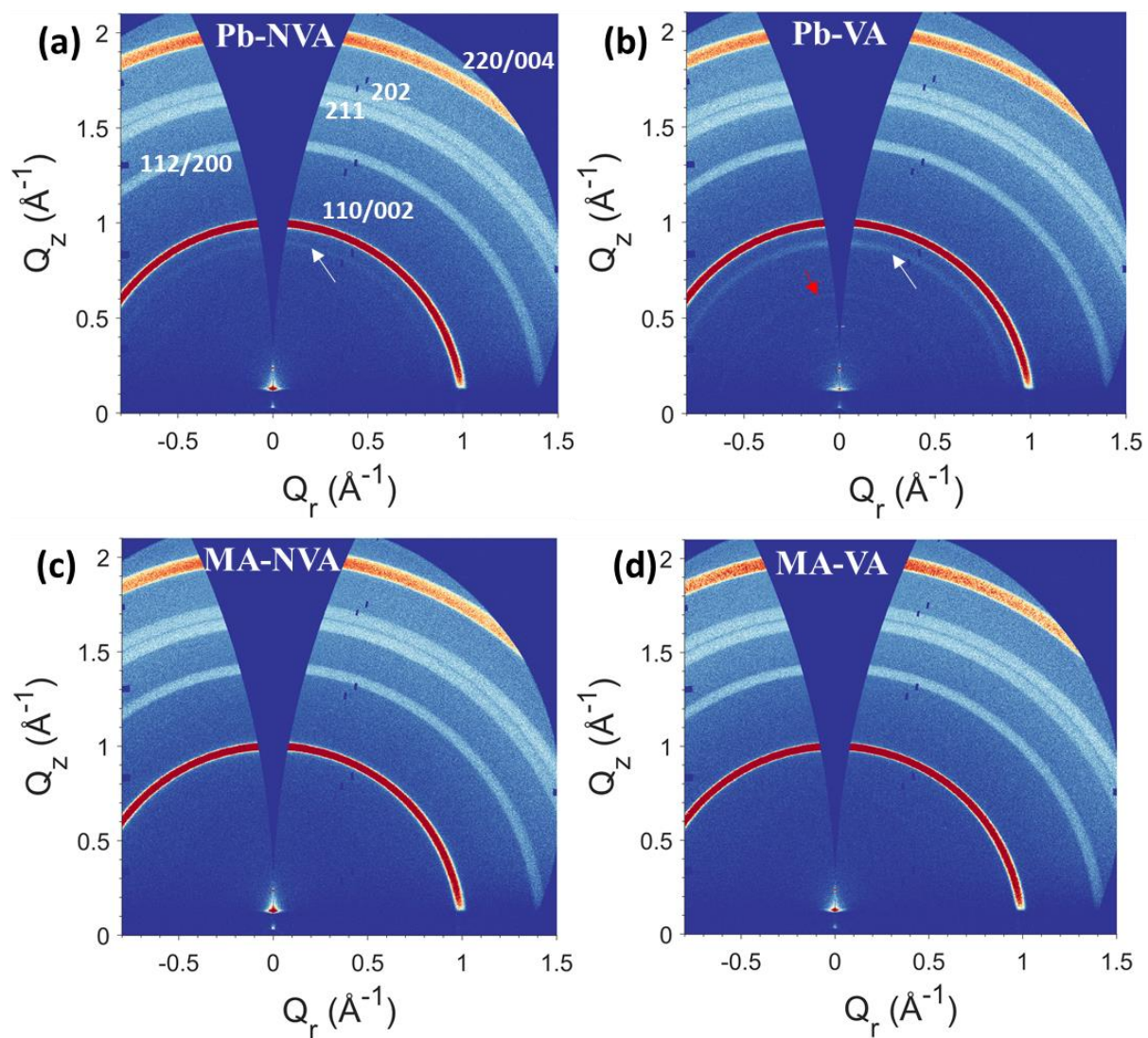


Figure S8: Grazing incidence (1.5°) wide angle X-ray scattering 2D patterns collected for a) Pb-NVA, b) Pb-VA, c) MA-NVA and d) MA-VA films. Here, scatter from Pbl_2 is indicated by a white arrow in the Pbl_2 excess samples. The red arrow shows additional weakly scattering features at low Q (or low 2θ) for Pb-VA.

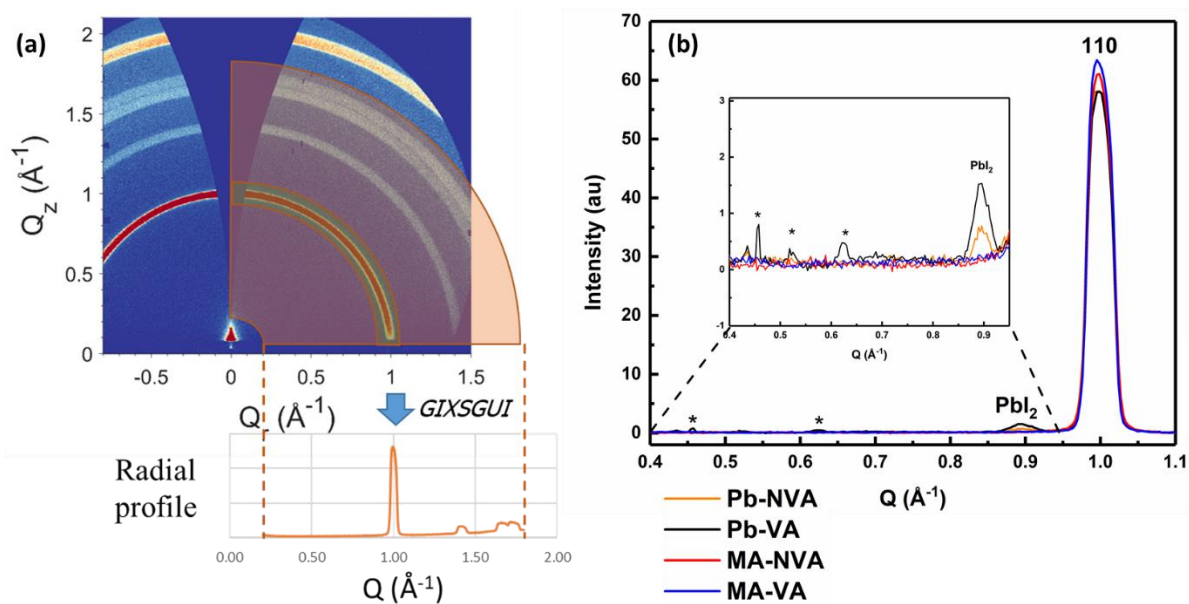


Figure S9: (a) Schematic of the reduction of the 2D detector scattering patterns to a profile of azimuthally integrated intensity data (integrated for all χ as a function of Q), also known as a 'cake remapping'. (b) 1D profiles for all samples obtained after azimuthal integration of 2D patterns in Figure S8 (a) – (d). Inset shows the magnified view of 1D radial profile in the range of $Q = 0.4$ to 0.95 \AA^{-1} (equivalent to $2\theta = 5.6^\circ$ to 13.5°).

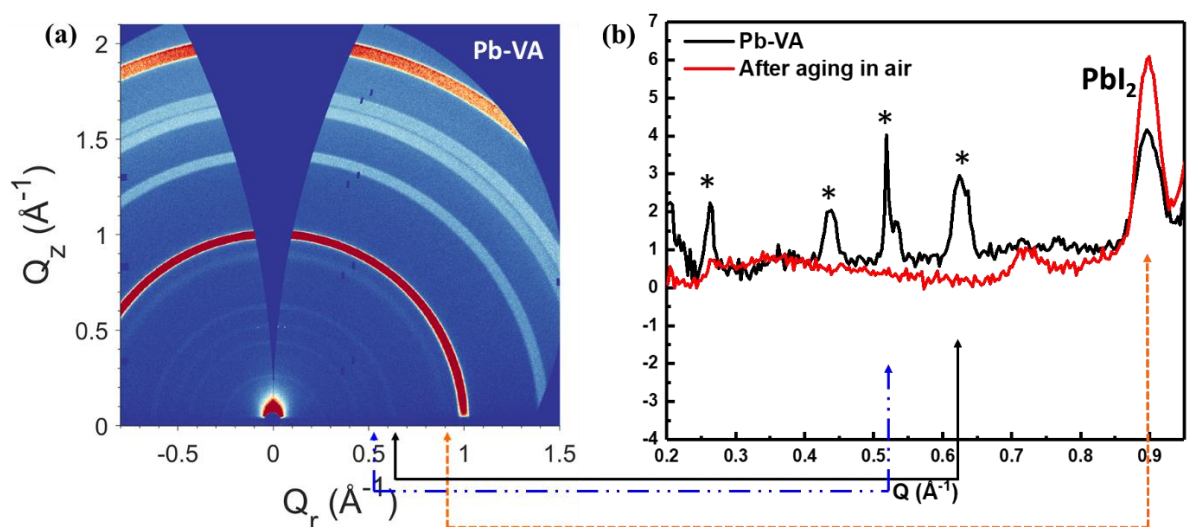


Figure S10: (a) Extended accumulation grazing incidence (0.5°) wide angle X-ray 2D scattering pattern of PbI_2 excess solvent vapour annealed film. (b) 1D radial profile of 2D pattern in the range of $Q = 0.2$ to 0.95 \AA^{-1} , showing crystalline PbI_2 and additional peaks at low Q marked with asterisks (*). These features were no longer present after overnight storage in ambient air, as shown in the radial profile for an aged sample (red). We also observed a small increase in the PbI_2 scattering signal; a finding consistent with our proposed mechanism shown in Figure 9 of the main paper.

Composition	Device code	Scan	Voc (V)	Jsc (mA/cm ²)	FF(%)	Eff(%)
Pb excess	Pb-NVA	Fw	1.06	20.30	57.2	12.3
		Rev	1.07	20.40	73.6	16.0
Pb excess	Pb-VA	Fw	1.01	20.32	33.7	6.91
		Rev	1.06	20.18	74.1	15.8
Stoichiometric	MAPI-NVA	Fw	1.06	20.7	70.5	15.5
		Rev	1.07	20.7	77.2	17.1
Stoichiometric	MAPI-VA	Fw	1.03	20.54	64.2	13.6
		Rev	1.05	20.51	76.3	16.4
MAI-excess	MA-NVA	Fw	1.10	20.98	70.2	16.2
		Rev	1.10	21.00	77.2	17.8
MAI-excess	MA-VA	Fw	1.07	20.93	71.0	15.9
		Rev	1.09	20.91	77.8	17.7

Table S1 Photovoltaic parameters of best devices for each case. –NVA and –VA stand for non-vapour annealed and vapour annealed respectively. Pb-, MA- and MAPI- compositions correspond to lead excess, MAI excess and stoichiometric MAPbI₃ respectively.

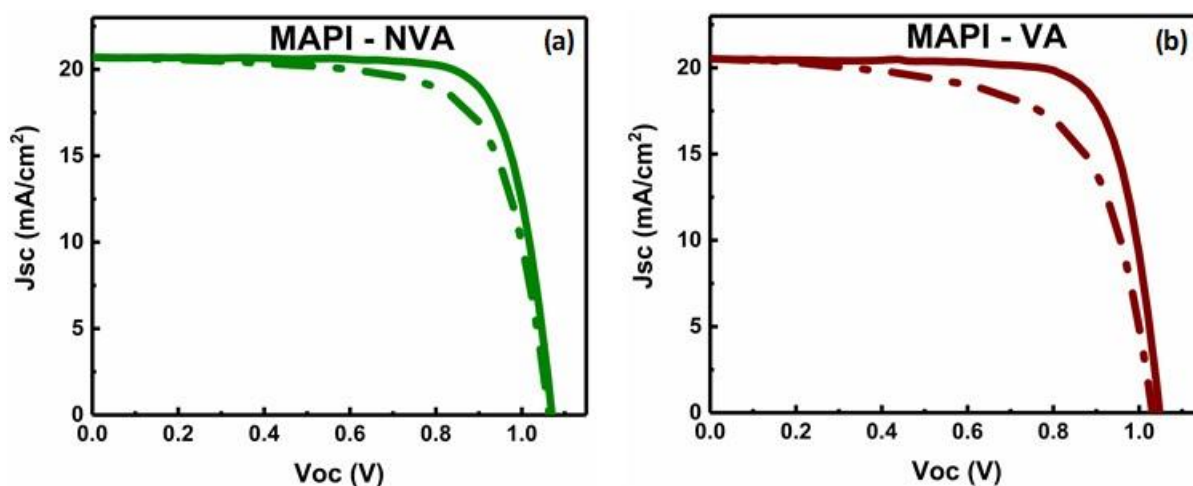


Figure S11: J-V curves of stoichiometric (MAI:PbI₂ = 1:1) MAPbI₃ based devices (a) without and (b) with solvent-vapour annealing.

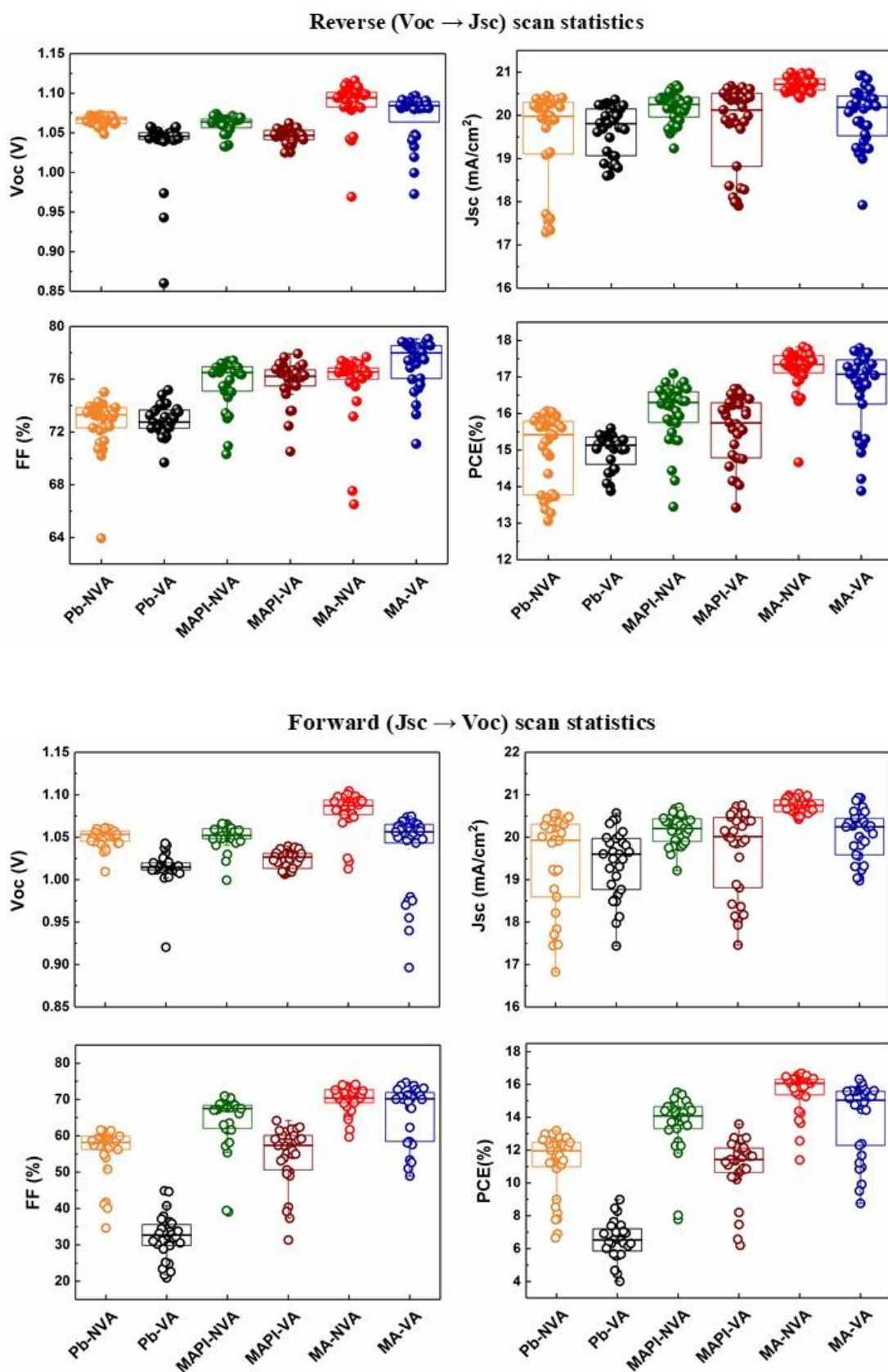


Figure S12: Reverse and forward scan statistic of lead excess (Pb-), stoichiometric (MAPI-) and MAI excess (MA-) compositions in planar architecture without (-NVA) or with (-VA) solvent vapour annealing. Horizontal line in the box shows the median value.

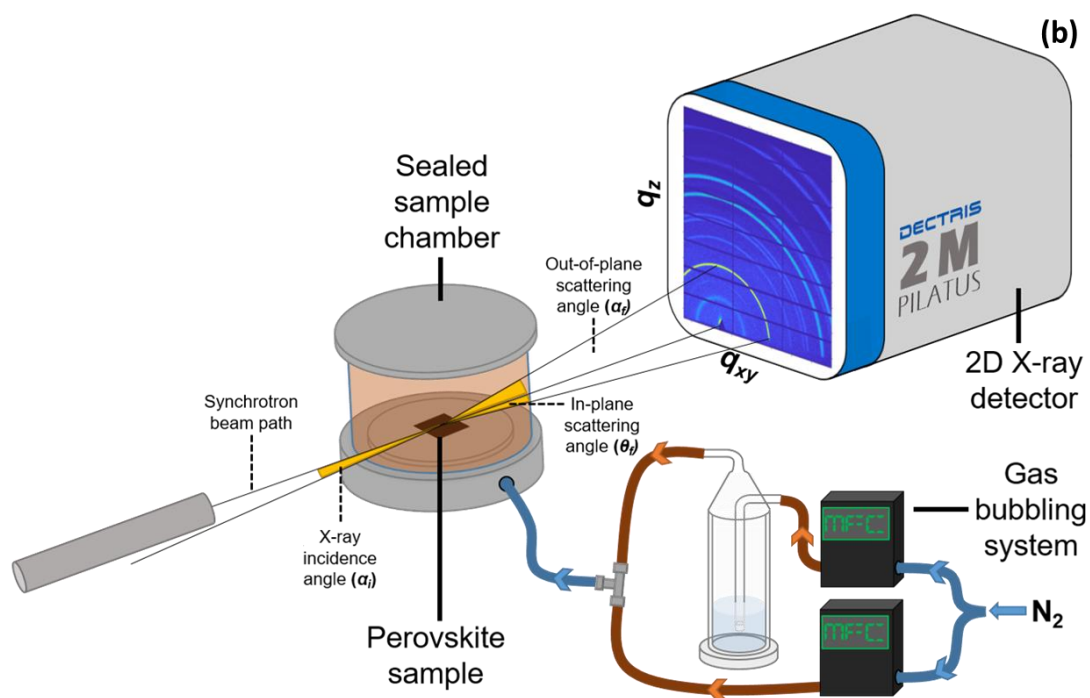
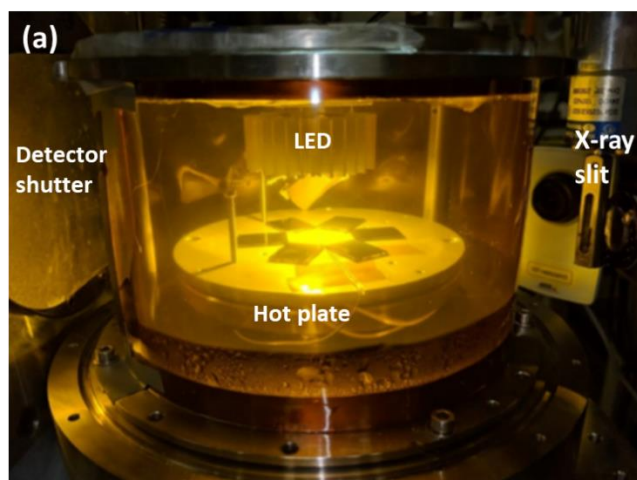


Figure S13: (a) Photograph of moisture chamber that was used to study degradation using in situ GIWAXS measurements on perovskite films. The chamber walls were composed of a thick Kapton film that is transparent to X-rays. (b) Schematic of the in situ GIWAXS measurements performed at the Diamond Light Source I22 synchrotron beamline with an X-ray beam energy set at 10 keV. Here the beam was incident at 0.3° with scattered X-rays detected using a Pilatus P3-2M detector.

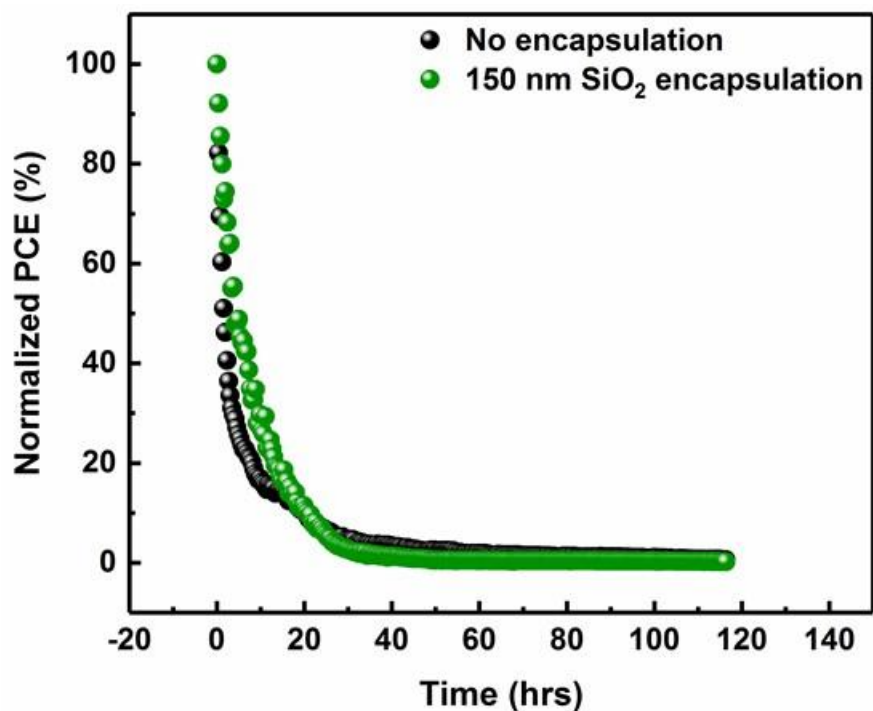


Figure S14: Continuous illumination device lifetime (PCE vs time) of Pb-excess solvent vapour annealed (Pb-VA) composition without (black) and with (green) 150 nm SiO₂ encapsulation.

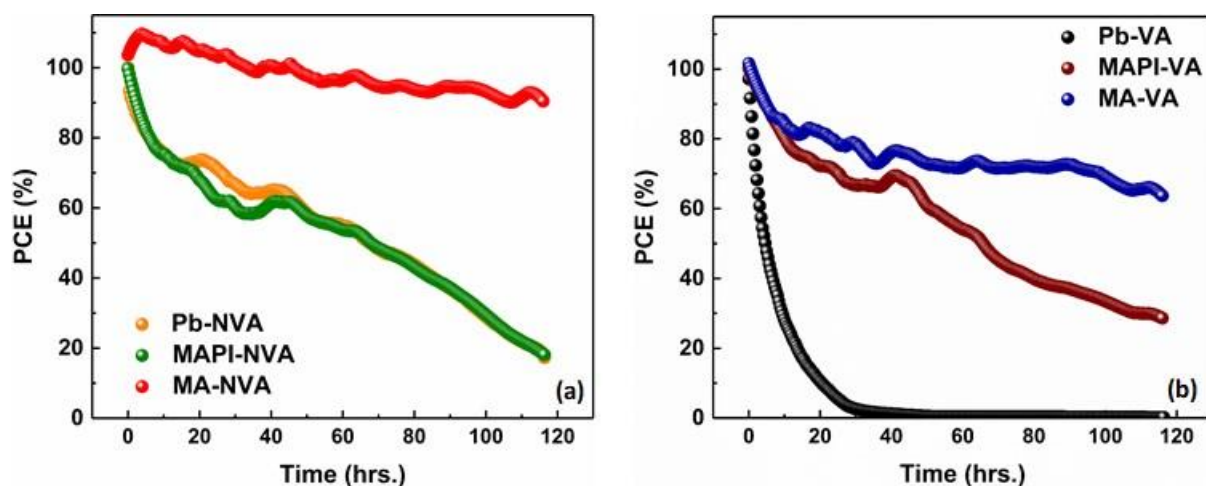


Figure S15: Composition dependence of continuous illumination device lifetimes (PCE vs time) (a) without and (b) with solvent vapour annealing. Compositions are abbreviated as Pb-excess (Pb-), Stoichiometric (MAPI-) and MA-excess (MA-).

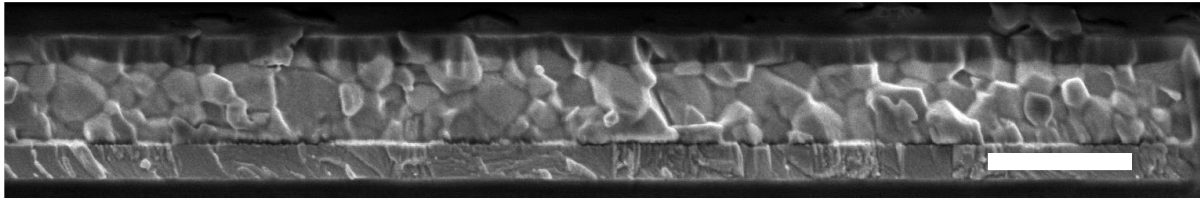


Figure S16: Representative device cross-section of 6% PbI_2 -excess (Pb-NVA) device before subjecting to 120 hrs lifetime testing. The grain structure within the perovskite film is well defined, with grain sizes ranging from 100 – 300 nm. Scale bar is 500 nm.

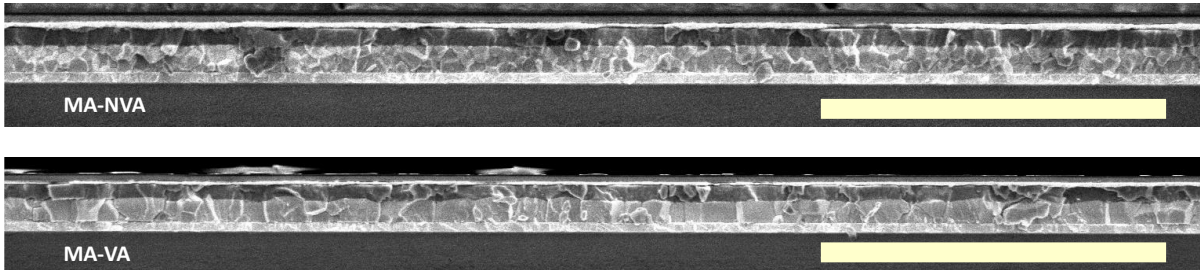
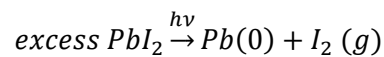


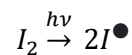
Figure S17: Cross-sectional SEM images of MA-NVA and MA-VA on a wide scale (Scale bar: 4 μm). MA-NVA did not show any voids at the ETL-perovskite interface, implying good mechanical contact between the perovskite film and ETL. This behaviour persisted even after solvent vapour annealing as evident from the cross-sectional SEM of MA-VA.

Scheme S18: Degradation pathways in PbI_2 -excess perovskite devices under illumination.^{43,44}

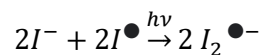
1. Under illumination, the excess PbI_2 undergoes photodecomposition process according to



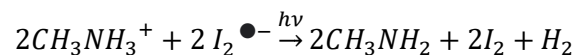
2. Iodine gas formed in process 1 undergoes atomic iodide generation^{44,65} under illumination



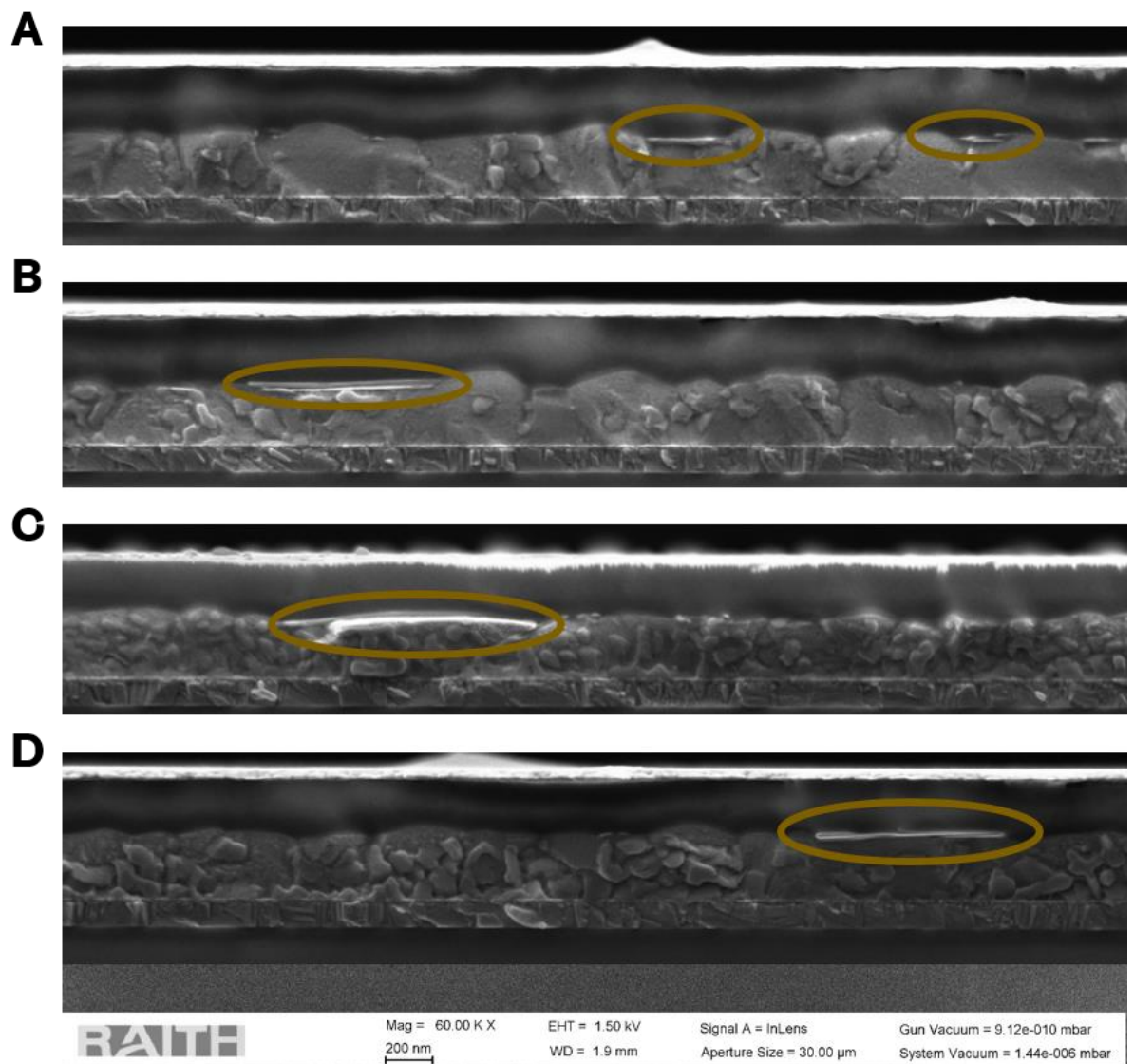
3. Atomic iodine reacts with mobile iodide species (I^-) from $MAPbI_3$



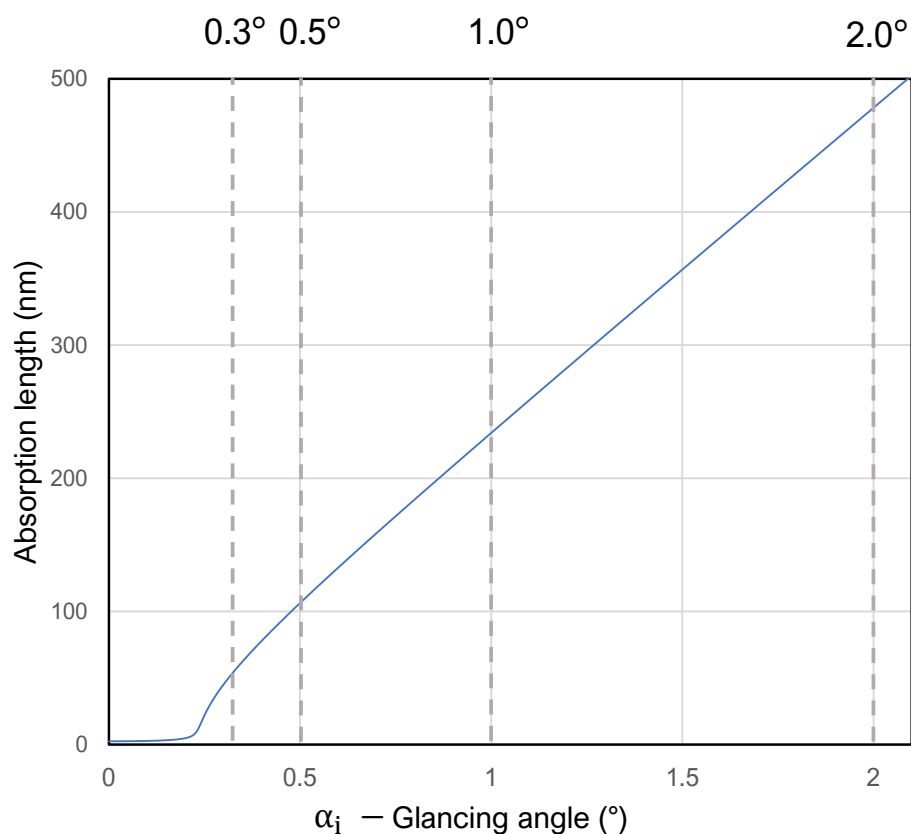
4. Mobile MA^+ ($CH_3NH_3^+$) ions react with $I_2^{\bullet-}$ species to form gaseous methylamine (CH_3NH_2), iodine (I_2) and hydrogen (H_2).



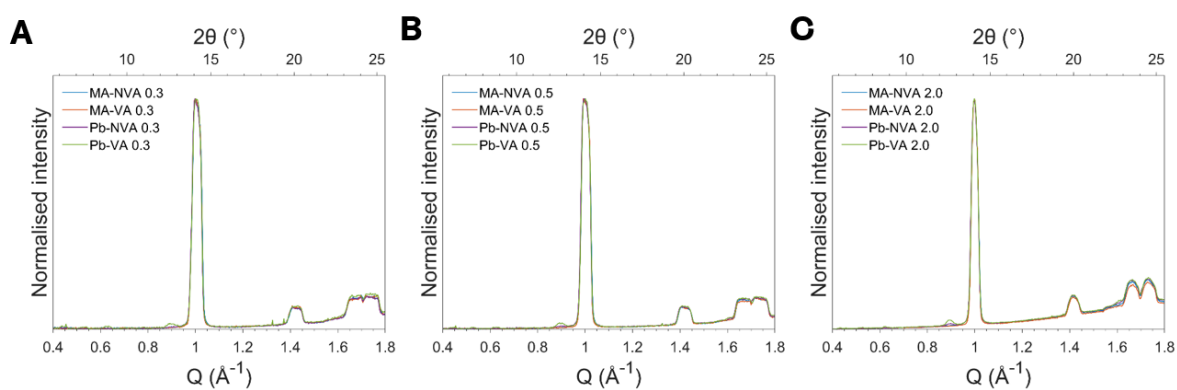
5.4: Additional data



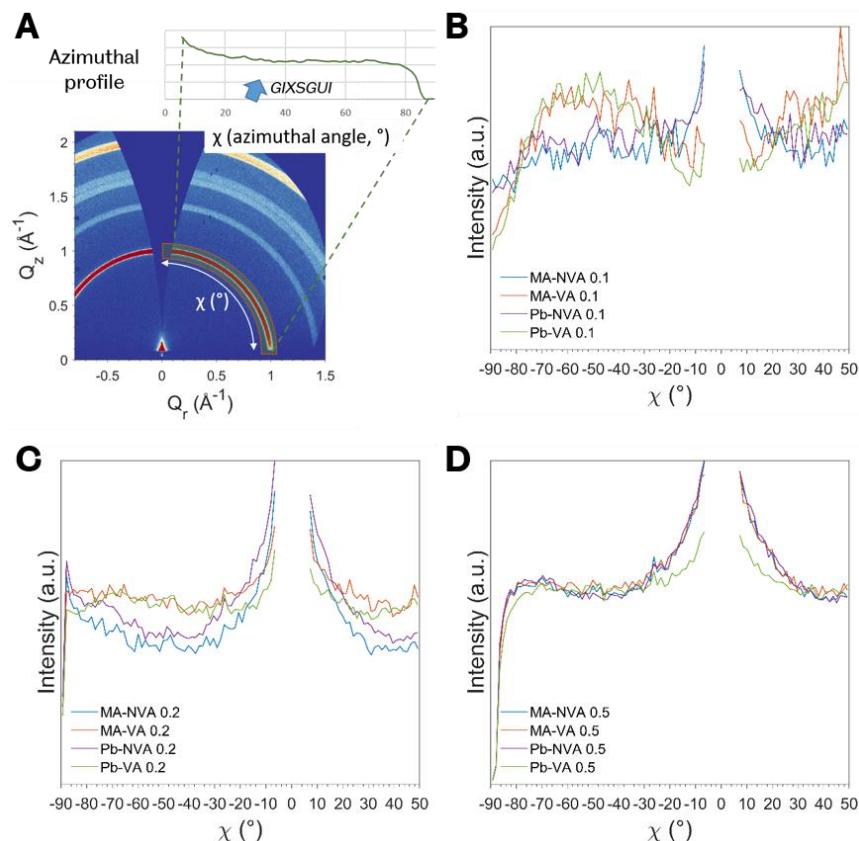
Additional Figure 1: Further cross-sectional SEM images showing the formation of flat, bright platelets at the top region of the perovskite active layer for a Pb-VA sample. These regions of PbI_2 are seen in *pc*-AFM images as non-conducting, with no photogenerated carriers produced (Figure 1). Some roughness and small features are seen in the grain surface for images C and D as a result of fracturing of the perovskite layer (during substrate breaking for SEM sample preparation), masking the true large grain structure which is better represented in parts A and B. These insulating regions may also somehow contribute to the hysteretic effects described in the manuscript.



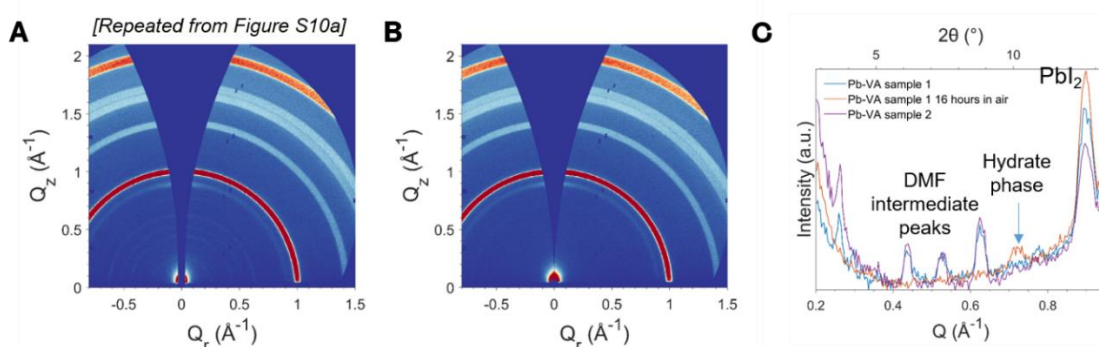
Additional Figure 2: the calculated penetration depth x (normal to the sample surface) for the Ga MetalJet X-ray beam, indicating (by the Beer-Lambert law) the depth at which the beam intensity $I(x)$ has dropped to $1/e$ of its initial intensity (I_0). This is calculated using the method of B.L. Henke,⁶⁷ with the material composition CH_3NPbI_3 and taking the MAPbI_3 density to be 4.16g/cm^3 .⁶⁸



Additional Figure 3: Further azimuthally integrated scattering profiles for different incidence angles (α_i) A) = 0.3°, B) = 0.5°, and C) = 2°. Here, PbI_2 scatter is observed $\sim Q = 0.9 \text{ \AA}^{-1}$ and low intensity peaks from an intercalated DMF phase can be seen in the range $0.4 < Q < 0.7 \text{ \AA}^{-1}$. This data illustrates a small angle-dependent (penetration depth) change in the scattering intensity from the weakly scattering DMF intermediate features which are more visible at shallower angles, suggesting they may be concentrated towards the film top surface.



Additional Figure 4: Crystal orientation as a function of sample depth. A) Shows the extraction of azimuthal profiles (radial integrations) of the $0.95 < Q < 1.05 \text{ \AA}^{-1}$ MAPbI_3 (110)/(002) scattering at α_i (grazing incidence) angles of B) 0.1° , C) 0.2° and D) 0.5° corresponding to $1/e$ absorption lengths normal to the sample surface of 3, 5 and 106 nm respectively. Parts B and C indicate the top surface is oriented with slightly greater out-of-plane scattering intensity for the MA-NVA and MA-VA samples. In contrast the Pb-NVA and Pb-VA samples show a broad maximum around $\chi = 50^\circ$, indicating some variation in the surface termination of the crystal.



Additional Figure 5: 2D GIWAXS scattering patterns of A) an additional freshly prepared Pb-VA sample (repeat measurement of Figure S10a to confirm the presence of the same scattering features), B) Pb-VA sample after 16 hours of ambient air exposure. C) shows the radial profiles through both samples and the duplicate sample (Figure S10a). As discussed earlier, the additional features at low Q for the sample which has not been exposed to air are attributed to DMF intercalation. After aging in air, a small peak is observed at $Q = 0.72 \text{ \AA}^{-1}$ which we attribute to some hydrate formation and the PbI_2 intensity has also increased, confirming the two decomposition products of the intermediate phase.

5.5: References

1. M. Ke, W. Longlong, L. Zhou, W. Xiao, X. Qiaofei, H. Youdi, H. Sanfeng, L. Xiaolong, L. Tao and C. Gang, *Advanced Materials*, 2018, **30**, 1706401.
2. P. K. Nayak, S. Mahesh, H. J. Snaith and D. Cahen, *Nature Reviews Materials*, 2019, **4**, 269-285.
3. A. K. Jena, A. Kulkarni and T. Miyasaka, *Chemical Reviews*, 2019, **119**, 3036-3103.
4. R. Wang, M. Mujahid, Y. Duan, Z.-K. Wang, J. Xue and Y. Yang, *Advanced Functional Materials*, **0**, 1808843.
5. W. A. Dunlap-Shohl, Y. Zhou, N. P. Padture and D. B. Mitzi, *Chemical Reviews*, 2019, **119**, 3193-3295.
6. NREL, Best Research-Cell Efficiency Chart <https://www.nrel.gov/pv/cell-efficiency.html>, 2020, Accessed April 2020.
7. C. C. Boyd, R. Cheacharoen, T. Leijtens and M. D. McGehee, *Chemical Reviews*, 2019, **119**, 3418-3451.
8. D. A. Egger, A. Bera, D. Cahen, G. Hodes, T. Kirchartz, L. Kronik, R. Lovrincic, A. M. Rappe, D. R. Reichman and O. Yaffe, *Advanced Materials*, 2018, **30**, 1800691.
9. J.-W. Lee, S.-H. Bae, N. De Marco, Y.-T. Hsieh, Z. Dai and Y. Yang, *Materials Today Energy*, 2018, **7**, 149-160.
10. Y. Shao, Y. Fang, T. Li, Q. Wang, Q. Dong, Y. Deng, Y. Yuan, H. Wei, M. Wang, A. Gruverman, J. Shield and J. Huang, *Energy & Environmental Science*, 2016, **9**, 1752-1759.
11. J. S. Yun, J. Seidel, J. Kim, A. M. Soufiani, S. Huang, J. Lau, N. J. Jeon, S. I. Seok, M. A. Green and A. Ho-Baillie, *Advanced Energy Materials*, 2016, **6**, 1600330.
12. Q. Wang, B. Chen, Y. Liu, Y. Deng, Y. Bai, Q. Dong and J. Huang, *Energy & Environmental Science*, 2017, **10**, 516-522.
13. T. Niu, J. Lu, R. Munir, J. Li, D. Barrit, X. Zhang, H. Hu, Z. Yang, A. Amassian, K. Zhao and S. Liu, *Advanced Materials*, 2018, **30**, 1706576.
14. A.-F. Castro-Méndez, J. Hidalgo and J.-P. Correa-Baena, *Advanced Energy Materials*, 2019, **0**, 1901489.
15. T. Leijtens, K. Bush, R. Cheacharoen, R. Beal, A. Bowring and M. D. McGehee, *Journal of Materials Chemistry A*, 2017, **5**, 11483-11500.
16. R. Xia, Z. Fei, N. Drigo, F. D. Bobbink, Z. Huang, R. Jasiūnas, M. Franckevičius, V. Gulbinas, M. Mensi, X. Fang, C. Roldán-Carmona, M. K. Nazeeruddin and P. J. Dyson, *Advanced Functional Materials*, 2019, **0**, 1902021.
17. P.-W. Liang, C.-Y. Liao, C.-C. Chueh, F. Zuo, S. T. Williams, X.-K. Xin, J. Lin and A. K. Y. Jen, *Advanced Materials*, 2014, **26**, 3748-3754.
18. Z. Xiao, Q. Dong, C. Bi, Y. Shao, Y. Yuan and J. Huang, *Advanced Materials*, 2014, **26**, 6503-6509.
19. J. Liu, C. Gao, X. He, Q. Ye, L. Ouyang, D. Zhuang, C. Liao, J. Mei and W. Lau, *ACS Applied Materials & Interfaces*, 2015, **7**, 24008-24015.
20. X. Cao, L. Zhi, Y. Li, F. Fang, X. Cui, L. Ci, K. Ding and J. Wei, *ACS Applied Energy Materials*, 2018, **1**, 868-875.
21. S. K. Yadavalli, Y. Zhou and N. P. Padture, *ACS Energy Letters*, 2018, **3**, 63-64.
22. J.-Y. Ma, H.-J. Yan, M.-H. Li, J.-K. Sun, Y.-X. Chen, D. Wang and J.-S. Hu, *Nanoscale*, 2020, **12**, 7759-7765.
23. H. Khassaf, S. K. Yadavalli, Y. Zhou, N. P. Padture and A. I. Kingon, *The Journal of Physical Chemistry C*, 2019, **123**, 5321-5325.
24. S.-H. Chin, J. W. Choi, H. C. Woo, J. H. Kim, H. S. Lee and C.-L. Lee, *Nanoscale*, 2019, **11**, 5861-5867.
25. A. M. Zeidell, C. Tyznik, L. Jennings, C. Zhang, H. Lee, M. Guthold, Z. V. Vardeny and O. D. Jurchescu, *Advanced Electronic Materials*, 2018, **4**, 1800316.
26. W. Li, S. K. Yadavalli, D. Lizarazo-Ferro, M. Chen, Y. Zhou, N. P. Padture and R. Zia, *ACS Energy Letters*, 2018, **3**, 2669-2670.
27. M. Wong-Stringer, O. S. Game, J. A. Smith, T. J. Routledge, B. A. Alqurashy, B. G. Freestone, A. J. Parnell, N. Vaenas, V. Kumar, M. O. A. Alawad, A. Iraqi, C. Rodenburg and D. G. Lidzey, *Advanced Energy Materials*, 2018, **8**, 1801234.
28. N. K. Noel, S. N. Habisreutinger, B. Wenger, M. T. Klug, M. T. Hörantner, M. B. Johnston, R. J. Nicholas, D. T. Moore and H. J. Snaith, *Energy & Environmental Science*, 2017, **10**, 145-152.
29. A. J. Ramadan, N. K. Noel, S. Fearn, N. Young, M. Walker, L. A. Rochford and H. J. Snaith, *Chemistry of Materials*, 2018, **30**, 7737-7743.
30. B.-w. Park, N. Kedem, M. Kulbak, D. Y. Lee, W. S. Yang, N. J. Jeon, J. Seo, G. Kim, K. J. Kim, T. J. Shin, G. Hodes, D. Cahen and S. I. Seok, *Nature Communications*, 2018, **9**, 3301.
31. C. Roldán-Carmona, P. Gratia, I. Zimmermann, G. Grancini, P. Gao, M. Graetzel and M. K. Nazeeruddin, *Energy & Environmental Science*, 2015, **8**, 3550-3556.
32. T. Meier, T. P. Gujar, A. Schönleber, S. Olthof, K. Meerholz, S. van Smaalen, F. Panzer, M. Thelakkat and A. Köhler, *Journal of Materials Chemistry C*, 2018, **6**, 7512-7519.
33. Q. Chen, H. Zhou, T.-B. Song, S. Luo, Z. Hong, H.-S. Duan, L. Dou, Y. Liu and Y. Yang, *Nano Letters*, 2014, **14**, 4158-4163.
34. Y. Kutes, Y. Zhou, J. L. Bosse, J. Steffes, N. P. Padture and B. D. Huey, *Nano Letters*, 2016, **16**, 3434-3441.

35. S. Y. Leblebici, L. Leppert, Y. Li, S. E. Reyes-Lillo, S. Wickenburg, E. Wong, J. Lee, M. Melli, D. Ziegler, D. K. Angell, D. F. Ogletree, Paul D. Ashby, F. M. Toma, J. B. Neaton, I. D. Sharp and A. Weber-Bargioni, *Nat Energy*, 2016, **1**, 16093.
36. M. U. Rothmann, W. Li, J. Etheridge and Y.-B. Cheng, *Advanced Energy Materials*, 2017, **7**, 1700912.
37. N. C. Halder and T. R. Williams, *Solar Cells*, 1983, **8**, 201-223.
38. V. Kumar, J. Barbé, W. L. Schmidt, K. Tsevas, B. Ozkan, C. M. Handley, C. L. Freeman, D. C. Sinclair, I. M. Reaney, W. C. Tsoi, A. Dunbar and C. Rodenburg, *Journal of Materials Chemistry A*, 2018, **6**, 23578-23586.
39. A. A. Petrov, I. P. Sokolova, N. A. Belich, G. S. Peters, P. V. Dorovatovskii, Y. V. Zubavichus, V. N. Khrustalev, A. V. Petrov, M. Grätzel, E. A. Goodilin and A. B. Tarasov, *The Journal of Physical Chemistry C*, 2017, **121**, 20739-20743.
40. J. Luo, R. Z. Qiu, Z. S. Yang, Y. X. Wang and Q. F. Zhang, *RSC Advances*, 2018, **8**, 724-731.
41. A. Yi, S. Chae, H. Lee and H. J. Kim, *Journal of Materials Chemistry A*, 2019, **7**, 27267-27277.
42. M. V. Khenkin, A. K. M. E. A. Katz and I. Visoly-Fisher, *Energy & Environmental Science*, 2019, **12**, 550-558.
43. E. J. Juarez-Perez, L. K. Ono, M. Maeda, Y. Jiang, Z. Hawash and Y. Qi, *Journal of Materials Chemistry A*, 2018, **6**, 9604-9612.
44. S. Wang, Y. Jiang, Emilio J. Juarez-Perez, Luis K. Ono and Y. Qi, *Nat Energy*, 2016, **2**, 16195.
45. Y. Yuan and J. Huang, *Accounts of Chemical Research*, 2016, **49**, 286-293.
46. F. Ambrosio, D. Meggiolaro, E. Mosconi and F. De Angelis, *Journal of Materials Chemistry A*, 2020, **8**, 6882-6892.
47. B.-A. Chen, J.-T. Lin, N.-T. Suen, C.-W. Tsao, T.-C. Chu, Y.-Y. Hsu, T.-S. Chan, Y.-T. Chan, J.-S. Yang, C.-W. Chiu and H. M. Chen, *ACS Energy Letters*, 2017, **2**, 342-348.
48. K. M. Fransishyn, S. Kundu and T. L. Kelly, *ACS Energy Letters*, 2018, **3**, 2127-2133.
49. Y. Guo, K. Shoyama, W. Sato, Y. Matsuo, K. Inoue, K. Harano, C. Liu, H. Tanaka and E. Nakamura, *Journal of the American Chemical Society*, 2015, **137**, 15907-15914.
50. Y. Zhang, S.-G. Kim, D. Lee, H. Shin and N.-G. Park, *Energy & Environmental Science*, 2019, **12**, 308-321.
51. L. T. Schelhas, Z. Li, J. A. Christians, A. Goyal, P. Kairys, S. P. Harvey, D. H. Kim, K. H. Stone, J. M. Luther, K. Zhu, V. Stevanovic and J. J. Berry, *Energy & Environmental Science*, 2019, **12**, 1341-1348.
52. A. Cicciooli and A. Latini, *The Journal of Physical Chemistry Letters*, 2018, **9**, 3756-3765.
53. G. P. Nagabhushana, R. Shivaramaiah and A. Navrotsky, *Proceedings of the National Academy of Sciences*, 2016, **113**, 7717.
54. Y. Zhao, W. Zhou, H. Tan, R. Fu, Q. Li, F. Lin, D. Yu, G. Walters, E. H. Sargent and Q. Zhao, *The Journal of Physical Chemistry C*, 2017, **121**, 14517-14523.
55. T. Zhang, X. Meng, Y. Bai, S. Xiao, C. Hu, Y. Yang, H. Chen and S. Yang, *Journal of Materials Chemistry A*, 2017, **5**, 1103-1111.
56. B. Conings, J. Drijkoningen, N. Gauquelin, A. Babayigit, J. D'Haen, L. D'Olieslaeger, A. Ethirajan, J. Verbeeck, J. Manca, E. Mosconi, F. D. Angelis and H.-G. Boyen, *Advanced Energy Materials*, 2015, **5**, 1500477.
57. C. Pareja-Rivera, A. L. Solís-Camero, M. Sánchez-Torres, E. Lima and D. Solís-Ibarra, *ACS Energy Letters*, 2018, **3**, 2366-2367.
58. L. Fangzhou, D. Qi, W. M. Kwong, D. A. B., N. Annie, R. Zhiwei, S. Qian, S. Charles, C. W. Kin, W. Jian, N. A. M. Ching, L. Changzhong, L. Hangkong, S. Kaimin, W. Chengrong, S. Huimin and D. Junfeng, *Advanced Energy Materials*, 2016, **6**, 1502206.
59. T. P. Gujar, T. Unger, A. Schönleber, M. Fried, F. Panzer, S. van Smaalen, A. Köhler and M. Thelakkat, *Physical Chemistry Chemical Physics*, 2018, **20**, 605-614.
60. J. Filik, A. W. Ashton, P. C. Y. Chang, P. A. Chater, S. J. Day, M. Drakopoulos, M. W. Gerring, M. L. Hart, O. V. Magdysyuk, S. Michalik, A. Smith, C. C. Tang, N. J. Terrill, M. T. Wharmby and H. Wilhelm, *Journal of Applied Crystallography*, 2017, **50**, 959-966.
61. Z. Jiang, *Journal of Applied Crystallography*, 2015, **48**, 917-926.
62. D. P. McMeekin, S. Mahesh, N. K. Noel, M. T. Klug, J. Lim, J. H. Warby, J. M. Ball, L. M. Herz, M. B. Johnston and H. J. Snaith, *Joule*, 2019, **3**, 387-401.
63. J.-a. Yang, A. Xiao, L. Xie, K. Liao, X. Deng, C. Li, A. Wang, Y. Xiang, T. Li and F. Hao, *Electrochimica Acta*, 2020, **338**, 135697.
64. J. Euvrard, O. Gunawan and D. B. Mitzi, *Advanced Energy Materials*, 2019, **9**, 1902706.
65. N. Pant, A. Kulkarni, M. Yanagida, Y. Shirai, T. Miyasaka and K. Miyano, *Advanced Materials Interfaces*, 2019, **7**, 1901748.
66. J. Chang, H. Zhu, J. Xiao, F. H. Isikgor, Z. Lin, Y. Hao, K. Zeng, Q.-H. Xu and J. Ouyang, *Journal of Materials Chemistry A*, 2016, **4**, 7943-7949.
67. Henke, B. L., Gullikson, E. M., & Davis, J. C. (1993). *Atomic data and nuclear data tables*, 54(2), 181-342
68. C. C. Stoumpos, C. D. Malliakas and M. G. Kanatzidis, *Inorganic Chemistry*, 2013, **52**, 9019-9038.

Chapter 6

Understanding the role of methylamine in the crystallisation of halide perovskites using *in-situ* X-ray scattering

6.0: Publication Foreword

A particularly fascinating method for rapid crystallisation of perovskite materials uses methylamine (CH_3NH_2) gas to dissolve and then reform the solid phase. Methylamine can fully recrystallise MAPbI_3 films, with liquification occurring at modest vapour pressures – completely overcoming the solid-state bonding - and films spontaneously convert back to a photoactive film upon removal from the gas environment. The perovskite reforms with crystallographic orientation, which has proven critical to achieve the highest performance for the best photovoltaic absorbers (GaAs and Si), either as uniaxial or epitaxial growth. Methylamine has also been used in novel solvent systems by effectively trapping the liquid state inside another solvent, which is another approach for fast crystallisation with huge potential. The mechanisms for these industrially applicable processes are not well understood in literature, so in this chapter, we attempted to bridge the understanding of solution chemistry and how it relates to crystal formation. The primary investigation involved monitoring the recrystallisation process *in situ* using GIWAXS from synchrotron radiation, allowing for 0.1 s time resolution. With this we were able to identify several possible previously undetected intermediate phases which play a crucial role in the film formation. This was repeated at three temperatures in the available window (above which the film spontaneously crystallised) to understand the nucleation and growth kinetics. The conclusion we have drawn is that methylamine plays a dual role, first in hydrogen-bonding with methylammonium, but secondly in solubilising the Pb directly as a donor ligand. In the final section, the reasons for this process being ineffectual with formamidinium perovskites is investigated and explained. We conclude that novel vapour treatments will be required to expand the range of perovskite compositions possible with this kind of recrystallisation process or related solution chemistries.

6.1: Author contributions

JAS conceived and coordinated the project, fabricated all samples, devices and analysed all data. OS acquired FTIR and absorption data, assisted with solution samples and acquired the GIWAXS in Figure 6. AS performed rigid body modelling and related structural refinements. RK acquired *ex-situ* GIWAXS data and assisted with synchrotron measurements. NM performed DFT calculations. MOK assisted with beamline and NMR measurements. JM assisted with NMR measurements and analysis. MF performed SAXS and XRD measurements. HN assisted with *in-situ* GIWAXS and data analysis for Figure 6. JR assisted with beamline measurements. AD acquired NMR data. NRM assisted with structural analysis. DW, DB, EU, AA, OG and DGL supervised various aspects of the project.

6.2 Publication: Understanding the role of methylamine in the crystallisation of halide perovskites using *in-situ* X-ray scattering

Joel A. Smith,¹ Oleksandra Shargaieva,² Adam Shnier,³ Rachel Kilbride,¹ Natalia Martsinovich,⁴ Mary O’Kane,¹ Jorge Mielgo,⁵ Marion Flatken,⁵ Hampus Näsström,² Jonathan Rawle,⁶ André Dallman,⁷ Nik Reeves-Mclaren,⁸ Daniel Wamwangi,⁹ David Billing,³ Eva Unger,² Antonio Abate,⁵ Onkar Game,¹ and David G. Lidzey.^{1*}

1) Department of Physics and Astronomy, University of Sheffield, Sheffield, S3 7RH, UK.

2) Young Investigator Group ‘Hybrid Materials Formation and Scaling’, Helmholtz-Zentrum Berlin, Kekuléstraße 5, 12489 Berlin, Germany.

3) School of Chemistry, University of the Witwatersrand, Johannesburg 2050, South Africa.

4) Department of Chemistry, University of Sheffield, S3 7RH, UK.

5) Young Investigator Group ‘Active Materials and Interfaces for Stable Perovskite Solar Cells’, Helmholtz-Zentrum Berlin, Kekuléstraße 5, 12489 Berlin, Germany.

6) Beamline I07, Diamond Light Source, Harwell Campus, Oxfordshire OX11 0DE, UK

7) Institut für Chemie, Humboldt Universität zu Berlin, AG NMR, Berlin, Germany.

8) Department of Materials Science and Engineering, University of Sheffield, Sheffield, S1 3JD, UK.

9) School of Physics, University of the Witwatersrand, Johannesburg 2050, South Africa.

*e-mail: Prof. David G. Lidzey, d.g.lidzey@sheffield.ac.uk.

6.2.1: Abstract

Hybrid organic-inorganic perovskites offer the unique possibility to rapidly form high-quality crystalline semiconducting materials from solution at low temperatures. This can be achieved using methylamine (CH_3NH_2) for either vapour-induced recrystallisation ('healing') to enhance crystallographic orientation of the film, or as a component in volatile solvent systems, both of which enable perovskite formation in seconds. However, the beneficially fast crystallisation via these processing routes has proved a challenge for understanding the structural mechanisms underpinning them. In this work, the role of methylamine in structure formation in both use cases is systematically addressed using synchrotron-based *in-situ* X-ray scattering with high temporal resolution. For the vapour treatment solvation process, between the perovskite and a fully methylamine-solvated liquid, a metastable crystalline intermediate phase is identified (1). During recrystallisation, instead a textured intermediate nucleates (2) with strong dependency on processing temperature and methylamine vapour pressure. This subsequently influences the rapid conversion into MAPbI_3 , with the resulting textured film exhibiting complex non-uniaxial grain orientation which is masked by conventional 1D diffraction methods. The fully solvated liquid state is next compared to the acetonitrile/methylamine solvent system, highlighting the critical role of amine ligands for Pb solvation. With a high concentration of acetonitrile present, perovskite crystallisation can proceed via a more typical $\text{MA}_2\text{Pb}_3\text{I}_8$ -type intermediate phase (3), explaining the typically isotropic orientation via this route. Finally, *in-situ* X-ray scattering is used to rationalise the inability of methylamine vapour to heal formamidinium-perovskite films. This is found to be due to irreversible addition-elimination reactions between methylamine and formamidinium, resulting in bulky cations which are incorporated into two 1D iodoplumbate structures which form during liquification (4) and recrystallisation (5). This work progresses current understanding of perovskite structure formation from solution, highlighting the importance of synchrotron-based two-dimensional X-ray scattering data in analysing such material systems.

6.2.2: Introduction

Metal halide perovskite materials have been realised to great effect in numerous optoelectronic applications including X-ray detectors, LEDs and thermal sensors over the last decade of intense research. Enabled by their high absorption, long charge-carrier lifetimes and benign defects in many compositions, in photovoltaic solar cells their power conversion efficiency (PCE) has rapidly advanced to 25.5% in single-junction and 29.5% in tandem architectures; primarily through compositional control, interface engineering and surface

passivation.¹⁻⁴ Processing these materials from solution at low-temperature is a unique benefit, but leads to significant challenges in controlling the solution chemistry, deposition and crystallisation. As the field progresses, effective management of crystallographic orientation, such that lattice planes of the crystal are aligned with respect to the substrate, is becoming critical for maximising performance. It has been shown that films with crystallographically oriented grains exhibit enhanced carrier transport between charge selective interfaces.^{5,6} Sub-grain boundaries, dislocations and twinning domains within a crystal, or grain misorientation between adjacent crystals, can deteriorate optoelectronic performance through nonradiative losses or suppressed charge-carrier diffusion.⁷⁻⁹ Having a continuous grain structure between the selective contacts also simplifies trap passivation, enabling targeted approaches specific to the bulk and to vertical grain boundaries.³ Combined with uniaxial orientation, this would enable enhanced interface design and control by limiting the possible surface termination environments of the crystal.^{10,11} More generally, oriented growth may help to mitigate the formation of undesirable amorphous or crystalline secondary phases which, at best, do not contribute to photovoltaic activity or, more concerningly, act as centres for degradation or introduce loss channels within the active layer.¹²⁻¹⁴

Several strategies have been employed to fabricate oriented perovskite films, such as incorporating alkylammonium or alkylamine additives, solvent engineering and intermediate phase control.^{6,15,16} As the workhorse research material, methylammonium (CH_3NH_3^+ or MA^+) lead iodide (MAPbI_3) continues to provide insight for more exotic alloys with better suitability for commercial application. One such approach to control orientation in MAPbI_3 is the use of methylamine (CH_3NH_2 or MA^0) gas vapour interactions, whereby methylamine can dissolve the perovskite to a liquid phase ($\text{MA}^0\cdot\text{MAPbI}_3$) and upon removal of the MA^0 , films recrystallize with strong texture.¹⁷⁻¹⁹ This process has been expanded to a range of film compositions, notably by partial MACl incorporation,²⁰ as well as being investigated extensively for phase conversion and cation interchange phenomena.²¹⁻²⁵ Beyond gas-induced recrystallisation, methylamine-based precursor solutions,²⁶ typically using acetonitrile (ACN),²⁷⁻³² tetrahydrofuran (THF), ethanol (EtOH) or mixtures thereof,^{33,34} have also been developed with promising device performance and scalable coating approaches. Compositional variations of this system using Br-based,³⁵ mixed Pb-Sn,³⁰ and partially mixed-cation systems have also been reported,^{28,36} but very little has investigated texture formation from these systems. Both the vapour recrystallisation and related solution chemistries have huge potential to combine textured perovskite films with rapid crystallisation, which is a critical design parameter for the fabrication of roll-to-roll perovskite solar cells to be competitive with existing market technologies.³⁷⁻⁴⁰ However, for

these to become industrially-relevant processes, understanding the compositional limits, controlling the film formation, and expanding the range of potential gases and solvent systems is key; all of which require insight into the mechanism underlying these crystallization routes.

X-ray scattering techniques, particularly grazing incidence wide-angle X-ray scattering (GIWAXS), are gaining increasing usage in the metal halide perovskite field.^{41–44} Benefitting from extensive development in the small-angle regime for the analysis of thin film nanostructure formation,⁴⁵ the advent of higher flux lab-based X-ray sources and 2D detectors, analysis of film texture *ex situ* is ever more accessible.^{11,46–48} *In-situ* GIWAXS has proven invaluable for monitoring perovskite crystallization,^{16,49–52} phase behaviour,^{53–55} as well as material stability.^{56–58} Correlating device performance with material changes with *in operando* stability measurements has also been demonstrated with realistic device configurations.^{59–61} While these measurements are generally over several hours, the high flux available at synchrotron light sources, combined with ultrafast 2D hybrid photon counting detector response,⁴² allows for the analysis of rapid processes such as short-lived metastable phases,^{62,63} which can provide unique mechanistic insight.

In this work, we monitored the MA⁰ gas liquification and crystallisation processes *in situ* using synchrotron-based GIWAXS with high time resolution. During liquification, we identify an intermediate phase (I₁) which rapidly forms as the perovskite decomposes, which is metastable - determined by the MA⁰ vapour pressure and processing temperature. In the reverse recrystallisation process, at low temperatures a different face-sharing intermediate (I₂) is formed, which is not observed at higher temperatures. Nucleation becomes more homogeneous at higher temperature, resulting in multiple grain orientations which are highly constrained through interactions with adjacent crystal domains. Importantly, these orientations are hidden in typically employed 1D X-ray diffraction (XRD) measurements. The dissolved liquid state (MA⁰·MAPbI₃) is then investigated alongside an ACN MA⁰·MAPbI₃ solution using ¹H, ¹³C and ²⁰⁷Pb NMR, absorption and FTIR spectroscopies as well as small-angle X-ray scattering to rationalise the differences in structure and solvation between these two systems. From these measurements we propose a scheme for the dissolution process by methylamine in the ACN solution, with structural analysis of the intermediate phase via this route confirming the formation of MA⁰-Pb coordination covalent bonding. We show that scalable coating of this solvent system does not always result in film orientation due to the possibility of forming an intermediate which surprisingly incorporates ACN (I₃), despite its weak co-ordinating ability. Lastly, we explore methylamine gas treatment of formamidinium (HC(NH₂)₂⁺ or FA⁺) containing perovskites. We identify that during vapour exposure, an irreversible *in situ* reaction occurs

between MA⁰ and FA⁺. This results in a large cation (methyl formamidinium) forming which is directly incorporated into a 1D iodoplumbate phase (I₄) prior to MA⁰ solvation. A secondary reaction occurs in the solvate with prolonged MA⁰ vapour exposure, and during recrystallisation the reaction product (dimethyl formamidinium) forces a different configuration 1D iodoplumbate phase (I₅) to be adopted. This work comprehensively evaluates the behaviour of MA⁰ in perovskite crystallisation and solutions, providing new understanding of the phase behaviour possible in these material systems. Crucially we highlight the necessity of alternative solvent vapours for the expansion of vapour treatments and related solution chemistries for thermally-stable MA⁺-free compositions.

6.2.3: Results

6.2.3.1: *In-situ* recrystallisation

To investigate the effect of MA⁰ interaction with perovskite films, mimicking a typical lab-based vapour exposure method, we used a synchrotron-based *in-situ* GIWAXS setup depicted in **Figure S1** at the I07 beamline at Diamond Light Source.⁶⁴ With this configuration, samples were inside a sealed, X-ray transmissive chamber, while N₂ and MA⁰ gas was flowed into the sample environment from a bubbler containing ethanol:methylamine solution (**Figure S2**). During this process, X-rays were scattered from films onto a 2D detector operating at ~10 frames s⁻¹. This reciprocal space imaging is azimuthally integrated to 1D plots of Q vs. intensity, enabling simultaneous monitoring of crystalline structure at different length scales within the film (remapping and explanation of data processing is shown in **Figure S3**). In **Figure 1a** we show the evolution of the 1D integrated scattering from a film of MAPbI₃ as MA⁰ is introduced into the chamber. Shortly into the experiment, intensity from the tetragonal MAPbI₃ phase reduces rapidly, commensurate with the emergence of scattering features from another crystalline phase (I₁). This phase has prominent peaks at $Q = 0.59, 0.61, 0.83, 1.2$ and 1.86 \AA^{-1} , and reaches maximum intensity as the perovskite phase becomes undetectable. After around 3 s, the intermediate structure has completely dissolved to a co-ordinated amorphous phase, with a broad scattering feature at $Q \sim 0.6 \text{ \AA}^{-1}$. **Figure 1b** shows azimuthal integrations at key time points, combining the intensity from multiple frames. Initially we confirm the film is MAPbI₃, with the simulated tetragonal $I4cm$ 1D diffraction pattern⁶⁵ shown below with Miller indices marked. This phase is gradually converted into the I₁ intermediate, which then becomes solvated at later times (additional peaks here are backgrounds including ITO and the environmental chamber – see **Figure S4**). Illustrative GIWAXS patterns (combined data over all available frames) for the perovskite, intermediate, and solvate phase are shown in **Figures**

1c-e. The 2D diffraction shows complete Debye-Scherrer rings on the detector, confirming isotropic orientation for all phases; the scattering domains are randomly oriented on the substrate surface.

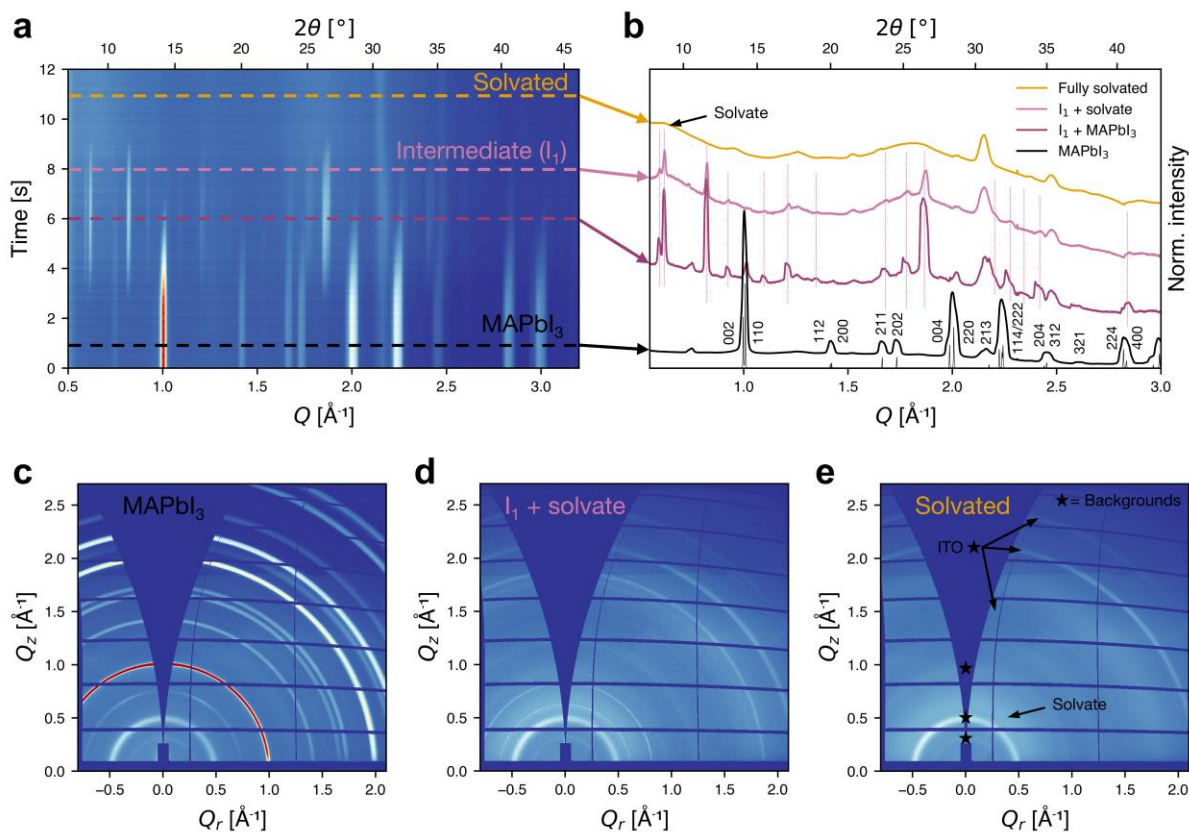


Figure 1 In-situ X-ray diffraction during methylamine vapour-induced liquification of MAPbI₃. a) Contour plot and b) azimuthal integrations showing that the structural evolution from MAPbI₃ to the solvate phase (MA⁰·MAPbI₃) proceeds via a crystalline intermediate phase, I₁. 2D GIWAXS patterns for each phase integrated over many frames for the c) initial MAPbI₃ which has isotropic orientation, d) I₁ with some solvate also forming and e) the fully solvated system (additional backgrounds are starred, further explanation in Figure S4).

Next, we monitored the reverse - recrystallisation - process by flowing N₂ into the chamber whilst applying a mild vacuum to remove the MA⁰ gas from the environment (**Figure S2**). The waterfall plot in **Figure 2a** shows the initial disordered solvate phase persists until, scattering features from an intermediate phase (I₂) emerge at $Q = 0.83, 1.2$ and 1.86 \AA^{-1} , followed soon after by scattering from MAPbI₃. An initial rapid increase in scattering intensity from both the MAPbI₃ and intermediate last for around 2 s, after which the intensity of I₂ gradually decreases, whereas MAPbI₃ scatter increases monotonically as more of the remaining intermediate phase in the film is converted to perovskite. At the end of the experiment, the intermediate scatter has almost disappeared and only perovskite and a low intensity feature at $Q \sim 0.7 \text{ \AA}^{-1}$ are present. This weakly scattering phase is most likely due to adsorbed solvent or moisture at the

thicker film surface towards the edge of the substrate and was observed before and after vapour treatment (**Figure S5**). Looking at azimuthal integrations of the data in **Figure 2b**, the pattern, I_2 exhibits significantly fewer scattering features than I_1 , which will be discussed later. To verify this, we repeated the liquification and recrystallisation processes with a further two samples, which confirmed that both phases were repeatably formed (**Figure S6**). Comparing combined GIWAXS images across multiple frames in **Figures 2c-e**, we observe anisotropic scattering rings and Bragg spots, indicating this process induces crystal orientation (texturing) of both the I_2 and perovskite phases.

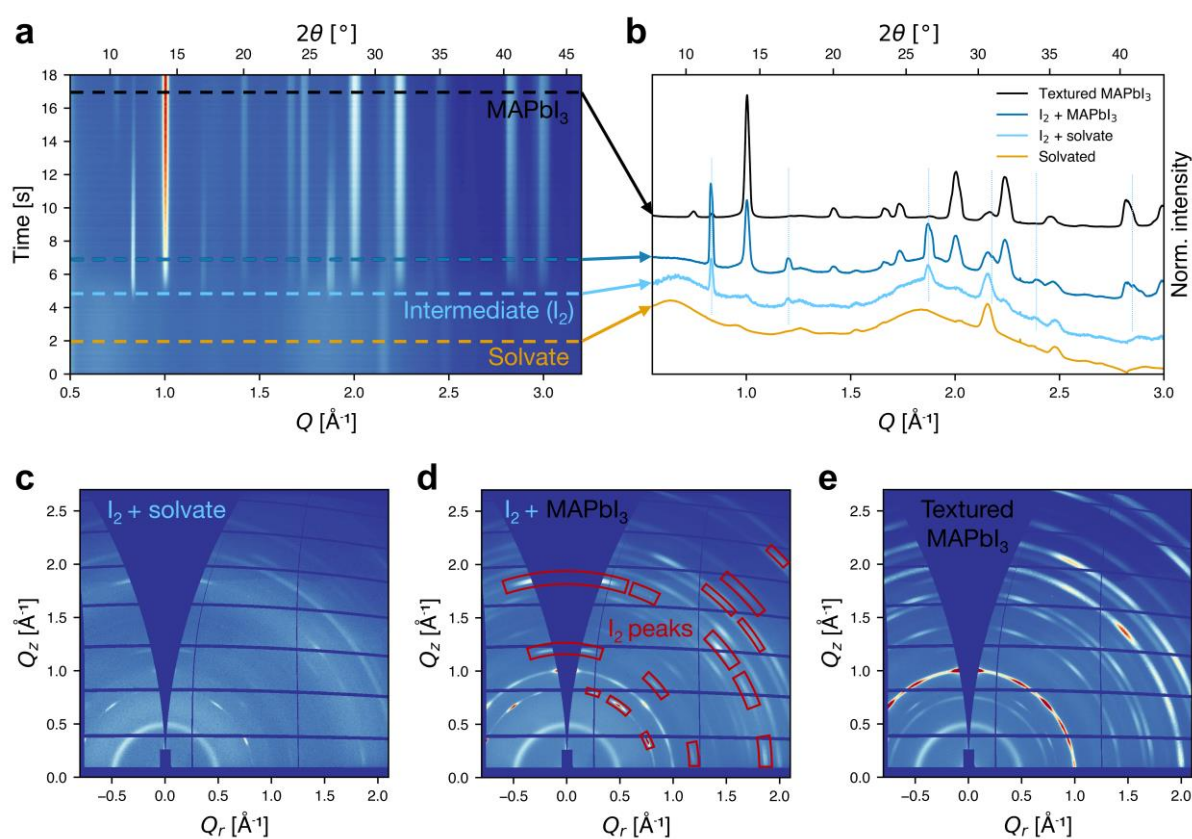


Figure 2: In-situ X-ray diffraction acquired during the vapour removal process. a) A face-sharing intermediate (I_2) nucleates from the solvate phase, slightly preceding the perovskite. b) Different stages of the process as I_2 gradually converts to the corner-sharing perovskite structure as MA^0 continues to be removed from the film. c) 2D GIWAXS over several frames showing the I_2 phase with the solvate and later d) with $MAPbI_3$. Here, I_2 forms with strong crystallographic texture. Marked I_2 peak positions are given in Table S1. e) The final perovskite exhibits multiple Bragg spots within the (110)/(002) ring at $Q \sim 1.0 \text{ \AA}^{-1}$, indicating multiple texture directions are present in the film.

6.2.3.2: Phase identification

In general, reported crystalline solvate and intermediate phases in literature adopt a variety of different 'ID' structures with mixtures of face- and edge-sharing octahedral structures

intercalated with solvent (denoted 'S' below). These phases can have varying widths of octahedral units extending in one dimension: 1-wide face-sharing structures with repeating units of PbI_3^- octahedra such as the hexagonal δ -FAPbI₃ (2H polytype) or dimethylammonium lead iodide; 2-wide Pb_2I_6 phases such as the reported monohydrate phase $\text{MAPbI}_3 \cdot \text{H}_2\text{O}$ or for larger solvents $\text{MA}_2(\text{S})_2\text{Pb}_2\text{I}_6$; or 3-wide with composition $\text{MA}_2(\text{S})_3\text{Pb}_3\text{I}_8$. Other common solvent intermediates include $\text{PbI}_2(\text{S})$ phases (reported for NMP, DMF and DMSO) as well as a variety of '0D' phases and corner-sharing A_3PbX_5 phases. Two recent works have proposed phases that mediate the methylamine liquification and recrystallisation processes, both relying on single crystal XRD at low temperature.^{31,66} Simulated powder X-ray diffraction (XRD) patterns from these phases in **Figure S7** shows that they are not a perfect match with the scattering features observed in the true processes, but it is highly likely that the room temperature phases are related or similar. In particular, work by Huang *et al.* highlights the strong hydrogen bonding interaction between MA^0 and MA^+ , resulting in a dimerized ionic-liquid-like pseudocation which then determines the phase behaviour.³¹

Identifying structures with grazing incidence wide-angle scattering data can be challenging for several reasons. Most critically these are the issues of sample texture (which can mask certain reflections and alter scattering intensities), sample footprint broadening,^{62,67} and the use of a flat area detector observing an incomplete fraction of the Ewald sphere in reciprocal space about the scattering centre,⁶⁷ the last of which leads to the incidence-angle-dependent 'missing wedge' of data in the Q_z direction.⁶⁸ In our experiment, direct structural solution methods are not possible due to the phase metastability and unknown $\text{MA}^0:\text{MA}^+$ stoichiometry. Instead, we carefully identified scattering features related to the two intermediate phases directly from the 2D data and integrated over many frames for specific sections of the kinetic datasets to make the background subtracted 1D patterns shown in **Figure S7**.

Beginning with the crystallisation intermediate **I**₂ as the higher symmetry case, we highlight the known diffraction peaks and their respective scattering vectors in **Figure S8** and **Table S1**, although additional scattering vectors coincident with those from the perovskite are also possible. This can seemingly be indexed as a 2H polytype (hexagonal) phase with repeated face-sharing PbI_3^- units. However, from the apparent c-axis length of $\sim 7.3 \text{ \AA}$, this is insufficiently long to accommodate 2 face-sharing units, and so is an imperfect match. This phase would be isostructural to other 2H phases (δ -FAPbI₃ and DMA^+PbI_3 where DMA^+ is dimethylammonium) with modified unit cell dimensions. To best match the observed scattering intensities and confirm the iodine positions with respect to the Pb sites we used a rigid body modelling approach. By rotating the face-sharing polymeric structure about the Pb-Pb axis (c-axis),

simulating the diffraction and comparing the quality of fitting to the data, we confirmed the same orientation of the iodoplumbate as is present in the other reported 2H phases (**Figure S9**). In particular, we observe little-to-no scattering intensity at $2\theta = 20.2^\circ$ and 23° , which constrains the allowed iodine positions.

The **I₁** intermediate pattern bears striking resemblance to that of the crystallisation intermediate, with most peaks observed at similar scattering angles (**Figure 3c**). In addition, a multitude of additional reflections are present at lower angles, most notably at $q = 0.59, 0.62 \text{ \AA}^{-1}$ ($2\theta = 8.33^\circ, 8.67^\circ$). The full peak list for this intermediate is given in **Table S2**. This suggests either that the liquification pattern is a superposition of two phases, or that **I₁** is a related structure with similar lattice dimensions but lower symmetry due to distortions of the iodoplumbate chain. Referring to Figure 1a, the kinetics of the lower angle peak evolution indicates that the latter is true, with the additional reflections coming from the same phase. At this point, we also note that the liquification and crystallisation intermediate scattering features over several repeated cycles were comparable each time (but were accompanied by significant morphological changes in the films). By integrating all frames on a second cycle of the same sample, i.e. liquifying from textured MAPbI₃ to induce partial orientation of the otherwise isotropic liquification intermediate, we identified a 3rd order relationship between the peaks at $q = 0.59, 0.62 \text{ \AA}^{-1}$ and those at $q = 1.76, 1.86 \text{ \AA}^{-1}$ ($25.0^\circ, 26.3^\circ$) based on their co-orientation (**Figure S10**). Using this, the pattern can be indexed with a monoclinic unit cell with lattice parameters $a = 10.5, b = 20.1, c = 8.3$ and $\beta = 97.7^\circ$. This c-axis length would accommodate the required chain length for an all face-sharing phase, however the arrangement of the iodoplumbate within this unit cell is unclear.

We additionally investigated computational solutions with density functional theory (DFT) calculations, to investigate how the MA⁰·MA⁺ dimer might affect the observed intermediate phases. Terminal iodine atoms (with a single Pb-I bond) in reported Pb₂I₆ and Pb₃I₈ structures are generally in close proximity to the MA⁺ cation and are stabilised by Coulombic attraction with the cation.^{69–71} Interestingly, we found that in several calculated geometries based on such double edge-sharing iodoplumbate structures, there was a tendency towards more highly coordinated iodine and Pb species. Specifically, we performed ab initio DFT calculations of MAPbI₃·H₂O, and (DMF)₂MA₂Pb₂I₆ (both 2-wide but with slightly different structural motifs¹⁹) and the same structures but with H₂O or DMF replaced with MA⁰, i.e. structures containing an MA⁰·MA⁺ dimer. Comparing the calculated geometries, we found that for structures with MA⁰·MA⁺, in some cases terminal iodine atoms preferred to form a second Pb-I bond, resulting in 2-coordinated iodine atoms and 7-coordinated Pb atoms. This indicates that the resultant

effect of the proton being shared in the $\text{MA}^0\text{-MA}^+$ dimer, with the positive charge now delocalised over the large cationic dimer species, reduces attractive $\text{MA}^+\text{-I}$ interactions at these terminal iodine sites and makes MA^+ less able to stabilise terminal iodines. Additionally, in both the DMF and H_2O structures hydrogen-bonded chains of solvent- MA^+ are present along the same crystal axis as the iodoplumbate, due to each solvent forming two hydrogen bonds. This may affect the iodine interactions and the phase metastability as compared to isolated $\text{MA}^0\text{-MA}^+$ dimers. The resulting DFT-derived phases and simulated diffraction patterns are shown in **Figure S11**, showing some similarity with the I_1 scattering pattern.

As is clear from several reports, the methylamine vapour pressure, film temperature and measurement protocol can all affect the observed intermediate structures.^{21,24,31,66,72–76} The variety of competing $\text{MA}^+\text{-I}$, $\text{MA}^+\text{-MA}^0$ and $\text{MA}^0\text{-Pb}$ interactions are likely the underlying cause for the multiple polymorphs reported in this system, with this work highlighting the critical role of the rapid $\text{MA}^+\text{-MA}^0$ complex formation in both process directions, and the kinetically stabilized oriented I_2 phase in the crystallization process and resulting texture formation.

6.2.3.3: Temperature and orientation

The data shown thus far have shown the recrystallisation process with the MAPbI_3 films held on a hotplate set at 23 °C. We noted in our initial investigations that after exposing films inside the methylamine environment, maintaining the partial pressure and subsequently ramping the hotplate temperature, that above ~65°C the transparent film spontaneously converted back into perovskite. This is in line with observations by Jacobs *et al.* of a temperature and MA^0 vapour pressure-dependent phase behaviour in this system,⁷⁷ and Wheeler *et al.* who highlighted the role of partial pressure and temperature in the gas uptake process, proposing a thermodynamic model for $\text{MA}^0\text{-MAPbI}_3$ complex formation which was exploited to great effect in the design of photothermal photovoltaic windows.⁷³ More recently, Hao *et al.* illustrated that exposing MAPbI_3 films held at various temperatures prior to exposure to methylamine vapour could alter the nucleation process, resulting in significant device performance variation when layers were integrated into solar cells.⁷⁸

We thus repeated the liquification and crystallisation experiments with the films held in the environmental chamber at two temperatures, 37 °C and 50 °C. During liquification, we first note that the previously identified I_1 intermediate phase is present with the same diffraction pattern (comparison of azimuthally integrated patterns is shown in **Figure S12**). Considering this as a two-step process (conversion from MAPbI_3 to I_1 and from the intermediate to the liquid state) and given that the kinetics for both are dictated by MA^0 gas uptake, as might be expected at

higher temperatures these processes were retarded (**Figure S13**). Conversely, during recrystallisation, higher temperature resulted in more rapid conversion to the perovskite phase (**Figure S14**). Interestingly, scattering from the crystallisation intermediate I_2 was not observed at 37 °C or 50 °C; if this phase is present the coherent scattering domains are undetectably small.

We replicated the healing process using a similar vapour exposure system in our labs, and in **Figure 3** we compare the *ex-situ* GIWAXS patterns for perovskite films fabricated at each temperature. Before treatment, the perovskite scattering is isotropic (**Figure 3a**), confirming randomly oriented grains as in the *in-situ* experiment. At 23 °C (**Figure 3b**), we see in the (110)/(002) scattering ring that the perovskite grain orientations have been restricted to a small number of directions, with the out-of-plane direction being the dominant orientation (partially masked by the GIWAXS geometry). At higher temperatures (**Figure 3c,d**), more Bragg spots are present in the first order diffraction ring, indicating more texture directions are present within the film. Taking radial integrations along the (110)/(002) ring we can illustrate the azimuthal angle (χ) dependent scattering intensity (see **Figure S3** for explanation). Comparing these azimuthal profiles for each temperature, we see both the additional texture directions clearly and that the distribution of intensity for each orientation is narrower; at higher temperatures we have a greater number of grain orientations but each orientation is highly constrained. We confirmed this behaviour was comparable between the *in-situ* and *ex-situ* GIWAXS patterns in **Figure S15**, which showed the same trends in azimuthal intensity.

In all cases, the crystallographic orientation is significantly different from the expected GIWAXS pattern for a close-to-uniaxial film, as is commonly observed for various perovskite compositions including MAPbBr₃,⁷⁹ or through addition of PEACl or MACl as a processing additive.^{80–82} In **Figure S16** we index an example 2D diffraction pattern, illustrating the two primary grain orientations. Beyond this, we confirmed that this scattering pattern must be a superposition of many texture directions by simulating GIWAXS patterns for various orientations, which are depicted in **Figure S17**.

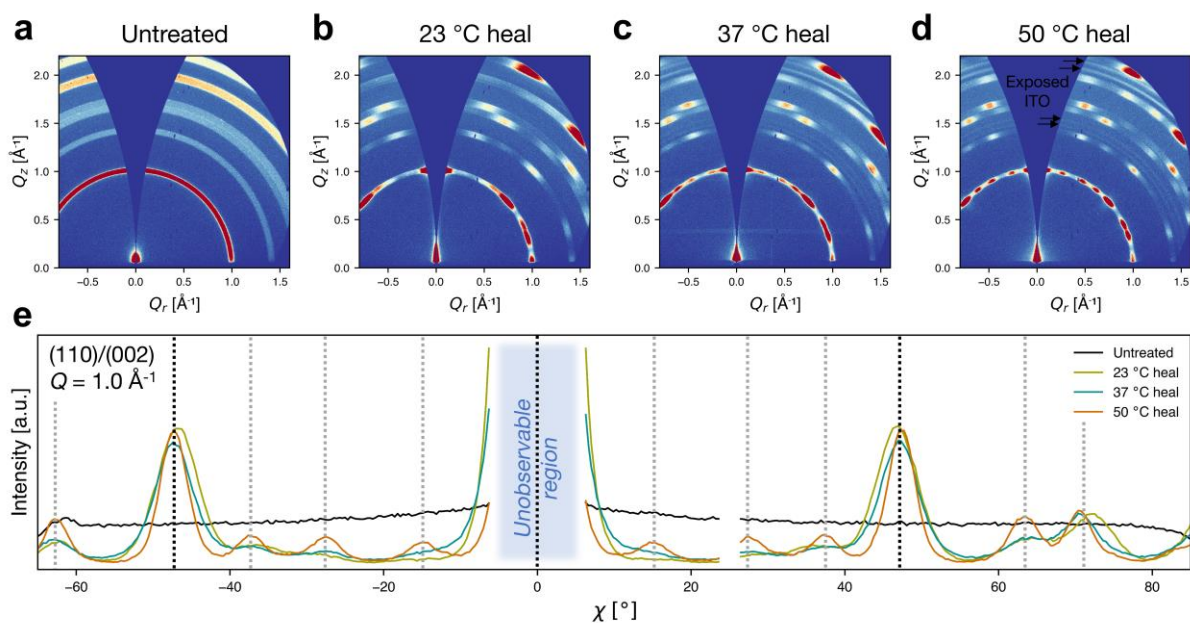


Figure 3: Ex-situ GIWAXS investigating the effect of temperature on crystal orientation. 2D GIWAXS patterns from a) an untreated (as prepared) spin-coated MAPbI₃ film and films held in a methylamine vapour environment on a hotplate at b) 23 °C, c) 37 °C and d) 50 °C before rapidly removing the vapour to recrystallise the film. e) Shows an azimuthal scattering intensity profile along the primary perovskite reflection, showing a greater number of texture directions (marked with dashed lines) are present with faster crystallisation at higher temperatures. Each direction is also more narrowly distributed, and we note that the narrow, intense out-of-plane scattering for the 50 °C sample is particularly masked by the ‘missing wedge’.

To understand the mechanism, we first confirmed whether the nucleation and crystallisation is primarily top-down (a concentration field) or bottom-up (nucleating at the substrate interface). If the nucleation is bottom-up, then we would expect to see some differences in the recrystallised film texture depending how the nuclei form at the buried interface. To explore this, we spin-coated and recrystallised *ex-situ* samples on both nanoparticle SnO₂ electron-transport layers and a hole-transporting self-assembled monolayer (SAM).^{83,84} Whilst we observed some changes in film coverage (due to the surface energy of the substrate affecting the MA⁰·MAPbI₃ wetting), the perovskite diffraction was near-identical (**Figure S18**), indicating that rapid change in MA⁰ partial pressure induces rapid nucleation from the top surface. We next compared the temporal evolution of the *in-situ* azimuthal intensity profiles for the 23 °C and 50 °C healing processes in **Figure S19**. In both cases, we observe that the primary texture directions emerge almost simultaneously. From this we conclude that multiple corner-sharing orientations are equally stable when forming (directly or from I₂) at the top surface upon vapour removal. At 50 °C, additional orientations are apparent as discrete spots in the azimuthal intensity profile, which could be caused by secondary nucleation events from the nuclei initially formed for the dominant orientations. Alternatively, this could be because the

rapid surface nucleation causes nuclei to encounter neighbouring crystals more quickly, minimising any time for nuclei to reorient before growing. In short at the highest temperature, the additional orientations present in the final film are most likely discretized because of:

- An oriented attachment mechanism, with adjacent particle interactions constraining grain orientations.
- Equivalent energetically favoured orientations of the MAPbI₃ nuclei.
- Specific favoured directions for secondary nucleation events.

We therefore interpret that at higher temperatures the face-sharing I₂ intermediate phase is present briefly as small domains before rapid conversion, based on the comparable crystal orientations in the treated films. Equivalently to the prolongation of observable I₁ scattering during liquification at higher temperatures (temperature slowing the MA⁰ uptake), in the reverse process the higher temperature accelerates MA⁰ removal and conversion to a corner-sharing octahedral arrangement. Achieving uniaxial growth within the possible temperatures at this pressure therefore is unlikely to be possible. We do however note recent efforts to finely control the MA⁰ partial pressure and process temperature simultaneously via this route have enabled enhanced orientation control, resulting in champion cells with 21.3% PCE.⁸⁵

We studied the effect of modifying the nucleation process and film orientation on photovoltaic device performance with an *n-i-p* device stack (ITO/np-SnO₂/perovskite/spiro-OMeTAD/Au, full details in the Methods). To preclude the possibility of Ostwald ripening or other secondary grain growth, we fabricated the perovskite films with no further annealing of the active layer after MA⁰ treatment. The results of this study are shown in **Figure S20**. We found that the orientation-constrained 50 °C healing resulted in the highest performance devices, with a champion stabilised power output of 18.1% PCE, with reverse-sweep performance metrics $V_{OC} = 1.05$ V, $J_{SC} = 22.1$ mA cm⁻² and 18.5 % PCE. Devices prepared at 23 °C exhibited significantly lower average performance, which we attribute to worsened film coverage (pinholes and voids) at lower temperature, with the MA⁰·MAPbI₃ substrate wetting enhanced with both higher temperatures.

In our initial experiments, it was possible to further engineer the concentration field to a temperature field by maintaining a high MA⁰ vapour pressure and ramping the temperature. This significantly altered the nucleation on both SnO₂ and SAM substrates, resulting in a rough film. However, on a lattice-matched KCl single-crystal substrate, we were able to form a close-to-uniaxially oriented perovskite film (**Figure S21**). We hope that the enhanced understanding presented in this work will enable further process development in this area.

6.2.3.4: Relating to solution chemistry

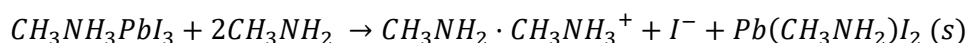
Beyond pure methylamine re-crystallisation, various related solution chemistries have been reported which utilise the coordinating ability and volatility of MA⁰ to enable rapid perovskite crystallisation. With a more complete understanding, it may be possible to engineer the same preferential orientation control as with the healing process. So to better understand the role of the methylamine in the dissolved state, as well as how it relates to methylamine-based solution chemistries, we investigated the liquid phase (MA⁰·MAPbI₃) and compared it to acetonitrile MAPbI₃ (ACN MA⁰·MAPbI₃). The MA⁰·MAPbI₃ liquid phase was prepared by flowing methylamine over fine-powdered MAPbI₃, and the ACN MA⁰·MAPbI₃ by flowing gas through a septum-sealed vial of acetonitrile/PbI₂/MAI (**Figure S22**), with both procedures explained in the Methods section.

Considering phase behaviour in the ACN MA⁰·MAPbI₃ system first, upon addition of acetonitrile to the precursor materials MAI/PbI₂ we observe the spontaneous formation of a black suspension of MAPbI₃, which may be coating other unreacted material (**Figure 4a**). As methylamine gas is flowed through this under anhydrous conditions, after some time a white precipitate begins to form. This material displaces the MAPbI₃ in solution, as shown in **Figure 4a**. We recovered this material by centrifugation, removed excess solvent and then performed pXRD, with the powder sample sealed under N₂ to avoid any solvent volatilisation (**Figure 4b**). From this, we identified the white phase to be a [Pb(CH₃NH₂)I₂]_n '2D co-ordination polymer' recently reported by Febriansyah and co-workers (depicted in **Figure 4c**).⁸⁶ This phase has repeating units of [Pb(CH₃NH₂)I₄]²⁻ occupying a ribbon-like sheet structure with five- or seven-coordinate, hemi-directed Pb anions. In their work, this material was synthesised by reacting MAI, PbI₂, ethanol and ethanol:methylamine solution, resulting in a final compound seemingly deficient of MA⁺ and I⁻ from the solution stoichiometry. This counter-intuitive behaviour agrees with our experiments when using acetonitrile and a stoichiometric MAPbI₃ solution composition. We rationalise this again by the hydrogen-bonding interaction between CH₃NH₃⁺ and CH₃NH₂. The formation constant for a complex of a base with its conjugate acid in solution is given by:

$$K_{f_1} = \frac{[B \cdot BH^+]}{[B][BH^+]}$$

where here *B* is CH₃NH₂, *BH*⁺ is CH₃NH₃⁺ and *B · BH*⁺ is a homo-conjugated complex (MA⁰·MA⁺ dimer). For MA⁰·MA⁺ in acetonitrile the formation constant is reported to be $K_{f_1} = 32$, indicating extensive dimerization.⁸⁷ MAI, and ammonium cations generally, are only weakly soluble in acetonitrile due its weak hydrogen bond accepting ability.

Our model for the dissolution process (**Figure 4d**) illustrates that as methylamine flows into the acetonitrile solution, $\text{MA}^0 \cdot \text{MA}^+$ dimers are formed at the perovskite reaction surface, with this species then dissipated into the solvent along with I^- either as a free ion or together in an ion pair. Simultaneously, further methylamine reacts with the remaining PbI_2 , with the methylamine covalently bonding to Pb and gradually converting the black MAPbI_3 into the coordination polymer (white precipitate). The initial dissolution process in anhydrous conditions can therefore be described as:



as depicted in **Figure 4e**. After this reaction has gone to completion and the perovskite has been fully converted to the co-ordination polymer, as further MA^0 is added we observe the white precipitate rapidly dissolves. Sudden dissolution likely then occurs as the Pb-I bonding in the co-ordination polymer is disrupted, resulting in a fully solvated system (**Figure 4f**).

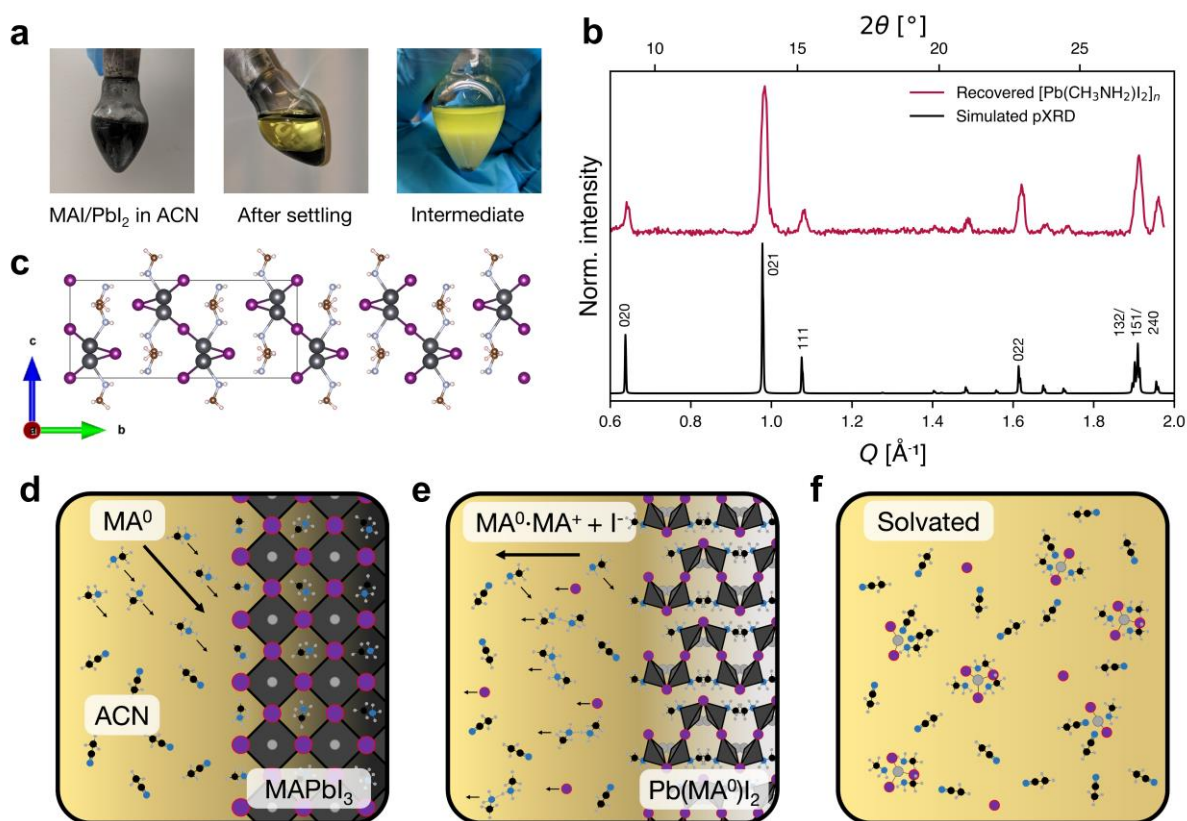


Figure 4: a) Photographs MAPbI_3 in acetonitrile, after settling for several minutes, and during the MA^0 gas bubbling process before complete dissolution. The white precipitate intermediate was recovered by centrifugation and part b) shows the powder XRD pattern corresponds with a 2D co-ordination polymer with composition $[\text{Pb}(\text{MA}_0)_2]_n$, as shown in part c). A scheme illustrating the dissolution process illustrates d) MA^0 gas reacting at the MAPbI_3 grain surface, e) the hydrogen-bonded $\text{MA}^0 \cdot \text{MA}^+$ is removed into the acetonitrile solution with I^- , converting the perovskite to the $[\text{Pb}(\text{MA}_0)_2]_n$ phase, before f) complete solvation, depicted as a mixture of solvated PbI_2 , PbI_3^- and free I^- .

Three possible interpretations seem plausible for the role of methylamine in solvating this system. Firstly, either the primary environment in the solution phase has $\text{MA}^0 \cdot \text{MA}^+$ distributed in the solvent, with the Pb and I solvated primarily by the acetonitrile, and with the methylamine simply minimising $\text{MA}^+ \cdot \text{I}^-$ h-bonding interactions. This would provide a larger population of I^- , indirectly solvating the Pb through enhanced complex formation. Secondly, in the final state, the amine may instead mostly be coordinated to the Pb via the nitrogen lone pair. This could cause the sudden dissolution if, at a critical methylamine concentration, the amine lone-pair ligand interaction becomes energetically favourable instead of h-bonding. A third scenario has methylamine exchanging between these two, partly in the dimer environment and behaving as a Pb ligand on ultrafast timescales. These possibilities can be explored with spectroscopic techniques.

Firstly, UV-Vis absorption spectroscopy data (**Figure 5a**) shows an absorption onset characteristic of ligand to metal charge transfer states in PbI_3^- species in the case of ACN $\text{MA}^0 \cdot \text{MAPbI}_3$. The steep onset with no longer wavelength absorption bands indicates limited formation of higher order iodide plumbate complexes such as $\text{PbI}_4^{2-}(\text{S})_n$ despite using a high concentration for this solvent system of 0.8 M.⁸⁸ The co-ordinating strength of solvents, quantified for example by Gutmann's donor number (D_N), has been shown to correlate with the inhibition of higher order iodoplumbate complexes in solution.⁸⁹⁻⁹¹ Thus if the material was dissolved purely in the weakly co-ordinating acetonitrile, $D_N = 14.1 \text{ kcal mol}^{-1}$,⁹² we might expect to see higher order iodide complexes such as PbI_4^{2-} to form. In contrast, the absorbance spectrum for pure $\text{MA}^0 \cdot \text{MAPbI}_3$ shows a redshifted onset (**Figure 5a**). This may indicate some $\text{PbI}_4^{2-}(\text{S})_2$ species, this could be due to the significantly higher concentration without additional ACN present. In both cases, it seems that complex formation is prevented by the strongly co-ordinating MA^0 (estimated from reported primary amines to be $D_N \sim 29 \text{ kcal mol}^{-1}$,³⁸ comparable to DMSO with $D_N = 29.8 \text{ kcal mol}^{-1}$) or otherwise hindered in the combined ACN MA^0 system compared to other polar solvent ligands.⁹³

Investigating possible MA^0 ligand formation further, we used several NMR probes. Firstly, we performed ^1H NMR on the two samples (**Figure 5b**, full spectra in **Figure S23**), which confirmed a single methyl peak in both samples, as well as a second proton environment related to the NH_3/NH_2 protons. The shifts between these peaks were comparable at 1.78 ppm for the $\text{MA}^0 \cdot \text{MAPbI}_3$ and 1.7 ppm for the ACN $\text{MA}^0 \cdot \text{MAPbI}_3$ (all shift values are given in **Table S3**). The proton ratios were also confirmed for the two cases, giving x values in CH_3NH_x of 2.45 for ACN $\text{MA}^0 \cdot \text{MAPbI}_3$ and 2.39 for $\text{MA}^0 \cdot \text{MAPbI}_3$. Both the relative shift and the absolute proton numbers point to the solvation mechanism being similar in the two systems. The $\text{MA}^0 \cdot \text{MAPbI}_3$

also showed a remarkable upfield shift for the whole spectrum with only CH_3NH_2 as the solvent, likely due to the strongly basic conditions and extensive lone pair interactions. Additionally, the methyl protons from acetonitrile were observed and a small amount of ethanol contamination was present from the MA^0 solution. These environments were further confirmed with ^{13}C NMR, which again illustrated a single methyl peak for the combined amine/ammonium system (**Figure S24**). We also note that the $\text{CH}_3\text{CH}_2\text{OH}$ environment in the ethanol was shifted upfield, most likely due to shielding by greater electron density on the oxygen as the OH proton is donated in the heavily basic conditions with so much methylamine present. ^{207}Pb NMR on the solution state showed the Pb is also shifted upfield in $\text{MA}^0\text{-MAPbI}_3$, which could be due to shielding by N lone pair (MA^0) ligands or I^- being coordinated more strongly to Pb without ACN present (**Figure 5c**).

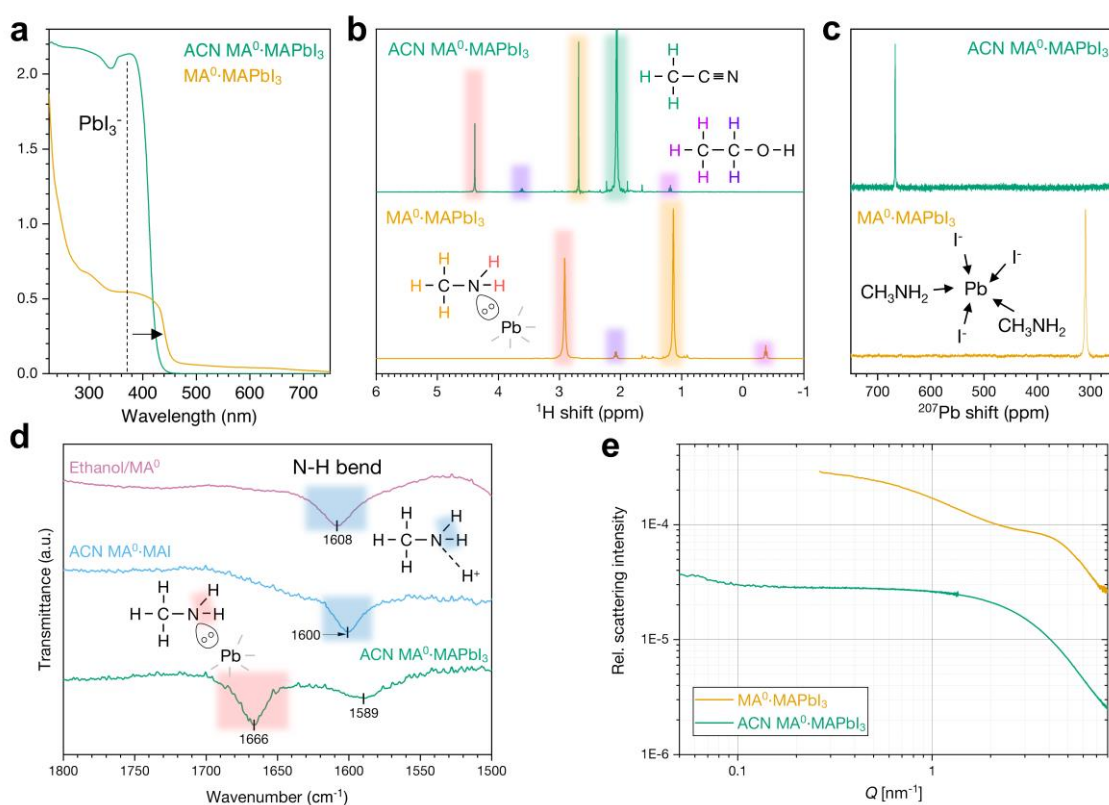


Figure 5: Comparison of acetonitrile (ACN) and pure MA^0 -solvated MAPbI_3 solutions. a) Absorbance spectra acquired from a quartz cuvette of 0.8 M ACN $\text{MA}^0\text{-MAPbI}_3$ solution and a wet film of the highly concentrated $\text{MA}^0\text{-MAPbI}_3$ sandwiched between layers of quartz glass. b) ^1H NMR spectroscopy from the two samples, confirming the NMR shifts of the methyl and amine environments to be comparable in both samples aside from a significant upfield shift of the pure- MA^0 spectrum (full spectra are given in Figure S23). c) ^{207}Pb NMR on the same solutions showing the Pb to be heavily shielded in the pure MA^0 sample. d) FTIR spectrum of the N-H bends in ACN $\text{MA}^0\text{-MAPbI}_3$ compared to two solutions with no Pb where hydrogen bonding dominates; an ethanol/ MA^0 solution and MAI dissolved in ACN by flowing MA^0 . e) 1D SAXS profiles for the two solvent systems, showing no preferred cluster size or aggregation in the ACN solution and intense scattering from the pure $\text{MA}^0\text{-MAPbI}_3$ solution.

To validate the theory that MA^0 is co-ordinated to Pb, we additionally performed FTIR spectroscopy on the ACN $\text{MA}^0\cdot\text{MAPbI}_3$ and two other systems where h-bonding would instead be present: the ethanol/ MA^0 solution, and pure MAI dissolved in ACN by the addition of MA^0 . We find in **Figure 5d** that the observable N-H stretch modes in CH_3NH_x are different for h-bonded environments ($\sim 1600\text{ cm}^{-1}$), whereas in the ACN $\text{MA}^0\cdot\text{MAPbI}_3$, the N-H bend mode is shifted to 1660 cm^{-1} . We also acquired small-angle X-ray scattering measurements on the two systems, as shown in **Figure 5e**. This illustrated very little aggregation in the ACN $\text{MA}^0\cdot\text{MAPbI}_3$ system and significantly higher scattering intensity in the highly concentrated $\text{MA}^0\cdot\text{MAPbI}_3$. Crucially, in neither system do we observe crystalline peaks in the solution. Taken together with the solvate scattering shown in Figure 1, we preclude the possibility of pre-ordered crystalline sheets existing in the solution, as has been proposed for this system.³⁴

We therefore believe that the single aminic environment observed in NMR is not due to $\text{MA}^+\cdot\text{MA}^0$ dimers in solution. We instead conclude that complete solvation in both systems occurs as the basicity increases to the point that, with no further proton-donating species available, the further added methylamine has the effect of converting the large population of $\text{MA}^0\cdot\text{MA}^+$ dimer species to become available as protophilic ligands. For the ACN $\text{MA}^0\cdot\text{MAPbI}_3$, we base this on the rapid dissolution of the white precipitate, which indicates there is a critical pH above which the dimer species can instead co-ordinate to the metal ligand centre. With low MA^0 , the combined MA^0/MA^+ system has ammonium-like character, with the equilibrium in solution instead favours hydrogen bond accepting through $\text{MA}^0\cdot\text{MA}^+$ dimer formation, gradually becoming more aminic until the threshold for co-ordination to Pb is met. In the pure $\text{MA}^0\cdot\text{MAPbI}_3$, the dimers and I^- instead remain localised to the metal halide in the 1D iodoplumbate structure prior to liquefaction. The role of MAI in the solvation for these systems is therefore two-fold: firstly, providing a large population of I^- for the formation of iodoplumbate complexes which enhance the metal solubility, and secondly, making an additional population of pseudo-amine ligands available during the basic conditions afforded by the additionally bubbled MA^0 . In this sense the cation itself participates in the solvation of the anion, much like an ionic liquid. This explanation does however lead to the question of where the MA^+ proton is in the final state.

It has been proposed that the Pb environment in these systems is predominantly the homoleptic amine species $\text{Pb}(\text{MA}^0)_6^{2+}$.⁶⁶ This is perhaps confirmed by the observation of a large population of free I^- in solution.⁸⁶ However the PbI_3^- absorbance band and $\text{MA}^0:\text{Pb}$ stoichiometry point to another explanation, with a mixture of species present. We performed a rudimentary titration experiment which found that as little as 2 moles of MA^0 are required to solvate MAPbI_3

in ACN (**Figure S25**). This is far lower than the proposed $4\text{MA}^0\cdot\text{MAPbI}_3$ stoichiometry required when processing the organohalide and metal halide individually.²⁶ This lower stoichiometry would preclude $\text{Pb}(\text{MA}^0)_6^{2+}$ and further support the notion that the cation exists in its conjugate base form co-ordinated to the Pb in solution. Clearly, the precise makeup of the Pb-coordination sphere in these co-ordinating solvent systems merits further investigation, extending to a wider-range of non-nucleophilic bases⁷⁴ which may offer similar potential in unconventional solvent systems.

We next investigated the reasons why spin-coated ACN $\text{MA}^0\cdot\text{MAPbI}_3$ does not result in preferentially oriented perovskite films. Using an *in-situ* drop-casting system at the mySpot beamline at BESSY II, we acquired GIWAXS from a droplet of solution as it dried on a substrate surface. The waterfall plot showing the evolution of the diffraction pattern from this droplet over time is shown in **Figure 6a**. An example reshaped 2D diffraction pattern from this experiment is shown in **Figure S26**. To our surprise, the 1D pattern was a perfect match for an $\text{MA}_2\text{Pb}_3\text{I}_8$ solvate phase with an orthorhombic *Pnnm* space group (**Figure 6b**). The fitted unit cell dimensions for this I_3 phase were $a = 17.07$, $b = 21.82$ and $c = 4.54$, which is remarkably isostructural to the reported $(\text{DMF})_2\text{MA}_2\text{Pb}_3\text{I}_8$ and $(\text{GBL})_2\text{MA}_2\text{Pb}_3\text{I}_8$ phases.^{71,89} From the size of the available cavity between the iodoplumbate chains for the cation and solvent to occupy, we conclude acetonitrile must be incorporated into this phase as an intercalated solvent (**Figure 6c**). The size of the $\text{MA}^0\cdot\text{MA}^+$ dimer would clearly be insufficient to fill this void, however it is possible that methylamine is also present given the smaller molecular size of ACN compared to DMF/GBL, giving a composition $(\text{ACN})_2(\text{MA}^0\cdot\text{MA}^+)_2\text{Pb}_3\text{I}_8$.

In **Figure 6d**, we show the *ex-situ* GIWAXS pattern from a blade-coated perovskite film produced from a 0.5 M ACN $\text{MA}^0\cdot\text{MAPbI}_3$ solution, which shows no preferred orientation (**Figure 6d**). In one literature report by Dou *et al.* utilising a highly concentrated ACN $\text{MA}^0\cdot\text{MAPbI}_3$ solution (with ACN removed by N_2 blowing before deposition), a slot-die coated MAPbI_3 film was observed to form with film texture almost identical to our observations. We reasonably speculate that in their work crystallisation proceeded via the I_2 phase, because of the higher ratio of $\text{MA}^0\cdot\text{ACN}$. This highlights that the effect of solvent concentration at the point of nucleation is more critical in determining the intermediate phase formed than the co-ordinating ability of the solvent.⁸⁹

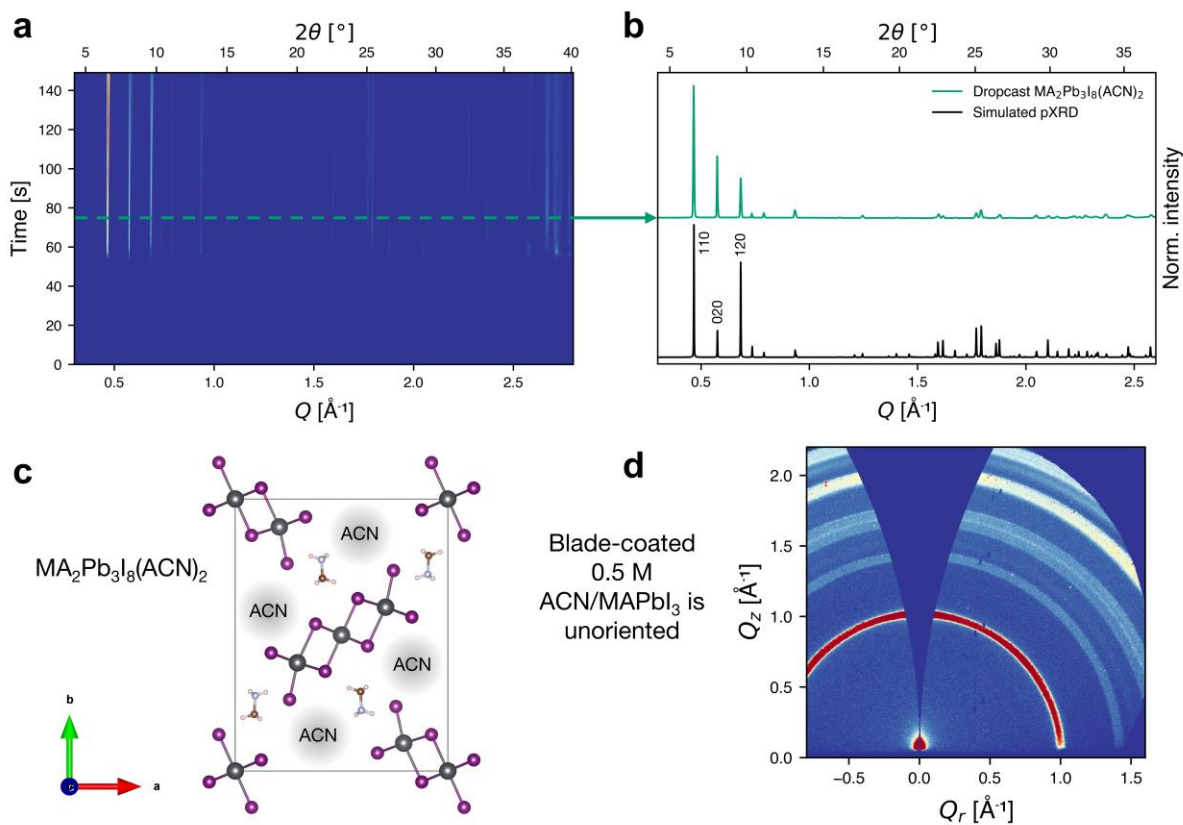


Figure 6: a) In-situ integrated X-ray scattering collected from a droplet of 0.8M ACN MA^0 -MAPbI₃ during drying. b) The diffraction pattern is consistent with a solvate intermediate phase I_3 with composition $MA_2Pb_3I_8(ACN)_2$ with the refined inorganic structure for I_3 shown in part c). d) Ex-situ GIWAXs pattern for a blade-coated 0.5 M ACN MA^0 -MAPbI₃ solution showing isotropic scattering rings, indicating that the MA^0 present in solution has not completely dictated crystal growth (such as via the I_2 phase).

6.2.3.5: Compositions beyond MAPbI₃

Using gas healing approaches and related co-ordinating solvent chemistries is of real interest for perovskite compositions beyond MAPbI₃ which, as is widely reported, suffers most acutely from irreversible chemical and thermal instabilities.^{94,95} Some progress has been made with small inclusions of other cations such as formamidinium during both healing and related solutions,^{28,36,96} as well as with Pb-Sn and mixed-halide ACN/MA solutions.^{30,35} We investigated the effect of treating films of FAPbI₃ with methylamine to inform our understanding of the healing process and to elucidate why in these cases the perovskite phase does not readily recrystallise.

We prepared films of FA(MA)PbI₃ by a reported two-step method incorporating MAI and MAI as additives, detailed in the Methods.⁹⁷ We first confirmed the material quality by preparing photovoltaic devices using the same *n-i-p* device configuration described above, achieving a champion PCE of 20.5% (**Figure S27**). Using the *in-situ* environmental chamber and protocol,

we created a low-moisture environment and exposed films to MA⁰ gas, with associated waterfall plots shown in **Figure 7a**. 2D diffraction patterns combined over a series of images are shown in **Figure S28** illustrating the film is initially α -FAPbI₃, PbI₂ and 2H/4H-FAPbI₃. Again, as the film is exposed to methylamine, an intermediate phase (**I₄**) formed prior to complete melting.

As shown in **Figure 7b**, we indexed this as a 1D hexagonal face-sharing iodoplumbate phase with space group *P63/mmc*. This resulted in a unit cell with lattice parameters $a = b = 8.87$ Å and $c = 8.12$ Å. This unit cell is therefore isostructural with 2H-FAPbI₃, DMAPbI₃ and other reported face-sharing hexagonal perovskites but with a larger a, b lattice parameter. The side length here corresponds to the Pb-Pb distance between chains - 8.67 Å for 2H-FAPbI₃⁹⁸ and 8.77 Å for DMAPbI₃⁹⁹ - signifying a larger cation occupies this space than either FA⁺ or DMA⁺.

Recent work by Wang *et al.* has highlighted the possible adverse reaction between FA⁺ and MA⁰ (formed by the deprotonation of MA⁺) in perovskite solutions.¹⁰⁰ In this reaction, the CH₃NH₂ amine lone pair nucleophile attacks the electropositive C in FA⁺ (HC(NH₂)₂). An NH₃ leaving group forms, and the resulting cation is 'methyl formamidinium' (MFA⁺): CH₃N⁺H₂CH=NH and its isomer CH₃NH=CHNH₂⁺. In a secondary reaction, a similar nucleophilic attack can form 'dimethyl formamidinium' (DMFA⁺) with two isomers, CH₃NHCH=N⁺HCH₃ and CH₃N⁺H₂CH=NCH₃. We therefore considered these two cations and a hypothetical FA⁺-MA⁰ dimer as three possible cationic species in the **I₄** phase.

To determine which is present in the structure, we performed first-principles calculations on modified 2H polytype phases to determine their stability. Pb and I positions were first determined through Pawley refinement of the diffraction pattern and the cation site was one of MFA⁺, DMFA⁺ and an FA⁺-MA⁰ dimer. For the structures with DMFA⁺ and an FA⁺-MA⁰ dimer, the iodoplumbate arrangement was unstable, and the resulting computational solutions were significantly expanded from the initial state, which precludes them from this phase (unit cells for these computational solutions are given in **Table S4**). The DFT-refined organic positions (representing a relaxed static cation) were then combined with the inorganic positions, calculated using a rigid-body modelling approach. The resulting (MFA)PbI₃ phase is shown in **Figures 7c-e** - we note this an idealised structure with only MFA⁺ and I. In Figure 7b, we observe a gradual shift of the **I₄** intermediate peaks to lower angles, meaning the unit cell is gradually increasing in volume. This supports the mechanism of the smaller FA⁺ cation being gradually converted into MFA⁺, before the crystalline phase decomposes entirely and the system is fully

solvated (**Figure S29** shows the diffraction from the solvated FA(MA)PbI₃ and MAPbI₃ are identical).

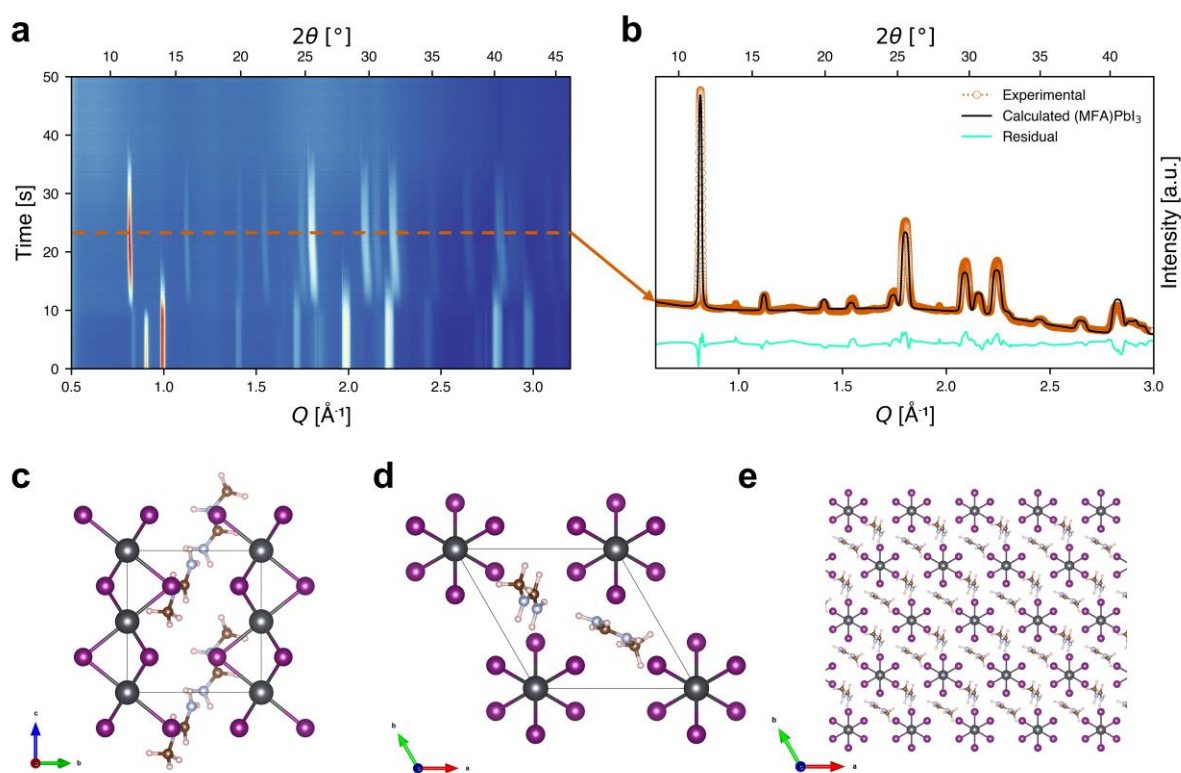


Figure 7: a) In-situ X-ray diffraction as formamidinium-rich perovskite films were exposed to MA⁰ vapour. b) Prior to solvation, an intermediate phase (**I**₄) forms, which was indexed as a hexagonal 2H polytype phase. Parts c)-e) are illustrative views of the proposed **I**₄ phase containing face-sharing iodoplumbates with a methyl formamidinium (MFA⁺) cation which forms by a reaction between FA⁺ and MA⁰.

Upon vapour removal, we observed different scattering features from **I**₄ emerging from the solvate phase (**Figure 8a**). The diffraction pattern for this **I**₅ intermediate phase was identified based on its similarity to a reported low-temperature methylamine dimer phase.³¹ The unit cell for the **I**₅ phase is also comprised of 1D PbI₃⁻ chains, but compared to the hexagonal phases above has a translational offset along the *c*-axis (along the Pb-Pb chains) amongst other small transformations. It therefore occupies a monoclinic structure with *P21/c* space group and the unit cell parameters were refined to $a = 10.67$, $b = 15.12$, $c = 7.94$ and $\beta = 106.0^\circ$ (**Figure 8b** shows the refinement to the 1D pattern, 2D patterns for **I**₅ and the solvate are shown in **Figure S30**). By the same first principles modelling approach as outlined above, we compared the using MFA⁺ and DMFA⁺ in the refined iodoplumbate structure, and found the calculated solution for MFA⁺ has a reduced unit cell volume from the structural refinement. This indicates instead that **I**₅ includes a larger cation than MFA⁺, or mixture of cations with average size larger than MFA⁺. This must be partially or fully DMFA⁺, which would continue to form in the solvate

by the continued addition of MA⁰. The **I₅** phase with composition (DMFA)PbI₃ with these DFT-estimated organic positions is shown in **Figures 8c-e**. Upon elevating the temperature of this film to close to 150°C, we observed a phase transition, and no conversion to a perovskite phase (**Figure S31**). These observations points toward the reactions between methylamine and formamidinium, resulting in the formation of large cations, being irreversible.

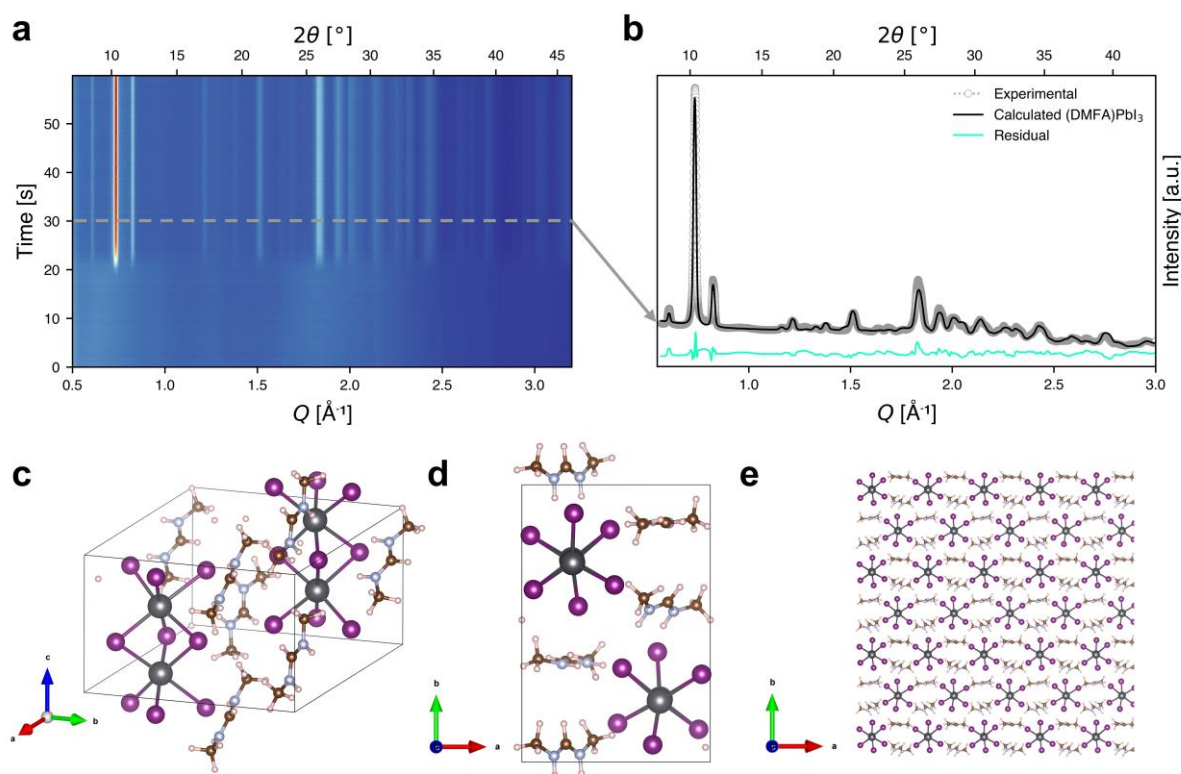


Figure 8: a) In-situ X-ray diffraction during removal of the MA⁰ vapour from the nominally FA(MA)PbI₃ film shows a different phase, **I₅** crystallises from the solvate. b) Measured and simulated diffraction for a proposed dimethyl formamidinium (DMFA⁺) iodoplumbate phase, shown in parts c)-e). c) Illustrating the monoclinic distortion, with adjacent face-sharing PbI₃ chains offset along the c-axis, with d) showing the view along this axis. e) Viewed over repeating units, the Pb sites in **I₅** are close to hexagonally-centred in the a-b plane.

To validate that this *in-situ* process (under anhydrous conditions) is an accurate representation of the true process, we repeated the MA⁰ treatment of FA(MA)PbI₃ films in air. These samples were prepared on an X-ray transmissive substrate, which was quickly encapsulated with a further transmissive foil after treatment to prevent moisture-induced changes. We acquired *ex-situ* transmission WAXS through this film, which confirmed the same **I₅** phase is present, in addition to a small amount of a pseudo-cubic perovskite phase (**Figure S32**). The perovskite may be able to reform either because the time under methylamine gas was shorter than the *in-situ* process, or because the presence of moisture mitigates or reverses some of the cation decomposition. We made further attempts to confirm the large

cationic species in our structure by performing ^1H NMR measurements on FAPbI_3 films which were first methylamine-treated in air before being dissolved in d_6 -DMSO. These confirmed two proton environments in the solution at the expected positions for the methyl peaks, indicating DMFAI was present in the films (**Figure S33**).

6.2.4: Conclusions

We have shown that in the methylamine vapour treatment of MAPbI_3 , rather than directly proceeding between a liquid ($\text{MA}^0\cdot\text{MAPbI}_3$) and perovskite phase, metastable crystalline intermediates form which dictate the liquification and recrystallization processes. During recrystallization, the intermediate phase rapidly crystallises from the liquid with preferred orientation, before converting to the perovskite phase. The 'healed' films typically produced via this route exhibit complex non-uniaxial orientation – multiple grain orientations – which are masked by conventional 1D XRD measurements. We illustrate that the MA^0 partial pressure and temperature parameters can be used to manipulate the nucleation and growth process to achieve uniaxial orientation, and note recent efforts to exploit this have resulted in high efficiency devices.^{85,101} Using a temperature-field driven recrystallization, we grew close to uniaxially-oriented MAPbI_3 on lattice-matched KCl substrates. Using absorption, nuclear magnetic resonance (NMR) and fourier-transform infrared (FTIR) spectroscopies, we elicited a new understanding of the $\text{MA}^0\cdot\text{MAPbI}_3$ liquid phase and the role played by methylamine in solvating this system, with applicability to related co-ordinating solvent systems. Finally, we explored the use of MA^0 vapour treatments of formamidinium-containing perovskites. We demonstrated an *in-situ* reaction between methylamine and FA^+ results in two bulky cations being formed, which are incorporated into temperature-stable 1D iodoplubate phases, preventing the recrystallisation of a photoactive perovskite layer. This study widens the current understanding of perovskite structure formation via the MA^0 gas-conversion route with insight for manipulating perovskite orientation, and for the future design of vapour treatments and volatile solvent systems which can be used with MA-free perovskite compositions.

6.2.5: Methods

Materials

All materials were purchased from Sigma Aldrich unless otherwise stated.

Sample substrate preparation

Unpatterned ITO substrates (Ossila) were cleaned by sonication sequentially for 15 minutes each in 2% Hellmanex/boiling de-ionised (DI) water, boiling DI water and isopropanol, with boiling DI and acetone rinsing between the sonication steps. Substrates were then UV ozone treated for 15 minutes before transport layer deposition.

Where used, np-SnO₂ layers⁸³ were spin-coated at 3000 rpm from a colloidal solution (15 wt% in H₂O, Alfa Aesar) diluted v:v 1:4 with ultrapure DI water. This solution was mixed plenty and sonicated before use, forming a highly uniform compact layer. Directly before use, np-SnO₂ films were annealed for 30 min at 150 °C and UV ozone treated for 15 minutes, which we found to be critical to maintain high V_{oc}.¹⁰²

For the self-assembled monolayer (SAM) substrates, MeO-2PACz layers on ITO were prepared according to the protocol by Al-Ashouri *et al.*⁸⁴ Briefly, MeO-2PACz was weighed into a vial, opened in air for 10 s, transferred back into a GB and dissolved in anhydrous ethanol (VWR) at 0.28 mg ml⁻¹. This solution was sonicated for 10 min and spin-coated statically onto freshly UVO-treated ITO at 3000 rpm for 30 s. Films were annealed for 10 minutes at 100 °C, with no further treatment before MAPbI₃ deposition.

Where used, samples for transmission measurements were prepared using Kapton tape on glass as the substrate. The cleaning and SnO₂ layer preparation was as above except for repeated dynamic spin coating of the np-SnO₂ solution prior to annealing to ensure good layer formation on the hydrophobic polyimide. For film fabrication on 1 cm² KCl crystal substrates (Agar Scientific), the crystal was cleaved using a razor blade and cleaned by polishing.

ACN:MAPbI₃

ACN MA⁰:MAPbI₃ solution was prepared using an acetonitrile and methylamine solvent system according to the procedure reported by Noel *et al.*²⁷ In a N₂-filled glovebox, MAI (Ossila) and PbI₂ (TCI) in a 1:1 stoichiometry were added to a vial or small volumetric flask. Acetonitrile was added for a solution concentration of 0.5 M, forming a black suspension, which was then covered with a rubber turnover stopper. Under a fume hood, N₂ was flowed into a gas washing bottle containing ethanol:methylamine solution (33 wt%) before passing through a desiccant tube containing fresh Drierite and CaO and into the solution (shown in Figure S22). Gas was passed from the bubbler into the vial until all material was completely dissolved, with additional mixing as required, before resealing in a N₂ glovebox. MAPbI₃ thin film samples were prepared by dynamically spin-coating the 0.5 M ACN MA⁰:MAPbI₃ solution in a glovebox at 3,000 rpm, before annealing at 100 °C for 15 minutes.

FAPbI₃

FA(MA)PbI₃ films were prepared using a previously reported two-step method by Jiang *et al.*⁹⁷ Specifically, a 1.5 M solution of PbI₂ dissolved in DMF:DMSO (9:1 v:v) was spin-coated on the freshly-prepared np-SnO₂ layer in an N₂ glovebox and directly transferred onto a hotplate to dry at 70 °C for 1 min. For the second step, a solution containing 180 mg of FAI (Ossila), 12.8 mg of MAI (Ossila) and 18 mg of MACl in 2 ml of IPA was freshly prepared. Films were removed from the glovebox (kept dry until use) and the organohalide solution was dynamically spin-coated onto the PbI₂ layers at 2,000 rpm in air (typically 30-40 % RH). Films were then immediately transferred onto a hotplate at 150 °C and annealed for 15 mins. After removing from the hotplate, films were kept dry before transferring back to the glovebox. For transmission measurements, films prepared on glass/Kapton/SnO₂ substrates were covered with a second piece of Kapton tape (before or after MA⁰ treatment) and the combined Kapton/SnO₂/FAPbI₃/Kapton sample was removed from the glass for measuring.

Methylamine treatment

Lab-based methylamine healing used a similar bubbling system as described for the preparation of the ACN MA⁰:MAPbI₃ solution. From the desiccant tube, gas was instead flowed slowly into an inverted funnel to create a small methylamine vapour environment. Samples were placed on a hotplate at various temperatures (23 °C, 37 °C or 50 °C) with the glass funnel placed on top to treat samples with the gas. After 5 seconds, the gas flow was stopped, and after 20 seconds the cone was rapidly removed vertically to minimise any airflow effects over the sample surface.

Device fabrication and testing

ITO/SnO₂ substrates were prepared as described above with etching using 4M HCl and Zn powder prior to cleaning. After UV ozone treatment, MAPbI₃ or FA(MA)PbI₃ layers were deposited as described above. For the healed devices, the MAPbI₃ layer was not annealed further after MA⁰ vapour treatment to confirm the influence of only the treatment. Devices were completed by dynamically spin-coating a spiro-OMeTAD solution onto the perovskite at 4,000 rpm in a GB. This solution contained 86 mg of spiro-OMeTAD (Ossila, sublimed) dissolved in 1 ml of chlorobenzene (by vortex mixing for ~5 minutes), 34 µl of *tert*-butyl pyridine, 20 µl of Li-TFSI solution (500 mg ml⁻¹ in ACN), and 11 µl of FK209 Co(II) PF₆ solution (Greatcell, 300 mg ml⁻¹ in ACN). ITO was exposed using a razor blade and after leaving overnight in a drybox, an Au electrode was evaporated under high vacuum (80 nm at 0.1 Ås⁻¹ for 2 nm then 1.2 Ås⁻¹).

All device performances were measured under a Newport 92251A-1000 solar simulator in ambient conditions, calibrated to AM1.5G 100 mWcm⁻² illumination with an NREL-certified

silicon reference cell. A metal aperture mask defined a cell area of 0.026 cm², and *J-V* curves were recorded with a Keithley 237 source measure unit. Measurements were made by forward and then reverse sweeping the bias between -0.1 and 1.2 V at 100 mVs⁻¹. The stabilised power output was determined by applying a bias voltage, defined by the reverse sweep V_{mpp} , and holding devices under this bias for several minutes. All device metrics were typically measured two days after perovskite deposition and no light-soaking or voltage pre-biasing were applied.

MA⁰·MAPbI₃ liquid preparation

First, MAPbI₃ powder was prepared by drop-casting 0.5 M ACN MA⁰·MAPbI₃ solution. The solution was gradually dropped onto a cleaned sheet of PTFE held at 65 °C on a hot plate under a fume hood. After the powder was completely crystallised, the temperature was increased to 75 °C for 30 min to remove any remaining solvent, before the material was recovered from the PTFE and transferred to a N₂ glovebox. The MAPbI₃ was then ground into a fine powder with a pestle and mortar, and ~2 g was added to a 10 ml round bottom flask with a stir bar and sealed with a rubber turnover stopper. Using the bubbling system described above, after extensive flushing with gas, an inlet needle was inserted into the stopper, with a second outlet needle passed into ethanol to collect the outgas and any disturbed MAPbI₃ powder. The MA₀ gas was flowed gradually over the fine powder until completely dissolved (~90 min) as a clear, viscous liquid which collected at the bottom of the flask. A low pressure/vacuum (LPV) NMR tube was filled with MA gas and maintained in this environment with a gas balloon above. The prepared MA⁰·MAPbI₃ solution was then rapidly transferred into this tube with minimal air contact using a wide needle syringe inserted into the neck of the balloon, before sealing with the tube piston (inside the balloon).

GIWAXS

In situ GIWAXS measurements were performed at the I07 surface and interface diffraction beamline at Diamond Light Source.⁶⁴ The experimental setup is shown and described in Figure S1. During liquification, N₂ was flowed into a bubbler containing ethanol:methylamine solution (33 wt%), with the evolved gas passing into an X-ray transparent sample environment. Crystallisation was induced by flowing N₂ and applying a mild vacuum to remove methylamine vapours from the chamber. X-rays with photon energy 10 keV were incident on samples at 0.5°, with the scattering detected by a PILATUS3 2M hybrid photon counting detector at a distance of 421 mm. Acquisition was for 100 ms with ~20 ms downtime between measurements. *Ex-situ* GIWAXS data was acquired with a Xenocs Xeuss 2.0 system using a monochromatic Ga MetalJet X-ray source (Excillum). X-rays with photon energy 9.243 keV were scattered from the sample surface and collected with a PILATUS3R 1M hybrid photon counting detector

(DECTRIS) with a sample to detector distance of ~330 mm and a grazing incidence angle of 0.5°. While measuring, the flight tube, sample chamber and detector were held under vacuum.

Additional *in-situ* GIWAXS measurements for analysing the ACN/MA solution were acquired at the mySpot beamline at the BESSY II synchrotron. A remote-controlled syringe was used to cast a droplet of 0.8 M ACN/MA solution onto a substrate surface in the path of X-rays with energy 9 keV ($\lambda = 1.3776 \text{ \AA}$) which were incident at 2°. Scattering from the droplet as it dried was collected using an Eiger 9M hybrid photon-counting detector (DECTRIS) positioned 295 mm from the sample, with the detector geometry calibrated using LaB₆.

Diffraction analysis

Data was corrected, processed and reshaped using PyFAI and modified scripts based on the pygix library (adapted for GI geometry).^{103,104} The GIXSGUI Matlab toolbox¹⁰⁵ was used to determine the expected diffraction peak positions for a given unit cell on the 2D data. GIWAXS SIIR-Kit was used for further 2D indexing.¹⁰⁶ Simulated 2D diffraction patterns used the simDiffraction Matlab toolbox,¹⁰⁷ using crystallographic information for the *I4cm* MAPbI₃ reported by Stoumpos *et al.*⁶⁵ Azimuthally integrated 1D data were indexed and refined using EXPO2014.¹⁰⁸ Further refinements and rigid body modelling were performed in TOPAS 5 (Bruker), using a fundamental parameters (FP) approach, in which an instrumental profile is concurrently refined, which describes the broadening characteristics of the diffractometer and geometry used.

Computational methods

Density functional theory (DFT) calculations were carried out using the SIESTA code (version 4.0)^{109,110}, using the same method as in our previous work.⁴⁷ The van der Waals functional¹¹¹ with C09 exchange¹¹² was used. Double-zeta polarised (DZP) finite-size numerical atomic orbitals were used in combination with Troullier-Martins norm-conserving pseudopotentials (relativistic for Pb, non-relativistic for C, N, H and I) downloaded from the SIESTA online basis sets database.¹¹³ For C, N, H and I, the standard DZP basis set cutoff radii were defined using the energy shift (i.e. the energy cost of confining the atomic orbital to a finite-range) of 10 meV; the basis set for Pb was downloaded from the SIESTA online database.¹¹³ The Brillouin zone was sampled using the *kgrid_cutoff* parameter of 30 Å, resulting in 105-256 *k*-points, depending on the cell size. All atomic positions and lattice parameters were fully optimised without applying any symmetry constraints, with the displacement threshold of 0.1 Å and the force of 0.04 eV Å⁻¹. This methodology resulted in accurate calculated lattice constants of cubic MAPbI₃ in our previous study.⁴⁷

Absorbance

For the ACN MA⁰·MAPbI₃, a 0.8 M solution was sealed in a 10 μm quartz cuvette. For the MA⁰·MAPbI₃, a thin film of MAPbI₃ was prepared on a quartz substrate. This was exposed to MA⁰ vapour under the healing funnel system above, and a second piece of quartz was transferred on top to trap the liquid phase, and edge sealed with a UV-curable epoxy. Both samples were measured using a Cary 5000 UV-Vis-NIR spectrometer (Agilent).

FTIR

Perovskite solutions as well as the reference solvents were measured in an ATR-cell with a Ge crystal at RT in vacuum with an FTIR spectrometer. For each measurement we averaged over 100 scans with 0.5 cm⁻¹ resolution.

NMR

Sample preparation – Both solution samples were prepared according to the procedures above, with the MA⁰·MAPbI₃ prepared directly into an LPV NMR tube and the ACN MA⁰·MAPbI₃ was sealed in a 100 MHz 7" NMR tube. In both cases, peak positions were calibrated using an isolated standard of lead acetate, Pb(CH₃COO)₂ 1M in d₆-DMSO in an internal capillary. This solution was also measured separately to ensure proper calibration. Additional measurements were acquired to understand healed FA(MA)PbI₃ films. These samples were prepared by redissolving films in d₆-DMSO and then transferring into a 100 MHz 7" NMR tube in a N₂ glovebox.

²⁰⁷Pb NMR - spectra were all acquired on a Bruker AVII 400MHz equipped with room-temperature TBO probe head. Typically a sweep width of 897 ppm was used and 8192 points were acquired, resulting in a total acquisition time of 54.48 ms. The centre frequency had to be adjusted from sample to sample to detect the desired signal, therefore, on new samples, a full scan of the possible shift range was acquired until the peak was detected. We used a 30° degree pulse in order to minimize the recycle delay down to 200 ms (for samples with very broad peaks and low concentrations acquisition time and recycle delay were adjusted down to 8ms and 50ms respectively). The number of scans thus ranged from 512 for the very concentrated MA⁰·MAPbI₃ sample up to several thousand scans for the more dilute ACN MA⁰·MAPbI₃ sample.

¹H- and ¹³C-NMR - All other spectra were measured with standardized parameter sets from Bruker Topspin version 2.1 (AV400) and 3.0 (AV500). Additional ¹H measurements were performed using a Bruker AVANCE III instrument operating at 400.2 MHz and 289 K. Spectra were acquired over 16 scans with an 8.2 kHz spectral window and 64k acquisition points, with 30 s relaxation delay to ensure full quantification.

6.2.6: Acknowledgements

We thank Dr. Andrew Parnell and Dr. Nga Phung for assistance with diffraction measurements as well as Dr. Sandra van Meurs and Khalid Doudin for assistance with NMR measurements. We thank the EPSRC for PhD studentship funding via the Centre for Doctoral Training in New and Sustainable PV (EP/L01551X/1, J.A.S.) and the Centre for Doctoral Training in Polymers, Soft Matter and Colloids (EP/L016281/1, M.E.O'K) and via the University of Sheffield DTG account (R.C.K.). J.A.S. also thanks Erasmus+ for funding and Dr Thomas Routledge and Elena Cassella for useful discussions. This work was supported through the Global Challenges Research Fund (GCRF) through Science & Technology Facilities Council (STFC), grant number ST/R002754/1: Synchrotron Techniques for African Research and Technology (START). O. S. and E. U. acknowledge funding from the German Science Foundation (DFG) provided in the framework of the priority program Grant No. SPP 2196, "Perovskite semiconductors: From fundamental properties to devices." A.S. hereby acknowledges the financial assistance of the South Africa National Research Foundation (NRF), University of the Witwatersrand – Material and Energy Research Group (MERG) and DST-NRF Centre of Excellence in Strong Materials (CoE-SM) toward this research. GIWAXS studies at the I07 beamline at Diamond Light Source were performed with beam time allocation SI22651-1. The allocation of beamtime at the mySpot synchrotron beamline, and the PTB four-crystal monochromator beamlines at BESSY II, Berlin is also gratefully acknowledged along with the assistance of beamline scientists with these measurements. We thank Armin Hoell and the PTB for allowing use of their facilities at BESSY II for the SAXS measurements. We also thank Xenocs for their ongoing support through the X-ray scattering user program at the University of Sheffield and we thank the EPSRC for funding the purchase of this instrument.

6.3: Supporting Information

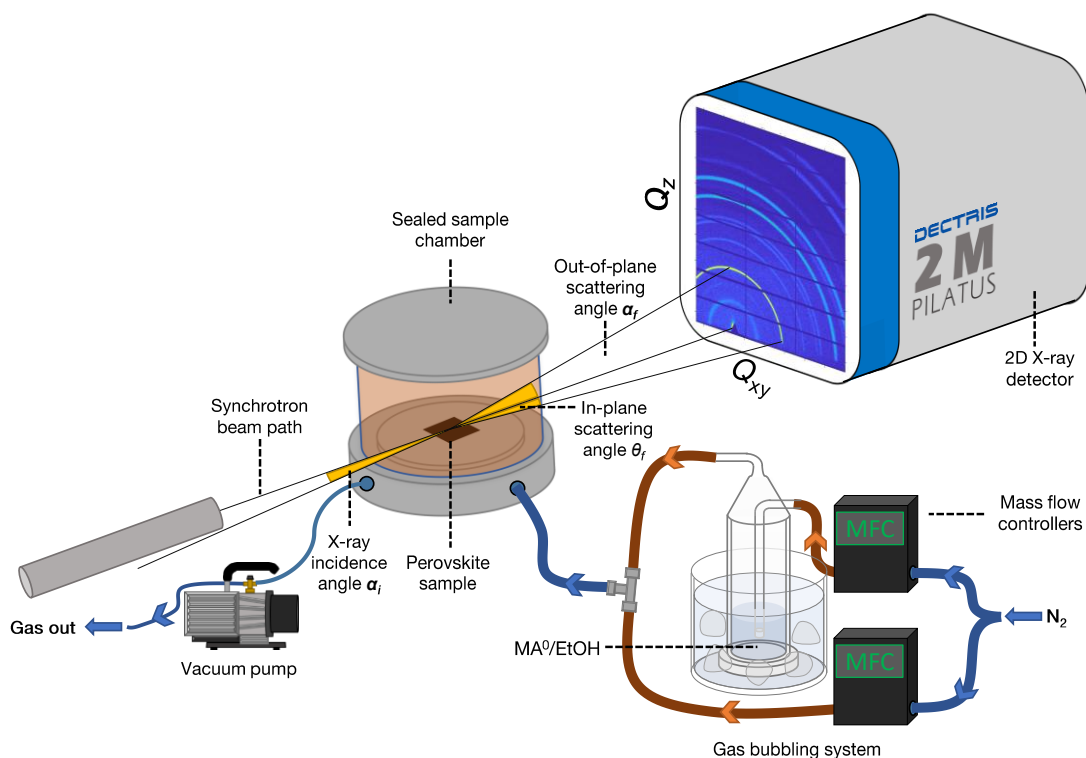


Figure S1: Experimental scheme for the in-situ experiments. Perovskite samples are placed in a closed environmental chamber, which was then flushed with N_2 . Two mass flow controllers were employed to deliver either MA^0 gas or further N_2 into the chamber. X-ray scattering was monitored typically over 30-60 seconds with ~ 10 frames s^{-1} .

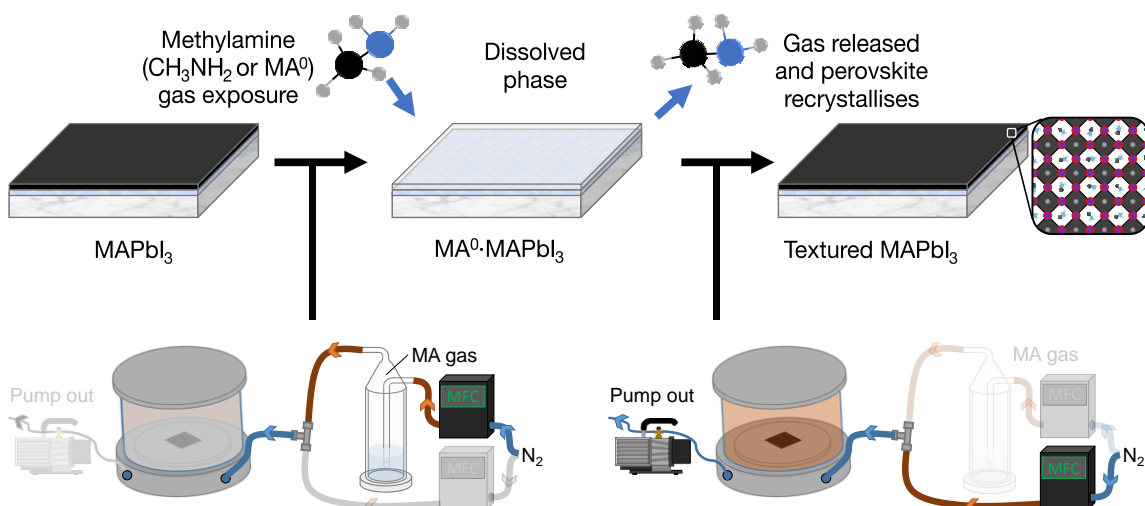


Figure S2: During the liquification and recrystallisation processes, the $MAPbI_3$ film was converted or recrystallised. For the liquification, MA^0 was flowed into the chamber, and for recrystallisation N_2 with an additional mild vacuum to accelerate MA^0 extraction.

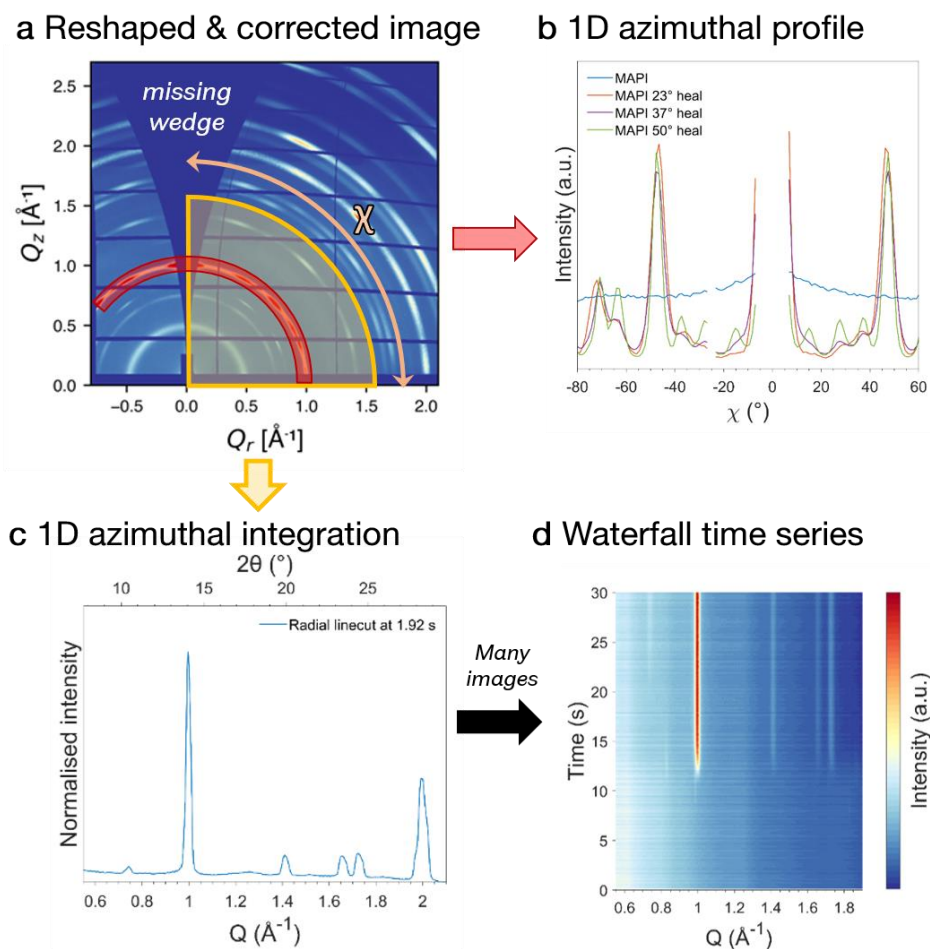


Figure S3: Illustration of the conversion of data from a) corrected and reshaped 2D GIWAXS pattern to b) an azimuthal intensity profile (intensity vs. χ) or c) azimuthally integrated to form radial profiles (intensity vs. Q). d) Sequences of radial profiles can be used to monitor phase evolution.

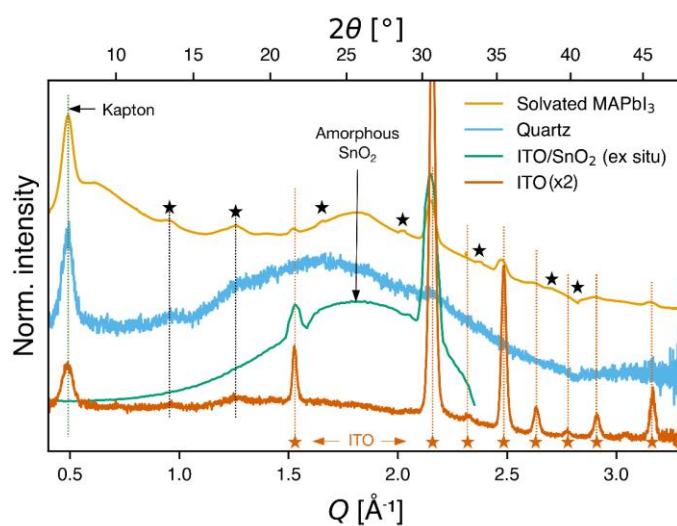


Figure S4: Additional scattering backgrounds from the in-situ experiment, confirming no additional crystalline scattering features are present in the solvate phase.

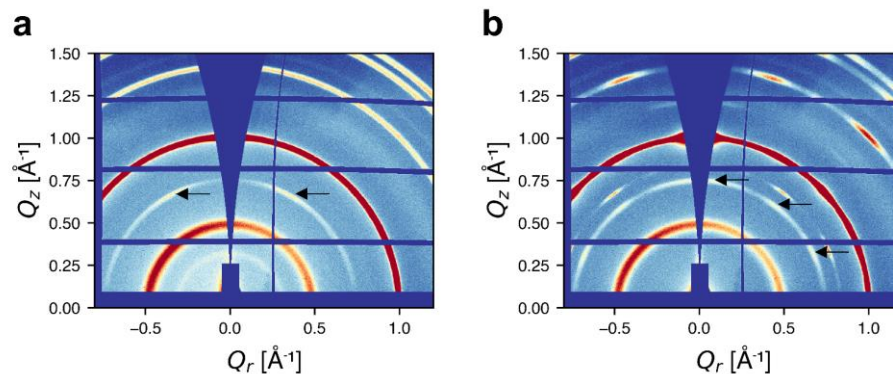


Figure S5: A weakly scattering phase was present in the in-situ data which we attribute to a surface phase forming at the thicker edges of the substrate. This phase is reoriented during the healing process, but was not apparent in ex situ measurements.

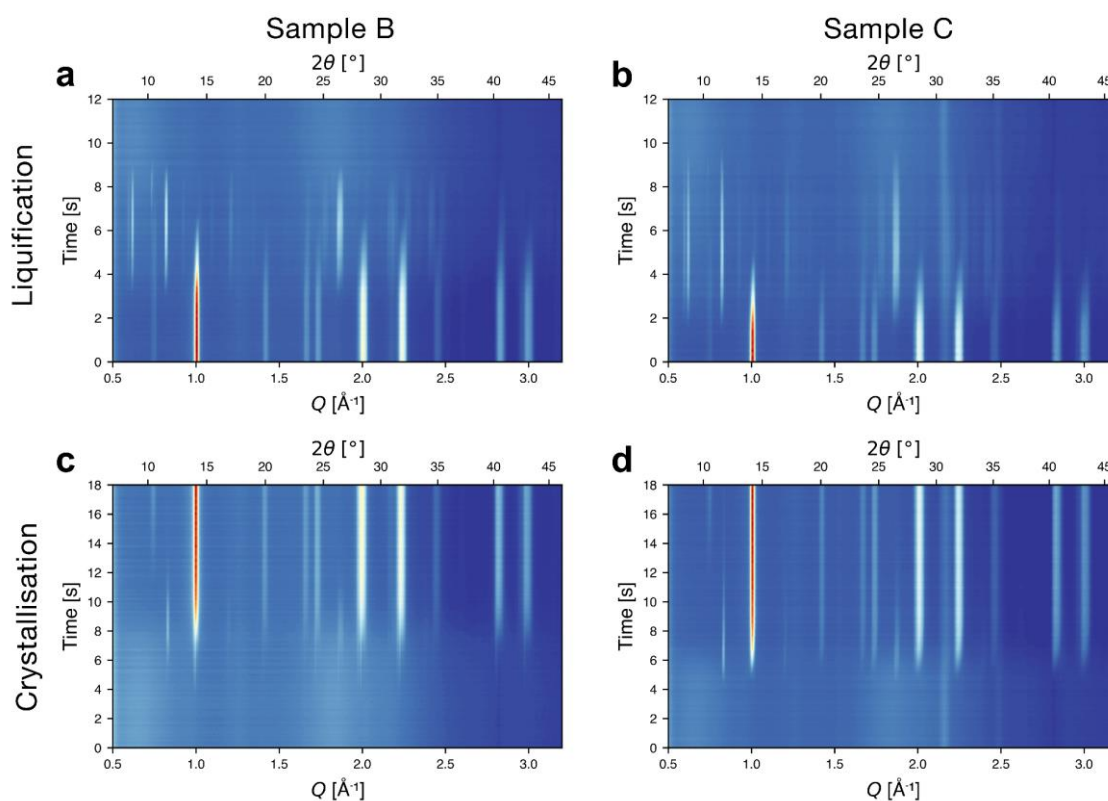


Figure S6: The in-situ experiment shown in the main text for 'Sample A' was repeated on a further two samples under the same conditions (hotplate temperature = 23 °C). Parts a) and b) show the waterfall plot of X-ray scattering during the liquification process for samples B and C. Parts c)-d) show the recrystallisation. In each case, the I_1 and I_2 intermediates are present, with the only difference being slight variation in the duration of the phase transformation.

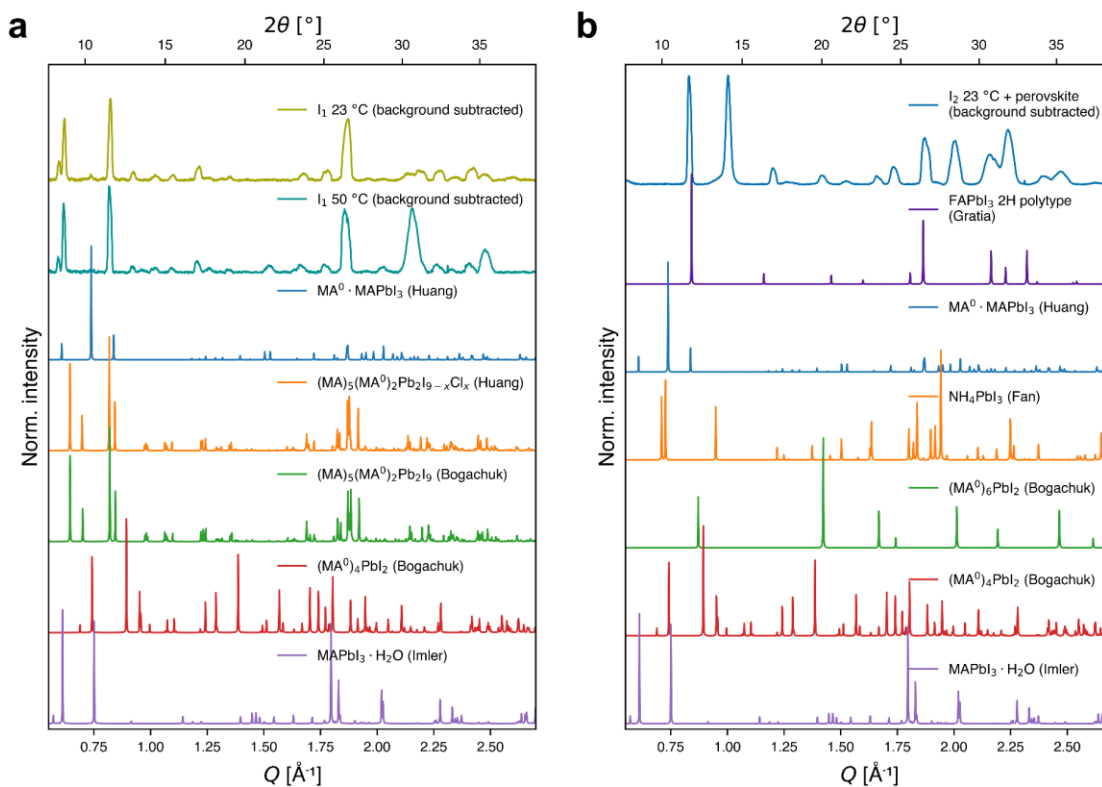


Figure S7: Comparison of background subtracted a) I_1 (liquification) and b) I_2 (crystallisation) intermediate diffraction patterns with a selection of simulated diffraction patterns for reported MA^0 and related 1D and 0D phases from an exhaustive search of crystallographic databases. Crystallographic information files simulated here were reported by Huang,³¹ Bogachuk,⁶⁶ Imler,¹¹⁴ Gratia⁹⁸ and Fan.¹¹⁵

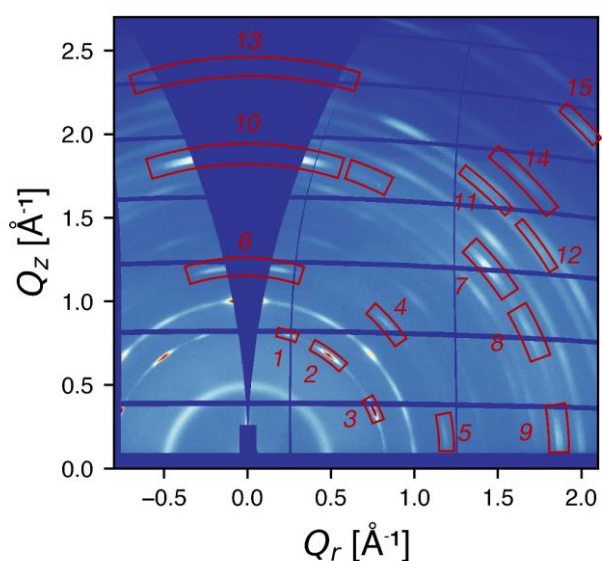


Figure S8: Diffraction spots associated with the I_2 intermediate phase. Numbered peak positions are given in Table S1.

No.	Q	χ [°]	Q_{xy}	Q_z
1	0.836	72.9	0.245	0.799
2	0.835	53.5	0.496	0.671
3	0.832	23.6	0.763	0.333
4	1.207	46.1	0.838	0.869
5	1.198	9.1	1.183	0.189
6	1.205	81.2 **	0.184	1.191
7	1.876	39.6	1.446	1.195
8	1.871	26.8	1.669	0.845
9	1.870	5.3	1.862	0.174
10	1.872	79.5 **	0.340	1.841
11	2.193	50.4	1.399	1.688
12	2.190	37.4	1.74	1.33
13	2.389	76.7 **	0.548	2.326
14	2.397	46.1	1.663	1.727
15	2.859	44.4	2.043	2.000

Table S1: Peak positions of the I_2 intermediate during crystallisation determined using SIIR-Kit.¹⁰⁶ Specular reflections are denoted by **, with the values given fitted close to the missing wedge.

No.	2 θ (°)	d (Å)	FWHM	100.*I/I _{max}
1	8.332	10.604	0.054	17.38
2	8.669	10.192	0.055	77.88
3	11.497	7.690	0.031	100.00
4	12.971	6.820	0.175	7.61
5	15.374	5.759	0.192	6.32
6	16.989	5.215	0.168	14.11
7	19.006	4.666	0.268	3.19
8	23.462	3.789	0.443	9.83
9	25.007	3.558	0.350	10.14
10	26.305	3.385	0.194	72.14
11	31.226	2.862	0.194	14.32
12	32.228	2.775	0.194	9.77
13	33.189	2.697	0.326	3.72
14	34.374	2.607	0.301	10.65
15	40.723	2.214	0.378	10.99

Table S2: Fitted peak positions for the 1D I_1 intermediate at 50 °C (1D pattern shown in Figure S7a).

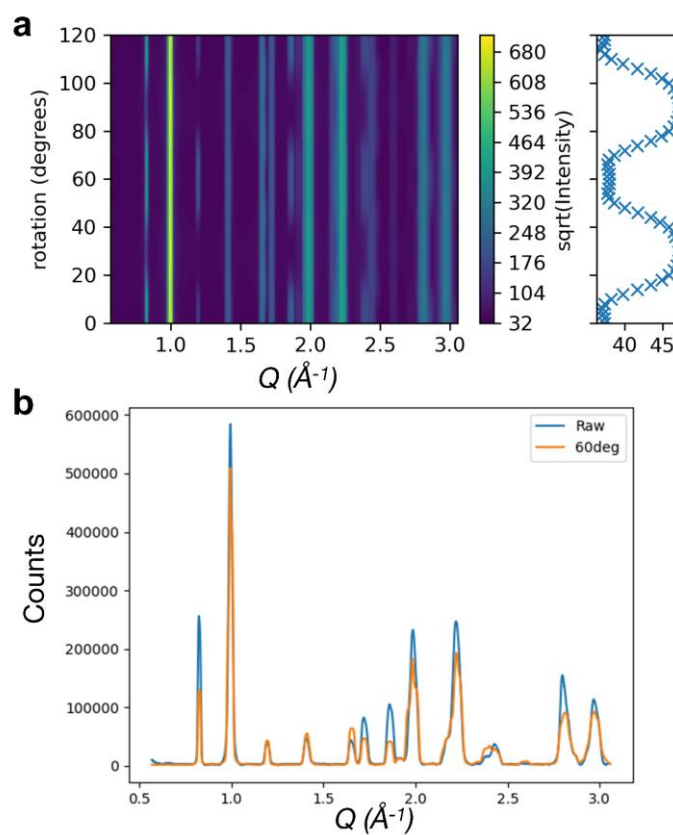


Figure S9: Optimal rotation of the iodoplumbate chains in a hypothetical 1D 2H phase which can reasonably fit the known 1D peaks from I_2 . However, we note that the Pb-Pb-Pb distance of $\sim 7.3 \text{ \AA}$ is not sufficiently long to allow for this face-sharing intermediate.

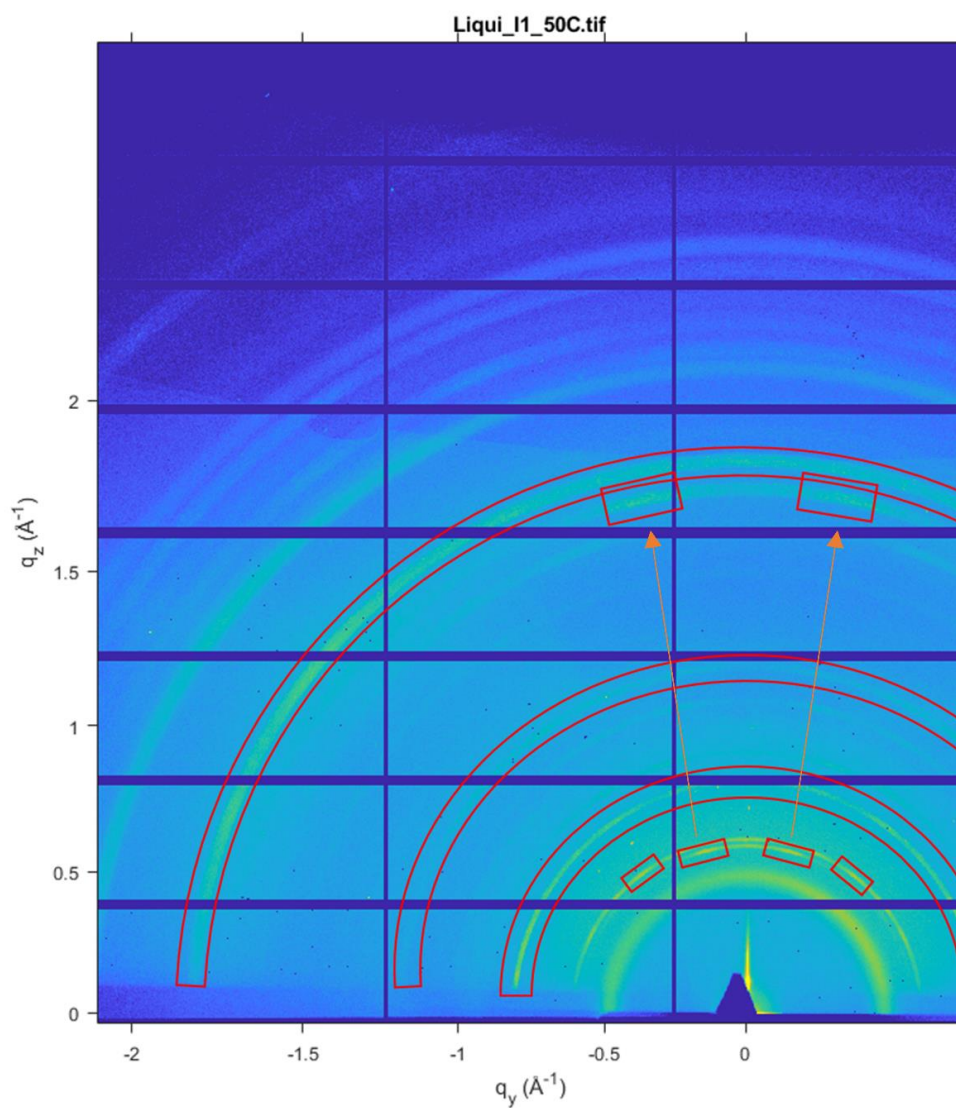


Figure S10: 2D diffraction pattern for re-dissolved 50 °C film (deposited->liquified->recrystallised->rehealed). By dissolving from an already textured MAPbI₃ we could induce some texturing of the I_r. Integrating over all possible frames, a third order relationship between the peaks at 2θ = 8.33° and 25° becomes clear.

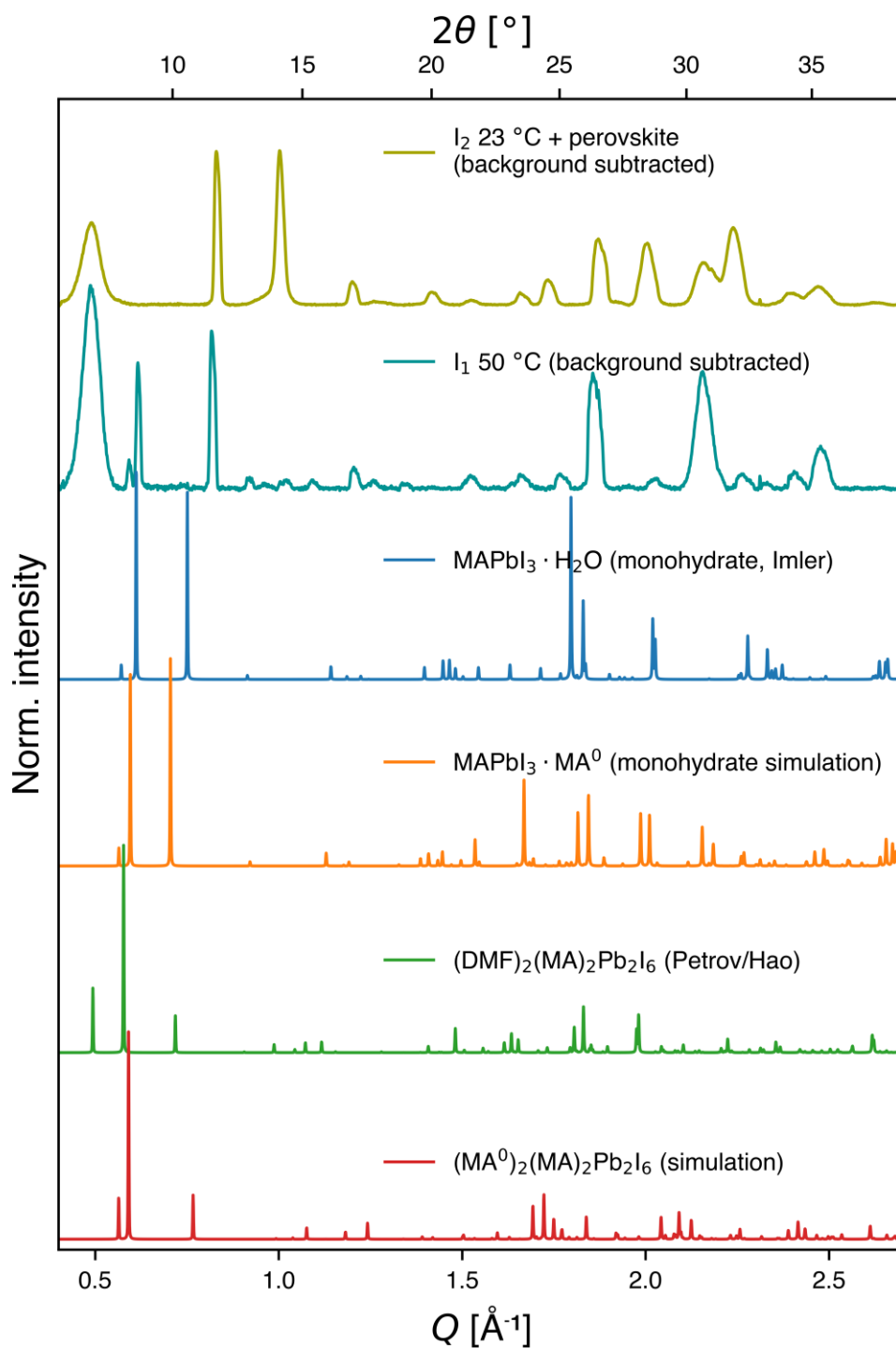


Figure S11: Computationally developed DFT structures compared to the I_1 and I_2 intermediate diffraction. These were developed by replacing the solvent (DMF or H_2O) in phases reported by Imler et al.¹¹⁴ (monohydrated MAPbI_3) and a $(\text{DMF})_2\text{MA}_2\text{Pb}_2\text{I}_6$ solvate phase first reported by Hao et al.¹⁹ and Petrov et al.⁷¹

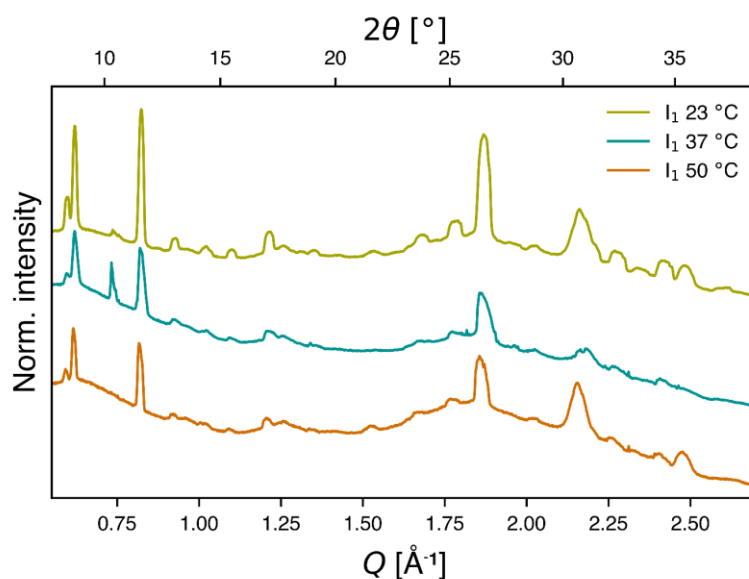


Figure S12: Comparison of azimuthally integrated I_1 intermediate diffraction patterns (combined over many frames) at each process temperature. Peaks for I_1 are consistent between each temperature condition.

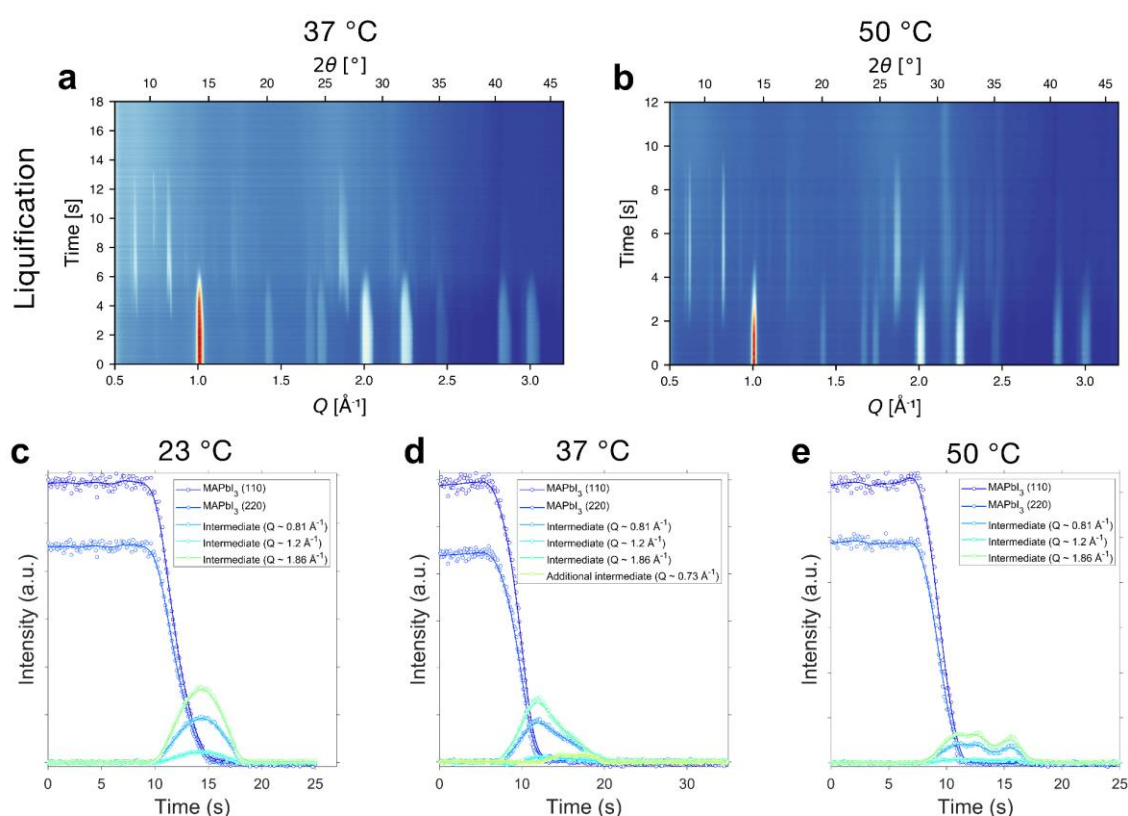


Figure S13: Temperature dependent liquification process. Waterfall plots are shown for a) 37 °C and b) 50 °C (23 °C shown in Figure 1a). Temperature dependent kinetics of phase transformation are shown for each temperature in parts c-e). Here, the scattering intensity for the intermediate and perovskite peaks was integrated at each timepoint. At 37 °C and 50 °C, the I_1 is more gradually converted to the solvate, with MA^0 uptake retarded. 50 °C, was close to the critical temperature for this system.

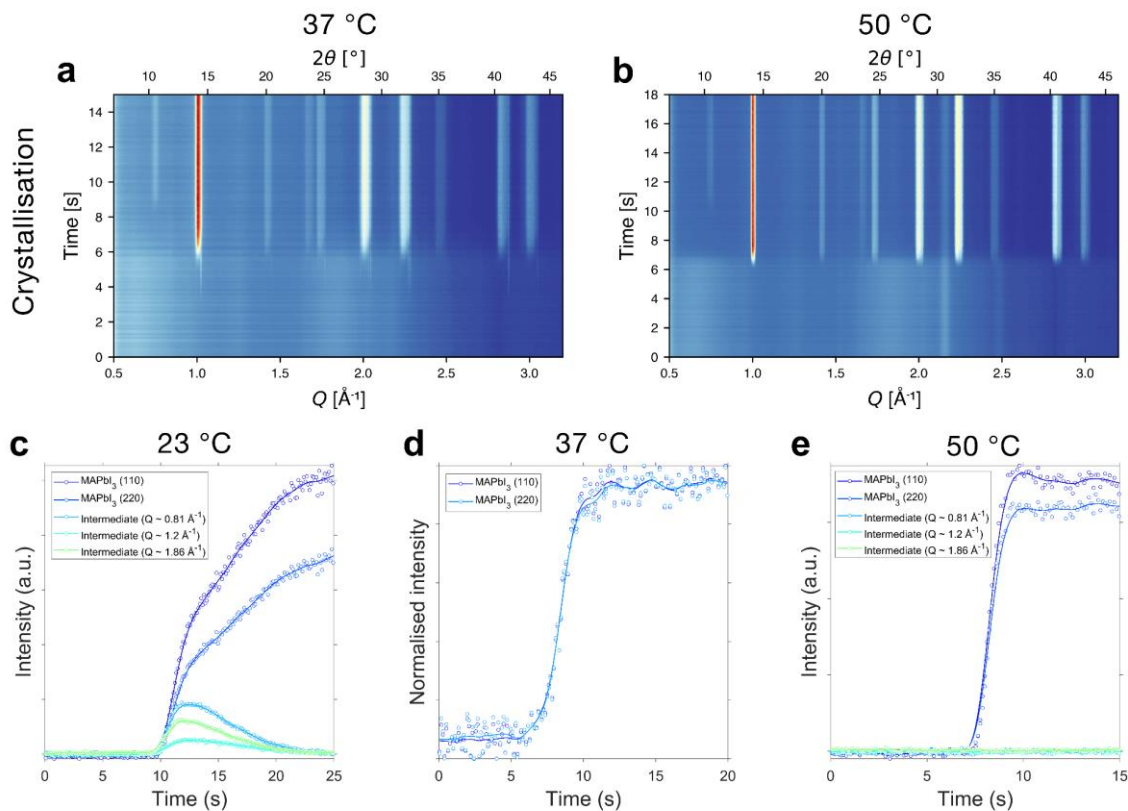


Figure S14: Temperature dependent recrystallisation process with waterfall plots for a) 37 °C and b) 50 °C (23 °C shown in Figure 2a). Parts c-e) illustrate the kinetics of phase transformation at each temperature by integrating the peak intensity at each time. No I_2 phase was observed at 37 °C and 50 °C, with crystalline domains of MAPbI₃ apparently formed directly. In part c) I_2 gradually converts to MAPbI₃ over tens of seconds.

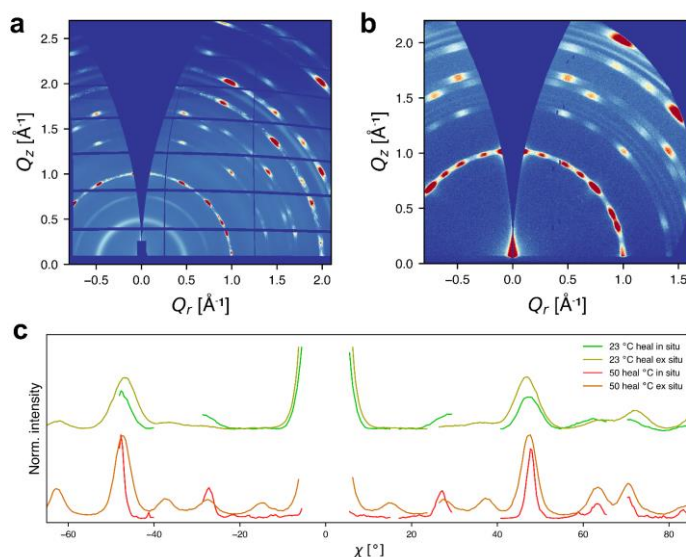


Figure S15: 2D diffraction for 50 °C healed MAPbI₃ a) in situ and b) ex situ (part b is repeated from Figure 3d for comparison). c) Azimuthal intensity profiles for two healing temperatures. Small variations in the intensity distribution are related to the slightly different MA⁰ partial pressures and ambient atmospheres in the in situ (flushing to N₂) vs ex situ (exposed to ambient) healing apparatus.

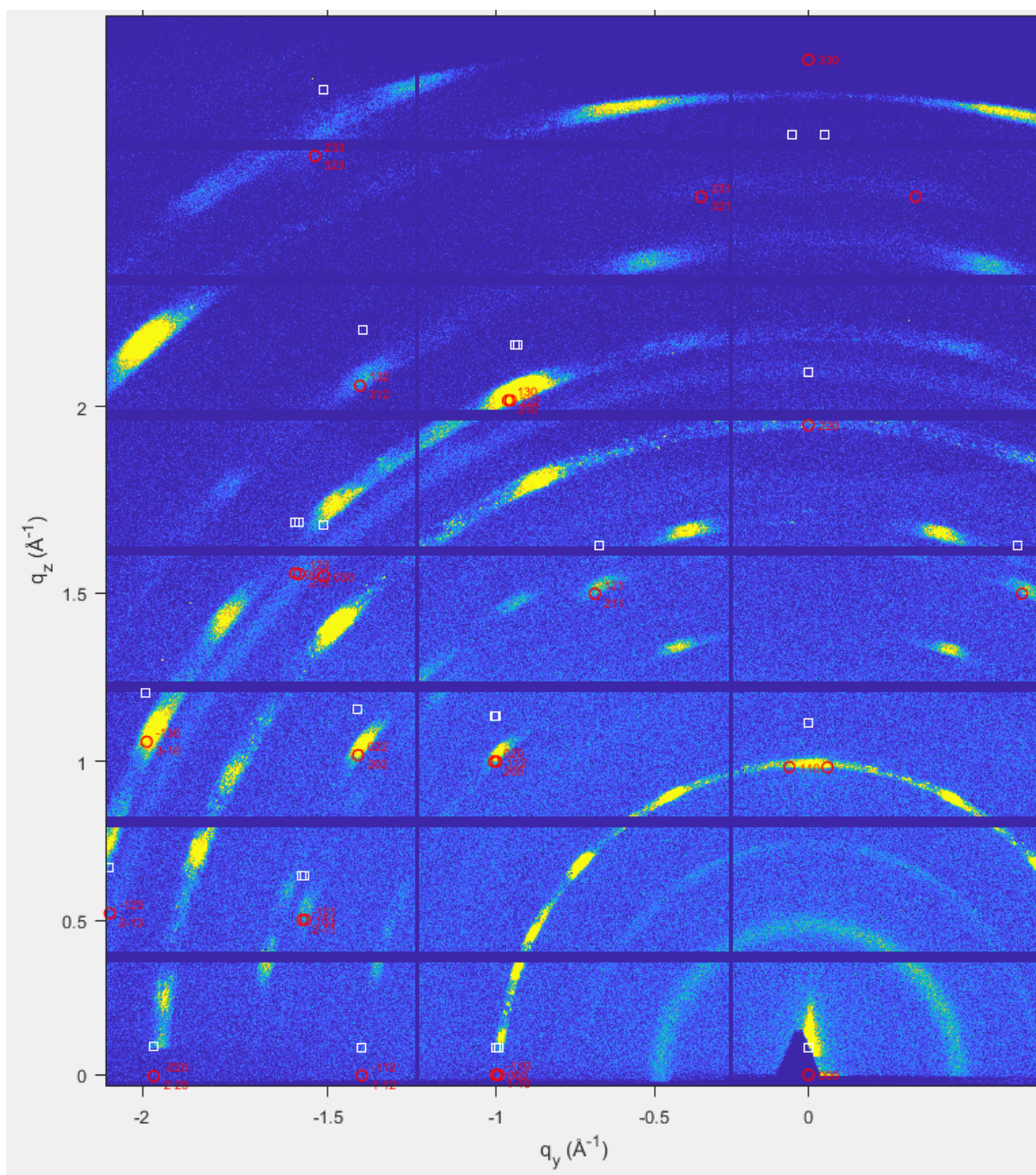


Figure S16: Calculated 2D peak positions expected for a uniaxially $\langle 110 \rangle$ oriented tetragonal MAPbI_3 phase. In red are the Miller indices associated with each peak. Clearly additional texture directions are present in the film to account for the diffraction pattern. Expected peak positions were simulated and overlaid using GIXSGUI.¹⁰⁵

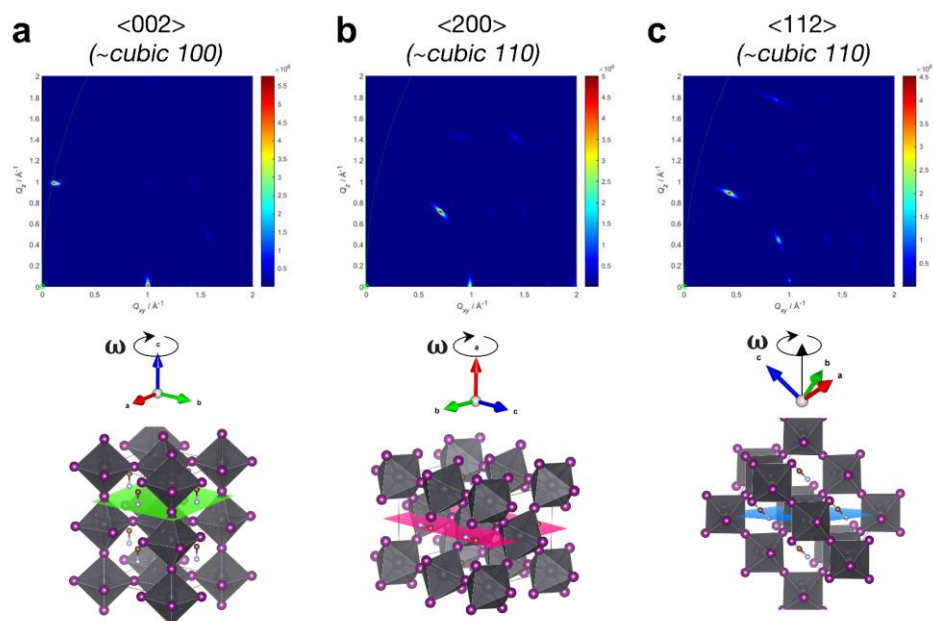


Figure S17: Simulated 2D diffraction patterns for several example texture directions in the film. Data were simulated using *simDiffraction*,¹⁰⁷ with crystallographic information from Stoumpos et al.⁶⁵

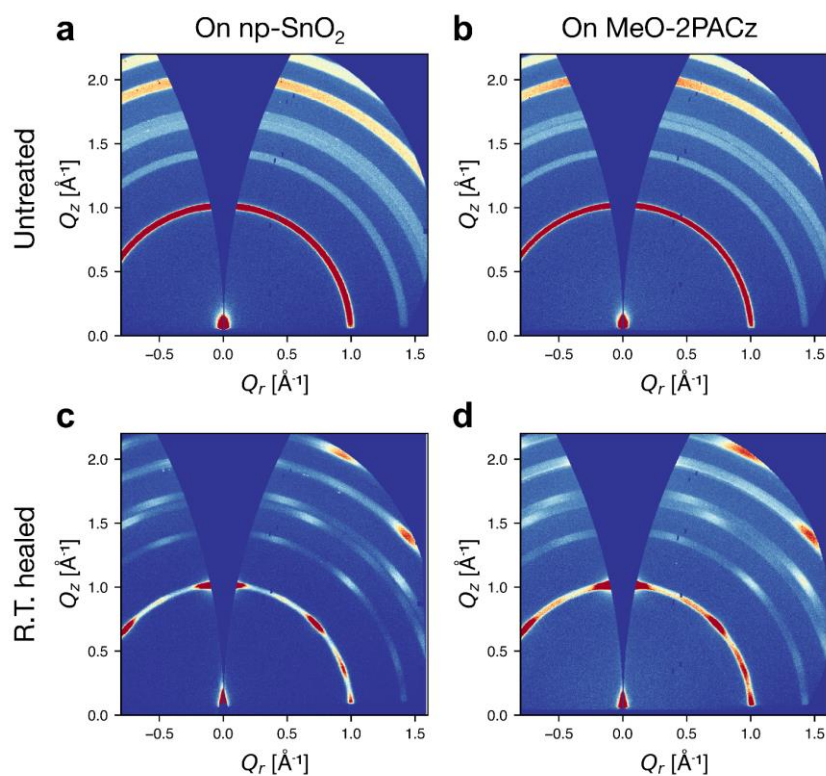


Figure S18: Investigating substrate dependent orientation effects. Films were spin-coated on *np*-SnO₂ and on MeO-2PACz (SAM), and the GIWAXS acquired from the as prepared films in a) and b) exhibits isotropic scattering features. In c) and d) the film has become textured by the room temperature healing process, with orientations consistent between the two substrates, confirming top-down growth.

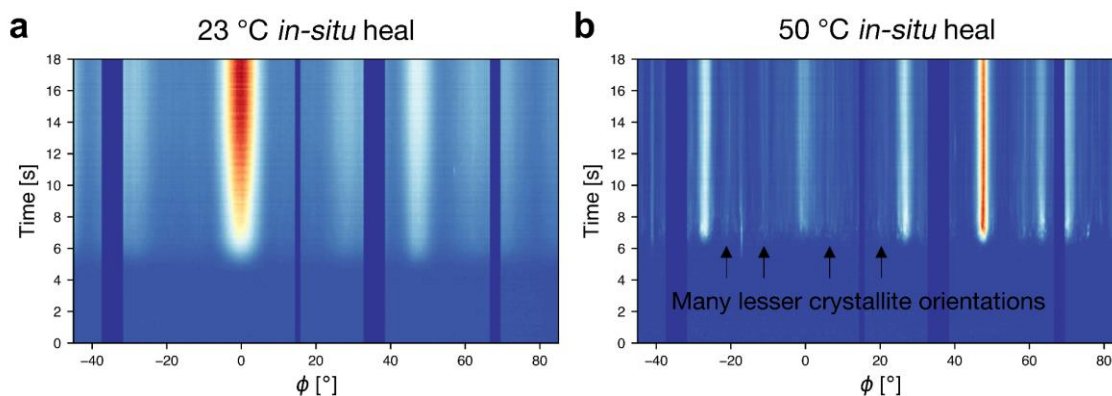


Figure S19: In-situ azimuthal profiles during a) 23 °C and b) 50 °C recrystallisation. These are directly integrated 'phi' profiles of the 2D detector image; the out-of-plane intensity is unrepresentative (as this direction is masked in grazing incidence geometry). Part a) confirms that the I_2 domains do not convert to specific perovskite orientations. At 50 °C, we observe many constrained texture directions due to either orientation locking as grain boundaries form, or possibly secondary nucleation events from the dominant orientations.

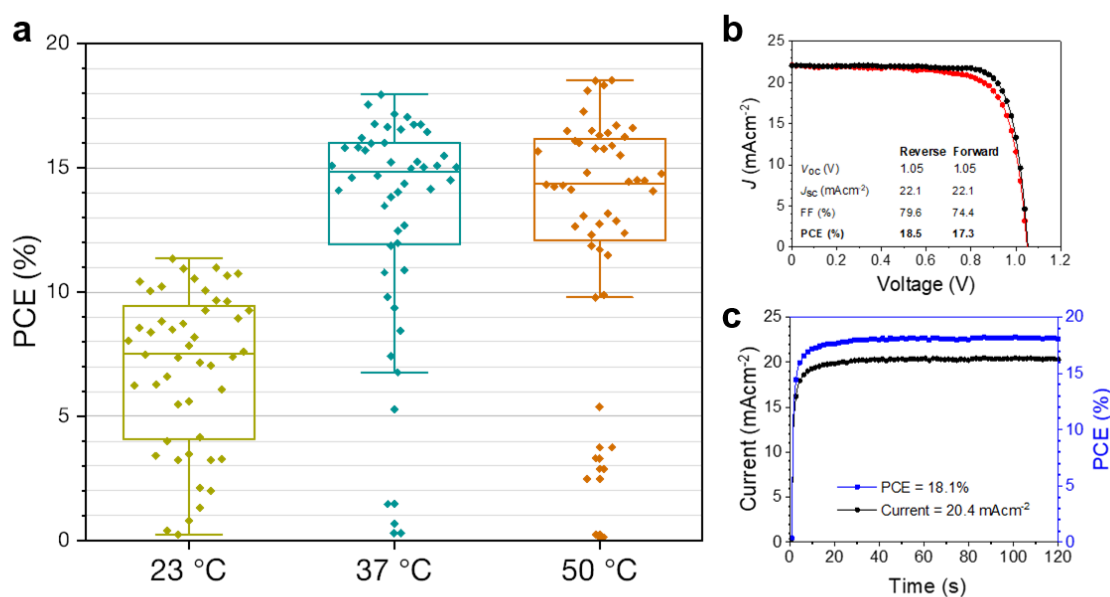


Figure S20: MAPbI₃ photovoltaic devices fabricated with an n-i-p stack (glass/ITO/np-SnO₂/MAPbI₃/spiro/Au). a) Statistical distribution of cell performances at each temperature condition (both forward and reverse sweep efficiencies are shown). b) Champion device fabricated with 50 °C healing to ambient air, with no further annealing. c) Stabilised power output of this champion device at the V_{mpp} bias voltage.

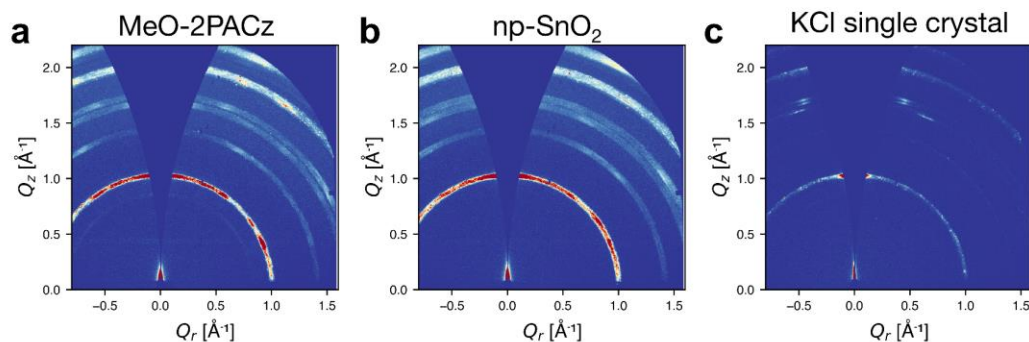


Figure S21: Temperature-field induced crystallisation. Here, the hotplate temperature was gradually increased whilst maintaining the films under an MA⁰ atmosphere under the perovskite phase spontaneously crystallised. In parts a) and b) the orientation is significantly different from the typical healing process (concentration field). In c) by repeating this process on a lattice-matched KCl single crystal substrate, the film orientation was close to uniaxial.

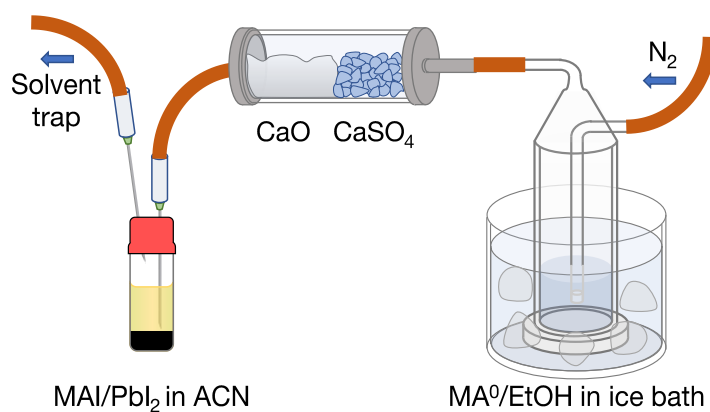


Figure S22: Illustration of the ACN MA⁰-MAPbI₃ solution preparation process under low-moisture conditions.

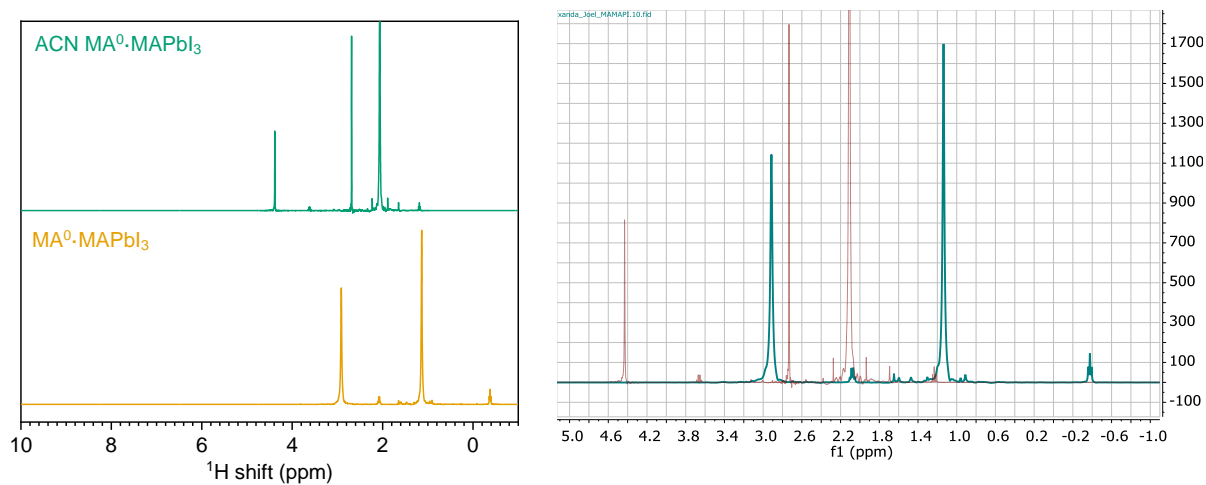


Figure S23: Full ^1H NMR spectra acquired from the ACN $\text{MA}^0\cdot\text{MAPbI}_3$ and $\text{MA}^0\cdot\text{MAPbI}_3$ solutions.

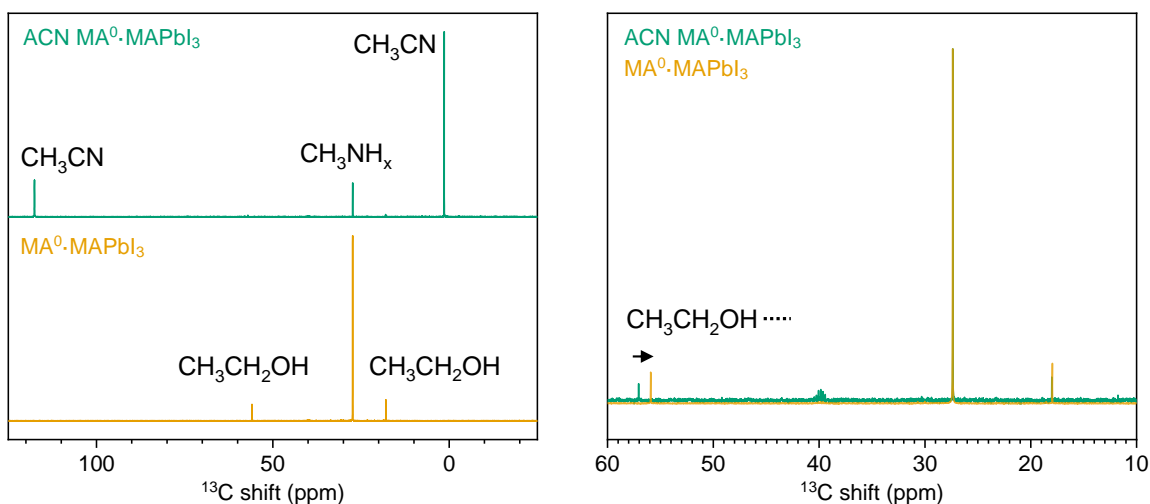


Figure S24: ^{13}C NMR spectra for ACN $\text{MA}^0\cdot\text{MAPbI}_3$ and $\text{MA}^0\cdot\text{MAPbI}_3$. One carbon environment is significantly more shielded (most caused by greater electron density on deprotonated O^-) in the $\text{MA}^0\cdot\text{MAPbI}_3$ sample.

Sample	^1H shift (ppm)					^{13}C shift (ppm)					^{207}Pb (ppm)
ACN $\text{MA}^0\cdot\text{MAPbI}_3$	4.43	3.66	2.73	2.11	1.23	117	55.4	26.8	17.4	0.93	666
$\text{MA}^0\cdot\text{MAPbI}_3$	2.91	2.08	1.14		-0.37		56.5	26.8	17.5		308
Compound	MA^0/MA^+	EtOH	MA^0/MA^+	ACN	EtOH	ACN	EtOH	MA^0/MA^+	EtOH	ACN	Pb
Environment	NH_2/NH_3	$\text{CH}_3\text{CH}_2\text{OH}$	CH_3	CH_3CN	$\text{CH}_3\text{CH}_2\text{OH}$	CH_3CN	$\text{CH}_3\text{CH}_2\text{OH}$	$\text{CH}_3\text{NH}_{2/3}$	$\text{CH}_3\text{CH}_2\text{OH}$	CH_3CN	$\text{MA}_0\cdot\text{MAPbI}_3$

Table S3: Summary of measured NMR shifts and the associated chemical environments.

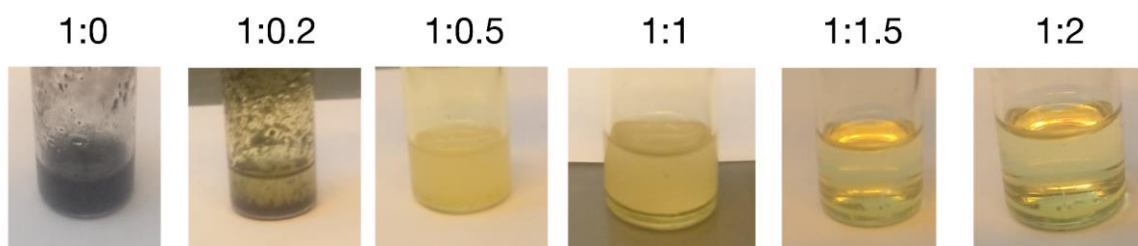


Figure S25: Simple titration of MAPbI_3 dispersed in ACN with liquid MA^0 gradually added.

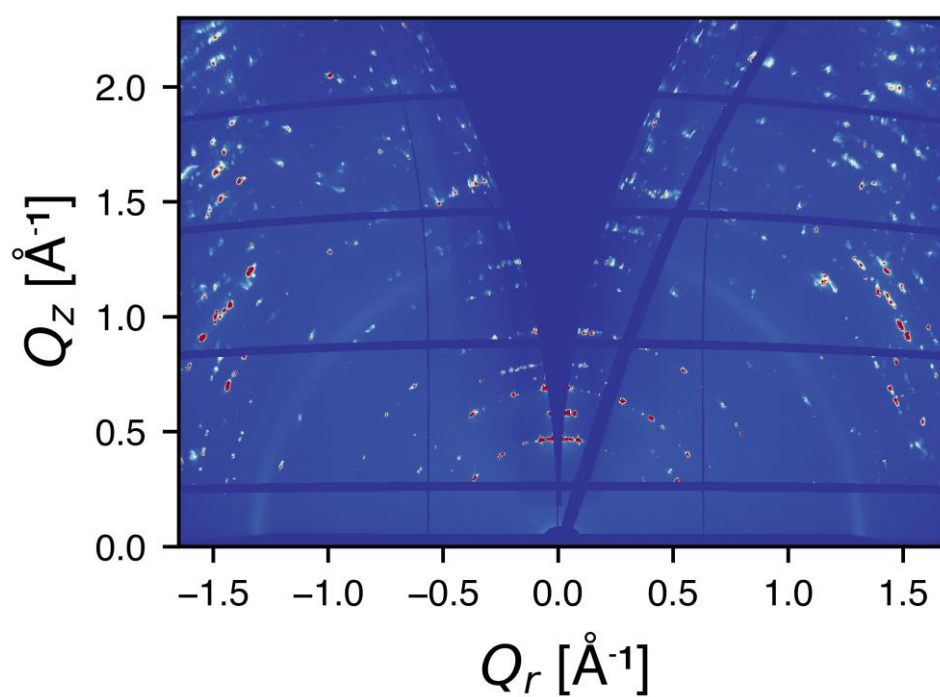


Figure S26: Example reshaped X-ray 2D diffraction pattern from the ACN MA^0 - MAPbI_3 droplet during crystallisation (at the droplet surface).

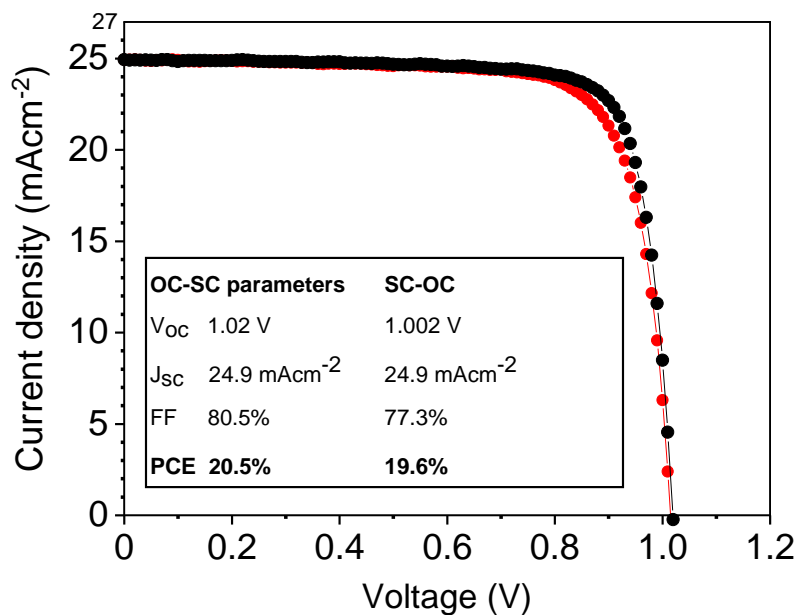


Figure S27: Champion two-step FA(MA)PbI₃ device, confirming appropriate material formation (fabrication protocol is described in the Methods).

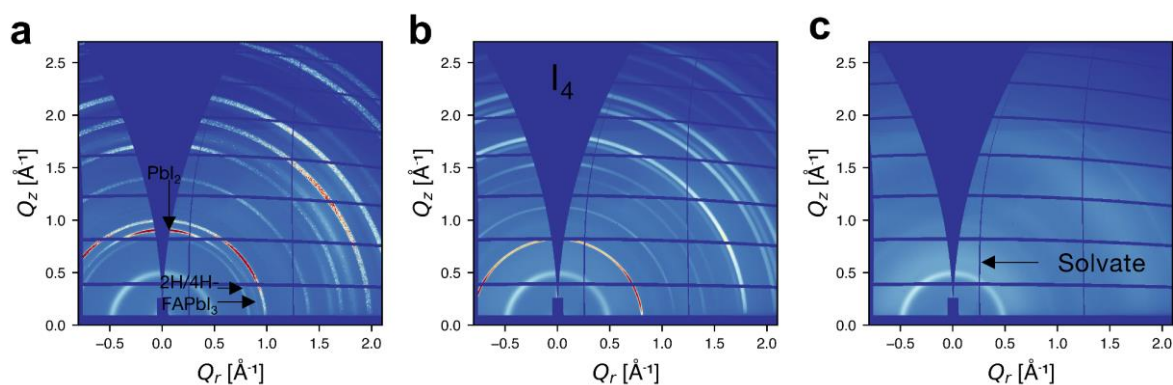


Figure S28: FAPbI₃ liquification. Integrated 2D diffraction patterns for a) FA(MA)PbI₃ b) I₄ (which is slightly textured) and c) solvate phase. We note additional scattering features from polytypic phases and PbI₂ in part a).

Cation	a (Å)	b (Å)	c (Å)	α (°)	β (°)	γ (°)	Volume	Note
N/A	8.935	8.935	8.143	90	90	120	563.0	Starting cell (iodoplumbate only)
MA-FA dimer	10.853	8.482	7.996	85.33	93.78	119.30	639.4	Not similar to the starting cell: increased lattice parameter a.
DMFA ⁺	10.625	8.703	8.082	82.81	106.54	123.29	598.4	
MFA ⁺	9.218	9.283	8.043	80.46	99.04	124.86	555.3	Similar to the starting cell

Table S4: DFT-simulated structural parameters for three possible cations in the I₄ intermediate.

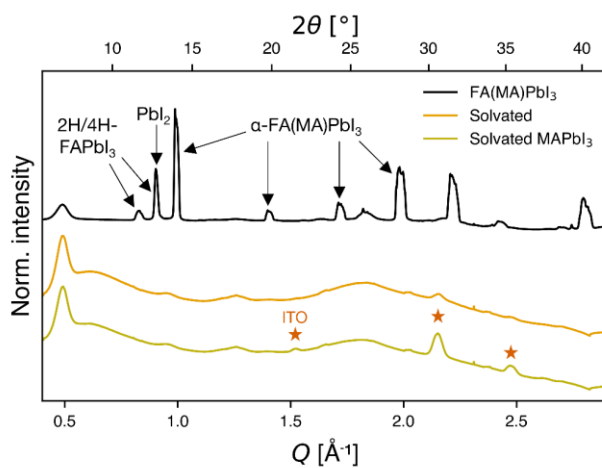


Figure S29: Comparison of solvated FA(MA)PbI₃ showing comparable scattering to the solvated MAPbI₃. All backgrounds are illustrated in Figure S4. Additionally, the 1D pattern of FA(MA)PbI₃ prior to healing shows scattering from polytype phases and PbI₂, which may be caused by air exposure before the in-situ experiment.

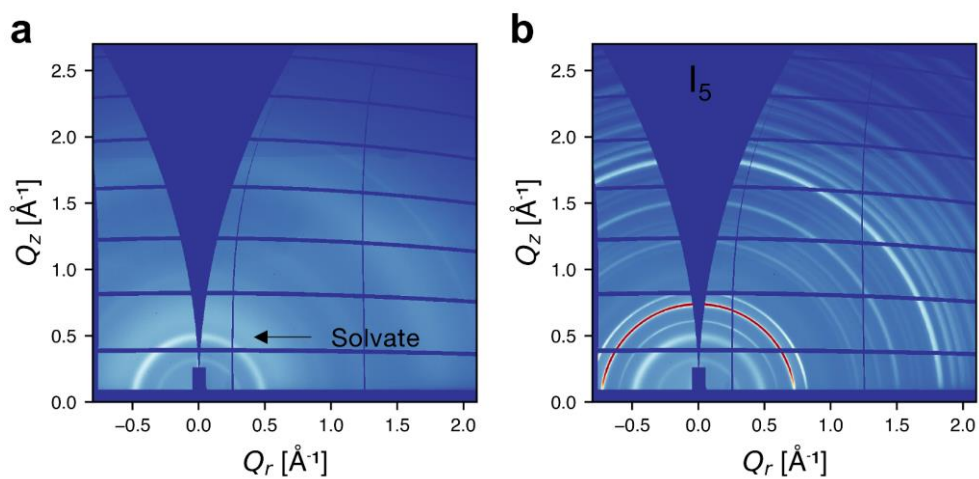


Figure S30: 2D diffraction patterns during recrystallisation of FA(MA)PbI₃. a) Solvate phase at the start of the experiment. b) The I₅ intermediate after treatment.

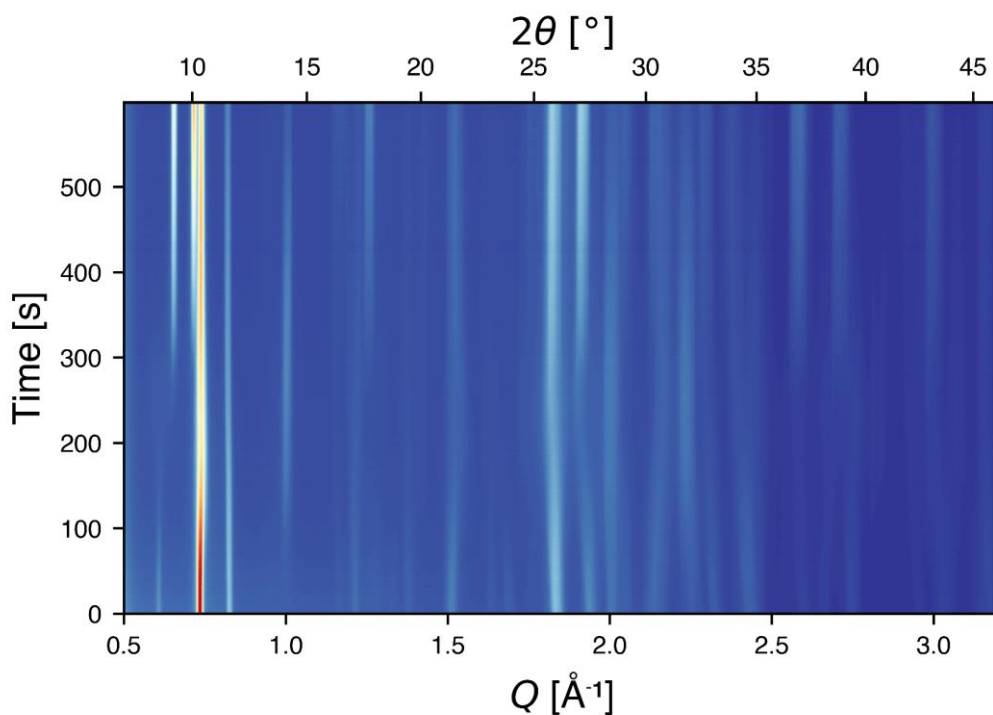


Figure S31: In-situ diffraction recorded from the heated FA(MA)PbI₃ film with a hotplate temperature setpoint of 150 °C. A phase transition occurs from around 50 s, with the final phase observed from ~250 s. Here the (100) reflection $2\theta = 8.6^\circ$ disappears and the (110) peak initially at 10.4° degrees splits, amongst other changes.

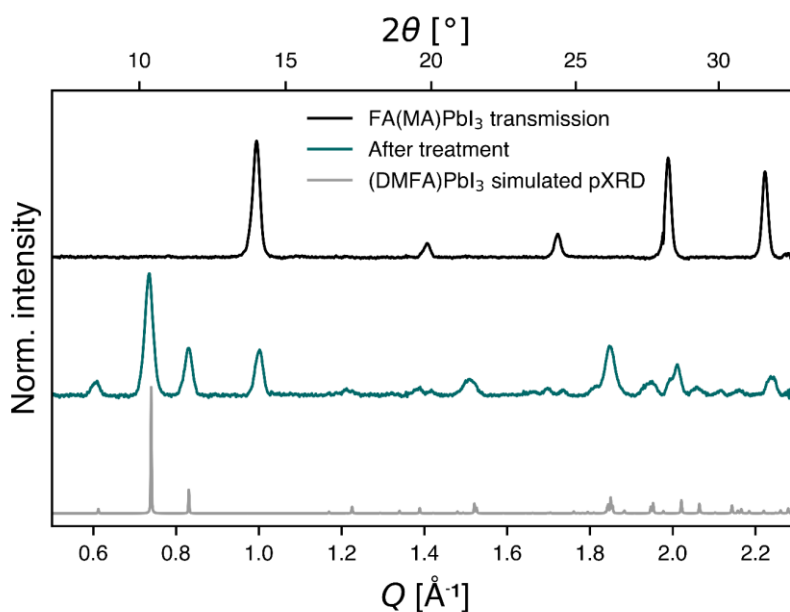


Figure S32: Ex-situ transmission WAXS acquired through samples prepared on X-ray transmissive substrate. The I_5 scattering features were observed, in good agreement with the simulated diffraction pattern for the proposed (DMFA)PbI₃ phase.

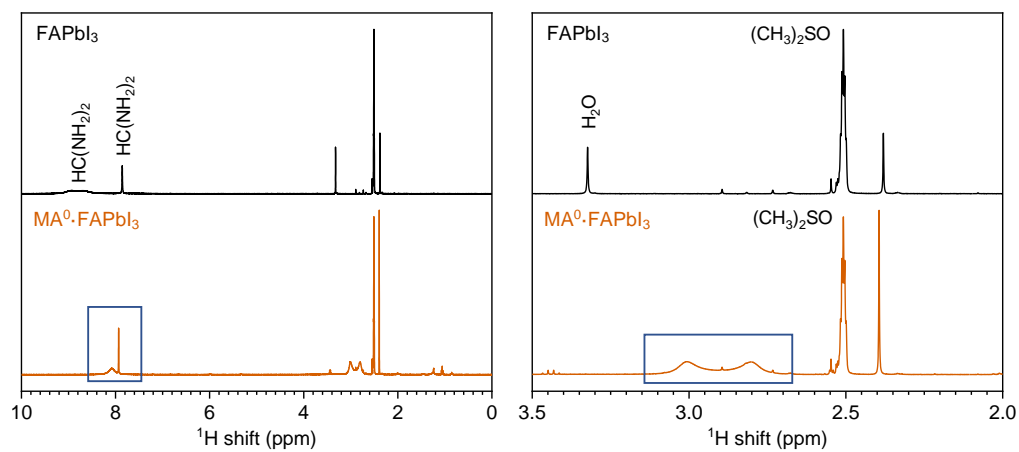


Figure S33: ^1H NMR on re-dissolved MA^0 -treated FAPbI_3 films (in d_6 -DMSO). Broadening of the marked methyl peaks (reported in Wang et al.¹⁰⁰) in part b) is thought to result from hydrogen bonding interactions between the aminic protons in the newly formed cation and either moisture or residual MA^0 .

6.4: References

- (1) National Renewable Energy Laboratory. Best Research-Cell Efficiencies <https://www.nrel.gov/pv/cell-efficiency.html> (accessed Jan 1, 2021).
- (2) Kim, G.; Min, H.; Lee, K. S.; Lee, D. Y.; Yoon, S. M.; Seok, S. I. Impact of Strain Relaxation on Performance of A-Formamidinium Lead Iodide Perovskite Solar Cells. *Science* (80-.). **2020**, *370* (6512), 108–112. <https://doi.org/10.1126/science.abc4417>.
- (3) Yoo, J. J.; Seo, G.; Chua, M. R.; Park, T. G.; Lu, Y.; Rotermond, F.; Kim, Y.; Moon, C. S.; Jeon, N. J.; Bulović, V.; Shin, S. S.; Bawendi, M. G. Efficient Perovskite Solar Cells via Improved Carrier Management. *Nature* **2021**, *590* (June 2020). <https://doi.org/10.1038/s41586-021-03285-w>.
- (4) Al-Ashouri, A.; Köhnen, E.; Li, B.; Magomedov, A.; Hempel, H.; Caprioglio, P.; Márquez, J. A.; Vilches, A. B. M.; Kasparavicius, E.; Smith, J. A.; Phung, N.; Menzel, D.; Grischek, M.; Kegelmann, L.; Skroblin, D.; Gollwitzer, C.; Malinauskas, T.; Jošt, M.; Matič, G.; Rech, B.; Schlattmann, R.; Topič, M.; Korte, L.; Abate, A.; Stannowski, B.; Neher, D.; Stolterfoht, M.; Unold, T.; Getautis, V.; Albrecht, S. Monolithic Perovskite/Silicon Tandem Solar Cell with >29% Efficiency by Enhanced Hole Extraction. *Science* (80-.). **2020**, *370* (6522), 1300–1309. <https://doi.org/10.1126/science.abd4016>.
- (5) Kim, D. H.; Park, J.; Li, Z.; Yang, M.; Park, J. S.; Park, I. J.; Kim, J. Y.; Berry, J. J.; Rumbles, G.; Zhu, K. 300% Enhancement of Carrier Mobility in Uniaxial-Oriented Perovskite Films Formed by Topotactic-Oriented Attachment. *Adv. Mater.* **2017**, *29* (23), 1–8. <https://doi.org/10.1002/adma.201606831>.
- (6) Zheng, X.; Hou, Y.; Bao, C.; Yin, J.; Yuan, F.; Huang, Z.; Song, K.; Liu, J.; Troughton, J.; Gasparini, N.; Zhou, C.; Lin, Y.; Xue, D.; Chen, B.; Johnston, A. K.; Wei, N.; Hedhill, M. N.; Wei, M.; Alsalloum, A. Y.; Maity, P.; Turedi, B.; Yang, C.; Baran, D.; Anthopoulos, T. D.; Han, Y.; Lu, Z.; Mohammed, O. F.; Gao, F.; Sargent, E. H.; Bakr, O. M. Managing Grains and Interfaces via Ligand Anchoring Enables 22.3%-Efficiency Inverted Perovskite Solar Cells. *Nat. Energy* **2020**, *5* (2), 131–140. <https://doi.org/10.1038/s41560-019-0538-4>.
- (7) Jariwala, S.; Sun, H.; Adhyaksa, G. W. P.; Lof, A.; Muscarella, L. A.; Ehrler, B.; Garnett, E. C.; Ginger, D. S. Local Crystal Misorientation Influences Non-Radiative Recombination in Halide Perovskites. *Joule* **2019**, *3* (12), 3048–3060. <https://doi.org/10.1016/j.joule.2019.09.001>.
- (8) Li, W.; Yadavalli, S. K.; Lizarazo-Ferro, D.; Chen, M.; Zhou, Y.; Padture, N. P.; Zia, R. Subgrain Special Boundaries in Halide Perovskite Thin Films Restrict Carrier Diffusion. *ACS Energy Lett.* **2018**, *3* (11), 2669–2670. <https://doi.org/10.1021/acsenergylett.8b01704>.
- (9) Hermes, I. M.; Best, A.; Winkelmann, L.; Mars, J.; Vorpahl, S. M.; Mezger, M.; Collins, L.; Butt, H. J.; Ginger, D. S.; Koynov, K.; Weber, S. A. L. Anisotropic Carrier Diffusion in Single MAPbI₃grains Correlates to Their Twin Domains. *Energy Environ. Sci.* **2020**, *13* (11), 4168–4177. <https://doi.org/10.1039/d0ee01016b>.
- (10) Canil, L.; Cramer, T.; Fraboni, B.; Ricciarelli, D.; Meggiolaro, D.; Singh, A.; Liu, M.; Rusu, M.; Wolff, C. M.; Phung, N.; Wang, Q.; Neher, D.; Unold, T.; Vivo, P.; Gagliardi, A.; De Angelis, F.; Abate, A. Tuning Halide Perovskite Energy Levels. *Energy Environ. Sci.* **2021**. <https://doi.org/10.1039/d0ee02216k>.
- (11) Jang, Y.-W.; Lee, S.; Yeom, K. M.; Jeong, K.; Choi, K.; Choi, M.; Noh, J. H. Intact 2D/3D Halide Junction Perovskite Solar Cells via Solid-Phase in-Plane Growth. *Nat. Energy* **2021**, *6* (1), 63–71. <https://doi.org/10.1038/s41560-020-00749-7>.
- (12) Doherty, T. A. S.; Winchester, A. J.; Macpherson, S.; Johnstone, D. N.; Pareek, V.; Tennyson, E. M.; Kosar, S.; Kosasih, F. U.; Anaya, M.; Abdi-Jalebi, M.; Andaji-Garmaroudi, Z.; Wong, E. L.; Madéo, J.; Chiang, Y.; Park, J.; Jung, Y.; Petoukhoff, C. E.; Divitini, G.; Man, M. K. L.; Ducati, C.; Walsh, A.; Midgley, P. A.; Dani, K. M.; Stranks, S. D. Performance-Limiting Nanoscale Trap Clusters at Grain Junctions in Halide Perovskites. *Nature* **2020**, *580* (7803), 360–366. <https://doi.org/10.1038/s41586-020-2184-1>.
- (13) Sun, Q.; Fassel, P.; Becker-Koch, D.; Bausch, A.; Rivkin, B.; Bai, S.; Hopkinson, P. E.; Snaith, H. J.; Vaynzof, Y. Role of Microstructure in Oxygen Induced Photodegradation of Methylammonium Lead Triiodide Perovskite Films. *Adv. Energy Mater.* **2017**, *7*, 1700977. <https://doi.org/10.1002/aenm.201700977>.
- (14) Di Girolamo, D.; Phung, N.; Kosasih, F. U.; Di Giacomo, F.; Matteocci, F.; Smith, J. A.; Flatken, M. A.; Köbler, H.; Turren Cruz, S. H.; Mattoni, A.; Cinà, L.; Rech, B.; Latini, A.; Divitini, G.; Ducati, C.; Di Carlo, A.; Dini, D.; Abate, A. Ion Migration-Induced Amorphization and Phase Segregation as a Degradation Mechanism in Planar Perovskite Solar Cells. *Adv. Energy Mater.* **2020**, *2000310*, 2000310. <https://doi.org/10.1002/aenm.202000310>.
- (15) Chen, A. Z.; Shiu, M.; Ma, J. H.; Alpert, M. R.; Zhang, D.; Foley, B. J.; Smilgies, D. M.; Lee, S. H.; Choi, J. J. Origin of Vertical Orientation in Two-Dimensional Metal Halide Perovskites and Its Effect on Photovoltaic Performance. *Nat. Commun.* **2018**, *9* (1), 1–7. <https://doi.org/10.1038/s41467-018-03757-0>.
- (16) Stone, K. H.; Gold-Parker, A.; Pool, V. L.; Unger, E. L.; Bowring, A. R.; McGehee, M. D.; Toney, M. F.; Tassone, C. J. Transformation from Crystalline Precursor to Perovskite in PbCl₂-Derived MAPbI₃. *Nat. Commun.* **2018**, *9* (1), 3458. <https://doi.org/10.1038/s41467-018-05937-4>.
- (17) Zhou, Z.; Wang, Z.; Zhou, Y.; Pang, S.; Wang, D.; Xu, H.; Liu, Z.; Padture, N. P.; Cui, G. Methylamine-Gas Induced Defect-Healing Behavior of CH₃NH₃PbI₃ Thin Films for Perovskite Solar Cells. *Angew. Chemie Int. Ed.* **2015**, *54* (33), 9705–9709. <https://doi.org/10.1002/anie.201504379>.
- (18) Zhou, Y.; Padture, N. P. Gas-Induced Formation/Transformation of Organic-Inorganic Halide Perovskites. *ACS Energy Lett.* **2017**, *2*, 7b00667. <https://doi.org/10.1021/acsenergylett.7b00667>.
- (19) Hao, F.; Stoumpos, C. C.; Liu, Z.; Chang, R. P. H. H.; Kanatzidis, M. G. Controllable Perovskite Crystallization at a Gas-Solid Interface for Hole Conductor-Free Solar Cells with Steady Power Conversion Efficiency over 10%. *J. Am. Chem. Soc.* **2014**, *136* (46), 16411–16419. <https://doi.org/10.1021/ja509245x>.
- (20) Ji, F.; Pang, S.; Zhang, L.; Zong, Y.; Cui, G.; Padture, N. P.; Zhou, Y. Simultaneous Evolution of Uniaxially Oriented Grains and Ultralow-Density Grain-Boundary Network in CH₃NH₃PbI₃ Perovskite Thin Films Mediated by Precursor Phase Metastability. *ACS Energy Lett.* **2017**, *2* (12), 2727–2733. <https://doi.org/10.1021/acsenergylett.7b00980>.
- (21) Zong, Y.; Zhou, Y.; Ju, M.; Garces, H. F.; Krause, A. R.; Ji, F.; Cui, G.; Zeng, X. C.; Padture, N. P.; Pang, S. Thin-Film Transformation of NH₄PbI₃ to CH₃NH₃PbI₃ Perovskite: A Methylamine-Induced Conversion-Healing Process. *Angew. Chemie Int. Ed.* **2016**, *55*, 1–6. <https://doi.org/10.1002/anie.201609529>.
- (22) Zhou, Y.; Yang, M.; Pang, S.; Zhu, K.; Padture, N. P. Exceptional Morphology-Preserving Evolution of Formamidinium Lead Triiodide Perovskite Thin Films via Organic-Cation Displacement. *J. Am. Chem. Soc.* **2016**, *138* (17), 5535–5538. <https://doi.org/10.1021/jacs.6b02787>.
- (23) Shao, Z.; Wang, Z.; Li, Z.; Fan, Y.; Meng, H.; Liu, R.; Wang, Y.; Hagfeldt, A.; Cui, G.; Pang, S. A Scalable Methylamine Gas Healing Strategy for High-Efficiency Inorganic Perovskite Solar Cells. *Angew. Chemie - Int. Ed.* **2019**, *58* (17), 5587–5591. <https://doi.org/10.1002/anie.201814024>.
- (24) Liu, Z.; Qiu, L.; Juarez-Perez, E. J.; Hawash, Z.; Kim, T.; Jiang, Y.; Wu, Z.; Raga, S. R.; Ono, L. K.; Liu, S.; Qi, Y. Gas-Solid Reaction Based over One-Micrometer Thick Stable Perovskite Films for Efficient Solar Cells and Modules. *Nat. Commun.* **2018**, *9* (1), 3880. <https://doi.org/10.1038/s41467-018-06317-8>.
- (25) Long, M.; Zhang, T.; Zhu, H.; Li, G.; Wang, F.; Guo, W.; Chai, Y.; Chen, W.; Li, Q.; Wong, K. S.; Xu, J.; Yan, K. Textured CH₃NH₃PbI₃ Thin Film with Enhanced Stability for High Performance Perovskite Solar Cells. *Nano Energy* **2017**, *33* (December 2016), 485–496. <https://doi.org/10.1016/j.nanoen.2017.02.002>.

- (26) Chen, H.; Ye, F.; Tang, W.; He, J.; Yin, M.; Wang, Y.; Xie, F.; Bi, E.; Yang, X.; Grätzel, M.; Han, L. A Solvent- and Vacuum-Free Route to Large-Area Perovskite Films for Efficient Solar Modules. *Nature* **2017**. <https://doi.org/10.1038/nature23877>.
- (27) Noel, N. K.; Habisreutinger, S. N.; Wenger, B.; Klug, M. T.; Hörantner, M. T.; Johnston, M. B.; Nicholas, R. J.; Moore, D. T.; Snaith, H. J. A Low Viscosity, Low Boiling Point, Clean Solvent System for the Rapid Crystallisation of Highly Specular Perovskite Films. *Energy Environ. Sci.* **2017**, *10* (1), 145–152. <https://doi.org/10.1039/C6EE02373H>.
- (28) Dou, B.; Whitaker, J. B.; Bruening, K.; Moore, D. T.; Wheeler, L. M.; Ryter, J.; Breslin, N. J.; Berry, J. J.; Garner, S. M.; Barnes, F. S.; Shaheen, S. E.; Tassone, C. J.; Zhu, K.; van Hest, M. F. A. M. Roll-to-Roll Printing of Perovskite Solar Cells. *ACS Energy Lett.* **2018**, *3* (10), 2558–2565. <https://doi.org/10.1021/acseenergylett.8b01556>.
- (29) Jeong, D. N.; Lee, D. K.; Seo, S.; Lim, S. Y.; Zhang, Y.; Shin, H.; Cheong, H.; Park, N. G.; Throughput, H.; Solar, P. Perovskite Cluster-Containing Solution for Scalable D-Bar Coating toward High-Throughput Perovskite Solar Cells. *ACS Energy Lett.* **2019**, *4* (11), 1189–1195. <https://doi.org/10.1021/acseenergylett.9b00042>.
- (30) McMeekin, D. P.; Mahesh, S.; Noel, N. K.; Klug, M. T.; Lim, J. C.; Warby, J. H.; Ball, J. M.; Herz, L. M.; Johnston, M. B.; Snaith, H. J. Solution-Processed All-Perovskite Multi-Junction Solar Cells. *Joule* **2019**, *3* (2), 387–401. <https://doi.org/10.1016/j.joule.2019.01.007>.
- (31) Huang, X.; Chen, R.; Deng, G.; Han, F.; Ruan, P.; Cheng, F.; Yin, J.; Wu, B.; Zheng, N. Methylamine-Dimer-Induced Phase Transition toward MAPbI₃ Films and High-Efficiency Perovskite Solar Modules. *J. Am. Chem. Soc.* **2020**, *142* (13), 6149–6157. <https://doi.org/10.1021/jacs.9b13443>.
- (32) Burkitt, D.; Swartwout, R.; McGettrick, J.; Greenwood, P.; Beynon, D.; Brenes, R.; Bulović, V.; Watson, T. Acetonitrile Based Single Step Slot-Die Compatible Perovskite Ink for Flexible Photovoltaics. *RSC Adv.* **2019**, *9* (64), 37415–37423. <https://doi.org/10.1039/c9ra06631d>.
- (33) Liu, Q.; Zhao, Y.; Ma, Y.; Sun, X.; Ge, W.; Fang, Z.; Bai, H.; Tian, Q.; Fan, B.; Zhang, T. A Mixed Solvent for Rapid Fabrication of Large-Area Methylammonium Lead Iodide Layers by One-Step Coating at Room Temperature. *J. Mater. Chem. A* **2019**, *7* (31), 18275–18284. <https://doi.org/10.1039/c9ta06084g>.
- (34) Wang, K.; Wu, C.; Hou, Y.; Yang, D.; Li, W.; Deng, G.; Jiang, Y.; Priya, S. A Nonionic and Low-Entropic MA(MMA)NPbI₃-Ink for Fast Crystallization of Perovskite Thin Films. *Joule* **2020**, 1–16. <https://doi.org/10.1016/j.joule.2020.01.004>.
- (35) Noel, N. K.; Wenger, B.; Habisreutinger, S. N.; Patel, J. B.; Crothers, T.; Wang, Z.; Nicholas, R. J.; Johnston, M. B.; Herz, L. M.; Snaith, H. J. Highly Crystalline Methylammonium Lead Tribromide Perovskite Films for Efficient Photovoltaic Devices. *ACS Energy Lett.* **2018**, *acsenergylett.8b00509*. <https://doi.org/10.1021/acseenergylett.8b00509>.
- (36) Vásquez-Montoya, M.; Montoya, J. F.; Ramirez, D.; Jaramillo, F. Understanding the Precursor Chemistry for One-Step Deposition of Mixed Cation Perovskite Solar Cells by Methylamine Route. *J. Energy Chem.* **2020**. <https://doi.org/10.1016/j.jechem.2020.08.059>.
- (37) Bruening, K.; Dou, B.; Simonaitis, J.; Lin, Y. Y.; van Hest, M. F. A. M.; Tassone, C. J. Scalable Fabrication of Perovskite Solar Cells to Meet Climate Targets. *Joule* **2018**, *2* (11), 2464–2476. <https://doi.org/10.1016/j.joule.2018.09.014>.
- (38) Swartwout, R.; Hoerantner, M. T.; Bulović, V. Scalable Deposition Methods for Large-area Production of Perovskite Thin Films. *ENERGY Environ. Mater.* **2019**, *2* (2), 119–145. <https://doi.org/10.1002/eem2.12043>.
- (39) Mathews, I.; Sofia, S.; Ma, E.; Jean, J.; Laine, H. S.; Siah, S. C.; Buonassisi, T.; Peters, I. M. Economically Sustainable Growth of Perovskite Photovoltaics Manufacturing. *Joule* **2020**, 1–18. <https://doi.org/10.1016/j.joule.2020.01.006>.
- (40) Bishop, J. E.; Smith, J. A.; Lidzey, D. G. Development of Spray-Coated Perovskite Solar Cells. *ACS Appl. Mater. Interfaces* **2020**. <https://doi.org/10.1021/acsmi.0c14540>.
- (41) Pearson, A. J. Structure Formation and Evolution in Semiconductor Films for Perovskite and Organic Photovoltaics. *J. Mater. Res.* **2017**, *1–27*. <https://doi.org/10.1557/jmr.2017.87>.
- (42) Mundt, L. E.; Schelhas, L. T. Structural Evolution During Perovskite Crystal Formation and Degradation: In Situ and Operando X-Ray Diffraction Studies. *Adv. Energy Mater.* **2019**, *1903074*, 1903074. <https://doi.org/10.1002/aenm.201903074>.
- (43) Zhou, Y.; Zhou, H.; Deng, J.; Cha, W.; Cai, Z. Decisive Structural and Functional Characterization of Halide Perovskites with Synchrotron. *Matter* **2020**, *2* (2), 360–377. <https://doi.org/10.1016/j.matt.2019.12.027>.
- (44) Schlipf, J.; Müller-buschbaum, P. Structure of Organometal Halide Perovskite Films as Determined with Grazing-Incidence X-Ray Scattering Methods. **2017**, 1–10. <https://doi.org/10.1002/aenm.201700131>.
- (45) Hexemer, A.; Müller-Buschbaum, P. Advanced Grazing-Incidence Techniques for Modern Soft-Matter Materials Analysis. *IUCrJ* **2015**, *2* (1), 106–125. <https://doi.org/10.1107/S2052252514024178>.
- (46) Taylor, A. D.; Sun, Q.; Goetz, K. P.; An, Q.; Schramm, T.; Hofstetter, Y.; Litterst, M.; Paulus, F.; Vaynzof, Y. A General Approach to High Efficiency Perovskite Solar Cells by Any Antisolvent. *Nat. Commun.* **2021**, No. 2021, 1–11. <https://doi.org/10.1038/s41467-021-22049-8>.
- (47) Freestone, B. G.; Smith, J. A.; Piana, G.; Kilbride, R. C.; Parnell, A. J.; Sortino, L.; Coles, D. M.; Ball, O. B.; Martsinovich, N.; Thompson, C. J.; Alanazi, T. I.; Game, O. S.; Tartakovskii, A. I.; Lagoudakis, P. G.; Lidzey, D. G. Low-Dimensional Emissive States in Non-Stoichiometric Methylammonium Lead Halide Perovskites. *J. Mater. Chem. A* **2019**, *7* (18), 11104–11116. <https://doi.org/10.1039/c8ta2184b>.
- (48) Hidalgo, J.; Perini, C. A. R.; Castro-Mendez, A. F.; Jones, D.; Köbler, H.; Lai, B.; Li, R.; Sun, S.; Abate, A.; Correa-Baena, J. P. Moisture-Induced Crystallographic Reorientations and Effects on Charge Carrier Extraction in Metal Halide Perovskite Solar Cells. *ACS Energy Lett.* **2020**, *5* (11), 3526–3534. <https://doi.org/10.1021/acseenergylett.0c01964>.
- (49) Meng, K.; Wu, L.; Liu, Z.; Wang, X.; Xu, Q.; Hu, Y.; He, S.; Li, X.; Li, T.; Chen, G. In Situ Real-Time Study of the Dynamic Formation and Conversion Processes of Metal Halide Perovskite Films. *Adv. Mater.* **2018**, *30* (11), 1–10. <https://doi.org/10.1002/adma.201706401>.
- (50) Munir, R.; Sheikh, A. D.; Abdelsamie, M.; Hu, H.; Yu, L.; Zhao, K.; Kim, T.; Tall, O. El; Li, R.; Smilgies, D.; Amassian, A. Hybrid Perovskite Thin-Film Photovoltaics: In Situ Diagnostics and Importance of the Precursor Solvate Phases. **2017**. <https://doi.org/10.1002/adma.201604113>.
- (51) Dong, J.; Shao, S.; Kahmann, S.; Rommens, A. J.; Hermida-Merino, D.; ten Brink, G. H.; Loi, M. A.; Portale, G. Mechanism of Crystal Formation in Ruddlesden–Popper Sn-Based Perovskites. *Adv. Funct. Mater.* **2020**, *30* (24). <https://doi.org/10.1002/adfm.202001294>.
- (52) Steele, J. A.; Solano, E.; Jin, H.; Prakasam, V.; Braeckevelt, T.; Yuan, H.; Lin, Z.; Kloe, R.; Wang, Q.; Rogge, S. M. J.; Van Speybroeck, V.; Chernyshov, D.; Hofkens, J.; Roeffaers, M. B. J. Texture Formation in Polycrystalline Thin Films of All-Inorganic Lead Halide Perovskite. *Adv. Mater.* **2021**, *2007224*, 1–9. <https://doi.org/10.1002/adma.202007224>.
- (53) Näsström, H.; Becker, P.; Márquez, J. A.; Shargaieva, O.; Mainz, R.; Unger, E.; Unold, T. Dependence of Phase Transitions on Halide Ratio in Inorganic CsPb(Br x I 1-x)₃ Perovskite Thin Films Obtained from High-Throughput Experimentation. *J. Mater. Chem. A* **2020**, *8* (43), 22626–22631. <https://doi.org/10.1039/D0TA08067E>.
- (54) Schelhas, L. T.; Christians, J. A.; Berry, J. J.; Toney, M. F.; Tassone, C. J.; Luther, J. M.; Stone, K. H. Monitoring a Silent Phase Transition in CH₃NH₃PbI₃ Solar Cells via Operando X-Ray Diffraction. *ACS Energy Lett.* **2016**, *1* (5), 1007–1012. <https://doi.org/10.1021/acseenergylett.6b00441>.
- (55) Rosales, B. A.; Mundt, L. E.; Allen, T. G.; Moore, D. T.; Prince, K. J.; Wolden, C. A.; Rumbles, G.; Schelhas, L. T.; Wheeler, L. M. Reversible Multicolor Chromism in Layered Formamidinium Metal Halide Perovskites. *Nat. Commun.* **2020**, *11* (1), 1–12. <https://doi.org/10.1038/s41467-020-19009-z>.
- (56) Kim, J.; Schelhas, L. T.; Stone, K. H. Effects of Oxygen and Water on the Formation and Degradation Processes of (CH₃NH₃)PbI₃ Thin Films. *ACS Appl. Energy Mater.* **2020**. <https://doi.org/10.1021/acsaem.0c02193>.

- (57) Alanazi, T. I.; Game, O. S.; Smith, J. A.; Kilbride, R. C.; Greenland, C.; Jayaprakash, R.; Georgiou, K.; Terrill, N. J.; Lidzey, D. G. Potassium Iodide Reduces the Stability of Triple-Cation Perovskite Solar Cells. *RSC Adv.* **2020**, *10* (66), 40341–40350. <https://doi.org/10.1039/d0ra07107b>.
- (58) Marchezi, P. E.; Therézio, E. M.; Szostak, R.; Loureiro, H. C.; Bruening, K.; Gold-Parker, A.; Melo, M. A.; Tassone, C. J.; Tolentino, H. C. N.; Toney, M. F.; Nogueira, A. F. Degradation Mechanisms in Mixed-Cation and Mixed-Halide Cs: XFA1-XPb(Bryl1- y)3 Perovskite Films under Ambient Conditions. *J. Mater. Chem. A* **2020**, *8* (18), 9302–9312. <https://doi.org/10.1039/d0ta01201g>.
- (59) Fransishyn, K. M.; Kundu, S.; Kelly, T. L. Elucidating the Failure Mechanisms of Perovskite Solar Cells in Humid Environments Using In Situ Grazing-Incidence Wide-Angle X-Ray Scattering. *ACS Energy Lett.* **2018**, *3*, 2127–2133. <https://doi.org/10.1021/acseenergylett.8b01300>.
- (60) Schelhas, L. T.; Li, Z.; Christians, J. A.; Goyal, A.; Kairys, P.; Harvey, S. P.; Kim, D. H.; Stone, K. H.; Luther, J. M.; Zhu, K.; Stevanovic, V.; Berry, J. J. Insights into Operational Stability and Processing of Halide Perovskite Active Layers. *Energy Environ. Sci.* **2019**, 1341–1348. <https://doi.org/10.1039/c8ee03051k>.
- (61) Chen, B. A.; Lin, J. T.; Suen, N. T.; Tsao, C. W.; Chu, T. C.; Hsu, Y. Y.; Chan, T. S.; Chan, Y. T.; Yang, J. S.; Chiu, C. W.; Chen, H. M. In Situ Identification of Photo- and Moisture-Dependent Phase Evolution of Perovskite Solar Cells. *ACS Energy Lett.* **2017**, *2* (2), 342–348. <https://doi.org/10.1021/acseenergylett.6b00698>.
- (62) Liman, C. D.; Choi, S.; Breiby, D. W.; Cochran, J. E.; Toney, M. F.; Kramer, E. J.; Chabinc, M. L. Two-Dimensional GIWAXS Reveals a Transient Crystal Phase in Solution-Processed Thermally Converted Tetrabenzoporphyrin. *J. Phys. Chem. B* **2013**, *117* (46), 14557–14567. <https://doi.org/10.1021/jp408220e>.
- (63) Kiligaridis, A.; Merdasa, A.; Rehermann, C.; Unger, E. L.; Scheblykin, I. G. Excitation Wavelength Dependence of Photoluminescence Flickering in Degraded MAPbI3 Perovskite and Its Connection to Lead Iodide Formation. *J. Lumin.* **2020**, *222* (February), 117129. <https://doi.org/10.1016/j.jlumin.2020.117129>.
- (64) Nicklin, C.; Arnold, T.; Rawle, J.; Warne, A. Diamond Beamline I07: A Beamline for Surface and Interface Diffraction. *J. Synchrotron Radiat.* **2016**, *23*, 1245–1253. <https://doi.org/10.1107/S1600577516009875>.
- (65) Stoumpos, C. C.; Malliakas, C. D.; Kanatzidis, M. G. Semiconducting Tin and Lead Iodide Perovskites with Organic Cations: Phase Transitions, High Mobilities, and Near-Infrared Photoluminescent Properties. *Inorg. Chem.* **2013**, *52* (15), 9019–9038. <https://doi.org/10.1021/ic401215x>.
- (66) Bogachuk, D.; Wagner, L.; Mastroianni, S.; Daub, M.; Hillebrecht, H.; Hinsch, A. The Nature of the Methylamine–MAPbI3 Complex: Fundamentals of Gas-Induced Perovskite Liquefaction and Crystallization. *J. Mater. Chem. A* **2020**, *8* (19), 9788–9796. <https://doi.org/10.1039/D0TA02494E>.
- (67) Smilgies, D. M. Scherrer Grain-Size Analysis Adapted to Grazing-Incidence Scattering with Area Detectors. *J. Appl. Crystallogr.* **2009**, *42* (6), 1030–1034. <https://doi.org/10.1107/S0021889809040126>.
- (68) Baker, J. L.; Jimison, L. H.; Mannsfeld, S.; Volkman, S.; Yin, S.; Subramanian, V.; Salles, A.; Alivisatos, A. P.; Toney, M. F.; Science, M.; Synchrotron, S.; Lightsource, R.; Park, M. Quantification of Thin Film Crystallographic Orientation Using X-Ray Diffraction with an Area Detector. *Langmuir* **2010**, *26* (11), 9146–9151. <https://doi.org/10.1021/la904840q>.
- (69) Breternitz, J.; Lehmann, F.; Barnett, S. A.; Nowell, H.; Schorr, S. Role of the Iodide–Methylammonium Interaction in the Ferroelectricity of CH3NH3PbI3. *Angew. Chemie - Int. Ed.* **2020**, *59* (1), 424–428. <https://doi.org/10.1002/anie.201910599>.
- (70) Cao, J.; Jing, X.; Yan, J.; Hu, C.; Chen, R.; Yin, J.; Li, J.; Zheng, N. Identifying the Molecular Structures of Intermediates for Optimizing the Fabrication of High-Quality Perovskite Films. *J. Am. Chem. Soc.* **2016**, *138* (31), 9919–9926. <https://doi.org/10.1021/jacs.6b04924>.
- (71) Petrov, A. V. A. V.; Sokolova, I. P.; Belich, N. A.; Peters, G. S.; Dorovatovskii, P. V.; Zubavichus, Y. V.; Khrustalev, V. N.; Petrov, A. V. A. V.; Grätzel, M.; Goodilin, E. A.; Tarasov, A. B.; Structure, C.; Phases, D.; Zubavichus, Y. V.; Khrustalev, V. N.; Petrov, A. V. A. V.; Grätzel, M.; Sokolova, I. P.; Belich, N. A.; Peters, G. S.; Dorovatovskii, P. V.; Zubavichus, Y. V.; Khrustalev, V. N.; Petrov, A. V. A. V.; Grätzel, M.; Goodilin, E. A.; Tarasov, A. B. Crystal Structure of DMF-Intermediate Phases Uncovers the Link Between CH3NH3PbI3 Morphology and Precursor Stoichiometry. *J. Phys. Chem. C* **2017**, *121* (38), 20739–20743. <https://doi.org/10.1021/acs.jpcc.7b08468>.
- (72) Pang, S.; Zhou, Y.; Wang, Z.; Yang, M.; Krause, A. R.; Zhou, Z.; Zhu, K.; Padture, N. P.; Cui, G. Transformative Evolution of Organolead Triiodide Perovskite Thin Films from Strong Room-Temperature Solid-Gas Interaction between HPbI3-CH3NH2 Precursor Pair. *J. Am. Chem. Soc.* **2016**, *138* (3), 750–753. <https://doi.org/10.1021/jacs.5b11824>.
- (73) Wheeler, L. M.; Moore, D. T.; Ihly, R.; Stanton, N. J.; Miller, E. M.; Tenent, R. C.; Blackburn, J. L.; Neale, N. R. Switchable Photovoltaic Windows Enabled by Reversible Photochemical Complex Dissociation from Methylammonium Lead Iodide. *Nat. Commun.* **2017**, *8* (1). <https://doi.org/10.1038/s41467-017-01842-4>.
- (74) Kerner, R. A.; Schloemer, T. H.; Schulz, P.; Berry, J. J.; Schwartz, J.; Sellinger, A.; Rand, B. P. Amine Additive Reactions Induced by the Soft Lewis Acidity of Pb2+ in Halide Perovskites. Part II: Impacts of Amido Pb Impurities in Methylammonium Lead Triiodide Thin Films. *J. Mater. Chem. C* **2019**, *7* (18), 5244–5250. <https://doi.org/10.1039/c8tc04872j>.
- (75) Raga, S. R.; Ono, L. K.; Qi, Y. Rapid Perovskite Formation by CH3NH2 Gas-Induced Intercalation and Reaction of PbI2. *J. Mater. Chem. A* **2016**, *4* (7), 2494–2500. <https://doi.org/10.1039/c5ta10055k>.
- (76) Zhao, T.; Williams, S. T.; Chueh, C.-C.; DeQuilettes, D. W.; Liang, P.-W.; Ginger, D. S.; Jen, A. K. Y. Design Rules for the Broad Application of Fast (<1 s) Methylamine Vapor Based, Hybrid Perovskite Post Deposition Treatments. *RSC Adv.* **2016**, *6* (33), 27475–27484. <https://doi.org/10.1039/C6RA03485C>.
- (77) Jacobs, D.; Zang, L. Thermally Induced Recrystallization of MAPbI3 Perovskite Under Methylamine Atmosphere: An Approach to Fabricating Large Uniform Crystalline Grains. *Chem. Commun.* **2016**, *52*, 10743–10746. <https://doi.org/10.1039/C6CC04521A>.
- (78) Hao, L.; Li, Z.; Wang, L.; Liu, R.; Shao, Z.; Zhou, Z.; Guo, X.; Cui, G.; Liu, S. F.; Pang, S. A Temperature Gradient-Induced Directional Growth of a Perovskite Film. *J. Mater. Chem. A* **2020**, *8* (33), 17019–17024. <https://doi.org/10.1039/D0TA04492J>.
- (79) Giesbrecht, N.; Schlipf, J.; Oesinghaus, L.; Binek, A.; Bein, T.; Müller-Buschbaum, P.; Docampo, P. Synthesis of Perfectly Oriented and Micrometer-Sized MAPbBr3 Perovskite Crystals for Thin-Film Photovoltaic Applications. *ACS Energy Lett.* **2016**, *1* (1), 150–154. <https://doi.org/10.1021/acseenergylett.6b00050>.
- (80) Chen, A. Z.; Foley, B. J.; Ma, J. H.; Alpert, M. R.; Niezgod, J. S.; Choi, J. J. Crystallographic Orientation Propagation in Metal Halide Perovskite Thin Films. *J. Mater. Chem. A* **2017**, *5* (17), 7796–7800. <https://doi.org/10.1039/c7ta02203d>.
- (81) Li, M.; Li, M.; Zuo, W. W.; Zuo, W. W.; Yang, Y. G.; Aldamasy, M. H.; Aldamasy, M. H.; Wang, Q.; Cruz, S. H. T.; Feng, S. L.; Saliba, M.; Saliba, M.; Wang, Z. K.; Abate, A.; Abate, A. Tin Halide Perovskite Films Made of Highly Oriented 2D Crystals Enable More Efficient and Stable Lead-Free Perovskite Solar Cells. *ACS Energy Lett.* **2020**, *5* (6), 1923–1929. <https://doi.org/10.1021/acseenergylett.0c00782>.
- (82) Oesinghaus, L.; Schlipf, J.; Giesbrecht, N.; Song, L.; Hu, Y.; Bein, T.; Docampo, P.; Müller-Buschbaum, P. Toward Tailored Film Morphologies: The Origin of Crystal Orientation in Hybrid Perovskite Thin Films. *Adv. Mater. Interfaces* **2016**, *3* (19), 1600403. <https://doi.org/10.1002/admi.201600403>.
- (83) Jiang, Q.; Zhang, L.; Wang, H.; Yang, X.; Meng, J.; Liu, H.; Yin, Z.; Wu, J.; Zhang, X.; You, J. Enhanced Electron Extraction Using SnO2 for High-Efficiency Planar-Structure HC(NH2)2PbI3-Based Perovskite Solar Cells. *Nat. Energy* **2017**, *2* (1), 16177. <https://doi.org/10.1038/nenergy.2016.177>.
- (84) Al-Ashouri, A.; Magomedov, A.; Roß, M.; Jošt, M.; Talaikis, M.; Chistiakova, G.; Bertram, T.; Márquez, J. A.; Köhnen, E.; Kasparavičius, E.; Levenco, S.; Gil-Escrig, L.; Hages, C. J.; Schlatmann, R.; Rech, B.; Malinauskas, T.; Unold, T.; Kaufmann, C. A.; Korte, L.; Niaura, G.; Getautis, V.; Albrecht, S. Conformal Monolayer Contacts with Lossless Interfaces for Perovskite Single Junction and Monolithic Tandem Solar Cells.

- Energy Environ. Sci.* **2019**, *12* (11), 3356–3369. <https://doi.org/10.1039/C9EE02268F>.
- (85) Fan, H.; Li, F.; Wang, P.; Gu, Z.; Huang, J. H.; Jiang, K. J.; Guan, B.; Yang, L. M.; Zhou, X.; Song, Y. L.; Guan, B.; Yang, L. M.; Jiang, K. J.; Song, Y. L. Methylamine-Assisted Growth of Uniaxial-Oriented Perovskite Thin Films with Millimeter-Sized Grains. *Nat. Commun.* **2020**, *11* (1), 1–10. <https://doi.org/10.1038/s41467-020-19199-6>.
- (86) Febriansyah, B.; Koh, T. M.; Rana, P. J. S.; Hooper, T. J. N.; Ang, Z. Z.; Li, Y.; Bruno, A.; Grätzel, M.; England, J.; Mhaisalkar, S. G.; Mathews, N. Hybrid 2D [Pb(CH₃NH₂)₂]_n Coordination Polymer Precursor for Scalable Perovskite Deposition. *ACS Energy Lett.* **2020**, *5* (7), 2305–2312. <https://doi.org/10.1021/acsenerylett.0c00781>.
- (87) Coetzee, J. F.; Padmanabhan, G. R. Properties of Bases in Acetonitrile as Solvent. IV. Proton Acceptor Power and Homoconjugation of Mono- and Diamines. *J. Am. Chem. Soc.* **1965**, *87* (22), 5005–5010. <https://doi.org/10.1021/ja00950a006>.
- (88) Shargaieva, O.; Kuske, L.; Rappich, J.; Unger, E.; Nickel, N. H. Building Blocks of Hybrid Perovskites: A Photoluminescence Study of Lead-Iodide Solution Species. *ChemPhysChem* **2020**, *21* (20), 2327–2333. <https://doi.org/10.1002/cphc.202000479>.
- (89) Shargaieva, O.; Näsström, H.; Smith, J. A.; Töbrens, D.; Munir, R.; Unger, E. L. Hybrid Perovskite Crystallization from Binary Solvent Mixtures: Interplay of Evaporation Rate and Binding Strength of Solvents. *Mater. Adv.* **2020**. <https://doi.org/10.1039/D0MA00815J>.
- (90) Radicchi, E.; Ambrosio, F.; Mosconi, E.; Alasmari, A. A.; Alasmary, F. A. S.; De Angelis, F. Combined Computational and Experimental Investigation on the Nature of Hydrated Iodoplumbate Complexes: Insights into the Dual Role of Water in Perovskite Precursor Solutions. *J. Phys. Chem. B* **2020**. <https://doi.org/10.1021/acs.jpcc.0c08624>.
- (91) Yoon, S. J.; Stamplecoskie, K. G.; Kamat, P. V. How Lead Halide Complex Chemistry Dictates the Composition of Mixed Halide Perovskites. *J. Phys. Chem. Lett.* **2016**, *7* (7), 1368–1373. <https://doi.org/10.1021/acs.jpclett.6b00433>.
- (92) Cataldo, F. A Revision of the Gutmann Donor Numbers of a Series of Phosphoramides Including TEPA. *Eur. Chem. Bull.* **2015**, *4* (2), 92–97. <https://doi.org/10.17628/ECB.2015.4.92>.
- (93) Radicchi, E.; Mosconi, E.; Elisei, F.; Nunzi, F.; De Angelis, F. Understanding the Solution Chemistry of Lead Halide Perovskites Precursors. *ACS Appl. Energy Mater.* **2019**, *2* (5), 3400–3409. <https://doi.org/10.1021/acsaem.9b00206>.
- (94) Juarez-Perez, E. J.; Ono, L. K.; Maeda, M.; Jiang, Y.; Hawash, Z.; Qi, Y. Photodecomposition and Thermal Decomposition in Methylammonium Halide Lead Perovskites and Inferred Design Principles to Increase Photovoltaic Device Stability. *J. Mater. Chem. A* **2018**, *6* (20), 9604–9612. <https://doi.org/10.1039/c8ta03501f>.
- (95) Conings, B.; Drijkoningen, J.; Gauquelin, N.; Babayigit, A.; D'Haen, J.; D'Olieslaeger, L.; Ethirajan, A.; Verbeeck, J.; Manca, J.; Mosconi, E.; Angelis, F. De; Boyen, H. H.-G. Intrinsic Thermal Instability of Methylammonium Lead Trihalide Perovskite. *Adv. Energy Mater.* **2015**, *5* (15), 1500477. <https://doi.org/10.1002/aenm.201500477>.
- (96) Zhang, Y.; Zhou, Z.; Ji, F.; Li, Z.; Cui, G.; Gao, P.; Oveisi, E.; Nazeeruddin, M. K.; Pang, S. Trash into Treasure: δ-FAPbI₃ Polymorph Stabilized MAPbI₃ Perovskites with Power Conversion Efficiency beyond 21%. *Adv. Mater.* **2018**, *30* (22), 1–8. <https://doi.org/10.1002/adma.201707143>.
- (97) Jiang, Q.; Zhao, Y.; Zhang, X.; Yang, X.; Chen, Y.; Chu, Z.; Ye, Q.; Li, X.; Yin, Z.; You, J. Surface Passivation of Perovskite Film for Efficient Solar Cells. *Nat. Photonics* **2019**, *13* (7), 460–466. <https://doi.org/10.1038/s41566-019-0398-2>.
- (98) Gratia, P.; Zimmermann, I.; Schouwink, P.; Yum, J.-H.; Audinot, J.-N.; Sivula, K.; Wirtz, T.; Nazeeruddin, M. K. The Many Faces of Mixed Ion Perovskites: Unraveling and Understanding the Crystallization Process. *ACS Energy Lett.* **2017**, 2686–2693. <https://doi.org/10.1021/acsenerylett.7b00981>.
- (99) Mancini, A.; Quadrelli, P.; Amoroso, G.; Milanese, C.; Boiocchi, M.; Sironi, A.; Patrini, M.; Guizzetti, G.; Malavasi, L. Synthesis, Structural and Optical Characterization of APbX₃ (A=methylammonium, Dimethylammonium, Trimethylammonium; X=I, Br, Cl) Hybrid Organic-Inorganic Materials. *J. Solid State Chem.* **2016**, *240*, 55–60. <https://doi.org/10.1016/j.jssc.2016.05.015>.
- (100) Wang, X.; Fan, Y.; Wang, L.; Chen, C.; Li, Z.; Liu, R.; Meng, H.; Shao, Z.; Du, X.; Zhang, H.; Cui, G.; Pang, S. Perovskite Solution Aging: What Happened and How to Inhibit? *Chem* **2020**, 1–10. <https://doi.org/10.1016/j.chempr.2020.02.016>.
- (101) Guan, Y.; Xu, M.; Zhang, W.; Li, D.; Hou, X.; Hong, L.; Wang, Q.; Zhang, Z.; Mei, A.; Chen, M.; Zhou, Y.; Padture, N. P.; Hu, Y.; Rong, Y.; Han, H. In Situ Transfer of CH₃NH₃PbI₃ Single Crystals in Mesoporous Scaffolds for Efficient Perovskite Solar Cells. *Chem. Sci.* **2019**, *68* (20), 42–61. <https://doi.org/10.1039/C9SC04900B>.
- (102) Smith, J. A.; Game, O. S.; Bishop, J. E.; Spooner, E. L. K.; Kilbride, R. C.; Greenland, C.; Jayaprakash, R.; Alanazi, T. I.; Alanazi, T. I.; Cassella, E. J.; Tejada, A.; Tejada, A.; Chistiakova, G.; Wong-Stringer, M.; Routledge, T. J.; Parnell, A. J.; Hammond, D. B.; Lidzey, D. G. Rapid Scalable Processing of Tin Oxide Transport Layers for Perovskite Solar Cells. *ACS Appl. Energy Mater.* **2020**, *3* (6), 5552–5562. <https://doi.org/10.1021/acsaem.0c00525>.
- (103) Ashiotis, G.; Deschildre, A.; Nawaz, Z.; Wright, J. P.; Karkoulis, D.; Picca, F. E.; Kieffer, J. The Fast Azimuthal Integration Python Library: PyFAL. *J. Appl. Crystallogr.* **2015**, *48*, 510–519. <https://doi.org/10.1107/S1600576715004306>.
- (104) Dane, T. G. The pygix library <https://github.com/tgdane/pygix>.
- (105) Jiang, Z. GIXSGUI: A MATLAB Toolbox for Grazing-Incidence X-Ray Scattering Data Visualization and Reduction, and Indexing of Buried Three-Dimensional Periodic Nanostructured Films. *J. Appl. Crystallogr.* **2015**, *48* (3), 917–926. <https://doi.org/10.1107/S1600576715004434>.
- (106) Savikhin, V.; Steinrück, H.-G.; Liang, R.-Z.; Collins, B. A.; Oosterhout, S. D.; Beaujuge, P. M.; Toney, M. F. GIWAXS-SIRKit: Scattering Intensity, Indexing and Refraction Calculation Toolkit for Grazing-Incidence Wide-Angle X-Ray Scattering of Organic Materials. *J. Appl. Crystallogr.* **2020**, *53* (4), 1108–1129. <https://doi.org/10.1107/S1600576720005476>.
- (107) Breiby, D. W.; Bunk, O.; Andreasen, J. W.; Lemke, H. T.; Nielsen, M. M. Simulating X-Ray Diffraction of Textured Films. *J. Appl. Crystallogr.* **2008**, *41* (2), 262–271. <https://doi.org/10.1107/S0021889808001064>.
- (108) Altomare, A.; Cuocci, C.; Giovacazzo, C.; Moliterni, A.; Rizzi, R.; Corriero, N.; Falcicchio, A. EXPO2013: A Kit of Tools for Phasing Crystal Structures from Powder Data. *J. Appl. Crystallogr.* **2013**, *46* (4), 1231–1235. <https://doi.org/10.1107/S0021889813013113>.
- (109) García, A.; Gale, J. D.; Soler, J. M.; Sánchez-Portal, D.; Artacho, E.; Ordejón, P.; Junquera, J. The SIESTA Method for Ab Initio Order-N Materials Simulation. *J. Phys. Condens. Matter* **2002**, *14* (11), 2745–2779. <https://doi.org/10.1088/0953-8984/14/11/302>.
- (110) Artacho, E.; Gale, J. D.; García, A.; Junquera, J.; Martín, R. M.; Ordejón, P.; Daniel, S.-P.; Soler, J. M. SIESTA 4.0 User's Guide.
- (111) Dion, M.; Rydberg, H.; Schröder, E.; Langreth, D. C.; Lundqvist, B. I. Van Der Waals Density Functional for General Geometries. *Phys. Rev. Lett.* **2004**, *92* (24), 22–25. <https://doi.org/10.1103/PhysRevLett.92.246401>.
- (112) Cooper, V. R. Van Der Waals Density Functional: An Appropriate Exchange Functional. *Phys. Rev. B - Condens. Matter Mater. Phys.* **2010**, *81* (16), 1–4. <https://doi.org/10.1103/PhysRevB.81.161104>.
- (113) SIESTA database (pseudopotentials and basis sets) <https://departments.icmab.es/leem/siesta/> (accessed Jan 31, 2019).
- (114) Imler, G. H.; Li, X.; Xu, B.; Dobereiner, G. E.; Dai, H.-L.; Rao, Y.; Wayland, B. B. Solid State Transformation of the Crystalline Monohydrate (CH₃NH₃)PbI₃ (H₂O) to the (CH₃NH₃)PbI₃ Perovskite. *Chem. Commun.* **2015**, *51* (56), 11290–11292. <https://doi.org/10.1039/C5CC03741G>.
- (115) Fan, L. Q.; Wu, J. H. NH₄PbI₃. *Acta Crystallogr. Sect. E Struct. Reports Online* **2007**, *63* (11). <https://doi.org/10.1107/S1600536807050581>.

Chapter 7

Conclusions & Future Work

In summary, the three results chapters presented have explored complementary approaches to enable the commercialisation of perovskite solar cells and materials. In these concluding remarks, the future outlook for these methods and results will be discussed.

7.1: Scalable processing of SnO₂

7.1.1: Conclusions

In Chapter 4, spray coating and slot-die coating processes were developed for the deposition and rapid post-processing of a nanoparticle SnO₂ electron-accepting layers. This work encompassed:

- New processing routes with relevance to industry (slot-die coating and spray-coating).
- Elucidation of the changes in the structure of the SnO₂ layer during annealing.
- An investigation into unusual phenomena at the SnO₂/perovskite interface dependent on the final surface treatment of these layers.
- A rapid annealing process suitable for transfer to scalable manufacture.

The 'pre-crystallised' nanoparticle approach offers an excellent opportunity for rapidly forming metal oxide layers with appropriate energy level alignment. It was concluded that a combination of hot-air annealing and UV-ozone treatment could dramatically reduce the processing time for this layer, meeting the requirements for rapid processing.

7.1.2: Future work

Large areas - Being formed of nanoparticles, a challenge is to form a truly conformal coating completely free from shunting pathways for perfect hole-blocking over large areas. Some of our follow-on work began to address this with scale-up of all active layers by coating an n-i-p structure triple-cation architecture solar cell over a large substrate, achieving over 12% PCE for an area larger than 1 cm².¹

Passivating ligand engineering - In this system, the potassium hydroxide colloidal stabilising component was fortuitously found to be beneficial for the devices, and in future work this could be engineered further with other stabilising ligands to combine better interface passivation into a single process.

Surface treatment process time - Whilst the UVO treatment was found to be successful for preparing the interface, as noted in the chapter this process duration is incompatible with R2R. It may be possible to achieve a similar effect either with a higher power UVO treatment or more likely a well-optimised, controlled and short O₂ plasma treatment which has more widespread industrial usage at present.²

Stability - Perhaps the most critical question remaining to be addressed by the field in this area is whether perovskite/metal oxide interfaces (particularly in *n-i-p* devices) can be made stable or whether they will intrinsically introduce redox-active sites for chemical decomposition of the perovskite, particularly of the organic cation. If so, appropriate stable organic interface modifiers or organic transport layers could be investigated to mitigate these issues and enable true material stability in the harsh conditions encountered by solar modules.

7.2: Solvent vapour annealing

7.2.1: Conclusions

In Chapter 5, the effects of DMF solvent-vapour recrystallisation of MAPbI₃ was investigated in relation to the morphology and properties of thin films and their incorporation into devices. The key observations were:

- A mechanism of stoichiometric change by the solvent annealing process was proposed, whereby the SVA process results in loss of organic or organohalide species.
- Subtle changes in the initial solution stoichiometry were found to dramatically affect both the SVA process, the material surface, and the PV device stability.
- The role of grain surfaces in dictating performance and stability was made clear and this was most striking in the case of PbI₂-excess films.
- Traces of DMF were found in the form of a metastable DMF intermediate phase, despite DMF being a more weakly co-ordinating solvent than DMSO,³ and was twinned with a dramatic loss in device performance through inadvertent loss of cationic species.

The SVA process introduces a secondary reaction, altering the crystallisation, but may to a lesser extent be occurring with all glovebox processing in solvent-rich environments. Overall these results highlight the critical need for a deeper understanding of solvent-solute interactions if solution-processable perovskites are to be deployed. Chapter 5 also contained some suggestions relating to the broader understanding of how material stoichiometry affects the electronic nature of grain boundaries, which would have other effects, for instance on ion migration and recombination losses. The variability between our different stoichiometries

highlights a key problem of inter- and intra-lab reproducibility and replicability, which are discussed further in the closing remarks.

7.2.2: Future work

Processing from other solvents - The work used the simple acetonitrile:methylamine solvent system through to isolate the solvent effects during SVA. However, looking at an expanded range of processing solvents, vapours and compositions to understand potential interactions would be valuable work, for instance by categorising based on hydrogen-bonding and donor ability.⁴ The process also has a large range of process control possible through solvent vapour pressure, temperature, duration, volume of solvent and so forth.

Trace solvent contamination - To find traces of this for certain compositions in the form of a more stable DMF intermediate phase was unusual. This begs the question whether solvent contamination (or other organic species) is commonplace within crystallised films, which would present an ongoing challenge for solution processing to overcome, as these would most likely introduce localised trap states or nucleation sites for phase degradation. Future work should certainly address these questions.

Weakly coordinating solvents – If trapped solvent is found to be an issue, then understanding the co-ordination to Pb will be important. In turn, how this can be engineered to ensure complete solvent removal would be worthy of investigation.

7.3: Methylamine

7.3.1: Conclusions

In Chapter 6, the role of methylamine gas was investigated in respect to vapour recrystallisation and related solution chemistries. The main findings were:

- During methylamine healing, metastable intermediate phases exist between the solid perovskite and the solvate liquid phase, identified using synchrotron-based GIWAXS with rapid acquisition.
- The recrystallisation intermediate phase dictates the crystal orientations present in vapour-treated films, which exhibit non-uniaxial orientation, with temperature dependency.
- The strong coordinating ability of the methylamine to methylammonium as a dimer, both structurally and in solution, was demonstrated, in addition to interactions with the lead centre as a ligand.

- It was also shown that methylamine causes an irreversible reaction with formamidinium, which prevents recrystallisation of FA-rich perovskite films.

Overall chapter this elucidates in greater detail the mechanism for methylamine recrystallisation and provides new insight into methylamine-MAPbI₃ interactions. It does however point to the disappointing conclusion that the rapid methylamine healing approach will be limited to predominantly methylammonium perovskites.

7.3.2: Future work

Other gases - Future work should address the possibility of other strongly coordinating bases which could recrystallise and aid in the dissolution of the perovskite precursor components for FA-rich perovskites, without undesired reactions. FA is a weaker Brønsted acid than MA⁺, so potentially there are other non-nucleophilic bases which could co-ordinate to the lead, enabling complex formation in volatile solvents without compromising the cation. For broader utility, ideally this would not be limited to pure-iodide, pure-FA compositions, which would expand the applicability to wider and lower bandgap materials.

Solution structure - We were not able to provide a conclusive understanding of the structure of the solution in this work. This should be addressed through more extensive SAXS, NMR or other methods, to determine how the colloidal chemistry or dissolved ions exist in this system compared to other solvents.

Intermediate phases - Despite several reports of MA⁰.MAPbI₃ intermediate phases, we were unable to provide conclusive structure determination for two phases due to their metastability, lasting only seconds (compared to >10s of seconds for the identified phases). Some additional data with different experimental protocols during the acquisition of the synchrotron measurements would have vastly simplified the structural analysis, also allowing for more in-depth process understanding. These were planned to take place in April 2020 but were unfortunately postponed indefinitely due to the COVID-19 pandemic.

Texture/orientation - Further demonstration that oriented perovskite films offer enhanced carrier transport, simplified interface and grain boundary passivation/secondary phase formation, reduced bulk defects and/or improved control over the buried interface would all be highly valuable demonstrations. However, 'bincontinuous' grains between the two interfaces will likely enhance ion transport, so instead small, well-passivated grains may offer a better route to consistent performance output. Perhaps this may negate the issues of day/night cycling, current losses and photochemical surface reactions.⁵⁻⁷

7.4 Revisiting the aims of the thesis

The objectives outlined in section 1.4 are given below, with how each has been addressed in this thesis.

- *Develop new lab-scale methods for processing functional optoelectronic layers for perovskite solar cells which are suitable with the requirements for scalable manufacture and rapid processing.*

This has been achieved with extensive process development in Chapter 4. The final process was compatible with R2R manufacture, but further development is required for the surface treatment process and to transfer to a scalable process as outlined in section 7.1.2.

- *Understand the fundamental crystallisation processes occurring during these deposition processes to gain new insight and enable the rational design of future novel processing routes.*

All chapters contain some element of this, particularly Chapter 6 which contains the most novel insight.

- *Elucidate the relationship between solution chemistry and early-stages crystallisation to bridge between a chemical and materials understanding of halide perovskites.*

This has been achieved to some extent in Chapters 5 and 6, but some specific details are lacking. In particular, the solution state of perovskite precursors and the nucleation process require further work.

- *At all stages, consider the efficiency/stability/cost triangle for economically viable PSC manufacture.*

High efficiency devices have been fabricated, and generally the processes used could be low cost. Perhaps the largest ongoing cost would be in maintaining a safe, low-toxicity working environment for workers in a PSC factory. Stability was investigated in Chapter 5, but more detailed understanding on *n-i-p* device stability with metal oxides is a necessity for future researchers.

7.5: Closing remarks

The outlook for perovskite solar cells is good, with many companies in varying stages of commercialisation. In 2022, the first perovskite-silicon tandem solar module from Oxford PV is likely to enter the market. If the planned trajectories of technological development and growth continue, this tandem pairing could heavily disrupt the silicon industry. In the longer term,

undoubtedly perovskite-perovskite tandems and multijunctions offer the lowest option EPBT, but would require major advances in the wide-gap (1.8 eV) and narrow-gap (1.25 eV) perovskites. Particularly the formation and stability of mixed B-site Pb-Sn perovskites require the most attention, with very few labs able to produce high efficiency devices at present.

In the academic setting, this and other works have highlighted one of the most challenging aspects for the PSC field, in that whilst good solar cells have been fabricated in hundreds of labs globally, subtle processing changes can significantly affect the perovskite layer formation and stability. Transferring ideal processes is therefore challenging and hindered (in some cases deliberately) by improper or incomplete methods in published works, which slows progress within the field to the benefit of few. Many reports with deeper insights on material properties are also reliant on films which have been fabricated in these varied conditions, and so conclusions which have been drawn require context. Some commendable attempts have been made to standardise various aspects of characterisation, device testing, stability measurements, and reporting between laboratories.⁸⁻¹⁴ Efforts such as these will be crucial for the field to move forward at the necessary pace for perovskite companies to avoid the valley of death which has befallen other PV technologies.

In general, this research has been, and continues to be, thoroughly interesting, varied and enjoyable. It is hoped that the insights gained in the works presented will be of benefit to others in the field. More broadly, it is expected that for the highest quality crystalline films, these kinds of approaches to understand crystallisation, perovskite solution chemistry and to manage film texture will be hugely important. It is fortunate that high efficiency devices can be made with comparative ease, but the lesson from other PV technologies is one of prolonged effort to produce devices truly operating at their limits. If halide perovskite solar cells can reach this technological maturity soon enough, they will be useful in the fight against anthropogenic global warming, but undoubtedly there are significant hurdles remaining to be addressed.

Appendix A

Key poster presentations

A1 “Performance and stability of planar perovskite solar cells using SnO₂ electron transport layers.”

Perovskite Solar Cells and Optoelectronics (PSCO), Oxford, 2017.

A2 “Electron beam evaporation of tin oxide transport layers for perovskite solar cells.”

Hybrid Organic PhotoVolatics (HOPV18), Benidorm, 2018.

A3 “Understanding texture formation in methylamine-recrystallised MAPbI₃.”

NanoGE Fall Meeting, Berlin, 2019.

A4 “Solvent Vapour Annealing of Methylammonium Lead Halide Perovskite: What’s the Catch?”

HOPV20 online, 2020.

Appendix A1



Performance and stability of planar perovskite solar cells using SnO₂ electron transport layer.

Joel A. Smith¹, Michael Wong-Stringer¹, Vikas Kumar², Benjamin G. Freestone¹, Onkar S. Game¹ and David G. Lidzey¹

¹ Department of Physics and Astronomy, University of Sheffield, Sheffield, S3 7RH, UK.

² Sorby Nano Investigation Centre, Sheffield S3 7HQ, UK.

Correspondence welcomed: jasmith3@sheffield.ac.uk

Question: Can SnO₂ be a more stable alternative metal oxide electron transport layer to TiO₂?

Context

- Current highest efficiency perovskite solar cell architectures up to 22.6% utilise a dual electron transport layer (ETL) comprising of a **compact TiO₂ layer and a mesoporous TiO₂ layer** which is infiltrated and capped by perovskite [1].
- UV irradiation on TiO₂ leads to reduced photocurrent** over time and increases with lower oxygen (which we need for encapsulating from moisture) [2].
- Many major **stability studies use UV filters**, luminescent downshifting to negate this and other superoxide formation effects [3, 4].
- The field has been moving towards alternative replacement planar ETL materials such as SnO₂ for improved stability, performance and processability.

	TiO ₂	SnO ₂
Processing temperature	150-500 °C	150-180 °C
Optical bandgap (UV stability)	~3.3 eV	~3.6 eV
Electron mobility	Lower	Higher
Light transmittance	Lower	Higher

Some motivations for the increased research interest in transitioning from TiO₂ to SnO₂.

Methods

Two prominent solution-processable, planar SnO₂ ETL deposition routes have recently been developed with preparation methods detailed below.

- Tin chloride route (Anaraki et al. [5])**
- Uses CsI_{0.05}((FAPbI₃)_{0.83}(MAPbBr₃)_{0.17})_{0.95}
 - Tin(IV) chloride pentahydrate 0.05M in IPA, >30 mins stirring.
 - 30 s spin at 3000 rpm.
 - Dry for 10 mins, gradual ramp to 60 mins anneal at 150 °C.
 - Max. PCE - 19.5%
 - Best performance also needs chemical bath deposition, + 4 hours.
 - Max. PCE - 20.8%
 - 3-7 hour preparation.

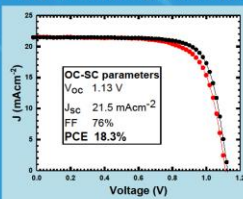
- Nanoparticle route (Jiang et al. [6])**
- Uses (FAPbI₃)_{0.83}(MAPbBr₃)_{0.17} (via 2 step deposition route).
 - 20% SnO₂ nanoparticle solution in H₂O (off the shelf product).
 - 6.5 parts DI water : 1 solution.
 - 30 s spin at 3000 rpm.
 - 30 mins baked at 150 °C.
 - Max. PCE - certified 19.9±0.06%
 - 2 hour preparation.
 - Easily compatible with scalable processing methods.

Conclusion: Nanoparticles are best, taken forward for stability work and development...

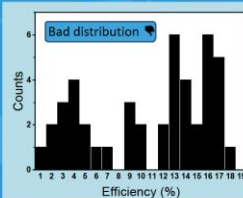
Results

Methods above transferred to our lab with perovskite (FAPbI₃)_{0.83}(MAPbBr₃)_{0.17}

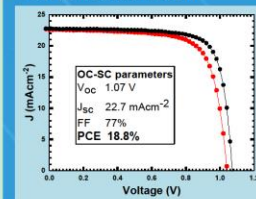
- Tin chloride route**
- High efficiencies possible but temperamental process.
 - Inconsistent device parameters, V_{oc} up to 1.17 V after aging for 28 days.



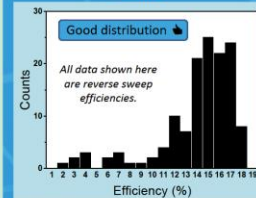
Best device run



- Nanoparticle route**
- Reliable efficiencies comparable or better than tin chloride route.
 - Lower V_{oc} than chloride route.
 - Best devices shown below.



All data



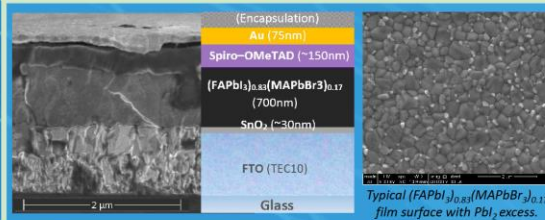
Future work

- Use a variety of deposition techniques to control SnO₂ defect density and correlate this with stability. Does a similar process to TiO₂ degradation occur?
- Develop a novel physical vapour deposition technique for SnO₂ ETL.
- Further investigate reversible & irreversible burn-in effects in the perovskite.

Objectives

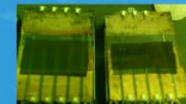
- Develop low temperature SnO₂ to match meso-TiO₂ efficiencies in our lab.
- Investigate long term stability of TiO₂ and SnO₂ (interfacial degradation).
- Understand SnO₂ driven degradation from some processing routes.

Device structure

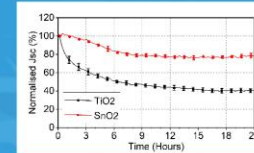
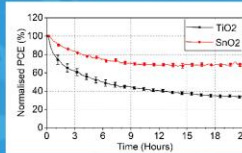


Preliminary stability

- Some devices encapsulated with 250 nm e-beam Al₂O₃ UV epoxy and glass cover.
- Aging was done in Suntest CPS+ illumination with 1500 W xenon lamp and coated quartz filters to approximate the AM1.5G solar spectrum, with low spectral mismatch in 350 - 600 nm range.
- Results show the burn in is reduced for SnO₂ devices. Recovery still to be studied.



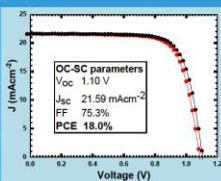
After 20 hours, TiO₂ device (left) has visibly degraded where not protected by Au, SnO₂ still optically dense.



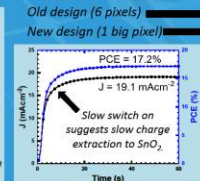
Normalised PCE and J_{sc} of un-encapsulated devices showing fast burn-in. TiO₂ is average of 4 devices and SnO₂ is average of 3 with standard deviation shown. Further work to follow.

Larger area development

- New larger area pixel design has been developed (2.6 to 16 mm²).
- FTO switched to ITO for enhanced planarity of SnO₂ layer.
- Perovskite switched to CsI_{0.05}((FAPbI₃)_{0.83}(MAPbBr₃)_{0.17})_{0.95} for stability.



Best devices show reduced hysteresis (forward & reverse sweeps closer).



Stabilised power output is close to values taken from sweep.

New data Ask me about this bit @

6x larger cell area

References

- Yang, Woon Seok, et al. "Iodide management in formamidinium-lead-halide-based perovskite layers for efficient solar cells." *Science* 356.6345 (2017): 1376-1379.
- Leijtens, Tomas, et al. "Overcoming ultraviolet light instability of sensitized TiO₂ with meso-structured organometal tri-halide perovskite solar cells." *Nature communications* 4 (2013): 2885.
- Tan, Haoren, et al. "Efficient and stable solution-processed planar perovskite solar cells via contact passivation." *Science* 355.6326 (2017): 722-726.
- Bella, Federico, et al. "Improving efficiency and stability of perovskite solar cells with photocurable fluoropolymers." *Science* (2016): aah4046.
- Anaraki, Elham Halvani, et al. "Highly efficient and stable planar perovskite solar cells by solution-processed tin oxide." *Energy & Environmental Science* 10 (2016): 3128-3134.
- Jiang, Qi, et al. "Enhanced electron extraction using SnO₂ for high-efficiency planar-structure HC (NH₂)₂PbI₃-based perovskite solar cells." *Nature Energy* 2 (2016): 16177.

Appendix A2



The University Of Sheffield.

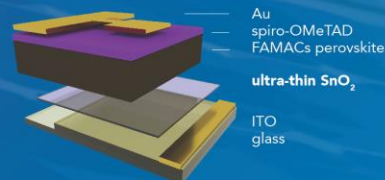
Electron beam evaporation of tin oxide transport layer for perovskite solar cells.

Joel A. Smith¹, Onkar S. Game¹, Michael Wong-Stringer¹, Claire Greenland¹, Benjamin G. Freestone, Thomas Routledge¹, David M. Coles¹ and David G. Lidzey¹.
¹ Department of Physics and Astronomy, University of Sheffield, Yorkshire, S3 7RH.

Correspondence: jasmith3@sheffield.ac.uk

Context

- Highest efficiency perovskite solar cell architectures up to 22.7% utilise a dual electron transport layer (ETL) comprising of a compact TiO₂ layer and a mesoporous TiO₂ layer which is infiltrated and capped by perovskite [1].
- UV irradiation on TiO₂ may lead to degradation over time [2], wider bandgap metal oxides such as SnO₂ may give improved transparency, stability and performance.

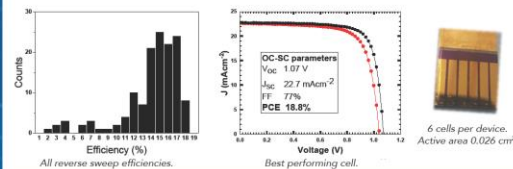


Objectives

- Develop annealed and annealing-free SnO₂ ETL deposited via electron beam evaporation.
- Understand charge transfer processes at ETL interfaces and the effect of band alignment and interface quality on this process.
- Understand the high performance, hysteresis-free behaviour of SnO₂ nanoparticle ETLs.

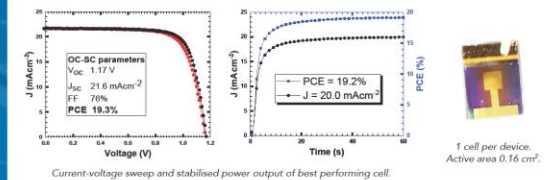
Solution processing

- SnO₂ nanoparticle ETL [3] on FTO with (FAPbI₂)_{0.83}(MAPbBr₃)_{0.17} perovskite.
- Layer doesn't perfectly cover FTO but good performance despite this.
- More reproducible results than tin chloride conversion routes to SnO₂ ETL.
- 6 cells per device, developed to larger one cell per device.



Solution processing development

- Shift to large 0.16 cm² one cell per device for improved reproducibility.
- SnO₂ nanoparticle ETL on ITO with Cs_{0.05}(FAPbI₂)_{0.83}(MAPbBr₃)_{0.17} perovskite.
- Highly reproducible 18% PCE and high device metrics.

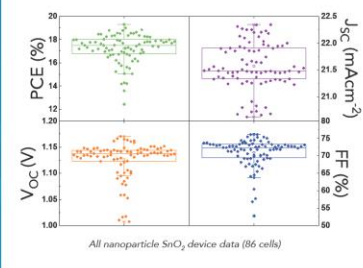
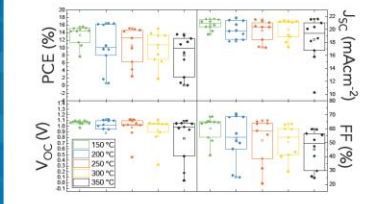


Electron-beam evaporation

- Evaporation allows for film uniformity over large areas, isn't subject to complex solution evolution, doesn't use toxic solvents, is widely used in the coatings and electronics industries and could be used as a roll-to-roll process.
- Faster than ALD or pulsed-CVD SnO₂, cheaper & more stable than C₂₀ [4, 5].
- May also allow for annealing-free transport layers if defects can be managed.

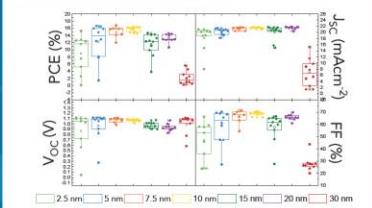
Annealing temperature optimisation

- At 350 °C we speculate indium migrates into the amorphous SnO₂ layer.



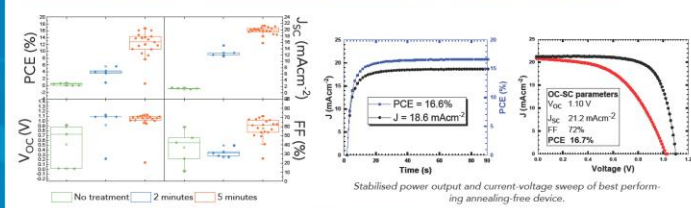
ETL thickness optimisation

- Comparable performance 5 nm - 10 nm.
- All devices annealed at 200 °C.



Annealing free

- Low temperature surface treatments required to properly managed the interface.
- Comparable efficiencies to annealed devices possible with careful interface management.



References

- [1] Yang, Woon Seok, et al. "Iodide management in formamidinium-lead-halide-based perovskite layers for efficient solar cells." *Science* 356.6345 (2017): 1376-1379.
- [2] Leijtens, Tomas, et al. "Overcoming ultraviolet light instability of sensitized TiO₂ with meso-structured organometal tri-halide perovskite solar cells." *Nature communications* 4 (2013): 2885.
- [3] Jiang, Qi, et al. "Enhanced electron extraction using SnO₂ for high-efficiency planar-structure HC (NH₂)₂PbI₃-based perovskite solar cells." *Nature Energy* 2 (2016): 16177.
- [4] Bush, Kevin A., et al. "23.6%-efficient monolithic perovskite/silicon tandem solar cells with improved stability." *Nature Energy* 2 (2017): 17009.
- [5] Avila, Jorge, et al. "Vapor-Deposited Perovskites: The Route to High-Performance Solar Cell production?." *Joule* (2017).



EPSC CENTRE FOR DOCTORAL TRAINING
 NEW AND SUSTAINABLE
 PHOTOVOLTAICS

EPSC
 Pioneering research
 and skills

Appendix A3

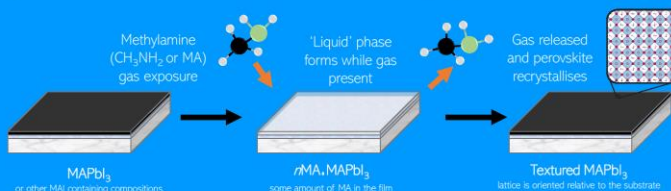


The University Of Sheffield.

Understanding texture formation in methylamine-recrystallised MAPbI₃

Joel A. Smith¹, Onkar Game¹, Natalia Martsinovich¹, Adam Shnier², Rachel Kilbride¹, Mary O'Kane¹, Marion Flatken³, Daniel Wamwangi², Andrew J. Parnell¹, David Billing², Antonio Abate³, David G. Lidzey¹

1) University of Sheffield, UK. 2) University of the Witwatersrand, SA. 3) Helmholtz Zentrum Berlin, DE.



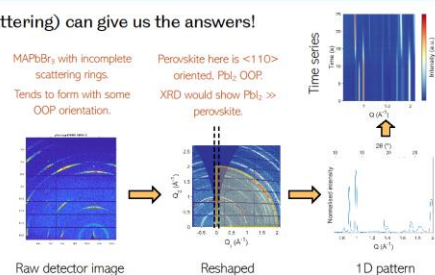
What is methylamine recrystallisation?

- When exposed to MA vapour, MAPbI₃ rapidly converts to transparent phase.
- Upon vapour removal, MAPbI₃ recrystallises with preferential orientation.¹
- Interpreted as 'uniaxial' orientation, lattice uniformly aligned out-of-plane.²
- Orientation of perovskite grains may benefit photovoltaic performance.^{2,4}
- Understanding the MA/MA⁺ interaction and phase behaviour may enable process development for new gases or perovskite compositions.³

How does this process work? *In situ* GIWAXS (grazing incidence wide-angle X-ray scattering) can give us the answers!

Interpreting GIWAXS data

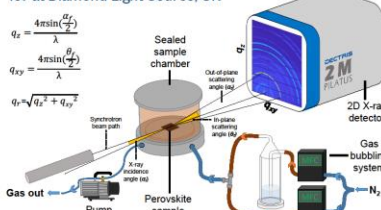
- 2D scattering patterns are collected from samples, like GI-XRD but capturing scatter in all directions.
- Peaks as would appear in powder XRD appear as Debye-Scherrer rings on the 2D X-ray detector.
- Films with isotropic (no preferred) orientation appear as semicircles of all scatter above the sample horizon.
- In samples showing some orientation, complete rings become diffuse, partial or incomplete rings (see MAPbBr₃).
- In strongly oriented or textured samples, scatter appears as Bragg spots, single peaks in the diffraction ring.
- XRD captures only out-of-plane (OOP) scatter, which can lead to misinterpretation in oriented samples, such as directly comparing PbI₂ and perovskite peak intensities to determine the ratio of phases present.



Experiment

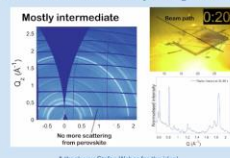
- Using a controlled sample environment, perovskite films were exposed to a flow of MA to understand the interaction between the gas and film.
- Afterwards, flow was switched to N₂ and a mild vacuum applied to remove MA from the chamber.
- We collected 2D scattering patterns with 0.1s time resolution during these liquification and crystallisation processes to understand the phase conversion mechanism and structures in the film.

107 at Diamond Light Source, UK

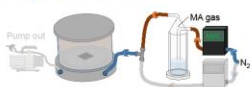


No screen?

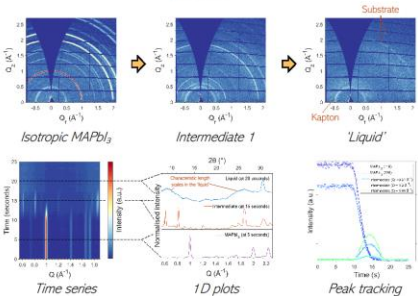
Watch the video - bit.ly/Magashealing



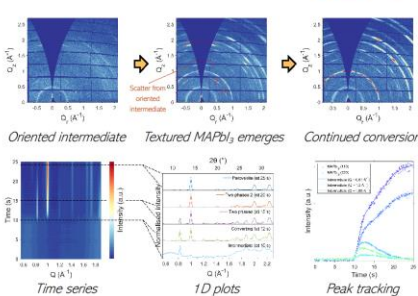
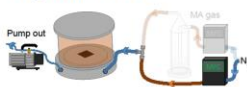
Liquification



- Metastable intermediate phases lasting only seconds as methylamine rapidly intercalates into or leaves the lattice.
- Orientation of the crystallisation intermediate governs the conversion process on into textured MAPbI₃.

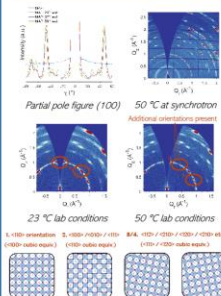


Crystallisation



Orientation

Multiple orientations present in the (100) diffraction ring. At 50 °C more orientations emerge, with increased constraint - less diffuse scatter.



Conclusions

- Methylamine liquification and recrystallization proceeds via metastable iodoplumbate crystalline phases, which are oriented and when recrystallising leads to textured MAPbI₃.
- Strong interaction between MA and MA⁺ forms a stable pseudo-cation in these structures, which is favourable with sufficient vapour pressure, ongoing work to understand the liquid.
- Methylamine-healed perovskite orientation more complex than just out-of-plane <110> texture, and has temperature-dependent degree of orientation, intermediate behaviour also affected by temperature.
- This complexity in texture is not revealed with XRD, and demonstrates the importance of 2D X-ray scattering in fully understanding structure in highly oriented systems.



1. Zhou, Z. et al. "Methylamine-Gas-Induced Defect-Healing Behavior of CH₃NH₂/PbI₂ Thin Films for Perovskite Solar Cells." *Angew. Chem. Int. Ed.* 54, 9705–9709 (2015).
2. Kim, D. H. et al. "300% Enhancement of Carrier Mobility in Uniaxially Oriented Perovskite Films Formed by Topotactic-Oriented Attachment." *Adv. Mater.* 29, 3–8 (2017).
3. Dou, B. et al. "Roll-to-Roll Printing of Perovskite Solar Cells." *ACS Energy Lett.* 3, 2558–2565 (2018).
4. Muscarella, L.A., et al. "Crystal orientation and grain size: do they determine optoelectronic properties of MAPbI₃ perovskite?" *The Journal of Physical Chemistry Letters* (2019).
5. Zhou, Y. et al. "Microstructures of organometal trihalide perovskites for solar cells: their evolution from solutions and characterization." *The Journal of Physical Chemistry Letters*, 4827–4839 (2015).

Appendix A4



Solvent Vapour Annealing of Methylammonium Lead Halide Perovskite: What's the catch?

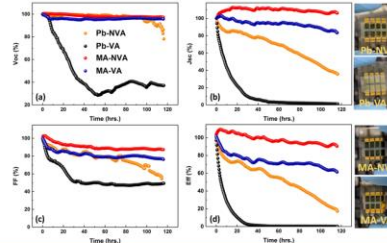
Onkar S. Game^a, Joel A. Smith^a, Tarek I. Alanazi^a, Michael Wong-Stringer^a, Vikas Kumar^b, Cornelia Rodenburg^b, Nick J. Terrill^c and David G. Lidzey^{a*}
 a) Department of Physics and b) Department of Material Science and Engineering, University of Sheffield, UK. c) Diamond Light Source, Harwell Campus, Oxford, UK.

Solvent vapour annealing (SVA) is a widely used post-processing treatment for grain growth of halide perovskites, with higher initial device performance possible. But are there downsides?

Key Results

- In our previous work, we found that SVA with DMF can increase initial device performance, but greatly worsens stability (untreated, encapsulated MAPbI₃ achieved 1500 hours T₉₀ lifetime with ISOS L-1 bias protocol).²
- We have now elucidated the mechanism using conducting AFM, SEM and a range of scattering techniques across different MAPbI₃ stoichiometries from acetonitrile/methylamine solvent.¹
- SVA treatment leads to a loss of organic species, leading to photo-inactive regions in the film, with PbI₂ excess ("Pb-VA") being particularly vulnerable and showing the worst stability.
- In the Pb-VA case, we find that a metastable solvent intermediate phase, which mediates the grain growth, persists even after annealing and leads to the loss of stability.

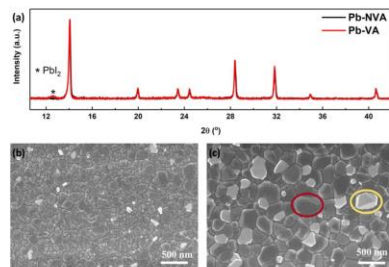
For more information: bit.ly/SolventAnnealing¹ and bit.ly/EncapsulatedMAPI²



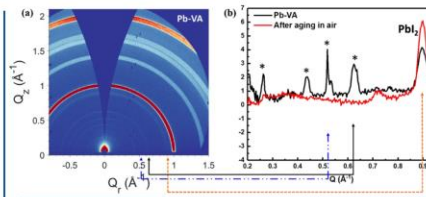
Device Instability

- a) V_{OC}, b) J_{sc}, c) FF and d) PCE for 4 compositions.
- Devices encapsulated with 150 nm SiO₂.¹
 - Stability: MA-NVA > MA-VA > Pb-NVA > Pb-VA
 - SVA is worse for stability regardless.
 - PbI₂-excess stoich. worse than MAI-excess.
 - Bad hysteresis for PbI₂-excess, worse after SVA.

	Vapour annealed (VA)	Non-VA(NVA)
PbI ₂ -excess	Pb-VA	Pb-NVA
MAI-excess	MA-VA	MA-NVA



- a) XRD and SEM of b) Pb-NVA and c) Pb-VA.
- Significant increase of apparent grain size in SEM.
 - Bright PbI₂-rich regions (yellow) correlate with photo-inactivity, and increase of PbI₂ in XRD after SVA treatment.

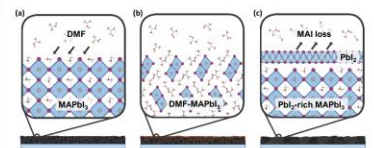


a) GIWAXS and b) azimuthal integrated linecut for Pb-VA.

- In treated films, solvent intermediate phase* present (even after further annealing) and leaving in glovebox for 24 H.
- Disappears after 24 H in air, or more gradually when encapsulated.
- In other stoichiometries this phase is less stable, so not observed.

References

- Game, Onkar S., Joel A. Smith, Tarek I. Alanazi, Michael Wong-Stringer, Vikas Kumar, Cornelia Rodenburg, Nick J. Terrill, and David George Lidzey. "Solvent Vapour Annealing of Methylammonium Lead Halide Perovskite: What's the catch?" *Journal of Materials Chemistry A* (2020).
- Wong-Stringer, Michael, Onkar S. Game, Joel A. Smith, Thomas J. Randle, Babbar A. Alqanashy, Benjamin G. Frenstone, Andrew J. Parrell, Naamun Sooran, Vikas Kumar, Miguel O. S. Hamed, Ahmed Inag, Cornelia Rodenburg, David G. Lidzey. "High-Performance Multilayer Encapsulation for Perovskite Photovoltaics." *Advanced Energy Materials* 8, no. 24 (2018): 1801234.



The Mechanism

- Film is annealed, then DMF vapour is added under a petri dish and rapidly intercalates into the film.
- '1D' iodoplumbate structure mediates crystal growth.
- As solvent is removed from the film, some organic species are liberated in the process, leading to a more PbI₂-rich MAPbI₃ film. This has a disorganised, highly-defective top surface which nucleates degradation.



Appendix B

Available solar energy

The oft-quoted adage that 1 hour of sunlight hitting the Earth's surface contains enough energy to power all of human civilisation for a year is elegant in its simplicity, but does not consider the practicalities of collecting this energy. To gain a more realistic estimate for the actual recoverable solar energy, a simple calculation was made using data from the World Bank, Solargis and ESMAP released as the Global Solar Atlas.* From this database, data for each country was taken:

- **Evaluated area** – the total area of the country which could be evaluated in the analysis, equal to the total area of the country for most countries.
- **Percentage level 1 area** – the proportion of the evaluated area suitable for solar power plants which excludes “areas due to physical/technical constraints, such as rugged terrain, presence of urbanized/industrial areas, forests and areas that are too distant from the centres of human activity”.
- **Average practical potential (daily)** - photovoltaic power potential for Level 1 areas, which is the total expected energy generation for a given installed utility-scale capacity (specific yield) factoring in “the theoretical potential, the air temperature affecting the system performance, the system configuration, shading and soiling, and topographic and land-use constraints”.

From this, the Level 1 area and annual specific yield for each country were calculated. Next, considering modules over the level 1 area with a density of 200 Wp/m², the total expected annual yield was computed. The table of calculated values for each country using this method is shown below.

* *ESMAP Global Solar Atlas*; World Bank, Washington, DC: Washinton DC, 2020. <https://doi.org/10.1596/34102>. Also accessible at www.globalsolaratlas.info.

Country	Evaluated area (km ²)	Percentage Level 1 area	Level 1 area (km ²)	Annual specific yield (kWh/kWp/yr)	Annual yield (kWh/m ² /yr)	Total recoverable energy (TWh/yr)
Aruba (Neth.)	180	85%	152.6	1812.1	362.4	55.3
Afghanistan	652860	59%	383457.4	1830.8	366.2	140407.0
Angola	1246700	75%	937310.6	1700.4	340.1	318758.5
Albania	27400	61%	16847.1	1475.5	295.1	4971.7
Andorra	470	11%	52.2	1532.6	306.5	16.0
United Arab Emirates	71020	59%	42144.8	1826.6	365.3	15396.1
Argentina	2475393	66%	1623920.3	1678.7	335.7	545217.6
Armenia	28470	69%	19776.9	1498.8	299.8	5928.3
American Samoa (U.S.)	200	27%	54.9	1453.6	290.7	16.0
Antigua and Barbuda	440	91%	402.4	1740.9	348.2	140.1
Australia	7692020	23%	1763504.1	1718.1	343.6	605972.3
Austria	82523	43%	35254.7	1188.8	237.8	8382.5
Azerbaijan	82670	82%	68063.4	1393.5	278.7	18968.7
Burundi	25680	82%	20995.0	1522.9	304.6	6394.6
Belgium	30280	79%	23788.7	1064.5	212.9	5064.5
Benin	112760	99%	111427.2	1532.2	306.4	34145.7
Burkina Faso	273600	98%	267036.3	1668.1	333.6	89087.9
Bangladesh	130170	92%	120152.1	1416.4	283.3	34037.1
Bulgaria	108560	76%	82390.2	1351.5	270.3	22270.4
Bahrain	778	76%	591.4	1777.0	355.4	210.2
The Bahamas	10010	69%	6899.5	1660.1	332.0	2290.7
Bosnia and Herzegovina	51200	62%	31906.3	1302.9	260.6	8314.4
Belarus	202988	74%	149428.8	1076.2	215.2	32163.1
Belize	22810	42%	9610.8	1524.5	304.9	2930.4
Bermuda (U.K.)	54	99%	53.3	1527.1	305.4	16.3
Bolivia	1083300	35%	380239.6	1803.9	360.8	137180.3
Brazil	8358140	54%	4501464.0	1607.5	321.5	1447250.4
Barbados	430	81%	347.6	1721.0	344.2	119.7
Brunei Darussalam	5270	12%	633.4	1423.8	284.8	180.4
Bhutan	38144	4%	1685.3	1429.3	285.9	481.7
Botswana	566730	47%	268783.3	1864.0	372.8	100203.4
Central African Republic	622980	57%	357026.1	1630.3	326.1	116412.6
Canada	5785872	22%	1252512.6	1392.7	278.5	348864.2
Switzerland	39516	39%	15464.3	1227.8	245.6	3797.5
Chile	536574	48%	256538.9	1958.1	391.6	100466.6
China	9388210	51%	4755994.2	1417.1	283.4	1347955.8
Côte d'Ivoire	318000	98%	311393.2	1460.0	292.0	90924.5
Cameroon	472710	68%	319253.8	1561.1	312.2	99680.1
Democratic Republic of Congo	2267050	47%	1065053.3	1553.3	310.7	330868.2

Congo	341500	37%	127425.9	1374.9	275.0	35040.0
Colombia	1109500	32%	358690.8	1478.0	295.6	106026.0
Comoros	1861	45%	830.5	1564.2	312.8	259.8
Cabo Verde	4030	71%	2854.1	1709.0	341.8	975.6
Costa Rica	51060	48%	24314.6	1493.9	298.8	7264.9
Cuba	104020	74%	76802.0	1657.4	331.5	25458.8
Curaçao (Neth.)	444	97%	432.1	1764.1	352.8	152.4
Cayman Islands (U.K.)	240	65%	156.1	1689.0	337.8	52.7
Cyprus	9240	88%	8159.4	1714.9	343.0	2798.5
Czech Republic	77220	75%	57928.2	1112.6	222.5	12889.7
Germany	349360	73%	256550.0	1080.7	216.1	55450.3
Djibouti	23180	93%	21460.5	1751.0	350.2	7515.4
Dominica	750	46%	343.5	1449.1	289.8	99.6
Denmark	41990	90%	37916.6	1037.8	207.6	7870.3
Dominican Republic	48310	61%	29417.1	1668.0	333.6	9813.4
Algeria	2381740	23%	552392.9	1794.6	358.9	198264.4
Ecuador	248360	35%	85921.0	1241.5	248.3	21335.0
Arab Republic of Egypt	995450	24%	242933.8	1915.0	383.0	93045.9
Eritrea	101000	72%	72291.9	1786.6	357.3	25831.4
Spain	499564	85%	427094.4	1610.6	322.1	137578.7
Estonia	43470	63%	27443.7	1035.5	207.1	5683.4
Ethiopia	1000000	83%	831563.1	1713.8	342.8	285030.0
Fiji	18270	27%	4856.7	1392.5	278.5	1352.6
France	547557	81%	443495.3	1235.9	247.2	109625.5
Federated States of Micronesia	700	23%	160.6	1419.1	283.8	45.6
Gabon	257670	44%	113183.8	1314.9	263.0	29764.5
United Kingdom	241930	85%	205932.1	953.6	190.7	39276.8
Georgia	69490	47%	32463.5	1353.6	270.7	8788.3
Ghana	227540	96%	218446.1	1467.4	293.5	64110.0
Guinea	245720	95%	233319.1	1619.7	323.9	75579.1
The Gambia	10120	97%	9803.1	1667.7	333.5	3269.7
Guinea-Bissau	28120	96%	27066.6	1627.0	325.4	8807.6
Equatorial Guinea	28050	69%	19318.1	1338.5	267.7	5171.4
Greece	128900	71%	91946.8	1512.2	302.4	27808.3
Grenada	340	50%	170.0	1624.9	325.0	55.2
Guatemala	107160	53%	56529.7	1600.7	320.1	18097.5
Guam (U.S.)	540	82%	444.9	1654.2	330.8	147.2
Guyana	196850	14%	28041.3	1531.5	306.3	8589.1
Hong Kong, SAR	1050	40%	424.8	1194.2	238.8	101.5
Honduras	111890	54%	60871.3	1556.0	311.2	18942.6
Croatia	55960	73%	40671.1	1325.2	265.0	10779.2
Haiti	27560	71%	19617.4	1707.0	341.4	6697.2
Hungary	90530	88%	79879.8	1255.7	251.1	20060.6
Indonesia	1811570	33%	591463.1	1375.1	275.0	162664.3
Isle of Man (U.K.)	570	84%	479.8	1008.8	201.8	96.8

India	2973190	87%	2598214.6	1577.5	315.5	819752.3
Ireland	68890	85%	58864.1	917.1	183.4	10796.8
Islamic Republic of Iran	1628760	73%	1182154.1	1794.3	358.9	424228.7
Iraq	434128	59%	254599.3	1707.6	341.5	86949.7
Israel	21640	93%	20070.2	1852.8	370.6	7437.4
Italy	294140	70%	206583.9	1457.6	291.5	60221.5
Jamaica	10830	41%	4447.7	1600.8	320.2	1424.0
Jordan	88780	52%	46497.5	1940.0	388.0	18040.8
Japan	364560	35%	127798.2	1257.6	251.5	32144.9
Kazakhstan	2699700	58%	1575528.9	1345.0	269.0	423825.2
Kenya	569140	82%	467425.2	1644.0	328.8	153692.5
Kyrgyz Republic	191800	37%	70757.6	1501.9	300.4	21254.7
Cambodia	176520	77%	136326.7	1505.6	301.1	41051.4
Kiribati	810	66%	532.9	1760.4	352.1	187.6
Saint Kitts and Nevis	260	60%	155.7	1695.6	339.1	52.8
Republic of Korea	97489	54%	52747.7	1392.9	278.6	14695.0
Kuwait	17820	83%	14843.4	1757.7	351.5	5217.9
Lao People's Democratic Republic	230800	36%	84209.9	1412.9	282.6	23795.7
Lebanon	10230	77%	7915.0	1763.5	352.7	2791.6
Liberia	96320	93%	89526.0	1417.4	283.5	25378.9
Libya	1759540	16%	281968.2	1870.4	374.1	105476.9
Saint Lucia	610	34%	210.3	1650.7	330.1	69.4
Liechtenstein	160	36%	58.3	1184.6	236.9	13.8
Sri Lanka	62710	73%	45877.8	1537.3	307.5	14105.7
Lesotho	30360	64%	19416.0	1874.2	374.8	7278.0
Lithuania	62642	81%	50868.2	1047.7	209.5	10658.9
Luxembourg	2430	81%	1957.2	1075.9	215.2	421.2
Latvia	62180	71%	44239.0	1041.4	208.3	9213.9
Macau, SAR	30	83%	24.8	1242.5	248.5	6.2
Morocco	446300	81%	362260.2	1827.4	365.5	132396.9
Moldova	32890	96%	31531.7	1259.0	251.8	7939.6
Madagascar	581800	77%	446115.9	1736.6	347.3	154948.0
Maldives	300	52%	155.6	1621.3	324.3	50.4
Mexico	1943950	69%	1335134.7	1797.3	359.5	479926.6
Marshall Islands	180	19%	34.4	1546.9	309.4	10.6
North Macedonia	25220	68%	17141.0	1416.7	283.3	4856.8
Mali	1220190	40%	490899.1	1706.8	341.4	167578.2
Malta	320	69%	222.2	1665.1	333.0	74.0
Myanmar	653080	52%	338175.8	1511.6	302.3	102238.0
Montenegro	13450	61%	8168.6	1393.4	278.7	2276.3
Mongolia	1553560	49%	754766.7	1736.4	347.3	262117.6
Northern Mariana Islands (U.S.)	460	27%	125.5	1698.9	339.8	42.7
Mozambique	786380	85%	668933.6	1618.8	323.8	216570.6
Mauritania	1030700	25%	254420.5	1733.4	346.7	88203.6
Mauritius	2030	76%	1536.5	1538.4	307.7	472.7

Malawi	94280	93%	87229.1	1679.2	335.8	29295.4
Malaysia	328550	26%	83896.2	1365.1	273.0	22904.7
Namibia	823290	73%	600760.0	1963.4	392.7	235903.0
New Caledonia (Fr.)	18280	46%	8319.8	1451.4	290.3	2415.1
Niger	1266700	30%	384579.3	1765.5	353.1	135795.4
Nigeria	910770	97%	887159.2	1568.7	313.7	278330.3
Nicaragua	120340	69%	83204.5	1499.6	299.9	24954.7
Netherlands	33690	82%	27699.6	1045.6	209.1	5792.6
Norway	54569	55%	29973.6	1007.8	201.6	6041.7
Nepal	143350	28%	39762.6	1458.5	291.7	11599.1
Nauru	20	100%	20.0	1697.6	339.5	6.8
New Zealand	263310	42%	109569.6	1342.3	268.5	29414.0
Oman	309500	45%	138387.4	1886.4	377.3	52211.6
Pakistan	770880	72%	556341.5	1720.1	344.0	191392.5
Panama	74340	48%	35984.5	1447.4	289.5	10416.8
Peru	1280000	25%	322163.7	1788.9	357.8	115261.5
Philippines	298170	46%	136526.4	1435.3	287.1	39192.0
Palau	460	22%	100.4	1461.8	292.4	29.4
Papua New Guinea	452860	18%	81425.6	1347.5	269.5	21944.9
Poland	306190	76%	234184.5	1089.3	217.9	51019.7
Puerto Rico (U.S.)	8870	66%	5842.3	1604.7	320.9	1875.0
D. P. R. of Korea	120410	53%	64084.5	1429.3	285.9	18318.8
Portugal	91606	92%	83994.3	1575.2	315.0	26460.8
Paraguay	397300	54%	215303.6	1562.7	312.5	67291.5
West Bank and Gaza	6020	90%	5408.2	1801.2	360.2	1948.2
French Polynesia (Fr.)	3660	10%	381.8	1603.8	320.8	122.5
Qatar	11610	90%	10411.9	1794.9	359.0	3737.6
Romania	230080	76%	174108.2	1286.1	257.2	44784.6
Russian Federation	8019565	45%	3595857.9	1224.6	244.9	880732.0
Rwanda	24670	78%	19215.1	1497.3	299.5	5754.0
Saudi Arabia	2149690	38%	827210.1	1883.0	376.6	311521.0
Sudan	1886068	46%	876030.0	1804.3	360.9	316118.6
Senegal	192530	83%	158961.8	1673.0	334.6	53187.9
Singapore	709	49%	345.0	1296.2	259.2	89.4
Solomon Islands	27990	8%	2205.2	1346.6	269.3	593.9
Sierra Leone	72180	97%	69921.1	1491.5	298.3	20857.0
El Salvador	20720	81%	16758.4	1761.9	352.4	5905.4
San Marino	60	86%	51.6	1372.2	274.4	14.2
Somalia	627340	90%	562596.7	1738.0	347.6	195560.9
Serbia	87460	84%	73705.2	1284.9	257.0	18940.9
South Sudan	619745	65%	400225.4	1626.8	325.4	130214.8
São Tomé and Príncipe	960	20%	189.8	1265.9	253.2	48.1
Suriname	156000	6%	9670.7	1558.2	311.6	3013.8
Slovakia	48080	59%	28589.6	1191.9	238.4	6815.2
Slovenia	20142	47%	9490.6	1253.6	250.7	2379.5

Sweden	142950	48%	68975.9	1035.6	207.1	14286.5
Eswatini	17200	92%	15776.3	1576.3	315.3	4973.6
Sint Maarten (Neth.)	34	69%	23.5	1776.9	355.4	8.3
Seychelles	460	20%	90.7	1586.9	317.4	28.8
Syrian Arab Republic	183630	79%	145121.8	1771.8	354.4	51424.9
Turks and Caicos Islands (U.K.)	950	85%	809.5	1723.6	344.7	279.0
Chad	1259200	46%	573512.3	1765.7	353.1	202524.5
Togo	54390	98%	53318.8	1505.4	301.1	16052.9
Thailand	510890	75%	384613.1	1483.6	296.7	114120.8
Tajikistan	138790	36%	49924.4	1584.3	316.9	15819.2
Turkmenistan	469930	36%	170996.2	1594.2	318.8	54522.0
Timor-Leste	14870	63%	9347.0	1583.8	316.8	2960.7
Tonga	720	41%	291.8	1462.8	292.6	85.4
Trinidad and Tobago	5130	39%	1977.7	1587.4	317.5	627.9
Tunisia	155360	76%	117697.8	1731.7	346.3	40764.5
Turkey	769630	79%	606414.3	1578.0	315.6	191380.5
Tuvalu	30	94%	28.1	1557.4	311.5	8.7
Tanzania	885800	81%	715230.3	1644.9	329.0	235303.0
Uganda	200520	82%	163636.3	1628.5	325.7	53295.8
Ukraine	579290	89%	518118.2	1203.1	240.6	124670.9
Uruguay	175020	95%	166687.3	1571.1	314.2	52375.5
United States of America	8039753	66%	5332699.7	1590.8	318.2	1696668.8
Uzbekistan	425400	48%	205932.2	1558.1	311.6	64173.1
Saint Vincent and the Grenadines	390	50%	195.0	1559.6	311.9	60.8
R. B. de Venezuela	882050	46%	405360.0	1589.4	317.9	128855.2
British Virgin Islands (U.K.)	150	53%	80.1	1772.0	354.4	28.4
United States Virgin Islands (U.S.)	350	62%	216.9	1733.9	346.8	75.2
Vietnam	310070	59%	183536.8	1297.4	259.5	47622.5
Vanuatu	12190	10%	1200.1	1288.6	257.7	309.3
Samoa	2830	9%	254.4	1479.3	295.9	75.3
Kosovo	10887	79%	8602.4	1349.0	269.8	2320.9
Republic of Yemen	527970	52%	272003.0	1903.0	380.6	103524.4
South Africa	1213090	84%	1021998.0	1826.3	365.3	373297.8
Zambia	743390	80%	598308.3	1762.3	352.5	210874.6
Zimbabwe	386850	95%	366379.7	1774.3	354.9	130013.6
Totals	115192995		60093763		Total:	18937314.0
						2161.8 TWy